

Immunological Role of Megakaryocytes and Platelets during Influenza A Virus Infection • A Compact Negative Group Delay Microstrip Diplexer with Low Losses for 5G Applications • Screening of Aflatoxin Production by *Aspergillus flavus* Isolates from Petroleum-contaminated Soil • Audio Encryption Framework Using the Laplace Transformation • Particle-Particle Collective Excitations of Sn isotopes • Blackberry (*Rubus fruticosus* L.) Fruit Extract Phytochemical Profile, Antioxidant Properties, Column Chromatographic Fractionation, and High-performance Liquid Chromatography Analysis of Phenolic Compounds • Radon Activity Concentration Measurements in the Water Collected from the Lower Zab River in the Kurdistan Region of Iraq • Natural Dye of Beetroot • Traffic Circulation Efficiency of Elliptical Roundabouts • Investigating and Studying the Modifications of Nano and Micro-sized Amorphous Materials Under the Influence of a High Energy Radiation • Evaluation of Radioactivity in Soil Sample from Al-Hadbaa Cement Plant in Nineveh Governorate, Iraq • Manufacturing and Evaluating of Indirect Solar Dryers • Design and Study of a Nanocavity-based One-dimensional Photonic Crystal for Potential Applications in Refractive Index Sensing • Enhancing Upper Limb Prosthetic Control in Amputees Using Non-invasive EEG and EMG Signals with Machine Learning Techniques • Investigating the Role of Metoclopramide and Hyoscine-N-Butyl Bromide in Colon Motility • The Local Anesthetic Activity of *Lavandula angustifolia* and *Eugenia caryophyllata* Essential Oils • Size Reduction and Harmonics Suppression in Microwave Power Dividers • Real-time Traffic Monitoring System Based on Deep Learning and YOLOv8 • Atherogenic Index of Plasma in the Three Trimesters of Pregnancy • Peperites • Effect of Waste Glass on Properties of Treated Problematic Soils • Magnetic and Electrical Properties of Electrodeposited Nickel Films • An Ultra-wideband Low-power Low-noise Amplifier Linearized by Adjusted Derivative Superposition and Feedback Techniques.



## **ARO-The Scientific Journal of Koya University**

ARO, meaning "Today" in Hewramí Kurdish, is an esteemed international scientific journal proudly published by Koya University with the following identifiers: p-ISSN: 2410-9355, e-ISSN: 2307-549X, and DOI: 10.14500/2307-549X. As a reputable open-access peer-reviewed journal, ARO is dedicated to publishing original scientific research, global news, and insightful commentary. Recognized for its impact in the academic community, ARO Journal has been awarded an Impact Factor by WoS-ESCI and covers diverse areas of Multidisciplinary Sciences, welcoming both original research articles and review articles. Notably, ARO Journal is committed to providing free access to its content and proudly boasts the absence of both APC (Article Processing Charges) and ASC (Article Submission Charges) fees.



### **ARO Executive Publisher**

Dr. Mohammed H. Zangana; President of Koya University and the Executive Publisher of ARO.

### **ARO Editor-in-Chief**

Dr. Dilan Majid Rostam is the Editor-in-Chief and member of the member Senior Executive Editorial Board.

### **ARO Editorial Board**

ARO takes pride in its robust and dedicated Editorial Board, comprising a distinguished twelve-member Senior Executive Editorial Board and a dynamic six-member Associate Editorial Board, both instrumental in shaping journal policies and ensuring editorial excellence. Additionally, ARO benefits from a highly esteemed Board of Reviewing Editors, consisting of over 250 prominent scientists from diverse fields. Their invaluable expertise and rigorous peer-review process contribute to the high standards and credibility of ARO, making it a leading platform for disseminating original scientific research, global news, and insightful commentary. The ARO editorial group consists of.

### **Senior Executive Editors**

Dilan M. Rostam, Salah I. Yahya, Basim M. Fadhil, Fahmi F. Muhammad, Wali M. Hamad, Jorge Correia, Fouad Mohammed, Jacek Binda, Nadhir Al-Ansari, Howri Mansurbeg, Tara F. Tahir and Yazan A. Khaleel.

### **Associate Editors**

Hamed M. Jassim, Ikbal M.G. Tahir, Saddon T. Ahmad, Sahar B. Mahmood and Layth I. Abd Ali and Mohammad Gh. Faraj.

### **This Issue Reviewers**

Abdulbasit Al-Talabani, Abubaker Hamad, Adeeb Jafir, Ali Abojassim, Ali Almehemdi, Areej Hussein, Asaad Ismail, Bestoon Mustafa, Bushra Oleiwi, Dalal Sinjare, Ali Mohammed, Dizar Ghafoor, Ehsan Nazemi, Fahmi Muhammadsharif, Farhad Ahmadnejad, Farzin Shama, Ganesh Loganathan, Ghassan Qasmarogy, Gulzar Ibrahim, Hamed Abbasi, Hanaa Muhammad, Hassan Bayram, Hayder Issa, Hazim Alhiti, Hersh Khizir, Hijran Jabbar, Hiwa Fatah, Ismail Mohammed, Javed Ahamad, Kawis Faraj, Kharman Faraj, Laith Najam, Layth Abd Ali, Maher Ali, Mohammad Zarei, Mohammad Faraj, Mohammed Mohammed Sabri, Mustafa Omar, Nabaz Hama-aziz, Nabeel Fattah, Nabil Fakhre, Nasreen Hussein, Navtej Ghumman, Omed Abdullah, Raja Parabathina, Safa Hameed, Salah Yahya, Saman Abdullah, Saman Mawlud, Saravana Mohan, Shaker Qaidi, Simko Ramadan, Sobhan Roshani. Sohrab Majidifar, Subasini Uthirapathy, Tariq Abbas, Yazan Khaleel and Zakariya Hussein

**ARO Editorial Web and New Media:** Dilan M. Rostam and Salah I. Yahya

**Managing Editor:** Salah I. Yahya

**Secretarial Office of the Journal:** Haneen H. Falah

**Journal Cover Designer:** Othman K. Ibrahim

ARO is a distinguished online open access scientific journal that releases hardcopies biannually. All published articles are freely accessible online under the Creative Commons Attribution License (CC-BY-NC-SA 4.0). It is important to note that the responsibility for the content lies solely with the authors and not with ARO or Koya University.

### **ARO the Scientific Journal Office**

Koya University, University Park  
Danielle Mitterrand Boulevard, Koya KOY45  
Kurdistan Region - F.R. Iraq

**E-mail:** aro.journal@koyauniversity.org

**url:** aro.koyauniversity.org

December 2023

# ARO

The Scientific Journal of Koya University

Vol XI, No 2(2023)

## Contents

<b>Aro Editorial Words</b> .....	iii
<b>Fryad M. Rahman</b> .....	1
Immunological Role of Megakaryocytes and Platelets during Influenza A Virus Infection	
<b>Leila Nouri, Salah I. Yahya, Abbas Rezaei, Fawwaz A. Hazzazi, Binh N. Nhu</b> .....	17
A Compact Negative Group Delay Microstrip Diplexer with Low Losses for 5G Applications: Design and Analysis	
<b>Sawan M. Mirkhan, Taha J. Omar</b> .....	25
Screening of Aflatoxin Production by <i>Aspergillus flavus</i> Isolates from Petroleum-contaminated Soil	
<b>Mardan A. Pirdawood, Shadman R. Kareem, Dashne Ch. Zahir</b> .....	31
Audio Encryption Framework Using the Laplace Transformation	
<b>Ali H. Taqi, Fahema A. Saber</b> .....	38
Particle-Particle Collective Excitations of Sn isotopes	
<b>Aryan F. Qader, Mehmet Yaman</b> .....	43
Blackberry ( <i>Rubus fruticosus</i> L.) Fruit Extract Phytochemical Profile, Antioxidant Properties, Column Chromatographic Fractionation, and High-performance Liquid Chromatography Analysis of Phenolic Compounds	
<b>Jahfer M. Smail, Hiwa H. Azeez, Habeeb H. Mansour, Saddon T. Ahmad</b> .....	51
Radon Activity Concentration Measurements in the Water Collected from the Lower Zab River in the Kurdistan Region of Iraq	
<b>Tara F. Tahir, Kurdistan F. Aziz, Dashne M. Kokhasmail</b> .....	59
Natural Dye of Beetroot: An Agent for Spectrophotometric Determination of Atenolol in the Pharmaceutical Formulations	
<b>Hardi S. Fathullah, Hirsh M. Majid, Chro H. Ahmed, Sulleyman H. Sourkan,</b> .....	65
<b>Karzan S. Ismael, Balen Z. Abdulsamad</b> Traffic Circulation Efficiency of Elliptical Roundabouts	

<b>Mohammed M. Sabri</b> .....	73
Investigating and Studying the Modifications of Nano and Micro-sized Amorphous Materials Under the Influence of a High Energy Radiation	
<b>Ali I. Yaseen, Laith A. Najam</b> .....	83
Evaluation of Radioactivity in Soil Sample from Al-Hadbaa Cement Plant in Nineveh Governorate, Iraq	
<b>Dara K. Khidir</b> .....	89
Manufacturing and Evaluating of Indirect Solar Dryers: A Case Study for the Kurdistan Region of Iraq	
<b>Khalid N. Sediq, Fahmi F. Muhammadsharif, Simko O. Ramadan, Shalaw Z. Sedeeq</b> .....	95
Design and Study of a Nanocavity-based One-dimensional Photonic Crystal for Potential Applications in Refractive Index Sensing	
<b>Huda M. Radha, Alia K. Abdul Hassan, Ali H. Al-Timemy</b> .....	99
Enhancing Upper Limb Prosthetic Control in Amputees Using Non-invasive EEG and EMG Signals with Machine Learning Techniques	
<b>Sleman Y. Omar, Dyari M. Mamand, Rebaz A. Omer, Rzgar F. Rashid, Musher I. Salih</b> .....	109
Investigating the Role of Metoclopramide and Hyoscine-N-Butyl Bromide in Colon Motility	
<b>Subasini Uthirapathy</b> .....	116
The Local Anesthetic Activity of Lavandula angustifolia and Eugenia caryophyllata Essential Oils	
<b>Sobhan Roshani, Salah I. Yahya, Yazeed Y. Ghadi, Saeed Roshani, Fariborz Parandin, Behnam D. Yaghouti</b> .....	122
Size Reduction and Harmonics Suppression in Microwave Power Dividers: A Comprehensive Review	
<b>Saif B. Neamah, Abdulamir A. Karim</b> .....	137
Real-time Traffic Monitoring System Based on Deep Learning and YOLOv8	
<b>Bana K. Hamadameen, Sara S. Hamad</b> .....	151
Atherogenic Index of Plasma in the Three Trimesters of Pregnancy	
<b>Jabbar M. A. Qaradaghi, Tola A. Merza</b> .....	157
Peperites: Insight into the Submarine Eruptions within Walash Volcano sedimentary Group, Mawat Area, Iraqi Kurdistan Region	
<b>Jaylan H. Sherwany, Jamal I. Kakrasul, Jie Han</b> .....	180
Effect of Waste Glass on Properties of Treated Problematic Soils: A Comprehensive Review	
<b>Musaab S. Sultan</b> .....	191
Magnetic and Electrical Properties of Electrodeposited Nickel Films	
<b>Mohsen Alirezapoori, Mohsen Hayati, Mohammad A. Imani, Farzin Shama, Pouria Almasi</b> .....	201
An Ultra-wideband Low-power Low-noise Amplifier Linearized by Adjusted Derivative Superposition and Feedback Techniques	

## ARO Editorial Words

Dear esteemed readers,

We are thrilled to unveil the 21st edition of Aro, the esteemed Scientific Journal of Koya University! This landmark issue marks a new chapter in Aro's remarkable journey, solidifying its position as a leading platform for groundbreaking research in the Kurdistan Region of Iraq and beyond.

Despite regional academic challenges, Aro has witnessed a surge in exceptional submissions this season. This, along with a growing flow of citations, underscores our journal's growing reputation in the global academic arena. This recognition is a tribute to the tireless dedication of our executive team, esteemed authors, reviewers, and editorial board members – all united in advancing Aro's global reach. We warmly welcome new editorial members whose expertise further strengthens our pursuit of international acclaim.

As we enter our 11th year, our vision is to amplify Aro's impact and visibility within the scholarly community. We are actively pursuing inclusion in the prestigious Science Citation Index Expanded™ (SCIE) by Clarivate Analytics, a testament to our unwavering commitment to scientific publishing excellence.

Aro remains committed to providing invaluable resources, support, and guidance to researchers throughout the publication process, while championing open access to scientific knowledge. We are proud recipients of the DOAJ Seal, affirming our dedication to trusted, high-quality open-access publishing.

While acknowledging the ongoing pursuit of dependable and proficient reviewers, we are actively working to enhance this crucial aspect of our journal. The overwhelming response from researchers over the past decade has prompted the expansion of our Editorial Board to efficiently manage the growing number of manuscript submissions.

This edition offers a diverse range of original research papers spanning numerous disciplines, reflecting Aro's multidisciplinary character. Our sincere gratitude goes to the authors who entrusted Aro with their groundbreaking research, and to the esteemed peer reviewers from prestigious universities worldwide who generously contributed their expertise to ensure the quality of this issue.

Looking ahead, we remain resolute in upholding the highest standards of scientific publishing and providing a valuable resource for researchers globally. Your continuous support and constructive feedback are crucial as we strive to establish Aro as a platform that fosters scientific excellence and facilitates the dissemination of knowledge.

Together, let us proceed on this exciting journey of continuous growth and innovation.

With warm regards,

Dilan M. Rostam  
*Editor-in-Chief*

Mohammed H. S. Zangana  
*Executive Publisher*

Salah I. Yahya, Basim M. Fadhil, Fahmi F. Muhammad, Wali M. Hamad, Jorge Correia, Fouad Mohammed, Jacek Binda, Nadhir Al-Ansari, Howri Mansurbeg, Tara F. Tahir and Yazen A. Khaleel.  
*Executive Editorial Board Members*



# Immunological Role of Megakaryocytes and Platelets during Influenza A Virus Infection

Fryad M. Rahman

Department of Biology, College of Science, University of Sulaimani,  
Kurdistan Region, F.R. Iraq.

Department of Medical Laboratory Analysis, College of Health Sciences, Cihan University - Sulaimaniya,  
Sulaimaniya 46001, Kurdistan region – F.R. Iraq

**Abstract**—Influenza viruses pose a serious threat to public health, with severe cases often characterized by lung damage and inflammation. However, the underlying mechanisms of these processes remain poorly understood. This study aimed to investigate the essential role of megakaryocytes (MKs) and platelets (PLTs) in influenza A virus (IAV) infections. Conducted at the Department of Rare Respiratory Diseases, Cystic Fibrosis, and Pulmonology, Nord University Hospital, Marseille, France, the study collected seventy blood samples between October 2018 and March 2019. Samples were obtained from healthy individuals and patients diagnosed with IAV. Messenger RNA was extracted from isolated PLTs and subjected to quantitative real-time-polymerase chain reaction using sets of primers targeting immune marker genes. Western blot analysis was also performed for confirmation, focusing on Fas Ligand (FasL). Results showed that PLTs from IAV-infected individuals expressed the FasL, tumor necrosis factor-related apoptosis-inducing ligand, and Granulysin (GNLY) receptors when activated. Furthermore, an *in vitro* assay revealed the presence of FasL receptors on infected CMK cell lines. *In vivo* investigations demonstrated that activated MKs and PLTs in mice also expressed FasL. Interestingly, none of the immune receptors under investigation were found in both MKs and PLTs in mouse model studies. In conclusion, MKs and PLTs play a significant role in influencing immune responses that may help prevent viral spread during infection. However, further examination of their mechanisms of action is warranted. Understanding the involvement of these cells in influenza pathogenesis could offer valuable insights for developing potential therapeutic strategies.

**Index Terms**—Influenza A virus, Megakaryocytes, Platelets, Killer activation receptors, FasL.

## I. INTRODUCTION

The Annual report of flu outbreaks indicated that this disease result in 250 000 to 500 000 mortalities worldwide (Organization, 2022). Recently, the GLaMOR Project has reported an uncertainty range of 294 000 - 518 000, which

is close to the previous global estimate by the World Health Organization (Paget, et al., 2019). Moreover, the H5N1 and H7N9 subtypes of human pathogenic avian viruses pose a serious threat to public health, highlighting the need for better understanding of influenza A viruses (IAV) and development of new therapies (Iuliano et al., 2018; Li et al., 2018; Paget, et al., 2019).

The multifactorial process of severe influenza is primarily influenced by the interaction between the virus' ability to replicate, the downregulation of host response to infection, and vascular hemorrhages that cause alveolar injury (Perrone, et al., 2008). The most frequent components in the inflamed lungs following endothelial cell injury are platelets (PLTs), which undertake immunological activities differently from leukocytes; but their actual function is still unknown (Tate, et al., 2009). In addition to their function in hemostasis, PLTs are crucial components of immunity. The production of cytokines by PLTs, which contribute to the acute inflammatory process, is well documented (Morrell, et al., 2014).

Megakaryocyte (MKs) is a key element of early thrombosis, hemostasis, and wound healing. More evidences are indicated that MKs may perform a different intrinsic biological function in addition to manufacturing PLTs (Arabian, et al., 2012). Furthermore, they are known to convey to PLTs a number of genes with well-known immunomodulatory properties (such as CD154, tumor necrosis factor-related apoptosis-inducing ligand [TRAIL], TNF-a, and FasL) (Crist, et al., 2004; Crist, et al., 2008).

PLTs are therefore crucial participants in IAV disease; however, their specific mechanisms of action are still unknown. The previous studies were believed that the MK precursor cells produced all of the PLTs at the bone marrow (Deutsch and Tomer, 2006; Machlus and Italiano, 2013; Patel, Hartwig and Italiano, 2005). However, recently, a milestone report provided evidence that a reservoir of MKs is also present in the lungs, which is believed the site for 50% of PLT biogenesis from total PLT (Lefrancais, et al., 2017). Furthermore, several studies emphasized that PLTs are cytotoxic to microorganisms and abnormal cells (Yeaman, 2010; Hamzeh-Cognasse, et al., 2015; Assinger, et al., 2019). *In vitro* studies highlighted similar to natural killer (NK) cells; PLTs destroy a range of tumor cell lines as



well as parasites (Ibele, et al., 1985; McMorran, et al., 2009). According the previous report, cell death is caused by an antibody-dependent cell-mediated cytotoxicity (Joseph, et al., 1983). However, the mechanisms driving PLT-mediated cell death remain unexplained, with the exception of new reports that show FasL may be involved (Schleicher, et al., 2015).

From this context, this study was designed to understand the immunological effects of MKs and PLTs during the pathology of influenza and help in the development of novel therapy. In addition, this highlights the critical requirement for innovative antiviral approaches, as the study's strategy focuses on cellular host characteristics rather than the virus.

## II. MATERIALS AND METHODS

### A. Study Design

The study was designed as a retrospective cohort study, aiming to investigate the significant immunological functions of MKs and PLTs in the progression of IAV pathogenesis. The total study population consisted of forty patients and thirty healthy individuals. The study was conducted between October 2018 and March 2019, at the Department of Rare Respiratory Diseases, Cystic Fibrosis, and Pulmonology at Nord University Hospital in Marseille-France.

### B. Reagents

The study used the reagents listed below: Anti-viral N1 protein, monoclonal anti-hemagglutinin (HA) and anti-viral M2 protein (Santa Cruz Biotechnology, Heidelberg, Germany, catalogue numbers [Cat. No.]: sc-56968, sc-393579, and MABF2165, respectively); Purified Mouse Anti-Human FasL CD178 (BD Bioscience, Cat No: 556372); monoclonal anti-tubulin antibody (Sigma Aldrich, Lyon, France, Cat No: T6199); anti-Glyceraldehyde-3-Phosphate Dehydrogenase (GAPDH) antibody (Millipore, Cat No: AB2302); Anti-Mouse CD178 (Fas Ligand) Monoclonal Antibody (MFL3), allophycocyanin (APC) (eBioscience, Cat No: 50-152-48); polyclonal antiplatelet CD41 (Bioss, Woburn, MA, Cat No: bsm-30032M-APC); monoclonal CD62P (P-Selectin) antibody (BioLegend, France, Cat No: 304903); ketamine/xylazine anesthesia (Bayer HealthCare, France, Cat No: 424946-01-6). The Coomassie (Bradford) Protein Assay Kit was used to measure total protein (Thermo Fisher Scientific, Cat No: 23236).

### C. Viruses

IAV (H1N1) strain A/PR/8/34 and IAV (H3N2) strain A/Udm/72 were used in this study. Virus stocks were produced on MDCK cells and stored at  $-80^{\circ}\text{C}$  with titer of  $10^7$  virus particles/mL.

### D. Cell Culture

Human acute megakaryocytic leukemia cells (CMK), DSMZ (Braunschweig, Germany, Cat No: ACC 392) was cultivated in RPMI 1640 (Gibco, Cergy, France, Cat No: 52400017), 10% fetal bovine serum (Gibco, Cat No: A3160501), 100 IU/mL penicillin/streptomycin,

2 mM L-glutamine, and 1% sodium pyruvate (Gibco, Cat No: 15070063, 25030149, and 11360039 respectively) were added as supplements. The cell line growth maintained at a density between  $5 \times 10^5$  cells/mL and  $1 \times 10^6$  cells/mL. A NucleoSpin RNA kit from (Macherey-Nagel, Cat No: 740955.50) was used to extract RNA from CMK cells. Quantitative real-time-polymerase chain reaction (qRT-PCR) was used to evaluate changes in gene expression, which will be detailed later. Primer sequences are available on request.

The American Type Culture Collection (ATCC, Manassas, VA, USA) provided the MDCK (Maddin-Darby canine kidney) cell line (ATCC CCL-34). Thermo Fisher Scientific provided 1% penicillin-streptomycin, 10% fetal bovine serum, 2 mM L-glutamine, and Eagle's Minimum Essential Medium (EMEM, Cat No: 12491) for the maintenance of MDCK cells. The DMEM Dulbecco's modified Eagle's media (Thermo Fisher Scientific, Cat No: A1443001) with or without phenol red, supplemented with 2 mM L-glutamine, 1% pen-strep, and 10% FBS was used to grow the human alveolar A549 cells (ATCC CCL-185) and mouse fibroblast NIH/3T3 cells (ATCC CRL-1658). All cell lines were kept at  $37^{\circ}\text{C}$  in 5%  $\text{CO}_2$  in a humid incubator. The RPMI 1640 culture media with the addition of 100 IU/ml interleukin-2 (IL-2) (Proleukin) (Chiron Corporation, Cat No: C210879), 10% FBS, 2 mM L-glutamine, 100 IU/ml penicillin, and 0.1 g/ml streptomycin was used for the cultivation of the human Natural Killer cell line, NK-92 (ATCC CRL-2407).

### E. IAV In Vitro Replication Experiment

RPMI 1640 was used to cultivate CMK cells in 96-well plates, accompanied by 2 mM L-glutamine, 1% sodium pyruvate, 10% fetal bovine serum, and 1% penicillin/streptomycin. At 70–80% of confluence cells had been infected by IAV A/PR/8/34 (H1N1) and IAV A/Udm/72 (H3N2) at a multiplicity of infection (MOI, 3), suspended in complete low-serum (2%) DMEM medium without phenol red. Virus infection was performed for 2 h at  $37^{\circ}\text{C}$  using gentle agitation to increase the rate of virus adsorption, then viral inoculate was removed. Unless otherwise stated, viral titers in all conditions were measured by plaque assay in the supernatant 16 h after inoculation. Then, CMK cells were harvested at (0, 3, and 6) days after infection and RNA was extracted according to the instruction protocols. All analysis was performed in duplicate for three times.

### F. Titration Experiment

In DMEM 10% fetal calf serum,  $1 \times 10^6$  MDCK cells were cultivated in each well of a 6 well culture plate. The diluted samples were prepared the following day by repeated dilution to a tenth of the original samples. For infection, diluted samples were added after the cells had been cleaned twice with phosphate buffer saline (PBS). The supernatant was removed following an hour of adsorption at  $37^{\circ}\text{C}$ , and MEM medium supplemented with 2% agarose and 1  $\mu\text{g}/\text{mL}$  trypsin was then added. To identify plaque lysis, live cells were stained with purple crystal for five minutes when agarose had been removed after 72 h. Then, each sample's



infectious viruses were assessed, with each plaque standing for one infectious virus, after the cells had undergone a thorough cleaning procedure.

### G. Human Sampling Experiment

A group of 22 women and 18 men, aged between 35 and 55, were referred to the Department of Rare Respiratory Diseases, Cystic Fibrosis, and Pulmonology at Nord University Hospital in Marseille, France, providing a demonstration for IAV infection; whereas the blood collecting center at la Timone Teaching Hospital in Marseille, France, received thirty volunteers who were then asked to provide control samples. None of the subjects were taking any medications or had any illnesses that are known to affect PLT function.

Regarding this study, which adhered to the principles of the Helsinki Declaration, all patients and healthy participants supplied written informed permission. In addition, the approval of this study was given by the research ethics committee of the University of Aix-Marseille.

### H. Evaluation of PLT and Leukocyte Numbers

The previously published methods for preparing human PLT-rich plasma (PRP), PLT-poor plasma (PPP), and washed PLTs were used (Miller, et al., 1988). Tyrode's buffer was used to resuspended washed PLTs (138 mM NaCl, 2.7 mM KCl, 12 mM NaHCO<sub>3</sub>, 0.4 mM NaH<sub>2</sub>PO<sub>4</sub>, 1 mM MgCl<sub>2</sub>, 2 mM CaCl<sub>2</sub>, 5 mM HEPES, 3.5 mg/ml HSA, and 5.5 mM glucose, pH 7.3) supplemented with 0.02 U/ml apyrase. Studies were carried out six hours after blood collection. RPMI 1640 was used to modify the PLT counts in PRP and washed PLTs to 3–4 10<sup>8</sup> cells/mL. On a BD-Accuri™ C6 flow cytometer (BD Biosciences), analysis was done using PE-CD62P (clone AK-4; eBioscience) and fluorescein isothiocyanate (FITC)-CD42b (clone HIP1; eBioscience) antibodies to assess granule secretion.

The mouse smart card 7030 was used to count PLTs on the Vet ABC Hematology Analyzer from (SCIL Animal Care Company Sarl, Altorf, France). Mouse PLTs in various sample fluids are distinguished by the automated cell counting according to their size.

### I. Flow Cytometry of Blood PLTs

Mouse blood was drawn by retrobulbar venous plexus puncture (The least amount of PLT activation is likely to occur when blood is collected through a retrobulbar venous plexus puncture) (Jiroukova, Shet and Johnson, 2007), while venipuncture is used to collect human blood into a plastic tube containing buffered 3.2% sodium citrate, which is then gently mixed right away after filling. In whole blood, PLT activation and CD41-positive cells were assessed utilizing FITC-conjugated P-selectin and APC and phycoerythrin (PE)-conjugated CD41/CD61 antibodies.

### J. In Vivo Experiments

Six-week-old C57BL/6 mice from Janvier Laboratories in (Le Genest Saint-Isle, France) were kept in a pathogen-free

environment and provided with unlimited access to food and water. Mice were kept in cages inside stainless steel isolation cabinets for infection tests, and the air was filtered with high-efficiency particle air ventilation. At day 0, mice were given a ketamine and xylazine mixture (43 mg/kg and 5 mg/kg, respectively) to make them unconscious before being given 20 µl of a PBS solution containing the A/PR/8/34 virus intranasally, as previously described (Rahman, et al., 2021). Infection was performed with either 500 or 750 Plaque-Forming Units (PFU). Then as a control (placebo), the same volume of PBS was used to treat mice intranasally. Daily survival rates and weight loss were measured following virus inoculation. Days three and six following infection, mice were anesthetized and peripheral blood were taken for PLTs isolation, while blood was collected on day 0 for isolation of PBMC or/and natural killer (NK) cells as a positive control for immune markers. A broncho-alveolar lavage (BAL) sample from euthanized mice was collected and processed with PBS to assess virus replication. Infectious virus titers were then calculated using a plaque assay. Statistical difference between control and treated groups was estimated by unpaired t-test or one-way ANOVA,  $p \leq 0.01$  was considered as statistically significant.

Ethical approval for the *in vivo* mouse studies was indeed obtained and adhered to the highest standards of animal welfare and regulatory guidelines. The experimental protocols were designed following the INRAE guidelines, which comply with the European animal welfare regulations. In addition, the study received explicit approval (number: G130555) from the Aix-Marseille University/ Faculty of Medicine la Timone's committee on animal research. This approval was further endorsed by the Directorate of Veterinary Services under the authority of the "Ministère de l'éducation nationale, de l'enseignement supérieur et de la recherche" with the authorization number 693881479 (APAFIS#14660). The animal welfare was taken seriously and ensured that all experimental procedures were conducted in a biosafety level 2 facility, adhering to strict safety measures.

### K. qRT-PCR Analysis

For every experiment, total RNA was isolated from MKs and PLTs of infected and non-infected mice, healthy individual and flu patient's, peripheral blood mononuclear cells (PBMC), [CMK, NK-92, A549, and NiH3T3] cell lines using QIAzol reagent (Qiagen) in accordance with the manufacturer's guidelines. Following that, the M-MLV Reverse Transcriptase kit (Invitrogen, Cat No: 10338842) was used to reverse-transcribe 5 µg of the obtained RNA. As previously mentioned, Uni12 primer was utilized for vRNA (viral RNA) reverse transcription (Hoffmann et al., 2001). As a housekeeping gene, GAPDH was reverse transcribed using a particular primer (Baier, et al., 1993) (All primer sequences are provided on request). The 5X HOT Pol EvaGreen qPCR Mix Plus (Euromedex, France, Cat No: 08-24-00001) was then used to conduct qRT-PCR. A Light-Cycler 480 type II apparatus (Roche, France) was carried out for the reactions,

amplifications, and measurements. The LC480 software (Roche) was employed to create amplification plots, and GAPDH was used to normalize the data. Fold induction was determined using the threshold cycle method  $2^{-\Delta\Delta C_t}$ . Changes were scaled to the control values' mean, which was set to 1.

#### L. Gene Expression Assays in Mouse Bone Marrow MKs

Following euthanasia, mice will have their tibias and femurs from both legs removed to collect their bone marrow. PBS/ethylenediaminetetraacetic acid (EDTA) will be used to flush bone marrow cells prior to filtering (using 70  $\mu$ m cell strainers), and flow cytometry will be used to sort MKs after red blood cells lysis. In addition, Ficoll gradient (Eurobio, Courtaboeuf, France, Cat No: CMSMSL01-01) was also used to enrich MKs from the bone marrow of infected and uninfected mice before they were chosen using fluorescence-activated cell sorting (Aria III SORP, Becton Dickinson) based on  $\geq 8$  N ploidy (Staining with 10  $\mu$ g/mL Hoechst 33342, Sigma-Aldrich, France) and CD41+ cells (anti-mouse-CD41-PE, Thermo Fischer Scientific, Cat No: CD4-112AP). Total RNA was extracted and gene expression assay was performed as mentioned before.

#### M. Western Blotting

Isolated PLTs from healthy individuals and flu patient's, MKs isolated from uninfected and infected mouse, PBMC, non-infected and infected CMK cell lines, NK-92 cell lines, NiH3T3 cells, and A549 cells were gathered as previously mentioned, lysed in buffer after being rinsed with PBS (Tris 50 mM, NaCl 250 mM, 0.1% NP-40, 0.1 mM PMSF, pH 7.4 added EDTA as a supplement – complementary combination of protease inhibitors) for 20 min on ice. The cell lysate was mixed with an equivalent volume of 2X Laemmli buffer, boiled for 5 minutes and was subjected to an SDS/PAGE. Proteins were then electro-transferred onto nitrocellulose membranes and stained with antibodies to FASLG (G247-4) (1:500) or mouse monoclonal anti- $\gamma$ -Tubulin antibody (1:1000) for one hour at ambient temperature (Immunoblots were performed along with antibodies directed against human and mouse). After washing in PBS-Tween 0.05% buffer (3 min, 3 times) an anti-mouse secondary HRP-conjugated antibody was applied to the membranes using this concentration (1:2000) or goat anti-mouse (1:10000) antibody for one hour at ambient temperature. Moreover, the membranes were then cleaned in PBS -Tween 0.05% buffer (5 min, 3 times) and revealed with Pierce ECL Plus Western Blotting Substrate. Chemiluminescent immunoassay (CLIA) CCD imager ImageQuant LAS 4000 was used for image acquisition (GE Healthcare, Velizy-Villacoublay, France).

#### N. Statistical Analysis

The software GraphPad Prism (version 9.0, GraphPad, La Jolla, CA, USA) was carried out for all statistical analyses. Some statistical analysis was performed using the Mann-Whitney test, and the findings were deemed statistically significant at  $p < 0.01$  (\*). To contrast the mean ranks

between groups, statistical analysis of other data was carried out using one-way ANOVA and multiple comparison tests,  $p < 0.01$  (\*) was used to determine if the results were statistically significant. Standard error of the mean ( $\pm$  SEM) is the measure used to displayed data.

### III. RESULTS

#### A. Contribution of MKs and PLTs to the Pathogenesis of IAV

To eliminate any risk of contamination in blood cells components, peripheral blood was taken from patients and healthy individuals, then after each of PLTs, MKs, and leucocytes were isolated as described in material and methods, then stained with specific antibodies corresponding to each blood cells and plotted by flow cytometry (Fig. 1a). It is noteworthy that in my experiments, PLTs and MKs (CD41-positive) were highly purified and were not contaminated (or at least undetectable with my technic) with leukocytes (PBMC) (CD45-positive cells) (Fig. 1a and e) and NK cells (CD56-positive) (Fig. 1a). In addition, the negative controls (A549 and NiH/3T3) cells were also stained to reduce any possible contamination with blood cell components (Fig. 1b and f). Importantly, in addition to PLTs and MKs purifications, the P-selectin surface expression was also observed on IAV infections in both PLTs and MKs compared to non-infected (Fig. 1c and d).

#### B. Definition of the IAV Infection Window

To determine the most powerful activity of IAV infection in MKs and PLTs. CMK cell lines were infected with IAV (MOI 3) for different indicated time points (Fig. 2d). Then mRNA was harvested and qRT-PCR was conducted with specific IAV primers to non-structural protein 1 (NS1). The result shows that pathogenicity of IAV was most active starting from day 3 to day 9 post-infection (Fig. 2d). Interestingly, the significant expression of NS1 gene was observed in infected mouse in day 3 and day 6 post-infection in both isolated MKs (Fig. 2b) and PLTs (Fig. 2c). The same results were also obtained for infected CMK cell lines at day 3 and day 6 post infections in comparison to uninfected CMK cells (Fig. 2a).

#### C. Analysis of the Expression of Cytotoxic Molecules in Human PLTs

Except for FASL, the analysis of killer molecules in PLTs was never investigated. To test this point, PLTs isolated from non-infected/IAV-infected patients at several stages of the disease were thus analyzed by flow cytometry (data not shown). Moreover, to examine the activities of immune markers in PLTs during IAV infection in healthy individuals and infected patients by IAV at (day 3) and (day 6) of sign and symptoms onset, peripheral blood was taken from both groups. First, after PLTs isolation, the PLT activations were checked by two specific PLT markers p-selectin (CD62P) (Fig. 1d) to differentiate between PLTs of uninfected (healthy individuals) and IAV-infected patients (Flu patients), and also PLTs population were determined by using CD41 polyclonal

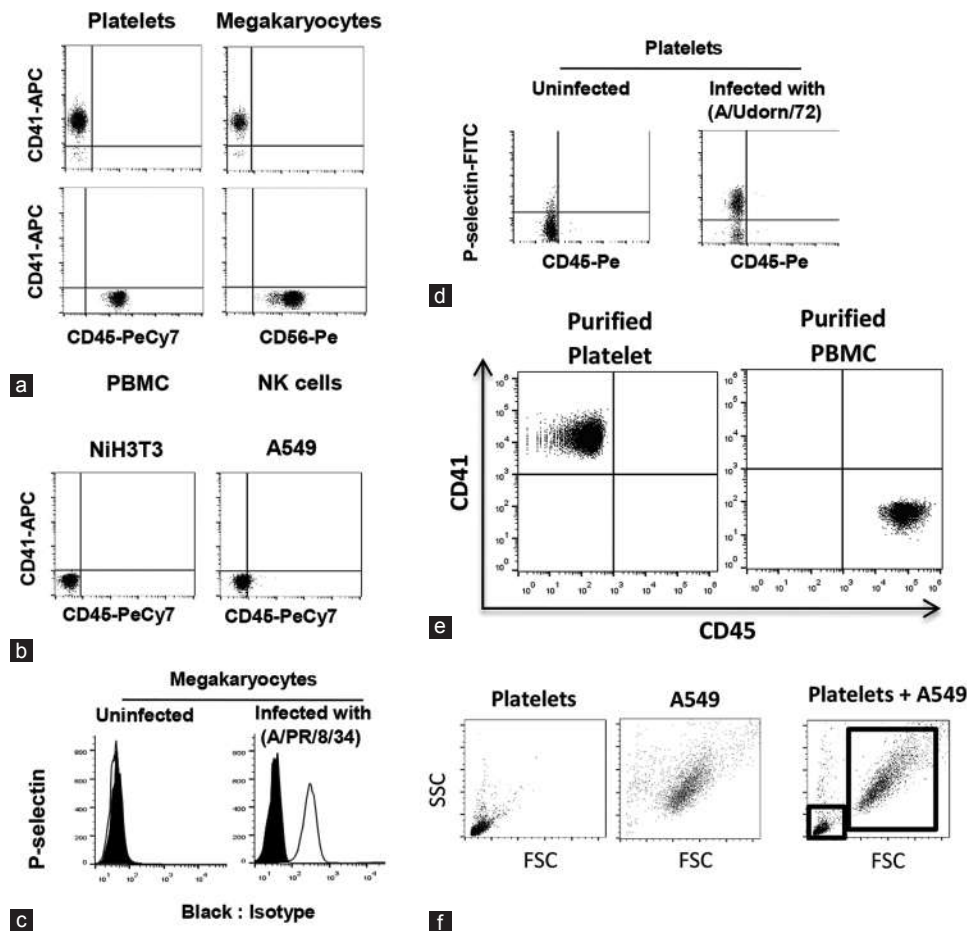


Fig. 1. During influenza A virus (IAV) infection, megakaryocytes (MKs) and platelets (PLTs) are stimulated and contribute to the pathogenesis of influenza. (a) Blood samples from uninfected or infected mice were double-stained with anti-CD45 and anti-CD41 antibodies as leukocytes and platelets identifiers, respectively from side then after double stained with anti-CD56 and anti-CD41 antibodies as NK cells and megakaryocytes identifiers from other side. (b) A549 and NIH/3T3 cell lines were double stained with anti-CD41 and anti-CD45 antibodies as platelets and leukocytes identifiers to confirm their purity and contamination rates by leukocytes and platelets/megakaryocytes throughout the study. (c) Isolated MKs from non-infected or infected mice with (A/PR/8/34) were evaluated for p-selectin secretion as indicator for MKs activation upon IAV infection, black color is correspond to Isotype. (d) Isolated PLTs from infected mouse by (A/Udorn/72) and non-infected were double stained with anti-CD62P (P-Selectin) as platelets activation marker and anti-CD45 antibody as leukocytes identifier. (e) Purification of isolated PLTs and PBMC were determined by double staining with anti-CD45 and anti-CD41 antibodies as PBMC and platelets identifiers, respectively. (f) PLTs and A549 were identified and gated alone or together in regards to size and shape by flow cytometry.

antiplatelet (Fig. 1a and e). Total RNAs were extracted and qRT-PCR was applied using specific probes and primers for the expression of different immune markers and receptors as a large panel of killer activation receptors (KARs) including (*CD16*, *CD56*, *Granulysin (GNLY)*, *FasL*, *Granzyme A*, *Granzyme B*, *NKG2C*, *NKG2D*, *TRAIL 1*, *TRAIL 2*, and *TRAIL 3*) (Fig. 3a) to indicate the important roles of PLTs through the expression of these markers during IAV infection. Inhibitory receptors (KIR) were also investigated (data not shown) such as (*ILT2*, *ILT4*, *KIR2DL-1-4*, *CD94/NKG2A*). NK92 and A549 cell lines have been used as positive and negative controls for receptors expression. Similar studies were also performed using infected versus non-infected mice (Figs. 4 and 5).

Result clearly shows that both PLTs of infected IAV patients and healthy individuals (control) were not significantly affected the expression of these markers except

for *FasL*, *TRAIL*, and *GNLY* which are markedly and significantly expressed in infected patients (activated PLTs) compared to healthy individuals (resting) PLTs (Fig. 3a). Interestingly, all mRNA coding for killer activation and inhibitory receptors were not upregulated for most cytotoxic molecules, suggesting that *FasL*, *TRAIL*, and *GNLY*, were highly upregulated upon IAV infection is MKs and PLTs specific and not due to contaminants of NK cells. Altogether, these data suggest that activated PLTs have important roles during IAV pathogenicity.

#### D. PLTs Activation by IAV Exhibits Membrane-bound FasL

To investigate the potential influence of PLT activation on *FasL* gene expression, a known pro-apoptotic molecule, this study is aimed to analyze the relationship between these two factors. To find this relation, peripheral blood was taken from non-infected and infected patients and PLTs were isolated

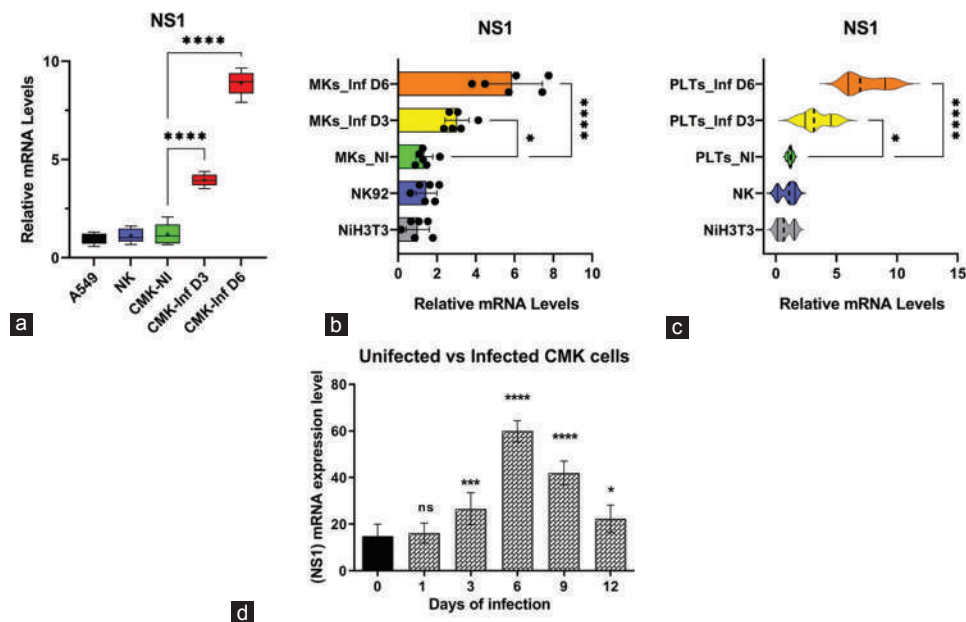


Fig. 2. Viral NS1 protein gene expression upon influenza A virus (IAV) infection. (a) CMK cells were non-infected or infected with IAV A/PR/8/34 virus (MOI 3), and then at day 3 and day 6 post-infection, RNA was extracted and real-time qPCRs were performed with specific primers to quantify gene expression of the non-structural protein 1 (NS1) of influenza A virus (mRNA or vRNA) at the indicated time point post-infection. A549 and NK92 cells were used as negative and positive controls for immune receptors, respectively. Data are represented as means  $\pm$  SEM,  $n = 3-6$  replicates. (b and c) Mice were non-infected or intranasally infected with (A/PR/8/34) virus (PFU 500), and then at day 3 and day 6 post-infection, megakaryocytes and platelets were isolated and RNA was extracted and real-time qPCRs were performed with specific primers to quantify (NS1) gene expression of influenza A virus (mRNA or vRNA) at the day 3 and day 6 post-infection. NiH3T3 and NK92 cells were used as negative and positive controls for immune receptors, respectively. Data are represented as means  $\pm$  SEM,  $n = 6$  mice. (d) CMK cell lines were grown on the 12 wells plates. At confluence 70-80% cells were non-infected (NI) or infected with A/PR/8/34 viruses (MOI 3) for the indicated time point (1, 3, 6, 9, and 12 days). CMK cell lines were then harvested and then after mRNA was extracted and converted to cDNA the quantitative real-time-polymerase chain reaction (qRT-PCR) were performed by using specific primers and probes for viral NS1 gene. Presence of the expressed gene was analyzed by qRT-PCR. Relative mRNA levels were calculated and plotted by GraphPad software as described in materials and methods. Analysis was performed three (3) times in duplicate for all experiments.

from both groups (as mentioned before); then after, RNAs were extracted and using specific primers for *FasL* gene, then qRT-PCR was performed for determining gene expression in activated (infected patients) and resting PLTs (healthy individuals). The present work shows that activated PLTs was significantly increased the expression of *FasL* gene when compared to inactivated (resting) PLTs in control group, A549 is used as negative and PBMC as positive control for the expression of *FasL* gene (Fig. 3a).

#### E. *FasL* mRNA Expression is Dependent on MKs Activation

To examine if MKs as PLTs precursor has the same response to *FasL* gene expression when it's activated much like PLT, CMK cell lines were cultivated and infected or not by IAV (see material and methods) then after were harvested at day 6 post infection, qRT-PCR was carried out after mRNA extraction using the same primers specific to *FasL* gene expression. The results show that like activated PLTs, *FasL* gene expression was greatly increased in activated CMK by IAV at day 6 post infection when compared to non-infected or resting CMK (Fig. 6a). An NK92 cell line was used as positive control, and A549 as negative control (data not shown). Thus, this finding

confirmed that *FasL* gene expression required activation of MKs by IAV as PLTs.

#### F. Infected Human MKs and PLTs Induces Expression of *FasL* Protein

To assess protein expression by immunoblot, proteins were extracted from non-infected and infected CMK cells in indicated time points (Fig. 6b), and from infected and uninfected PLTs (Fig. 3b), also from PBMC of infected patients, (NK-92 cell line as positive) and (A549 cells as negative) controls. Furthermore, the extracted proteins were examined using a western blot. The findings showed that *FasL* protein for size of (37-40) kDa were detected in PBMC and NK-92 cell lines as positive controls and not detected in A549 as negative control (Fig. 3b and 6b). *FasL* protein expression was only detectable in infected PLTs and CMK cell lines at day 1, day 3, and day 6 post infection in a dose dependent manner, while no *FasL* protein detection was observed in uninfected CMK cell line and resting PLTs (Fig. 3b and 6b). Thus, IAV infection is crucial for promoting *FasL* protein secretion in activated PLTs and CMK cell lines. This discovery supported some studies which suggested that killing was *FASL*-dependent.

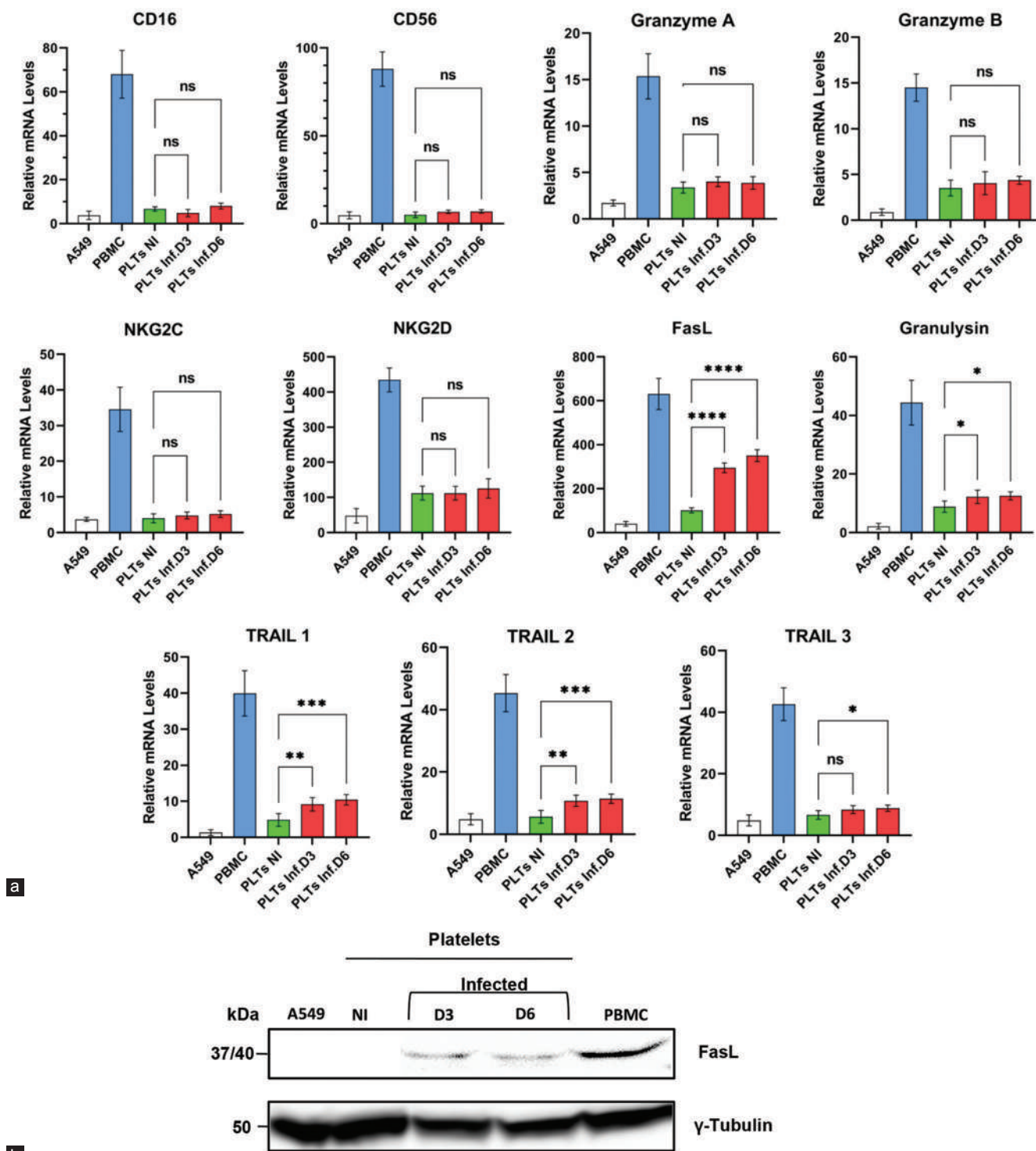


Fig. 3. Effect of influenza A virus (IAV) infection on killer activation receptors expression in human platelets (PLTs). (a) PLTs were isolated from patients infected by IAV (n = 10) and healthy individuals (n = 10), with isolated PBMC and A549 cells as positive and negative controls, respectively. PLTs and PBMC were isolated from healthy and flu patients and A549 was harvested as negative control. mRNA was extracted and converted to cDNA the quantitative real-time-polymerase chain reaction (qRT-PCR) were conducted using specific primers and probes for each known (KARs). Presence of the expressed genes was analyzed by qRT-PCR. Relative mRNA expression levels were calculated and plotted by GraphPad software as described in materials and methods. Analysis was performed 3 times in duplicate. (b) Platelets from healthy individuals (NI) and infected patients with IAV at day 3 (D3) and day 6 (D6) post influenza infections were isolated then lysed and presence of the FasL protein was analyzed by western blot. A549 cells and PBMC were lysed as negative and positive controls respectively, and presence of the FasL protein was analyzed by western blot. Presence of  $\gamma$ -Tubulin protein considered as internal loading control.

It is noteworthy that throughout this study, PLTs (CD41-positive) were highly purified and were not contaminated (or

at least undetectable with our technic) with leukocytes (CD45 positive cells) (Fig. 1a and e).

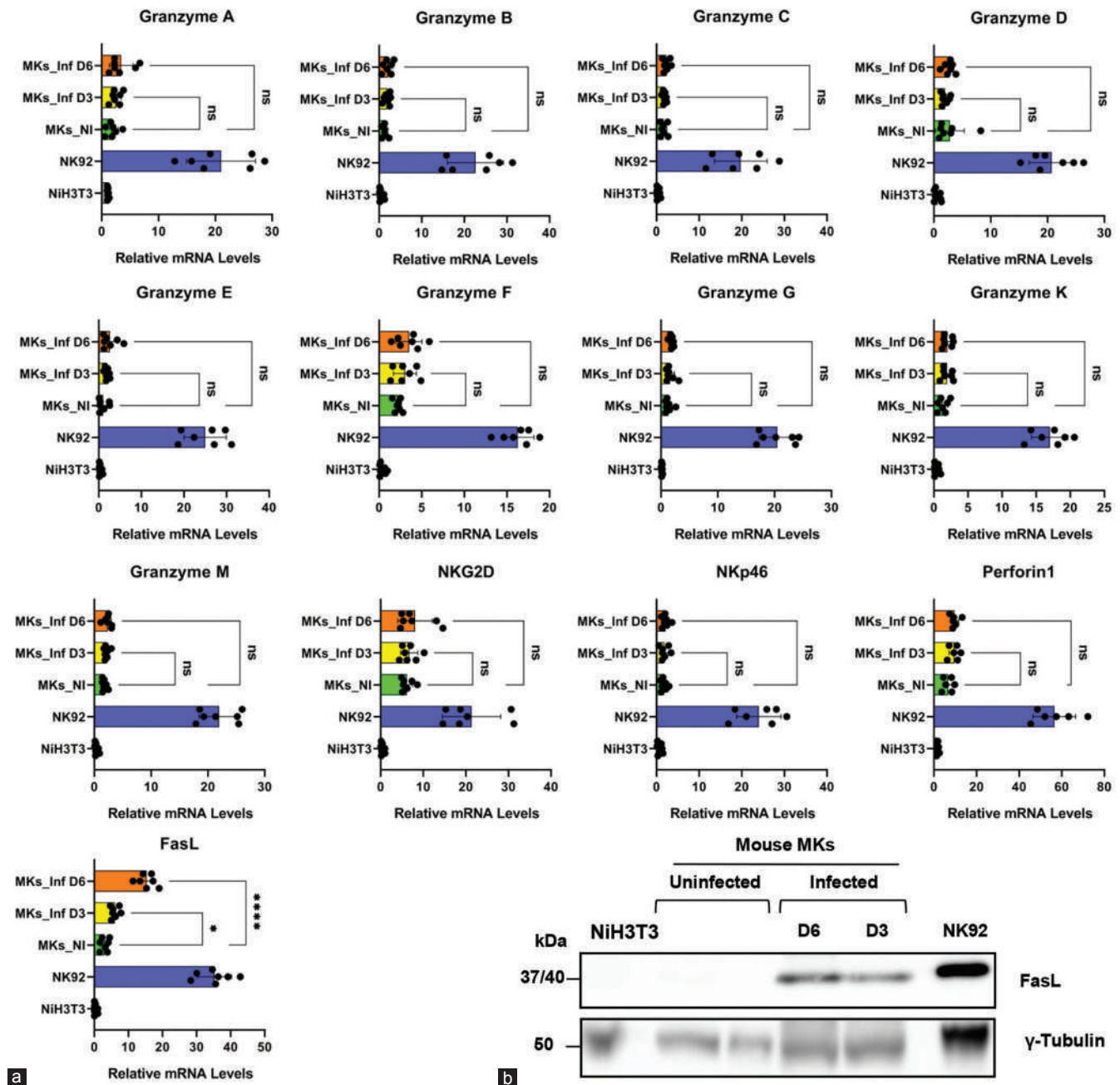


Fig. 4. Effect of influenza A virus infection on killer activation receptors expression in mouse megakaryocytes (MKs). (a) Three groups of mice ( $n = 7$  mice/group) were uninfected or infected and inoculated with A/PR/8/34 virus, at a 50% lethal dose ( $LD_{50}$ ) (500 pfu per mouse; Day 3 and 6 post-infection), and NK92 cells and NiH3T3 cell lines were used as positive and negative controls, respectively. MKs were isolated from bone marrow of infected mice or not and then NiH3T3 cells were harvested as negative control and NK92 cell lines were also harvested as positive control. mRNA was extracted and quantitative real-time-polymerase chain reaction (qRT-PCR) were performed by using specific primers and probes for each known genes of (KAR). Presence of the expressed genes was analyzed by qRT-PCR. Relative mRNA levels were calculated and plotted by GraphPad software as described in materials and methods. Analysis was performed 3 times in duplicate. (b) Mouse was uninfected (NI) or infected (inoculated) with A/PR/8/34 viruses (750 PFU) for 3 (D3) or 6 (D6) days post-infection, MKs were isolated from bone marrow (as described in materials and methods) then lysed and presence of the FasL protein was analyzed by western blot. NIH/3T3 and NK92 cell lines were lysed as negative and positive controls respectively, and presence of the FasL protein was analyzed by western blot. Presence of  $\gamma$ -Tubulin protein considered as internal loading control.

#### G. *GNLY* is Present in Human MKs and PLTs and is Released on Their Activation

To analyze whether the lysis granules secreted from the activated or/and resting PLTs and MKs. Specially to evaluate the secretion of *GNLY*, CMK cell lines, NK92,

and A549 cells were cultivated from side, then after, not infected or infected with IAV (Fig. 6a); In addition, *GNLY* gene expression was estimated from other side by infected PLTs versus uninfected (Fig. 3a). Moreover, total RNAs were extracted and converted to cDNA then qRT-

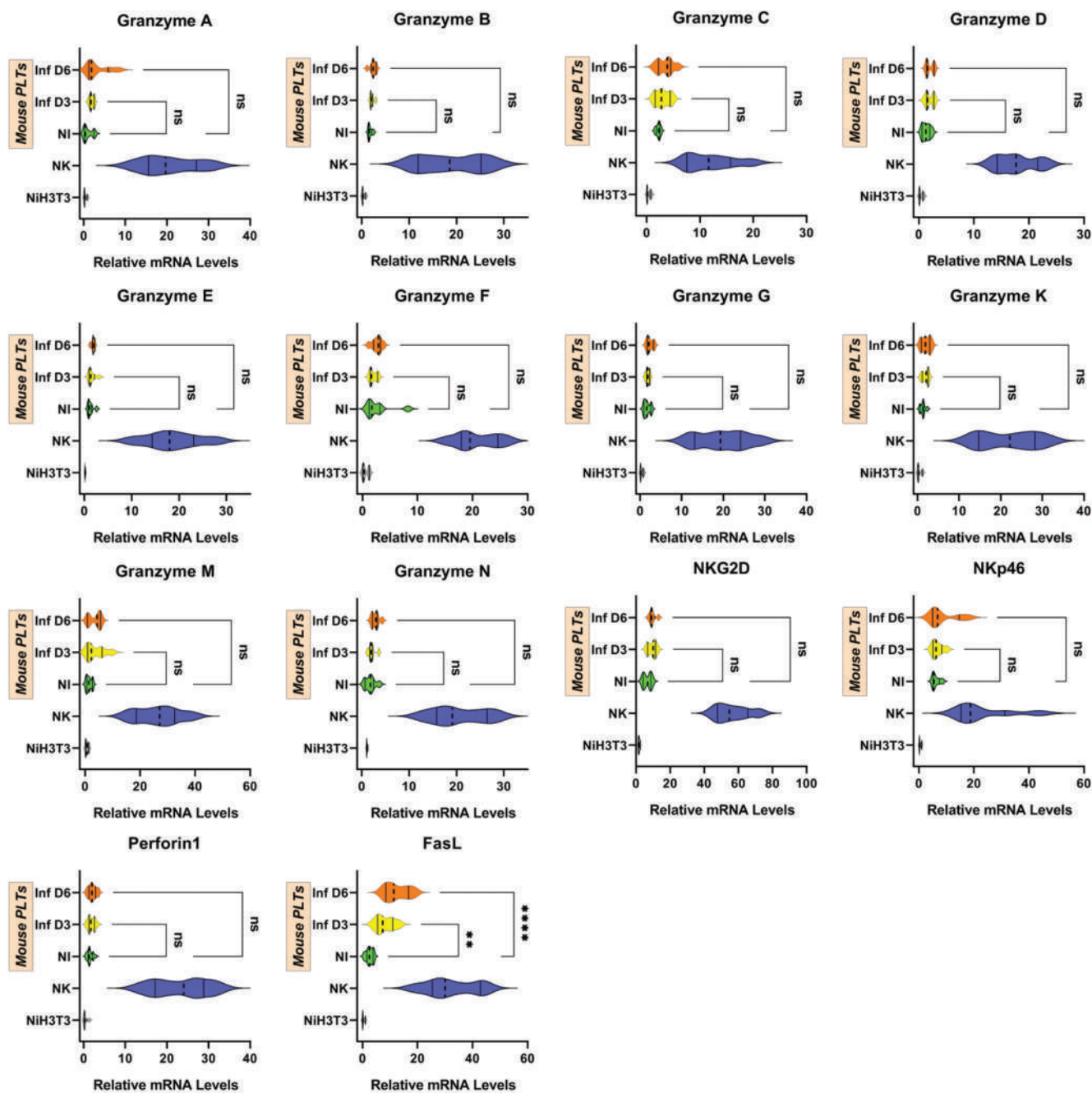


Fig. 5. Effect of influenza A virus (IAV) infection on killer activation receptors expression in mouse platelets (PLTs). Mouse PLTs (n = 7 mice/group) were infected or not by IAV at 3 days and 6 days post-infection, and NK92 cells and NiH3T3 cell lines were used as positive and negative controls, respectively. PLTs were isolated from non-infected or infected mice and then NiH3T3 cells and NK92 cell lines were harvested as negative and positive controls, respectively. mRNA was extracted and quantitative real-time-polymerase chain reaction (qRT-PCR) were conducted using specific primers and probes for each known genes of (KAR). Presence of the expressed genes was analyzed by qRT-PCR. Statistical analyses were performed using one-way ANOVA as mentioned in materials and methods. Analysis was performed 3 times in duplicate.

PCR was achieved to estimate the expression rates of *GNLY* gene among the infected and non-infected PLTs and CMK cell lines in parallel with NK cells and A549 cell lines as positive and negative controls, respectively. The present results demonstrated that expression of *GNLY* gene was moderately and significantly increased in infected CMK cells and PLTs in comparison to non-infected (Fig. 3a and 6a).

*H. Most of Lytic Granules with Cytotoxic Actions were not Secreted by Activated or Resting Human MKs*

Approximately most of KARs and KIRs were not expressed by CMK cells in resting situation or on their activation. To evaluate the secretion capabilities of lytic granules by MKs (CMK cells) in non-infected or IAV-infected status, CMK cell lines were harvested and total RNAs were extracted, upon its conversion to cDNA, qRT-PCR was conducted for

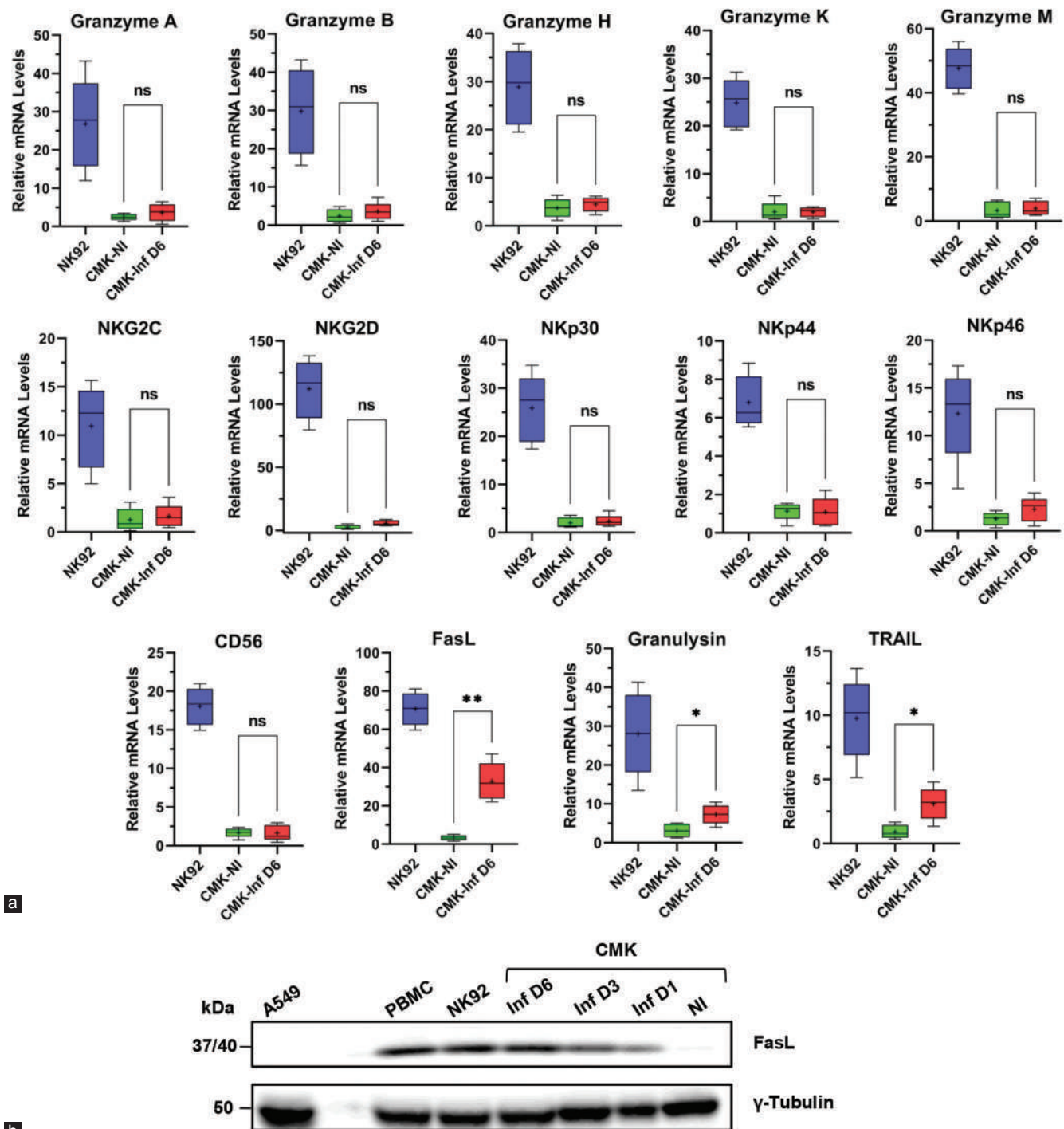


Fig. 6. Killer activation receptors (KARs) gene expression in CMK cell lines upon influenza A virus infection. (a) CMK cells were grown on the 6 wells plates. At confluence 70-80% cells were infected with A/PR/8/34 or A/Udorn/72 (MOI 3) or uninfected for 6 days post-infection, and then NK92 and A549 cells were used as positive and negative controls, respectively. Uninfected or infected CMK cells, NK92 cell lines and A549 cells (data not shown) were harvested, and then after mRNA was extracted and converted to cDNA the quantitative real-time-polymerase chain reaction (qRT-PCR) were conducted by using specific primers and probes for each known (KAR) genes. Presence of the expressed genes was analyzed by qRT-PCR. Relative mRNA levels were calculated and plotted by GraphPad software as described in materials and methods. Analysis was performed 3 times in duplicate. (b) CMK cell lines were non-infected (NI) or infected with A/PR/8/34 viruses (MOI 3) for the indicated time point (days), PBMC and NK92 cells were used as positive controls and A549 cells were included as negative control. All cell lines were then lysed and presence of the FasL protein was analyzed by western blot. Presence of  $\gamma$ -Tubulin protein considered as internal loading control.

approximately all of lytic granule's genes. Data indicated that there are no any significant differences between infected and uninfected CMK cells when compared to NK92 cell lines

as positive control (Fig. 4a, and Fig. 7). Furthermore, these outcomes emphasize that both non-infected and infected CMK cell lines were unable to secrete perforin and all



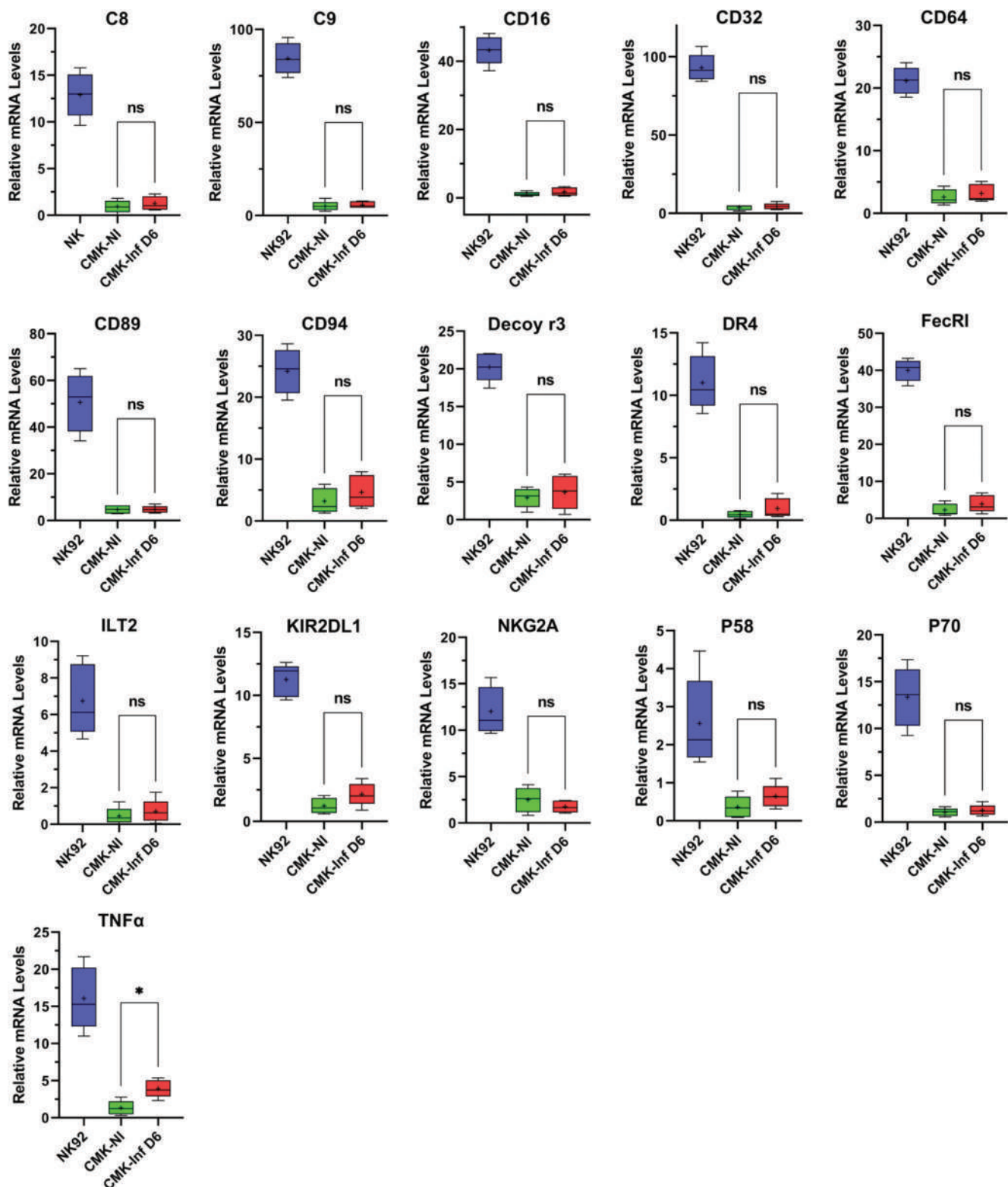


Fig. 7. Killer inhibitory receptors (KIRs) gene expression in CMK cell lines upon influenza A virus infection. CMK cells were grown on the 6 wells plates. At confluence 70-80% cells were infected with A/PR/8/34 or A/Udorn/72 (MOI 3) or uninfected for 6 days post-infection, and then NK92 and A549 cells were used as positive and negative controls, respectively. Uninfected or infected CMK cells, NK92 cell lines and A549 cells (data not shown) were harvested, and then after mRNA was extracted and converted to cDNA the quantitative real-time-polymerase chain reaction (qRT-PCR) were performed by using specific primers and probes for each known (KIRs) gene. Presence of the expressed genes was analyzed by qRT-PCR. Relative mRNA levels were calculated and plotted by GraphPad software as described in materials and methods. Analysis was performed 3 times in duplicate.

granzymes lytic granules. These results show that PLTs and MKs in human were not exhibits the cytotoxic activities and defense mechanisms as like immune cells. However, infected MKs was expressed membrane bound *FasL*, *TRAIL*, and *GNLY* lytic granule as KARs (Fig. 6a) and *TNF $\alpha$*  as KIRs (Fig. 7) on activation in contrast to resting status. Altogether, these findings suggest that activated MKs express some killer and inhibitory activation receptors, which point its pivotal roles during IAV pathogenicity.

#### *I. Analysis of the Expression of Cytotoxic Receptors among Mouse MKs and PLTs (In Vivo).*

As mentioned before, this work also tested whether the expression of killing receptors in murine PLTs on infection results from a modification of the transcriptome/proteome in the MKs (precursors of PLTs). To this end, mice had the infection intranasally by (A/PR/8/34) virus (500 PFU) and after 3 and 6 days, bone marrow MKs were isolated. The present result showed that *NKG2D*, *NKp46*, *perforin1* and all of granzyme types were not upregulated at the transcriptional level in bone marrow MKs upon mice infection; while *FasL* gene was significantly upregulated in infected mouse MK's when compared to resting MKs (uninfected mouse) in different time points (Fig. 4a). In addition, the expression of FasL protein was more certain through western blot. To do this study, MKs was isolated from bone marrow of infected and uninfected mouse, then after protein was extracted and lysed at (3 and 6) days post-infection (Fig. 4b), protein from negative control NIH/3T3 cells and NK92 cells as positive control were also extracted and lysed. Furthermore, the protein expression was analyzed by Immunoblot. The outcome amply demonstrates that FasL protein was observed in mice MKs at both day 3 and day 6 post-infection, while this protein was not detected in non-infected MKs (Fig. 4b). Altogether, this data is certainly indicated that MKs activation is required to express killing FasL.

As previously described, obtained outcome reveals that *FasL* gene is upregulated at the transcriptional level in bone marrow MKs upon mice infection. Moreover, the expressions of the same markers were screened for isolated PLTs from non-infected and infected mice at day 3 and day 6 as much like MKs (Fig. 5). Results demonstrated that except of *FasL* gene expression which was highly upregulated in infected PLTs in comparison to uninfected, while PLTs of both infected and non-infected mouse were unable to express genes related to all of *granzymes*, *perforin1*, *NKG2D*, and *NKp46* (Fig. 5). Thus, these results in the animals are important to investigate *in vivo* involvement of cytotoxic PLTs in IAV pathogenesis.

Here, this study extended to checking a large panel of other killing receptors. In all conditions, mRNA was extracted and whole-transcriptome analysis was performed on MKs and PLTs, the results of qRT-PCR revealed the differential gene expression in the different conditions. Indeed, no any receptors were significantly upregulated upon infected mice compared to uninfected (results not shown). Approximately all types of granzyme and perforin were not secreted by MKs and PLTs in resting situation or on their activation by IAV.

#### IV. DISCUSSION

The goal of the current research was to better understand the unexpected roles that PLTs and MKs play in immunity and as cytotoxic agents. Furthermore, to investigate the role of PLT activation and *FasL* gene expression in a physiological model of influenza virus infections, the current study aimed to comprehensively analyze their relationship and potential implications. A recent study shows that PLTs engulf influenza viruses *in vitro*, therefore, PLTs migration to the lungs is probably moving to do the same *in vivo* (Danon, Jerushalmy and De Vries, 1959). This could appear as the passive absorption of particles in a manner similar to bacterial ingestion (White, 2005). It is also possible to compare the uptake of IAVs by neutrophils and macrophages during the phagocytosis of human immunodeficiency viruses (Youssefian, et al., 2002). PLTs support the body's immunity against pathogenic bacterial infections by accelerating damage healing and reducing vascular lesions (Petaja, 2011; Engelmann and Massberg, 2013). PLT-neutrophil cross-talk mediates the early intrinsic resistance against influenza, it tightly controls host immune and complement responses but can potentially cause thrombotic vascular blockage (Koupenova, et al., 2019).

Supporting previous observations, obtained results demonstrated that plasma from infected mice contained signs of PLT activation. In response to a fatal IAV infection, PLTs and MKs were subsequently activated in the peripheral circulation and bone marrow, respectively. It's interesting to understand that the influenza virus activates PLTs by producing thrombin (Boilard, et al., 2014); thrombin primarily activates PAR4 and PAR1 to facilitate signal transduction (Kahn, et al., 1999; Kataoka, et al., 2003). This increases the possibility that thrombin may have a negative impact on IAV infection.

PAR4 and GPIIIa are two molecules that are crucial for PLT function. Due to the absence of PAR1 in mouse PLTs, thrombin-mediated PLT activation most likely happens through activating PAR4. As a result, fibrinolysis is a method by which PAR1 and plasminogen control pathogenesis. In addition, the results of the current study showed that IAV infection activated MKs and PLTs. This method was used to demonstrate several activation markers *in vivo* and *in vitro* (Figs. 3-5). These results specified that MKs and PLTs were highly activated upon infection with different strains of IAV in murine and in humans.

Additional result support current study which demonstrates that through thrombin production or Fc $\gamma$ R1IA signaling, the influenza virus stimulates PLTs (Boilard, et al., 2014). Moreover, PLTs' TXA2 and serotonin are released upon the thrombin activation, which later activates the GPIIb/IIIa complex, and enhances the movement of P-selectin to the PLT plasma membrane (Polley, et al., 1981).

The arsenal is potent proinflammatory chemicals generated by active PLTs that improve adhesion, recruitment, and neutrophil rolling (Mayadas, et al., 1993; Diacovo, et al., 1996; Von Hundelshausen, et al., 2001; Zarbock, Polanowska-Grabowska and Ley, 2007). According to recent study, during

the intense inflammation brought on by influenza, PLT interaction with neutrophils is anticipated to be considerable. The physical interaction from neutrophils to PLTs is another element in neutrophil retention and activation (Zarbock, Polanowska-Grabowska and Ley, 2007).

The particular *in vivo* and *in vitro* expression of killer receptors in MKs and PLTs has not yet been described. This study also showed that the *FasL* gene was highly expressed and upregulated among activated PLTs in both mice and humans, which is consistent with some reports suggesting that killing was FASL-dependent (Garcia-Garcia and Ramos, 2006). However, it was suggested that murine PLTs induce apoptosis through FasL on activation (Volpe, et al., 2016).

These findings were also confirmed among human PLTs, when apoptosis was induced in Fas-positive tumor cells after human PLTs activation (Ahmad, et al., 2001). These observations open a door to the discovery of a novel immunological role of PLTs and their regulation function during pathological conditions.

To the best of our knowledge, this investigation is the initial to use *in vivo* models to investigate the expression of immunological receptors in MKs and PLTs as viral infections progress. The member of the tumor necrosis factor (TNF) family includes Fas and Fas Ligand (FasL). Apoptosis, which is governed by the protein Fas-FasL, is a crucial process for maintaining immunological homeostasis (Volpe, et al., 2016). A caspases cascade that starts apoptosis is activated when Fas ligates with FasL (Ashkenazi and Dixit, 1998).

The present results show that MKs and PLTs exhibit *FasL* expression (see figures) which effectively shielded mice from the IAV pathogenesis brought on by a variety of influenza strains (data not shown). These outcomes are in agreement with earlier research demonstrating that through membrane-bound FasL, PLTs trigger apoptosis (Schleicher, et al., 2015). It is interesting to note that membrane-bound FasL was shown to be expressed by activated MKs; however, its exact purpose is yet unknown (Arabianian, et al., 2012).

The present study's findings showed that MKs and PLTs express *FasL* (see figures), which is successfully protecting mice from multiple influenza strains that cause IAV pathology in mice (data not shown). These findings align with those of prior research papers indicating that through membrane-bound FasL, PLTs trigger apoptosis (Schleicher, et al., 2015). It is interesting that activated MKs have been proven to express membrane-bound FasL, but its specific function is yet unknown (Arabianian, et al., 2012).

There are two main hypotheses that can be formulated to explain this increased PLT content in immune properties molecules. First, as PLTs arise from the membrane budding of MKs, they largely inherit their transcriptome and proteome from them. Differences in the expression of intracellular PLT cytotoxic molecules might be the result of their upregulation in MKs on direct virus infection or an exposition of an inflammatory environment (cytokines). Second, PLTs have mRNA and the entire translational machinery for protein synthesis, even though they lack a nucleus (Han and Baker, 1964; Rowley, et al., 2011). Accordingly, PLTs that are directly exposed to viruses might also differ in their protein

profile compared to uninfected PLTs. Both hypotheses are not exclusive and could act synergistically.

To test the first hypothesis, we isolated MKs from bone marrow of uninfected (NI) or infected mice (days 3 or 6 post-infection – ID3, ID6) by flow cytometry (based on the ploidy of MKs) and found that on IAV infection, the content of murine MKs in mRNA coding for most (KARs) *Granzymes*, *perforin1*, and *NKG2D* was significantly not upregulated [except *FasL*] when compared to MKs of uninfected mice (Fig. 4a), whereas western blot analysis revealed that infected mice had higher levels of FasL protein expression than uninfected (Fig. 4b). NIH/3T3 cells and peripheral blood mononuclear cells (PBMC) were used as negative and positive controls, respectively. Interestingly, all mRNA coding for cytotoxic molecules were not upregulated such as *NKp46*, suggesting that this regulation is MK specific and not due to contaminants of NK cells.

It has previously been proven that T cells require the membrane-bound form of FasL (LA, et al., 2009). Following PLT activation, the cell membrane has FasL exposed is triggered the apoptosis of the target cell in 6 h (Schleicher, et al., 2015). Moreover, as a result of viral infection in the eye, it has been discovered that FasL-dependent apoptosis can stop damaging inflammatory reactions (Griffith, et al., 1995). As a result, the protein profile of PLTs that are directly exposed to IAV or an inflammatory environment (cytokines) may be different from uninfected PLTs. In addition, the current study found that, despite the highly upregulated *FasL* gene in activated MKs and PLTs in both humans and mice, the *TRAIL*, *GNLY*, and *TNF* genes, which function as killer activation receptors and inhibitory receptors, respectively, were all significantly upregulated in infected human PLTs and CMK cell lines at the indicated time points compared to non-infected. These findings were consistent with some recent studies, which indicated that *TRAIL* (Morrell, et al., 2014), *CD154* (Arabianian, et al., 2012; Henn, et al., 2001), and *TNF $\alpha$*  (Liu, et al., 2001; Morrell, et al., 2014) were markedly expressed on MKs and PLTs activation. In addition, soluble and membrane-bound forms of functional *FasL* are expressed by activated PLTs and MKs (Josefsson, et al., 2014; Schleicher, et al., 2015).

This work show, for the first time, that neither in humans nor in mice were nearly all of the NK cytotoxic receptors expressed by MKs and PLTs in the resting or active states. Hence, the current investigation showed that MKs and PLTs have no cytotoxic role during the pathogenesis of *in vivo* and *in vitro* influenza virus infections. However, it's important to mention, these results show that PLTs and MKs were efficiently expressed (*FasL*, *TRAIL* and *TNF $\alpha$* ) after activation by IAV in human and mouse, while cytotoxic granules production were not demonstrated either among human or in murine in resting PLTs and MKs and also on their activations by IAV, except of *GNLY* granule gene expression in Flu patient *in vivo* (Fig. 3a) and among infected CMK cell lines *in vitro* (Fig. 6a).

The current data suggest that a novel treatment strategy for treating severe influenza would require looking into *FasL* expression in activated MKs and PLTs. FasL was found in

this work as an apoptotic receptor that is produced from MKs and PLTs. This finding requires additional work to investigate the part that possible pathways play in PLT-induced apoptosis. In addition, it also highlights the importance of FasL as an apoptotic immune element in activated MKs and PLTs during IAV pathogenicity.

It was suggested that PLTs express several pattern recognition receptors (PRRs) families as C-type lectin receptors (CLRs), toll-like receptors (TLRs), and NOD-like receptors (NLRs), which are highly conserved receptors, identify virus as a stranger (Chao, et al., 2019). Due to the activation of these receptors, the initial inflammation following IAV infection is linked to the release of cytokines and chemokine's (Koupenova, et al., 2019). It's interesting to note that PLT activation's increased cytokine production was only discovered later following infection (Dib, et al., 2020; Koupenova, et al., 2019).

Moreover, several immune cells are modulated by PLTs, which help to coordinate the immunological response (e.g., monocytes, lymphocytes, neutrophils, and dendritic cells). As well, during this process, immune cells, and PLTs work together to generate a physical barrier that stops pathogens from escaping and triggers immune system reactions that are innate and adaptive (Ebermeyer, et al., 2021).

Due to the fact that severe influenza virus infections are defined by the dysregulation of inflammation, it's probable that PLTs have a role in promoting inflammation and play a significant role in the development of IAV. In view of IAV outbreaks that consistently result in severe human infections, serious concerns have been raised about the therapeutic options available for these pathogens. This shows how urgently new antiviral techniques are required. New approaches that use drugs that target cellular proteins are thought to be less likely to promote resistance. Such cellular targets would be valuable for the treatment of most if not all influenza strains infections. In addition, the anti-influenza medications that are now on the market are only (modestly) effective when taken within 48 hours of infection. This treatment interval is usually exceeded in patients who are admitted to the hospital with severe influenza. It is well known that infectious respiratory viruses such as influenza A/B viruses, severe acute respiratory syndrome coronavirus 2 (SARS-CoV-2), and respiratory syncytial virus (RSV) infection, they attack from prominently the respiratory system and PLTs play a central role during this pathogenesis. Thus, antiplatelet drugs can circumvent the severity of the pathogenicity of these viruses.

In fact, the distinct role of PLTs is poorly understood, and the few findings that are available have been published in top publications. Considering that (KIRs) and (KARs) are little understood, this study investigated (KIRs) and (KARs) in PLTs and MKs in both physiological and pathological contexts using *in vitro*, *in vivo*, and clinical tools. Indicating that this study will definitely have an impact on the medical field and ultimately on the definition of PLT as a completely new type of immune cell. It is also noteworthy that many antiplatelet medications are already approved for humans use and are commercially available. Antiplatelet drugs are

well-known and documented; their pharmacovigilance (PV) and adverse effects have also been extensively established. Interestingly, future research is most required to offer a long-term perspective and provides an alternative management option for severe influenza, especially if the disease is caused by viral strains resistant to any of the currently available anti-influenza drugs.

## V. CONCLUSIONS

Altogether, these results suggest that MKs and PLTs have no cytotoxic function that can be induced in response to IAV infection. However, their role is limited to membrane-bound *FasL*, *TRAIL*, *GPLY*, and *TNFA* expressions and might open a new window to explore their immunological role during viral pathogenicity.

## VI. ACKNOWLEDGMENT

A great thanks to Prof. Marie-Christine ALESSI (PUPH) head of the C2VN research laboratory, Faculty of Medicine, Aix-Marseille University, for having provided all the facilities throughout the present study. Special thanks to Prof. Pierre MORANGE (Service d'Hématologie Biologique, CHU de Marseille - Hôpital de la Timone) and Prof. Pascal CHANEZ (APHM HOPITAL NORD) and their staff for providing patients samples and facilities.

## REFERENCES

- Ahmad, R., Menezes, J., Knafo, L., and Ahmad, A., 2001. Activated human platelets express Fas-L and induce apoptosis in Fas-positive tumor cells. *Journal of Leukocyte Biology*, 69(1), pp.123-128.
- Arabianian, L.S., Kujawski, S., Habermann, I., Ehninger, G., and Kiani, A., 2012. Regulation of fas/fas ligand-mediated apoptosis by nuclear factor of activated T cells in megakaryocytes. *British Journal of Haematology*, 156(4), pp.523-534.
- Ashkenazi, A., and Dixit, V.M., 1998. Death receptors: Signaling and modulation. *Science*, 281(5381), pp.1305-1308.
- Assinger, A., Schrottmaier, W.C., Salzman, M., and Rayes, J., 2019. Platelets in sepsis: An update on experimental models and clinical data. *Frontiers in Immunology*, 10, p.1687.
- Baier, G., Telford, D., Gulbins, E., Yamada, N., Kawakami, T., and Altman, A., 1993. Improved specificity of RT-PCR amplifications using nested cDNA primers. *Nucleic Acids Research*, 21(5), pp.1329-1330.
- Boilard, E., Pare, G., Rousseau, M., Cloutier, N., Dubuc, I., Levesque, T., Borgeat, P., and Flamand, L., 2014. Influenza virus H1N1 activates platelets through FcγRIIA signaling and thrombin generation. *Blood*, 123(18), pp.2854-2863.
- Chao, C.H., Wu, W.C., Lai, Y.C., Tsai, P.J., Perng, G.C., Lin, Y.S., and Yeh, T.M., 2019. Dengue virus nonstructural protein 1 activates platelets via Toll-like receptor 4, leading to thrombocytopenia and hemorrhage. *PLOS Pathogens*, 15(4), pp.e1007625.
- Crist, S.A., Elzey, B.D., Ludwig, A.T., Griffith, T.S., Staack, J.B., Lentz, S.R., and Ratliff, T.L., 2004. Expression of TNF-related apoptosis-inducing ligand (TRAIL) in megakaryocytes and platelets. *Experimental Hematology*, 32(11), pp.1073-1081.
- Crist, S.A., Sprague, D.L., and Ratliff, T.L., 2008. Nuclear factor of activated T cells (NFAT) mediates CD154 expression in megakaryocytes. *Blood*, 111(7), pp.3553-3561.

- Danon, D., Jerushalmy, Z., and De Vries, A., 1959. Incorporation of influenza virus in human blood platelets *in vitro*. Electron microscopical observation. *Virology*, 9, pp.719-722.
- Deutsch, V.R., and Tomer, A., 2006. Megakaryocyte development and platelet production. *British Journal of Haematology*, 134(5), pp.453-466.
- Diacovo, T.G., Roth, S.J., Buccola, J.M., Bainton, D.F., and Springer, T.A., 1996. Neutrophil rolling, arrest, and transmigration across activated, surface-adherent platelets via sequential action of P-selectin and the beta 2-integrin CD11b/CD18. *Blood*, 88(1), pp.146-157.
- Dib, P.R.B., Quirino-Teixeira, A.C., Merij, L.B., Pinheiro, M.B.M., Rozini, S.V., Andrade, F.B., and Hottz, E.D. 2020. Innate immune receptors in platelets and platelet-leukocyte interactions. *Journal of Leukocyte Biology*, 108(4), pp.1157-1182.
- Ebermeyer, T., Cognasse, F., Berthelot, P., Mismetti, P., Garraud, O., and Hamzeh-Cognasse, H., 2021. Platelet innate immune receptors and TLRs: A double-edged sword. *International Journal of Molecular Sciences*, 22(15): 7894.
- Engelmann, B., and Massberg, S., 2013. Thrombosis as an intravascular effector of innate immunity. *Nature Reviews Immunology*, 13(1), pp.34-45.
- Garcia-Garcia, J., and Ramos, C., 2006. Influenza, an existing public health problem. *Salud Pública de México*, 48(3), pp.244-267.
- Griffith, T.S., Brunner, T., Fletcher, S.M., Green, D.R., and Ferguson, T.A., 1995. Fas ligand-induced apoptosis as a mechanism of immune privilege. *Science*, 270(5239), pp.1189-1192.
- Hamzeh-Cognasse, H., Damien, P., Chabert, A., Pozzetto, B., Cognasse, F., and Garraud, O., 2015. Platelets and infections-complex interactions with bacteria. *Frontiers in Immunology*, 6, p.82.
- Han, S.S., and Baker, B.L., 1964. The ultrastructure of megakaryocytes and blood platelets in the rat spleen. *The Anatomical Record*, 149, pp.251-267.
- Henn, V., Steinbach, S., Buchner, K., Presek, P., and Kroczyk, R.A., 2001. The inflammatory action of CD40 ligand (CD154) expressed on activated human platelets is temporally limited by coexpressed CD40. *Blood*, 98(4), pp.1047-1054.
- Hoffmann, E., Stech, J., Guan, Y., Webster, R.G., and Perez, D.R., 2001. Universal primer set for the full-length amplification of all influenza A viruses. *Archives of Virology*, 146(12), pp.2275-2289.
- Ibele, G.M., Kay, N.E., Johnson, G.J., and Jacob, H.S., 1985. Human platelets exert cytotoxic effects on tumor cells. *Blood*, 65(5), pp.1252-1255.
- Iuliano, A.D., Roguski, K.M., Chang, H.H., Muscatello, D.J., Palekar, R., Tempia, S., Cohen, C., Gran, J.M., Schanzer, D., Cowling, B.J., Wu, P., Kyncl, J., Ang, L.W., Park, M., Redlberger-Fritz, M., Yu, H., Espenhain, L., Krishnan, A., Emukule, G., van Asten, L., Pereira da Silva, S., Aungkulanon, S., Buchholz, U., Widdowson, M.A., Bresee, J.S., and Global Seasonal Influenza-associated Mortality Collaborator, N., 2018. Estimates of global seasonal influenza-associated respiratory mortality: a modelling study. *Lancet*, 391(10127), pp.1285-1300.
- Jirouskova, M., Shet, A.S., and Johnson, G.J., 2007. A guide to murine platelet structure, function, assays, and genetic alterations. *Journal of Thrombosis and Haemostasis*, 5(4), pp.661-669.
- Josefsson, E.C., Burnett, D.L., Lebois, M., Debrincat, M.A., White, M.J., Henley, K.J., Lane, R.M., Moujalled, D., Preston, S.P., O'Reilly, L.A., Pellegrini, M., Metcalf, D., Strasser, A., and Kile, B.T., 2014. Platelet production proceeds independently of the intrinsic and extrinsic apoptosis pathways. *Nature Communications*, 5, pp.3455.
- Joseph, M., Aurialt, C., Capron, A., Vorng, H., and Viens, P., 1983. A new function for platelets: IgE-dependent killing of schistosomes. *Nature*, 303(5920), pp. 810-812.
- Kahn, M.L., Nakanishi-Matsui, M., Shapiro, M.J., Ishihara, H., and Coughlin, S.R., 1999. Protease-activated receptors 1 and 4 mediate activation of human platelets by thrombin. *Journal of Clinical Investigation*, 103(6), pp.879-887.
- Kataoka, H., Hamilton, J.R., McKemy, D.D., Camerer, E., Zheng, Y.W., Cheng, A., Griffin, C., and Coughlin, S.R., 2003. Protease-activated receptors 1 and 4 mediate thrombin signaling in endothelial cells. *Blood*, 102(9), pp.3224-3231.
- Koupenova, M., Corkrey, H.A., Vitseva, O., Manni, G., Pang, C.J., Clancy, L., Yao, C., Rade, J., Levy, D., Wang, J.P., Finberg, R.W., Kurt-Jones, E.A., and Freedman, J.E., 2019. The role of platelets in mediating a response to human influenza infection. *Nature Communications*, 10(1), pp.1780.
- LA, O.R., Tai, L., Lee, L., Kruse, E.A., Grabow, S., Fairlie, W.D., Haynes, N.M., Tarlinton, D.M., Zhang, J.G., Belz, G.T., Smyth, M.J., Bouillet, P., Robb, L., and Strasser, A. 2009. Membrane-bound Fas ligand only is essential for Fas-induced apoptosis. *Nature*, 461(7264), pp.659-663.
- Lefrancais, E., Ortiz-Munoz, G., Caudrillier, A., Mallavia, B., Liu, F., Sayah, D.M., Thornton, E.E., Headley, M.B., David, T., Coughlin, S.R., Krummel, M.F., Leavitt, A.D., Passegue, E., and Looney, M.R. 2017. The lung is a site of platelet biogenesis and a reservoir for haematopoietic progenitors. *Nature*, 544(7648), pp.105-109.
- Li, L., Wong, J.Y., Wu, P., Bond, H.S., Lau, E.H.Y., Sullivan, S.G., and Cowling, B.J., 2018. Heterogeneity in estimates of the impact of influenza on population mortality: A systematic review. *American Journal of Epidemiology*, 187(2), pp.378-388.
- Liu, S., Yu, Y., Zhang, M., Wang, W., and Cao, X., 2001. The involvement of TNF-alpha-related apoptosis-inducing ligand in the enhanced cytotoxicity of IFN-beta-stimulated human dendritic cells to tumor cells. *Journal of Immunology*, 166(9), pp.5407-5415.
- Machlus, K.R., and Italiano, J.E., Jr. 2013. The incredible journey: From megakaryocyte development to platelet formation. *Journal of Cell Biology*, 201(6), pp.785-796.
- Mayadas, T.N., Johnson, R.C., Rayburn, H., Hynes, R.O., and Wagner, D.D., 1993. Leukocyte rolling and extravasation are severely compromised in P selectin-deficient mice. *Cell*, 74(3), pp.541-554.
- McMorran, B.J., Marshall, V.M., de Graaf, C., Drysdale, K.E., Shabbar, M., Smyth, G.K., Corbin, J.E., Alexander, W.S., and Foote, S.J., 2009. Platelets kill intraerythrocytic malarial parasites and mediate survival to infection. *Science*, 323(5915), pp.797-800.
- Miller, S.A., Dykes, D.D., and Polesky, H.F. 1988. A simple salting out procedure for extracting DNA from human nucleated cells. *Nucleic Acids Research*, 16(3), pp.1215.
- Morrell, C.N., Aggrey, A.A., Chapman, L.M., and Modjeski, K.L., 2014. Emerging roles for platelets as immune and inflammatory cells. *Blood*, 123(18), pp.2759-2767.
- Organization, W.H. 2022. *Up to 650 000 People Die of Respiratory Diseases Linked to Seasonal Flu Each Year*. Available from: <https://www.who.int/news/item/13-12-2017-up-to-650-000-people-die-of-respiratory-diseases-linked-to-seasonal-flu-each-year-2022> [Last accessed on 2023 May 01].
- Paget, J., Spreeuwenberg, P., Charu, V., Taylor, R.J., Iuliano, A.D., Bresee, J., Simonsen, L., Viboud, C., Global Seasonal Influenza-associated Mortality Collaborator, N., and Teams, G.L.C., 2019. Global mortality associated with seasonal influenza epidemics: New burden estimates and predictors from the GLaMOR Project. *Journal of Global Health*, 9(2), pp.020421.
- Patel, S.R., Hartwig, J.H., and Italiano, J.E., Jr. 2005. The biogenesis of platelets from megakaryocyte proplatelets. *Journal of Clinical Investigation*, 115(12), pp.3348-3354.
- Perrone, L.A., Plowden, J.K., Garcia-Sastre, A., Katz, J.M., and Tumpey, T.M., 2008. H5N1 and 1918 pandemic influenza virus infection results in early and excessive infiltration of macrophages and neutrophils in the lungs of mice. *PLOS Pathogens*, 4(8), pp.e1000115.
- Petaja, J., 2011. Inflammation and coagulation. An overview. *Thrombosis Research*, 127(Suppl 2), pp.S34-S37.
- Polley, M.J., Leung, L.L., Clark, F.Y., and Nachman, R.L., 1981. Thrombin-induced platelet membrane glycoprotein IIb and IIIa complex formation.

- An electron microscope study. *Journal of Experimental Medicine*, 154(4), pp.1058-1068.
- Rahman, F., Libre, C., Oleinikov, A., and Tcherniuk, S., 2021. Chloroquine and pyrimethamine inhibit the replication of human respiratory syncytial virus A. *Journal of General Virology*, 102(8), 001627.
- Rowley, J.W., Oler, A.J., Tolley, N.D., Hunter, B.N., Low, E.N., Nix, D.A., Yost, C.C., Zimmerman, G.A., and Weyrich, A.S., 2011. Genome-wide RNA-seq analysis of human and mouse platelet transcriptomes. *Blood*, 118(14), pp.e101-e111.
- Schleicher, R.I., Reichenbach, F., Kraft, P., Kumar, A., Lescan, M., Todt, F., Gobel, K., Hilgendorf, I., Geisler, T., Bauer, A., Olbrich, M., Schaller, M., Wesselborg, S., O'Reilly, L., Meuth, S.G., Schulze-Osthoff, K., Gawaz, M., Li, X., Kleinschnitz, C., Edlich, F., and Langer, H.F., 2015. Platelets induce apoptosis via membrane-bound FasL. *Blood*, 126(12), pp.1483-1493.
- Tate, M.D., Deng, Y.M., Jones, J.E., Anderson, G.P., Brooks, A.G., and Reading, P.C. 2009. Neutrophils ameliorate lung injury and the development of severe disease during influenza infection. *Journal of Immunology*, 183(11), pp.7441-7450.
- Volpe, E., Sambucci, M., Battistini, L., and Borsellino, G., 2016. Fas-Fas Ligand: Checkpoint of T Cell Functions in Multiple Sclerosis. *Frontiers in Immunology*, 7, pp.382.
- Von Hundelshausen, P., Weber, K.S., Huo, Y., Proudfoot, A.E., Nelson, P.J., Ley, K., and Weber, C., 2001. RANTES deposition by platelets triggers monocyte arrest on inflamed and atherosclerotic endothelium. *Circulation*, 103(13), pp.1772-1777.
- White, J.G., 2005. Platelets are coverocytes, not phagocytes: Uptake of bacteria involves channels of the open canalicular system. *Platelets*, 16(2), pp.121-131.
- Yeaman, M.R., 2010. Platelets in defense against bacterial pathogens. *Cellular and Molecular Life Sciences*, 67(4), pp.525-544.
- Youssefian, T., Drouin, A., Masse, J.M., Guichard, J., and Cramer, E.M. 2002. Host defense role of platelets: Engulfment of HIV and *Staphylococcus aureus* occurs in a specific subcellular compartment and is enhanced by platelet activation. *Blood*, 99(11), pp.4021-4029.
- Zarbock, A., Polanowska-Grabowska, R.K., and Ley, K., 2007. Platelet-neutrophil-interactions: Linking hemostasis and inflammation. *Blood Reviews*, 21(2), pp.99-111.

# A Compact Negative Group Delay Microstrip Diplexer with Low Losses for 5G Applications: Design and Analysis

Leila Nouri<sup>1,2</sup>, Salah I. Yahya<sup>3,4</sup>, Abbas Rezaei<sup>5</sup>, Fawwaz Hazzazi<sup>6</sup> and B. N. Nhu<sup>1,2</sup>

<sup>1</sup>Institute of Research and Development, Duy Tan University, Da Nang, Vietnam

<sup>2</sup>School of Engineering and Technology, Duy Tan University, Da Nang, Vietnam

<sup>3</sup>Department of Communication and Computer Engineering, Cihan University-Erbil, Erbil, Iraq

<sup>4</sup>Department of Software Engineering, Faculty of Engineering, Koya University, Koya, KOY45, Iraq

<sup>5</sup>Department of Electrical Engineering, Kermanshah University of Technology, Kermanshah, Iran

<sup>6</sup>Department of Electrical Engineering, College of Engineering in Al-Kharj, Prince Sattam bin Abdulaziz University, AlKharj 11492, Saudi Arabia

**Abstract**—A novel compact microstrip diplexer based on spiral cells is presented in this paper. The proposed resonator primarily consists of two spiral thin lines connected to a pair of coupled lines. This novel resonator is analyzed mathematically to find its behavior and tune the dimensions of the final layout easily. Using the analyzed resonator, two bandpass filters (BPFs) are designed. Then, a novel high-performance microstrip diplexer is obtained by designing and integrating these BPFs. The proposed diplexer boasts a remarkably small size of  $0.004 \lambda g^2$  and features flat channels with low insertion losses of only 0.048 dB and 0.065 dB. The maximum group delays of  $S_{21}$  and  $S_{31}$  are 0.31 ns and 0.86 ns, respectively, which are good values for modern communication system. Meanwhile, inside its passbands for some frequency ranges its group delays are negative. Thus, using this diplexer can decrease the signal dispersion. The first and second passbands are wide with 47.3% and 47.1% fractional bandwidths, respectively. Therefore, this diplexer can be easily used in designing high-performance radio frequency communication systems.

**Index Terms**—5G, Diplexer, Group delay, Microstrip.

## I. INTRODUCTION

There has been a growing demand for passive filtering microstrip devices with a planar structure and low cost by modern radio frequency (RF) communication systems (Jamshidi, et al., 2023; Yahya, Rezaei and Khaleel, 2021; Yahya and Rezaei, 2021; Rezaei and Yahya, 2022; Yahya,

Rezaei and Nouri, 2020; Hosseini and Rezaei, 2020; Yahya and Rezaei 2020; Fadaee, et al., 2023; Afzali, et al., 2021). A microstrip diplexer is an electronic device that allows two different frequency bands to be transmitted and received simultaneously through a single antenna. It consists of two bandpass filters (BPFs) with different center frequencies, connected in parallel. The main application of a diplexer is in wireless communication systems, such as cellular networks and satellite communication. It enables the sharing of a single antenna for multiple frequency bands, reducing the number of antennas needed, and hence the cost and complexity of the system (Al-Majdi and Mezaal, 2023; Deng, Xu and Zheng, 2023; Chaudhary, Roshani and Shabani, 2023). Several different microstrip configurations are presented to create diplexers for wireless RF applications. A cross-band microstrip diplexer is presented in (Duan, et al., 2023). The dual-mode squared shape BPFs are used to obtain a microstrip diplexer in (Alnagar, et al., 2022). The common problems of the proposed diplexers in (Al-Majdi and Mezaal, 2023; Deng, Xu and Zheng, 2023; Chaudhary, Roshani and Shabani, 2023; Duan, et al., 2023; Alnagar, et al., 2022) are their high insertion losses and large dimensions. Based on a new resonator, a compact diplexer is proposed in (Yahya, Rezaei and Nouri, 2021) which works at 3 GHz and 1.4 GHz for S-band and L-band wireless applications. Various techniques have been employed to achieve microstrip diplexers, including folded open-loop ring resonators, stub-loaded coupled U-shape cells, meandrous and patch cells, a transmission line that is composite right/left handed and free of vias, and stub-loaded coupled open loops. These techniques have been applied to be effective in designing microstrip diplexers with desired characteristics such as high selectivity, low insertion loss, and compact size. Each of these techniques has its advantages and disadvantages and the selection of

ARO-The Scientific Journal of Koya University  
Vol. XI, No. 2 (2023), Article ID: ARO.11237, 8 pages  
DOI: 10.14500/aro.11237

Received 06 July 2022; Accepted: 25 July 2022

Regular research paper: Published 25 August 2023

Corresponding author's, e-mail: leilanouri@duytan.edu.vn

Copyright © 2023 Leila Nouri, Salah I. Yahya, Abbas Rezaei, Fawwaz Hazzazi and B. N. Nhu. This is an open access article distributed under the Creative Commons Attribution License.



technique depends on the particular requirements of the diplexer application. Folded open-loop ring resonators in (Feng, Zhang and Che, 2017), stub-loaded coupled U-shape cells in (Huang, et al., 2016), the meandrous and patch cells in (Rezaei and Noori, 2018), a transmission line that is composite right/left handed and free of vias in (Kumar and Upadhyay, 2019), and stub-loaded coupled open loops in (Rezaei, et al., 2019) are utilized to achieve microstrip diplexers. The patch and thin cells are combined in (Rezaei, Yahya and Jamaluddin, 2020) for designing a microstrip diplexer, which is suitable for GSM applications. The reported diplexers in (Zhou, et al., 2018; Rezaei and Noori, 2020; Danaeian, 2020; Roshani and Roshani, 2019; Rezaei, et al., 2019) have narrow channels. On the other hand, the common problem of the microstrip diplexers in (Feng, Zhang and Che, 2017; Huang, et al., 2016; Rezaei and Noori, 2018; Kumar and Upadhyay, 2019; Rezaei, et al., 2019; Rezaei, Yahya and Jamaluddin, 2020; Zhou, et al., 2018; Rezaei and Noori, 2020; Danaeian, 2020; Roshani and Roshani, 2019; Rezaei, et al., 2019) is their large implementation areas. Meanwhile, they could not improve group delay. Although group delay is important, only a few diplexer designers have made attempts to improve it. However, a number of designers of the other passive microstrip filtering devices have investigated group delay (Nouri, Yahya and Rezaei, 2020; Xu, Chen and Wan, 2020; Rezaei, Yahya and Nouri, 2023; Hayati, Rezaei and Noori, 2019; Hayati, et al., 2021; Liu, 2010; Chen et al., 2015; Noori and Rezaei, 2017; Lin, 2011). Since, the negative group delay circuits can be used to compensate dispersion, designing microwave circuits with a negative group delay is very important (Ahn, Ishikawa and Honjo, 2009; Chaudhary, Jeong and Lim, 2014; Ravelo, et al., 2020; Shao, et al., 2017).

This work presents the design of a diplexer for 5G mid-band applications, which utilizes a novel and compact microstrip structure. This diplexer operates at 1.86 GHz and 4.62 GHz, which are the two frequency bands of interest for 5G mid-band communication. The channels of this diplexer are wide and flat, ensuring that the signal loss is minimized and that the diplexer has a high selectivity. In addition, the group delays of  $S_{21}$  and  $S_{31}$  are negative at some frequencies, which is desirable for some specific applications. To achieve this design, a perfect mathematical method consisting of the resonator design is applied. This method allows for the tuning of the operating frequency and miniaturization of the diplexer simultaneously. The resonator is used to obtain two BPFs, which are then integrated to form the proposed diplexer. The resonator design plays a crucial role in the performance of the diplexer. The resonator is designed using a combination of a rectangular patch and a meander line. The rectangular patch acts as the radiating element, while the meander line is used to increase the resonant frequency of the patch. The resonator is then coupled to a microstrip transmission line to form a BPF.

The design of the BPF is optimized using a simulation tool, which allows for the adjustment of the dimensions of the resonator to achieve the desired frequency response.

The optimized BPF is then integrated with another BPF to form the proposed diplexer. The final diplexer design is compact and has a low insertion loss, making it suitable for use in 5G mid-band communication systems. The performance of the proposed diplexer is confirmed using simulation and comparison with the other designs. The results show that the diplexer has a high selectivity and low insertion loss at the desired frequencies of 1.86 GHz and 4.62 GHz.

## II. THE PROPOSED RESONATOR: DESIGN AND ANALYSIS

Fig. 1 depicts the proposed resonator and its approximated LC circuit. It includes a pair of coupled lines and two spiral cells. If we set the physical lengths of coupled lines equal to  $2l_3$ , then an approximated equivalent of them consists of the inductors and capacitors  $L_3$  and  $C$  respectively. In this case, we assume that the equivalent of the physical length  $l_3$  is the inductor  $L_3$ . Furthermore, the open ends of coupled lines are depicted by the capacitors  $C_o$ . The equivalent of spiral cell1 and the physical length  $l_1$  is presented by  $L_1$ . Similarly,  $L_2$  is an equivalent of spiral cell 2 and the physical length  $l_2$ .

The open end capacitors are small so that we can remove them for easier calculations. Under this condition, the equivalent impedance between the terminals ( $Z_{eq}$ ) is:

$$Z_{eq} = \frac{1}{\frac{1}{\frac{1}{2j\omega L_3 + \frac{1}{j\omega C}} + j\omega C} + j\omega(L_1 + L_2)} \quad (1)$$

Where  $\omega$  is an angular frequency. After simplifying Equation (1), it can be written as:

$$Z_{eq} = \frac{1 - 3\omega^2 C(2L_3 + L_1 + L_2) + 4\omega^4 C^2 L_3(L_3 + 2L_1 + 2L_2)}{j\omega C(3 - 8\omega^2 L_3 C + 4\omega^4 C^2 L_3^2)} \quad (2)$$

The coupling capacitor  $C$  (in fF) is usually a small capacitor and the inductors are in nH ranges. To easy calculation, the following approximations can be used:

$$\begin{aligned} &3\omega^2 C(2L_3 + L_1 + L_2) \gg 4\omega^4 C^2 L_3(L_3 + 2L_1 + 2L_2) \\ &3\omega^2 C(2L_3 + L_1 + L_2) \gg 4\omega^6 C^3 L_3^2(L_1 + L_2) \\ &j\omega C(3 - 8\omega^2 L_3 C + 4\omega^4 C^2 L_3^2) \approx 3j\omega C \end{aligned} \quad (3)$$

The presented approximations in Equation (3) should be used for an angular frequency in GHz. By applying Equation (3) in Equation (2), the approximated equivalent impedance can be derived as follows:

$$Z_{eq} \approx \frac{1 - 3\omega^2 C(2L_3 + L_1 + L_2)}{3j\omega C} \quad (4)$$

Using  $Z_{eq}$ , the  $ABCD$  matrix of the proposed resonator ( $T$ ) can be given by:



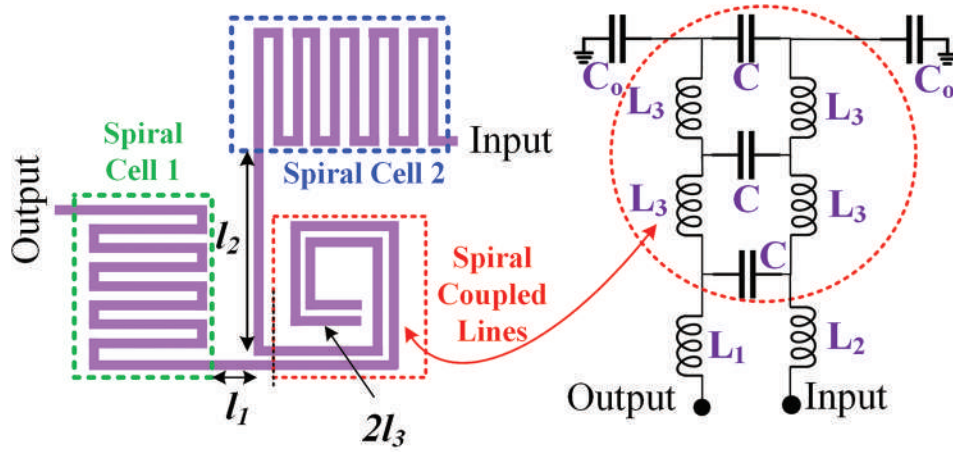


Fig. 1. Proposed basic resonator: Layout and equivalent LC model.

$$T = \begin{bmatrix} A & B \\ C & D \end{bmatrix} = \begin{bmatrix} 1 & \frac{1-3\omega^2 C(2L_3+L_1+L_2)}{3j\omega C} \\ 0 & 1 \end{bmatrix} \quad (5)$$

The  $ABCD$  matrix can be used to calculate the scattering parameters. For example  $S_{21}$  is calculated as follows:

$$S_{21} = \frac{6j\omega CZ_0}{6j\omega CZ_0 + 1 - 3\omega^2 C(2L_3 + L_1 + L_2)} \quad (6)$$

In Equation (6),  $Z_0$  is the impedance of the terminals, which is  $50 \Omega$  for this work. At the operating frequency, the insertion loss should be a very small value. Since the insertion loss is  $-20 \log|S_{21}|$ , for minimizing we can set  $|S_{21}|=1$  as follows:

$$\begin{aligned} |S_{21}|=1 &\rightarrow 1 - 3(2\pi f_0)^2 C(2L_3 + L_1 + L_2) \\ &= 0 \rightarrow f_0 = \frac{1}{2\pi \sqrt{3C(2L_3 + L_1 + L_2)}} \end{aligned} \quad (7)$$

In Equation (7),  $f_0$  is the operating frequency of the proposed basic resonator. If the gap of coupled lines is adjusted so that the capacitor  $C$  becomes in the range of  $10^{-12} F$ , the inductors can be selected in the nH ranges. In this case, the operating frequency will be in GHz ranges. For a predetermined operating frequency, the values of  $L_1$ ,  $L_2$ , and  $L_3$  can be tuned with a high degree of freedom. Therefore, by adjusting the physical lengths of spiral cells, we can miniaturize the resonator size easily. Using the analyzed resonator, we presented two BPFs (BPF1 and BPF2). These filters and their frequency responses are presented in Fig. 2, where all dimensions are in mm. Moreover, the widths of all thin lines are 0.1 mm. The proposed BPFs are simulated on a Rogers RT/Duroid5880 substrate with 2.22 dielectric constant,  $\tan(\delta)=0.0009$  and  $h = 31$  mil. All simulation results are extracted using ADS software (EM simulator) in 5MHz linear steps. The information about the frequency responses is shortened in Table I.

As shown in Table I, both filters have low insertion losses which was the purpose of our mathematical analysis. The maximum group delays of  $S_{21}$  for both filters are low. By

integrating the proposed BPFs, our diplexer can be obtained as shown in Fig. 3. We did not change the dimensions of our filters in the final diplexer structure. Therefore, all dimensions are in mm and the widths of all thin lines are 0.1 mm. Both filters are connected directly without needing to any extra matching circuits. Thus, the overall size is saved again. The proposed diplexer has a total size of just  $11.3 \text{ mm} \times 5.7 \text{ mm}$  (equivalent to  $0.004 \lambda_g^2$ ), with  $\lambda_g$  being the guided wavelength calculated at the first operating frequency of the presented diplexer.

The important parameters in determining the frequency response are specified, which are shown in Fig. 3 as  $l_A$ ,  $l_B$ ,  $S_C$ ,  $S_D$ ,  $l_E$ , and  $l_F$ . The frequency responses as functions of these parameters are shown in Fig.4. As shown in this figure, by decreasing the physical length of spiral cell  $l_A$ , the insertion loss at the lower channel will be increased. However, we should try to increase the dimensions of this cell so that it does not lead to an increase in the overall size. Since spiral cell B is directly connected to the common port, its dimension has a direct impact on the both channels. Decreasing the length of this cell increases the insertion loss at the lower channel. Increasing the length of spiral cell B shifts the first channel to the left. However, it creates some harmonics inside the higher channel. Changing the gaps between coupled lines  $S_C$  and  $S_D$  affects the insertion losses of the first and second passbands, respectively. Changing the physical lengths  $l_E$  and  $l_F$  has no impact on the first channel. However, reducing the lengths  $l_E$  and  $l_F$  destroys the second passband.

### III. RESULTS AND COMPARISON

Fig. 5a and b show the simulated scattering parameters of the designed diplexer. Operating at 1.8 GHz and 4.6 GHz, the introduced diplexer exhibits exceptionally low insertion losses of only 0.048 dB and 0.065 dB, respectively. Both channels are flat and wide, where both of them have 47% fractional bandwidths (FBW). Meanwhile, The lower and upper channels exhibit return losses of 43.8 dB and 27.6 dB, respectively. The isolation of the output ports is better than  $-19.88$  dB from DC to 7 GHz. As can be seen, after the first channel we could suppress harmonics up to 7GHz

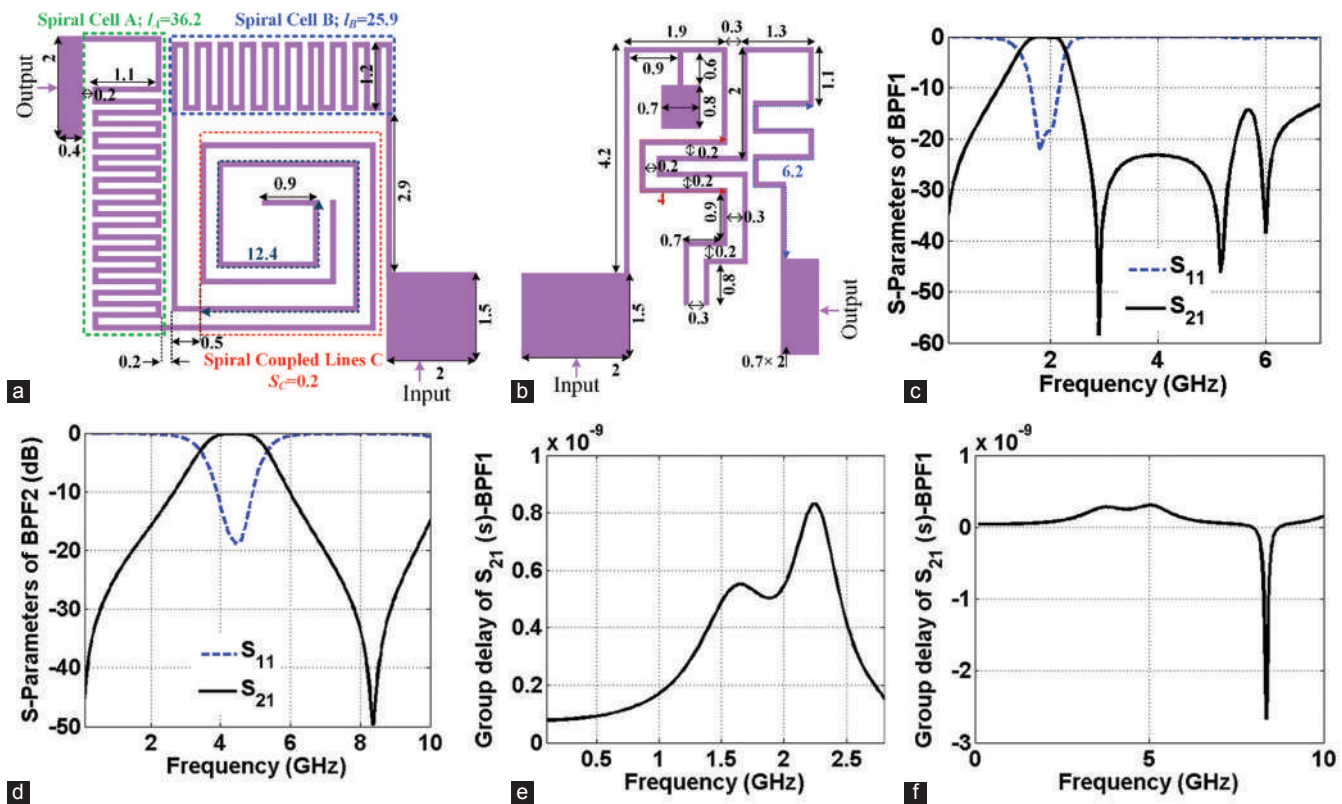


Fig. 2. Proposed bandpass filters (BPFs) and their simulated frequency responses, (a) BPF1, (b) BPF2, (c) BPF1 frequency response, (d) BPF2 frequency response, (e) group delay of BPF1, and (f) group delay of BPF2.

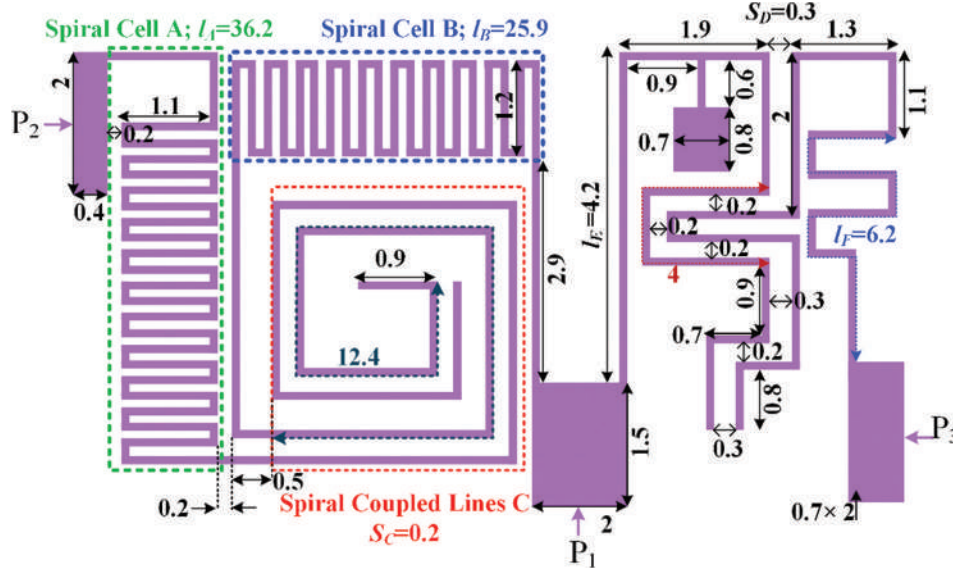


Fig. 3. Layout of the proposed microstrip diplexer.

with  $-14.4$  dB maximum level. Consequently, it is capable of suppressing harmonics from the first up to the sixth harmonics after the lower passband. The group delays of  $S_{21}$  and  $S_{31}$  (related to the suggested diplexer) are presented in Fig. 5c and d. As can be seen, in some frequencies inside the channels, the group delays have negative values which is an advantage (Ahn, Ishikawa and Honjo, 2009; Chaudhary, Jeong and Lim, 2014; Ravelo, et al., 2020; Shao, et al.,

2017). At the lower and upper channels, the maximum group delays are  $0.3$  ns and  $0.8$  ns, which are acceptable for modern wireless communication systems.

To verify the advantages of the designed microstrip diplexer, a comparison was made with the previously reported microstrip diplexers. The comparison was based on the main diplexer parameters such as insertion loss, operating frequency, return loss, group delay, and FBW. The obtained

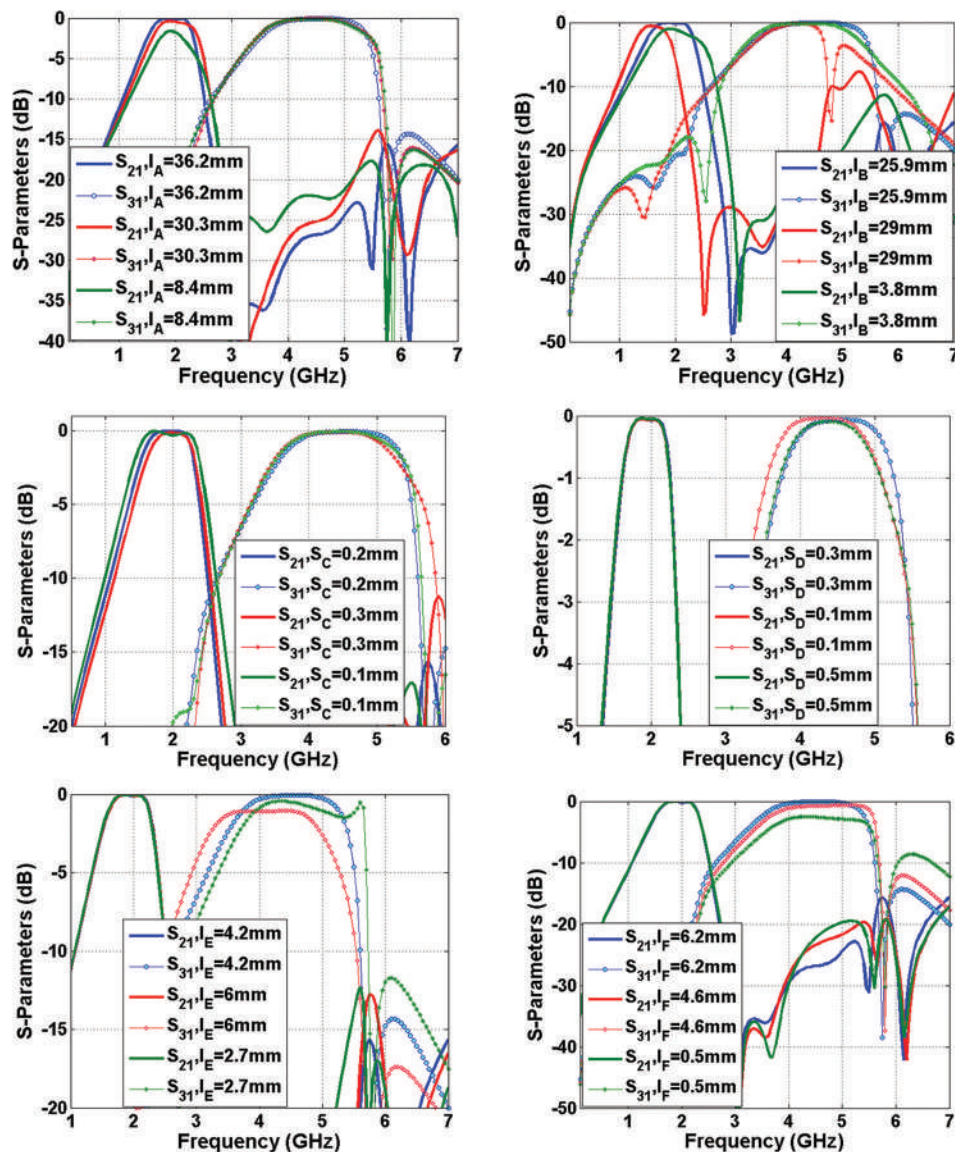


Fig. 4. Frequency responses of the proposed diplexer as functions of  $I_A$ ,  $I_B$ ,  $S_C$ ,  $S_D$ ,  $I_E$ , and  $I_F$ .

TABLE I  
SUMMARIZED SIMULATION RESULTS OF THE PROPOSED BPFs

Filters	BPF1	BPF2
$f_o$ (GHz)	1.82	4.5
Insertion loss (dB)	0.042	0.098
Return loss (dB)	22.66	18.8
Maximum harmonic level (dB)	-15	-15
Last frequency with suppressed harmonics (GHz)	6.94	10
Maximum group delay at passband (NS)	0.83	0.3
Fractional bandwidth (%)	50.14	28.2

BPF: Bandpass filters, NS: Not significant

results of the comparison are summarized in Tables II and III. In the comparison tables, the parameters  $f_o$ , IL, RL, and FBW are the operating frequency, insertion loss, return loss, and FBW, respectively. In addition, index 1 corresponds to the first channel, while index 2 corresponds to the second channel. According to Table II, the designed diplexer has

significant advantages over the previously reported microstrip diplexers. It has the smallest size and the widest channels, with the lowest insertion losses and best return loss at all channels. These results demonstrate the effectiveness of the designed novel compact structure in achieving high performance microstrip diplexers. In Table III, the group delay of our diplexer is compared with the previous passive filtering microstrip devices. It was found that the group delay of the designed diplexer is better than all of the previously reported devices. This indicates that the diplexer has better phase characteristics, which is essential for applications such as signal processing and data communication. Overall, the comparison results demonstrate that the designed microstrip diplexer using the novel compact structure has significant advantages over the previous microstrip diplexers in terms of size, performance, losses, and group delay. These advantages make it a promising candidate for use in wireless

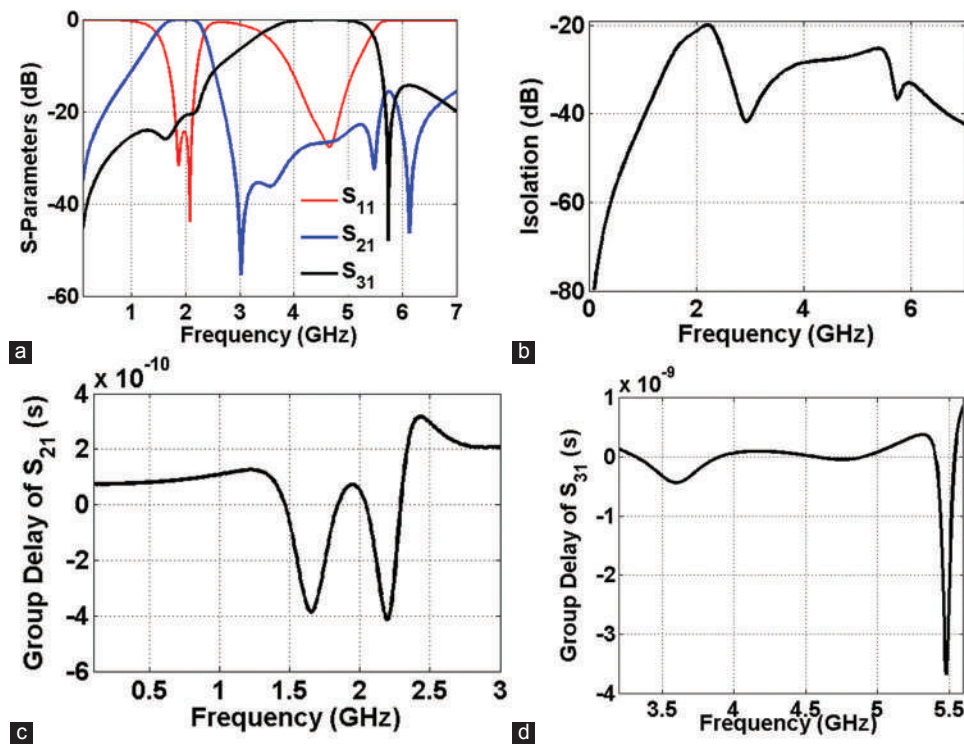


Fig. 5. Proposed diplexer, (a) scattering parameters, (b)  $S_{23}$ , (c) group delay of  $S_{21}$ , and (d) group delay of  $S_{31}$ .

TABLE II  
COMPARISON BETWEEN THE DESIGNED DIPLEXER AND THE PREVIOUS WORKS

References	$f_{o1}-f_{o2}$ (GHz)	$IL_1-IL_2$ (dB)	$RL_1-RL_2$ (dB)	$FBW_1\%-FBW_2\%$	Size ( $\lambda g^2$ )
This diplexer	1.86–4.62	0.048–0.065	43.8–27.6	47.3–47.1	0.004
Al-Majdi and Mezaal, 2023	2.84–4.08	0.7–0.9	21.2–17	1.41–2.2	-
Deng, Xu and Zheng, 2023	16–18.3	1.3–1.36	19–17	2.5–2.3	-
Chaudhary, Roshani and Shabani, 2023	2.1–5.1	0.3–0.4	10–18	14–4	0.083
Duan, et al., 2023	-	1.6–2.6	15.6–15	-	-
Alnagar, et al., 2022	1.82–2	1.1–1.2	35–45	3.2–3	0.26
Yahya, Rezaei and Khaleel, 2021	1.4–3	0.06–0.07	28.6–20	47–45	0.004
Feng, Zhang and Che, 2017	0.9–1.8	1.4–2.3	15–20	6.1–4	0.089
Huang, et al., 2016	2.3–2.72	1–0.9	20–20	6.1–5.8	0.127
Rezaei and Noori, 2018	0.8–0.9	0.28–0.29	21.2–24.3	3.2–3.2	0.01
Kumar and Upadhyay, 2019	3.5–5.6	0.87–1.25	17–15.5	21.2–13.29	0.12
Rezaei, et al., 2019	1.6–2.1	0.1–0.16	33–22	16.8–11	0.054
Rezaei, Yahya and Jamaluddin, 2020	0.78–1.85	0.17–0.30	19–21	12.5–4.2	0.026
Zhou, et al., 2018	1.8–2.4	0.5–0.2	12–20	-	0.04
Rezaei and Noori, 2020	1–1.3	0.21–0.21	32–25	4.6–4.6	0.018
Danaeian, 2020	2.4–3.5	1.45–1.55	13–30	5.9–8.8	0.029
Roshani and Roshani, 2019	0.9–2.6	0.7–0.5	19.6–22	-	0.017
Rezaei, et al., 2019	2.12–3.94	0.25–0.26	18.45–17.47	5.7–6.5	0.038

communication systems and other applications requiring high-performance diplexers.

#### IV. CONCLUSION

In this paper, the mathematical design, simulation, and optimization of a microstrip diplexer with a high performance is proposed. An estimated LC model of the proposed basic structure is analyzed to find the scattering parameters. Subsequently, the operating frequency of the basic resonator

is calculated to help the miniaturization and tune the resonance frequency simultaneously. The designed diplexer operates at 1.86 GHz and 4.62 GHz, which makes it suitable for the mid-band 5G applications. It occupies a compact size of 64.4 mm<sup>2</sup>. The other advantages of this diplexer are low insertion and return losses, wide FBW, flat channels, and low group delays, while the isolation between the output ports is acceptable. Moreover, after the lower channel, the harmonics are suppressed from the 1<sup>st</sup> up to 6<sup>th</sup> harmonics.

TABLE III  
GROUP DELAYS COMPARISON (\*: APPROXIMATED VALUES).

References	Type	Maximum group delays at each channel
This work	Bandpass-bandpass diplexer	0.31 ns, 0.86 ns
Jamshidi, et al., 2023	Lowpass-bandpass diplexer	0.34 ns, 1.7 ns, 0.34 ns
Al-Majdi and Mezaal, 2023	Bandpass-bandpass diplexer	4 ns*, 3 ns*
Yahya, Rezaei and Nouri, 2021	Bandpass-bandpass diplexer	0.94 ns, 0.48 ns
Rezaei, et al., 2019	Bandpass-bandpass diplexer	Maximum 2.6 ns for both channels
Danaeian, 2020	Bandpass-bandpass diplexer	1.5 ns, 0.8 ns
Nouri, Yahya and Rezaei, 2020	Bandpass-bandpass diplexer	3.15 ns, 2.98 ns
Xu, Chen and Wan, 2020	Lowpass-bandpass diplexer	1.62 ns, 1.75 ns, 2.07 ns
Rezaei, Yahya and Nouri, 2023	Lowpass-bandpass diplexer	1.43 ns, 1.68 ns
Hayati, Rezaei and Noori, 2019	Lowpass-bandpass diplexer	2 ns, 1.24 ns
Hayati, et al., 2021	Lowpass-bandpass diplexer	0.65 ns*, >2.5 ns*
Liu, 2010	Tri-channel bandpass filter	Better than 8 ns at all channels
Chen, et al., 2015	Lowpass-bandpass triplexer	1.5 ns, 6 ns, 4.4 ns
Noori and Rezaei, 2017	Quad-channel bandpass diplexer	2.76 ns, 3.31 ns, 0.91 ns, 2.15 ns
Lin, 2011	Quad-channel bandpass filters	9 ns, 6 ns, 6 ns, 5 ns

## REFERENCES

- Afzali, B., Abbasi, H., Shama, F., and Dehdasht-Heydari, R., 2021. A microstrip bandpass filter with deep rejection and low insertion loss for application at 2.4 GHz useful wireless frequency. *AEU-International Journal of Electronics and Communications*, 138, p.153811.
- Ahn, K.P., Ishikawa, R., and Honjo, K., 2009. Group delay equalized UWB InGaP/GaAs HBT MMIC amplifier using negative group delay circuits. *IEEE Transactions on Microwave Theory and Techniques*, 57(9), pp.2139-2147.
- Al-Majdi, K., and Mezaal, Y.S., 2023. New miniature narrow band microstrip diplexer for recent wireless communications. *Electronics*, 12, p.716.
- Alnagar, I.A., Mahmoud, N.M., Khames, S.A., and Hussein, A.H., 2022. Efficient microstrip diplexer employing a new structure of dual-mode bandpass filter. *American Scientific Research Journal for Engineering, Technology, and Sciences*, 88(1), pp.68-76.
- Chaudhary, G., Jeong, Y., and Lim, J., 2014. Microstrip line negative group delay filters for microwave circuits. *IEEE Transactions on Microwave Theory and Techniques*, 62(2), pp.234-243.
- Chaudhary, M.A., Roshani, S., and Shabani, S., 2023. A miniaturized dual-band diplexer design with high port isolation for UHF/SHF applications using a neural network model. *Micromachines (Basel)*, 14, p.849.
- Chen, F.C., Qiu, J.M., Hu, H.T., Chu, Q.X., and Lancaster, M.J., 2015. Design of microstrip lowpass-bandpass triplexer with high isolation. *IEEE Microwave and Wireless Components Letters*, 25(12), pp.805-807.
- Danaeian, M., 2020. Miniaturized half-mode substrate integrated waveguide diplexer based on SIR-CSRR unit-cell. *Analog Integrated Circuits and Signal Processing*, 102, pp.555-561.
- Deng, S., Xu, F., and Zheng, Z., 2023. Compact diplexer with high isolation based on mixed-mode triangular substrate integrated waveguide cavities. *Electronics Letters*, 59(7), pp.1-3.
- Duan, S., Zhou, Y., Li, L., Li, L., and Kang, D., 2023. Cross-band microstrip diplexer design. *Proceedings of SPIE*, 12462, p.1246219.
- Fadaee, M.D., Shama, F., Feali, M.S., and Gilan, M.S., 2023. A miniaturized wide stopband low-pass filter using T and modified L shapes resonators. *ARO-the Scientific Journal of Koya University*, 11(1), pp.116-120.
- Feng, W., Zhang, Y., and Che, W., 2017. Tunable dual-band filter and diplexer based on folded open loop ring resonators. *IEEE Transactions on Circuits and Systems*, 64, pp.1047-1051.
- Hayati, M., Rezaei, A., and Noori, L., 2019. Design of a high-performance lowpass-bandpass diplexer using a novel microstrip structure for GSM and WiMAX applications. *IET Circuits, Devices and Systems*, 13(3), pp.361-367.
- Hayati, M., Zarghami, A.R., Zarghami, S., and Alirezaee, S., 2021. Designing a miniaturized microstrip lowpass-bandpass diplexer with wide stopband by examining the effects between filters. *AEU-International Journal of Electronics and Communications*, 139, p.153912.
- Hosseini, S.M., and Rezaei, A., 2020. Design of a branch-line microstrip coupler using spirals and step impedance cells for WiMAX applications. *ARO-the Scientific Journal of Koya University*, 8(1), pp.1-4.
- Huang, F., Wang, J., Zhu, L., and Wu, W., 2016. Compact microstrip balun diplexer using stub-loaded dual-mode resonators. *Electronic Letters*, 52, pp.1994-1996.
- Jamshidi, M., Yahya, S.I., Nouri, L., Dezaki, H.H., Rezaei, A., and Chaudhary, M.A., 2023. A high-efficiency diplexer for sustainable 5G-enabled IOT in metaverse transportation system and smart grids. *Symmetry*, 15(4), p.821.
- Kumar, A., and Upadhyay, D.K., 2019. A compact planar diplexer based on via-free CRLH TL for WiMAX and WLAN applications. *International Journal of Microwave and Wireless Technologies*, 11, pp.130-138.
- Lin, S.C., 2011. Microstrip dual/quad-band filters with coupled lines and quasi-lumped impedance inverters based on parallel-path transmission. *IEEE Transactions on Microwave Theory and Techniques*, 59(8), pp.1937-1946.
- Liu, Y., 2010. A tri-band bandpass filter realized using tri-mode T-shape branches. *Progress in Electromagnetics Research*, 105, pp.425-444.
- Noori, L., and Rezaei, A., 2017. Design of a microstrip diplexer with a novel structure for WiMAX and wireless applications. *AEU-International Journal of Electronics and Communications*, 77, pp.18-22.
- Nouri, L., Yahya, S.I., and Rezaei, A., 2020. Design and fabrication of a low-loss microstrip lowpass-bandpass diplexer for WiMAX applications. *China Communications*, 17(6), pp.109-120.
- Ravelo, B., Wu, L., Wan, F., Rahajandraibe, W., and Murad, N.M., 2020. Negative group delay theory on Li topology. *IEEE Access*, 8, pp.47596-47606.
- Rezaei, A., and Noori, L., 2018. Novel compact microstrip diplexer for GSM applications. *International Journal of Microwave and Wireless Technologies*, 10, pp.313-317.
- Rezaei, A., and Noori, L., 2020. Miniaturized microstrip diplexer with high performance using a novel structure for wireless L-band applications. *Wireless Networks*, 26, pp.1795-1802.
- Rezaei, A., and Yahya, S.I., 2022. A new design approach for a compact microstrip diplexer with good passband characteristics. *ARO-the Scientific Journal of Koya University*, 10(2), pp.1-6.
- Rezaei, A., Yahya, S.I., and Jamaluddin, M.H., 2020. A novel microstrip diplexer with compact size and high isolation for GSM applications. *AEU-International*

*Journal of Electronics and Communications*, 114, p.153018.

Rezaei, A., Yahya, S.I., and Nouri, L., 2023. Design and analysis of a compact microstrip lowpass–bandpass diplexer with good performance for wireless applications. *International Journal of Microwave and Wireless Technologies*, pp.1-9.

Rezaei, A., Yahya, S.I., Noori, L., and Jamaluddin, M.H., 2019. Design of a novel wideband microstrip diplexer using artificial neural network. *Analog Integrated Circuits and Signal Processing*, 101, pp.57-66.

Rezaei, A., Yahya, S.I., Noori, L., and Jamaluddin, M.H., 2019. Design and fabrication of a novel compact low-loss microstrip diplexer for WCDMA and WiMAX applications. *Journal of Microwaves, Optoelectronics and Electromagnetic Applications*, 18(4), pp.482-491.

Roshani, S., and Roshani, S., 2019. Design of a very compact and sharp bandpass diplexer with bended lines for GSM and LTE applications. *AEU-International Journal of Electronics and Communications*, 99, pp.354-360.

Shao, T., Wang, Z., Fang, S., Liu, H., and Fu, S., 2017. A compact transmission-line self-matched negative group delay microwave circuit. *IEEE Access*, 5, pp.22836-22843.

Xu, J., Chen, Z.Y., and Wan, H., 2020. Lowpass-bandpass triplexer integrated

switch design using common lumped-element triple-resonance resonator technique. *IEEE Transactions on Industrial Electronics*, 67(1), pp.471-479.

Yahya, S.I., and Rezaei, A., 2020. An area-efficient microstrip diplexer with a novel structure and low group delay for microwave wireless applications. *Aro-the Scientific Journal of Koya University*, 8(2), pp.71-77.

Yahya, S.I., and Rezaei, A., 2021. Design and fabrication of a novel ultra compact microstrip diplexer using interdigital and spiral cells. *ARO-The Scientific Journal of Koya University*, 9(1), pp.103-108.

Yahya, S.I., Rezaei, A., and Khaleel, Y.A., 2021. Design and analysis of a wide stopband microstrip dual-band bandpass filter. *ARO-The Scientific Journal of Koya University*, 9(2), pp.83-90.

Yahya, S.I., Rezaei, A., and Nouri, L., 2020. Design and performance of microstrip diplexers: A review. *ARO-the Scientific Journal of Koya University*, 8(1), pp.38-49.

Yahya, S.I., Rezaei, A., and Nouri, L., 2021. The use of artificial neural network to design and fabricate one of the most compact microstrip diplexers for broadband L-band and S-band wireless applications. *Wireless Networks*, 27, pp.663-676.

Zhou, J., Li, J.L., Sun, C.G., Li, H., and Gao, S.S., 2018. A novel microstrip diplexer based on coupled line. *Electromagnetics*, 38, pp.87-95.

# Screening of Aflatoxin Production by *Aspergillus flavus* Isolates from Petroleum-contaminated Soil

Sawan M. Mirkhan and Taha J. Zrary

Department of Biology, Faculty of Science and Health, Koya University,  
Danielle Mitterrand Boulevard, Koya KOY45, Kurdistan Region – F.R. Iraq

**Abstract**—Fungi are eukaryotic, heterogeneous, unicellular to filamentous, spore-bearing, and chemoorganotrophic organisms which lack chlorophyll. This present study was carried out to isolate and identify fungi from petroleum-contaminated soil. Several fungal genera which included *Rhizopus* spp., *Mucor* spp., *Penicillium* spp., *Rhizoctonia* spp., *Aspergillus* spp., *Alternaria* spp., and *Cladosporium* spp. were isolated using potatoes dextrose agar, Czapek-Dox Agar, and *Aspergillus flavus* Differentiation Agar culture media that comparable with co-amoxiclav (1g) and chloramphenicol to prevent the growth of any bacteria. The direct plate and serial dilution agar plate methods were used for the isolation of fungi. Based on the results, *Aspergillus* and *Mucor* spp. were the most predominant genera and had the highest number of colonies in the soil samples. In this investigation, seven out of 27 soil samples were morphologically (macroscopically and microscopically) identified, such as *A. flavus*. Aflatoxigenicity of *A. flavus* was detected using characteristics in *Aspergillus* differentiation agar and colony fluorescence on exposure to ultraviolet light. In addition, molecular approaches were used for the detection of aflatoxigenic of the *A. flavus* isolates. Three structural (*aflD*, *aflO*, and *aflP*) and one regulatory (*aflR*) gene of the aflatoxin gene cluster of *A. flavus* were targeted for amplification by the polymerase chain reaction method. The aflatoxigenic of all six *A. flavus* isolates was detected molecularly which contained two structural (*aflD*, *aflP*) genes out of three structural genes, while there was no specific amplification of the *aflO* gene in the fourth, fifth, and sixth *A. flavus* which is similar to the *aflR* gene in the first and second *A. flavus*.

**Index Terms**—Fungus, Aflatoxin, Aflatoxin genes, *Aspergillus flavus*, Petroleum-contaminated soil, Polymerase chain reaction.

## I. INTRODUCTION

Fungi do not photosynthesize; therefore, they get their food by the absorption of dissolved molecules due to their ability to secrete some digestive enzymes to their environment as they are heterotrophs. Thus, they are considered to be the

main decomposers in ecological systems (Harris, 2008; Soni, 2007).

Microfungi contribute to the degradation of synthetic and natural pollutants because fungi similarly emit primary and secondary metabolites (antibiotics, protein, toxins, ethanol, etc.). Soil fungi are a potential and abundant source of highly bioactive secondary metabolites. Mycoflora colonizes, reproduces, and stays alive in several environments including microecological niches. They can survive in risky environments, such as thermal springs, cold places, hot springs, and run-off hydrocarbon-contaminated soil (Hanson, 2008).

Mycotoxins are non-volatile, and they are mainly produced by filamentous fungi; however, it should be taken into consideration that the majority of fungi are non-toxic and many secondary metabolites from fungi are non-toxic. Mycotoxins occur in varieties of fungi, some of these mycotoxins are important and intensive, together with ochratoxin, citrinin, ergot alkaloid, patulin, fusarium, and aflatoxin. Aflatoxins are potent carcinogenic, mutagenic, and teratogenic secondary metabolites and are produced predominantly by *Aspergillus flavus* and *Aspergillus parasiticus* (Abdel-Hadi, 2011). *A. flavus* is a saprotrophic and pathogenic fungus with a cosmopolitan distribution (Ramírez-Camejo, et al., 2012).

Petroleum-based products are complex mixtures that contain numerous aliphatic, alicyclic, and aromatic compounds depending on the definition. It is well known as a great important source of daily energy during the exploration, production, refining, transport, storage of petroleum, and petroleum products (Kvenvolden and Cooper, 2003).

This saprotrophic *A. flavus* can survive on most of the sources of organic nutrients, such as tree leaves, animal fodder, outdoor and indoor air environments, dead insects and animal carcasses, and etcetera; therefore it is so common. It is a pathogenic fungus with a cosmopolitan distribution (Ramírez-Camejo, et al., 2012; Machida and Gomi, 2010).

Aflatoxin is a type of mycotoxin produced by *Aspergillus* species of fungi, such as *A. flavus* and *A. parasiticus* (Martins, Martins and Bernardo, 2001). Aflatoxins consist of a group of approximately 20 related fungal metabolites. Yin, et al. (2008) declared that the term aflatoxin comes from four different types of the production of mycotoxins, which are B<sub>1</sub>, B<sub>2</sub>, G<sub>1</sub>, and G<sub>2</sub>. Aflatoxin B<sub>1</sub> is the most toxic and potent carcinogen that can cause liver cancer in many different

ARO-The Scientific Journal of Koya University  
Vol. XI, No. 2 (2023), Article ID: ARO.11144. 6 pages  
DOI: 10.14500/aro.11144

Received: 01 February 2023; Accepted: 28 July 2023  
Regular research paper: Published: 25 August 2023

Corresponding author's e-mail: sawan.majid@koyauniversity.org  
Copyright © 2023 Sawan M. Mirkhan and Taha J. Zrary. This is an open access article distributed under the Creative Commons Attribution License.



animal species (Martins, Martins and Bernardo, 2001). Besides, it contributes to the production of the tropics and subtropics commodities, such as pistachios, cotton, spices, and maize (Yin, et al., 2008; Martins, Martins and Bernardo, 2001).

## II. MATERIALS AND METHODS

### A. Scanning Location

Twenty-seven soil samples were collected from different ecosystems at Hawler governorate (Taq Taq Operating Company) and Sulaymaniyah governorate (Bazian Oil Refinery and Directory Refinery of Sulaymaniah) that were contaminated with petroleum. Where the samples of soil were taken from, growing plants were noticed. All samples were collected from the 2<sup>nd</sup> of December 2015 to the 10<sup>th</sup> of March 2016.

### B. Soil Sampling

Soil samples (about 500 g each) were taken from a depth of 0–15 cm from petroleum-contaminated soil in each refinery field. The distance between every two samples was 25 m; however, three of them were taken randomly (as replication) at three different points with a trowel after removing litter or weed plants.

### C. Morphological Identification of *Aspergillus* Species

*Aspergillus* isolates were grown on potatoes dextrose agar (PDA), Czapek-Dox Agar (CZA), and AFPA at 28°C incubation to identify macroscopic characters including color, diameter, and number of colonies, and microscopic characters, such as conidia, conidiophore, phialides, and vesicles. After that, slides were prepared from these new cultures using Lacto phenol cotton blue by growing medium and then observed under a light microscope (Rodrigues, et al., 2007).

### D. Cultural Methods for Aflatoxin Detection

#### Detection of aflatoxin based on cultural characteristics in AFPA

For the aflatoxin detection that creates *Aspergillus* species from soil samples, *Aspergillus* differentiation agar was used, which is a differential and selective medium. Then, aflatoxigenic *A. flavus* was distinguished after 7 days of incubation at 28 °C depending on the appearance of the reverse orange color on the plates. The cause of this color change is the reaction between the aspergillic acid molecules that are produced by *Aspergillus* species with the ferric ions from ferric citrate, which exists in the medium (Rodrigues, et al., 2007).

### E. Molecular Identification of *A. flavus* Isolates

Classical techniques were used for the identification and detection of *Aspergillus* isolates in samples based on morphological studies. These methods have a low degree of sensitivity and do not allow the specification of

mycotoxigenic species. PCR methods are used to detect aflatoxigenic strains of *A. flavus*, as they can target DNA accurately due to their high sensitivity and specificity (Almoammar, et al., 2013).

### F. DNA Extraction Method

DNA extraction kit (Fungal/Bacterial DNA MiniPrep™) is used to extract the genomic DNA from all the isolates. The kit is used according to the manufacturer.

### G. Molecular Discovery of Aflatoxigenic *A. flavus* Isolates

Aflatoxigenic strains of *A. flavus* was distinguished and identified from other fungi by developing Molecular methods. A polymerase chain reaction (PCR) is one of those techniques that are used for this purpose as it can be handy and easy to use (Hussain, et al., 2015; Criseo, Bagnara and Bisignano, 2001). Cluster genes contain *nor1*, *omtB*, and *omt-1* structural genes in the aflatoxin biosynthesis pathway, which is coding for key enzymes and regulatory gene (*aflR*) which is vital for aflatoxin production; besides, it affects the structural genes and activates transcription. Four primer pairs have been used for a specific consequence of *aflO*, *aflD*, *aflR*, and *aflP* (Erami, et al., 2007). Numerous research assemblies have tested the possibility of applying PCR-based diagnostic methods to detect the presence (genomic PCR) or real-time PCR of the aflatoxin biosynthetic genes or the expression reverse transcription (RT) (Dheeb, et al., 2014; Abdel-Hadi, Carter and Magan, 2011; Degola, et al., 2007) (Tables I-IV).

The PCR products were detected on 2% agarose at 5 volts/cm<sup>2</sup>. 1x TBE buffer for 1:30 h, DNA ladder (100 bp), visualized under U.V light Agreed by (Scherer, et al., 2005).

### H. Statistical Analysis

Data analysis was performed using the Statistical Package for the Social Sciences (SPSS) Version 17.0. Results are expressed as mean ± S.E. The analysis of variance (ANOVA) was applied.

TABLE I  
THE COMPONENTS OF THE MAXIME PCR PREMIX KIT (I-TAQ)

Materials	Volume
i-Taq DNA polymerase (U)	2.5
DNTPs (mm)	2.5
Reaction buffer (10X)	1X
Gel loading buffer	1X

PCR: Polymerase chain reaction

TABLE II  
MIXTURE OF THE SPECIFIC INTERACTION FOR DIAGNOSIS GENE

Components	Concentration
Maxime PCR PreMix kit (i-Taq) (μL)	5
Forward primer	10 pmol/μ (1 μL)
Reverse primer	10 pmol/μ (1 μL)
DNA (μL)	1–1.5
Distill water (μL)	16.5
Final volume (μL)	25

PCR: Polymerase chain reaction



TABLE III  
PRIMERS THAT ARE USED (SCHERM, ET AL., 2005)

Gene	Primer code	Sequence (5'–3')	Temperature (°C)	GC (%)	Estimated size (bp)
<i>aflD</i>	Nor1 (F)	ACGGATCACTTAGCCAGCAC	57.3	55.0	990
	Nor1 (R)	CTACCAGGGGAGTTGAGATCC	56.4	57.1	
<i>aflO</i>	OmtB (F)	GCCTTGACATGGAACCATC	54.1	50.0	1333
	OmtB (R)	CCAAGATGGCCTGCTCTTA	54.9	50.0	
<i>aflP</i>	Omt1 (F)	GCCTTGCAAACACACTTTCA	54.4	54.0	1490
	Omt1 (R)	AGTTGTTGAACGCCCCAGT	57.3	52.6	
<i>aflR</i>	AflR (F)	CGAGTTGTGCCAGTTCAAAA	53.8	45.0	999
	AflR (R)	AATCCTCGCCACCATACTA	57.3	52.6	

III. RESULTS

A. Isolation of Fungi

Direct method

Approximately 27 soil samples were taken from three different refineries from December 2015 to March 2016. The samples were cultured on PDA with co-amoxiclav (1g), CZA with co-amoxiclav (1g), and *A. flavus* Differentiation Agar (AFDA) with chloramphenicol (Table V).

B. Morphological Identification of *A. flavus*

*Aspergillus* has several morphological and growth responses to different nutrients, so it is significant to regulate conditions for the morphological detection of *A. flavus*, as species identification depends on pure cultures grown on known media.

The plates were incubated for 7 days at 28°C on CZA and PDA, and then, they were observed for macroscopic (colony color and diameter) (Fig. 1) and microscopic characteristics (conidia, conidiophore, vesicle, and phialides) (Figs. 2 and 3).

C. Cultural Method for Detection of Aflatoxin

There are several methods for the detection of aflatoxin in cultures of fungus. Here, the colony fluorescence on exposure to ultraviolet (UV) and orange color features in AFPA was used (Yazdani, et al., 2010).

Detection of aflatoxin producers based on reverse color change on AFDA

Aflatoxin-producing *Aspergillus* species were detected on *Aspergillus* differentiation agar (AFPA), which is a selective and differential medium. In Fig. 4a, a white colony can be seen after 7 days of incubation at 28°C, while in Fig. 4b, an orange colony can be seen on the reverse side of the plate.

D. Molecular Identification of *A. flavus*

Extraction of DNA

Six out of 27 *A. flavus* isolates were identified by KAPA Universal Ladder and contain four reference bands (500, 1000, 1600, and 4000) for orientation, (Fig. 5).

Detection of aflatoxin-producing strains by conventional PCR method

PCR was used to diagnose aflatoxin-making strains of *A. flavus* molecularly, which are three structural genes (*aflD*,

TABLE IV  
THE OPTIMUM CONDITION OF THE DETECTION GENE (SCHERM, ET AL., 2005)

Phase	Temperature (°C)	Time	Number of cycle
Initial denaturation	94	5 min	35 cycles
Denaturation 2	94	30 s	
Annealing	50	60 s	
Extension	72	90 s	
Final extension	72	7 min	

TABLE V  
THE INCIDENCE PERCENTAGE OF FUNGI ISOLATED FROM CONTAMINATED SOIL BY THE DIRECT METHOD

Isolated fungi	Frequency (%)	Location
<i>Rhizopus</i> spp.	2 (6.9)	Bazyan
<i>Mucor</i> spp.	7 (24.1)	Bazyan, DRS, TTOPCO
<i>Penicillium</i> spp.	3 (10.4)	Bazyan, DRS, TTOPCO
<i>Rhizoctonia</i> spp.	1 (3.5)	Bazyan
<i>Aspergillus</i> spp.	7 (24.1)	DRS, TTOPCO
<i>Alternaria</i> spp.	6 (20.7)	DRS, TTOPCO
<i>Cladosporium</i> spp.	3 (10.3)	DRS
Total	29 (100)	

DRS: Directory Refinery of Sulaymaniyah, TTOPCO: Taq Taq Operating Company

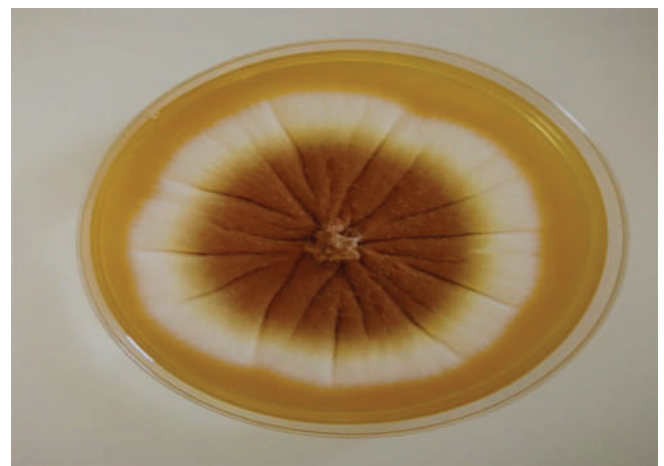


Fig. 1. Colony of *Aspergillus flavus* on CZA attaining diameter 36 mm within 7 days of incubation at 28°C, colony color becoming brown to white.

*aflO*, and *aflP*), and a regulatory gene (*aflR*). The results of the toxigenicity of all *A. flavus* isolates have shown that only *aflD* and *aflP* among the structural genes and *aflR* as a regulatory gene were identified as the most toxigenic isolates (Fig. 6).

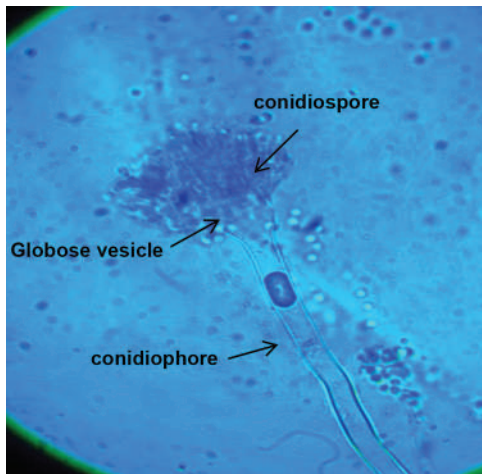


Fig. 2. Microscopic characteristic of *Aspergillus flavus*, Aspergillum-like spore-bearing, globose vesicle, bear chain of conidiospores; microscopic observation of the fungal isolate under  $\times 400$  magnification (lactophenol cotton).

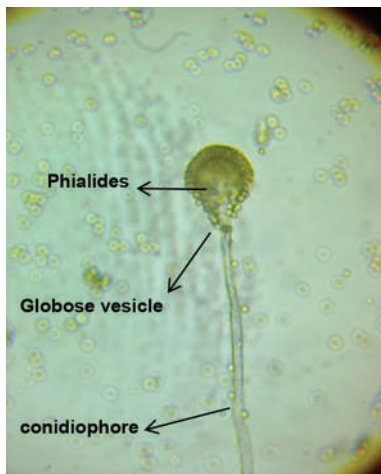


Fig. 3. Uniseriate Conidia head of *Aspergillus flavus*, Aspergillum-like spore-bearing conidiophore, Globose vesicle, directly borne vesicles. Microscopic observation of the fungal isolate under  $\times 400$ .

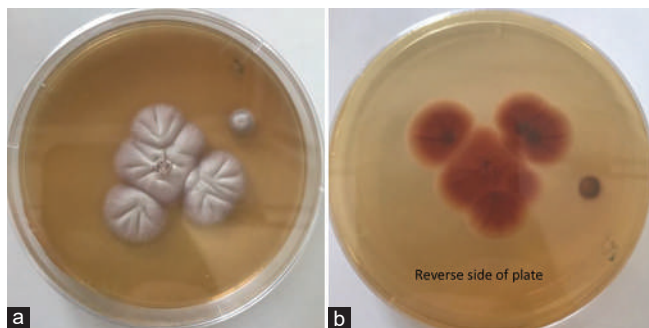


Fig. 4. (a and b) *Aspergillus flavus* on AFPA, after 7 days of incubation at 28°C, with characteristic orange color on the reverse side of the plate.

#### IV. DISCUSSION

In the investigation, seven isolated genera were obtained from the 27 soil samples that were isolated from various locations. From the fungal isolates, most of the species belonging to the genera *Aspergillus* and *Mucor* were

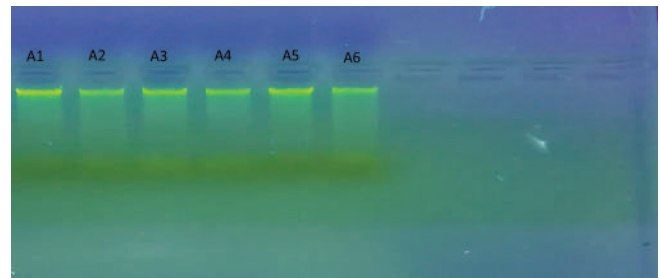


Fig. 5. Gel electrophoresis of genomic DNA extraction from *Aspergillus flavus*, 1% agarose gel at 5 vol/cm for 1:15 h, A: *A. flavus*.

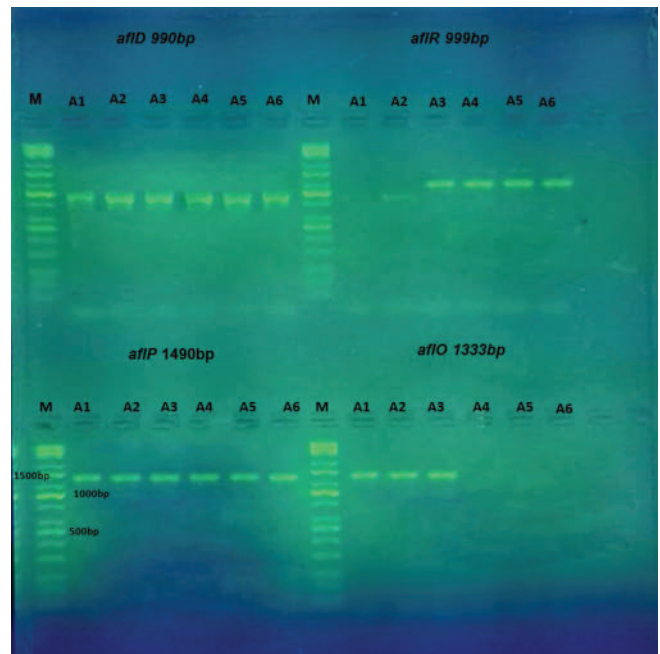


Fig. 6. The polymerase chain reaction product of the band size (*aflD* 990 pb) (*aflO* 1333 bp) (*aflP* 1490 bp) (*aflR* 1498 bp). The product was electrophoresis on 2% agarose at 5 volt/cm<sup>2</sup>.  $\times 1$  TBE buffer for 1:30 h. N: DNA ladder (100), lane (1-6), visualized under UV light, A: *Aspergillus flavus*.

dominant. The same results were achieved by Raja, Praveena and William in 2017. These results were achieved with those found by Rohilla and Salar (2012) as well. 24.1% of *Aspergillus* spp. and 20.7% of *Alternaria* spp. were found in the Directory Refinery of Sulaymaniyah (DRS), and Taq Taq Operating Company (TTOPCO), while 24.1% of *Mucor* spp. and 10.1% of *Penicillium* spp. found in DRS, TTOPCO, and Bazyan. Finally, *Rhizoctonia* spp., *Rhizopus* spp., and *Cladosporium* spp. from Bazyan were 3.5%, 6.9%, and 10.3%, respectively. These results correspond with Raja, Praveena and William in 2017.

Results from the present study show a correlation between dilution with the diameter and the number of colonies of isolate fungi in different soil contaminated with petroleum locations which were reported by Farrag, et al. (2017); Agarwal (2017), and Jasuja, Saxena and Joshi (2013).

Possibly, due to differences in the cell wall structure, fungi are considered to be more tolerant of high concentrations of polluting chemicals than other organisms. In fungi, the

cell wall is the outer-most layer, external to the plasma membrane. The fungal cell wall is a matrix of three main components chitin, glucans, and proteins (Blakely, et al., 2002). Based on Khalid, Hussain and Imran (2018); Farrag, et al. (2017), and Giusiano, et al. (2017), all *A. flavus* isolates were identified depending on the features' description and the isolates' characteristics. *A. flavus* is morphologically characterized by brown to white smooth colonies on CZA. As stated by Hedayati, et al., (2007), the colonies were flat, with radial grooves. It was observed that the diameter of *A. flavus* colonies was smaller on CZA, PDA, and CMA than on AFPA. This difference in the diameter of the colony of fungi may have been caused by the difference in the nutrient ingredients of the media.

To differentiate aflatoxigenic from non-aflatoxigenic *Aspergillus*, three different cultural-based methods were used. These were the blue fluorescence of aflatoxin B, orange color on the reverse of the AFPA plates, and color change on exposure to ammonium hydroxide vapor which agreed with Yazdani, et al. (2010) and Rodrigues, et al. (2007). However, in 2014, Nair, et al. demonstrated that mycotoxins cannot be produced by all strains of *Aspergillus*, as *A. flavus* producing aflatoxin needs using techniques such as ELISA, TLC, and HPLC to obtain aflatoxin concentration.

In this study, seven *Aspergillus* spp. were isolated out of 27 samples, while six samples of *A. flavus* were used for the molecular method by correlating between the presence-absence of genes and also the ability-inability of aflatoxins production. Nowadays, to identify and detect aflatoxin-producing fungi, DNA-based detection systems are frequently used, such as PCR, which is used to distinguish between the aflatoxin-producing and non-producing *A. flavus* strains (Hussain, et al., 2015; Degola, et al., 2007). In 2016, Temu declared that there are three structural genes (*aflD*, *aflM*, and *aflO*) with *aflR* as a regulatory gene that was followed by 5.8S ITS rDNA nucleotide sequence analysis; besides, the spices quality with safety prediction to consumers can be assessed by PCR. The presence of fungi in a substrate does not necessarily relate to the presence or amount of aflatoxin, however, bands of the fragments of *aflD* and *aflP* genes at 990 bp and 1490 bp were visualized, respectively, as the result of the test for the detection of aflatoxigenic *A. flavus* isolates using the molecular method. While *aflR* was seen frequently in *A. flavus* samples in our condition and even with using the same pair of primers, *aflO* was seen in three *A. flavus* and not visualized in other *Aspergillus* strains, as shown in Fig. 6. The lack of aflatoxin production in the strains of *A. flavus* may be due to the lack of genes in their genome, as reported by Houshyarfard, et al. (2014). Deletion of portions of the aflatoxin biosynthesis gene cluster within the aflatoxigenic *A. flavus* strain is not rare. In 2016, Temu stated that the genetic variation in aflatoxin production can arise from mutations in the aflatoxin biosynthetic gene cluster which may include gene loss, DNA inversion, recombination, partial deletions, or other genomic rearrangements of the cluster (Carbone, et al., 2007). However, a species may have all genes involved in the pathway but not necessarily produce aflatoxin till certain favorable conditions trigger its

production. However, a species missing aflatoxin biosynthetic genes cannot produce aflatoxin. The presence of biosynthetic genes has been used as a diagnostic tool for aflatoxigenic fungi in certain foodstuffs (Gallo, et al., 2012).

## V. CONCLUSIONS

From this presented study, we have concluded that the most frequent fungi isolates were *Aspergillus* spp. and *Mucor* spp.; however, the amplification of *aflD* and *aflP* genes from *A. flavus* isolates from the petroleum-contaminated could confirm the aflatoxin production. Hence, not necessarily all *Aspergillus* spp. excrete aflatoxin (note: all the structural aflatoxin genes were not detected in current local isolates of *A. flavus*).

## REFERENCES

- Abdel-Hadi, A., 2011. Molecular Ecology of *Aspergillus* Section Flavi Species: Approaches to Understanding the Role of Aflatoxin Genes in Aflatoxin Biosynthesis.
- Abdel-Hadi, A., Carter, D., and Magan, N., 2011. Discrimination between aflatoxigenic and non-aflatoxigenic *Aspergillus* section Flavi strains from Egyptian peanuts using molecular and analytical techniques. *World Mycotoxin Journal*, 4(1), pp.69-77.
- Agarwal, P., 2017. Isolation and characterization of Tyrosinase (a carbon trapping enzyme) producing microorganisms, in the agricultural soil of Western Uttar Pradesh and the study of enzymatic activity of Tyrosinase produced. *Biochemistry and Molecular Biology Letters*, 3(1), p.105.
- Almoammar, H., Bahkali, A.H., and Abd-Elsalam, K.A., 2013. A polyphasic method for the identification of aflatoxigenic '*Aspergillus*' species isolated from Camel feeds. *Australian Journal of Crop Science*, 7(11), p.1707.
- Blakely, J.K., Neher, D.A. and Spongberg, A.L., 2002. Soil invertebrate and microbial communities, and decomposition as indicators of polycyclic aromatic hydrocarbon contamination. *Applied Soil Ecology*, 21(1), p.71-88.
- Carbone, I., Jakobek, J.L., Ramirez-Prado, J.H., and Horn, B.W., 2007. Recombination, balancing selection and adaptive evolution in the aflatoxin gene cluster of *Aspergillus parasiticus*. *Molecular Ecology*, 16(20), pp.4401-4417.
- Criseo, G., Bagnara, A., and Bisignano, G., 2001. Differentiation of aflatoxin-producing and non-producing strains of *Aspergillus flavus* group. *Letters in Applied Microbiology*, 33(4), pp.291-295.
- Degola, F., Berni, E., Dall'Asta, C., Spotti, E., Marchelli, R., Ferrero, I., and Restivo, F.M., 2007. A multiplex RT-PCR approach to detect aflatoxigenic strains of *Aspergillus flavus*. *Journal of Applied Microbiology*, 103(2), pp.409-417.
- Dheeb, B.I., Ismail, E.N., AL-mishhadani, I.I.H., Majeed, S.M., and Majeed, D.M., 2014. A study of the expression of aflatoxin B1 regulatory gene in clinical and environmental *Aspergillus flavus* using real-time PCR. *International Journal of Sciences: Basic and Applied Research*, 17(1), pp.417-427.
- Erami, M., Hashemi, S.J., Pourbakhsh, S.A., Shahsavandi, S., Mohammadi, S., Shoushtari, A., and Jahan, S.Z., 2007. Application of PCR on detection of aflatoxinogenic fungi; short communication. *Archives of Razi Institute*, 62, pp.95-100.
- Farrag, A.A., Shehata, R.M., EL-Sheikh, H.H., Abo-Dahab, N.F., and Ali, A.M., 2017. Diversity and biotechnological applications of some fungi that isolated from unusual soil samples in Egypt. *Journal of Ecology of Health and Environment*, 5(1), pp.23-33.
- Gallo, A., Stea, G., Battilani, P., Logrieco, A.F., and Perrone, G., 2012. Molecular characterization of an *Aspergillus flavus* population isolated from maize during the first outbreak of aflatoxin contamination in Italy. *Phytopathologia*

*Mediterranea*, 51, pp.198-206.

Giusiano, G.E., Piontelli, E., Fernández, M.S., Mangiaterra, M.L., Cattana, M.E., Kocsubé, S., and Varga, J., 2017. Biodiversity of species of *Aspergillus* section Fumigati in semi-desert soils in Argentina. *Revista Argentina de microbiología*, 49(3), pp.247-254.

Hanson, J.R., 2008. *Chemistry of Fungi*. Royal Society of Chemistry, United Kingdom.

Harris, S.D., 2008. Branching of fungal hyphae: Regulation, mechanisms and comparison with other branching systems. *Mycologia*, 100(6), pp.823-832.

Hedayati, M.T., Pasqualotto, A.C., Warn, P.A., Bowyer, P., and Denning, D.W., 2007. *Aspergillus flavus*: Human pathogen, allergen and mycotoxin producer. *Microbiology*, 153(6), pp.1677-1692.

Houshyarfard, M., Rouhani, H., Falahati-Rastegar, M., Malekzadeh-Shafaroudi, S., Mehdikhani-Moghaddam, E., and Chang, P.K., 2014. Gene deletion patterns in non-aflatoxigenic isolates of *Aspergillus flavus*. *Mycologia Iranica*, 1(2), pp.87-97.

Hussain, A., Afzal, A., Irfan, M., and Malik, K.A., 2015. Molecular detection of aflatoxin-producing strains of *Aspergillus flavus* from peanut (*Arachis hypogaea*). *Turkish Journal of Agriculture-Food Science and Technology*, 3(5), pp.335-341.

Jasuja, N.D., Saxena, R., and Joshi, S.C., 2013. Isolation and identification of microorganisms from playhouse agriculture soil of Rajasthan. *African Journal of Microbiology Research*, 7(41), pp.4886-4891.

Khalid, S., Hussain, N., and Imran, M., 2018. Detection of aflatoxigenicity of *Aspergillus flavus*, based on potential gene marker, from food and feed samples. *Journal of Food Safety*, 38, p.e12448.

Kvenvolden, K.A., and Cooper, C.K., 2003. Natural seepage of crude oil into the marine environment. *Geo-Marine Letters*, 23(3-4), pp.140-146.

Machida, M., and Gomi, K., Eds., 2010. *Aspergillus: Molecular Biology and Genomics*. United Kingdom: Horizon Scientific Press.

Martins, M.L., Martins, H.M., and Bernardo, F., 2001. Aflatoxins in spices marketed in Portugal. *Food Additives and Contaminants*, 18(4), pp.315-319.

Nair, S.C., Bhagobaty, R.K., Nampoothiri, K., Kalaigandhi, V., and

Menon, K.R.K., 2014. Detection of Aflatoxin production by fungi in spice samples using HPLC and direct visual cultural methods. *Innovative Romanian Food Biotechnology*, 14, pp.1-12.

Raja, M., Praveena, G., and William, S.J., 2017. Isolation and identification of fungi from soil in Loyola College campus, Chennai, India. *International Journal of Current Microbiology and Applied Sciences*, 6(2), pp.1789-1795.

Ramírez-Camejo, L.A., Zuluaga-Montero, A., Lázaro-Escudero, M., Hernández-Kendall, V., and Bayman, P., 2012. Phylogeography of the cosmopolitan fungus *Aspergillus flavus*: Is everything everywhere? *Fungal Biology*, 116(3), pp.452-463.

Rodrigues, P., Soares, C., Kozakiewicz, Z., Paterson, R., Lima, N., and Venâncio, A., 2007. Identification and characterization of *Aspergillus flavus* and aflatoxins. In: *Communicating Current Research and Educational Topics and Trends in Applied Microbiology*. Formatex, Mumbai.

Rohilla, S.K., and Salar, R.K., 2012. Isolation and characterization of various fungal strains from agricultural soil contaminated with pesticides. *Research Journal of Recent Sciences ISSN*, 2277, p.2502.

Scherm, B., Palomba, M., Serra, D., Marcello, A., and Migheli, Q., 2005. Detection of transcripts of the aflatoxin genes aflD, aflO, and aflP by reverse transcription-polymerase chain reaction allows differentiation of aflatoxin-producing and non-producing isolates of *Aspergillus flavus* and *Aspergillus parasiticus*. *International Journal of Food Microbiology*, 98(2), pp.201-210.

Soni, S.K., 2007. *Microbes: A Source of Energy for the 21<sup>st</sup> Century*. New India Publishing, New Delhi.

Temu, G.E., 2016. Molecular Identification of *Aspergillus* strains and quick detection of aflatoxin from selected common spices in Tanzania. *Journal of Scientific Research and Reports*, 10, pp.1-8.

Yazdani, D., Zainal, A.M., Tan, Y.H., and Kamaruzaman, S., 2010. Evaluation of the detection techniques of toxigenic *Aspergillus* isolates. *African Journal of Biotechnology*, 9(45), pp.7654-7659.

Yin, Y.N., Yan, L.Y., Jiang, J.H., and Ma, Z.H., 2008. Biological control of aflatoxin contamination of crops. *Journal of Zhejiang University Science B*, 9(10), pp.787-792.

# Audio Encryption Framework Using the Laplace Transformation

Mardan A. Pirdawood<sup>1</sup>, Shadman R. Kareem<sup>1,2</sup> and Dashne Ch. Zahir<sup>1</sup>

<sup>1</sup>Department of Mathematics, Faculty of Science and Health, Koya University,  
Kurdistan Region – F.R. Iraq

<sup>2</sup>Department of Computer Science, College of Information Technology and Computer Sciences, Catholic University in Erbil,  
Kurdistan Region – F.R. Iraq

**Abstract**—Digital information, especially multimedia and its applications, has grown exponentially in recent years. It is important to strengthen sophisticated encryption algorithms due to the security needs of these innovative systems. The security of real-time audio applications is ensured in the present study through a framework for encryption. The design framework protects the confidentiality and integrity of voice communications by encrypting audio applications. A modern method of securing communication and protecting data is cryptography. Using cryptography is one of the most important techniques for protecting data and ensuring the security of messaging. The main purpose of this paper is to present a novel encryption scheme that can be used in real-time audio applications. We encrypt the sound using a combination of an infinite series of hyperbolic functions and the Laplace transform, and then decrypt it using the inverse Laplace transform. The modular arithmetic rules are used to generate the key for the coefficients acquired from the transformation. There is no loss of data or noise in the decryption sound. We also put several sound examples to the test.

**Index Terms**—Cryptography, Laplace transformations, Maclaurin series, Sound encryptions.

## I. INTRODUCTION

Since the invention of written language, people have yearned to communicate in secret. Imagine sending a message to someone, but being concerned that someone else might view it, read the letter, or hear the electronic message (Mel and Baker, 2001). Conventionally, cryptography is used to provide confidentiality and integrity through encryption methods. Plaintext is the message to be communicated, and it can be text, numerical data, audio, executable programs, or anything else. In a cryptographic system, the original message to be transmitted is called the plaintext. In cryptography, mathematical techniques can be incredibly

beneficial. The encryption method varies depending on the key, which alters the algorithm's technical operation. The cryptographic framework transfers plaintext to ciphertext (we keep messages secret by turning them into a code) so only the intended recipient can understand it (Delfs, Knebl and Knebl, 2002).

A considerable scope of investigation pertains to the governance and administration of security imperatives within the modern context framework of multimedia systems see (Ghadi, Laouamer and Moulahi, 2016) (El-Zoghdy, El-sayed and Faragallah, 2020). Audio data applications are extremely important and frequently used in multimedia systems (Kaur and Dutta, 2018; Liu, et al., 2017). The present research focuses on the creation of audio encryption algorithms that show attributes of low-power consumption, high real-time audio presence, and fast multimedia processing (Ghasemzadeh and Esmaeili, 2017; El-Zoghdy, El-sayed and Faragallah, 2020; Al-kateeb and Mohammed, 2020; Dutta, et al., 2020).

The creation of a physical phenomenon called sound is when anything vibrates. A sound wave requires a medium since sound is pressure variations traveling as waves. As previously mentioned, they could form this medium of solids, liquids, or gases. If these variances in specified weight fall within the run of human hearing, which contains a recurrence constraint of 20 Hz to 20 kHz, human eardrums will detect sound (Adriansyah, 2010).

Modern audio or voice applications also demand quick processing durations and low-power consumption. Traditional encryption techniques include symmetric algorithms such as ASE, DES, and public key algorithms such as RSA. While these techniques possess robust cryptographic features, they are unsuitable for low-profile audio applications considering their significant computational complexity. The development of audio encryption algorithms with calculative efficiency, real-time applicability, and effective multimedia processing capabilities is heavily emphasized in current research in digital security.

As Shannon (1998) suggested, diffusion and confusion are two of the key concepts in cryptography, and it is based on this idea that substitution and permutation operations networks (SPNs) become the foundation for many modern cryptography systems.

ARO-The Scientific Journal of Koya University  
Vol. XI, No.2 (2023), Article ID: ARO.11165, 7 pages  
DOI: 10.14500/aro.11165

Received: 20 February 2023; Accepted: 05 August 2023  
Regular research paper: Published: 25 August 2023

Corresponding author's e-mail: mardan.ameen@koyauniversity.org  
Copyright © 2023 Mardan A. Pirdawood, Shadman R. Kareem and Dashne Ch. Zahir. Pirdawood. This is an open access article distributed under the Creative Commons Attribution License.



A single nonlinear component, such as a “substitution box,” creates confusion. In this case, we permute the data value based on a key parameter. As part of the diffusion operation, the data value is replaced by a random number or series of numbers instead of the actual data value. According to this study, both terms have intricate relationships among ciphertexts, plaintexts, and encryption algorithms with symmetric keys; substitution-permutation networks are used as fundamental structural components of algorithms that use symmetric keys by analysts and designers.

In recent years, a multitude of encryption techniques have been put forward for encrypting digital audio. Lima and da Silva Neto (2016), they proposed a cryptographic technique based on the cosine number transform (CNT) to encrypt digital audio, which is applied recursively to two blocks of samples of a non-compressed digital audio signal and specified over a finite field. He chooses the blocks by applying a straightforward overlapping rule, which makes sure that the ciphered data are diffused throughout all the blocks that have been processed.

Elliptic curve cryptography (ECC), a method of encrypting data using elliptic curves (EC), was first suggested by Miller (August 1985). The security provided by ECC, which employs the Public Key encryption technique and security it offers, is based on how difficult the discrete logarithm problem (DLP) is to solve. In later applications, elliptic curve (ECC) public key cryptography is gaining traction. The public key approach for audio encryption is provided by Singh, et al. (2014) using a cryptographic scheme based on the ECC mathematical operation. The presented work illustrates how each value of the audio file is converted to an EC point and uses the ECC encryption algorithm. To show how ECC is implemented, the audio file is first converted into an affine point on the EC over the finite field  $GF(p)$ . The starting point for ECC,  $P_m(x, y)$ , is an affine point that is on the EC. In this work, he provides how the encryption and decryption processes work.

The combination of different techniques allows us to create more security modules when it comes to security issues, as well as more reliable results when it comes to image processing. As stated by (Al-Khazraji, Abbas, and Jamil, 2022), they have developed an innovative approach that combines neural style transfer (NST) and deep dream techniques to generate a novel image that merges both these advancements. The utilization of pre-trained networks, namely VGG-19 for NST and Inception v3 for deep dream, was integral to their methodology. As a result, by combining these two techniques, you are able to enhance the images that simulate hallucinations that are being experienced by both psychiatric patients and drug addicts.

The works of Hayat, Azam, and Asif (2018) and Hayat and Azam (2019), as cited in the references, involved the development of an EC-based system designed to produce  $8 \times 8$  S-boxes. This system took into account the significant influence of Modell’s Error-Correcting Codes (ECs) within a finite field context. Their research entailed the synthesis of a set of S-boxes utilizing both MEC and  $S_8$  as symmetric groups. In the work by Khalid, et al. (2022), they explored

the creation of a novel digital audio encryption method utilizing the Mordell EC (MEC) over a finite prime field within the context of the SPN. Their proposed approach consisted of two distinct components within the framework: the first aimed at managing confusion, while the second dealt with diffusion.

In recent years, unique characteristics of chaotic solutions, such as hypersensitive dependency, ergodicity, and pseudo-randomness, add a significant amount of unpredictability to deterministic nonlinear systems. Chaotic maps were widely used in various audio encryption frameworks. Kordov (2019) designed an audio encryption technique using an SPN structure and chaotic maps. In the study conducted by Shah, Shah, and Jamal (2020), they employed the SPN to propose an alternative method for audio encryption. Within their framework, they developed robust S-boxes for confusion by employing the Mobius transformation and the Hénon chaotic map. These S-boxes were then utilized for pixel-wise permutation to achieve diffusion.

The Laplace transform is a technique with several uses, such as wave equations, signals, systems, electrical circuit analysis, heat conduction, solar systems, hydrodynamics, communication systems, nuclear physics, and solar systems (Ramana, 2017). Lakshmi, Kumar and Sekhar, (2011) proposed a new cryptographic technique based on a new mathematical transformation for cryptography by employing Laplace transforms. In their work, a new approach to cryptography was introduced, involving the combination of a power series derived from the specific function  $f(t)$  and Laplace transforms. They created the key from the coefficients gained from the transformation by applying the modular arithmetic rules. Later, Hiwarekar (2013, July.) improved that cryptography technique in which the plain text was encrypted using the Laplace transform and cipher text decrypted using the inverse Laplace transform. Using Laplace transforms and infinite series expansion of the hyperbolic function, a new iterative encryption and decryption method has been developed (Hiwarekar, 2013).

We created a novel mathematical transformation for cryptography in this research, based on mixing hyperbolic functions and the Laplace transform for encrypting digital audio data and the corresponding inverse Laplace transform for decryption. The transform, defined over a finite field, is performed recursively to blocks of samples from a non-compressed digital audio input, where the secret key is used to determine how many times the transform is done to each of these blocks. Confusion approached with a power series coefficient. The technique we have employed has been previously utilized across various subjects by several researchers. For instance, Gencoglu (2019) innovatively employed the power series transform in cryptography to encrypt a specific sentence. This was accomplished through the utilization of the extended Laplace transform of an exponential function. The key is constructed by applying the principles of modular arithmetic to the transformation coefficients, while we use this method for encrypting digital audio files through the Maclaurin series of the cosine-hyperbolic transform in conjunction with the Laplacian

transformation which is applied to the coefficients of the Maclaurin series.

## II. DEFINITIONS AND BASIC CONCEPTS

The science of information security is the art and science of secret writing or cryptography. The message's original format is plaintext. They reference the message in disguise in the encrypted text. They encased the last message to be conveyed in a cryptogram. Transforming plaintext into ciphertext is known as encryption. Translating plaintext from cipher text in the other direction is known as decryption. We know the person who decodes the communication as the encipherer (Nichols, 1996).

### A. The Laplace Transform

The Laplace transform is a well-known integral transform in mathematics with several applications in science and engineering. It is the most essential integral transformation. Due to a variety of unique characteristics, the Laplace Transform can be thought of as a transformation from the time domain, where inputs and outputs are functions of time, to the frequency domain, where inputs and outputs are functions of complex angular frequency. Modern engineering system analysis and design strategies mainly rely on Laplace transform methods. The concepts of Laplace transforms are employed in a variety of scientific and technological domains, such as electric circuit analysis, communication engineering, control engineering, and nuclear physics (Lakshmi, et al., 2011). It is required to know the following Laplace transform findings:

### B. Definition

If  $f(t)$  is a function defined for all  $t \geq 0$ , then its Laplace transform is defined as

$$L\{f(t)\} = F(s) = \int_0^{\infty} e^{-st} f(t) dt \quad (1)$$

for all values of  $s$  for which the improper integral converges.

Assuming the integral is present. A real or complex number (Hiwarekar, 2013, July.) is used here as the parameter  $s$ . The inverse Laplace transform is of the form:

$$L^{-1}\{F(s)\} = f(t) \quad (2)$$

that a limit of integrals across bounded intervals defines an inappropriate integral over an infinite interval that is,

$$\int_0^{\infty} e^{-st} f(t) dt = \lim_{M \rightarrow \infty} \int_0^M e^{-st} f(t) dt \quad (3)$$

The improper integral is said to converge if the limit in (3) exists; otherwise, it diverges or doesn't exist.

### C. Linearity Property

The Laplace transform is a linear transform. It means that, if  $L\{f_1(t)\} = F_1(s), L\{f_2(t)\} = F_2(s), \dots, L\{f_n(t)\} = F_n(s),$

then

$$L\{c_1 f_1(t) + c_2 f_2(t) + \dots + c_n f_n(t)\} = c_1 F_1(s) + c_2 F_2(s) + \dots + c_n F_n(s), \quad (4)$$

where  $c_1, c_2, \dots, c_n$  are constants.

## III. PROPOSED METHOD

The application steps that boost the data security and privacy of this suggested hybrid model by combining cryptography and encryption technology are as follows.

### D. Encryption

The Maclaurin series of  $t \cosh t$  as follow:

$$t \cosh t = \sum_{i=0}^{\infty} \frac{t^{2i+1}}{2i!} \quad (5)$$

The suggested technique feeds an "audio1.wav" as a carrier input to do simulation studies. MATLAB was used to implement this proposed approach, and we use it with two data sound files (.wav). Figs. 2, 5, and 7 illustrate how the technique behaved during the encryption and decryption phases. Using the Matlab code  $[x, Fs] = \text{outright}(\text{"audio1.wav"})$ , we can get the vector that includes the values of the amplitude of our sample voice per second, which is the message that needs encryption. We consider the plot of the audio message to be as shown in Fig. 1. We convert the values of the vector  $x$  from decimal to integer form. To do this, we can choose the number of digits that should follow the decimal point. Let's say that there are a certain amount of digits following the decimal points (i.e.,  $m$  is number of digits after decimal points.).

Then, the vector  $y = x * 10^m$ , where  $m = 15$ , as shown in Fig. 3. If we take  $m$  large, then the error will become small (i.e., the difference between the original audio and the decrypted audio depends on the value of  $m$ ). Depending on the value of  $m$ , we ignore the decimal places while converting digital sound values, which are ordinarily decimal numbers, into

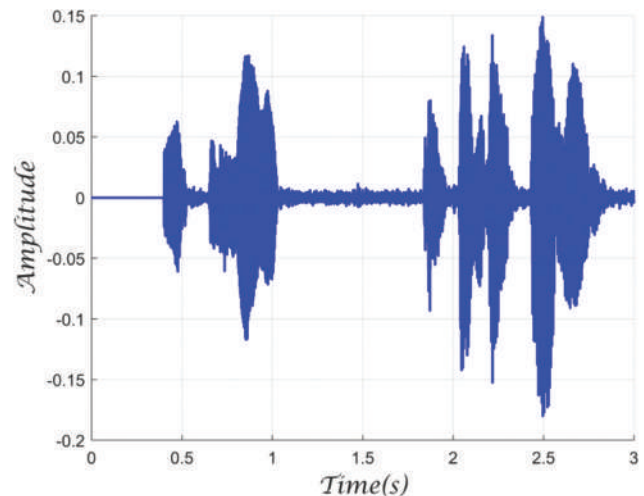


Fig. 1. Time domain plot of the "audio1.wav" signal.

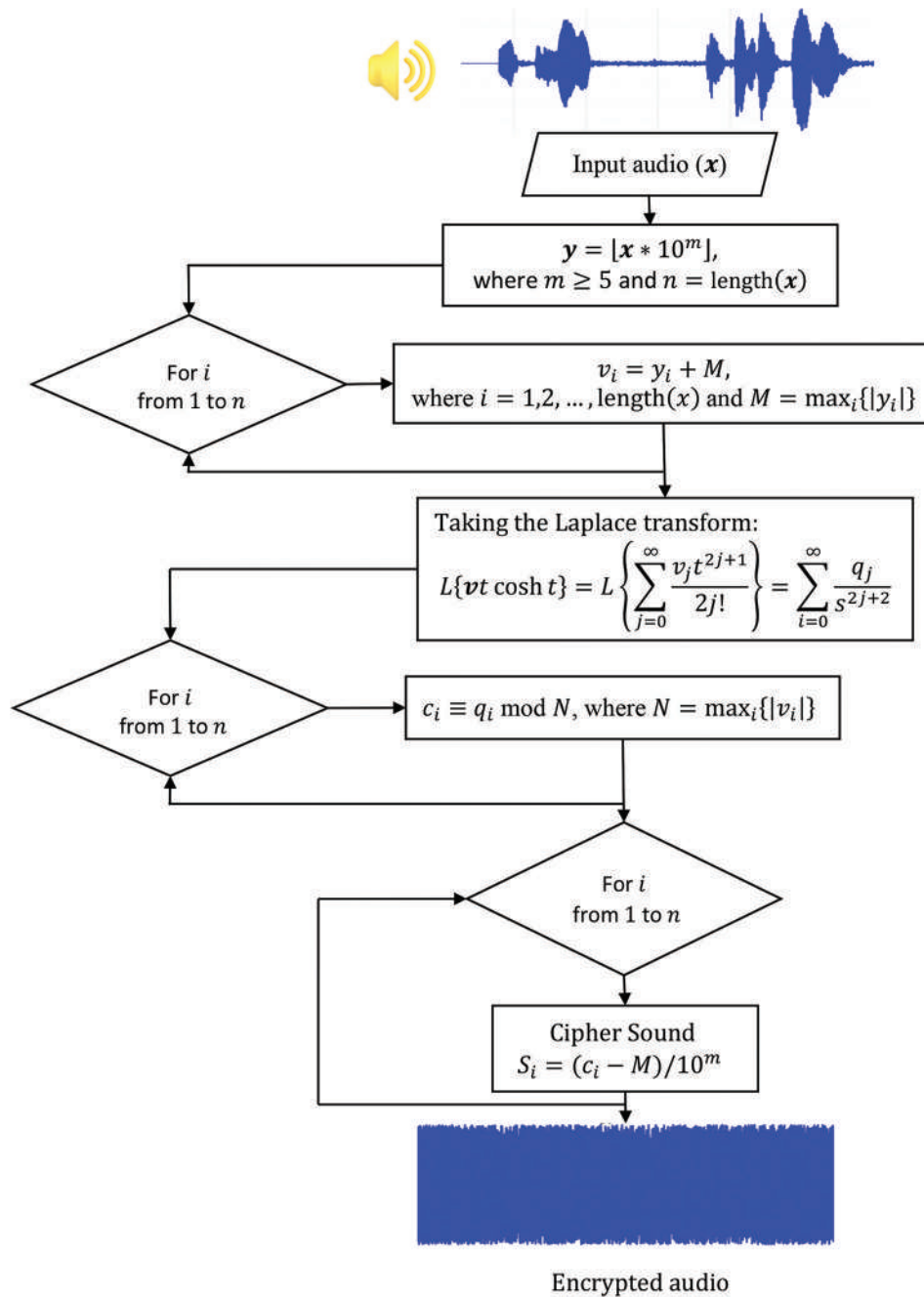


Fig. 2. Flow diagram of the proposed Laplace transformation audio encryption system.

integer numbers using the congruence module  $N$ .

For making the values of amplitude become non-negative, we do this calculation  $v_i = y_i + M$  where  $M = \max |y_i|$ . We did these calculations because we want the values to become between 0 and  $N = \max_i |v_i|$ , for  $i = 0, 1, 2, \dots, \text{length}(x)$  not face problems during the encryption and decryption when we take the congruence module  $N$ . Then, the plot of the amplitude per second of our audio signal sample is shown in Fig. 3. We can make the entries of on the vector  $v$ , as shown in Fig. 3 as a coefficients of the series as in equation (6) as follows:

$$f(t) = vt \cosh t = \sum_{i=0}^{\infty} \frac{v_i t^{2i+1}}{2i!} \quad (6)$$

By taking the Laplace transform for  $f(t)$ , we will have

$$L\{f(t)\} = L\{vt \cosh t\} = L\left\{\sum_{i=0}^{\infty} \frac{v_i t^{2i+1}}{2i!}\right\} = \sum_{i=0}^{\infty} \frac{q_i}{s^{2i+2}} \quad (7)$$

where  $q_i = v_i (2i-1)$  for  $i = 0, 1, 2, \dots$

Changing the results values of  $q_i$  to mod  $N$ , where  $N = \max_i |v_i| = 3288 \times 10^{11}$ . The amplitude of our sample audio gets converted to cipher amplitude value, with key  $k_i$  for  $i=0, 1, 2, 3, \dots$ . Hence, after calculating the amplitude sound vector  $s = (c-M)/10^m$  the message audio ‘audio1.wav’ of Fig. 1 gets converted to Fig. 5, and it was encrypted.

Note that the amplitude of the audio in terms of  $i$ ,  $i = 0$ ,



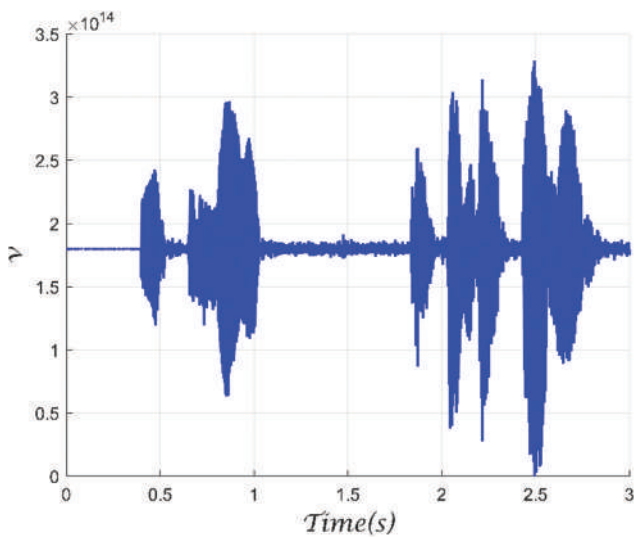


Fig. 3. The positive integer values of the amplitude per second need to be encrypted.

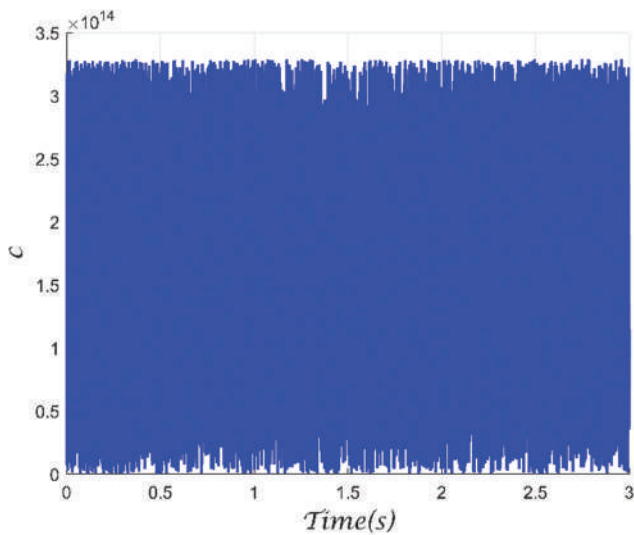


Fig. 4. The encrypted positive integer values of the vector  $c$ .

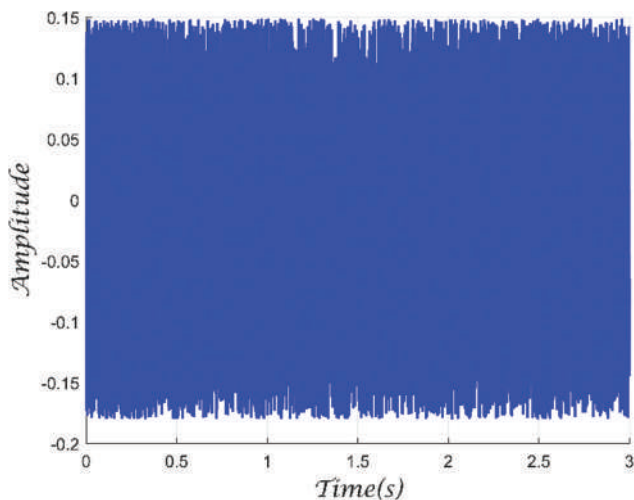


Fig. 5. The encrypted audio.

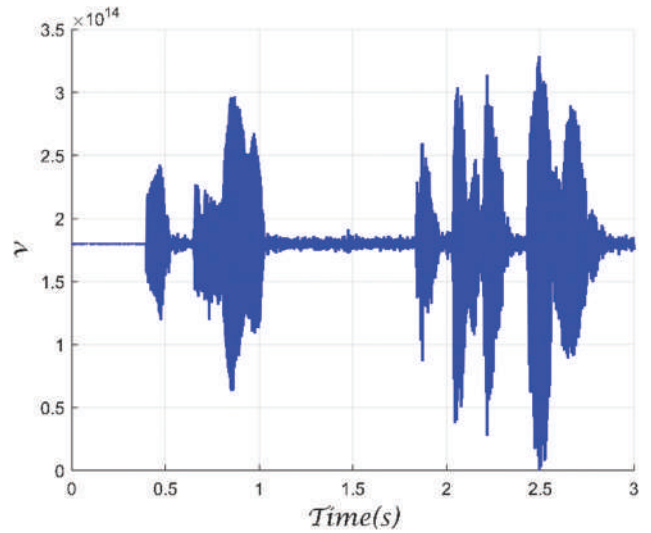


Fig. 6. The decrypted positive integer values of the vector  $v$ .

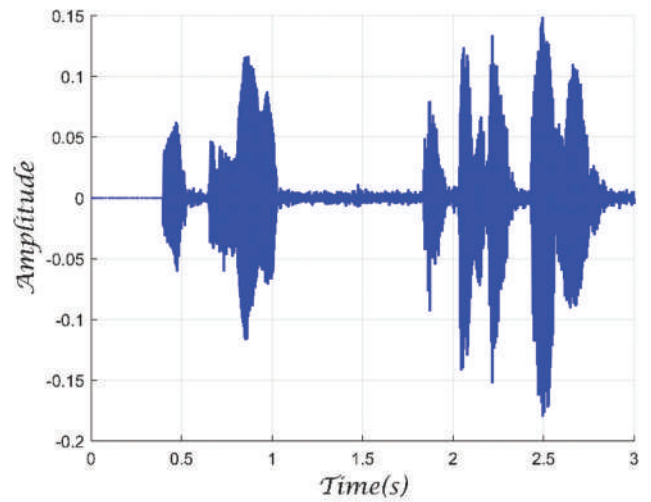


Fig. 7. The decrypted audio.

1, 2, ..., length ( $x$ ) under Laplace transform of  $vt \cosh t$  can be converted to cipher vector  $c$  where the components of this vector are given by

$$c_i = q_i - Nk_i, \text{ for } i = 0, 1, 2, \dots, \text{length}(x) \quad (8)$$

and

$$q_i = (2i + 1)v_i, \text{ for } i = 0, 1, 2, \dots, \text{length}(x) \quad (9)$$

with key

$$k_i = \frac{q_i - c_i}{N}, \text{ for } i = 0, 1, 2, \dots, \text{length}(x) \quad (10)$$

#### E. Decryption

We assume that the received cipher amplitude of the audio is shown in Fig. 4 as a vector  $c$ . The given key  $k_i$  for  $i = 0, 1, 2, \dots$ , as defined in equation (10). Let

$$q_i = Nk_i + c_i, \text{ for } i = 0, 1, 2, \dots, \text{length}(x) \quad (11)$$

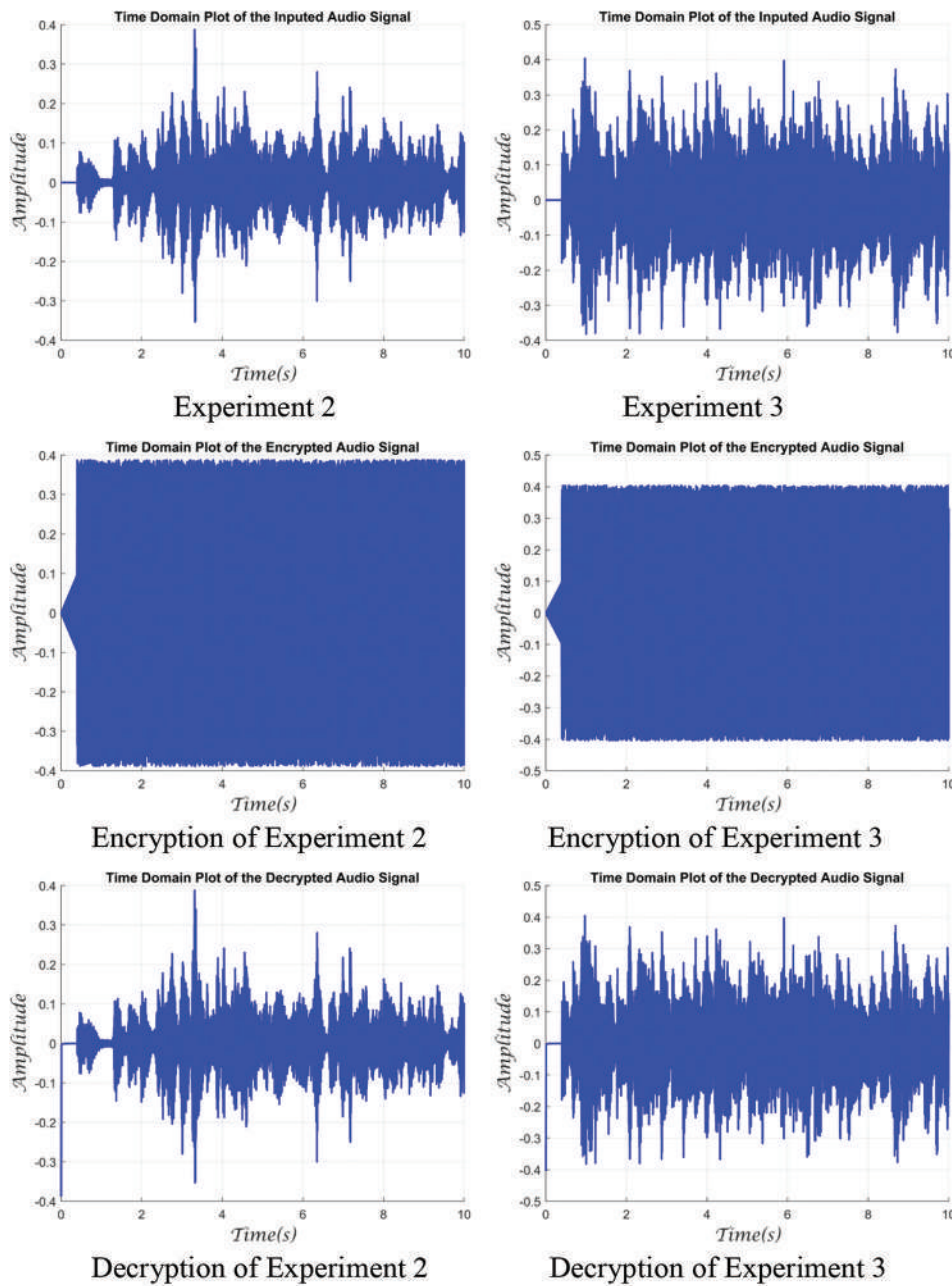


Fig. 8. The results of simulations for the proposed scheme were applied to other audio samples.

We will take the inverse Laplace transform for  $\sum_{i=0}^{\infty} \frac{q_i}{s^{2i+2}}$ , we obtain:

$$vt \cosh t = \sum_{i=0}^{\infty} \frac{v_i t^{2i+1}}{2i!} \tag{12}$$

The decrypted positive integer values of the vector  $v$  are shown in the Fig. 6.

Hence, after calculating the amplitude of the sound vector  $s = \frac{v - M}{10^m}$ , we have the decrypted audio, as shown in Fig. 7.

We can do other experiments on the other audios for more understanding and see how this technique works on them (Fig. 8).

TABLE I  
COMPARISON OF THE ERROR RATES OF THREE AUDIO ENCODING TECHNIQUES

Method	Cipher Key ( $N, m$ )	Error rate
LOG Method	$(a, b) = (0.0003, 300000)$	0.00017
RSA Method	$(e, n) = (5, 35)$	0.973701
Our proposed Method	$(N, m) = (3288 \times 10^{11,15})$	$1.1348 \times 10^{-14}$

The first goal, lossless, was accomplished by this approach since there was no data loss throughout the encryption and decryption operations when we took very large value of  $m$ , as seen from the aforementioned experiment results. The original audio stream and the decoded version are identical.

#### IV. ERROR RATE

By comparing the audio signals that have been decrypted to the original input signals, we may have obtained the error rate. For instance, in Figs. 1 and 7, the MATLAB Simulink system for measuring error rates is approaches to  $10^{-15}$ . The error rates of the RSA method and the LOG method proposed by Khalil (2016) are 0.00017 and 0.973701, respectively. These values indicate that our technique performs significantly better, as demonstrated in Table I. The proposed method outperforms the RSA and LOG methods in terms of error rate, as shown in table. Since the encryption algorithms use encoding techniques, it is obvious that some signals may have been lost during the recovery steps in (Khalil, 2016).

#### V. CONCLUSION

The security of real-time audio applications makes sure in the current study through a framework for encryption. The design framework protects the confidentiality of military voice communications by encrypting audio applications. The private key in the proposed work is the sum of multiples of the mod, and it suggests a novel cryptographic technique for the encryption of digital audio through the combination of infinity series of particular hyperbolic functions and employing Laplace transforms for encryption and corresponding inverse Laplace transforms for decryption. Due to this, it is highly challenging for an eyedropper to find the secret key using either a brute-force attack or any other assault. The performance and documented outcomes of the procedure clearly indicate that our method was successful in achieving its primary aim of sound data encryption.

#### ACKNOWLEDGMENT

The authors thank Koya University for their financial assistance.

#### REFERENCES

- Adriansyah, Y., 2010. *Simple Audio Cryptography*. Institute Teknologi Bandung Indonesia, Indonesia.
- Al-Kateeb, Z.N., and Mohammed, S.J., 2020. A novel approach for audio file encryption using hand geometry. *Multimedia Tools and Applications*, 79(27-28), pp.19615-19628.
- Al-Khazraji, L.R., Abbas, A.R., and Jamil, A.S., 2022. Employing neural style transfer for generating deep dream images. *Aro-The Scientific Journal of Koya University*, 10(2), pp.134-141.
- Delfs, H., Knebl, H., and Knebl, H., 2002. *Introduction to Cryptography*. Vol. 2. Springer, Heidelberg.
- Dutta, H., Das, R.K., Nandi, S., and Prasanna, S.M., 2020. An overview of digital audio steganography. *IETE Technical Review*, 37(6), pp.632-650.
- El-Zoghdy, S.F., El-sayed, H.S., and Faragallah, O.S., 2020. Transmission of chaotic-based encrypted audio through OFDM. *Wireless Personal Communications*, 113, pp.241-261.
- Gencoglu, M., 2019. Embedded image coding using laplace transform for Turkish letters. *Multimedia Tools and Applications*, 78(13), pp.17521-17534.
- Ghadi, M., Laouamer, L., and Moulahi, T., 2016. Securing data exchange in wireless multimedia sensor networks: Perspectives and challenges. *Multimedia Tools and Applications*, 75, p.3425-3451.
- Ghasemzadeh, A., and Esmaceli, E., 2017. A novel method in audio message encryption based on a mixture of chaos function. *International Journal of Speech Technology*, 20, pp.829-837.
- Hayat, U., and Azam, N.A., 2019. A novel image encryption scheme based on an elliptic curve. *Signal Processing*, 155, pp.391-402.
- Hayat, U., Azam, N.A., and Asif, M., 2018. A method of generating  $8 \times 8$  substitution boxes based on elliptic curves. *Wireless Personal Communications*, 101, p.439-451.
- Hiwarekar, A., 2013. A new method of cryptography using Laplace transform of hyperbolic functions. *International Journal of Mathematical Archive*, 4(2), pp.208-213.
- Kaur, A., and Dutta, M.K., 2018. An optimized high payload audio watermarking algorithm based on LU-factorization. *Multimedia Systems*, 24, pp.341-353.
- Khalid, I., Shah, T., Almarhabi, K.A., Shah, D., Asif, M., and Ashraf, M.U., 2022. The SPN network for digital audio data based on elliptic curve over a finite field. *IEEE Access*, 10, pp.127939-127955.
- Khalil, M., 2016. Real-time encryption/decryption of audio signal. *International Journal of Computer Network and Information Security*, 8(2), pp.25-31.
- Kordov, K., 2019. A novel audio encryption algorithm with permutation-substitution architecture. *Electronics*, 8(5), p.530.
- Lakshmi, G.N., Kumar, B.R., and Sekhar, A.C., 2011. A cryptographic scheme of laplace transforms. *International Journal of Mathematical Archive*, 2(12), pp.2515-2519.
- Lakshmi, G.N., Kumar, B.R., Suneetha, C., and Chandra, A., 2011. A cryptographic scheme of finite fields using logical operators. *International Journal of Computer Applications*, 975, p.8887.
- Lima, J.B., and da Silva Neto, E.F., 2016. Audio encryption based on the cosine number transform. *Multimedia Tools and Applications*, 75, pp.8403-8418.
- Liu, Z., Huang, J., Sun, X., and Qi, C., 2017. A security watermark scheme used for digital speech forensics. *Multimedia Tools and Applications*, 76, pp.9297-9317.
- Mel, H., and Baker, D., 2001. *Cryptography Decrypted*. Addison-Wesley, Reading, MA.
- Miller, V., 1985. Use of Elliptic Curves in Cryptography. In: *Conference on the Theory and Application of Cryptographic Techniques*. Springer, Berlin, Heidelberg, pp.417-426.
- Nichols, R., 1996. *Classical Cryptography Course*. Vol. 2. Aegean Park Press, California.
- Ramana, B., 2017. *Higher Engineering Mathematics*. Tata McGraw-Hill Education, United States.
- Shah, D., Shah, T., and Jamal, S.S., 2020. Digital audio signals encryption by Mobius transformation and Henon map. *Multimedia Systems*, 26, pp.235-245.
- Shannon, C., 1998. Communication theory of secrecy systems. 1945. *MD Computing: Computers in Medical Practice*, 15(1), pp.57-64.
- Singh, R., Chauhan, R., Gunjan, V.K., and Singh, P., 2014. Implementation of elliptic curve cryptography for audio-based application. *International Journal of Engineering Research and Technology (IJERT)*, 3(1), pp.2210-2214.

# Particle-Particle Collective Excitation of Sn isotopes

Ali H. Taqi and Fahema A. Saber

Department of Physics, College of Science, Kirkuk University,  
Kirkuk, Iraq

**Abstract**—In this paper, energy-level schemes and reduced electric transition strengths of neutron-rich Tin isotopes  $^{102,110,116,120,122}\text{Sn}$  ( $Z=50$ ) are studied using collective models, that is, particle-particle Tamm-Dancoff Approximation and particle-particle Random Phase Approximation. According to these models, the excited states of closed-core  $A+2$  systems with multipolarity  $J$  and isospin  $T$  can be described as a linear combination of particle-particle pairs. In our investigation, the low-lying states of the investigated isotopes  $^{102,110,116,120,122}\text{Sn}$  are described by acting two-particle operators on a correlated core  $^{100}\text{Sn}$ ,  $^{108}\text{Sn}$ ,  $^{114}\text{Sn}$ ,  $^{118}\text{Sn}$ , and  $^{120}\text{Sn}$ , respectively. The Hamiltonian is diagonalized within the model space include  $\{1g_{7/2}, 2d_{5/2}, 2d_{3/2}, 3s_{1/2}, \text{ and } 1h_{11/2}\}$  orbits, using the matrix elements of neutron-neutron interaction and modified surface delta interaction. The calculated values are checked by using the resultant eigenvalues and eigenvectors to calculate the excitation energies and reduced electric transition strengths. Our calculated results are compared to the available experimental data, and these comparisons led to reasonable agreements. Effective charges are also used to account for the core polarization effect.

**Index Terms**—Collective excitations, Energy-level schemes, Particle-particle Random Phase Approximation; Particle-particle Tamm-Dancoff Approximation.

## I. INTRODUCTION

Elsasser in 1934 observed that there are some nucleon numbers correspond to greater stability (given the name magic numbers) than other numbers (Sorkin, 2014). Subsequently, Mayer (1949); Haxel, Jensen and Suess (1949), indicated that the nuclear potential could be constituted by a one-body Harmonic Oscillator with a spin-orbit potential for creating the shell gaps at 8, 20, 28, 50, 82, and 126 (Elliott and Lane, 1954).

The main goal of theoretical nuclear physics is to develop a universal approach that can describe the excited state of all nuclear systems with the same accuracy. Nuclear structure problems, as in many branches of physics (theoretical atomic, solid-state, nuclear, and elementary particle physics), are many-body problems,

which can cause the dimension of Hilbert space to grow rapidly as the number of particles increases, and the dimension of such space becomes very large in many cases, preventing complete calculations. With such systems, the calculation of all possible truncated model spaces and various approximate approaches exists (Rowe, 1970; Brussaard and Glaudemans, 1977; Ring and Schuck, 1980).

The nuclear structure can be described according to the nuclear shell model where each nucleon in moving in single-particle orbits within some potential and regulates the energy levels in terms of quantum numbers ( $n\ell$ ) (Bhatt, Nestor Jr. and Raman, 1992). The nuclear shell model treats nucleons as occupying various orbits of a single particle orbits that are occupied and bound according to the principle of Pauli exclusion (Nichols, 2014; Tajima and Suzuki, 2001; Hasan, Obed and Rahim, 2020).

There are many correlations that cannot be reproduced using a simple shell model and Hartree-Fock (HF) calculations. These correlations can be taken into account by breaking the HF core and raising a nucleon from below to above Fermi level (Taqi, 2013; Rowe, 1970). According to the collective models, the excited states of  $A+2$  nuclei can be described as a linear combination of particle-particle ( $pp$ ) pairs (Ring and Schuck, 1980; Heyde, 1994). Such approximations are called particle-particle Tamm-Dancoff approximation ( $pp$  TDA). A more general model can be obtained by treating the ground and the excited states more symmetrically, that is, both the ground states and the excited states can be described as a linear combination of particle-particle and hole-hole states. Such an approximation is referred to as the particle-particle random phase approximation ( $pp$  RPA) (Taqi, 2007; Taqi, Rasheed and Amin, 2010).

Several theories and interaction have been used to explain the shell model calculations of Sn isotopes, for neutron-deficient Sn isotopes (Engeland, et al., 1995; Covello, et al., 1997; Schubert, et al., 1995) taking  $^{100}\text{Sn}$  as core, for  $^{106,107,108,109}\text{Sn}$  isotopes using CD-Bonn and Nijmegen1 interactions (Dikmen, 2009), for exotic  $^{134,136,138,140}\text{Sn}$  isotopes with a realistic effective interaction (Covello, et al., 2011), for even  $^{102-108}\text{Sn}$  and odd  $^{103-107}\text{Sn}$  isotopes using different interactions (Trivedi, et al., 2012), for  $^{104,106,108}\text{Sn}$  based on the CD-Bonn nucleon-nucleon (N-N) interaction (Jassim, 2013), and for even-even  $^{100-108}\text{Sn}$  isotopes by with the effective interactions Snet, SN100PN Delta interaction (Al-Attiah, Majeed and Al-Kawwaz, 2013).

ARO-The Scientific Journal of Koya University  
Vol. XI, No. II (2023), Article ID: ARO.11153, 5 pages  
DOI: 10.14500/aro.11153

Received: 09 February 2023; Accepted: 08 August 2023  
Regular research paper: Published: 25 August 2023

Corresponding author's e-mail: [alitaqi@uokirkuk.edu.iq](mailto:alitaqi@uokirkuk.edu.iq)  
Copyright © 2023 Ali H. Taqi and Fahema A. Saber. This is an open access article distributed under the Creative Commons Attribution License.



The energy levels, binding energy, and reduced transition probabilities  $B(E2;0^+ \rightarrow 2^+)$  were calculated for even-even  $^{134,136}\text{Sn}$ , and  $^{134,136}\text{Te}$  around doubly magic core  $^{132}\text{Sn}$  using shell model code Nushellx@MSU for Windows and employing the effective interactions jj56pna, jj56pnb, kh5082, cw5082, jj56cdb, and khhe (Majeed and Obaid, 2016). The surface delta interaction (SDI) and modified SDI (MSDI) are used by applying the nuclear shell model to calculate values of excitation energies for isotopes of equal mass number containing two nucleons outside the closed core  $^{114}\text{Sn}$ , these nuclei are that the isotope  $^{116}\text{Sn}$  contains two neutrons within the model space ( $3s_{1/2}, 2d_{3/2}, 1h_{11/2}$ ) and the other isotope is that  $^{116}\text{Te}$  contains two protons within the model space ( $1g_{7/2}, 2d_{5/2}, 3s_{1/2}, 2d_{3/2}, 1h_{11/2}$ ) (Obeed and Abed, 2020).

Theoretical nuclear physics is the development of models for describing structure and properties of atomic nuclei. A successful model must reasonably well account for previously measured nuclear properties and must predict additional properties that can be measured in new experiments. Therefore, in this paper, particle-particle excitations of some even-even Tin isotopes were investigated using particle-particle random phased approximation PPRPA code version 1, 2015 (Taqi, 2016) in the presence of MSDI and N-N interactions. Our approach assumes that the low-lying states of  $^{102}\text{Sn}$ ,  $^{110}\text{Sn}$ ,  $^{116}\text{Sn}$ ,  $^{120}\text{Sn}$ , and  $^{122}\text{Sn}$  by acting two-particle operators on a correlated core  $^{100}\text{Sn}$ ,  $^{108}\text{Sn}$ ,  $^{114}\text{Sn}$ ,  $^{118}\text{Sn}$ , and  $^{120}\text{Sn}$ , respectively. A comparison had been made between our theoretical predictions and the recent available experimental data.

## II. THEORY

The collective excited states of multipolarity  $J$  and isospin  $T$  for the  $A + 2$  systems can be constructed by operating  $Q_{\omega, JT}^\dagger$  on the core  $|0\rangle$  (Ring and Schuck, 1980),

$$Q_{\omega}^\dagger |0\rangle = |A+2, \omega, JT\rangle = \left( \sum_{m \leq n} X_{mn}^{\omega, JT} a_m^\dagger a_n^\dagger - \sum_{i \leq j} Y_{ij}^{\omega, JT} a_i^\dagger a_j^\dagger \right) |A, 0\rangle \quad (1)$$

where  $mn$  and  $ij$  represents orbits above and below the Fermi level, respectively. In  $pp$  RPA, two types of variations  $\delta Q_{\omega, JT} |0\rangle$  are available, they are:  $a_m^\dagger a_n^\dagger |0\rangle$  and  $a_i^\dagger a_j^\dagger |0\rangle$  which gives two sets of the equation of motion (Rowe, 1970; Ring and Schuck, 1980),

$$\left. \begin{aligned} RPA \left[ a_n a_m \left[ H, Q_{\omega, JT}^\dagger \right] \right] |RPA = E_x RPA \left[ a_n a_m, Q_{\omega, JT}^\dagger \right] |RPA \\ RPA \left[ a_i a_j \left[ H, Q_{\omega, JT}^\dagger \right] \right] |RPA = E_x RPA \left[ a_i a_j, Q_{\omega, JT}^\dagger \right] |RPA \end{aligned} \right\} \quad (2)$$

within the quasi-boson approximation, the amplitudes  $X_{mn}^{\omega, JT}$  and  $Y_{ij}^{\omega, JT}$  for  $|A+2, \omega, JT\rangle$  systems approximate as follows,

$$\left. \begin{aligned} X_{mn}^{\omega, JT} = A, 0 |a_n a_m |A+2, \omega, JT \cong HF | \left[ a_n a_m, Q_{\omega, JT}^\dagger \right] | HF \\ Y_{ij}^{\omega, JT} = A, 0 |a_i a_j |A+2, \omega, JT \cong HF | \left[ a_i a_j, Q_{\omega, JT}^\dagger \right] | HF \end{aligned} \right\} \quad (3)$$

The compact matrix of  $pp$  RPA can be written as (Ring and Schuck, 1980),:

$$\begin{pmatrix} A_{mmn}^{\omega, JT} & B_{mnij}^{\omega, JT} \\ B_{mnij}^{\omega, JT} & C_{iji'j'}^{\omega, JT} \end{pmatrix} \begin{pmatrix} X_{mn}^{\omega, JT} \\ Y_{ij}^{\omega, JT} \end{pmatrix} = E_x \begin{pmatrix} 1 & 0 \\ 0 & -1 \end{pmatrix} \begin{pmatrix} X_{mn}^{\omega, JT} \\ Y_{ij}^{\omega, JT} \end{pmatrix} \quad (4)$$

$$\left. \begin{aligned} A_{mmn}^{\omega, JT} &= (\varepsilon_m + \varepsilon_n) \delta_{mm} \delta_{nn} + V_{mmn} \\ C_{iji'j'}^{\omega, JT} &= (\varepsilon_m + \varepsilon_n) \delta_{mm} \delta_{nn} + V_{mmn} \\ B_{mnij}^{\omega, JT} &= -V_{ijmn} \end{aligned} \right\} \quad (5)$$

Where  $E_x$  and  $\varepsilon$  are the excited and single-particle energies, respectively, while  $V_{mmn}$  is the two-particle matrix element of the effective interaction. If sub matrices  $B_{mnij}^{\omega, JT}$  and  $C_{iji'j'}^{\omega, JT}$  set equal to zero, then the RPA equation reduces to the TDA equation.

The antisymmetric matrix elements of the MSDI used in this work have the form of the following (Brussaard and Glaudemans, 1977),:

$$V_{ab, cd}^{JT} = \frac{1}{2} A_T (-1)^{n_a + n_b + n_c + n_d} \times \sqrt{\frac{(2j_a + 1)(2j_b + 1)(2j_c + 1)(2j_d + 1)}{(1 + \delta_{ab})(1 + \delta_{cd})}} \times \left\{ \begin{aligned} &(-1)^{j_a + j_b + j_c + j_d} \begin{pmatrix} j_a & j_b & J \\ \frac{1}{2} & \frac{-1}{2} & 0 \end{pmatrix} \times \begin{pmatrix} j_c & j_d & J \\ \frac{1}{2} & \frac{-1}{2} & 0 \end{pmatrix} \\ &\left[ 1 - (-1)^{J+T+1} \right] - \begin{pmatrix} j_a & j_b & J \\ \frac{1}{2} & \frac{1}{2} & 1 \end{pmatrix} \begin{pmatrix} j_c & j_d & J \\ \frac{1}{2} & \frac{1}{2} & -1 \end{pmatrix} \\ &\left[ 1 + (-1)^T \right] + \left\{ [2T(T+1) - 3] B + C \right\} \delta_{ac} \delta_{bd} \end{aligned} \right\} \quad (6)$$

with

where  $B$ ,  $C$ ,  $A_0$ , and  $A_1$  are the strength parameters of the (MSDI).

## III. RESULTS AND DISCUSSIONS

In the present study, the nuclear structures of Tin isotopes:  $^{102}\text{Sn}$ ,  $^{110}\text{Sn}$ ,  $^{116}\text{Sn}$ ,  $^{120}\text{Sn}$ , and  $^{122}\text{Sn}$  are studied in the framework of  $pp$  TDA and RPA using PPRPA code version 1, 2015 (Taqi, 2016). The Hamiltonian is diagonalized within the model space including  $\{1g_{7/2}, 2d_{5/2}, 2d_{3/2}, 3s_{1/2}, \text{ and } 1h_{11/2}\}$  orbits, using MSDI and N-N interaction. The models assume that the low-lying states of  $^{102}\text{Sn}$  are obtained by acting  $pp$  operator on a correlated  $^{100}\text{Sn}$  core, of  $^{110}\text{Sn}$  are obtained by acting  $pp$  operator on a correlated core of  $^{108}\text{Sn}$  isotope, of  $^{116}\text{Sn}$  are obtained by acting  $pp$  operator on a correlated core of  $^{114}\text{Sn}$  isotope, of  $^{120}\text{Sn}$  are obtained by acting  $pp$  operator on a correlated core of  $^{118}\text{Sn}$  isotope, and of  $^{122}\text{Sn}$  are obtained by acting

$pp$  operator on a correlated core  $^{120}\text{Sn}$  isotope. The single particle energies are given in Table I.

The calculated  $pp$  TDA eigenvalues for  $^{102}\text{Sn}$  that were calculated using N-N interactions and MSDI along with the corresponding experimental data of energy levels (<https://www.nndc.bnl.gov>) are tabulated in Table II and are also plotted in Fig. 1.

Few excited states with  $J^\pi = 2^+, 4^+$ , and  $6^+$  are known from experiments. For instance, the first  $2^+$  experimental excited states are obtained at 1.472 MeV, the values of  $pp$  TDA with MSDI were found at 1.848 MeV, and the same state was found at 1.934 MeV with the N-N interaction.

The calculated eigenvalues and experimentally known energy levels for  $^{110}\text{Sn}$ ,  $^{116}\text{Sn}$ ,  $^{120}\text{Sn}$ , and  $^{122}\text{Sn}$  are tabulated in Tables III-VI and are also plotted in Figs. 2-5. The  $pp$

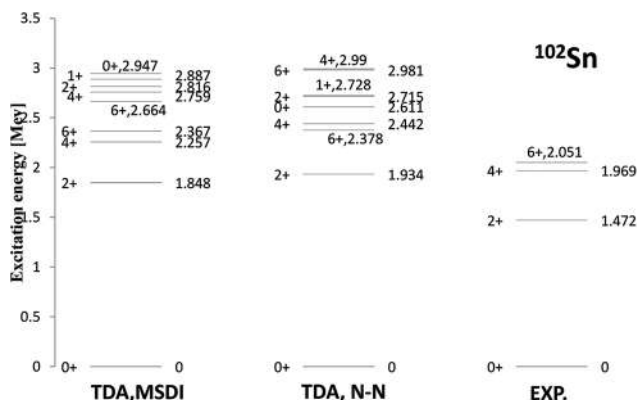


**Fig. 1.** Energy levels scheme of  $^{102}\text{Sn}$  isotope using particle-particle Tamm-Dancoff approximation with modified surface delta interaction and neutron-neutron interactions in comparison with the experimental energies (<https://www.nndc.bnl.gov>).

TABLE I  
SINGLE PARTICLE ENERGIES

ORBITS ( $NLJ$ )	S.P. ENERGY (MEV)
$1g_{7/2}$	-5.6014
$2d_{5/2}$	-5.2819
$2d_{3/2}$	-3.7090
$3s_{1/2}$	-3.7077
$1h_{11/2}$	-3.9843

TABLE II  
THE CALCULATED LOW-LYING STATES (MEV) OF  $^{102}\text{Sn}$  USING MSDI AND N-N INTERACTIONS FOR THE  $pp$  TDA IN COMPARISON WITH THE EXPERIMENTAL DATA ([HTTPS://WWW.NNDC.BNL.GOV](https://www.nndc.bnl.gov))

$J^\pi$	EXP.	$J^\pi$	TDA, MSDI	$J^\pi$	TDA, N-N
$0^+$	0	$0^+$	0	$0^+$	0
$2^+$	1.472	$2^+$	1.848	$2^+$	1.934
$4^+$	1.969	$4^+$	2.257	$6^+$	2.378
$6^+$	2.051	$6^+$	2.367	$4^+$	2.442
		$6^+$	2.664	$0^+$	2.611
		$4^+$	2.759	$2^+$	2.715
		$2^+$	2.816	$1^+$	2.728
		$1^+$	2.887	$6^+$	2.981
		$0^+$	2.947	$4^+$	2.99

N-N: Neutron-neutron,  $pp$  TDA: Particle-particle Tamm-Dancoff Approximation, MSDI: Modified surface delta interaction

TABLE III  
THE CALCULATED LOW-LYING STATES (MEV) OF  $^{110}\text{Sn}$  USING MSDI AND N-N INTERACTIONS FOR  $pp$  TDA AND  $pp$  RPA IN COMPARISON WITH THE EXPERIMENTAL DATA ([HTTPS://WWW.NNDC.BNL.GOV](https://www.nndc.bnl.gov))

$J^\pi$	EXP.	$J^\pi$	TDA, MSDI	$J^\pi$	TDA, N-N	$J^\pi$	RPA, N-N	$J^\pi$	RPA, MSDI
$0^+$	0	$0^+$	0	$0^+$	0	$0^+$	0	$0^+$	0
$2^+$	1.212	$1^+$	0.548	$1^+$	0.948	$1^+$	1.008	$1^+$	0.607
$4^+$	2.197	$2^+$	1.048	$2^+$	1.137	$2^+$	1.213	$2^+$	1.121
$2^+$	2.546	$4^+$	1.21	$4^+$	1.493	$4^+$	1.571	$4^+$	1.287
$4^+$	2.695	$2^+$	2.428	$2^+$	2.641	$2^+$	2.716	$2^+$	2.501
$6^+$	3.335	$4^+$	2.588	$4^+$	2.788	$4^+$	2.865	$4^+$	2.664
$7^+$	4.004	$11^+$	3.45	$11^+$	3.849	$11^+$	3.927	$11^+$	3.527
$8^+$	4.138	$7^+$	3.685	$7^+$	4.084	$7^+$	4.163	$7^+$	3.762
$10^+$	4.317	$6^+$	3.777	$6^+$	4.223	$6^+$	4.301	$6^+$	3.854
		$8^+$	3.815	$8^+$	4.295	$8^+$	4.374	$8^+$	3.893
		$10^+$	3.846	$10^+$	4.362	$10^+$	4.374	$10^+$	3.923
		$0^+$	4.29	$0^+$	4.762	$0^+$	4.838	$0^+$	4.366
		$2^+$	4.437	$2^+$	4.928	$2^+$	5.006	$2^+$	4.514

$pp$  TDA: Particle-particle Tamm-Dancoff Approximation,  $pp$  RPA: Particle-particle Random Phase Approximation, MSDI: Modified surface delta interaction, N-N: Neutron-neutron

TABLE IV  
THE CALCULATED LOW-LYING STATES (MEV) OF  $^{116}\text{Sn}$  USING MSDI AND N-N INTERACTIONS FOR  $pp$  TDA AND  $pp$  RPA IN COMPARISON WITH THE EXPERIMENTAL DATA ([HTTPS://WWW.NNDC.BNL.GOV](https://www.nndc.bnl.gov))

$J^\pi$	EXP.	$J^\pi$	RPA, MSDI	$J^\pi$	RPA, N-N	$J^\pi$	TDA, MSDI	$J^\pi$	TDA, N-N
$0^+$	0	$0^+$	0	$0^+$	0	$0^+$	0	$0^+$	0
$2^+$	1.293	$2^+$	1.531	$2^+$	1.104	$2^+$	1.386	$2^+$	0.905
$0^+$	2.027	$5^+$	1.788	$0^+$	1.567	$5^+$	1.636	$0^+$	1.349
$2^+$	2.112	$4^+$	1.807	$4^+$	1.603	$4^+$	1.654	$4^+$	1.386
$4^+$	2.391	$6^+$	1.871	$5^+$	1.64	$6^+$	1.718	$5^+$	1.421
$0^+$	2.545	$2^+$	2.289	$6^+$	1.769	$2^+$	2.138	$6^+$	1.551
$2^+$	2.65	$3^+$	2.319	$2^+$	2.076	$3^+$	2.168	$2^+$	1.858
$2^+$	2.843	$0^+$	2.378	$2^+$	2.141	$0^+$	2.225	$2^+$	1.924
$3^+$	2.996	$2^+$	2.385	$3^+$	2.171	$2^+$	2.231	$3^+$	1.953
$6^+$	3.032	$1^+$	2.403	$0^+$	2.203	$1^+$	2.248	$0^+$	1.998
		$2^+$	2.533	$1^+$	2.254	$2^+$	2.378	$1^+$	2.034
		$0^+$	2.534	$2^+$	2.465	$0^+$	2.379	$2^+$	2.245

$pp$  TDA: Particle-particle Tamm-Dancoff Approximation,  $pp$  RPA: Particle-particle Random Phase Approximation, MSDI: Modified surface delta interaction, N-N: Neutron-neutron

TABLE V  
THE CALCULATED LOW-LYING STATES (MEV) OF  $^{120}\text{Sn}$  USING MSDI AND N-N INTERACTIONS FOR  $pp$  TDA AND  $pp$  RPA IN COMPARISON WITH THE EXPERIMENTAL DATA ([HTTPS://WWW.NNDC.BNL.GOV](https://www.nndc.bnl.gov))

$J^\pi$	EXP.	$J^\pi$	TDA, MSDI	$J^\pi$	TDA, N-N	$J^\pi$	RPA, MSDI	$J^\pi$	RPA, N-N
$0^+$	0	$0^+$	0	$0^+$	0	$0^+$	0	$0^+$	0
$2^+$	1.171	$1^+$	0.671	$1^+$	0.619	$1^+$	0.758	$1^+$	0.745
$0^+$	1.875	$2^+$	1.102	$2^+$	0.695	$2^+$	1.24	$2^+$	0.865
$4^+$	2.194	$9^+$	1.187	$4^+$	1.133	$9^+$	1.343	$4^+$	1.32
$5^-$	2.284	$4^+$	1.246	$9^+$	1.135	$4^+$	1.396	$9^+$	1.33
$1^+$	2.297	$6^-$	1.267	$0^+$	1.194	$6^-$	1.423	$0^+$	1.383
$5^-$	2.54	$6^+$	1.307	$6^-$	1.215	$6^+$	1.46	$6^-$	1.41
$6^+$	2.685	$8^+$	1.344	$6^+$	1.297	$8^+$	1.499	$6^+$	1.488
$6^-$	2.749	$10^+$	1.373	$8^+$	1.369	$10^+$	1.528	$8^+$	1.564
$8^+$	2.802	$5^-$	1.458	$5^-$	1.411	$5^-$	1.614	$5^-$	1.605
$1^+$	2.835	$5^-$	1.496	$10^+$	1.436	$5^-$	1.652	$10^+$	1.63
$6^-$	2.844	$6^-$	1.687	$5^-$	1.444	$6^-$	1.843	$5^-$	1.639
$10^+$	2.902	$1^+$	1.85	$6^-$	1.667	$1^+$	2.001	$6^-$	1.862
		$0^+$	1.904	$1^+$	1.798	$0^+$	2.058	$1^+$	1.988

$pp$  TDA: Particle-particle Tamm-Dancoff Approximation,  $pp$  RPA: Particle-particle Random Phase Approximation, MSDI: Modified surface delta interaction, N-N: Neutron-neutron

RPA results are plotted in columns (second and third) for both interactions MSDI and N-N, respectively, while the *pp* TDA results are plotted in columns (fourth and fifth) for both interactions MSDI and N-N, respectively. The calculated results are compared with the experimental data (first

column). The sequence of levels is very predictable based on both interactions.

The calculated low-lying states of  $^{110}\text{Sn}$  and  $^{116}\text{Sn}$  using MSDI and N-N interactions for *pp* TDA and *pp* RPA are in agreement with the experimental data, notably,  $1^+$  and  $5^+$  levels cannot be predicted experimentally or are not available.

The first experimental  $2^+$  excited states for  $^{120}\text{Sn}$  occur at 1.171 MeV. The same state was found at 1.240 MeV when using *pp* RPA with the MSDI, but it was found at 0.865 MeV when using the N-N interaction. Similarly, the same state was found at 1.102 MeV when using *pp* TDA with the MSDI, but it was found at 0.695 MeV when using the N-N interaction.

There are only a few known experimentally excited states for  $^{122}\text{Sn}$  ( $J^\pi = 2^+, 4^+, 6^+, 8^+, \text{and } 10^+$ ), more states were predicted by *pp* TDA and *pp* RPA calculations for MSDI and N-N than by experimental evidence.

TABLE VI

THE CALCULATED LOW-LYING STATES (MeV) OF  $^{122}\text{Sn}$  USING MSDI AND N-N INTERACTIONS FOR *pp* TDA AND *pp* RPA IN COMPARISON WITH THE EXPERIMENTAL DATA ([HTTPS://WWW.NNDC.BNL.GOV](https://www.nndc.bnl.gov))

$J^\pi$	EXP.	$J^\pi$	TDA, MSDI	$J^\pi$	TDA, N-N	$J^\pi$	RPA, N-N	$J^\pi$	RPA, MSDI
$0^+$	0	$0^+$	0	$0^+$	0	$0^+$	0	$0^+$	0
$2^+$	1.14	$1^+$	0.587	$2^+$	0.566	$2^+$	0.72	$1^+$	0.664
$4^+$	2.142	$11^+$	0.803	$1^+$	0.617	$1^+$	0.737	$11^+$	0.944
$6^+$	2.555	$2^+$	0.906	$11^+$	0.834	$11^+$	1.017	$2^+$	1.023
$8^+$	2.69	$3^+$	0.945	$3^+$	0.975	$3^+$	1.144	$3^+$	1.071
$10^+$	2.765	$9^+$	0.987	$4^+$	1.005	$4^+$	1.179	$9^+$	1.128
		$5^+$	1.009	$9^+$	1.017	$9^+$	1.2	$5^+$	1.145
		$7^+$	1.018	$5^+$	1.039	$5^+$	1.218	$7^+$	1.158
		$4^+$	1.043	$7^+$	1.048	$7^+$	1.231	$4^+$	1.176
		$6^+$	1.101	$6^+$	1.169	$6^+$	1.348	$6^+$	1.24
		$8^+$	1.136	$8^+$	1.24	$8^+$	1.423	$8^+$	1.277
		$10^+$	1.163	$10^+$	1.307	$10^+$	1.49	$10^+$	1.304

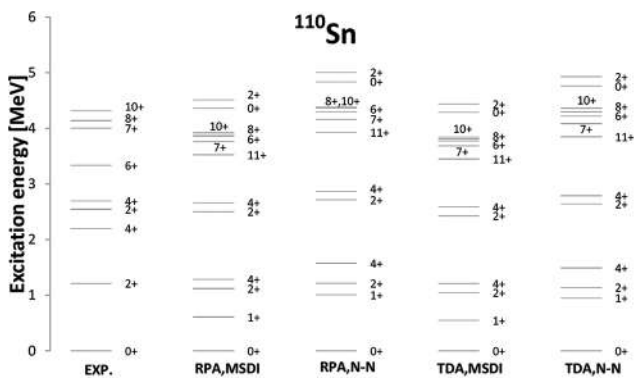


Fig. 2. Energy levels scheme of  $^{110}\text{Sn}$  isotope using particle-particle Tamm-Dancoff approximation and particle-particle random phase approximation with modified surface delta interaction and neutron-neutron interactions in comparison with the experimental energies (<https://www.nndc.bnl.gov>).

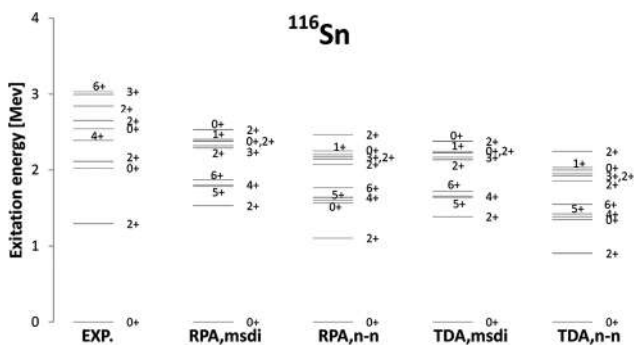


Fig. 3. Energy levels scheme of  $^{116}\text{Sn}$  isotope using particle-particle Tamm-Dancoff approximation and particle-particle random phase approximation with modified surface delta interaction and neutron-neutron interactions in comparison with the experimental energies (<https://www.nndc.bnl.gov>).

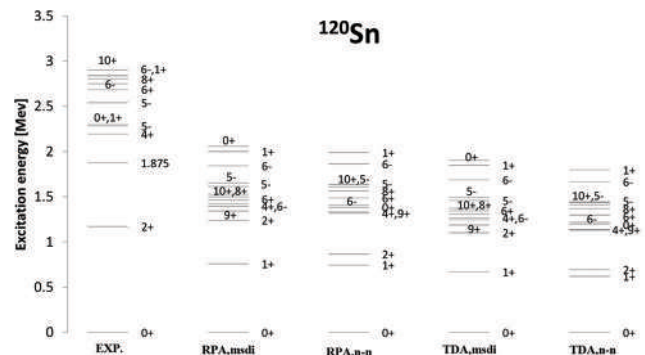


Fig. 4. Energy levels scheme of  $^{120}\text{Sn}$  isotope using particle-particle Tamm-Dancoff approximation and particle-particle random phase approximation with modified surface delta interaction and neutron-neutron interactions in comparison with the experimental energies (<https://www.nndc.bnl.gov>).

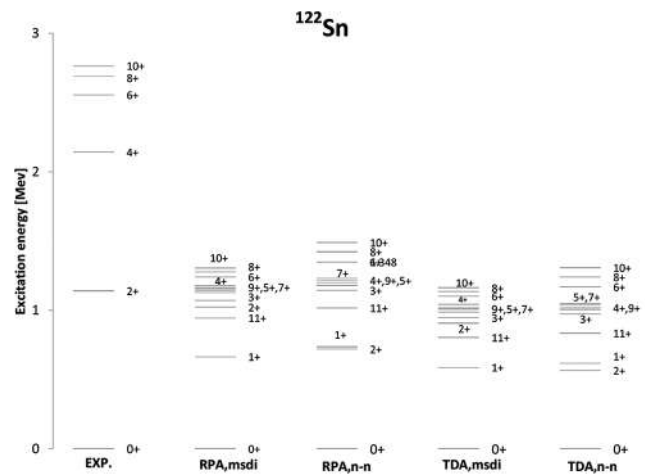


Fig. 5. Energy levels scheme of  $^{122}\text{Sn}$  isotope using particle-particle Tamm-Dancoff approximation and particle-particle random phase approximation with modified surface delta interaction and neutron-neutron interactions in comparison with the experimental energies (<https://www.nndc.bnl.gov>).

## IV. CONCLUSION

When the Hamiltonian is diagonalized in the presence of N-N interactions and MSDI, the calculated results of *pp* RPA and *pp* TDA are obtained in reasonable agreement to those of experimental data for the investigated Sn isotopes. Both the interactions predict very well the ordering of levels. However, for  $^{102}\text{Sn}$ , the N-N interaction has the same experimental  $2^+$  state. The ground states of  $^{110}\text{Sn}$  and  $^{116}\text{Sn}$  are very nicely predicted. The calculated first  $2^+$  excited state of  $^{120}\text{Sn}$  using *pp* RPA with the MSDI obtained at 1.24 MeV is in good agreement with the experimental value at 1.171 MeV.

## REFERENCES

- Al-Attiah, K.H.H., Majeed, F.A., and Al-Kawwaz, T.J., 2013. Calculations of even-even  $^{100-108}\text{Sn}$  isotopes using shell model in the vicinity of  $^{100}\text{Sn}$ . *Journal of Babylon University/Pure and Applied Sciences*, 21(8), pp.2831-2836.
- Bhatt, K.H., Nestor C.W. Jr., and Raman, S., 1992. Do nucleons in abnormal-parity states contribute to deformation. *Physical Review C, Nuclear Physics*, 46(1), pp.164-180.
- Brussaard, P.J., and Glaudemans, P.W.M., 1977. *Shell Model Applications in Nuclear Spectroscopy*. North-Holland Publishing Company, Amsterdam.
- Covello, A., Andreozzi, F., Coraggio, L., Gargano, A., Kuo, T.T.S., and Porrino, A., 1997. Nuclear structure calculations with realistic effective interactions. *Progress in Particle and Nuclear Physics*, 38, pp.165-172.
- Covello, A., Coraggio, L., Gargano, A., and Itaco, N., 2011. Shell-model study of exotic Sn isotopes with a realistic effective interaction. *Journal of Physics Conference Series*, 267, p.012019.
- Dikmen, E., 2009. Shell model description of neutron-deficient Sn isotopes. *Communications in Theoretical Physics*, 51(5), p.899.
- Elliott, J.P., and Lane, A.M., 1954. Evidence for two-body spin-orbit forces in nuclei. *Physical Review*, 96(4), p.1160.
- Engeland, T., Hjorth-Jensen, M., Holt, A., and Osnes, E., 1995. Large shell model calculations with realistic effective interaction. *Physica Scripta*, 1995(T56), p.58.
- Hasan, A.K., Obeed, F.H., and Rahim, A.N., 2020. Positive parity levels of  $^{21,23}\text{Na}$  isotopes by using the nuclear shell model. *Ukrainian Journal of Physics*, 65(1), p.3.
- Haxel, O., Jensen, J.H.D., and Suess H.E., 1949. On the magic numbers in nuclear structure. *Physical Review*, 75(11), p.1766.
- Heyde, K.L.G., 1994. *The Nuclear Shell Model*. Springer-Verlag, Berlin, Heidelberg.
- Jassim, K.S., 2013. Nuclear structure of  $^{104,106,108}\text{Sn}$  isotopes using the nushell computer code. *Chinese Journal of Physics*, 51(3), p.441.
- Majeed, F.A., and Obaid, S.M., 2016. Large-scale shell model calculations of  $^{134,136}\text{Sn}$ ,  $^{134,136}\text{Te}$  around doubly-magic  $^{132}\text{Sn}$ . *International Journal of Scientific and Technology Research*, 5(4), p.106.
- Mayer, M.G., 1949. On closed shells in nuclei. *Physical Review*, 75(12), p.1969.
- National Nuclear Data Center. Available from: <https://www.nndc.bnl.gov> [Last accessed on 2023 Feb 01].
- Nichols, A.J., 2014. *Gamma-ray Spectroscopy and Lifetime Measurements of Nuclei in the A=70, N =Z Region, PhD Thesis*. University of York, United Kingdom.
- Obeed, F.H., and Abed, B.S., 2020. Study of energy spectrum of  $^{116}\text{Sn}$  and  $^{116}\text{Te}$  nuclei by using surface delta and modified surface delta interactions. *Journal of Physics Conference Series*, 1664, p.012145.
- Ring, P., and Schuck, P., 1980. *The Nuclear Many-body Problem*. 1<sup>st</sup> ed., Springer-Verlag, New York.
- Rowe, D.J., 1970. *Nuclear Collective Motion: Models and Theory*. Butler and Tanner Ltd., London.
- Schubart, R., Grawe, H., Heese, J., Kluge, H., Maier, K.H., and Schramm, M., 1995. Shell model structure at 100Sn-the nuclides  $^{98}\text{Ag}$ ,  $^{103}\text{In}$ , and  $^{104,105}\text{Sn}$ . *Zeitschrift Für Physik a Hadrons and Nuclei*, 352, pp.373-390.
- Sorkin, O., 2014. Shell evolutions and nuclear forces. *EPJ Web of Conferences*, 66, p.01016.
- Tajima, N., and Suzuki, N., 2001. Prolate dominance of nuclear shape caused by a strong interference between the effects of spin-orbit and  $l^2$  terms of the Nilsson potential. *Physical Review C*, 64, p.037301.
- Taqi, A.H., 2007. The electroexcitation of low-lying, collective, positive parity, T=1 states in  $^{18}\text{O}$ , based on the particle-particle random phase approximation. *Chinese Journal of Physics*, 45(5), p.530.
- Taqi, A.H., 2013. Particle-particle Tamm-Dancoff approximation and particle-particle random phase approximation calculations for  $^{18}\text{O}$  and  $^{18}\text{F}$  nuclei. *Pramana Journal of Physics*, 80(2), pp.355-360.
- Taqi, A.H., 2016. A visual Fortran 90 program for the two-particle or two-hole excitations of nuclei: The PPRPA program. *SoftwareX*, 5, pp.51-61.
- Taqi, A.H., Rasheed, A.A., and Amin, S.H., 2010. Particle-particle and hole-hole random phase approximation calculations for  $^{42}\text{Ca}$  and  $^{38}\text{Ca}$  nuclei. *Acta Physica Polonica B*, 41(6), p.1327.
- Trivedi, T., Srivastava, P.C., Negi, D., and Mehrotra, I., 2012. Shell model description of  $^{102-108}\text{Sn}$  isotopes. *International Journal of Modern Physics E*, 21(4), p.1250049.



# Blackberry (*Rubus fruticosus* L.) Fruit Extract Phytochemical Profile, Antioxidant Properties, Column Chromatographic Fractionation, and High-performance Liquid Chromatography Analysis of Phenolic Compounds

Aryan F. Qader<sup>1,2</sup> and Mehmet Yaman<sup>2</sup>

<sup>1</sup>Department of Chemistry, Faculty of Science and Health, Koya University, Danielle Mitterrand Boulevard, Koya KOY45, Kurdistan Region – F.R. Iraq

<sup>2</sup>Department of Chemistry, Faculty of Science, Firat University, Elazig, Turkey

**Abstract**—This groundbreaking study explores the untapped potential of blackberries, a member of the *Rubus* genus in the Rosaceae family, and sheds light on their remarkable health and medicinal properties. Unlike previous research conducted in other regions, this investigation focuses specifically on the blackberry fruit's phytochemical constituents, chromatographic fractionations, and antioxidant activities in the Koisinjaq and Erbil villages of Northern Iraq. The research unveils seven distinct fractions obtained through column chromatography, with Fractions 2 and 3,5 found to contain p-coumaric acid and rutin, respectively, while Fraction 2 also houses chlorogenic acid. The analysis reveals the impressive richness of the methanolic blackberry extract in phenolic content (38.08 mg gallic acid equivalent/g dry weight [DW]), flavonoids (14.58 mg quercetin equivalent/g DW), flavonols (6.95 mg rutin equivalent/g DW), and anthocyanins (7.73 mg/kg DW), underlining the fruit's potent antioxidant activity. Furthermore, blackberries display exceptional ferric-reduction and metal-chelating capabilities, with 20.53 mg FeSO<sub>4</sub>/g and 182.12 mg Fe<sup>2+</sup>/g DW, respectively. Remarkably, blackberries also exhibit a remarkable ability to inhibit amylase activity (76.01%). These findings open up exciting prospects for utilizing blackberry fruit as a natural and potent source of phytochemicals and antioxidants in the food and pharmaceutical industries, promising transformative applications in health and well-being.

**Index Terms**—*Rubus fruticosus*, Phytochemical, Antioxidants, Column chromatography, Phenolic.

ARO-The Scientific Journal of Koya University  
Vol. XI, No. 2 (2023), Article ID: ARO.11189, 8 pages  
DOI: 10.14500/aro.11189

Received: 27 April 2023; Accepted: 16 August 2023

Regular research paper: Published: 25 August 2023

Corresponding author's e-mail: aryan.qader@koyauniversity.org

Copyright © 2023 Aryan F. Qader and Mehmet Yaman. This is an open access article distributed under the Creative Commons Attribution License.



## I. INTRODUCTION

Plants play a significant role in the food industry because of their sensory and nutritional properties, serving as sources of antioxidants to maintain food quality. They are used in medicine as medicinal herbs, providing healthcare and disease prevention for much of the global population (Hama, et al., 2016). Natural antioxidants can be found abundantly in medicinal herbs, making them an excellent source for creating contemporary medications. As various ailments such as cancer, liver disease, and arthritis do not have allopathic solutions, medicinal herbs have played a significant role in modern medicine (Shibu Prasanth and Chandran, 2017). Fruits and vegetables provide a variety of tastes and have been linked to an increased quality of life, making them essential for human health (Soquetta, Terra, and Bastos, 2018). Berries, with their unique color, flavor, aroma, high vitamin and mineral content, and range of food service applications, are a vital part of the fruit kingdom (Okatan, 2020). Blackberries, belonging to the *Rubus* genus in the Rosaceae family, are extensively grown globally. These fruits are native to tropical America, primarily Colombia and Ecuador (Sanín, Navia, and Serna-Jiménez, 2020). The global commercial output of blackberries is estimated to be approximately 154,578 tons/year, with North America, Europe, and Asia being the primary producers (Monforte, et al., 2018). Blackberries comprise several small drupes on a 1–2.5 cm long receptacle and are recognizable by their dark crimson color and bitter flavor (Fig. 1) (Sanín, Navia, and Serna-Jiménez, 2020).

The attractive color and flavor of blackberries (*Rubus fruticosus*) have made them a popular fruit, and they may also offer health benefits to humans (Santos, et al., 2019). Blackberries are rich in various bioactive



Fig. 1. Blackberry (*Rubus fruticosus* L.) fruit.

compounds, such as flavonoids, phenolic acids, tannins, vitamins, and antioxidants (Kitrytė, et al., 2020). The fruit of blackberries contains phenolic compounds such as anthocyanins, flavonols, chlorogenic acid, and procyanidins that have a positive impact on human health (Zafra-Rojas, et al., 2018). Blackberries have been used medicinally in Europe since the 16<sup>th</sup> century, where they were used for treating eye and mouth diseases (Oszmiański, et al., 2015). Various studies have suggested that consuming blackberries regularly can be beneficial to human health, especially in preventing and treating chronic degenerative disorders (Padilla-Jimenez, et al., 2019). Thus, this study aimed to establish an experimental set-up to extract and then fractionate the fruits, to isolate and explain new/novel phytochemical content. Thus, this study aimed to establish an experimental set-up to extract and then fractionate the fruits, isolate and explain new/novel phytochemical content, evaluate the antioxidant activity of the fraction, and identify potential new bioactive compounds or drugs.

## II. MATERIALS AND METHODS

### A. Chemicals

Only analytical-grade chemicals and solvents were used in this study. Silica gel for column chromatography (70–230 mesh ASTM), thin-layer chromatography (TLC), aluminum sheets 20 × 20 cm (60 F254), aluminum chloride, sodium acetate trihydrate, potassium ferricyanide, iodine, phenanthroline monohydrate, ferrous sulfate heptahydrate, dipotassium hydrogen phosphate, sodium carbonate, Folin-Ciocalteu's phenol reagent, sodium hydroxide, trichloroacetic acid, ferric chloride trihydrate, potassium hydroxide, and HCO<sub>2</sub>H was purchased from Merck (Germany). Methanol, ethanol, hexane, and sodium dihydrogen phosphate were got from Carlo Erba in Sabadell (Spain). Quercetin and ethyl acetate were purchased from Sigma-Aldrich (Germany). Gallic acid dry was supplied by ISOLAB GmbH. Rutin trihydrate was got from (Dr Ehrenstorfer™).

### B. Plant Acquisition

In October 2020, villagers in Northern Iraq's Koy Sanjaq/Erbil area (Fig. 2) gathered blackberries (*Rubus fruticosus* L.) fruit.

The fruit was washed, dried in the shade, and then ground into a fine powder in an electric grinder. The powder was then sealed in airtight vials and kept for future analysis.

### C. Plant Extraction

Using maceration achieved success in extracting plant components. The powder material was extracted at room temperature 3 times for 24 h using 75 ml of MeOH. Whatman filter paper No. 1 was used to filter the extract and the filtrate was concentrated under decreased pressure and at 40°C. Hexane was used to remove the fat after the evaporation of the extract. Dry methanolic extract (3.44 g) was kept at 4–6°C for further analysis.

### D. Total Phenolic Content (TPC)

The TPC extract was determined by altering the Folin–Ciocalteu procedure (Akyüz, et al., 2020). A 1.5 mL of distilled water was added to 0.1 mL of extract (3 mg/mL MeOH) and vigorously agitated for 5 min with 0.1 mL of Folin–Ciocalteu reagents, followed by 1.5 mL of sodium carbonate, 10% (w/v). After 60 min in the dark, the mixture's absorbance was determined at 765 nm using a Thermo Scientific GENESYS 10S ultraviolet-visible spectrophotometer (USA). A regression equation derived from the gallic acid standard calibration curve (Fig. 3a) was used to calculate the extract's TPC equivalents (mg gallic acid equivalent [GAE]/g dry weight [DW]).

### E. Total Flavonoid Content (TFC)

The aluminum chloride colorimetric technique was used to determine the flavonoid content of fruit extract with minimal development (Iqbal, Salim, and Lim, 2015). In total, 0.2 mL of extract (3 mg/mL) was combined with 1 mL of 5% AlCl<sub>3</sub> solution, followed by 0.1 mL of 1.0 M CH<sub>3</sub>COOK solution and 2.7 mL of MeOH then allowed to stand for 60 min. The absorbance was measured at 420 nm. A calibration curve (Fig. 3b) was used to compute the TFC, expressed as (mg quercetin equivalent [QE]/g DW).

### F. Total Flavonol Content (TF)

TF was quantified using a colorimetric approach using aluminum chloride (Binici, ŞAT, and Aoudeh, 2021), which was significantly changed. A standard calibration curve for this method was generated using rutin. A 0.5 mL solution of the extract (3 mg/mL) was added to a test tube, followed by 0.5 mL of 2% aluminum chloride and 5% sodium acetate (6 mL). After constant stirring, all tubes were incubated for 150 min at room temperature in a dark place. The absorbance was measured for the reference (Fig. 3c) and sample at 440 nm to get mg rutin equivalent (RE)/g DW values for the results.

### G. Total Anthocyanin Content (TAC)

The differential pH approach determined the amount of monomeric anthocyanin in its totality (Sutharut and Sudarat, 2012). The anthocyanin concentration of blackberry extract was measured by diluting it with potassium chloride (0.025 M) and sodium acetate (0.40 M) solutions and then

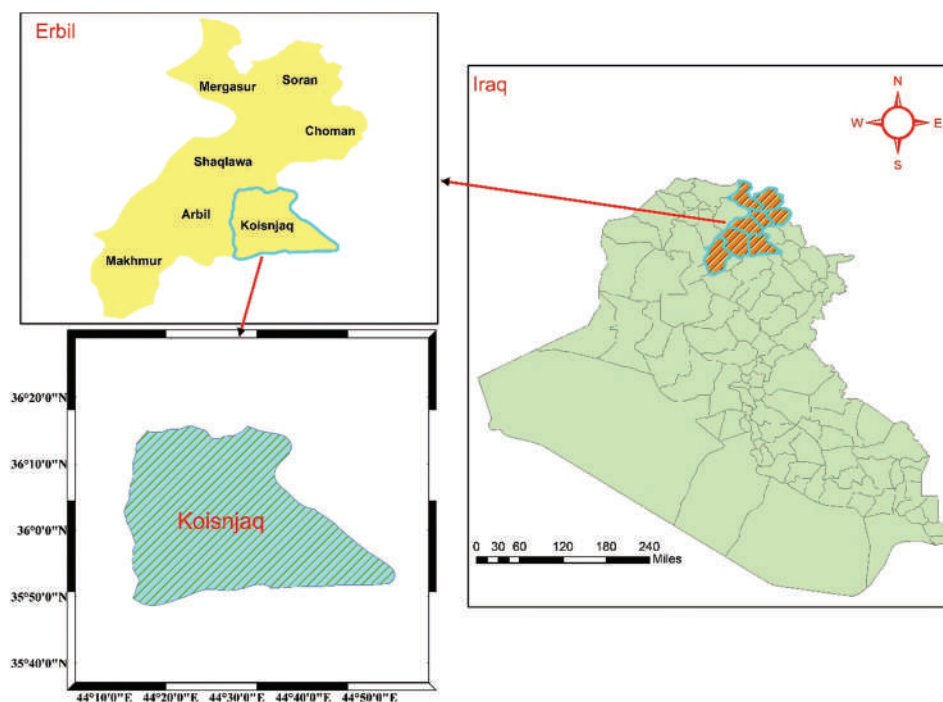


Fig. 2. GIS Map: Iraqi map, Erbil governorate location, and Koysnjaq study area location.

adjusting the pH with HCl to 1.0 or 4.5 as appropriate. The cyanidin-3-glucoside standard was used for absorbance measurement against a distilled water blank. The absorbance of each diluted solution was measured at two wavelengths, 520 nm, and 700 nm.

Calculation of absorption (A):

$$A = (A_{520} - A_{700})_{\text{pH 1.0}} - (A_{520} - A_{700})_{\text{pH 4.5}}$$

The following formula was used to calculate the absorption (A):

$$\text{Anthocyanin extraction yield (mg/g)} = \frac{A \times MW \times DF \times V \times 1000}{\epsilon \times L \times \text{wt}}$$

Where;

DF=Dilution factor, MW=Molar mass of cyanidin-3-glucoside (449.2 g/mol),  $\epsilon$ =molar extinction coefficient of cyanidin-3-glucoside (26900 L/mol.cm), V=Extract volume (L), L=Sample cell Length (cm), 1000=Conversion factor from g to mg, wt=Sample weight (g). Data represented in mg of cyanidin-3-glucoside/g.

#### H. Antioxidant Power for Reducing Ferric (FRAP)

Potassium ferricyanide made a colored complex containing antioxidant properties to test the reducing power (Günsel, et al., 2019). A 0.1 mL extract sample of 3 mg/mL concentration was added to a tube containing 2.5 mL of 1%  $K_3Fe(CN)_6$  and 2.5 mL of 0.2 M phosphate buffer (pH: 6.6). After 30 min at a temperature of 50°C, a 2.5 mL of 10% Trichloroacetic acid was added to the mixture and then centrifuged at 3000 rpm for 10 min. The supernatant was pipetted into a second tube

containing 2.5 mL water and 0.5 mL of newly prepared 0.1%  $FeCl_3$  concentration. The same approach was used to develop a standard calibration curve for quercetin (Fig. 3d). The absorbances were recorded at 700 nm.

#### I. Metal Chelating Ability (MCA)

The metal-chelating activity of blackberry extract was studied using the 1,10-phenanthroline technique (Akbaba, 2021) by filling the tube with 0.1 mL of sample solution (3 mg/mL). Then, 1.5 mL of water, 1 mL of 0.2%  $FeCl_3$ , 1 mL of 0.2% phenanthroline, and 1.4 mL of water were added. The tubes were vigorously shaken before incubation for 20 min in a dark place. The absorbance was determined at 510 nm. The equivalent iron II sulfate concentrations are given in mg  $Fe^{2+}$ /g DW (Fig. 3e).

#### J. $\alpha$ -amylase Inhibition (AAI)

A modified starch iodine approach was used (Ademiluyi and Oboh, 2013). A 0.25 mL of  $\alpha$ -amylase was incubated with 0.25 mL (3 mg/mL) of plant extract for 15 min at 37°C. After the addition of 0.25 mL of starch solution, the mixture was reincubated for 30 min. A 0.1 mL of HCl (1.0 M) was added to halt the reaction. Adding 1.0 mL of iodine reagent to 3.0 mL of distilled water, the mixture was continuously vortexed. A spectrophotometer was used to quantify the absorbance at 580 nm. Individual blanks were prepared to change the background absorbance of the measurements. The controls were done the same way as the trials, where plant extract for 0.25 ml of distilled water was substituted. The commonly used drug for antidiabetic is acarbose, which was used as a positive control.

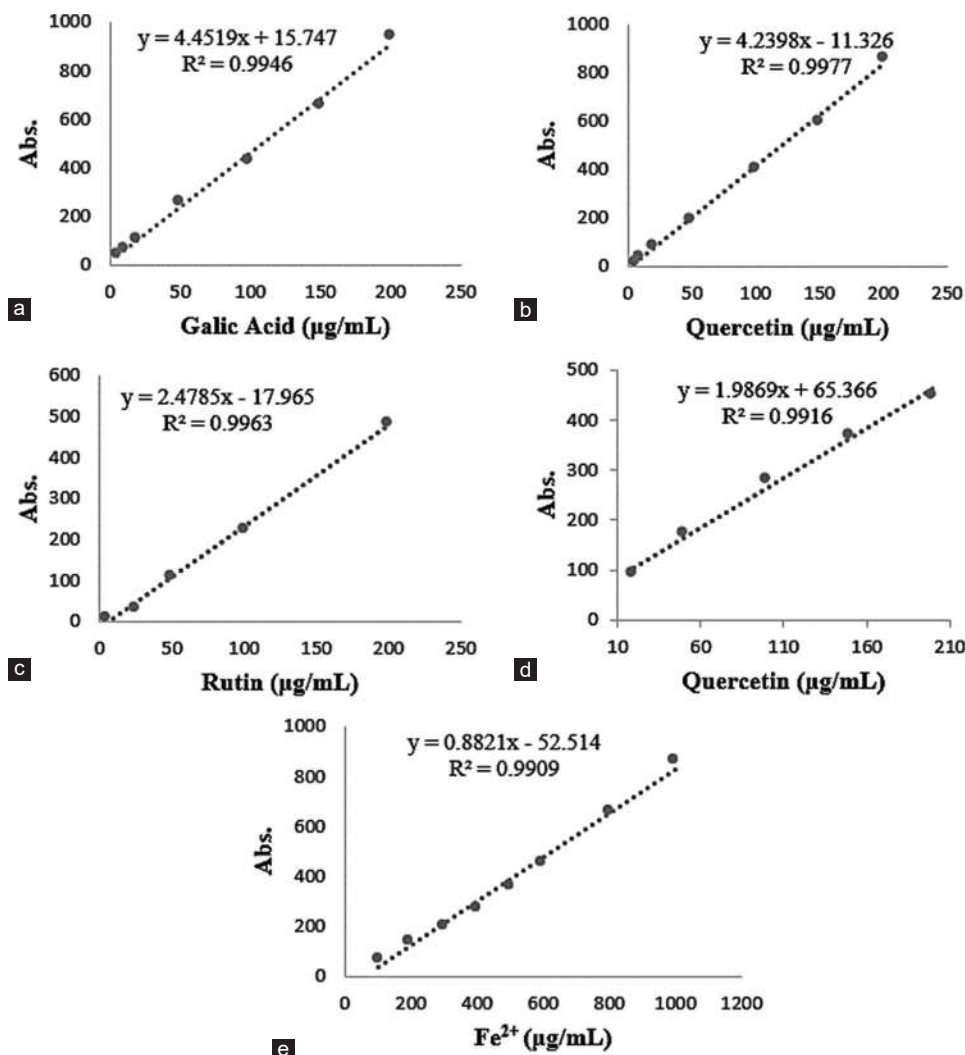


Fig. 3. Calibration curve of (a) gallic acid standard for the total phenolic content analysis, (b) quercetin standard for the total flavonoid content analysis, (c) rutin standard for the total flavonol content analysis, (d) quercetin standard for the ferric reducing antioxidant power analysis, and (e) Ferrous sulfate standard for the metal chelating ability analysis.

### K. Select a Plant Separation Solvent

TLC confirmed the bioactive component separation from the methanolic extract. Many solvent systems were tested to choose the optimum one. The chromatogram was examined under UV light (254 nm and 365 nm) to see whether it could detect spots in an iodine chamber. The mobile phase employed was toluene-ethyl acetate-formic acid. Because of its higher  $R_f$  value, chemical separation in column chromatography was achieved using toluene-ethyl acetate-formic acid (65:45:25).

### L. Chromatographic Separation in a Column

Column chromatography is one of the best ways to separate phytochemicals. This study innovated an appropriate mobile solvent system. Therefore, the chromatography was done on an empty glass column filled with activated silica gel (70–230 mesh) and washed with the mobile phase. It was mixed with a solvent solution and put on the column (Fig. 4). TLC plates were applied to monitor the 85 collected fractions, and the relevant fractions were mixed, and then

concentrated under low pressure. In the end, seven unique blackberry extract fractions were available.

### M. High-performance Liquid Chromatography (HPLC) Phenolic Components Analysis

A Shimadzu HPLC equipped with a Shimadzu DGU-20A5 vacuum degasser and a Shimadzu 20 ADXR solvent pump was employed to determine the polyphenol concentrations. Separations were performed using a reversed-phase Cliepus C18 5 m column (250 mm × 4.6 mm). Detection was performed using a Shimadzu SPD-M20A photodiode array detector. Stock solutions for analytically pure polyphenol standards were prepared by dissolving 0.01 g of polyphenol in deionized clean water and adding 10 mL of MeOH and water in a (1:1) ratio. Essential stock solutions were prepared from the prepared stock solution for each polyphenol. HPLC-DAD method was used to identify the phenolic chemicals (Erkan, 2012). Gradient elution using solvent A: 4.5% of acetic acid solution and solvent B: acetonitrile as mobile phases at a flow rate of 1.0 mL/min and an injection volume of 20 µL

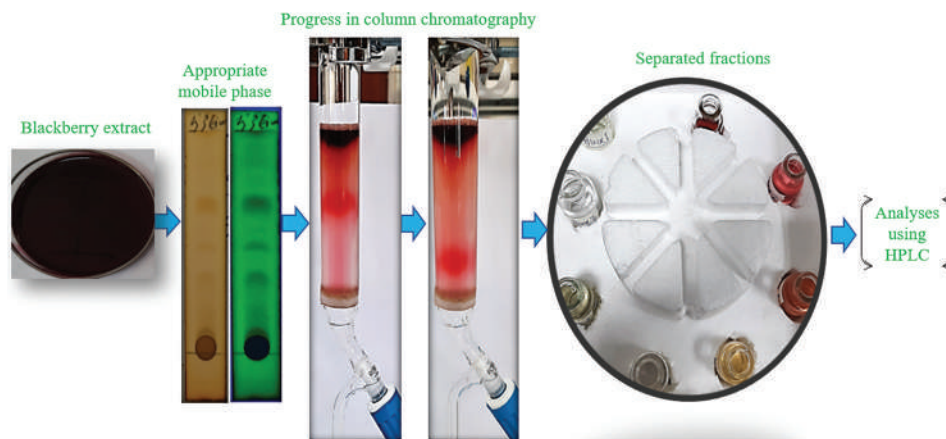


Fig. 4. Column chromatography produced seven fractions using a suitable mobile phase and thin-layer chromatography confirmation.

was used to detect the concentration. The diluted extract and the fractions were injected straight into the HPLC apparatus and screened using a photodiode array detector.

### III. RESULTS AND DISCUSSION

#### A. Total Phenolic, Flavonoid, Flavonol, and Anthocyanin Contents

*Rubus fruticosus* L.'s phenolic, flavonoid, flavonol, and anthocyanin content and the corresponding quantities are listed in Table I. The TPC of an extract was measured using the Folin–Ciocalteu method, which depends on transferring electrons from phenolic compounds to the Folin–Ciocalteu reagent in alkaline conditions. This method is a standard and straightforward one. TPC of 38.08 mg GAE/g dry extract was the most significant one. Many studies have been conducted to evaluate the correlation between phenolic content and antioxidant activity. Researchers observed a correlation between phenolic concentration and antioxidant activity, although others found no evidence (Ismail, Marjan, and Foong, 2004).

The human body's capacity to combat illnesses is aided by flavonoids, which are a subset of polyphenols (Rajanandh and Kavitha, 2010). Flavonoids are secondary metabolites that exhibit antioxidant activity based on the amount and position of free OH groups (Aryal, et al., 2019). This extract had 14.58 mg QE/g of dry extract of TFC, showing that it possessed the greatest TFC.

Many plant foods include flavonols, a class of flavonoids and polyphenols that critically prevent coronary heart disease and other age-related diseases such as dementia (Fang, Tang and Huang, 2013). Quercetin, the most abundant flavonol with antioxidant activity, has all the structural characteristics required for free radical scavenging (Kalita, et al., 2013). Blackberry extract had the greatest flavonols, with 6.95 mg RE/g dry extract of TF. The values of TPC and TFC in this study were more significant than the range previously reported by researchers. According to a study of the preceding literature, Zafra-Rojas, et al. reported a TPC of 40.16 mg GAE/g DW and a TAC of 3.65 mg cy-3-glu/g DW (Zafra-Rojas, et al., 2018). Diaconeasa et al. observed that the

TABLE I  
ANALYSES OF BLACKBERRY EXTRACT'S PHYTOCHEMICAL CONTENT

Phytochemicals	Present quantity
TPC (mg GAE/g)	38.08±0.19
TFC (mg QE/g)	14.58±0.83
TF (mg RE/g)	6.95±0.76
TAC (mg cy-3-glu/kg)	7.73±1.17

TPC: Total phenolic content, TFC: Total flavonoid content, TF: Total flavonol content, TAC: Total anthocyanin content, GAE: Gallic acid equivalent, QE: Quercetin equivalent, RE: Rutin equivalent, Results are reported as mean±SD of three determinations

TPC of blackberry methanol extract was 4.61 mg GAE/g DW and the TFC was 0.07 mg QE/g DW (Diaconeasa, et al., 2019). Koca and Karadeniz (2009) determined that the methanol extract of blackberry contained 3.26 mg of GAE/g and 1.59 mg of cy-3-glu/g of the dry weight of TPC and TAC (Koca and Karadeniz, 2009).

Phytochemicals called anthocyanins are naturally occurring pigments that give fruits, vegetables, and plants color. They stand head and shoulders above chlorophyll in readily observable plant pigments (Kong, et al., 2003). Glucosil residues and polar substituent groups (hydroxyl, carboxyl, and methoxyl) combined in anthocyanins, making them polar molecules in their own right (Navas, et al., 2012). *In vitro* and *in vivo* studies have shown anthocyanins' antiallergic, anti-inflammatory, antiviral, and antioxidant effects (Al-Sane, Povero, and Perata, 2011). Besides their various roles, they were reduced agents, hydrogen donors, and single oxygen quenchers. The presence of electron-donating and electron-withdrawing substituents in the ring structure and the amount and location of OH groups play an essential role in this property (Lapornik, Prošek, and Wondra, 2005). The most frequently used method for analyzing anthocyanin is the pH differential approach, because of its speed and simplicity. Blackberries had a 7.73 mg cy-3-glu/kg DW (Table II).

#### B. Antioxidant Power for Reducing Ferric

One of the most used methods for evaluating antioxidant capability is the FRAP test. The ability of antioxidants to reduce  $Fe^{3+}$  to  $Fe^{2+}$  is the basis of the FRAP test's colorimetric technique. FRAP test directly reveals a substance's reducing capacity, which is essential for assessing whether a compound

is an efficient antioxidant (Rehakova, et al., 2014). In this study, a compound's potency as a reducing agent was evaluated by reducing Fe [(CN)<sub>6</sub>]<sup>3+</sup> to Fe [(CN)<sub>6</sub>]<sup>2+</sup>. The complex formation results in an increase in absorbance, which shows that the reduction capacity has improved. Blackberry methanol extract had 20.53 mg FeSO<sub>4</sub>/g DW (Table II). The antioxidant activity of blackberries has been reported in earlier studies to be typically lower than the value observed in this research. In the previous work, Zafra-Rojas, et al. discovered a FRAP of 12511.44 μmol Fe (II)/100 g DW (Zafra-Rojas, et al., 2018). Koca and Karadeniz (2009) previously determined FRAP equals 59.36 μmol Fe (II)/g DW (Koca and Karadeniz, 2009).

### C. Capacity for Chelating Metal Ions

Oxygen transport and respiration depend on iron, which acts as a cofactor for several iron-metallic enzymes. Fenton reactions, which are the breakdown of hydrogen or lipid peroxide to create highly reactive and physiologically hazardous hydroxyl and lipid peroxy radicals catalyzed by transition metals, may cause the creation of reactive oxygen species if there is an excess of free iron (Islam, Yu and Xu, 2016).

The iron-chelating agent 1,10-phenanthroline is assumed to chelate primarily Fe<sup>2+</sup> as [Fe (phenanthroline)]<sup>2+</sup>. Fe<sup>2+</sup>-phenanthroline combination absorbs visible wavelength light at 510 nm, and the measurement is directly proportional to the sample's Fe<sup>2+</sup> level in the pH range of 2.5 to 8.0 (Zohlen, 2000). Antioxidants are oxidized when they are exposed to FeCl<sub>3</sub>. Antioxidants undergo oxidation upon exposure to FeCl<sub>3</sub>, causing a reduction of Fe (III) to Fe (II). The Fe-phenanthroline generated matches a sample's antioxidant content (Yefrida, et al., 2018). The data show that blackberry

extract can chelate metals at 182.12 mg Fe<sup>2+</sup>/g DW (Table II). The blackberry methanol extract was shown to have FRAP of 955.4 μM Fe<sup>2+</sup>/g DW and MCA of 437 μg/mL DW by Bhagat and Thusoo (2015).

### D. AAI Assay

Antidiabetic drugs might be identified by investigating natural extracts from readily available traditional medicinal plants. Several plants have been showed to inhibit α-amylase, making them potentially effective in treating diabetic patients (Rahimzadeh, et al., 2014). The human body needs to have an enzyme called α-amylase that breaks down starch into simpler sugars (Nickavar and Yousefian, 2011). AAI slows the hydrolysis of α-1,4-glycosidic bonds in carbohydrates (such as starch and maltose), resulting in decreased glucose absorption into the circulation (Anigboro, et al., 2021).

Inhibitory effects of blackberry extract on α-amylase have been shown in inhibition studies. The amounts of plant extract in test samples were compared to those in control samples in all trials. Acarbose was used as a positive control. A plant extract's α-amylase inhibitory activity was investigated using a quantitative starch-iodine method. The amylase inhibition effect on a plant extract is shown in Table II. Table III compares the phytochemical profile and antioxidant activity of the Kurdistan region to those of other regions.

### E. HPLC Analysis of the Extract and Fractions

A total of 85 fractions were collected using glass column chromatography. Using comparable thin-layer chromatograms, they were combined into seven separate fractions. Complex natural chemicals make it very difficult to investigate the structure of active plant components and evaluate their antioxidant and biological capabilities. High-resolution chromatographic technologies, such as HPLC, identified and characterized some of the bioactive compounds discovered in the extract and its fractions. (Gómez-Caravaca, et al., 2006). A fruit extract and seven blackberry fractions (F1-F7) were tested. As shown in Table IV, the fruit methanolic extract lacked significant phenolic components, while fraction two contained two different compounds and Fractions 4 and 5 included just one significant component. Other phenolics were detected; however, they could not be identified because of insufficient criteria.

TABLE II  
BLACKBERRY EXTRACT FERRIC REDUCTION ANTIOXIDANT POWER, METAL CHELATING CAPABILITY, AND AAI

Antioxidants	Present quantity
FRAP (mg FeSO <sub>4</sub> /g DW)	20.53±0.47
MCA (mg Fe <sup>2+</sup> /g DW)	182.12±0.26
AAI%	76.01±1.57

Results are reported as mean±SD of three determinations. DW: Dry weight, FRAP: Ferric reducing antioxidant power, MCA: Metal chelating ability, AAI: α-amylase Inhibition

TABLE III  
COMPARISON OF THE PHYTOCHEMICAL PROFILES OF BLACKBERRIES FROM KURDISTAN AND OTHER REGIONS

Phytochemicals	Kurdistan region	Other regions	References
TPC (mg/g) DW	38.08±0.19	40.16	Zafra-Rojas, et al., 2018
		4.61	Diaconeasa, et al., 2019
		3.26	Koca and Karadeniz, 2009
TFC (mg/g) DW	14.58±0.83	0.07	Diaconeasa, et al., 2019
TF (mg/g) DW	6.95±0.76		
TAC (mg cy-3-glu/kg) DW	7.73±1.17	3.65	Zafra-Rojas, et al., 2018
		1.59	Koca and Karadeniz, 2009
FRAP (mg/g) DW	20.53±0.47	6.98	Zafra-Rojas, et al., 2018
		0.03	Koca and Karadeniz, 2009
		0.053	Bhagat and Thusoo, 2015
MCA (mg/g) DW	182.12±0.26	0.437	Bhagat and Thusoo, 2015

DW: Dry weight, TPC: Total phenolic content, TFC: Total flavonoid content, TF: Total flavonol content, TAC: Total anthocyanin content, FRAP: Ferric reducing antioxidant power, MCA: Metal chelating ability

TABLE IV  
QUANTITIES OF PHENOLIC COMPOUNDS (MG/KG DM) IN VARIOUS BLACKBERRY FRACTIONS AND FRUIT EXTRACT

Phenolic compounds	Extract	F1	F2	F3	F4	F5	F6	F7
Chlorogenic acid	n.d.	n.d.	0.084	n.d.	n.d.	n.d.	n.d.	n.d.
Catechin	n.d.	n.d.	n.d.	n.d.	n.d.	n.d.	n.d.	n.d.
p-Coumaric acid	n.d.	n.d.	0.961	n.d.	n.d.	n.d.	n.d.	n.d.
Epicatechin	n.d.	n.d.	n.d.	n.d.	n.d.	n.d.	n.d.	n.d.
Rutin	n.d.	n.d.	n.d.	n.d.	0.404	3.134	n.d.	n.d.
Resveratrol	n.d.	n.d.	n.d.	n.d.	n.d.	n.d.	n.d.	n.d.
Naringin	n.d.	n.d.	n.d.	n.d.	n.d.	n.d.	n.d.	n.d.

n.d.: Not detected, DW: Dry weight

#### IV. CONCLUSION

This research gives a complete analysis of the antioxidant potency of a blackberry fruit concentrate, fractionated by column chromatography. The extract was found to contain anthocyanin, flavonoids, flavonols, and polyphenolics, all of which have antioxidant properties. The high level of phenolic compounds, which have strong antioxidant and free radical scavenging properties, makes up around twice the amount of phenolic content compared to the total flavonoid content. Testing using FRAP and MCA revealed that this plant has a significant capacity for scavenging free radicals. The extract tested for its  $\alpha$ -amylase inhibitory capacity exhibited the most substantial inhibition. Related to validation parameters, standard deviations were given in the Tables of the results got. Linearity ranges were given on the calibration graphs. The limit of quantification (LOQ) values was found from the calibration graphs to be 5.0  $\mu\text{g/mL}$  for TPC, TFC, and TF. For FRAP and MCA analyses, LOQs were determined as 20 and 100  $\mu\text{g/mL}$ , respectively. The LODs values are one-third of the LOQ values given. For accuracy, the recovery tests were examined and it was found that those values are >90%. For the first time, column chromatography isolated seven different blackberry extract fractions. As part of the HPLC investigation, certain phenolic compounds, including p-coumaric acid, chlorogenic acid, and rutin, were discovered in fractions. For example, methanolic blackberry extract did not find any phenolic compounds similar to F1, F3, F6, and F7. While F4 and F5 had only rutin, F2 had p-coumaric acid plus chlorogenic acid. This study's discoveries could help identify the particular molecule that is causing the increased antioxidant activity in food.

#### ACKNOWLEDGMENT

We would like to thank the heads of the chemistry departments at Koya University in Iraq and Firat University in Turkey for allowing us to conduct research in their laboratories.

#### REFERENCES

Ademiluyi, A.O., and Oboh, G., 2013. Aqueous extracts of Roselle (*Hibiscus sabdariffa* Linn.) varieties inhibit  $\alpha$ -amylase and  $\alpha$ -glucosidase activities *in vitro*. *Journal of Medicinal Food*, 16(1), pp.88-93.

Akbaba, E., 2021. Characterization of bioactive and antioxidant composition of

mountain tea (*Sideritis montana* ssp. *Montana*): Microwave-assisted technology. *International Journal of Secondary Metabolite*, 8(2), pp.159-171.

Akyüz, E., TÜRkoğlu, S., BaŞkan, K.Sö., TÜtem, E., and Apak, M.R., 2020. Comparison of antioxidant capacities and antioxidant components of commercial bitter melon (*Momordica charantia* L.) products. *Turkish Journal of Chemistry*, 44(6), pp.1663-1673.

Al-Sane, K.O., Povero, G., and Perata, P., 2011. Anthocyanin tomato mutants: Overview and characterization of an anthocyanin-less somaclonal mutant. *Plant Biosystems-An International Journal Dealing with all Aspects of Plant Biology*, 145(2), pp.436-444.

Anigboro, A.A., Avwioroko, O.J., Ohwokevw, O.A., Pessu, B., and Tonukari, N.J., 2021. Phytochemical profile, antioxidant,  $\alpha$ -amylase inhibition, binding interaction and docking studies of *Justicia carnea* bioactive compounds with  $\alpha$ -amylase. *Biophysical Chemistry*, 269, p.106529.

Aryal, S., Baniya, M.K., Danekhu, K., Kunwar, P., Gurung, R., and Koirala, N., 2019. Total phenolic content, flavonoid content and antioxidant potential of wild vegetables from Western Nepal. *Plants*, 8(4), p.96.

Bhagat, M., and Thusoo, S., 2015. Phytochemical, cytotoxic and immunomodulatory analysis of an Indian blackberry *Rubus fruticosus*. *Journal of Biologically Active Products from Nature*, 5(5), pp.339-348.

Binici, H.I., ŞAT, İ.G., and Aoudeh, E., 2021. The effect of different drying methods on nutritional composition and antioxidant activity of purslane (*Portulaca oleracea*). *Turkish Journal of Agriculture and Forestry*, 45(5), pp.680-689.

Diaconeasa, Z., Iuhas, C.I., Ayvaz, H., Rugină, D., Stanilă, A., Dulf, F., Bunea, A., Socaci, S.A., Socaciu, C., and Pintea, A., 2019. Phytochemical characterization of commercial processed blueberry, blackberry, blackcurrant, cranberry, and raspberry and their antioxidant activity. *Antioxidants (Basel)*, 8(11), p.540.

Erkan, N., 2012. Antioxidant activity and phenolic compounds of fractions from *Portulaca oleracea* L. *Food Chemistry*, 133(3), pp.775-781.

Fang, F., Tang, K., and Huang, W.D., 2013. Changes of flavonol synthase and flavonol contents during grape berry development. *European Food Research and Technology*, 237(4), pp.529-540.

Gómez-Caravaca, A.M., Gómez-Romero, M., Arráez-Román, D., Segura-Carretero, A., and Fernández-Gutiérrez, A., 2006. Advances in the analysis of phenolic compounds in products derived from bees. *Journal of Pharmaceutical and Biomedical Analysis*, 41(4), pp.1220-1234.

Günsel, A., Alici, E.H., Bilgiçli, A.T., Arabaci, G., and Yaraşir, M.N., 2019. Antioxidant properties of water-soluble phthalocyanines containing quinoline 5-sulfonic acid groups. *Turkish Journal of Chemistry*, 43(4), pp.1030-1039.

Hama, J.R., Omer, R.A., Rashid, R.S.M., Mohammad, N.E.A., and Thoss, V., 2016. The diversity of phenolic compounds along defatted kernel, green husk and leaves of walnut (*Juglans regia* L.). *Analytical Chemistry Letters*, 6(1), pp.35-46.

Iqbal, E., Salim, K.A., and Lim, L.B.L., 2015. Phytochemical screening, total phenolics and antioxidant activities of bark and leaf extracts of *Goniothalamus velutinus* (Airy Shaw) from Brunei Darussalam. *Journal of King Saud University-Science*, 27(3), pp.224-232.

Islam, T., Yu, X., and Xu, B., 2016. Phenolic profiles, antioxidant capacities and metal chelating ability of edible mushrooms commonly consumed in China. *LWT-Food Science and Technology*, 72, pp.423-431.

Ismail, A., Marjan, Z.M., and Foong, C.W., 2004. Total antioxidant activity and phenolic content in selected vegetables. *Food Chemistry*, 87(4), pp.581-586.

Kalita, P., Tapan, B.K., Pal, T.K., and Kalita, R., 2013. Estimation of total flavonoids content (TFC) and anti oxidant activities of methanolic whole plant extract of *Biophytum sensitivum* Linn. *Journal of Drug delivery and Therapeutics*, 3(4), pp.33-37.

Kitrytė, V., Narkevičiūtė, A., Tamkutė, L., Syrpas, M., Pukalskienė, M., and Venskutonis, P.R., 2020. Consecutive high-pressure and enzyme assisted fractionation of blackberry (*Rubus fruticosus* L.) pomace into functional

- ingredients: Process optimization and product characterization. *Food Chemistry*, 312, p.126072.
- Koca, I., and Karadeniz, B., 2009. Antioxidant properties of blackberry and blueberry fruits grown in the Black Sea Region of Turkey. *Scientia Horticulturae*, 121(4), pp.447-450.
- Kong, J.M., Chia, L.S., Goh, N.K., Chia, T.F., and Brouillard, R., 2003. Analysis and biological activities of anthocyanins. *Phytochemistry*, 64(5), pp.923-933.
- Lapornik, B., Prošek, M., and Wondra, A.G., 2005. Comparison of extracts prepared from plant by-products using different solvents and extraction time. *Journal of Food Engineering*, 71(2), pp.214-222.
- Monforte, M.T., Smeriglio, A., Germanò, M.P., Pergolizzi, S., Circosta, C., and Galati, E.M., 2018. Evaluation of antioxidant, antiinflammatory, and gastroprotective properties of *Rubus fruticosus* L. fruit juice. *Phytotherapy Research*, 32(7), pp.1404-1414.
- Navas, M.J., Jiménez-Moreno, A.M., Bueno, J.M., Saez-Plaza, P., and Asuero, A.G., 2012. Analysis and antioxidant capacity of anthocyanin pigments. Part IV: Extraction of anthocyanins. *Critical Reviews in Analytical Chemistry*, 42(4), pp.313-342.
- Nickavar, B., and Yousefian, N., 2011. Evaluation of  $\alpha$ -amylase inhibitory activities of selected antidiabetic medicinal plants. *Journal für Verbraucherschutz und Lebensmittelsicherheit*, 6(2), pp.191-195.
- Okatan, V., 2020. Antioxidant properties and phenolic profile of the most widely appreciated cultivated berry species: A comparative study. *Folia Horticulturae*, 32(1), pp.79-85.
- Oszmiański, J., Nowicka, P., Teleszko, M., Wojdyło, A., Cebulak, T., and Oklejewicz, K., 2015. Analysis of phenolic compounds and antioxidant activity in wild blackberry fruits. *International Journal of Molecular Sciences*, 16(7), pp.14540-14553.
- Padilla-Jimenez, S.M., Angoa-Pérez, M.V., Mena-Violante, H.G., Oyoque-Salcedo, G., Renteria-Ortega, M., and Oregel-Zamudio, E., 2019. Changes in the aroma of organic blackberries (*Rubus fruticosus*) during ripeness. *Analytical Chemistry Letters*, 9(1), pp.64-73.
- Rahimzadeh, M., Jahanshahi, S., Moein, S., and Moein, M.R., 2014. Evaluation of alpha-amylase inhibition by *Urtica dioica* and *Juglans regia* extracts. *Iranian Journal of Basic Medical Sciences*, 17(6), pp.465-469.
- Rajanandh, M.G., and Kavitha, J., 2010. Quantitative estimation of  $\beta$ -sitosterol, total phenolic and flavonoid compounds in the leaves of *Moringa oleifera*. *International Journal of PharmTech Research*, 2(2), pp.1409-1414.
- Rehakova, Z., Koleckar, V., Jahodar, L., Opletal, L., Macakova, K., Cahlikova, L., Jun, D., and Kuca, K., 2014. Evaluation of the antioxidant activity of several naturally occurring coumarins and their synthesized analogues by "ferric reducing antioxidant power" assay. *Journal of Enzyme Inhibition and Medicinal Chemistry*, 29(1), pp.49-54.
- Sanín, A., Navia, D.P., and Serna-Jiménez, J.A., 2020. Functional foods from crops on the northern region of the South American Andes: The importance of blackberry, yacon, açai, yellow pitahaya and the application of its biocompounds. *International Journal of Fruit Science*, 20(Supl 3), pp.S1784-S1804.
- Santos, S.S., Rodrigues, L.M., Costa, S.C., and Madrona, G.S., 2019. Antioxidant compounds from blackberry (*Rubus fruticosus*) pomace: Microencapsulation by spray-dryer and pH stability evaluation. *Food Packaging and Shelf Life*, 20, p.100177.
- Shibu Prasanth, S.C.R., and Chandran, P., 2017. Phytochemical and antimicrobial analysis of leaf samples of different *Rubus* species. *International Journal of ChemTech Research*, 10(4), pp.359-368.
- Soquetta, M.B., Terra, L.M., and Bastos, C.P., 2018. Green technologies for the extraction of bioactive compounds in fruits and vegetables. *CyTA-Journal of Food*, 16(1), pp.400-412.
- Sutharut, J., and Sudarat, J., 2012. Total anthocyanin content and antioxidant activity of germinated colored rice. *International Food Research Journal*, 19(1), pp.215-221.
- Yefrida, S.H., Alif, A., Efdi, M., and Aziz, H., 2018. Modification of phenanthroline method to determine antioxidant content in tropical fruits methanolic extract. *Research Journal of Chemistry and Environment*, 22, pp.28-35.
- Zafra-Rojas, Q., Cruz-Cansino, N., Delgadillo-Ramírez, A., Alanís-García, E., Añorve-Morga, J., Quintero-Lira, A., Castañeda-Ovando, A., and Ramírez-Moreno, E., 2018. Organic acids, antioxidants, and dietary fiber of Mexican blackberry (*Rubus fruticosus*) residues cv. Tupy. *Journal of Food Quality*, 2018, p.5950761.
- Zohlen, A., 2000. Use of 1, 10-phenanthroline in estimating metabolically active iron in plants. *Communications in Soil Science and Plant Analysis*, 31(3-4), pp.481-500.



# Radon Activity Concentration Measurements in the Water Collected from the Lower Zab River in the Kurdistan Region of Iraq

Jahfer M. Smail<sup>1</sup>, Hiwa H. Azeez<sup>2</sup>, Habeeb H. Mansor<sup>2</sup> and Saddon T. Ahmad<sup>3</sup>

<sup>1</sup>Department of Physics, Faculty of Science and Health, Koya University,  
Koya KOY45, Kurdistan Region – F.R. Iraq

<sup>2</sup>Department of Physics, College of Education, Salahaddin University – Erbil,  
Erbil, Kurdistan Region – F.R. Iraq

<sup>3</sup>Faculty of Medicine, Koya University,  
Koya KOY45, Kurdistan Region – F.R. Iraq

**Abstract**—This study aims to assess radon levels in the water of the Lower Zab River. Knowing the radon concentrations is crucial for understanding the potential risks to human health and implementing protective measures. A RAD7-H<sub>2</sub>O detector has been used to measure the radon concentration in 28 water samples from the Lower Zab River in the Kurdistan Region of Iraq. Results show that the radon activity concentrations ranged from 0.5 to 4 Bq.L<sup>-1</sup>, with an average of 0.61 Bq.L<sup>-1</sup>, and the resulting annual effective dose (AED) varied from 0.137 to 60.06 Sv.y<sup>-1</sup>, with an average of 12.08 Sv.y<sup>-1</sup>. The average radon concentration and AED in the measured samples are below the reference levels recommended by the ICRP and the World Health Organization. Consequently, the LZR water is suitable for human consumption and use and does not present any health hazards related to radon exposure.

**Index Terms**—Activity concentration, Annual effective dose, Lower zab river, RAD-H<sub>2</sub>O, Radon gas, Water.

## I. INTRODUCTION

Radon, a naturally occurring radioactive gas resulting from uranium and radium decay in rocks and soil, can contaminate groundwater. Physical properties of radon are a colorless, odorless, and tasteless gas at room temperature and pressure. Radon is denser than air and is about 9 times denser than the air we breathe (Ismail, 2008). Radon's melting point is around  $-71^{\circ}\text{C}$ , and its boiling point is about  $-61.7^{\circ}\text{C}$ . Radon is sparingly soluble in water, which means it can dissolve to some extent in water (Baskaran, 2016). Radon is highly radioactive. It is a decay product of uranium and thorium,

which are naturally present in the Earth's crust. It decays into various radioactive isotopes known as radon decay products, some of which are also radioactive and can attach to airborne particles (Hussein, et al., 2018).

And chemical properties of radon are classified as a noble gas (Group 18 of the periodic table), making it chemically inert. It does not readily form chemical compounds with other elements. Due to its high ionization energy and electron configuration, radon does not readily react with other elements or compounds. It does not typically form stable compounds under normal conditions. While radon's chemical reactivity is low, some compounds containing radon have been synthesized under specialized laboratory conditions (Baskaran, 2016). These compounds are generally unstable and fleeting. The most significant aspect of radon's chemical behavior is its radioactive decay. Radon (<sup>222</sup>Rn), a naturally occurring radioactive gas, possesses a half-life of 3.824 days. It arises immediately following the decay of radium (<sup>226</sup>Ra). It undergoes alpha decay, emitting alpha particles (helium nuclei) and transforming into different elements in a decay chain. This decay chain eventually leads to stable lead isotopes (Aziz, et al., 2015). Radon activity concentrations in water vary due to geographic and geological conditions (UNSCEAR, 1988). Over 90% of the overall radiation dose from radon exposure is contributed by two of the <sup>222</sup>Rn daughters emitters, <sup>214</sup>Po and <sup>218</sup>Po (Gruber, Maringer and Landstetter, 2009). Radon is a by-product of the decay of <sup>226</sup>Ra, which comes from the natural decay series of <sup>238</sup>U. Radon daughters are generally solids that follow to the surface of airborne dust particles, unlike radon itself which is a gas. The risk of developing lung cancer rises if such contaminated dust is inhaled because the particles might follow to the lung's airways (Baykara, Karatepe and Doğru, 2011). When radon enters the human body through inhalation and ingestion, health risks associated with radon arise due to its short-lived progenies.

Most radon gas that enters the lungs is excreted and does not accumulate in the alveoli. Although only a small amount

ARO-The Scientific Journal of Koya University  
Vol. XI, No. 11 (2023), Article ID: ARO.11192. 08 pages  
Doi: 10.14500/aro.11192

Received: 09 May 2023; Accepted: 09 September 2023  
Regular research paper: Published: 18 September 2023

Corresponding author's e-mail: jahfer.majeed@koyauniversity.org  
Copyright © 2023 Jahfer M. Smail, Hiwa H. Azeez, Habeeb H. Mansor and Saddon T. Ahmad. This is an open access article distributed under the Creative Commons Attribution License.



of radon enters the lining of the lungs, it has the potential to cause DNA damage in vulnerable lung tissue and lead to cancer. Furthermore, when we inhale, we can take in radon decay products that are present in the air (Corrêa, et al., 2009). Because the half-life of radon decay products is brief, they mostly decay entirely inside the lungs (Hussein, 2018).

Radon can enter homes through two primary sources: Soil and water. Radon gas that emanates from soil is responsible for health issues associated with radon exposure (Najam, et al., 2018). Inhaling Radon from household water can cause lung cancer, while drinking water contaminated with radon can lead to stomach cancer (Al-Alawy, et al., 2018). A recent study found that the level of naturally occurring radioactive materials present in soil samples taken from the LZR was below the allowed limit (Smail, et al., 2021). The activity concentration of prompt radon gas in the Jale and Mersaid springs in Koya region has been measured using an HPGe spectrometer. These warm springs contain a considerable activity level arranged between  $19.04 \pm 0.55 \text{ Bq.L}^{-1}$  and  $30.11 \pm 0.67 \text{ Bq.L}^{-1}$  (Ahmad, Almuhsin and Hamad, 2021). The relationship between radon activity concentration and physicochemical parameters in groundwater of 24 different wells in Erbil city, Iraq, has been investigated using the RAD 7/H<sub>2</sub>O detector (Qadir, et al., 2021). The main purpose of this research is to determine the activity concentration of radon in water samples collected from the LZR in the Kurdistan Region of Iraq using a RAD-H<sub>2</sub>O semi-conductor radon detector, and its implications for human health. Furthermore, the relationship between radon concentration and physicochemical parameters was estimated for water samples collected from various locations. The most commonly used parameters by researchers are pH, Temperature, and EC.

## II. MATERIALS OF METHODS

### A. Study Area

The Zab River gathers most of its water from the mountains in Iran (around 80%) and the rest from the mountains in the Kurdistan region of Iraq. The Dukan Lake generates 150 megawatts of electricity, irrigates 3,000 dunums of farmland,

and supports the establishment of 400 fish farms (Smail, et al., 2023). It lies between  $36^{\circ} 11' 28.4'' \text{ N}$  and  $35^{\circ} 47' 23.3'' \text{ N}$  latitude and  $45^{\circ} 15' 43.6'' \text{ E}$  and  $44^{\circ} 10' 26.3'' \text{ E}$  longitude. Fig. 1 shows the geographic location of LZR in the Kurdistan region of Iraq, as well as the location of the sampling sites. The LZR is regarded as the primary source of potable water for a significant portion of the Raparin administration, as well as the cities of Sulaimaniyah, Kirkuk, Chamchamal, and Duzkhurmatu.

### B. Sample Collection

The researchers gathered 28 water samples from various locations on the surface of the (LZR). These samples were collected in polyethylene containers with a capacity of 2 L, placed in a cool box, and then transported to the laboratory at Koya University. They were preserved at room temperature for radon exhalation. When collecting water samples, it is important to close the tubes so that the internal radon gas of the water does not evaporate to the outside, and to preserve the amount of real radon inside.

### C. Sample Counting

The active-method RAD-H<sub>2</sub>O solid-state detector was used to analyze the samples in a timely manner. The bottles were 250 mL filled with 200 mL of the water sample, and then the instrument was set up. The RAD-H<sub>2</sub>O was programmed with the test Wat250 and has a 4-cycle of 5-min protocol, which uses this protocol with the use of a tube of 250 ml for the Rad device, and is usually used when there are samples of water in a large amount. The RAD - H<sub>2</sub>O system consists of three primary units, which are depicted in Fig. 2.

The RAD7 radon monitor, a water vial with an aerator, and a small desiccant tube, which are all shown. Before taking measurements, the RAD7 was connected to the dry unit and purged for 30 min to eliminate any radioactive particles from the measurement chamber. Then, the RAD7 was connected to 250 mL water vials, and the test began by bubbling water for 5 min to extract radon from the sample. The RAD7 pump cycled air between the measurement chamber and the vials, at the end of the process, the RAD7 produced a summary of

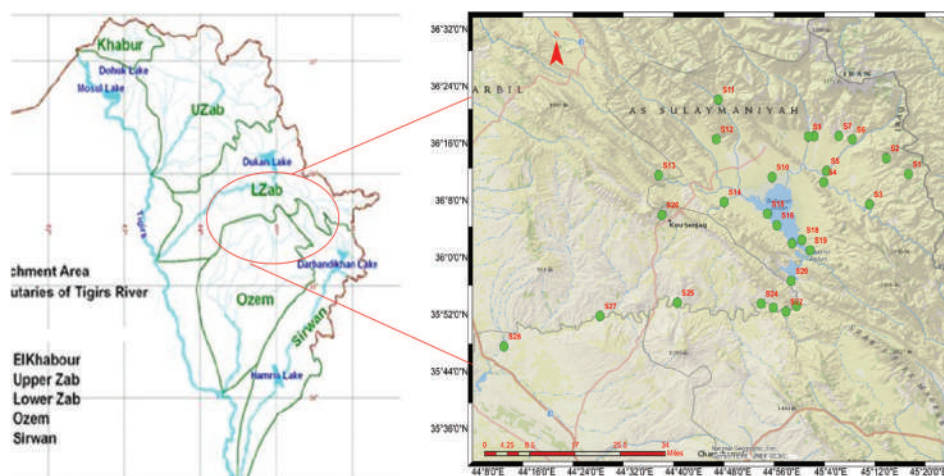


Fig. 1. The geographic location of LZR.

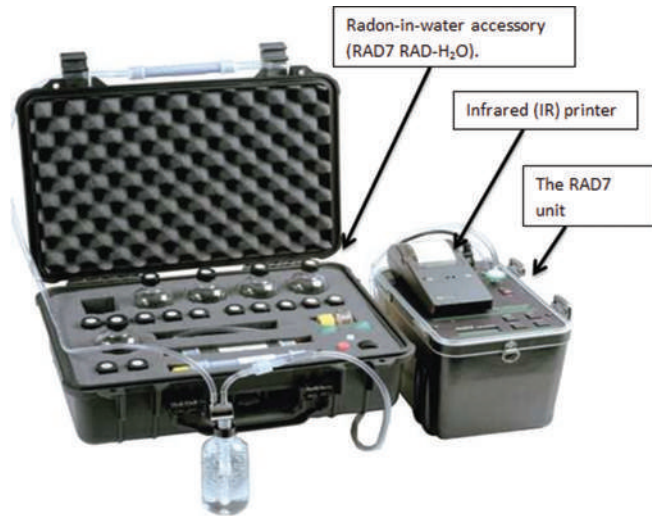


Fig. 2. RAD - H<sub>2</sub>O instrument comprises three units: The RAD7 unit, the infrared printer, and the radon - in-water accessory.

the radon activity concentration in the water samples from the <sup>218</sup>Po source.

### III. CALCULATION

#### A. Activity Concentration

The corrected radon concentration in the water during the sampling period was calculated using the equation provided below.

$$C_{(Rn)_0} = C_{Rn} e^{\lambda t} \quad (1)$$

Where  $C_{(Rn)_0}$  represent the actual radon concentration in the water,  $C_{Rn}$  is the radon concentration readied by the RAD7,  $\lambda$  is the decay constant of radon ( $\lambda = 0.181 \text{ day}^{-1}$ ), and  $t$  is the time interval between sampling and testing (Ezzulddin and Mansour, 2020).

#### B. Annual Effect Dose (AED)

The AED resulting from radon in water can be classified into two categories: the dose that is received from ingesting radon and the dose that is received from inhaling radon. When radon and its offspring are present in drinking water, they can mainly cause a radiation dose in the stomach through ingestion. Nonetheless, radon gas that is present in water can escape into the indoor air during daily activities such as showering, washing dishes, and using water in homes, which can significantly increase the risk of lung cancer from the radon that is inhaled. The calculation for the AED resulting from radon ingestion can be determined using the equation below (Abdullah, et al., 2023):

$$AED_{ing} = C_{RnW} \times C_w \times DCF \quad (2)$$

$C_{RnW}$  =Represents the radon concentration present in the water.

$C_w$  =For infants, children, and adults, the annual water intake is respectively equivalent to (150, 350, and 500) liters per year.

$DCF$  =The Dose Conversion Factor varies according to age and is equal to (23, 5.9, and 3.5) Nano Sieverts per

Becquerel for infants, children, and adults, respectively. To calculate the dose resulting from the inhalation of radon, the following equation can be utilized.

$$AED_{iha} = C_{RnW} \times R \times F \times O \times DCF \quad (3)$$

$R$ , which denotes the ratio of radon in the air to water and has a value of;  $F$ , which represents the equilibrium factor between radon and its progeny and has a value of 0.4;  $O$ , which refers to the average time that an individual spends indoors and has a value of 7000 h/year; and  $DCF$ , which is the factor used to convert radon exposure into health risks and has a value of 9 Nano Sieverts per (Becquerel hour per meter cubed).

## IV. RESULTS AND DISCUSSION

### A. Activity Concentration

The RAD-H<sub>2</sub>O electronic device is utilized for gauging the amount of radon gas concentration. In sniff mode, the device exclusively relies on alpha particles emitted by <sup>218</sup>Po to calculate the concentration of <sup>222</sup>Rn. Table I contain a measured summary of the average radon activity concentrations in the surface water samples collected from LZR. The concentrations ranged from  $(0.15 \pm 0.01) \text{ Bq.L}^{-1}$  to  $(4 \pm 0.06) \text{ Bq.L}^{-1}$ , with an average concentration of  $(0.61 \pm 0.02) \text{ Bq.L}^{-1}$ . The results indicate that the highest level of contamination was found in sample S12 (Sarwchawa), which was below the recommended limit of  $11.1 \text{ Bq.L}^{-1}$  set by the EPA. The lowest concentration of radon gas was observed in samples S17 and S18, located in the central part of the Dukan Lake construction, where the water is stagnant. Radon gas was released to the open air, leading to a lower concentration of radon gas. The variation in radon gas concentration in the water samples is due to the varying geological formations and radium content in different areas of the study region. Table II presents a comparison of the present study's results with the average values obtained from the previous studies on water samples, both locally and internationally.

### B. AEDs of Radon

Equations (2) and (3) can be used to calculate the AED for ingestion through the stomach and inhalation through the lungs, respectively. Table III presents the average AED for ingestion, inhalation.

The AED for ingestion had a range of  $4.17\text{--}114.46 \text{ }\mu\text{Sv.y}^{-1}$ , with an average of  $17.62 \text{ }\mu\text{Sv.y}^{-1}$ . In the case of infants aged 1–2 years who consume an average of 150 L of water annually, the  $AED_{ing}$  values varied between 0.5 and  $13.78 \text{ }\mu\text{Sv.y}^{-1}$ , with an average of  $2.12 \text{ }\mu\text{Sv.y}^{-1}$ . The dose received by this age group was lower than the recommended limit of  $100 \text{ }\mu\text{Sv.y}^{-1}$  set by UNSCEAR in 2000 and the World Health Organization (WHO) for the general public.

The ICRP age groups for children range from 7 to 12 years old and have an average annual water intake of 350 L. The corresponding  $AED_{ing}$  values ranged from 0.31 to  $8.25 \text{ }\mu\text{Sv.y}^{-1}$ , with an average of  $1.269 \text{ }\mu\text{Sv.y}^{-1}$ . The dose received by children in the 7–12 age groups was lower than

the recommended limit of  $100 \mu\text{Sv.y}^{-1}$  by UNSCEAR in 2000 and the WHO for the general public. Adults in ICRP age groups above 17 years have an average annual water intake of 500 L and the corresponding  $\text{AED}_{\text{ing}}$  values ranged from 0.25 to  $6.99 \mu\text{Sv.y}^{-1}$ , with an average of  $1.07 \mu\text{Sv.y}^{-1}$ . The dose rates received by adults in the ICRP age group

were lower than the recommended limit of  $100 \mu\text{Sv.y}^{-1}$  set by UNSCEAR in 2000 and the WHO for the general public. Children and adults have a similar level of susceptibility to radon exposure. These findings emphasize the significance of calculating the AED separately for infants, children, and adults. These results are consistent with the earlier findings (Wallner and Steininger, 2007).

As per the guidelines set by the European Union (E.U. 1998) and the World Health Organization (WHO, 2004), drinking water is considered safe if the dose of radiation it contains is  $100 \mu\text{Sv.y}^{-1}$  or lower. In such cases, no further steps need to be taken. However, if the dose exceeds this limit, steps to lower the radiation levels are recommended.

The AED from inhaling radon released into the air through water varied between 3.97 and 108.92, with an average of  $16.76 \mu\text{Sv.y}^{-1}$ . The total AED for adults the whole body (including the stomach and lungs) ranged from 3.92 to 107.67, with an average of  $16.57 \mu\text{Sv.y}^{-1}$ . According to UNSCEAR's 2000 guidelines, the recommended mean dose for drinking and inhaling are 0.002 and  $0.025 \text{mSv.y}^{-1}$ , respectively. Except for samples S12 and S13, all samples were within the recommended values for infants, children, and adults for both ingestion and inhalation.

Table IV provides information on the mean yearly effective dose for the entire body, ingestion, and inhalation.

The AED for ingestion of radon gas ranged from 4.17 to  $114.46 \mu\text{Sv.y}^{-1}$ , with an average of  $17.62 \mu\text{Sv.y}^{-1}$ . The AED for inhalation of radon released into the air varied from 3.97 to  $108.92 \mu\text{Sv.y}^{-1}$ , with an average of  $16.76 \mu\text{Sv.y}^{-1}$ . The total yearly effective dose for adults the entire body (stomach and lungs) ranged from 3.92 to  $107.67 \mu\text{Sv.y}^{-1}$ , with an average of  $16.57 \mu\text{Sv.y}^{-1}$ . All samples, except for S12 and S13, were within the UNSCEAR-recommended mean dose for drinking and breathing value which is 0.002 and  $0.025 \text{mSv.y}^{-1}$ , respectively, for infants, children, and adults for both ingestion and inhalation (UNSCEAR, 2000). From Table IV, it is clear that infants are more affected by the dose of radon

TABLE I

THE MEASURED RADON ACTIVITY CONCENTRATIONS IN THE SURFACE WATER COLLECTED FROM LZR

Code of samples	Location	$^{222}\text{Rn}$ Activity concentration ( $\text{Bq.L}^{-1}$ )
S1	Halsho	0.33±0.02
S2	Shekh awdalan	1.17±0.03
S3	Kawya	0.40±0.02
S4	Sndolan	0.26±0.02
S5	Braym awa	1.32±0.12
S6	Grd ester	0.15±0.01
S7	Sharwet	0.26±0.02
S8	Kona Mase	0.22±0.01
S9	Dole shahedan	0.51±0.02
S10	Darband	0.29±0.02
S11	Daraban	0.40±0.02
S12	Sarwchawa	4.00±0.06
S13	Jaly	3.59±0.06
S14	Khdran	0.20±0.01
S15	Kalkan	0.73±0.03
S16	Aleqa	0.22±0.01
S17	Merza Rostam	0.19±0.01
S18	Tangzha	0.15±0.01
S19	Khoshaw	0.15±0.01
S20	Lower Dukan	0.68±0.03
S21	Sartk	0.33±0.02
S22	Dwawan	0.29±0.02
S23	Klesa	0.22±0.01
S24	Bogd	0.22±0.01
S25	Mokharas	0.22±0.01
S26	Hamamok	0.15±0.01
S27	Segrdkan	0.34±0.02
S28	Prde	0.26±0.02
Average		0.61±0.02

TABLE II

COMPARISON OF THE ACTIVITY OF RADON IN THE PRESENT STUDY WITH THAT OF LOCAL AND FOREIGN COUNTRIES

Country	$^{222}\text{Rn}$ concentration $\text{Bq.L}^{-1}$	Source of water	References
Iraq – Erbil (Barserin village) Winter season	33.86±2.4	Drink water	Are and Mansour, 2022
Iraq - Kurdistan (Erbil)	0.06–13.06	Drink water	Ezzulddin and Mansour, 2020
Iraq Kurdistan (Darbandikhan Lake)	0.151–34.21	Drink water	Jafir, Ahmed and Saridan, 2016
Iraq (Kirkuk)	0.31–0.36	Drink water	Kareem, Ibrahim and Ibrahiem, 2020
Iraq (Baghdad province)	94.9±10.81	Drink water	Najam, et al., 2018
Iraq (Anbar)	2.1–6.4	Drink water	Farhan, et al., 2020
Iraq (Bagdad)	0.07–0.29	Drink water	Kadhim, 2015
Saudi Arabia	4.39–11.02	Drink water	Tayyeb, Kinsara and Farid, 1998
Pakistan	8.8	Drink water	Khattak, et al., 2011
Malaysia	0.041–3.97	Drink water	Nuhu, et al., 2020
Poland	0.42–10.52	Drink water	Bem, et al., 2014
Nigeria	4.3–42	Drink water	Avwiri, Tchokossa and Mokobia, 2007
Spain	0.22–52	Drink water	Dueñas, et al., 1999
Barzil	1.88–196	Drink water	Corrêa, et al., 2009
Iraq (Shatt-Al-Arab)	0.062	Surface water	Jebur and Subber, 2015
Turkey	0.091	Surface water	Canbazoğlu, et al., 2012
Iran (Mashhad City)	2.15	Surface water	Binesh, Mowlavi and Mohammadi, 2012
LZR	0.15–4.02	Surface water	Present study

TABLE III

THE AEDs RESULTING FROM THE INGESTION OF RADON IN WATER SAMPLES IN THE LZr AREA AND THE AED CAUSED BY INHALING RADON THAT HAS ESCAPED INTO THE INDOOR AIR OF HOMES FOR INFANTS, CHILDREN, AND ADULTS

Code of samples	Location	AED <sub>ing</sub> (μSv.y <sup>-1</sup> )			AED <sub>inh</sub> of radon gas by water in homes (μSv.y <sup>-1</sup> )
		Infant	Children	Adult	
S1	Halsho	1.13±0.06	0.68±0.04	0.57±0.03	8.26±0.46
S2	Shekh awdalan	4.03±0.12	2.41±0.07	2.04±0.06	29.42±0.86
S3	Kawya	1.39±0.07	0.83±0.04	0.71±0.04	10.16±0.50
S4	Sndolan	0.88±0.05	0.53±0.03	0.45±0.03	6.43±0.38
S5	Braym awa	4.55±0.41	2.73±0.24	2.31±0.21	33.26±2.99
S6	Grd ester	0.50±0.04	0.30±0.02	0.26±0.02	3.68±0.30
S7	Sharwet	0.88±0.06	0.53±0.03	0.45±0.03	6.46±0.40
S8	Kona Mase	0.76±0.05	0.45±0.03	0.38±0.03	5.54±0.37
S9	Dole shahedan	1.76±0.08	1.06±0.05	0.89±0.04	12.88±0.55
S10	Darband	1.01±0.06	0.60±0.04	0.51±0.03	7.36±0.43
S11	Daraban	1.39±0.07	0.83±0.04	0.7±0.04	10.12±0.50
S12	Sarwchawa	13.78±0.21	8.25±0.12	6.99±0.10	100.67±1.51
S13	Jaly	12.39±0.21	7.42±0.12	6.29±0.10	90.53±1.51
S14	Khdran	0.67±0.05	0.40±0.03	0.34±0.02	4.92±0.35
S15	Kalkan	2.52±0.09	1.51±0.06	1.28±0.05	18.41±0.68
S16	Aleqa	0.76±0.05	0.45±0.03	0.38±0.03	5.52±0.37
S17	Merza Rostam	0.67±0.05	0.40±0.03	0.34±0.02	4.91±0.35
S18	Tangzha	0.50±0.04	0.30±0.02	0.25±0.02	3.67±0.30
S19	Khoshaw	0.50±0.04	0.30±0.02	0.25±0.02	3.67±0.30
S20	Lower Dukan	2.35±0.09	1.41±0.05	1.19±0.05	17.15±0.66
S21	Sartk	1.13±0.06	0.68±0.04	0.57±0.03	8.27±0.46
S22	Dwawan	1.01±0.06	0.60±0.04	0.51±0.03	7.35±0.43
S23	Klesa	0.75±0.05	0.45±0.03	0.38±0.03	5.51±0.37
S24	Bogd	0.75±0.05	0.45±0.03	0.38±0.03	5.51±0.37
S25	Mokharas	0.75±0.05	0.45±0.03	0.38±0.03	5.51±0.37
S26	Hamamok	0.50±0.04	0.30±0.02	0.26±0.02	3.68±0.30
S27	Segrdkan	1.17±0.06	0.70±0.04	0.60±0.03	8.57±0.46
S28	Prde	0.88±0.06	0.53±0.03	0.45±0.03	6.43±0.40
Average		2.12±0.082	1.269±0.049	1.07±0.04	15.45±0.60

present in water than children and adults in all regions under study. Due to some reasons, infants have a higher respiratory rate than older children and adults. This means they inhale a larger volume of air relative to their body weight, which can result in a higher intake of radon gas if it is present in the indoor air. An infant’s respiratory system is still developing and may be less efficient at filtering and clearing harmful substances from the air compared to older children and adults. This can lead to a greater accumulation of radon and its decay products in their lungs. Rapid cell division and growth are characteristic of infancy. This increased cellular activity can make developing tissues more vulnerable to the damaging effects of ionizing radiation, such as that emitted by radon and its decay products. They have less developed DNA repair mechanisms compared to adults. Ionizing radiation from radon can cause damage to DNA, and a less efficient DNA repair system in infants may lead to a higher likelihood of genetic mutations (Berglund, et al., 1992; Tong et al., 2012).

Infants tend to consume a higher proportion of liquids relative to their body weight compared to older children and adults. Radon can dissolve in water, and this can result in increased ingestion of radon-contaminated water in infants, potentially contributing to their overall exposure. They spend more time indoors, especially in their homes, compared to

older children who might spend more time outside. If a home has elevated radon levels, infants may experience prolonged exposure during critical developmental stages. Infants have a relatively larger body surface area compared to their body volume, which could lead to a higher proportion of radon absorption through their skin (Kumar et al., 2021). Furthermore, all water in the study is suitable for use by populations.

*C. Correlation between Water Quality Parameter and Radon Activity Concentration*

Table V summarizes the outcomes of measuring several physicochemical parameters such as temperature, electrical conductivity, and pH for all samples to determine their impact on radon concentrations.

The electrical conductivity of surface water ranged from 247 to 716 μS.cm<sup>-1</sup>, with an average of 352.43 μS.cm<sup>-1</sup>. The World Health Organization (WHO) has set a limit of 600 μS cm<sup>-1</sup> for the permissible electrical conductivity level in water.

A weak correlation was observed between electrical conductivity and radon concentration in surface water, with a correlation coefficient of (R<sup>2</sup> = 0.29), except for samples S11 and S13. These samples are unsuitable for drinking due to their high sulfide content, which results in high electrical conductivity. The evaluated radon with an increase

TABLE IV

THE COMBINED YEARLY EFFECTIVE DOSE RESULTING FROM CONSUMING AND INHALING RADON IN WATER SAMPLES OVER AN EXTENDED PERIOD AT LZR IS REFERRED TO AS AED<sub>TOTAL</sub>

Code of samples	Location	AED <sub>TOTAL</sub> (μSv.y <sup>-1</sup> )		
		Infant	Childern	Adult
S1	Halsho	9.39±0.52	8.94±0.49	8.83±0.49
S2	Shekh awdalan	33.45±0.98	31.83±0.93	31.46±0.92
S3	Kawya	11.55±0.57	10.99±0.55	10.86±0.54
S4	Sndolan	7.31±0.43	6.96±0.41	6.88±0.40
S5	Braym awa	37.82±3.40	35.99±3.23	35.57±3.2
S6	Grd estr	4.18±0.34	3.98±0.33	3.93±0.32
S7	Sharwet	7.35±0.46	6.99±0.44	6.91±0.43
S8	Kona mase	6.3±0.42	5.99±0.4	5.92±0.40
S9	Dole shahedan	14.65±0.63	13.94±0.6	13.78±0.59
S10	Darband	8.37±0.49	7.96±0.47	7.87±0.46
S11	Daraban	11.5±0.57	10.95±0.55	10.82±0.54
S12	Sarwchawa	114.46±1.72	108.92±1.63	107.67±1.61
S13	Jaly	102.93±1.72	97.95±1.63	96.82±1.62
S14	Khdran	5.60±0.40	5.33±0.38	5.26±0.38
S15	Kalkan	20.93±0.77	19.92±0.74	19.69±0.73
S16	Aleqa	6.27±0.42	5.97±0.40	5.9±0.40
S17	Merza Rostam	5.58±0.40	5.31±0.38	5.25±0.38
S18	Tangzha	4.17±0.35	3.97±0.33	3.93±0.33
S19	Khoshaw	4.17±0.35	3.97±0.33	3.92±0.33
S20	Lower Dukan	19.5±0.75	18.56±0.71	18.34±0.7
S21	Sartk	9.4±0.52	8.94±0.49	8.84±0.49
S22	Dwawan	8.35±0.49	7.95±0.47	7.86±0.46
S23	Klesa	6.27±0.42	5.96±0.40	5.9±0.40
S24	Bogd	6.27±0.42	5.96±0.40	5.9±0.40
S25	Mokharas	6.26±0.42	5.96±0.40	5.89±0.40
S26	Hamamok	4.18±0.35	3.98±0.33	3.93±0.33
S27	Segrdkan	9.74±0.53	9.27±0.50	9.16±0.50
S28	Prde	7.31±0.46	6.96±0.44	6.88±0.43
Average		17.62±0.69	17.62±0.69	16.76±0.66

TABLE V

THE MEASURED RADON ACTIVITY CONCENTRATION AND PHYSICO-CHEMICAL WATER QUALITY PARAMETERS

Code of Samples	Location	<sup>222</sup> Rn concentration (Bq.L <sup>-1</sup> )	Water quality parameter		
			E.C. μs.cm <sup>-1</sup>	Temp °C	pH
S1	Halsho	0.33±0.02	338	20	9
S2	Shekh awdalan	1.17±0.03	355	20	8.8
S3	Kawya	0.4±0.02	266	19	8.9
S4	Sndolan	0.26±0.02	273	16	9
S5	Braym awa	1.32±0.12	295	20	7.5
S6	Grd estr	0.15±0.01	247	22	9.1
S7	Sharwet	0.26±0.02	369	20	7.5
S8	Kona mase	0.22±0.01	290	20	7.8
S9	Dole shahedan	0.51±0.02	398	22	7.6
S10	Darband	0.29±0.02	255	16	8.3
S11	Daraban	0.4±0.02	716	12	9.4
S12	Sarwchawa	4±0.06	558	14	8.7
S13	Jaly	3.59±0.06	615	15	9.2
S14	Khdran	0.2±0.01	367	20	7.8
S15	Kalkan	0.73±0.03	257	18	8.5
S16	Aleqa	0.22±0.01	292	19	8.3
S17	Merza Rostam	0.19±0.01	247	17	8.5
S18	Tangzha	0.15±0.01	257	21	8.5
S19	Khoshaw	0.15±0.01	247	15	8.5
S20	Lower Dukan	0.68±0.03	330	15	7.7
S21	Sartk	0.33±0.02	324	18	7.9
S22	Dwawan	0.29±0.02	335	19	7.7
S23	Klesa	0.22±0.01	332	20	7.9
S24	Bogd	0.22±0.01	336	18	7.8
S25	Mokharas	0.22±0.01	337	12	7.9
S26	Hamamok	0.15±0.01	532	22	8.1
S27	Segrdkan	0.34±0.02	347	15	8
S28	Prde	0.26±0.02	353	10	8.4
Average		0.61±0.02	352.43	17.67	8.30

in electrical conductivity has been reported by (Tabar and Yakut, 2014). Fig. 3 illustrates the correlation between radon concentration in water and electrical conductivity.

The correlation between water temperature and radon concentration for surface water is presented in Fig. 4. From the samples analyzed for the effect of water temperature on the radon concentration, the results are presented in Table V. It was shown that there is no correlation between water temperature and the radon concentration for surface water with a correlation coefficient of (R<sup>2</sup> = 0.057).

The measured pH values for all water samples are presented in Table V. The average pH value of surface water was found to be 8.30, with a range of 7.5–9.4. The water tends to be more alkaline when it passes through the carbonate (Nilsson and Sandberg, 2017), and this may tend to decrease the radon concentration due to the capturing of radon by carbonate. It was observed that there is no correlation between radon concentration and pH with a correlation coefficient of (R<sup>2</sup> = 0.078) for surface water. The variation in pH water for drinking water is due to contact with the carbonate rocks such as limestone and dolomite (Alharbi, Abbadly and El-Taher, 2015). All the measured values are within the acceptable ranges (6.5–8.5) declared by the WHO for drinking water, except for the samples

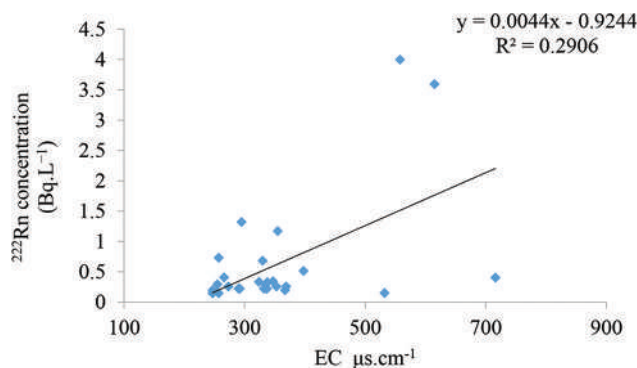


Fig. 3. The correlation between electrical conductivity and radon activity concentration for surface water.

(S1, S2, S3, S4, S11, S12, and S13) which are not suitable for drinking due to weak contact with the carbonate rocks such as limestone and dolomite.

Several studies have reported a similar negative correlation among dissolved radon, and some studies revealed a positive correlation between <sup>222</sup>Rn and pH. On the other hand, some studies show no correlation between pH and <sup>222</sup>Rn concentration. This is mainly because that radon is an inert gas. The correlation between water pH and radon concentration for surface water is presented in Fig. 5.

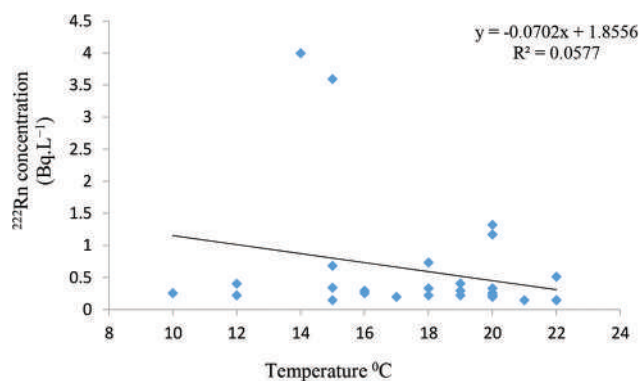


Fig. 4. The correlation between temperature and radon activity concentration for surface water.

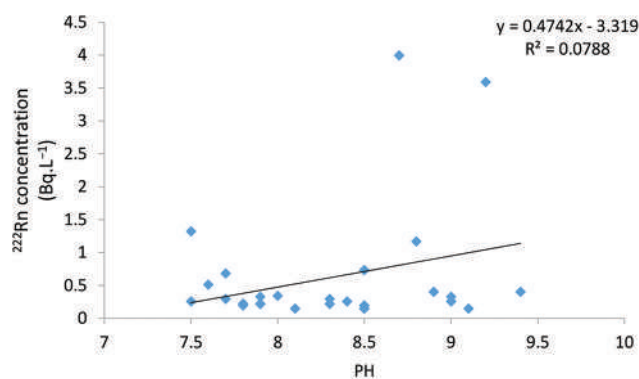


Fig. 5. The correlation between pH and radon activity concentration for surface water.

## V. CONCLUSION

This study is to determined radon levels in surface water along the LZR. It is evident from the results that the radon levels in all examined surface water samples remain comfortably below the EPA's recommended limit of 11.1 Bq.L<sup>-1</sup>, as stipulated in the guidelines from LZR. Furthermore, the investigation into the AEDs of radon for various age groups underscores the heightened vulnerability of infants compared to children and adults. However, reassuringly, the calculated AEDs to internal organs such as the stomach and lungs, arising from radon in surface water, remain well below the thresholds recommended by UNSCEAR for both ingestion and inhalation pathways. Interestingly, the lack of correlation between radon concentrations and key water quality parameters such as electrical conductivity and pH for surface water highlights the complex and multifaceted nature of radon distribution and behavior in aquatic environments. These findings hold significant implications, especially for governmental agencies entrusted with the responsibility of managing drinking water resources and ensuring their long-term sustainability. The insights gained from this study can serve as a foundational basis for informed decision-making, contributing to more effective strategies for the utilization and preservation of water resources. As such, this work stands to make a meaningful contribution to the

broader goals of ensuring safe and sustainable drinking water sources for the well-being of communities and the environment.

## ACKNOWLEDGMENTS

The authors are appreciative to the Koya University and Salahaddin University-Erbil Research Centre teams for assisting with the completion of this work.

## DISCLOSURE STATEMENT

No potential conflict of interest was reported by the author(s).

## REFERENCES

- Abdullah, G.M., Azeez, H.H., Mustafa, H.T., and Ismaeel, A.O., 2023. A study of radon concentration and physicochemical parameters in spring water of Erbil City, Iraqi Kurdistan Region. *Journal of Radioanalytical and Nuclear Chemistry*, 332(3), pp.775-784.
- Ahmad, S.T., Almuhsin, I.A., and Hamad, W.M., 2021. Radon activity concentrations in Jale and Mersaid warm water springs in Koya District, Kurdistan Region-Iraq. *Journal of Radioanalytical and Nuclear Chemistry*, 328, pp.753-768.
- Al-Alawy, I.T., Mohammed, R.S., Fadhil, H.R., and Hasan, A.A., 2018. Determination of radioactivity levels, hazard, cancer risk and radon concentrations of water and sediment samples in Al-Husseiniya River (Karbala, Iraq). *Journal of Physics Conference Series*, 1032(1), p.012012.
- Alharbi, W.R., Abbady, A.G.E., and El-Taher, A., 2015. Radon concentrations measurement for groundwater using active detecting method. *American Scientific Research Journal for Engineering Technology and Sciences (ASRJETS)*, 14, pp.1-11.
- Ameen, A.I.M., and Mansour, H.H., 2022. <sup>222</sup>Rn activity concentration measurement and its radiological risks in the environment of Barserin village, Erbil-Iraq. *Zanco Journal of Pure and Applied Sciences*, 34(2), pp.6-21.
- Avwiri, G.O., Tchokossa, P., and Mokobia, C.E., 2007. Natural radionuclides in borehole water in Port Harcourt, rivers state, Nigeria. *Radiation Protection Dosimetry*, 123(4), pp.509-514.
- Aziz, H.H., Samil, J.M., Ismail A.H., and Karim, H.H., 2015. Asses of indoor Radon dose and its risks on children's health using track detectors: Case study in Koya Kindergartens. *Journal of Kerbala University*, 11(2), pp.106-113.
- Baskaran, M., 2016. *Radon: A Tracer for Geological, Geophysical and Geochemical Studies*. Springer, Berlin.
- Baykara, O., Karatepe, Ş., and Dođru, M., 2011. Assessments of natural radioactivity and radiological hazards in construction materials used in Elazig, Turkey. *Radiation Measurements*, 46(1), pp.153-158.
- Bem, H., Plota, U., Staniszewska, M., Bem, E.M., and Mazurek, D., 2014. Radon (<sup>222</sup>Rn) in underground drinking water supplies of the Southern Greater Poland Region. *Journal of Radioanalytical and Nuclear Chemistry*, 299(3), p.1307-1312.
- Berglund, B., Bert, B., Helmut, K., Thomas, L., Molhave, M.M.L., and Skov, P., 1992. Report no. 10 effect of indoor air pollution on human health. *Indoor Air*, 25, pp.2-25.
- Binesh, A., Mowlavi, A.A., and Mohammadi, S., 2012. Estimation of the effective dose from Radon ingestion and inhalation in drinking water sources of Mashhad, Iran. *Iranian Journal of Radiation Research*, 10(1), pp.37-41.
- Canbazoglu, C., Dođru, M., Çelebi, N., and Kopuz, G., 2012. Assessment of natural radioactivity in Elazig Region, eastern Turkey. *Journal of Radioanalytical and Nuclear Chemistry*, 292(1), pp.375-380.

- Corrêa, J.N., Paschuk, S.A., Schelin, H.R., Barbosa, L., Sadula, T., and Matsuzaki, C.A., 2009. Measurements of Radon Concentration Levels in Drinking Water at Urban Area of Curitiba (Brazil). In: *2009 International Nuclear Atlantic Conference-INAC 2009*.
- Dueñas, C., Fernández, M.C., Carretero, J., Liger, E., and Cañete, S., 1999.  $^{226}\text{Ra}$  and  $^{222}\text{Rn}$  concentrations and doses in bottled waters in Spain. *Journal of Environmental Radioactivity*, 45(3), pp.283-290.
- Ezzulddin, S.K., and Mansour, H.H., 2020. Radon and radium activity concentration measurement in drinking water resources in Kurdistan Region-iraq. *Journal of Radioanalytical and Nuclear Chemistry*, 324(3), pp.963-976.
- Farhan, A.O., Ahmed, A.M., Awadh, S.M., and Al-Sultani, A.H., 2020. Radon gas and effective dose in groundwater in Abu-jir village in Anbar, Western iraq. *Iraqi Geological Journal*, 53(2C), pp.26-33.
- Gruber, V., Maringer, F.J., and Landstetter, C., 2009. Radon and other natural radionuclides in drinking water in Austria: Measurement and assessment. *Applied Radiation and Isotopes*, 67(5), pp.913-917.
- Hussein, A.M., 2018. Natural radioactivity and Radon exhalation in the sediment river used in Sulaymaniyah governorate, Iraq, dwellings. *ARO-The Scientific Journal of Koya University*, 6(2), pp.7-12.
- Hussein, Z.A., Ismail, A.H., Battawy, A.A., Karim, H.H., and Smail, J.M., 2018. Indoor Radon levels in apartments of Erbil city by using long and short term techniques. *Tikrit Journal of Pure science*, 21(3), pp.150-154.
- Ismail, A.H., 2008. Analysis of Radon concentrations in drinking water in Erbil governorate (Iraqi Kurdistan) and its health effects. *Tikrit Journal of Pure Science*, 13(3), p.9.
- Jafir, A.O., Ahmed, A.A., and Saridan, W.M., 2016. Seasonal Measurements of Natural Radionuclides in the Water Resources and Sediments of Darbandikhan Lake in Kurdistan Region, Northeastern Iraq. In: *AIP Conference Proceedings*. Vol. 1718.
- Jebur, J.H., and Subber, A.R.H., 2015. Level of radionuclide contents in surface water from Shutt-al-arab river in Basrah governorate, Iraq. *International Journal of Advanced Research in Physical Science (IJARPS)*, 2(5), pp.1-6.
- Kadhim, I.H., 2015. Analysis of radon concentration in drinking water in some locations at Baghdad City/Iraq. *Journal of University of Babylon for Pure and Applied Sciences*, 23(4), pp.1686-1692.
- Kareem, D.O., Ibrahim, A.A., and Ibrahim, O.S., 2020. Heavy metal and radon gas concentration levels in Khasa River in Kirkuk City (NE Iraq) and the associated health effects. *Arabian Journal of Geosciences*, 13(19), p.1023.
- Khattak, N.U., Khan, M.A., Shah, M.T., and Javed, M.W., 2011. Radon concentration in drinking water sources of the main campus of the University of Peshawar and surrounding areas, Khyber Pakhtunkhwa, Pakistan. *Journal of Radioanalytical and Nuclear Chemistry*, 290(2), pp.493-505.
- Kumar, A., Arora, T., Singh, P., Singh, K., Singh, D., Pathak, P.P., and Ramola, R.C., 2021. Quantification of radiological dose and chemical toxicity due to Radon and uranium in drinking water in Bageshwar Region of Indian Himalaya. *Groundwater for Sustainable Development*, 12, p.100491.
- Najam, L.A., Ebrahiem, S.A., Abbas, S.A., and Mahdi, H.A., 2018. Assessment of Radon gas concentrations levels and radiation hazards in the dwellings of Baghdad province, Iraq. *Rasayan Journal of Chemistry*, 11(1), pp.37-40.
- Nilsson, A.C., & Sandberg, B. (2017). *Elevated pH Values in Groundwater Observations from SKB investigations*. Skb. Available from: <https://www.skb.com/publication/2485482/R-16-04.pdf> [Last accessed on 2023 Apr 06].
- Nuhu, H., Hashim, S., Sanusi, M.S.M., and Saleh, M.A., 2020. Radon activity concentration measurements in water sources from Perak State Malaysia. *Journal of Radiation Research and Applied Sciences*, 13(1), pp.665-671.
- Qadir, R.W., Asaad, N., Qadir, K.W., Ahmad, S.T., and Abdullah, H.Y., 2021. Relationship between radon concentration and physicochemical parameters in groundwater of Erbil City, Iraq. *Journal of Radiation Research and Applied Sciences*, 14(1), pp.61-69.
- Smail, J.M., Ahmad, S.T., and Mansour, H.H., 2021. Estimation of the natural radioactivity levels in the soil along the little Zab River, Kurdistan Region in Iraq. *Journal of Radioanalytical and Nuclear Chemistry*, 331, pp.1-10.
- Smail, J.M., Mansour, H.H., and Ahmad, S.T., 2023. Evaluation of radiological hazards in lower zab river sediments. In: *Radiation Effects and Defects in Solids*. Taylor & Francis, United Kingdom.
- Tabar, E., and Yakut, H., 2014. Determination of  $^{226}\text{Ra}$  concentration in bottled mineral water and assessment of effective doses, a survey in Turkey. *International Journal of Radiation Research*, 12, pp.193-202.
- Tayyeb, Z.A., Kinsara, A.R., and Farid, S.M., 1998. A study on the radon concentrations in water in Jeddah (Saudi Arabia) and the associated health effects. *Journal of Environmental Radioactivity*, 38(1), pp.97-104.
- Tong, J., Qin, L., Cao, Y., Li, J., Zhang, J., Nie, J., and An, Y., 2012. Environmental Radon exposure and childhood leukemia. *Journal of Toxicology and Environmental Health Part B Critical Reviews*, 15(5), pp.332-347.
- UNSCEAR, 1988. *1988 Report to the General Assembly*. 647. Available from: [https://www.unscear.org/docs/publications/1988/unscear\\_1988\\_report.pdf](https://www.unscear.org/docs/publications/1988/unscear_1988_report.pdf) [Last accessed on 2023 Apr 10].
- Wallner, G., and Steining, G., 2007. Radium isotopes and  $^{222}\text{Rn}$  in Austrian drinking waters. *Journal of Radioanalytical and Nuclear Chemistry*, 274(3), pp.511-516.



# Natural Dye of Beetroot: An Agent for Spectrophotometric Determination of Atenolol in the Pharmaceutical Formulations

Tara F. Tahir<sup>1</sup>, Kurdistan F. Aziz<sup>2</sup> and Dashne M. Kokhasmail<sup>2</sup>

<sup>1</sup>Department of Medical Microbiology, Faculty of Science and Health, Koya University, Danielle Mitterrand Boulevard, Koya KOY45, Kurdistan Region – F.R. Iraq

<sup>2</sup>Department of Chemistry, Faculty of Science and Health, Koya University, Danielle Mitterrand Boulevard, Koya KOY45, Kurdistan Region – F.R. Iraq

**Abstract**—In this study, a simple and indirect spectrophotometric method for the quantification of atenolol in pharmaceutical formulations, utilizing a natural food dye extracted from red beet root, is presented. The process involves the oxidation of atenolol in a 1 mol/L HCl acidic medium, using an excess of potassium persulfate. Subsequently, the resulting tablet solution is employed to fade the red beetroot dye, and the solution is measured spectrophotometrically. The optimized reaction conditions consist of a 16 µg/mL atenolol solution, 2.1 mL (100 µg/mL) of potassium persulfate, and 5 mL (100 µg/mL) of red beetroot dye. Spectrophotometric measurements were performed at 535 nm, and the linear range for quantification was found to be 4–22 µg/mL ( $R^2 = 0.9987$ ). The method exhibited a limit of detection of 0.01 µg/mL. Notably, the proposed method was successfully applied to analyze various commercial brands of pharmaceutical formulations; yielding results consistent with those obtained using the pharmacopeia method. This research offers a valuable and accessible technique for atenolol quantification, demonstrating potential significance in pharmaceutical analysis and quality control processes.

**Index Terms**—Atenolol, Beetroot dye, Indirect measurement, Redox reaction, Spectrophotometric method.

## I. INTRODUCTION

The analytical procedures that are comprised less harmful, non-toxic reagents used, and the wastes produced are important analytical features. This concept is one of the 12 principles of green chemistry regulations and rules (Vidotti, et al., 2006, Anastas, 1999). Consequently, this urges the claim to use ecofriendly reagents and instruments that are

less convoluted in relation to consumption of solvents and the possibility to achieve swift and accurate measurements. Red beetroot natural dye is an organic pigment that absorbs selective wavelengths in the range of purple to red color and contains a high concentration of betaines compound which oversees the red color (Nisa, et al., 2021). The red natural pigment of beetroot is extracted in the highest yield when 5 g of the beetroot sample is heated to 100°C in 10 ml distilled water for 10 min at pH 4 (Hussin, 2022). The organic dye that is friendly to the environment has different application in painting, optical, and industrial fields (Thankappan, Thomas, and Nampoori, 2012, Abdelrahman, Abdelrahman, and Elbadawy, 2013).

Hypertension is a disease of the century. Pharmaceutical industries are competing to manufacture drugs for all diseases particularly chronic diseases such as hypertension. A major issue worldwide is the falsification and tampering of medications that are consumed by the populace. The utilization of these pharmaceuticals presents a risk to individuals' well-being. In Brazil, this concern came to light in 1998, when a range of medications including birth control pills, antibiotics, anticancer drugs, and fever reducers was counterfeited with severe outcomes (Pastore and Capriglione, 1998). Therefore, the examination of pharmaceutical compositions aims not only to ensure the quality control in the manufacturing process but also to demonstrate the appropriateness of the product (Pezza, et al., 2000). Furthermore, within the framework of green chemistry, there is a clear need for effective approaches to regulate the quantity of medication present in pharmaceutical formulations. Atenolol, a  $\beta_1$ -selective (cardioselective) adrenoceptor antagonist, is a medication frequently employed in the treatment of hypertension. It is also utilized for the prevention of heart conditions such as angina pectoris and the regulation of certain types of cardiac arrhythmias (Hoffman, et al., 1987). Atenolol is chemically identified as 4-(2-hydroxy-3-[(1-methylethyl) amino] propoxy) benzeneacetamide.

Several analytical methods have been recorded to detect the existence of atenolol in pharmaceutical products.

ARO-The Scientific Journal of Koya University  
Vol. XI, No. 11 (2023), Article ID: ARO.11286. 6 pages  
DOI: 10.14500/aro.11286

Received: 23 July 2023; Accepted: 04 September 2023  
Regular research paper: Published: 18 September 2023

Corresponding author's e-mail: tara.fuad@koyauniversity.org  
Copyright © 2023 Tara F. Tahir, Kurdistan F. Aziz and Dashne M. Kokhasmail. This is an open access article distributed under the Creative Commons Attribution License.



Various techniques have been reported in scientific literature for quantifying atenolol in pharmaceutical formulations, such as high-performance liquid chromatography (Weich, et al., 2007), high-performance thin-layer chromatography (Argekar and Powar, 2000), potentiometry (Nikolelis, Petropoulou, and Mitrokotsa, 2002, Saad, et al., 2003, Shamsipur and Jalali, 2005), capillary electrophoresis (Bonato and Briguenti, 2005), and voltammetry (Goyal, et al., 2006, Goyal and Singh, 2006). However, many of these methods are lengthy, requiring significant amounts of organic solvents, or necessitate costly and advanced equipment.

Various cost-effective, precise, and resource-efficient methods have been observed for the analysis of atenolol, such as diffuse reflectance spectroscopy (Gotardo, et al., 2008), visible spectrophotometry (Gülcü, Yücesoy and Serin, 2004, Salem, 2002, Al-Ghannam and Belal, 2002, Amin, Ragab and Saleh, 2002, Al-Ghannam, 2006), and UV derivative spectrophotometry (Ferraro, Castellano and Kaufman, 2004). Among these, the UV-visible spectrophotometer remains the most widely used technique globally due to its simplicity, rapidity, accuracy, sensitivity, and suitability for routine pharmaceutical quality control (Wati, Chandra, and Rivai, 2020).

To adhere to the principles of green chemistry, this study employed a spectrophotometer to analyze the presence of atenolol in a pharmaceutical formulation utilizing beetroot natural dye.

## II. MATERIALS AND METHODS

### A. Instruments

The measurement of absorbance was conducted using the Agilent Technologies Cary Series UV-Visible double beam Spectrophotometer, which was equipped with a glass cell having an optic path length of 1.0 cm.

### B. Materials, Chemicals, and Solutions

A stock solution of atenolol, with a purity of 99.9%, was obtained from Awamedica Pharmaceutical Company in the Kurdistan Region of Iraq and used as received. To prepare a solution of 1000  $\mu\text{g/mL}$ , 0.1 g of atenolol was dissolved in 20 mL of distilled water and warmed for approximately 10 min. The resulting solution was then diluted to 100 mL with distilled water in a volumetric flask. Daily working standard solutions were prepared by diluting the stock solution appropriately with distilled water. A solution of potassium persulfate (100  $\mu\text{g/mL}$ ) was prepared by dissolving 0.1 g of solid potassium persulfate (Fluka) in a small amount of warm water and then diluting it to 1000 mL with distilled water. A solution of hydrochloric acid (SCP) with an approximate concentration of 1.0 M was created by diluting 8.3 mL of concentrated HCl in a 100 mL volumetric flask using distilled water. To produce a dye solution of red beetroot with a concentration of 100  $\mu\text{g/mL}$ , 0.1 g of fresh red beetroot was dissolved in 10 mL of distilled water, heated to 100°C for 10 min at pH 4, and then further diluted to 1000 mL using distilled water.

### C. Interfering Solutions

Individual solutions of glucose (SCP), lactose (BDH), and starch (Difco) with concentrations of 1000  $\mu\text{g/mL}$  were prepared by dissolving 0.1 g of each respective solid compound in 100 mL of distilled water.

### D. Pharmaceutical Formulations

Pharmaceutical tablets from two distinct commercial brands, specifically Novaten (50 mg) and Vascoten (100 mg), were subjected to analysis. These formulations were obtained from local drug stores and underwent testing before their designated expiration dates.

For each pharmaceutical company, 28 tablets of Novaten and 20 tablets of Vascoten were weighed, crushed, and the resulting sample powder from each company was carefully measured and placed into separate 50 mL beakers. Subsequently, the powder was dissolved in 20 mL of distilled water, heated, and continuously stirred for 10 min to improve solubility. Any insoluble excipients were then removed through filtration using Whatman No. 41 membrane filter paper. The filtered solution was further diluted to a final volume of 100 mL in a volumetric flask, using the same solvent.

### E. Method

An indirect spectrophotometric method was employed to determine the content of pharmaceutical tablets (Kokhasmail, Tahir, and Azeez, 2020) and atenolol in the previously reported method (Basima, Afyaa, and Najih, 2022). The determination of atenolol involved two steps. In the first step, atenolol was oxidized using an excess of potassium persulfate reagent as the oxidizing agent, under acidic conditions with HCl as illustrated in Fig 1 (Shadjou, et al., 2011). The second step involved the determination of the excess potassium persulfate reagent by measuring the bleaching reaction of the red beetroot food dye in an acidic medium.

### F. Analytical Procedure

In a 25.0 mL volumetric flask, either a standard solution or a sample solution containing atenolol (100  $\mu\text{g/mL}$ ) was mixed with varying concentrations ranging from 4 to 22  $\mu\text{g/mL}$ , along with 2.1 mL of potassium persulfate solution (100  $\mu\text{g/mL}$ ) and 1.0 mL of HCl (1 mol/L). The mixture was vigorously shaken and left to stand for 10 min at a controlled temperature of  $40 \pm 2^\circ\text{C}$ . Subsequently, 5 mL of red beetroot solution (100  $\mu\text{g/mL}$ ) was added, and the mixture was further diluted to the mark with distilled water. The absorbance of the resulting solution was measured at 535 nm, relative to a reagent blank prepared under similar conditions but without the presence of atenolol. This process allows for precise analysis and quantification of atenolol using spectrophotometric measurements.

## III. RESULTS AND DISCUSSION

### A. Absorption Spectra

The molecular absorption spectrum of the red beetroot solution (5.0 mL, 100  $\mu\text{g/mL}$ ) exhibited its maximum

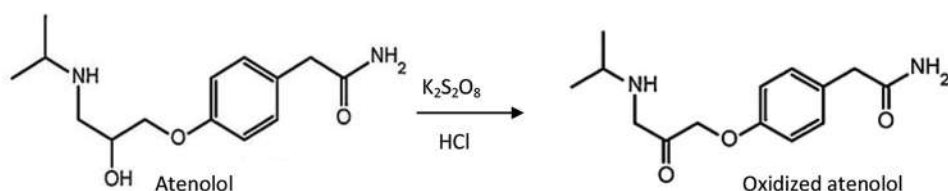


Fig. 1. Oxidation reaction mechanism of atenolol by oxidizing agent potassium persulfate in HCl acidic medium.

absorbance at 535 nm when compared against the blank solution of distilled water (Fig. 2a). On the other hand, a remarkable decrease in absorbance was observed for the resulting bleaching solution containing 10  $\mu\text{g/mL}$  of atenolol at the same wavelength (Fig. 2b). Conversely, the blank solution comprising 2.1 mL (100  $\mu\text{g/mL}$ ) of potassium persulfate and red beetroot dye displayed no significant absorbance (Fig. 2c). These observations illustrate the distinctive spectral responses and indicate the effectiveness of the method in detecting and quantifying atenolol in the presence of the specific reagents.

### B. Different Proton Providers

The reaction of 16  $\mu\text{g/mL}$  atenolol with 2.1 mL (100  $\mu\text{g/mL}$ ) of potassium persulfate and the 5.0 mL (100  $\mu\text{g/mL}$ ) solution of red beetroot dye was investigated using different acidic solutions, namely, 1 mol/L of HCl, HNO<sub>3</sub>, H<sub>2</sub>SO<sub>4</sub>, and CH<sub>3</sub>COOH, individually (Fig. 3a). Among these acids, Muriatic acid (HCl), being the strongest acid, proved to be the most effective in achieving sufficient oxidation of atenolol and bleaching of the red beetroot dye. The optimal volume of 1.0 mL (1 mol/L) HCl solution was identified and used for subsequent studies (Fig. 3b). These findings highlight the significance of using HCl as the acidic medium to attain the desired reactions for the analysis of atenolol and red beetroot dye in the method.

### C. Sequence of Addition

The effect of different sequences of addition for the components, namely, 2.1 mL (100  $\mu\text{g/mL}$ ) potassium persulfate, 16  $\mu\text{g/mL}$  atenolol solution, 5.0 mL (100  $\mu\text{g/mL}$ ) red beetroot dye, and 1.0 mL (1 mol/L) HCl, was investigated by measuring the absorbance at 535 nm (Fig. 4). The optimal absorbance was achieved when the sequence of addition was as follows: Atenolol, potassium persulfate, HCl, and finally red beetroot dye. These results validate the mechanism of the redox reaction between atenolol and potassium persulfate, followed by the bleaching of the red beetroot dye by the resulting solution from the drug reaction in the acidic medium. The preferred order of addition ensures the most efficient and accurate determination of atenolol content in the presence of red beetroot dye, allowing for reliable analysis using the described method.

### D. Bleacher and Dye Concentrations

Elementary experiments were conducted to determine the optimal amount of red beetroot dye to be added, and it was found that adding 5 mL of 100  $\mu\text{g/mL}$  red beetroot dye

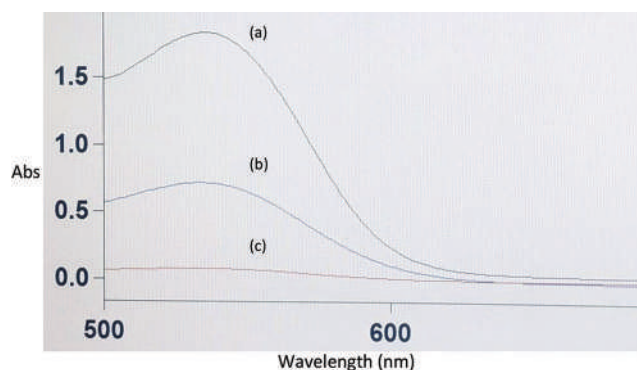


Fig. 2. Absorption spectra of (a) 5.0 mL of (100  $\mu\text{g/mL}$ ) red beetroot, (b) 10  $\mu\text{g/mL}$  atenolol, 2.1 mL (100  $\mu\text{g/mL}$ ) of potassium persulfate, and 5.0 mL red beetroot dye, and (c) blank reagent of 2.1 mL (100  $\mu\text{g/mL}$ ) of potassium persulfate and red beetroot solution against distilled water.

yielded stable and intense absorbance, making it a reasonable concentration for the procedure.

On the other hand, it was observed that higher concentrations of potassium persulfate, exceeding 100  $\mu\text{g/mL}$ , led to diminish in the intensity of the red beetroot dye's color. To establish the appropriate volume for the procedure, different volumes ranging from 0.5 mL to 2.4 mL of 100  $\mu\text{g/mL}$  potassium persulfate were tested under the experimental conditions, and it was determined that 2.1 mL of the oxidant provided the best results, as shown in Fig. 5.

### E. Temperature, Time, and Stability

The absorbance of the redox reactions involving 16  $\mu\text{g/mL}$  of atenolol, 2.1 mL (100  $\mu\text{g/mL}$ ) of potassium persulfate solution in 1.0 mL acidic medium of (1 mol/L) HCl, along with 5 mL (100  $\mu\text{g/mL}$ ) of red beetroot dye, was examined at various heating temperatures and times, as shown in Table I. It was observed that increasing the heating temperature to  $40 \pm 2^\circ\text{C}$  for 10 min resulted in the maximum absorbance of the resulting bleaching solution. This is attributed to the fact that at higher temperatures, the electrons possess more energy, allowing them to overcome the activation energy required to break bonds with the current molecule and move to the next. In essence, the temperature represents the average kinetic energy of the particles in the reaction system. Therefore, higher temperatures provide more energy, making it easier for electrons to transition between molecules. In addition, increased temperature enhances diffusion rates, leading to more frequent interactions between molecules that have yet to undergo the reaction, thus facilitating the overall reaction process (Meixner, Renneberg and Kuhn, 2002).

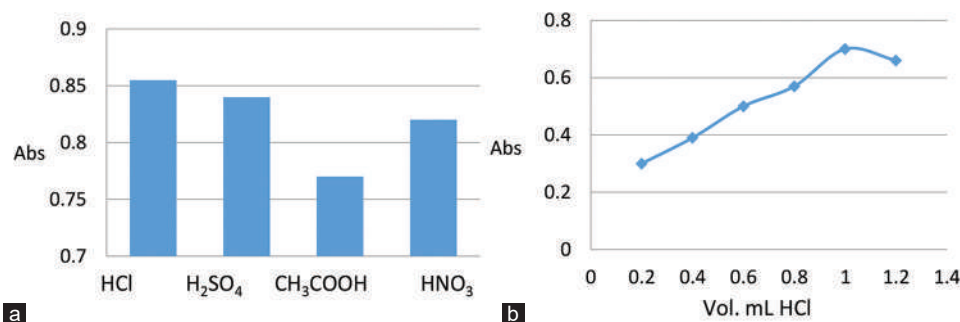


Fig. 3. Absorbance of yielded bleaching solutions of atenolol with (a) 1 mol/L of HCl, H<sub>2</sub>SO<sub>4</sub>, CH<sub>3</sub>COOH, and HNO<sub>3</sub>, individually, (b) different volumes (0.2–1.2 mL) of 1 mol/L HCl solution.

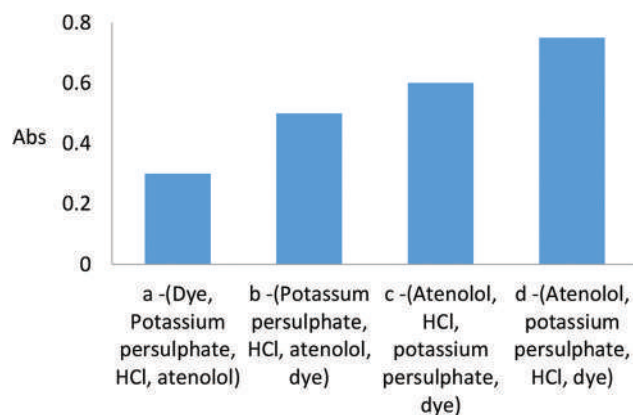


Fig. 4. Absorbance of different sequences of mixing atenolol, potassium persulfate, HCl, and red dye of beetroot.

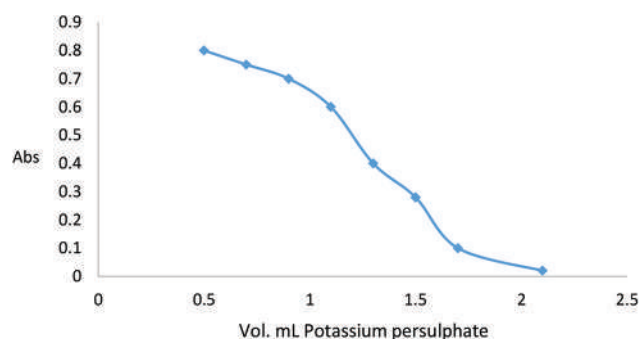


Fig. 5. Amount of bleacher potassium persulfate solution of red beetroot dye in an acidic medium.

Time plays a crucial role in completing the redox reaction of 16 µg/mL atenolol with 2.1 mL (100 µg/mL) of potassium persulfate solution in a 1.0 mL (1 mol/L) HCl solution, as well as the subsequent bleaching of 5 mL (100 µg/mL) of red beetroot dye. The maximum absorbance was achieved after 10 min at 40 ± 2°C, as indicated in Table I. It is notable that a higher temperature near to 50°C causes decomposition of the oxidizing agent potassium persulfate.

Moreover, the color intensity of the resulting bleached dye solution remained stable for at least 24 h at room temperature (25 ± 3°C) after 40 min of completion. This demonstrates that the reaction is not only efficient but also exhibits good stability over time, providing reliable and consistent results.

TABLE I.  
HEATING TEMPERATURES AND TIMES OF YIELDED BLEACHING REACTION OF ATENOLOL DRUG OF THE RED BEETROOT DYE

Temperature °C	Absorbance					
	10 min	20 min	30 min	40 min	50 min	60 min
5±2	0.2055	0.2022	0.2043	0.2173	0.1983	0.2076
10±2	0.5673	0.5723	0.4751	0.4832	0.5394	0.4890
25±2	0.7137	0.7109	0.7097	0.7122	0.7096	0.7105
40±2	0.8102	0.8102	0.8079	0.8089	0.8043	0.8076
45±2	0.8101	0.8102	0.8077	0.8085	0.8043	0.8077

TABLE II  
COMMON EXCIPIENTS IN THE DETERMINATION OF ATENOLOL WITH THEIR RELATIVE ERRORS

Interference	Allowance concentration (µg/mL)	E %
Lactose	30	-3.97
Glucose	25	1.38
Starch	20	2.70

TABLE III  
ACCURACY AND PRECISION OF THE CALIBRATION CURVE

Concentration of atenolol (µg/mL)	Obtained concentration (µg/mL)	SD	RSD%	E%*
4	3.86	0.0001	0.77	-3.50
16	16.08	0.0001	0.01	0.50
22	21.70	0.0010	0.10	-1.36

\*Average of five determinations

#### F. Interferences

Pharmaceutical tablets were prepared with the addition of common excipients to assess atenolol under optimum conditions. The excipient solutions, namely, lactose, glucose, and starch, were each prepared at a concentration of 1000 µg/mL. These solutions were then mixed individually with 16 µg/mL of pure atenolol to achieve a final volume of 25 mL. The obtained spectra were compared with the spectrum of the 16 µg/mL atenolol standard solution.

In the evaluation, it was found that there were no significant levels of interferences, and the errors observed in the determination of atenolol in the presence of common excipients were lower than 5% (Table II). This indicates that the presence of these common excipients in pharmaceutical tablets does not significantly affect the accuracy and reliability of the determination of atenolol using the proposed method under the specified optimum conditions.

TABLE IV  
DETERMINATION OF ATENOLOL IN PHARMACEUTICAL TABLETS

Sample	Label to content (mg/tablet)	Found by proposed <sup>a</sup> method (mg/tablet)	t value (2.78)	F value (19)	Found by reference <sup>a</sup> method (mg/tablet)
A	100	101.8±0.6	0.340	4.69	99.7±0.4
B	50	48.5±0.9	0.254	7.88	49.8±0.5

<sup>a</sup>Average±standard deviation (SD), n=3

TABLE V  
COMPARISON OF THE PROPOSED AND THE EXISTING VISIBLE SPECTROPHOTOMETRIC METHODS

Method	Linear range (µg/mL)	Detection limit (µg/mL)	Quantification limit (µg/mL)	References
coupling with 4-chloro-7-nitrobenzo-2-oxa-1,3-diazole	5–50	1.3	Non	Al-Ghannam, and Belal, 2002
Complexation reaction	3–48	0.26	0.80	Prashanth and Basavaiah, 2012
Oxidation reaction with chromate, indigo carmine dye	1.2–60	0.3259	1.0863	Saleem, 2019
Complex with bromocresol green	2.66–26.63	0.22	0.66	Antakli, Nejem and Joumaa, 2020
Indirect determination Beet root dye bleaching	4–22	0.01	0.60	Suggested method

### G. Calibration Curve and Application

An analytical curve conforming to Beer's law was created by employing atenolol standard solutions across a concentration range of 4–22 µg/mL (Fig. 6). The plotted graph of absorbance versus concentration (µg/mL) exhibited a good correlation coefficient ( $R^2 = 0.9987$ ), indicating a linear relationship between absorbance and atenolol concentration.

The limit of detection for the method was determined to be 0.01 µg/mL, signifying the lowest concentration of atenolol that can be reliably detected and quantified using this spectrophotometric technique. Overall, the analytical curve's characteristics demonstrate the method's precision and sensitivity in accurately determining the concentration of atenolol in the specified concentration range.

In the proposed procedure, accuracy and precision were achieved by measuring the absorbance of the resulting bleaching solution of the red beetroot dye, which indirectly determined the concentration of atenolol at three different levels (4, 16, and 22 µg/mL). Each concentration was subjected to five replicate measurements (Table III).

The suitability of the suggested procedure was assessed based on two key parameters: The relative standard deviation (RSD %) and the relative error (E %) values. By examining the RSD% and E% values for the three different concentrations of atenolol, the procedure's robustness and accuracy can be ascertained. These parameters help to establish the reliability and practicality of the suggested procedure for the analysis of atenolol in pharmaceutical formulations.

The proposed method was employed to assess commercial atenolol tablets, and the obtained results were statistically compared with the tablet contents determined using the UV spectrophotometry technique which is the procedure of the pharmacopoeia analysis (Table IV). The reference method involved the quantitative determination of atenolol using UV spectrophotometry at 275 nm, which required successive dilutions with methanol and heating at 60°C under shaking for 15 min (Gotardo, et al., 2008, Wati, et al., 2020).

The proposed method was applied to several commercially available pharmaceutical tablets containing atenolol, and the

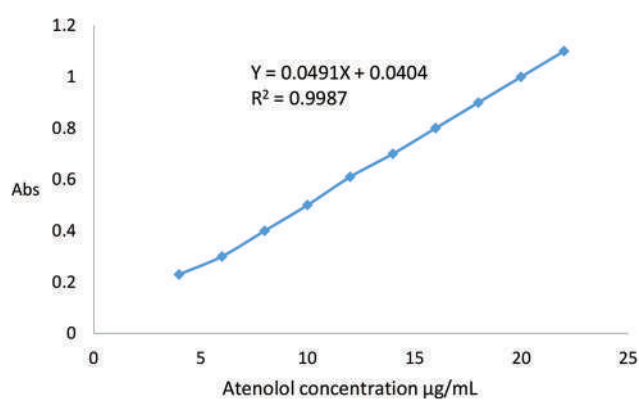


Fig. 6. Calibration curve of indirect spectrophotometric determination of atenolol.

results showed excellent agreement with those obtained using the pharmacopoeia method. To further validate the consistency and accuracy of both methods, the results for the formulations assayed by both approaches were compared using the F test and t test at a 95% confidence level.

The calculated F and t values were found to be within the theoretical range, indicating that there is no significant difference between the two methods concerning precision and accuracy. This statistical analysis supports the reliability and suitability of the proposed method for the quantitative determination of atenolol in commercial pharmaceutical tablets and confirms its capability to yield results comparable to those obtained using the established pharmacopoeia method.

The results obtained by the recommended method were compared with those in some of the literature corresponding to the linear range of the calibration curve, quantification limit, and detection limit (Table V).

## IV. CONCLUSION

The proposed method offers an indirect spectrophotometric approach for accurately quantifying atenolol in tablets. Its notable advantages include its simplicity, utilization of an eco-friendly red beetroot dye, and minimal consumption of reagents and solvents, making it a greener and more cost-

effective option. The method relies on the redox reaction between atenolol and the oxidizing agent potassium persulfate, resulting in the bleaching of the red beetroot dye within the pharmaceutical tablet. The determination of atenolol is accomplished using a spectroscopic technique, which proved successful in yielding reliable results.

By applying the proposed method, atenolol concentrations were determined in tablet samples from various commercial brands. The method exhibited good precision and accuracy, confirming its reliability and suitability for practical use in pharmaceutical analysis.

In summary, the proposed indirect spectrophotometric method presents an efficient and environmentally friendly solution for quantifying atenolol in tablets, making it a valuable tool for pharmaceutical quality control and analysis of different commercial formulations.

## REFERENCES

- Abdelrahman, A.H., Abdelrahman, M.A., and Elbadawy, M.K., 2013. Possibility of using the beet dyes as a laser gain medium. *Natural Science*, 5(11), pp.1183-1188.
- Al-Ghannam, S.M., 2006. A simple spectrophotometric method for the determination of beta-blockers in dosage forms. *Journal of Pharmaceutical and Biomedical Analysis*, 40(1), pp.151-156.
- Al-Ghannam, S.M., and Belal, F., 2002. Kinetic spectrophotometric determination of atenolol in dosage forms. *Journal of AOAC International*, 85(4), pp.817-823.
- Amin, A.S., Ragab, G.H., and Saleh, H., 2002. Colorimetric determination of beta-blockers in pharmaceutical formulations. *Journal of Pharmaceutical and Biomedical Analysis*, 30(4), pp.1347-1353.
- Anastas, P.T., 1999. Green chemistry and the role of analytical methodology development. *Critical Reviews in Analytical Chemistry*, 29(3), pp.167-175.
- Antakli, S., Nejem, L., and Joumaa, M.A., 2020. Determination of atenolol in tablet formulation by analytical spectrophotometry. *Research Journal of Pharmacy and Technology*, 13(2), pp.609-614.
- Argekar, A.P., and Powar, S.G., 2000. Simultaneous determination of atenolol and amlodipine in tablets by high-performance thin-layer chromatography. *Journal of Pharmaceutical and Biomedical Analysis*, 21(6), pp.1137-1142.
- Basima, A.A.S., Afyaa, M.Y., and Najih, H.S., 2022. Visible spectrophotometric method for quantitative estimation of atenolol drug using cerium (III and IV). *AIP Conference Proceedings*, 2660(1), p.20097.
- Bonato, P.S., and Briguenti, A.C.C., 2005. Quantitative analysis of beta-blockers in pharmaceutical preparations by capillary electrophoresis. *Drug Development and Industrial Pharmacy*, 31(2), pp.209-214.
- Ferraro, M.C.F., Castellano, P.M., and Kaufman, T.S., 2004. Chemometric determination of amiloride hydrochloride, atenolol, hydrochlorothiazide and timolol maleate in synthetic mixtures and pharmaceutical formulations. *Journal of Pharmaceutical and Biomedical Analysis*, 34(2), pp.305-314.
- Gotardo, M.A., Sequinel, R., Pezza, L., and Pezza, H.R., 2008. Determination of atenolol in pharmaceutical formulations by diffuse reflectance spectroscopy. *Ecletica Quimica*, 33(4), pp.7-12.
- Goyal, R.N., and Singh, S.P., 2006. Voltammetric determination of atenolol at C<sub>60</sub>-modified glassy carbon electrodes. *Talanta*, 69(4), pp.932-937.
- Goyal, R.N., Gupta, V.K., Oyama, M., and Bachheti, N., 2006. Differential pulse voltammetric determination of atenolol in pharmaceutical formulations and urine using nanogold modified indium tin oxide electrode. *Electrochemistry Communications*, 8(1), pp.65-70.
- Gülcü, A., Yücesoy, C., and Serin, S., 2004. Spectrophotometric determination of some beta-blockers in dosage forms based on complex formation with Cu(II) and Co(II). *Farmaco*, 59(6), pp.487-492.
- Hoffman, B.B., Hardman, J.G., Limbird, L.E., and Gilman, A.G. (eds.), 1987. *Goodman and Goodman's. The Pharmacological Basis of Therapeutics*. 10<sup>th</sup> ed., Vol. 10. MacGraw-Hill, Rio de Janeiro, pp.1011-1021.
- Hussin, S.H.S., 2022. Optical properties of beetroot dye and its different applications. *bn AL-Haiitham Journal For Pure and Applied Sciences*, 35(2), pp.17-27.
- Kokhasmail, D.M., Tahir, T.F., and Azeez, K.F., 2020. Spectrophotometric indirect determination of captopril through redox reaction with n-bromosuccinimide and RB dye in pharmaceutical products. *ARO-The Scientific Journal*, 8(2), pp.8-14.
- Meixner, T., Renneberg, H., and Kuhn, A.J., 2002. Temperature effects on redox reactions of the nitrogen cycle: A review. *European Journal of Soil Science*, 53(4), pp.539-556.
- Nikolelis, D.P., Petropoulou, S.E., and Mitrokotsa, M.V., 2002. A minisensor for the rapid screening of atenolol in pharmaceutical preparations based on surface-stabilized bilayer lipid membranes with incorporated DNA. *Bioelectrochemistry*, 58(1), pp.107-112.
- Nisa, A.U., Hina, S., Kalim, I., Saeed, M.K., Ahmad, I., Zahra, N., Mazhar, S., Masood, S., Ashraf, M., Syed, Q.A., and Shad, R., 2021. Quality assessment and application of red natural dye from beetroot (*Beta vulgaris*). *Pakistan Journal of Agricultural Research*, 34(3), pp.552-558.
- Pastore, K., and Capriglione, L., 1998. O feitiço do corpo ideal. *Revista Veja*, 1532, pp.62-69.
- Pezza, L., Tubino, M., Melios, C.B., and Pezza, H.R., 2000. Rapid spot test analysis for the detection of dipyron in pharmaceutical preparations. *Analytical Sciences*, 16(3), pp.313-315.
- Prashanth, K.N., and Basavaiah, K., 2012. Simple, sensitive and selective spectrophotometric methods for the determination of atenolol in pharmaceuticals through charge transfer complex formation reaction. *Acta Poloniae Pharmaceutica and Drug Research*, 69(2), pp.213-223.
- Saad, S.M.H., Abou-Sekkina, M.M., El-Ries, M.A., and Wassel, A.A., 2003. Polymeric matrix membrane sensors for sensitive potentiometric determination of some beta-blockers in pharmaceutical preparations. *Journal of Pharmaceutical and Biomedical Analysis*, 32(1), pp.175-180.
- Saleem, B.A.A., 2019. Spectrophotometric determination of atenolol using indigo carmine dye. *Kirkuk University Journal for Scientific Studies*, 14(2), pp.15-39.
- Salem, H., 2002. Spectrophotometric determination of beta-adrenergic blocking agents in pharmaceutical formulations. *Journal of Pharmaceutical and Biomedical Analysis*, 29(3), pp.527-538.
- Shadjou, N., Hasanzadeh, M., Saghatforoush, L., Mehdizadeh, R., and Jouyban, A., 2011. Electrochemical behavior of atenolol, carvedilol and propranolol on copper-oxide nanoparticles. *Electrochimica Acta*, 58, pp.336-347.
- Shamsipur, M., and Jalali, F., 2005. Preparation of an atenolol ion-selective electrode and its application to pharmaceutical analysis. *Analytical Letters*, 38(3), pp.401-410.
- Thankappan, A., Thomas, S., and Nampoori, V.P.N., 2012. Effect of betanin natural dye extracted from red beet root on the non linear optical properties ZnO nanoplates embedded in polymeric matrices. *Journal of Applied Physics*, 112(12), pp.104-123.
- Vidotti, E.C., Costa, W.F., and Oliveira, C.C., 2006. Development of a green chromatographic method for determination of colorants in food samples. *Talanta*, 68(3), pp.516-521.
- Wati, E.J., Chandra, B., and Rivai, H., 2020. Overview of the analysis methods of atenolol in pharmaceutical preparations and biological matrices during 2000-2020. *Indian Journal of Preventive and Social Medicine*, 5(11), pp.13-23.
- Weich, A., De Oliveira, D.C., De Melo, J., Goebel, K., and Rolim, C.M.B., 2007. Validation of UV spectrophotometric and HPLC methods for quantitative determination of atenolol in pharmaceutical preparations. *Latin American Journal of Pharmacy*, 26(5), pp.765-770.

# Traffic Circulation Efficiency Analysis of Elliptical Roundabouts

Hardi S. Fathullah<sup>1</sup>, Hirsh M. Majid<sup>2</sup>, Chro H. Ahmed<sup>3</sup>, Sulleyman H. Sourkan<sup>4</sup>, Karzan S. Ismael<sup>5</sup> and Balen Z. Abdulsamad<sup>6</sup>

<sup>1</sup>Department of Engineering, Kurdistan Institution for Strategic Studies and Scientific Researches, Sulaimani, 46001, Kurdistan Region – F.R. Iraq

<sup>2</sup>Department of Civil Engineering, College of Engineering, University of Sulaimani, Sulaimani, Kurdistan Region – F.R. Iraq

<sup>3</sup>Department of Civil Engineering, College of Engineering, University of Sulaimani, Sulaimani, Kurdistan Region – F.R. Iraq

<sup>4</sup>Sulaimani Polytechnic University - Digital Cultural Heritage Research Group, Kurdistan Region – F.R. Iraq

<sup>5</sup>Department of City Planning Engineering, Technical College of Engineering, Sulaimani Polytechnic University, Kurdistan Region – F.R. Iraq

<sup>6</sup>Department of Geotechnical Engineering, Faculty of Engineering, Koya University, Koya KOY45, Kurdistan Region – F.R. Iraq

**Abstract**— This paper investigates the impact of a roundabout's central island geometry on operational performance. A case study roundabout with an elliptical central island, characterized by major and minor axes of 63 and 44 meters respectively, is examined. Using SIDRA intersection software, two simulation models were developed, one with an elliptical shape and the other circular. The investigation commenced by assigning peak traffic volumes to both models, followed by the generation of twelve diverse scenarios. These scenarios encompassed gradual increases in lane volumes, spanning from levels of service A to F. Each approach received 100% of the assigned volume for one run and 75% for the other, with this allocation alternating in successive runs. The results demonstrated that at high degrees of saturation, the elliptical roundabout outperformed the circular roundabout in terms of delay and capacity. The performance index of the elliptical roundabout was 16.9% lower than that of the circular roundabout, confirming its superior performance. Moreover, recognizing the importance of accommodating heavy vehicles in urban settings, a parametric study was conducted. Eight additional simulation scenarios, encompassing varying heavy vehicle percentage (HV%) were executed. Results indicated at higher HV% levels, particularly around 8% and 12%, control delay increases by 28.9% and 35.2% for elliptical and circular roundabouts, respectively. These results confirm

that the performance of the elliptical roundabout outperforms the circular roundabout under various scenarios. However, it's crucial to highlight that the elliptical roundabout displayed higher susceptibility to increasing heavy vehicle percentages compared to the circular roundabout.

**Index Terms**—Circular roundabout, Elliptical roundabout, Heavy vehicle percentage, Performance evaluation, Traffic simulation.

## I. INTRODUCTION

The history of roundabouts dates back to the early 1900s when the first ones were established in Paris and New York. However, these initial attempts were intended as pedestrian traffic islands rather than efficient traffic management solutions. These early models led to traffic jams and accidents, revealing the need for improved designs. In 1966, the British government enacted legislation to guide the construction and utilization of roundabouts, marking a pivotal shift towards their modern form. This legislation played a significant role in reducing crashes and delays by about 40%, while enhancing roundabout capacity by approximately 10% (Moran, 2009).

A modern roundabout is characterized by a circular junction where traffic flows counterclockwise around a central island. It differs from traditional intersections as it lacks traffic signals or stop signs. Drivers entering a roundabout must yield to oncoming traffic, proceed through the junction, and exit onto their selected street (WSDOT, 2021; Qu, et al., 2014; Mohammed Ali, et al., 2023). This modern design not only enhances traffic flow but also elevates the aesthetics of roads while providing improved safety compared to

ARO-The Scientific Journal of Koya University  
Vol. XI, No. 2 (2023), Article ID: ARO.11150. 8 pages  
Doi: 10.14500/aro.11150

Received: 08 February 2023; Accepted: 08 September 2023

Regular research paper: Published: 20 September 2023

Corresponding author's e-mail: hirsh.majid@univsul.edu.iq

Copyright © 2023 Hardi S. Fathullah, Hirsh M. Majid,

Chro H. Ahmed, Sulleyman H. Sourkan, Karzan S. Ismael and

Balen Z. Abdulsamad. This is an open access article distributed under the Creative Commons Attribution License.



conventional intersections. In modern roundabouts, traffic signals or stop signs are absent. When entering, drivers yield to oncoming traffic, proceed to the junction, and exit onto their chosen street (WSDOT, 2021). This design significantly improves traffic flow, enhances road esthetics, and ensures greater safety compared to traditional intersections.

Research by the University of Maine found a 39% reduction in crashes, a 76% decrease in injury-producing crashes, and a remarkable 90% reduction in collisions resulting in fatal or incapacitating injuries across a sample of 25 intersections converted into roundabouts. Similarly, (Davies, 2011) found that roundabouts not only improve safety but also possess the potential to reduce traffic delay by up to 75%.

The performance assessment of the roundabouts has been a focal point for researchers over the past few decades. (Sisiopiku and Oh, 2001) delved into the performance comparison between roundabouts and four-leg intersection using SIDRA package. This study considered diverse geometric configurations and traffic conditions. The results confirmed the general superiority of roundabouts in terms of higher capacities compared to other traffic control intersection types, such as yield control, two- and four-way stop control, and signal control. (Mabuchi and Nakamura, 2007) conducted a comparison between roundabouts and signalized intersections. Their results showed that when the approaching traffic volume is below 600 veh/h, roundabouts experience significantly fewer delay and traffic conflict issues compared to signalized intersections. In addition, the study found that as the difference in traffic volume between each approach increases, the performance of roundabouts decreases. (Al Momani, 2009) investigated the operational performance of roundabouts and pre-timed signalized intersections using MITSIMLab microscopic traffic simulator. This study utilized a virtual network for comparisons based on various traffic volume and green times for pre-timed signalized intersections. The results revealed that roundabouts statistically outperformed pre-timed signalized intersections across all traffic volumes. Similarly, (Tracz and Chodur, 2012) compared traffic performance of signalized intersection, signalized roundabouts, and signalized turbo roundabout. Their results showed that signalized turbo roundabouts exhibited enhanced safety and efficiency, even under the conditions of higher accident risk for public transport (buses and trams) when halting at bus/tram stop stations within the intersections.

In a more recent study, (Hatami and Aghayan, 2017) undertook a comparison of three types of roundabouts (modern, turbo, and elliptical roundabouts) with varying circulating widths and speed limits. Their simulations were conducted using Aimsun simulation software. However, the study faced limitations due to the overestimation of roundabout capacities derived from the simulation, impacting its practical applicability. In addition, the lack of clarity in the roundabout geometric design further hindered the study's relevance. (Mohamed, *et al.*, 2022) utilized the VISSIM simulator to simulate a mega elliptical roundabout on rural multilane highways. They considered various scenarios of mega elliptical roundabouts at different traffic flows for intersection entrances.

The parameters of comparisons included minimum delay, minimum emissions, and minimum fuel consumption. The findings highlighted instances where the elliptical roundabout outperformed traditional interchanges (full cloverleaf), and they proposed the optimal time for transitioning from a mega elliptical roundabout to an interchange (full cloverleaf).

(Akçelik, 2011a) examined differences in capacities estimated by the HCM 2010 and SIDRA standard models for multilane roundabouts. The study emphasized the need to incorporate driver behavior parameters, as in the SIDRA standard method, into roundabout capacity models. Moreover, NCHRP 672(TRB, 2010b) emphasized that lane-by-lane modeling of roundabouts is pivotal for understanding the impact of roundabout geometry on the capacity. Other factors, such as lane width and number of lanes, were found to be of secondary significant. Continuing from his previous research (Akçelik, 2017) conducted an assessment of the HCM Edition 6 model and then comparing it with that of the HCM2010 and SIDRA standard capacity for roundabouts. In the light of results mentioned in this study, it can be concluded that there exists a broad consensus regarding the superior performance of roundabouts in terms of safety, traffic performance, vehicle time consumption, fuel consumption, and air pollution compared to other control modes.

There are various types of roundabouts categorized based on shape, configuration, and size: (i) Circular and elliptical roundabouts as the most prevalent shapes; (ii) configuration-wise, there exist mini roundabout, normal roundabout, and double roundabout; and (iii) concerning size, roundabouts can be single-lane or multi-lane (AASHTO, 2011). In Kurdistan Region of Iraq, the proliferation of roundabouts is rapidly increasing, especially within newly developed urban areas and even along high-speed rural highways. This surge necessitates a well-structured and effectively managed plan to regulate the flow of incoming traffic at these roundabouts. Consequently, this study focuses on assessing the capacity and efficiency of a standard multilane elliptical roundabout. For this purpose, Shari Spi intersection situated in the eastern-north of Sulaymaniah city is selected as a case study location. The selection of Shari Spi intersection is rooted in its distinct attributes, being the sole elliptical roundabout within the city featuring multiple entry points and high traffic volume.

Furthermore, the roundabout experiences noticeable traffic congestion issues on its approaches, particularly during peak periods. Fig. 1 provides a visual representation of the chosen roundabout.

The rest of this research is organized as follows. Section 2 presents the framework of the proposed methodology with the detailed steps of data collection. Section 3 demonstrates calibration, analysis results, and comparisons between different roundabout shapes. Finally, Section 4 provides concluding remarks on the study.

## II. METHODOLOGY

This study was conducted by collecting traffic volume from a roundabout with an elliptical central island using



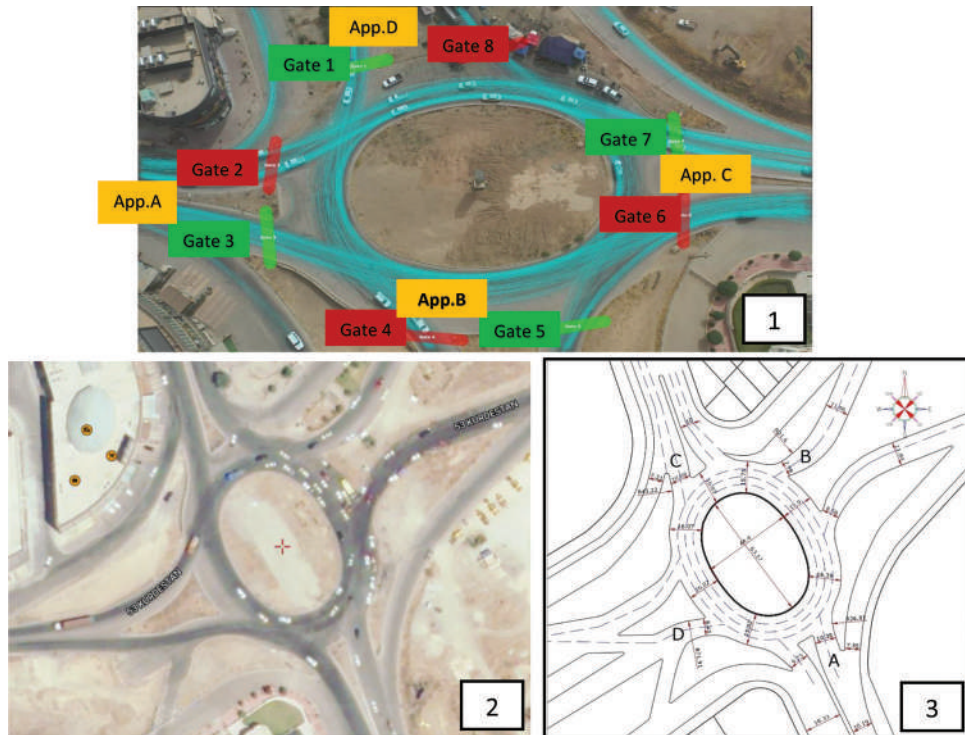


Fig. 1: Shari Spi roundabout (1-taken from drone camera, 2-Google map, 3- AutoCAD 2D).

video recording for approximately 5 h of the morning peak period. The determination of the peak hour was based on a comprehensive and pilot study over various days of different weeks spanning two distinct months. This selection ensured that the generated traffic volume was at its highest.

The turning proportions for each approach movements were calculated using Corel studio software. This approach was necessary because, at roundabouts, when lane movements mix with the circulating volumes, it becomes challenging to track individual car movements effectively. Table I shows the peak hour volume and flow rate of each approach roads.

This study utilized Sidra Intersection software as the simulation tool. Sidra intersection is an advanced, lane-based micro-analytical tool that is used worldwide for the purpose of design and evaluation of individual intersections and networks. The software offers a range of design and evaluation measures, including capacity, level of service (LOS), and various performance metrics such as delay, queue length, stops per vehicle, and for pedestrians, as well as factors like fuel consumption, pollutant emissions, and operational cost. SIDRA intersection 8.0, in particular, offers significant improvements in network modeling and processing (Akçelik, 2018). Furthermore, this software version, especially for roundabout, exhibits remarkable capabilities compared to some other software in use. It is recognized by Highway Capacity Manual and the TRB Roundabout Guide (TRB, 2010b). This software version includes the SIDRA Standard roundabout capacity model, alongside HCM and other common models. It takes into account roundabout geometry parameters, including roundabout diameter, entry radius, entry angle, entry lane width, circulating lane width, the number of entry lanes, and circulating lanes, as well as

TABLE I  
SUMMARY OF 5 H TRAFFIC VOLUME (PEAK 15 MIN OF EACH DAY)

Summary of peak hour traffic volume					
Time	Duration	Approach A	Approach B	Approach C	Approach D
07:51–08:06	15 min	147	261	275	238
08:06–08:21	15 min	157	239	302	281
08:21–08:36	15 min	175	201	293	320
08:36–08:51	15 min	141	233	234	304
Flow rate		700	1044	1208	1280

other geometric parameters, when calculating capacity. The capacity model offered in SIDRA intersection is based-on gap-acceptance theory and employs empirical (regression) equations to model gap-acceptance parameters including the effect of roundabout geometry. In contrast, the HCM 6 capacity model is an empirical (exponential regression) model firmly grounded in gap acceptance theory without taking roundabout geometry into consideration (Akçelik, 2011a, 2011b).

HCM2010 Capacity Model for two-lane entries conflicted by two circulating lanes given as follows (TRB, 2010a):

$$c_{e,R,pce} = 1130e^{(-0.7 \times 10^{-3})v_{c,pce}} \tag{1}$$

$$c_{e,L,pce} = 1130e^{(-0.7 \times 10^{-3})v_{c,pce}} \tag{2}$$

Where

$c_{e,R,pce}$  = capacity of the right entry lane in (pc / h)

$c_{e,L,pce}$  = capacity of the left entry lane in (pc / h)

$v_{c,pce}$  = conflicting flowrate (total of both lanes) in (pc / h)

$$Q = s u \quad (3)$$

Where:

$s$  = saturation flow rate (veh/h) and  $u$  = unblocked time ratio

For any gap-acceptance process, the saturation flow rate is

$$s = 3600/\beta \quad (4)$$

Where:

$\beta$  = follow-up headway of the entry stream (sec.), and the unblocked time ratio is  $u = g/c$ , where  $g$  = average unblocked time (sec.) and  $c$  = average gap-acceptance cycle time (sec.)

The unblocked time ratio used in SIDRA roundabout model is calculated by;

$$u = \max \left\{ u_{\min}, f_{od} (1 - \Delta_c q_c + 0.5 \beta \varphi_c q_c) e^{-\lambda(\alpha - \Delta_c)} \right\} \quad (5)$$

$$u_{\min} = Q_m / s \quad (6)$$

$$\lambda = \varphi_c q_c / (1 - \Delta_c q_c) \quad \text{subject to } q_c \leq 0.98 / \Delta_c \quad (7)$$

Where:

$u_{\min}$  is the minimum value of the unblocked time ratio,  $f_{od}$  is the origin-destination factor,  $Q_m$  is the minimum capacity per lane (veh/h),  $s$  is the saturation flow rate (veh/h),  $\beta$  is follow-up headway (sec.) and  $\alpha$  is critical gap (sec.) for the entering stream,  $\varphi_c$  is the intrabunch headway (sec.) and  $\varphi_c$  is the proportion unbunched for the circulating stream, and  $q_c$  is the circulating flow rate (pcu/s) (Akgelik and Besley, 2005).

Two roundabout models were created in this simulation software. The first model represented the existing study area with an elliptical central island, while the second model featured a roundabout with circular central of 63 m radius. This radius value was derived from the major axis of the elliptical central island in the existing model. Although the utilized version of SIDRA intersection was not capable of visually depicting the elliptical layout of the roundabout, the impact of the geometry was accounted for, and it was reflected in the output layouts. To evaluate the impact of the central island's shape on the performance of roundabout, several measures of effectiveness were compared. These measures included control delay, geometric delay, queue length, average travel time, speed efficiency, and performance index assessed at different levels of detail such as lane, movement, approach, and intersection.

### III. DATA ANALYSIS AND RESULTS

#### A. Calibration

To ensure that the software's output accurately represents the real condition of the site, it must undergo calibration using *in situ* control delay parameter. Traffic data were collected over several hours at various time of the day to account for oversaturated and undersaturated conditions at the intersection. The data were extracted using Data from Sky platform (Fig. 1) and the HCM 2010 procedure was employed to calculate the approach delays of the roundabout. The same data set used as the input to the SIDRA software to simulate delays. To align the delay output with the actual conditions, a correlation equation was derived between the simulated and calculated delays

for each approach and the intersection, as depicted in Table II and Fig. 2. Microsoft Excel tools were utilized for these correlation derivations.

It is important to note that a comprehensive analysis was conducted to determine the most suitable correlation between the simulated and calculated delays. The findings revealed that polynomial correlations outperformed linear correlations. These polynomial equations were capable of more accurately capturing the intricate relationships between the simulated and calculated delays, thus reflecting the complex dynamics of the intersection.

As discussed in Section 2, the required traffic volume and vehicle movement data were collected through video recording for approximately 5 h during the peak period. The maximum volumes for each approach within a 15-min are presented in Table I. The turning proportions for each approach movements were calculated using Corel studio software. The traffic volume of each approach road was utilized in the simulation for different scenarios and roundabout shapes, as presented in Table III. These volumes were subsequently assigned to the corresponding approaches within the proposed models to assess the operational performance of the roundabouts.

#### B. Effect of the Roundabout Geometric Shape

In this section, the effect of roundabout geometric shapes on the performance measures is examined by applying two test scenarios. In the first scenario, an identical traffic volume was assigned to each movement type, ensuring that the (LOS) of the roundabout remained above LOS F. Specifically, in a simulation case, 100% of capacity was used for each approach road. Subsequently, virtual volumes were allocated to the SW and NE approaches, while the SE and NW approaches were loaded with 75% of the maximum capacity. In the second scenario, the volumes assigned to the approaches were reversed. This approach is employed to investigate the impact of the short and long axes of the elliptical roundabout on traffic movement.

It is noteworthy that the utilization of values of 100% and 75%, both less than and greater than the roundabout's maximum capacity, contributes to a more comprehensive understanding of the LOS and the effects of geometric variations. This approach enables an evaluation of the roundabout's performance under different loading conditions and provides valuable insights into its behavior at various levels of congestion.

The results showed that there were evident differences in the performance parameters of the two models. The circular and elliptical roundabout were compared in terms of various performance measures, including delay, degree of saturation, travel speed, travel time, and others. Furthermore, the performance index of the elliptical roundabout was found to be 16.9% lower than that of the circular roundabout confirming its superior performance. Fig. 3 depicts the degree of saturation for each scenario implemented for both the circular (63 m dia.) and elliptical shapes.

TABLE II  
SUMMARY OF THE DATA USED FOR THE CALIBRATION OF SIDRA SOFTWARE

Delay s/veh.								
Gate-1			Gate-3			Intersection		
Calculated delay s/veh	Simulated delay s/veh	Calibrated delay s/veh	Calculated delay s/veh	Simulated delay s/veh	Calibrated delay s/veh	Calculated delay s/veh	Simulated delay s/veh	Calibrated delay s/veh
183.55	173.9	183.24	325.78	234.3	324.06			
86.45	102.7	89.78	196.315	166.3	196.99			
41.032	47.6	38.33	96.206	96.8	96.74			
24.577	24.8	22.36	40.595	40.5	37.49			
17.785	15.8	16.92	22.372	20.9	21.48			
14.256	11.3	14.38	15.820	13.4	15.98			
12.138	8.6	12.92	12.705	9.9	13.53			
10.708	6.6	11.86	10.908	7.2	11.70			
9.699	5.3	11.19	9.739	5.6	10.63			
Gate-5			Gate-7			Intersection		
Calculated delay s/veh	Simulated delay s/veh	Calibrated delay s/veh	Calculated delay s/veh	Simulated delay s/veh	Calibrated delay s/veh	Calculated delay s/veh	Simulated delay s/veh	Calibrated delay s/veh
391.28	124.1	380.91	100.89	68	101.26	238.67	149.4	238.95
219.478	100.1	220.00	51.773	40	49.77	134.360	102.6	133.23
98.525	82.7	131.43	28.329	25.4	29.45	64.860	62.6	66.84
41.914	42.8	17.50	19.095	17.6	20.43	31.050	31.1	30.09
24.143	22.4	7.23	14.921	12.6	15.32	19.490	17.5	18.46
17.146	14.3	12.15	12.552	9.7	12.60	14.740	12	14.48
13.614	10.1	16.72	11.065	7.7	10.83	12.250	8.9	12.42
11.505	7.4	20.38	10.040	6.2	9.55	10.710	6.8	11.10
10.110	5.7	22.98	9.299	5.1	8.64	9.660	5.4	10.26

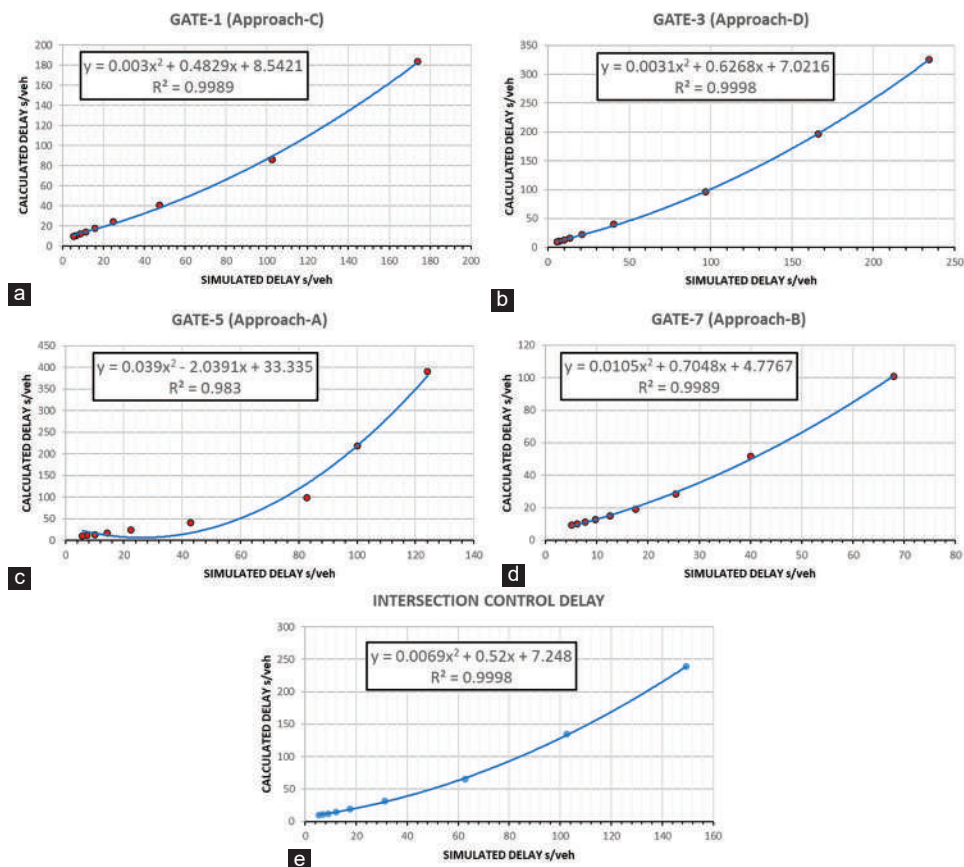


Fig. 2. Intersection control delay to perform calibration process (a) Gate 1 (approach-C). (b) Gate 3 (approach-D). (c) Gate 5 (approach-A). (d) Gate 7 (approach-B). (e) Intersection control delay.

It should be noted that in the simulations, the approach speed and exit speed were set at 50 km/h. This decision was based on the data collected from video recordings and the posted speed limits at the roundabout approaches. However, it is important to highlight that the average travel speed, calculated by the software using input approach volumes and traffic composition, consistently remained below 50 km/h, with values ranging from 40 km/h to 45 km/h.

As depicted in the Fig. 3, at a low degree of saturation ( $<0.748$ ), no changes in LOS were observed for both roundabout geometric shapes. However, at a higher degree of saturation ( $>0.748$ ), the impact of changing approach volumes began to manifest in both roundabout geometric shapes, resulting in a decrease in LOS from A to B level. Further increments in the degree of saturation beyond 0.987 with the first scenario, tended to raise the LOS of the elliptical roundabout by one level compared to the circular one, while when the second scenario was applied both of them dropped to the next lower LOS.

In the last two simulations (11 and 12), the degree of saturations exceeded one for both scenarios 1 and 2. As illustrated in Fig. 3 in Scenario 1, the elliptical roundabout consistently outperforms the circular roundabout. However, in Scenario 2, both roundabouts experienced a drop to the next two lower LOS levels. This variation can be primarily attributed to two factors: (i) The circular roundabout, with a diameter of 63 m, necessitated vehicles to traverse a longer path compared to the elliptical roundabout, which featured major and minor axes of 63 m and 44 m, respectively; and (ii) the elliptical shape caused difficulty for some approach movement's turning maneuver while significantly facilitated the turning maneuver for others, as compared to the circular shape.

Furthermore, average control delay, which serves as the main indicator of LOS, was determined for each of the twelve-simulation test as shown in Fig. 4. The results indicate that the lower the demand, the less the difference between both roundabouts' performance in terms of control delay. However, as demand increased (especially on NW-SE approaches perpendicular to the major axis of the elliptical roundabout), this difference became more pronounced.

### C. Effect of Heavy Vehicles

In this section, the effect of heavy vehicles on the roundabout performance is investigated through the application of two test scenarios presented in Section 3.2. It is important to note that for each scenario, four simulation tests were conducted with varying percentages of heavy vehicles, ranging from 2% to 12% as detailed in Table IV. These specific percentages were selected to assess the influence of traffic composition on the efficiency of both elliptical and circular roundabouts. In addition, these percentages were grouped into intervals, as displayed in Table IV, to evaluate the effects of varying

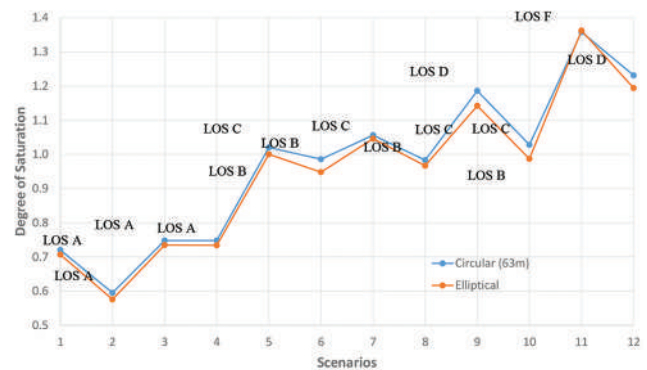


Fig. 3. Degree of saturation for different roundabout shape and loading configuration.

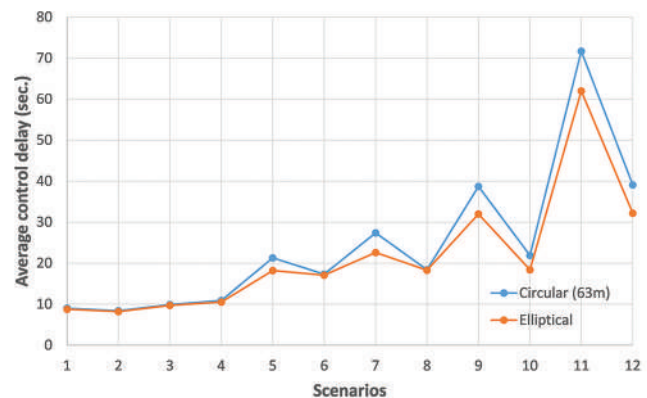


Fig. 4. Average control delay of both models with alternate approach volumes.

heavy vehicle percentages on roundabout performance systematically.

Furthermore, it should be emphasized that these percentage values closely approximate real-world data. By replicating the traffic compositions encountered in practical scenarios, insights can be gained into how varying proportions of heavy vehicles impact roundabout performance. Consequently, the utilization of these percentages serves a dual purpose: It reflects real-world conditions and allows for the analysis of roundabout performance under different traffic compositions.

The results showed that increasing the percentage of heavy vehicles from 2% to 5% tended to be inefficient in improving the LOS of the elliptical roundabout, while the LOS of the circular roundabout dropped from B to C level. At higher percentages of heavy vehicles, especially from 8% and 12%, the control delay increased by 28.9% and 35.2% for the elliptical and circular roundabouts, respectively, as demonstrated in Fig. 5. These results confirm that the performance of the elliptical roundabout consistently outperforms the circular roundabout under various scenarios. However, it is important to note that the elliptical roundabout was more susceptible to the changes in the percentage of heavy vehicles compared to the circular roundabout.

TABLE III  
LOADING CONFIGURATION FOR DIFFERENT SCENARIOS USED IN SIDRA

1						2					
U	Movement Volume veh/approach/15 min.			Approach	Volume Assignment	U	Movement Volume veh/approach/15 min.			Approach	Volume Assignment
	L	R	TH				L	R	TH		
5	80	80	120	NE-SW	100%	8	90	90	130	NE-SW	100%
4	60	60	90	SE-NW	75%	6	68	68	98	SE-NW	75%
3						4					
5	80	80	120	SE-NW	100%	8	90	90	130	SE-NW	100%
4	60	60	90	NE-SW	75%	6	68	68	98	NE-SW	75%
5						6					
10	100	100	150	NE-SW	100%	12	115	115	125	NE-SW	100%
8	75	75	113	SE-NW	75%	9	87	87	94	SE-NW	75%
7						8					
10	100	100	150	SE-NW	100%	12	115	115	125	SE-NW	100%
8	75	75	113	NE-SW	75%	9	87	87	94	NE-SW	75%
9						10					
12	120	120	130	NE-SW	100%	12	120	120	150	NE-SW	100%
9	90	90	97	SE-NW	75%	11	98	98	113	SE-NW	75%
11						12					
12	120	120	130	SE-NW	100%	14	130	130	150	SE-NW	100%
9	90	90	97	NE-SW	75%	11	98	98	113	NE-SW	75%

TABLE IV  
ALTERNATE APPROACH VOLUME ASSIGNMENT FOR VARYING HV%

Applying uniform approach volume alternately with varying HV%					
Alternate approach volume with HV% assignment		Circular 63		Elliptical	
		Degree of saturation	LOS	Degree of saturation	LOS
1	C2 (2%) and E2 (2%)	0.999	B	0.995	B
2	C1 (2%) and E1 (2%)	0.972	B	0.951	B
3	C2 (5%) and E2 (5%)	1.065	C	1.02	B
4	C1 (5%) and E1 (5%)	1.008	C	0.972	B
5	C2 (8%) and E2 (8%)	1.146	D	1.099	C
6	C1 (8%) and E1 (8%)	1.008	C	0.984	B
7	C2 (12%) and E2 (12%)	1.232	E	1.217	D
8	C1 (12%) and E1 (12%)	1.13	C	1.072	C

C1-E1 : SW and NE Approaches 100% – SE and NW Approaches 75% of volumes assigned, C2-E2 : SW and NE Approaches 75% – SE and NW Approaches 100% of volumes assigned, LOS: Level of service

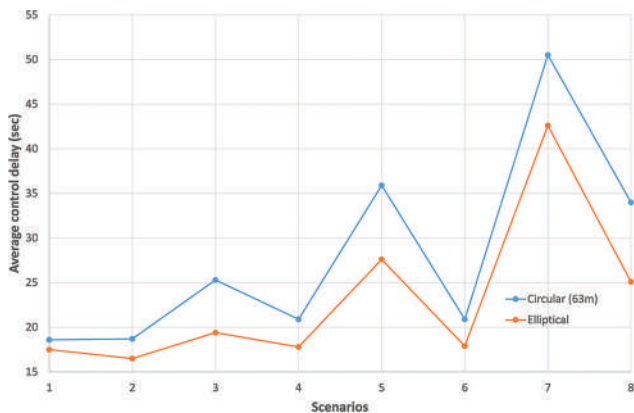


Fig. 5. Average control delay of C63m and elliptical models with alternate approach volumes for various percentage of heavy vehicles.

IV. CONCLUSION

In this study, two simulation models were developed using SIDRA Intersection software, featuring different geometric shapes of central islands: One with an elliptical shape and the other with a circular shape. The study assessed the operational performance of roundabouts, specifically comparing the delay and capacity of elliptical and circular geometric shapes. Various factors, including traffic volume, traffic composition, and degree of saturation, were considered. The investigation was initiated by assigning peak traffic volumes to both models, followed by the generation of twelve diverse scenarios. These scenarios encompassed gradual increases in lane volumes, spanning from levels of service A to F.

The results demonstrated that the elliptical roundabout exhibited superior operational performance compared to the circular roundabout, particularly in terms of capacity, LOS, and performance index parameters. The performance index of the elliptical roundabout was 16.9% lower than that of the circular roundabout, confirming its superior performance.

In addition, recognizing the importance of accommodating heavy vehicles in urban settings, a parametric study was conducted. It included eight simulation scenarios with varying heavy vehicle percentages (HV%). Results indicated at higher HV% levels, particularly around 8% and 12%, control delay increases by 28.9% and 35.2% for elliptical and circular roundabouts, confirming the elliptical roundabout’s superior performance. However, it is crucial to highlight that the elliptical roundabout displayed higher susceptibility to increasing heavy vehicle percentages compared to the circular roundabout.

In conclusion, the findings suggest that the implementation of an elliptical central island can offer practical advantages

and contribute to the enhanced performance of a roundabout. This trend becomes particularly prominent when the traffic volume along the approaches parallel to the longer axis of the elliptical roundabout surpasses the volume on the approach's perpendicular to this axis.

Moving forward, future research should explore specific design parameters and operational conditions contributing to elliptical central island advantages. In addition, a comprehensive study of traffic composition's impact on roundabout performance could provide valuable insights. Overall, this study underscores the potential benefits of adopting elliptical geometric shapes in certain traffic scenarios, calling for further research.

#### REFERENCES

- AASHTO., 2011. A Policy on Geometric Design of Highways and Streets. American Association of State Highway and Transportation Officials, Washington DC.
- Akçelik, R., 2011. An Assessment of the Highway Capacity Manual 2010 Roundabout Capacity Model. In: International Roundabout Conference. Transportation Research Board, Carmel, Indiana, USA.
- Akçelik, R., 2011. Some Common and Differing Aspects of Alternative Models for Roundabout Capacity and Performance Estimation. In: International Roundabout Conference. Carmel, Indiana, USA: Transportation Research Board.
- Akçelik, R., 2017. An Assessment of the Highway Capacity Manual Edition 6 Roundabout Capacity Model. In: 5<sup>th</sup> International Roundabout Conference. Transportation Research Board, Green Bay, WI, USA.
- Akçelik, R., 2018. SIDRA Intersection 8.0 User Guide. Akçelik and Associates Pty Ltd., Greysthorne, Australia.
- Akçelik, R., and Besley, M., 2005. Differences between the AUSTROADS roundabout guide and AUSIDRA roundabout analysis methods. *Road and transport Research Journal*, 14(1), pp.44-64.
- AL Momani, M., 2009. A Comparison of Traffic Flow Performance of Roundabouts and Signalized Intersections using MITSIMlab. Master's Thesis, Near East University. Graduate School of Applied Sciences, Nicosia.
- Davies, C., 2011. A Brief History of Roundabouts: Once Bitten Twice Shy. Canada: Miovision.
- Hatami, H., and Aghayan, I., 2017. Traffic efficiency evaluation of elliptical roundabout compared with modern and turbo roundabouts considering traffic signal control. *PROMET-Traffic and Transportation*, 29(1), pp.1-11.
- Mabuchi, T., and Nakamura, H., 2007. Performance evaluation of roundabouts considering traffic conflicts. *J East Asia Society for transportation Studies*, 7, pp.2412-2424.
- Mohamed, A.I., Ci, Y., and Tan, Y., 2022. Mega elliptical roundabouts versus grade-separation interchange. *Proceedings of the Institution of Civil Engineers-Transport*, 175(6), pp.323-343.
- Mohammed Ali, H.K., and Majid, H.M., 2023. Comparative evaluation of roundabout capacities methods for single-lane and multi-lane roundabout. *Journal of Engineering*, 29(3), pp.76-97.
- Moran, J., 2009. Defining Moment: The British Invent the modern Round About, 1966. FT Magazine Europe.
- Qu, X., Ren, L., Wang S., and Oh E., 2014. Estimation of entry capacity for single-lane modern roundabouts: Case study in Queensland, Australia. *Journal of Transportation Engineering*, 140(7), pp. 1-5.
- Sisiopiku, V.P., and Oh, H.U., 2001. Evaluation of roundabout performance using Sidra. *Journal of Transportation Engineering*, 127(2), pp.143-150.
- TRB, 2010b. National cooperative highway research program and United States, federal highway administration 2010. In: Roundabouts: An Informational Guide. Washington, DC: Transportation Research Board.
- Tracz, M., and Chodur, J., 2012. Performance and safety roundabouts with traffic signals. *Procedia-Social and Behavioral Sciences*, 53, pp.788-799.
- WSDOT., 2021. What is Roundabout? Available from: <https://wsdot.wa.gov/Safety/roundabouts/basicfacts.htm#:~:text=A%20modern%20roundabout%20is%20a,exit%20at%20their%20desired%20street> [Last accessed on 2023 Aug 15].

# Investigation of Nano- and Micro-Sized Amorphous Materials under the Influence of High-Energy Radiation

Mohammed M. Sabri

Department of Physics, Faculty of Science and Health, Koya University,  
Koya KOY45, Kurdistan Region - F.R. Iraq

**Abstract**—This research explored the behavior of glass when bombarded by high-energy radiation, especially electron beams inside transmission electron microscopy (TEM). Six types of glasses are investigated under e-beam. The work is conducted using three types of TEMs of energies of 120, 200, and 300 keV. The findings show that these microscopies have a significant impact on the glass, as various observations were documented. Using a wide electron beam, morphology changes combined with bubble formation are observed in the glass. These changes are rounding and smoothening of glass edges and surfaces. In addition, the findings show that there is no material loss due to irradiation as confirmed by the energy dispersive X-ray spectroscopy. The results also show that high silica glass is very sensitive, while high boron glass is found to be less sensitive to irradiation. Using a smaller size electron beam, on the other hand, resulted in the fabrication of a nanoring/nanocrater in glass. The possible applications of this research can be in the protection and packaging of three-dimensional electronic equipment and nanoscale pattern formation through roughening of the external glass contour through phase separation and the opposite through local changing of a part of the glass through the pseudo-melting and the stability of loaded and un-loaded glasses to the irradiation. Furthermore, by generating a nanoring or a nanocrater through e-beam, the lithography process is successfully performed, as the effect of the electron beam is solely at the irradiation region, while the regions outside the e-beam remain unaffected.

**Index Terms**—Glass, Morphology changes, Nanoring, Quasi melting, Transmission electron microscopy.

## I. INTRODUCTION

Irradiation with high-energy radiation has been reported to perform changes in nano and micro-size amorphous materials, especially glass (Jiang, et al., 2004; Singh and Karmakar, 2011; Ehrt and Vogel, 1992; Sidorov, et al., 2021). This topic has become of great interest and, therefore, attracted a variety of researchers in the past and recently (Shelby, 1980; Abo Hussein, 2023). This is due to the fact that radiation has

an important impression on the structures, characteristics, morphologies, and compositions of these materials. A variety of changes have been reported to occur when the e-beam interacts with a material (Hobbs, 1987; Chen, et al., 2021). Various definitions have been reported on glass (Mauro, et al., 2013), focusing either on its physical properties or on its structure. Usually, all glasses were found to share two common properties. These are as follows: (i) glass has a short-range order of the atomic arrangement and (ii) glass has a behavior of time-dependent glass transformation (Guigo and Sbirrazzuoli, 2018; Shelby, 2005). The American Society for Testing and Materials defines glass as “an inorganic product of fusion which has cooled to a rigid condition without crystallization.” A typical type of glass is oxide glass. These glasses are considered to be prototype brittle materials that became significant member of nowadays nano and micro components in terms of structure and function (Bruns, et al., 2023). Usually, three fundamental types of oxides are available. Glass formers such as silica and boric oxide, glass modifiers such as soda and lithium oxide, and intermediates such as  $Al_2O_3$ . Changes due to radiation of glass with a high-energy particle include for instance the modifications in the external shapes of the glass, in particular, changing the external parts of the glass fragment (Gedeon, et al., 2007; Zheng, et al., 2010) and other amorphous materials (Shen, et al., 2022), phase separation (Chen, et al., 2015; DeNatale, et al., 1986; Sun, et al., 2004), ion migration (Yoshida and Tanaka, 1997; Jbara, et al., 1995; Gedeon, et al., 1999), phase alteration (Liu, et al., 2004), the production of bubbles (Leay and Harrison, 2019), which was considered to be oxygen, nanoprecipitation (Qiu, et al., 2002), crystallization (Klimenkov, et al., 2001; Jencic, et al., 1995), hole drilling (Furuya, 2008), and quasi-melting (Ajayan and Ijima, 1992; Ajayan and Marks, 1989; Marks, et al., 1986). Most of these changes were frequently reported in oxide glasses (Skuja, et al., 2005), while the phenomenon of shape transformations was rarely reported (Li, et al., 2019). The latter was sometimes noticed accidentally, while sometimes deliberately studied. Transmission electron microscopy (TEM) is a widely used technique and considered to be a powerful tool for irradiation-induced modifications, formation of nanoparticles, and also for the purpose of recording images (Duan, et al., 2018; Sigle, 2005; Egerton et al., 2004). Moreover, exploring electron beam-materials interaction is of a great interest

ARO-The Scientific Journal of Koya University  
Vol. XI, No. 2 (2023), Article ID: ARO.11290, 10 pages  
DOI: 10.14500/aro.11290

Received: 27 July 2023; Accepted: 09 September 2023

Regular research paper: Published: 24 September 2023

Corresponding author's e-mail: mohammed.mohammedsabri@koyauniversity.org

Copyright © 2023 Mohammed M. Sabri. This is an open access article distributed under the Creative Commons Attribution License.



(Dapor, 2003). Normally, scattering of both types elastic and inelastic is reported to occur when an e-beam hits a material, and this will be the source of giving essential knowledge on the structure and the composition of the sample. One of the significant importance of using a transmission electron microscope is to modify the amorphous materials and can track these modifications *in situ* (live) and this will allow the discovery of novel phenomena such as nanoscale and microscale phase changes and morphology changes in these materials (Rauf, 2008; Mackovic, et al., 2014; Butler, 1979). Usually, three various mechanisms are involved in the interaction of a high-energy radiation with materials. These are as follows: (i) ionization and electronic excitation processes through radiolysis (Ugurlu, et al., 2011), (ii) direct displacement of the atoms by fast high-energy radiation (elastic collisions) through knock-on (Ugurlu, et al., 2011), and (iii) heating (Liu, et al., 1994; Sidorov, et al., 2021). The first mechanism, on the one hand, involves damage to the electronic structure and bond breakage, which may lead to the displacement of atoms as a secondary effect converting excitonic energies generated during incident probe-atomic electron interactions into momentum by forming a Frenkel pair. The second mechanism, on the other hand, includes direct atom displacement, which may be followed by rearrangement of the electronic structure. Finally, under a high-energy radiation, the specimen will be saturated with energy through electron-phonon scattering and this will cause the specimen to be heated. It has been suggested that the quality of the heat flow connection to the sample support may affect the temperature alteration from a few degrees up to melting (Hobbs, 1987; Bysakh, et al., 2004). The effects of heating in the TEM can be minimized using several methods such as avoid the usage of thick samples and using thin sample instead, coating the sample with conducting materials, and using unheated holders.

The main purpose of the current research is to explore the influence of irradiation by the electron beam on different glasses and then explain the resulting phenomena that occurred in these materials.

## II. MATERIALS AND METHODS

The experimental procedure consists of three main stages. These stages are as follows: (i) glass preparation through typical melting process, (ii) TEM sample preparation, and (iii) the irradiation process. All the micrographs that obtained from the irradiation process were analyzed using image J software (Image J Launcher version 1.4.3.67 with an accuracy of about 100%). This software was used to determine the radius of curvature of the rounded corners of the glass fragments, to determine the size of the nanoparticles, as well as to determine the size of the nanorings.

### A. Producing the Glass through Melting Process

The initial step of the glass preparation is mixing the raw materials manually and then weight about 300 g of each glass batch for the melting process. All raw materials were oxides

and carbonates ( $\text{Na}_2\text{CO}_3$ ,  $\text{H}_3\text{BO}_3$ ,  $\text{SiO}_2$ ,  $\text{CaCO}_3$ ,  $\text{Al}_2\text{O}_3$ ,  $\text{Li}_2\text{O}$ ,  $\text{CeO}_2$ ,  $\text{Cr}_2\text{O}_3$ , and  $\text{ZrO}_2$ ) and they were all purchased from the company Sigma-Aldrich and their purity of about 99.9%. The batch was, then, transferred to the platinum crucible (of a cylindrical shape having a height of about 12 cm and base diameter of about 5 cm), and the latter was transferred to the electric furnace of an internal volume of about 148  $\text{cm}^3$  with silicon carbide elements for the purpose of melting. The entire melting process lasted 5 h. After that, about 20% of the product was fast-cooled (quenching process) in water to get a quenched glass and the rest (~ 80%) was transferred to another furnace for slow cooling (annealing process) to get an annealed glass. The degree of annealing temperature was 510°C for 1 h. Six different glasses were used. One of them is a silica-free (Si-free) glass and named as NB. The second glass is a high-Si glass and named as NBS-HS and the third is a high-B glass and named as NBS-HB. The fourth is a boron-free (B-free) glass and named as NCS. The fifth glass contains both Al and Ca and named as ACBS. The last glass is alkali-mixed glass and named as AMBS. Table I shows the chemical composition of the prepared glass along with the melting temperature of each glass.

### B. Sample Preparation for TEM Tests

TEM specimens were prepared by manually grinding the quenched glass into a very fine powder (the amount of the powder used was about 20–30 g) in acetone using a pestle and mortar. The mixture (powder and acetone) was, then, transferred to the ultrasonic machine and was left for about 15 min to decrease or remove the amount of the agglomeration. A fresh TEM sample holder (either gold or copper grids with carbon film) was, then, carried by tweezers and immersed into the mixture to pick up the glass. Finally, the TEM sample is transferred to the microscope for the irradiation study.

### C. e-beam Irradiation Procedure

Three different types of TEMs were used to conduct the irradiation. First, TEM of type Philips 420 thermionic tungsten at 120 kV is used to investigate the effect of the electron beam in modifying the shape of the glass fragment. The captured images in this microscope were saved in photographic plates and, then, collected and scanned using a normal scanning machine to get the final micrographs. Normally, the irradiation

TABLE I  
THE CHEMICAL COMPOSITION (MOL. %) OF THE GLASS AND THE MELTING TEMPERATURE (OC)

Glass name	Glass code	Glass composition	Melting temperature
Silica-free	NB	21.16Na <sub>2</sub> O-70.84B <sub>2</sub> O <sub>3</sub> -4CeO <sub>2</sub> -2Cr <sub>2</sub> O <sub>3</sub> -4ZrO <sub>2</sub>	1250
High silica	NBS-HS	16.6Na <sub>2</sub> O-20B <sub>2</sub> O <sub>3</sub> -63.4SiO <sub>2</sub>	1200
High boron	NBS-HB	16.6Na <sub>2</sub> O-62.55B <sub>2</sub> O <sub>3</sub> -20.85SiO <sub>2</sub>	1100
Boron-free	NCS	18.3Na <sub>2</sub> O-18.3CaO-63.4SiO <sub>2</sub>	1450
Al-Ca glass	ACBS	8Al <sub>2</sub> O <sub>3</sub> -27CaO-8B <sub>2</sub> O <sub>3</sub> -57SiO <sub>2</sub>	1450
Alkali-mixed glass	AMBS	8.6Na <sub>2</sub> O-4.3Li <sub>2</sub> O-25.7B <sub>2</sub> O <sub>3</sub> -51.4SiO <sub>2</sub> -4CeO <sub>2</sub> -2Cr <sub>2</sub> O <sub>3</sub> -4ZrO <sub>2</sub>	1400



process in this TEM has been conducted using the largest condenser aperture and spot size 1. Second, TEM of type JEOL JEM 2010F field emission gun (FEG) at 200 kV, which has the capability of getting a finer electron beam (few nm in size) than that in the TEM of type Philips 420 and also provides a charged coupled device (CCD) camera to take digital images and third, TEM of type JEOL JEM 3010 lanthanum hexaborides ( $\text{LaB}_6$ ) of a voltage of 300 kV. In this microscope, a higher current is available and this allows to irradiate of the samples with a higher accelerating voltage in comparison to the TEM 2010F at 200 kV and TEM 420 at 120 kV. However, the e-beam cannot be focused on that much compared to TEM 2010F (FEGTEM) due to the filament source of the former TEM. There is also a CCD camera in this TEM to record the images. It is worth mentioning that all the three TEMs used in this research are located at the University of Sheffield-United Kingdom. Fig. 1 illustrates a schematic diagram of the mechanisms used in this research. These include (i) morphology alteration experiments, (ii) hole drilling, and (iii) imaging.

### III. RESULTS AND DISCUSSION

#### A. Shape Alteration Due to e-beam Irradiation

It has been proven that an electron beam is a versatile tool for performing alterations into glass (Musterman, et al., 2022). In addition, *in situ* TEM is most widely used technique due to its various characteristics, and due to the fact that *in situ* TEM is enthusiastic by observing the real-time material modification, the effect of the e-beam cannot be neglected (Shen, et al., 2022). The experiment of shape alteration has been performed by reducing the diameter of the e-beam

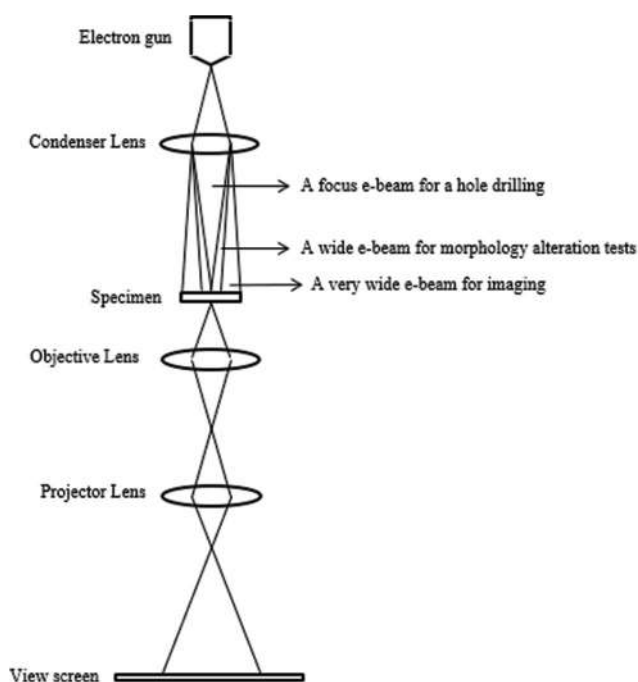


Fig. 1. A schematic diagram showing the three mechanisms used in the transmission electron microscopy.

in such a way that covering the entire glass fragment. The e-beam is then will be leaving at this condition for a selected period of time and monitoring the live morphology changes. When the irradiation process is completed, a micrograph of the irradiated glass fragment at a selected magnification will be captured. Fig. 2 shows a sample of the alkali-mixed glass before and subsequent 5 min of electron irradiation. This glass sample is of sharp corners and coarse edges, as shown in Fig. 2a. Our measurements of this fragment before the irradiation were as follows: position 1, position 2, and position 3 have a radius of curvature of about 4 nm, 7 nm, and 7.5 nm, respectively. The e-beam diameter has then been reduced to cover the whole glass particle (the size of the electron beam  $\sim 500$  nm). After about less than a minute of irradiation, the modifications were initiated. These modifications are smoothing of the rough surfaces and edges and rounding of the sharp corners, as shown in Fig. 2b. From Fig. 2b, it is clear that the morphology of the entire glass sample was altered and if the irradiation process continued for a longer time, the glass particle in Fig. 2a might be gotten more rounded to form a full ball-shape. The measurements after the entire 5 min of irradiation, however, were as follows: the radius of curvature of position 1 is about 5 nm, the radius of curvature of position 2 is about 26 nm, and the radius of curvature of position 3 is about 16 nm. The impacts of the e-beam on the glass fragment are obvious through noticing the shape-changing. The electron beam is wide enough to cover the entire glass fragment (the size of the electron beam is larger than the size of the glass fragment) and the first part subjecting to the alteration is the corner of the glass sample. Usually, the flow of materials due to e-beam irradiation was reported to be the reason for the phenomenon of morphology alteration in glass (Bruns, et al., 2023).

Now, a sample of a high-Si glass has been irradiated for 5 min. After  $\sim 1$  min of e-beam irradiation, this sample underwent a morphology modification. This glass sample is some sharp corners (positions 1 and 2 in Fig. 3a). These positions became rounded after the irradiation (the same positions shown in Fig. 3b). This is again proposed to be due to the movement of glass material (Bruns, et al., 2023). As such, the material will be moved into the middle of the glass fragment and accumulate there and therefore this fragment looks darker after irradiation (Fig. 3b). In addition, a little

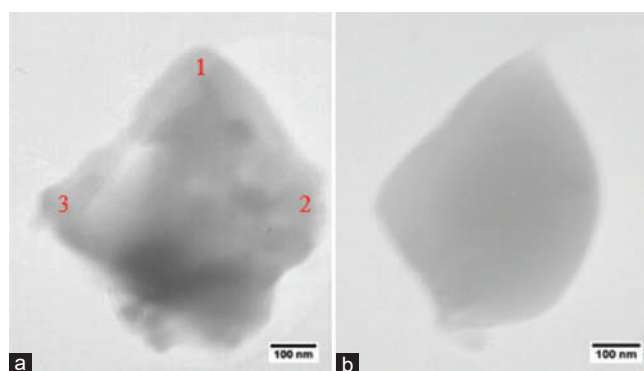


Fig. 2. An alkali-mixed glass (a) at  $t=0$  min and (b) at  $t=5$  min irradiation using a transmission electron microscopy of type Philips 420 at 120 kV.

smoothing effect on the bottom part of this fragment can be seen due to the irradiation. Our experiments showed that before the irradiation, the radius of curvatures of position 1 and position 2 was 5 nm and 6 nm, respectively (as shown in Fig. 3a). However, after 5 min of irradiation, the radius of curvatures of position 1 and position 2 dramatically increased to about 15 nm and 8 nm, respectively (Fig. 3b). This result is consistent with the results reported by Singh and Karmakar in which they observed morphological alterations (rounding of glass edges) of glass fragment in bismuth-doped oxide glass (Singh and Karmakar, 2011). In addition, the results observed in this research are agreed with what have been reported by Jiang and his group in terms of smoothing of the rough glass surface in germanium glass (Jiang, et al., 2005).

The chemical composition of this glass was explored before and after the irradiation using energy-dispersive X-ray spectroscopy (EDX), as shown in Fig. 4. Both spectra contain the glass elements of oxygen, sodium, silicon, and boron. It is obvious that before (Fig. 4a) and after irradiation (Fig. 4b), there is no difference in the composition of this fragment and this gives an indication and confirmation of no loss of materials occurred due to the e-beam irradiation. Furthermore, the copper (Cu) peaks (signals) that appeared in the energy dispersive spectroscopy spectra are belonging to the copper grid used to hold the glass specimen for TEM measurements.

A time-series irradiation of a fragment of the B-free glass has been performed, as shown in Fig. 5. Usually, time-series is an important process in the field of e-beam-induced modifications in glass. This process gives a chance to live observe and track the alteration of the irradiated glass sample. Fig. 5a shows a fragment of the B-free glass at  $t = 0$  min. When this glass was irradiated for about 1-min, a slight alteration can be evident, as shown in Fig. 5b. These alterations were not stopped when the glass sample was irradiated for extra 2 min and 5 min, as shown in Figs. 5c and d, respectively. All these alterations occurred to this sample are in terms of rounding of the corners as well as smoothing of the coarse surfaces (Singh and Karmakar, 2011; Jiang, et al., 2005).

A sample of the Si-free glass has been shown to be robust under irradiation, as shown in Fig. 6. This sample was analyzed using a JEOL 2010F TEM. The total irradiation process was 5 min. A slight modification in this glass fragment was noticed,

in which the bottom corner of the fragment shown in Fig. 6a underwent a slight rounding when subjected to the irradiation (Fig. 6b). This is due to the fact that this glass showed its robustness to the irradiation (Jiang, et al., 2023). In addition, the coarse edges of this fragment became smooth.

The spectrum shown in Fig. 7 is a point EDX spectrum of the high-B glass. The significance of these spectra is that it is obvious that there was a substantial decrease in the amount of boron. Furthermore, the amount of sodium was decreased from about 9.74% before the irradiation to about 3.20% due to subsequent irradiation. This effect is believed to be due to alkali migration under irradiation (Sidorov, et al., 2021; Hofmann, et al., 2023). However, the alteration of O and Si is not significant. In addition, the gold (Au) peaks (signals) appeared in the EDX spectra are belonging to the gold grid used to hold the glass specimen for the TEM measurements.

A sample of the AL-Ca glass was also time-series investigated under the e-beam, as shown in Fig. 8. Significant shape transformations were observed. The 300 kV e-beam irradiation was enough to perform these changes and also influenced the carbon film as can be seen in the left side of Fig. 8d-f. It was observed that increasing the irradiation time resulted in smoothing the rough edges and surfaces of the glass fragment. In addition, the rounding of the glass fragment's corners was increased with increasing the irradiation time. For example, the lower right corner of the glass fragment has the data tabulated in Table II below.

A thick B-free glass particle of about 500 nm in size has been explored under the influence of the irradiation, as seen in Fig. 9 using a time-series technique to track the changes that occurred with increasing the irradiation time. Obviously, from  $t = 0$  min (Fig. 9a) to  $t = 6$  min irradiation (Fig. 9g), substantial morphology transformations occurred due to the large amount of energy delivered by the e-beam (300 keV). The glass fragment gradually changed its shape into almost a sphere shape and all rough edges and surfaces became smooth on increasing the irradiation time.

Another phenomenon that can be occurred as a result of electron beam irradiation and is believed to be associated with the morphology alteration is bubble formation (Weber, et al., 1997). Fig. 10 represents a B-free glass irradiated between  $t = 1$  min to  $t = 5$  min. The sample shown in Fig. 10a is clean with free of any bubbles. However, after the irradiation was initiated, the bubble started to form and the number of bubbles increased with increasing the irradiation time (For example Fig. 10b and Fig. 10c). In Fig. 10d, it seems that at 3 min irradiation, the bubbles were merged producing larger bubbles. This was continued by increasing the irradiation time in which at  $t = 5$  min, all bubbles were merged

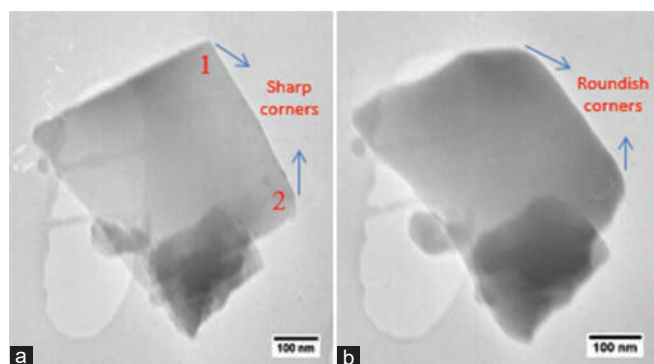


Fig. 3. A high-Si glass before (a) and after 5 min irradiation (b) using a transmission electron microscopy of type Philips 420 at 120 kV

TABLE II

THE AMOUNT OF ROUNDING OF A CORNER OF THE GLASS FRAGMENT

Irradiation time (min)	The amount of rounding (nm)
0	30
1	45
2	50
3	65
4	90
5	110

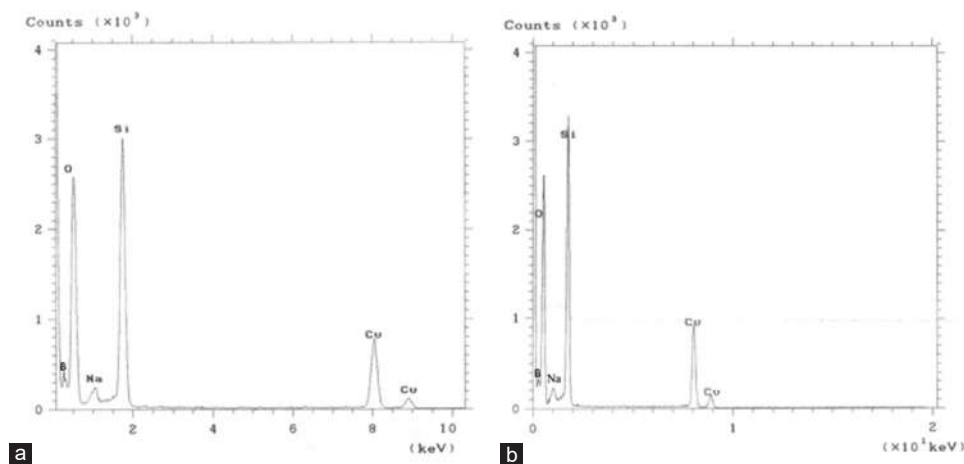


Fig. 4. Energy dispersive x-ray spectroscopy spectra of the high-Si glass before (a) and after irradiation (b).

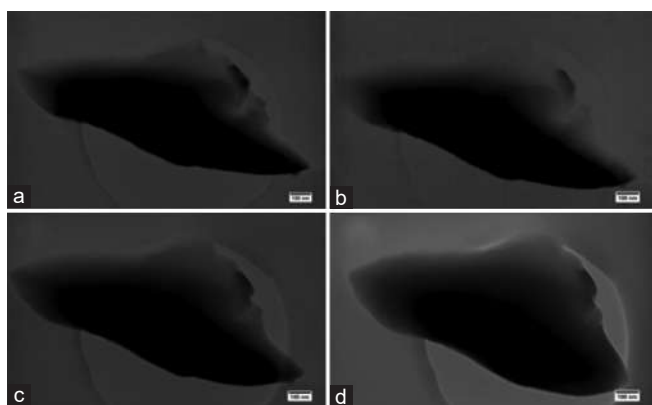


Fig. 5. A time-series irradiation of the B-free glass at (a) no irradiation, (b) 1 min, (c) 2 min and (d) 5 min using a transmission electron microscopy of type Philips 420 at 120 kV.

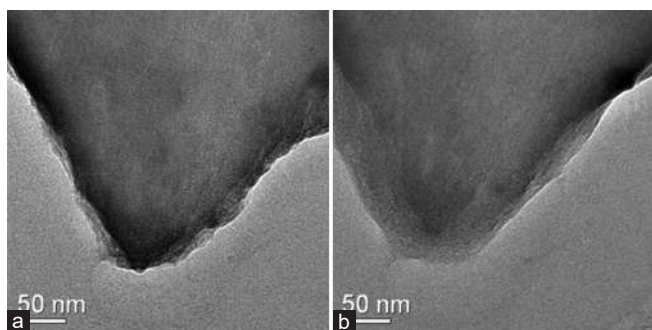


Fig. 6. A slight modification in a Si-free sample using transmission electron microscopy JEOL JEM 2010F at 200 kV. (a) before irradiation and (b) after 5 min irradiation.

and only a few were left. Moreover, the other effects of the irradiation that can be seen are rounding of the entire fragment and smoothing of the coarse surfaces. It seems that bubble formation is a secondary effect associated with the morphology alteration phenomenon. This is a beneficial to understand the mechanism of this phenomenon, as it is obviously very difficult to be produced by temperature, but rather the kinetic activation role in which the fast electrons play at a temperature well below the melting point (Ollier, et al., 2006; Leay and Harrison, 2019).

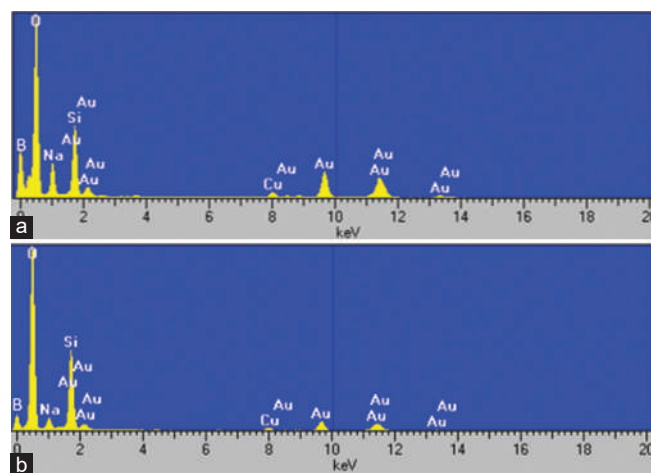


Fig. 7. The electron dispersive x-ray spectroscopy spectrum for the fragment of the high-B glass (a) without e-beam irradiation and (b) subsequent irradiation.

To confirm the robustness of a high-B glass, a fragment of this glass was inserted into the TEM of type JEOL JEM 3010 at 300 kV and irradiated for 1 and 2 min, respectively, as shown in Fig. 11. Before the irradiation, the fragment was of a rough edge as indicated by the red arrows in Fig. 11a. However, this rough edge has been smoothed and the roughness partially disappeared after 1 min of irradiation as indicated by the yellow arrows in Fig. 11b and continued to be smoothed at 2 min of irradiation, and now, there is no any trace of roughness and the entire edge became smooth, as shown in Fig. 11c. As a combined phenomenon of morphology alteration, a few bubbles were also formed as denoted by the green arrows in Fig. 11c.

This glass was also imaged using scanning electron microscopy (SEM) of type JEOL JEM 6400 combined with an EDX, as shown in Fig. 12.

### B. Fabrication of Nanostructures (Nanoring/Nanocrater) Using Electron Beam

It has been reported that an electron beam in TEM is a versatile tool to produce nanostructures including rings, crater,

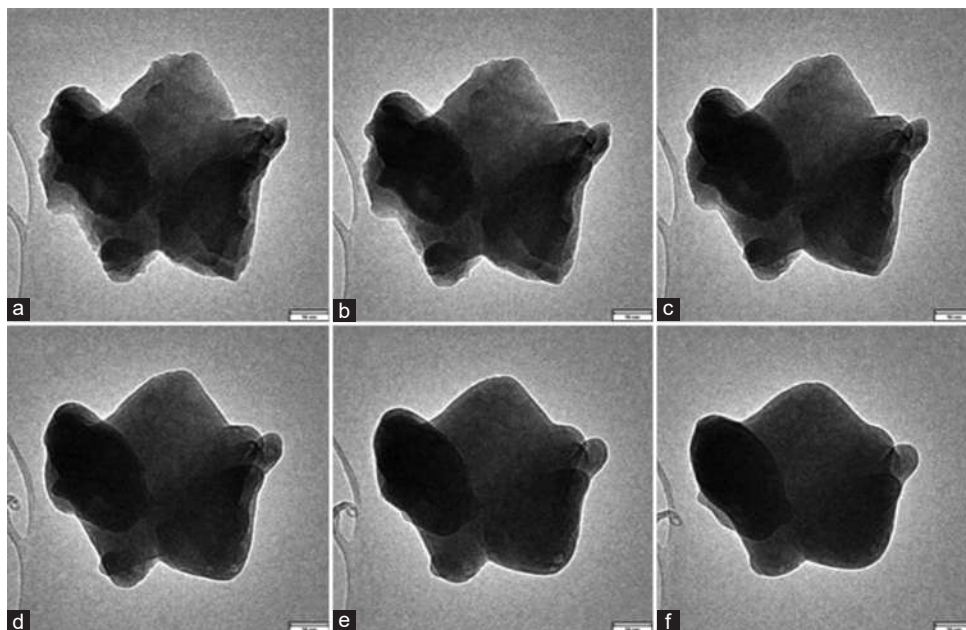


Fig. 8. A time-series irradiation of a fragment of the AL-Ca glass at (a) 0 min, (b) 1 min, (c) 2 min, (d) 3 min, (e) 4 min and (f) 5 min using a transmission electron microscopy of type JEOL JEM 3010 at 300 kV and showing significant shape alterations. The scale bar in all images is 90 nm.

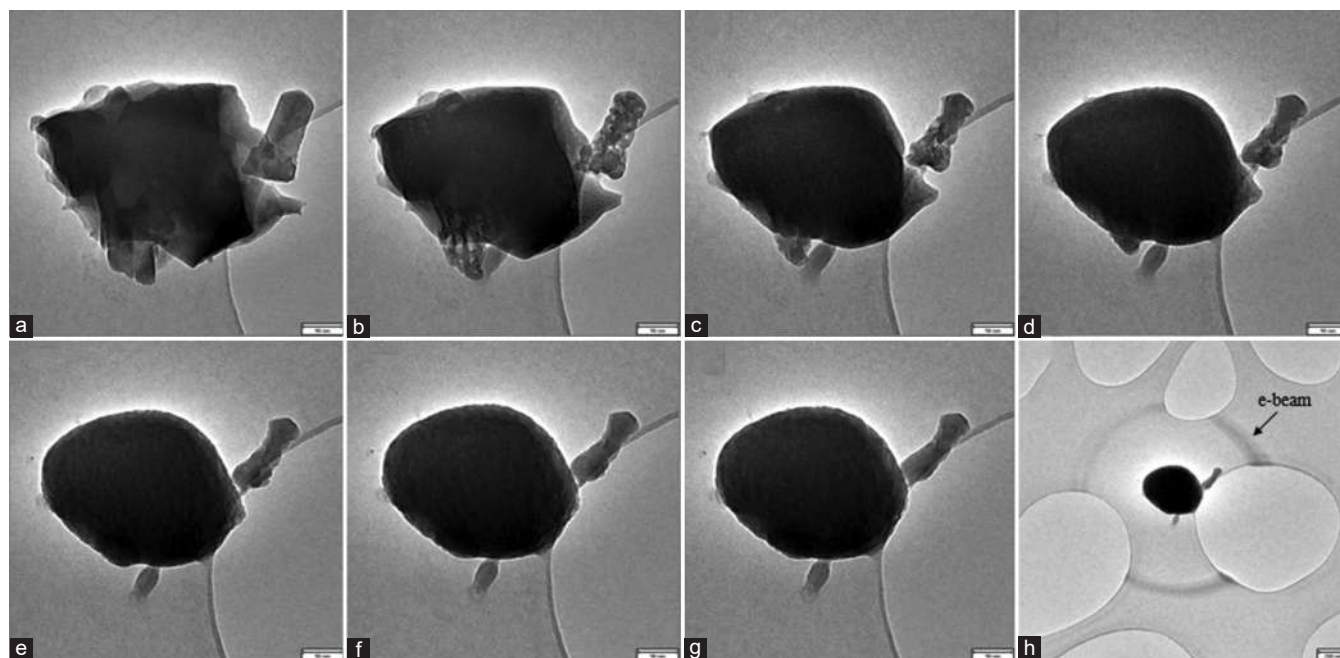


Fig. 9. A time-series irradiation of a fragment of the B-free glass at (a)  $t = 0$ -min, (b)  $t = 1$  min, (c)  $t = 2$  min, (d)  $t = 3$  min, (e)  $t = 4$  min, (f)  $t = 5$  min and (g)  $t = 6$  min irradiation using a transmission electron microscopy of type JEOL JEM 3010 at 300 kV. (h) is a higher magnification micrograph of (g) showing the diameter of the e-beam. The scale bar in (a-g) is 90 nm and in (h) is 200 nm.

and nanoparticles (Martinez, et al., 2016). An experiment has been performed to produce a hole (ring) in the glass using a TEM of type JEOL JEM 3010 at 300 kV, as shown in Fig. 13. Hole drilling through e-beam has been discussed as achieving very localized melting and ablation by evaporation even in metals on well-conductive support as a result of kinetic heat transport delays (Bysakh, et al., 2004). In Fig. 13a and b, a hole of a diameter of about 100 nm in the high-B glass and a hole of a diameter of about 100 nm in the high-Si glass have been successfully fabricated, respectively. Usually, holes

and rings are considered to be 2D structures in which their thickness is much smaller than their diameter (Jiang, et al., 2003). Moreover, rings fabrication in glasses by electron irradiation was believed to be due to the ionization and migration process. Our difficulties in the process of producing a hole in the glass is that live observation for tracking such a process from the beginning to the end is somewhat impossible due to the extremely high e-beam intensity when focusing on a spot and a 300 kV electron beam is enough to give an extremely high intensity. Therefore, the e-beam will

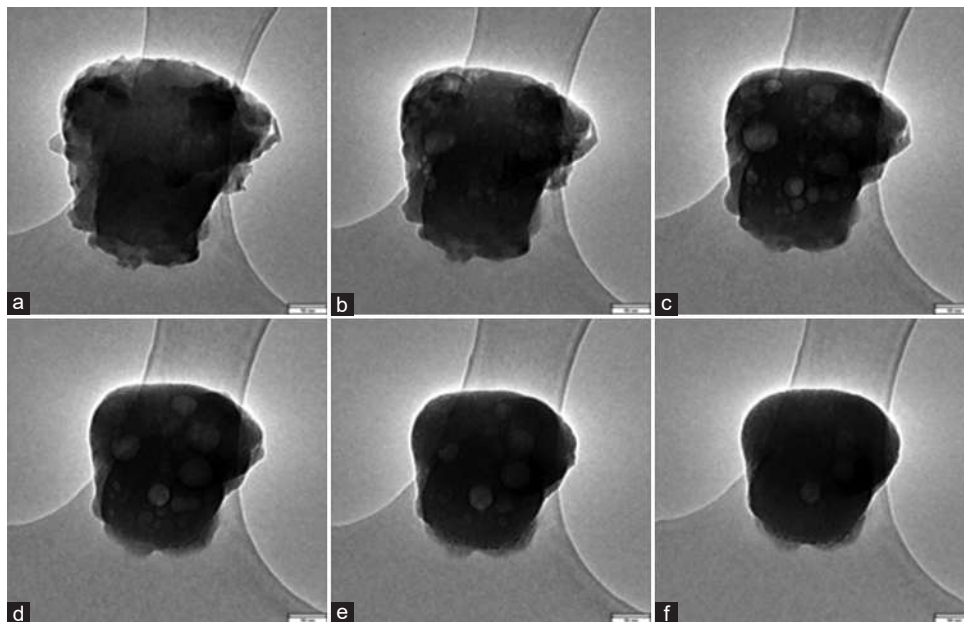


Fig. 10. A boron-free glass (a) at  $t = 0$  min and (b-f) at  $t = 1$  to  $t = 5$  min irradiation using a transmission electron microscopy of type JEOL JEM 3010 at 300 kV. The scale bar in all images is 90 nm.

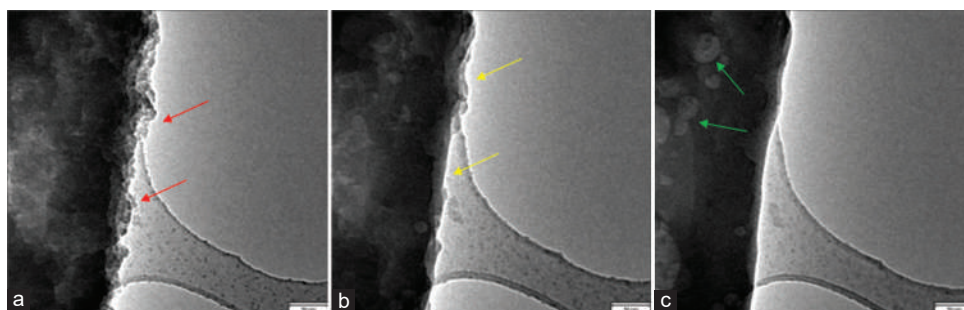


Fig. 11. A high-B glass (a) at  $t = 0$  min, (b) at  $t = 1$  and (c) at  $t = 2$  min irradiation using a transmission electron microscopy of type JEOL JEM 3010 at 300 kV. The scale bar in all images is 90 nm. The red and yellow arrows represent the roughness versus the smoothness of the fragment edge at  $t = 0$  min and  $t = 1$  min, respectively. The green arrows represent the bubbles formed as a result of e-beam irradiation.

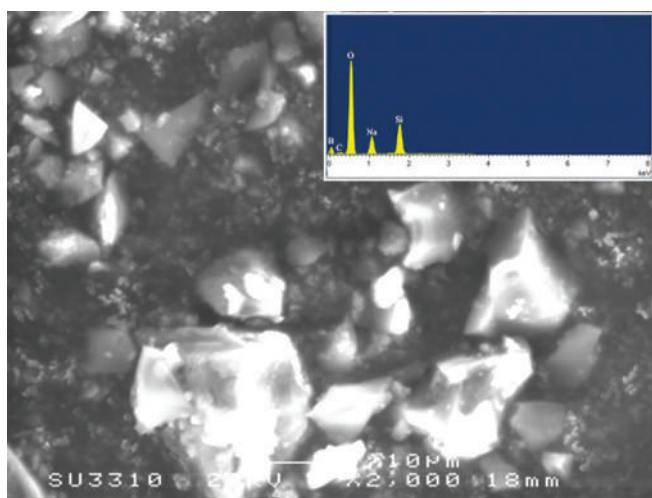


Fig. 12. A secondary electron image of a high-B glass using SEM of type JEOL JEM 6400. The inset is the EDX spectrum of the fragment.

be focused to fabricate the hole, and then, the e-beam will be spread to photograph the hole. The process in Fig. 13c is somewhat different and can be named a crater formation rather

than a hole (ring) formation. This is due to the fact that in the crater formation, many tiny spherical-shaped nanoparticles of the size of about 15 nm were formed inside and around the electron beam (the yellow square shape in Fig. 13c), which are believed to be one of the loaded elements in this glass (alkali-mixed), that is, cerium, chromium, or zirconium. It has been demonstrated that the electron beam irradiation increased the atom diffusion by several orders of magnitude compared to that in thermal treatment. The fabrication of nanoparticles occurs at both distinctly lower temperature and significantly higher rates of the irradiation. This explains that the electron beam irradiation can result in a fast grain growth of the primary nucleated nanoparticles leading to bigger smallest-sized particles (Ahn et al., 2015). Furthermore, A possible explanation for crater fabrication by the electron beam is the alkali migration (Gedeon, et al., 1999), as the two alkalis contained in this glass are Na and Li and they are both positive ions; hence, they migrate away from the negativity charged electron beam. It is believed that a highly focused electron beam (the intensity of about 180 pA/cm<sup>2</sup>) dominantly contributes to the sputtering effect (such as in Fig. 13a and

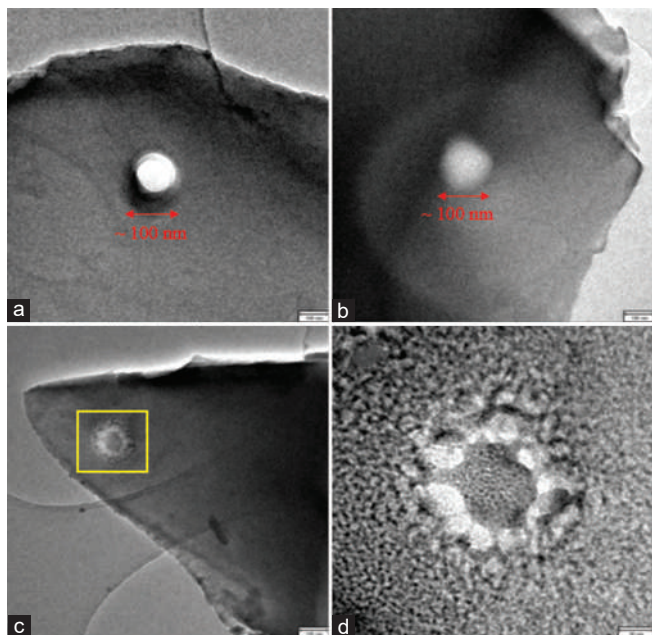


Fig. 13. The effect of a fully focused electron beam on (a) high-B glass, (b) high-Si glass, (c) alkali-mixed glass using a transmission electron microscopy of type JEOL JEM 3010 at 300 kV. (d) is a magnified micrograph of the irradiated area in (c) (the yellow square shape). The scale bar in (a-c) is 100 nm and in (d) is 30 nm.

b), while a slightly spread e-beam (the intensity of about 130 pA/cm<sup>2</sup>) mostly contributes to the diffusion of the atoms forming nanoparticles (such as in Fig. 13c and d).

In general, the speed of shape changes including rounding of the sharp corners and smoothening and flattening of the rough edges and surfaces is faster in TEM of type JEOL JEM 3010 at 300 kV and in TEM of type JEOL JEM 2010F at 200 kV than in TEM of type Philips 420 at 120 kV. This is true because the higher voltage TEM has the higher energy, and hence, the alteration that occurred in the irradiated glass will be faster. Usually, the phenomenon of shape transformation was believed to be due to the reduction of the surface energy anisotropy as the temperature is raised, that is, either the thermal or the electronic temperature. Through the *in situ* observations, the speed of glass rounding and flattening was faster in the high-Si glass and slower in the high-B glass. This is due to the relationship between this effect and the melting temperature ( $T_m$ ) and the glass transition temperature ( $T_g$ ) of those glasses and some other amorphous materials (Rao, et al., 2021; Mohammad, et al., 2016). Therefore, it can be supposed that the high-B glass is a robust glass under the influence of the electron beam. It has been reported that the migration of Na<sup>+</sup> increases with reducing the percentage of B<sub>2</sub>O<sub>3</sub> (We, et al., 2011). This is applicable to what has been found in this research, as the morphology alteration of glass were substantial in the high-Si glass, while these alterations were slight in the high-B glass due to the strongly bonded of Na and B in the glass network. It has also been proposed that the greatest significant technique for the movement of the glass material due to the radiation was the formation of point defects (Mayr, et al., 2003). Usually, glasses are sensitive to irradiation because

they are not in the thermodynamic minimum and hence the glass under irradiation can be readily altered (Gedeon, et al., 2007). Nanoring and crater formation, on the other hand, show the capability of electron beam in tailoring the glass material, especially in the fabrication of these structures. The fabrication of nanorings and nano-crater in glasses by the electron beam is believed to be a result of ionization and field-induced migration (Furuya, 2008). In addition, a changeable local structure in the medium range is existing in the amorphous materials and this permits fabricating rings with desired properties (Jiang, et al., 2003).

#### IV. CONCLUSION

The influence of high-energy radiation in different glasses has been investigated using three different types of TEMs. It has been concluded that irradiation through the electron beam has a considerable impact on the glasses. In this research, morphology alterations of the glasses were observed through the phenomenon of rounding the sharp corners and smoothening the rough edges and surfaces of the glass sample. It was also concluded that the radius of curvature (the amount of glass corner's rounding) increased when the irradiation time increased. Bubble formation, on the other hand, was observed as a combined effect with e-beam-induced morphology alteration, which was believed to be oxygen, and no materials loss was observed due to the irradiation. Moreover, nanoring and nanocrater fabrication in the glasses were successfully performed.

#### V. ACKNOWLEDGMENT

The author thanks and acknowledges Koya University, Faculty of Science and Health, Department of Physics for enabling this work as well as Dr. Guenter Moebus and Dr. Guang Yang for their help.

#### REFERENCES

- Abo Hussein, E.M., 2023. The impact of electron beam irradiation on some novel borate glasses doped V<sub>2</sub>O<sub>5</sub>; Optical, physical and spectral investigation. *Inorganic Chemistry Communications*, 147, pp.110232.
- Ahn, J.H., Eom, J.Y., Kim, J.H., Kim, H.W., Lee, B.C., and Kim, S.S., 2015. Synthesis of TiO<sub>2</sub> nanoparticles induced by electron beam irradiation and their electrochemical performance as anode materials for Li-ion batteries. *Journal of Electrochemical Science and Technology*, 6(3), pp.75-80.
- Ajayan, P.M., and Ijima, S., 1992. Electron irradiation-induced dynamical fluctuations in amorphous structures. *Journal of Non-Crystalline Solids*, 150, pp.423-428.
- Ajayan, P.M., and Marks, L.D., 1989. Experimental evidence for quasi melting in small particles. *Physical Review Letters*, 63(3), pp.279-282.
- Bruns, S., Minnert, C., Petho, L., Michler, J., and Durst, K., 2023. Room temperature viscous flow of amorphous silica induced by electron beam irradiation. *Advanced Science*, 10, pp.2205237.
- Butler, E.P., 1979. *In situ* experiments in the transmission electron microscope. *Reports on Progress in Physics*, 42, pp.834-889.
- Bysakh, S., Shimojo, M., Mitsuishi, K., and Furuya, K., 2004. Mechanisms of nano-hole drilling dye to nano-probe intense electron beam irradiation on a

- stainless steel. *Journal of Vacuum Science and Technology B*, 22(6), pp.2620-2627.
- Chen, L.T., Ren, X.T., Mao, Y.N., Mao, J.J., Zhang, X.Y., Wang, T.T., Sun, M.L., Wang, T.S., Smedskjaer, M.M., and Peng, H.B., 2021. Radiation effects on structure and mechanical properties of borosilicate glasses. *Journal of Nuclear Materials*, 552, pp.153025.
- Chen, X.Y., Zhang, S.G., Xia, M.X., and Li, J.G., 2015. Phase separation and crystallization induced by electron irradiation in nanoscale Fe<sub>36.5</sub>Mn<sub>11</sub>Cr<sub>8.5</sub>Ni<sub>3</sub>Si<sub>10</sub>C<sub>10</sub> metallic glass. *Acta Metallurgica Sinica*, 28, pp.1332-1335.
- Dapor, M., 2013. *Electron-beam Interactions with Solids*. Vol. 186. Springer, Berlin, Heidelberg, pp.1-110.
- DeNatale, J.F., Howitt, D.G., and Arnold, G.W., 1986. Radiation damage in Silicate glass. *Radiation Effects*, 98, pp.63-70.
- Duan, B.H., Chen, L., Lv, P., Du, X., Zhang, L.M., and Wang, T.S., 2018. *In situ* TEM study on electron irradiation effect in SiO<sub>2</sub>-Na<sub>2</sub>O-B<sub>2</sub>O<sub>3</sub> glasses. *International Journal of Applied Glass Science*, 10(2), pp.220-227.
- Egerton, R.F., Li, P., and Malac, M., 2004. Radiation damage in the TEM and SEM. *Micron*, 35, pp.399-409.
- Ehrt, D., and Vogel, W., 1992. Radiation effects in glasses. *Nuclear Instruments and Methods in Physics Research Section B: Beam Interactions with Materials and Atoms*, 65, pp.1-8.
- Furuya, K., 2008. Nanofabrication by advanced electron microscopy using intense and focused beam. *Science and Technology of Advanced Materials*, 9, pp.014110.
- Gedeon, O., Jurek, K., and Drbohlav, I., 2007. Changes in surface morphology of silicate glass induced by fast electron irradiation. *Journal of Non-Crystalline Solids*, 353, pp.1946-1950.
- Gedeon, O., Jurek, K., and Hulinsky, V., 1999. Fast migration of alkali ions in glass irradiated by electrons. *Journal of Non-Crystalline Solids*, 246, pp.1-8.
- Guigo, N., and Sbirrazzuoli, N., 2018. Thermal analysis of biobased polymers and composites. In: *Handbook of Thermal Analysis and Calorimetry*. Vol. 6. Elsevier, Netherlands, pp.399-429.
- Hobbs, L.W., 1987. Electron-beam sensitivity in inorganic specimens. *Ultramicroscopy*, 23, pp.339-344.
- Hofmann, M., Weigel, C., Strehle, S., and Holz, M., 2023. *A Paradigm Change: Focused Electron Beam Nanostructuring of Glass*. Research Square, North Carolina.
- Jbara, O., Cazaux, J., and Trebbia, P., 1995. Sodium diffusion in glasses during electron irradiation. *Journal of Applied Physics*, 78, pp.868-875.
- Jencic, I., Bench, M.W., Robertson, I.M., and Kirk, M.A., 1995. Electron-beam-induced crystallization of isolated amorphous regions in Si, Ge, GaP, and GaAs. *Journal of Applied Physics*, 78(2), pp.974-982.
- Jiang, N., Hembree, G.G., Spence, J.C.H., Qiu, J., Garcia de Abajo, F.J., and Silcox, J., 2003. Nanoring formation by direct-write inorganic electron-beam lithography. *Applied Physics Letters*, 83(3), pp.551-553.
- Jiang, N., Qiu, J., and Silcox, J., 2004. Effects of high-energy electron irradiation on heavy-metal fluoride glass. *Journal of Applied Physics*, 96(11), pp.6230-6233.
- Jiang, N., Qiu, J., and Spence, J.C.H., 2005. Precipitation of Ge nanoparticles from GeO<sub>2</sub> glasses in transmission electron microscope. *Applied Physics Letter*, 86, pp.143112-142113.
- Jiang, N., Qiu, J., Ellison, A., and Silcox, J., 2003. Fundamentals of high-energy electron-irradiation-induced modifications of silicate glasses. *Physical Review B*, 68(6), pp.064207.
- Jiang, Y.Z., Zhang, J.D., Wang, Z.J., Sun, Z., Deng, W.M., Zhao, Y.J., Lv, P., Zhang, L.M., Wang, T.S., and Chen, L., 2023. Composition dependence of element depth profiles in electron irradiated borosilicate glasses. *Journal of Non-Crystalline Solids*, 600, pp.121995.
- Klimenkov, M., Matz, W., Nepjiko, S.A., and Lehmann, M., 2001. Crystallization of Ge nanoclusters in SiO<sub>2</sub> caused by electron irradiation in TEM. *Nuclear Instruments and Methods in Physics Research B*, 179, pp.209-214.
- Leay, L., and Harrison, M.T., 2019. Bubble formation in nuclear glasses: A review. *Journal of Materials Research*, 34, pp.905-920.
- Li, S., Zhong, J., Cui, Z., Zhang, Q., Sun, M., and Wang, Y., 2019. Electron beam-induced morphology transformations of Fe<sub>2</sub>TiO<sub>3</sub> nanoparticles. *Journal of Materials Chemistry C*, 7, pp.13829-13838.
- Liu, M., Xu, L., and Lin, X., 1994. Heating effect of electron beam bombardment. *The Journal of Scanning Microscopies*, 16(1), pp.1-5.
- Liu, Z.Q., Hashimoto, H., Song, M., Mitsuishi, K., and Furuya, K., 2004. Phase transformation from Fe<sub>4</sub>N to Fe<sub>3</sub>O<sub>4</sub> due to electron irradiation in the transmission electron microscope. *Acta Materialia*, 52, pp.1669-1674.
- Mackovic, M., Niekiel, F., Wondraczek, L., and Spiecker, 2014. Direct observation of electron-beam-induced densification and hardening of silica nanoballs by *in situ* transmission electron microscopy and finite element method simulations. *Acta Materialia*, 79, pp.363-373.
- Marks, L.D., Ajayan, P.M., and Dundurs, J., 1986. Quasi-melting of small particles. *Ultramicroscopy*, 20, pp.77-82.
- Martinez, I.G.G., Bachmatiuk, A., Bezugly, V., Kunstmann, J., Gemming, T., Liu, Z., Guniberti, G., and Rummeli, M.H., 2016. Electron-beam induced synthesis of nanostructures: A review. *Nanoscale*, 8, pp.11340-11362.
- Mauro, J.C., Ellison, A.J., and Pye, L.D., 2013. Glass: The nanotechnology connection. *International Journal of Applied Glass Science*, 4(2), pp.64-75.
- Mayr, S.G., Ashkenazy, Y., Albe, K., and Averback, R.S., 2003. Mechanisms of radiation-induced viscous flow: Role of point defects. *Physical Review Letters*, 90, pp.055505.
- Mohammad, A., Al-Ahmari, A.M., AlFaify, A., and Mohammed, M.K., 2016. Effect of melt parameters on density and surface roughness in electron beam melting of gamma titanium aluminide alloy. *Rapid Prototyping Journal*, 23(3), pp.474-485.
- Musterman, E.J., Dierolf, V., and Jain, H., 2022. Electron beam heating as a tool for fabricating lattice engineered crystals in glass. *Optical Materials Express*, 12(8), pp.3248-3261.
- Ollier, N., Rizza, G., Boizot, B., and Petite, G., 2006. Effects of temperature and flux on oxygen bubble formation in Li borosilicate glass under electron beam irradiation. *Journal of Applied Physics*, 99, pp.073511.
- Qiu, J., Shirai, M., Nakaya, T., Si, J., Jiang, X., Zhu, C., and Hirao, K., 2002. Space-selective precipitation of metal nanoparticles inside glasses. *Applied Physics Letters*, 81(16), pp.3040-3042.
- Rao, N.R., Rao, T.V., Rao, B.S., and Shanmukhi, P.S.V., 2021. Electron beam irradiation modification on chemical, thermal and crystalline properties of poly (L-lactic acid). *Indian Journal of Pure and Applied Physics*, 59, pp.715-722.
- Rauf, I.A., 2008. Direct observation of the birth of a nanocrystalline nucleus in an amorphous matrix. *Applied Physics Letters*, 93, pp.143101-143103.
- Shelby, J.E., 1980. Effect of radiation on the physical properties of borosilicate glasses. *Journal of Applied Physics*, 51, pp.2561-2565.
- Shelby, J.E., 2005. *Introduction to Glass Science and Technology*. 2<sup>nd</sup> ed. New York State College of Ceramics at Alfred University School of Engineering, Alfred, NY, USA.
- Shen, Y., Zhao, X., Gong, R., Ngo, E., Maurice, J.L., Cabarrocas, P.R., and Chen, W., 2022. Influence of the electron beam and the choice of heating membrane on the evolution of Si nanowires' morphology in *in situ* TEM. *Materials*, 15, pp.5244.
- Sidorov, A.I., Kirpichenko, D.A., Yurina, U.V., and Podsvirov, O.A., 2021. Structural changes in silica glass under the action of electron beam irradiation: The effect of irradiation dose. *Glass Physics and Chemistry*, 47(2), pp.118-125.
- Sigle, W., 2005. Analytical transmission electron microscopy. *Annual Review of Materials Research*, 35, pp.239-314.

- Singh, S.P., and Karmakar, B., 2011. *In situ* electron beam irradiated rapid growth of bismuth nanoparticles in bismuth-based glass dielectrics at room temperature. *Journal of Nanoparticle Research*, 13, pp.3599-3606.
- Skuja, L., Hirano, M., Hosono, H., and Kajihara, K., 2005. Defects in oxide glasses. *Physica Status Solidi*, 2(1), pp.15-24.
- Sun, K., Wang, L.M., Ewing, R.C., and Weber, W.J., 2004. Electron irradiation induced phase separation in a sodium borosilicate glass. *Nuclear Instruments and Methods in Physics Research B*, 218, pp.368-374.
- Ugurlu, O., Haus, J., Gunawan, A.A., Thomas, M.G., Maheshwari, S., Tsapatsis, M., and Mkhoyan, K.A., 2011. Radiolysis to Knock-on damage transition in zeolites under electron beam irradiation. *Physical Review B*, 83, pp.113408.
- We, X., Varshneya, A.K., and Dieckmann, R., 2011. Sodium tracer diffusion in glasses of the type  $(\text{Na}_2\text{O})_{0.2}(\text{B}_2\text{O}_3)_y(\text{SiO}_2)_{0.8-y}$ . *Journal of Non-Crystalline Solids*, 357, pp.3661-3669.
- Weber, W.J., Ewing, R.C., Angell, C.A., Arnold, G.W., Cormack, A.N., Delaye, J.M., Griscom, D.L., Hobbs, L.W., Navrotsky, A., Price, D.L., Stoneham, A.M., and Weinberg, M.C., 1997. Radiation effects in glasses used for immobilization of high-level waste and plutonium disposition. *Journal of Materials Research*, 12, pp.1946-1978.
- Yoshida, N., and Tanaka, K., 1997. Ag migration in Ag-As-S glasses induced by electron-beam irradiation. *Journal of Non-Crystalline Solids*, 210, pp.119-129.
- Zheng, K., Wang, C., Cheng, Y.Q., Yue, Y., Han, X., Zhang, Z., Shan, Z., Mao, S.X., Ye, M., Yin, Y., and Ma, E., 2010. Electron-beam-assisted superplastic shaping of nanoscale amorphous silica. *Nature Communications*, 1(24), pp.1-8.



# Evaluation of Radioactivity in Soil Sample from Al-Hadbaa Cement Plant in Nineveh Governorate, Iraq

Ali I. Yaseen and Laith A. Najam

Department of Physics, College of Science, University of Mosul,  
Mosul, Iraq

**Abstract** — The fundamental goal of this study is to measure the level of radioactivity in the soil of the area around Al-Hadbaa cement plant, also to evaluate the radiological hazard of radionuclide, gamma-spectroscopy with an HPGe detector with the crystal diameter of 70.6 mm and length of 70 mm has been used to estimate the specific activity of natural radionuclides  $^{226}\text{Ra}$ ,  $^{232}\text{Th}$ ,  $^{40}\text{K}$ , and artificial radionuclides  $^{137}\text{Cs}$  in the fifteen soil samples collected. The results show that the average concentration of specific activity of  $^{226}\text{Ra}$ ,  $^{232}\text{Th}$ ,  $^{40}\text{K}$ , and  $^{137}\text{Cs}$  was  $11.17 \pm 1.69$ ,  $13.38 \pm 0.72$ ,  $158.36 \pm 5.35$  Bq/kg, and  $1.52 \pm 0.19$  Bq/kg, respectively. The average specific activity of these radionuclides is discovered to be lower than the global average which is 33 Bq/kg for  $^{226}\text{Ra}$ , 30 Bq/kg for  $^{232}\text{Th}$ , and 400 Bq/kg for  $^{40}\text{K}$ . Radiological hazard indices are determined according to the activity concentration of the radionuclides in the area under study. The outcome of the radiological hazard index is within the globally recognized limit proposed by UNSCEAR which is  $1000 \mu\text{Sv/y}$  for annual effective dose and  $290 \times 10^{-6}$  for cancer risk, so it is possible to conclude that there are no radiological hazards as a result of radiation exposure to the workers working in the cement plant as well as the organisms living in the region.

**Index Terms** — Ambient dose, Al-Hadbaa cement plant,  $^{137}\text{Cs}$ , Gamma-ray spectroscopy, Nineveh Governorate, Radiological hazard, Soil samples.

## I. INTRODUCTION

The emission of radiation from the disintegration of an unstable nucleus by less elementary particles ( $\alpha$  or  $\beta$  particles) is known as radioactivity (Abdullah and Ahmed, 2012), or emission of electromagnetic waves ( $\gamma$  ray) (Wais and Najam, 2021).

Life on Earth has developed under constant exposure to radiation, in addition to ionizing radiation from natural sources; a multitude of exposure from artificial sources produced by mankind came into play in the 20<sup>th</sup> century (Grupe and Rodgers, 2016).

Dating back to the origin of the earth, there has been an abundance of natural radioactivity in the environment and

the earth's crust. It may be found in plants, rocks, soil, and water, and since that time, people have been exposed to both internal and external radiation (Marie and Najam, 2022; Kang et al., 2020).

The natural radioactivity in soil produced by the  $^{238}\text{U}$  and  $^{232}\text{Th}$  decay series, as well as  $^{40}\text{K}$  (Isel et al., 2023) and natural radioactivity largely dependent on geological and geographical features of the region (UNSCEAR, 2000). The determination of radionuclides in soil and sand provides a valuable insight into human exposure to background radiation and a potential impact of natural radioactivity on human health (Lee et al., 2023). It is known that a significant part of gamma radiations originates from the surface layer at a depth of 0–25 cm (Küçükönder et al., 2023).

Artificial radioactivity – such as  $^{137}\text{Cs}$  (long life 30.2 y) – can be found in the environment and is significant for assessing both internal and external exposure. It has been on increase lately as a result of human activities (Kang et al., 2020) (Taqi and Namq, 2022).

Medical radiation use, nuclear accidents – such as Chernobyl nuclear power plant – and nuclear weapon testing, all make up the majority of artificial radiation sources (Hafizoğlu, 2023).

Many studies were performed to assess the natural and artificial radioactivity in soil, Isel et al., (2023) assessed natural and artificial radioactive pollution in sediment and soil samples of Bosphorus, Istanbul.

Another research, made by EL-Taher et al., (2017) measured the effect of cement plant factory exhaust on radiological content of surrounding soil samples in Assuit province, Egypt. In North Iran, Shahroudi and Poukimani, (2023) studied the emission pattern of NORMS and  $^{137}\text{Cs}$  in the sediment of Gas River and the Gorgan Bay. Furthermore, Ali et al., (2014) assessed the natural radioactivity of marl as a raw material at Kufa cement quarry in Najaf governorate, Iraq. A researcher Hussein (2019) assessed the levels of natural radioactivity and radiation hazards of soils from Erbil governorate, Iraq Kurdistan. Moreover, the researchers Smail et al.,(2021) measured the natural radioactivity levels in the soil along the Little Zab River, Kurdistan Region in Iraq.

The aim of this study is to determine the specific activities of ( $^{226}\text{Ra}$ ,  $^{232}\text{Th}$ ,  $^{40}\text{K}$ ) and ( $^{137}\text{Cs}$ ) in soil samples from the environment of Al-Hadbaa cement plant in Hamam Al-Alil, a sub-district in Nineveh government.

ARO-The Scientific Journal of Koya University  
Vol. XI, No. 2 (2023), Article ID: ARO.11283. 6 pages  
Doi: 10.14500/aro.11283

Received: 21 July 2023; Accepted: 09 September 2023  
Regular research paper: Published: 25 September 2023

Corresponding author's e-mail: ali.idriss.yaseen.phy@gmail.com  
Copyright © 2023 Ali I. Yaseen and Laith A. Najam. This is an open access article distributed under the Creative Commons Attribution License.



II. MATERIALS AND METHODS

A. Study Area

Al-Hadbaa cement plant is in Hamam Al-Alil sub-district which is at a distance of 20 km to the south of the city of Mosul, Nineveh governorate, as shown in Fig. 1, at coordinates of 36°09'29" N and 43°15'34" E. This plant was established by FCB (French Company) in 1963 and it produces Portland cement.

B. Samples Collection

In this study, on October 6, 2022, 15 samples were taken using a shovel from the soil near the Al-Hadbaa cement plant. The samples were taken at a depth of 10–15 cm within an area of (1 m × 1 m) for each sample. Then, the sample has been divided into three sections, all mixed to prepare homogenized samples. These samples were placed inside polyethylene bags with a mass of 2 kg.

Table I and Fig. 2. show the coordinates of the location of each sample located using the global position system.

C. Samples Preparing

All samples were air-dried before being placed in an electric oven set at 100°C for 2 h to completely remove the moisture. To create homogeneous samples, the samples were then sieved through a mesh size of 2 mm. To achieve the radioactive equilibrium between radionuclides and their daughters, the sieved soil was placed in (1 kg) Marinelli beakers and totally sealed for at least 1 month (Isel et al., 2023), (Cherie and Deressu, 2023).

D.  $\gamma$ -Spectroscopy Analysis

$\gamma$ -spectroscopy with high purity Germanium detector (HPGe) and p-type vertical closed-end coaxial from PGT (Princeton Gamma Tec-PGT Company-USA) in Koya university's nuclear radioactivity laboratory has been used to measure the specific activity of radionuclide in soil samples. The crystal of the detector has a diameter of 70.6 mm and a length of 70 mm, as shown in Fig. 3.

The gamma-ray spectrometry system was calibrated for

energy using standard point gamma-ray sources such as <sup>60</sup>Co (peaks of 1173.2 and 1322.5 keV), <sup>137</sup>Cs (peak 661.7 keV), and <sup>226</sup>Ra (peaks of 186,351,609, 1120, 1764) keV. The efficiency calibration was measured using three standard point gamma-ray sources <sup>226</sup>Ra, <sup>60</sup>Co, and <sup>137</sup>Cs. These samples were left for at least 4 h (PGT Company, 2002).

The resolution (FWHM) at 122 keV for <sup>57</sup>Co is 1.1 keV, and 1332 keV for <sup>60</sup>Co is 1.97 keV, with an efficiency of 73.8%. The specific activity of (<sup>226</sup>Ra, <sup>232</sup>Th, and <sup>40</sup>K) and (<sup>137</sup>Cs) in soil samples was measured by (HPGe) detector. The spectrum was collected for (36,000 s) and the background has been measured by putting an empty beaker on the detector for the same period of time.

III. THEORETICAL EQUATIONS

A. Specific Activity

Using the equation below, the specific activity of (<sup>226</sup>Ra, <sup>232</sup>Th, and <sup>40</sup>K) and (<sup>137</sup>Cs) in soil samples is determined (Xinwei and Xiaolan, 2006).

$$A_s \text{ (Bq/kg)} = C_a / \epsilon P^* M_s \tag{1}$$

Where ( $A_s$ ) is the radio nucleus activity concentration of the sample, ( $C_a$ ) is the net count rate below the corresponding peak, ( $\epsilon$ ) is the efficiency of detecting at the specific  $\gamma$  ray energy, ( $P^*$ ) is the absolute transition probability of the specific  $\gamma$  ray, and ( $M_s$ ) is the mass of the sample in kg.

The activity concentration of <sup>226</sup>Ra has been measured as the average of the activity found using the gamma-ray line at 351.9 keV from <sup>214</sup>Pb and at 609.31 keV, 1120 keV, and 1764.5 keV from <sup>214</sup>Bi. The activity concentration of <sup>232</sup>Th has been measured as the average of the activity found in gamma-ray lines at 238.36 keV from <sup>212</sup>Pb decay, 583.19 keV, and 2614.5 keV from <sup>208</sup>Tl. The gamma-ray line at 1460.8 keV has been used to directly measure the activity level of <sup>40</sup>K, the gamma-ray line at 661.7 keV has been used to directly measure the activity level of <sup>137</sup>Cs.

B. Radiological Hazard Indices



Fig. 1. A map of Nineveh governorate showing Hamam Al-Alil sub-district.

TABLE I  
COORDINATES OF SAMPLES TAKEN FROM THE AREA NEAR AL-HADBAA CEMENT PLANT.

Sample no	Sample code	Longitude E	Latitude N
1	H1	43°21'22.74"	36°20'8.58"
2	H2	43°21'26.5"	36°20'19.13"
3	H3	43°21'28.87"	36°20'14.3"
4	H4	43°21'15.69"	36°20'21.43"
5	H5	43°21'19.09"	36°20'24.68"
6	H6	43°21'21.41"	36°20'32.204"
7	H7	43°21'27.37"	36°20'35.52"
8	H8	43°21'28.96"	36°20'38.46"
9	H9	43°21'31.15"	36°20'41.97"
10	H10	43°21'31.02"	36°20'44.67"
11	H11	43°21'30.82"	36°20'48.31"
12	H12	43°21'33.02"	36°20'48.57"
13	H13	43°21'33.46"	36°20'53.37"
14	H14	43°21'34.34"	36°20'55.69"
15	H15	43°21'31.61"	36°20'56.56"



Fig. 2. A map of Al – Hadbaa cement plant showing the locations of samples.

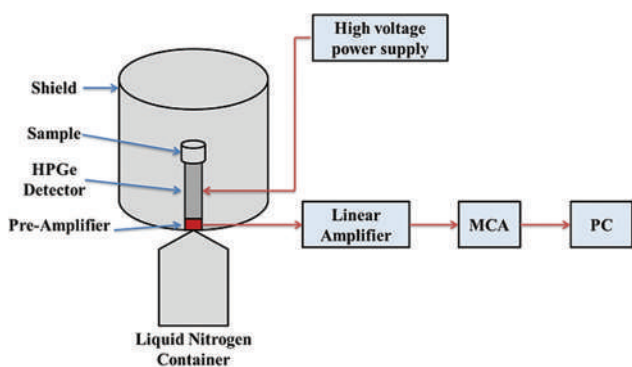


Fig. 3. Schematic layout of gamma-ray spectrometry system.

**Radium equivalent activity ( $Ra_{eq}$ )**

The presence of ( $^{226}\text{Ra}$ ,  $^{232}\text{Th}$ , and  $^{40}\text{K}$ ) in soil samples is typically used to estimate their normal radioactivity. Radium equivalent index is used to describe the total amount of radiation exposure from these radionuclides,  $Ra_{eq}$  measured in (Bq/kg), and the following equation is used to calculate it (Qureshi et al., 2014).

$$Ra_{eq} = A_{Ra} + 1.43A_{Th} + 0.077A_K \quad (2)$$

Where ( $A_{Ra}$ ,  $A_{Th}$ , and  $A_K$ ) are the specific activities of ( $^{226}\text{Ra}$ ,  $^{232}\text{Th}$ , and  $^{40}\text{K}$ ) in Bq/kg, respectively.

**Absorbed gamma dose rate ( $D'$ )**

The absorbed gamma dose rate in the air at (1 m) above the ground level can be calculated using the specific activity of natural radionuclide ( $^{226}\text{Ra}$ ,  $^{232}\text{Th}$ , and  $^{40}\text{K}$ ) (Örgün et al., 2007).

$$D_\gamma \text{ (nGy / h)} = 0.462A_{Ra} + 0.604A_{Th} + 0.0417A_K \quad (3)$$

Where  $D'$  is the absorbed dose rate in nGy/h.

**Annual effective dose equivalent (AEDE)**

The AEDE is calculated using the absorbed gamma dose rate which is measured in ( $\mu\text{Sv}/\text{y}$ ) to evaluate the level of health effects brought on by  $D'$ , the conversion factor (0.7 Sv/Gy) has been used to estimate the annual effective dose along with the indoor occupancy factor (0.8), and with the outdoor occupancy factor (0.2), the annual effective dose can be calculated by using the equations (Fisher et al, 1983, Kolo

et al, 2017).

$$AEDE_{indoor} (\mu\text{Sv} / \text{y}) = D(\text{nGy} / \text{h}) \times 0.7 \times 0.8 \times 8760 \times 10^{-3} \quad (4)$$

$$AEDE_{outdoor} (\mu\text{Sv} / \text{y}) = D(\text{nGy} / \text{h}) \times 0.7 \times 0.2 \times 8760 \times 10^{-3} \quad (5)$$

**Annual gonadal dose equivalent (AGDE)**

The most sensitive organs of human body to radiation exposure are the gonads. Their calculation is based on the specific activity of natural radionuclides in soil samples through the following equation (Kolo et al., 2017).

$$AGDE (\mu\text{Sv} / \text{y}) = 3.09A_{Ra} + 4.18A_{Th} + 0.314A_K \quad (6)$$

**Excess lifetime cancer risk (ELCR)**

ELCR can be used to determine the amount of extra cancer risk caused by exposure to ionizing radiation. ELCR measurement is based on AEDE by the equation (Taskin et al., 2009).

$$ELCR = (AEDE) \times D_L \times D_F \quad (7)$$

Where ( $D_L$ ) is the mean of human time of life (70 year), ( $D_F$ ) is the lethal risk factor per Sievert ( $0.05 \text{ Sv}^{-1}$ ).

**External and internal hazard indices**

The external hazard index ( $H_{ex}$ ) represents the exposure to natural radiation, while the internal hazard index ( $H_{in}$ ) represents the exposure to radon nuclide and its daughters. The ( $H_{ex}$ ) and the ( $H_{in}$ ) have been calculated by the equations (Najam et al., 2011, Mahur et al., 2008).

$$H_{ex} = \frac{A_{Ra}}{370} + \frac{A_{Th}}{259} + \frac{A_K}{4810} \leq 1 \quad (8)$$

$$H_{in} = \frac{A_{Ra}}{180} + \frac{A_{Th}}{259} + \frac{A_K}{4810} \leq 1 \quad (9)$$

**Gamma radiation level index ( $I_\gamma$ )**

The gamma radiation level index can be used to determine the extent of gamma radiation risk associated with the natural radionuclides in soil. ( $I_\gamma$ ) is calculated using the following equation (Kafala and Macmahon, 2007)

$$I_\gamma = \frac{A_{Ra}}{150} + \frac{A_{Th}}{100} + \frac{A_K}{1500} \leq 1 \quad (10)$$

The ambient dose equivalent rate  $H^*(10)$

It is a quantifiable quantity that offers a conservation estimation of the effective dose and evaluates the risk to human health caused by radiation exposure. The ambient dose equivalent rate of ( $^{226}\text{Ra}$ ,  $^{232}\text{Th}$ , and  $^{40}\text{K}$ ) and ( $^{137}\text{Cs}$ ) in the air at (1 m) above the ground was calculated as follows (Lee et al., 2023).

$$H^*(10) \text{ (nSv/h)} = 0.674 A_{\text{Ra}} + 0.749 A_{\text{Th}} + 0.0512 A_{\text{K}} + 0.192 A_{\text{Cs}} \quad (11)$$

#### IV. RESULTS AND DISCUSSION

##### A. Specific Activity

The results of the concentration of specific activity of ( $^{226}\text{Ra}$ ,  $^{232}\text{Th}$ , and  $^{40}\text{K}$ ) and ( $^{137}\text{Cs}$ ) radionuclides in soil samples from Al-Hadbaa cement plant are presented in Table II and Fig. 4 below. The specific activity of ( $^{226}\text{Ra}$ ) ranges from ( $7.861 \pm 0.948$  Bq/kg) for sample (H2) to ( $14.492 \pm 1.066$  Bq/kg) for sample (H4) with a mean value ( $11.172 \pm 1.085$  Bq/kg). The specific activity of ( $^{232}\text{Th}$ ) ranges from ( $7.687 \pm 0.434$  Bq/kg) for sample (H2) to ( $16.945 \pm 0.641$  Bq/kg) for sample (H13)

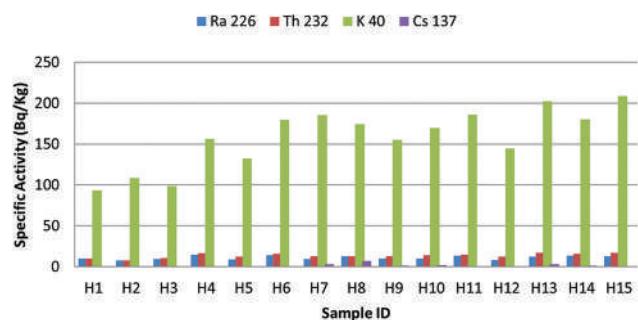


Fig. 4. Variations of specific activity of ( $^{226}\text{Ra}$ ,  $^{232}\text{Th}$ , and  $^{40}\text{K}$ ) and ( $^{137}\text{Cs}$ ) in the soil samples.

TABLE II  
SPECIFIC ACTIVITY OF ( $^{226}\text{Ra}$ ,  $^{232}\text{Th}$ , AND  $^{40}\text{K}$ ) AND ( $^{137}\text{Cs}$ ) IN THE SOIL SAMPLES COLLECTED FROM AL-HADBAA CEMENT PLANT

Sample ID	Specific Activity (Bq/kg)			
	$^{226}\text{Ra}$	$^{232}\text{Th}$	$^{40}\text{K}$	$^{137}\text{Cs}$
H1	10.179±0.9876	9.979±0.54	93.12±3.929	0.224±0.107
H2	7.861±0.948	7.687±0.434	108.7±4.018	0.433±0.102
H3	9.376±1.0666	10.424±0.65	98.7±3.966	ND
H4	14.492±1.0661	16.595±0.806	156.3±5.459	0.277±0.151
H5	9.053±1.0263	12.349±0.564	132.3±4.694	0.546±0.131
H6	13.978±1.1714	15.62±0.809	179.8±7.073	0.569±0.123
H7	9.619±1.0921	13.033±0.73	185.6±5.231	2.862±0.267
H8	12.619±1.0095	12.633±1.192	174.6±6.864	7.285±0.497
H9	9.968±0.9612	12.553±0.721	154.9±4.983	1.028±0.177
H10	9.922±1.0922	13.72±0.779	169.7±5.515	1.94±0.201
H11	13.563±1.0534	14.811±0.914	186.2±5.046	0.698±0.15
H12	8.454±1.0534	12.021±0.732	144.4±5.275	0.667±0.142
H13	12.181±1.6899	16.945±0.641	202.5±6.949	2.817±0.306
H14	13.524±0.9349	15.566±0.666	179.9±5.387	1.468±0.186
H15	12.799±1.132	16.82±0.728	208.8±5.945	0.604±0.148
Min	7.861±0.948	7.687±0.434	93.12±3.929	0.224±0.107
Max	14.492±1.0661	16.945±0.641	208.8±5.945	7.285±0.497
Ave.	11.172±1.085	13.383±0.727	158.368±5.356	1.529±0.192

with mean value ( $13.383 \pm 0.727$  Bq/kg). For ( $^{40}\text{K}$ ), the specific activity ranges from ( $93.12 \pm 3.929$  Bq/kg) for sample (H1) to ( $208.8 \pm 5.945$  Bq/kg) for sample (H15) with a mean value ( $158.368 \pm 5.356$  Bq/kg). The specific activity of ( $^{137}\text{Cs}$ ) ranges from ( $0.224 \pm 0.107$  Bq/kg) for sample (H1) to ( $7.285 \pm 0.497$  Bq/kg) for sample (H8) with a mean value ( $1.529 \pm 0.192$  Bq/kg).

The average specific activity values determined for the radionuclides ( $^{226}\text{Ra}$ ,  $^{232}\text{Th}$ , and  $^{40}\text{K}$ ) are below the global average recommended by the (UNSCEAR, 2000) which are: (33 Bq/kg) for  $^{226}\text{Ra}$ , (30 Bq/kg) for  $^{232}\text{Th}$ , and (400 Bq/kg) for  $^{40}\text{K}$ , as shown in Table III.

Table III shows a comparison of the average value of the specific activity level for radionuclides ( $^{226}\text{Ra}$ ,  $^{232}\text{Th}$ , and  $^{40}\text{K}$ ) and ( $^{137}\text{Cs}$ ) that results in this study with another local and global studies that are similar to this study, the result of the average specific activity of ( $^{226}\text{Ra}$ ) is comparable to the value of  $^{226}\text{Ra}$  in Turkey and Rabia region in Nineveh governorate, on the other side, the average value of ( $^{232}\text{Th}$ ) is comparable to the value in Egypt and South Korea, and the value of specific activity of ( $^{40}\text{K}$ ) is comparable to the value in Egypt. Finally, the average of specific activity for ( $^{137}\text{Cs}$ ) is comparable to the average in South Korea and Duhok governorate.

##### B. Radiological Hazard Indices

Radiological hazard indices have been determined according to the activity concentration of the radionuclides in the area under study. Table IV shows the radiological hazard indices of the soil samples collected from Al-hadbaa cement plant.

The values of radium equivalent  $\text{Ra}_{\text{eq}}$  range from ( $27.223$  Bq/kg) to ( $52.929$  Bq/kg), with a mean value of ( $42.506$  Bq/kg), all values of  $\text{Ra}_{\text{eq}}$  are below the allowed limit ( $370$  Bq/kg) suggested by (UNSCEAR, 2000).

While the values of absorbed dose ( $D^y$ ) range between ( $12.808$  nGy/h) and ( $24.779$  nGy/h) with a mean value

TABLE III  
A COMPARISON OF THE AVERAGE SPECIFIC ACTIVITY IN UNITE (BQ/KQ) OF ( $^{226}\text{Ra}$ ,  $^{232}\text{Th}$ , AND  $^{40}\text{K}$ ) AND ( $^{137}\text{Cs}$ ) IN THIS STUDY WITH SIMILAR STUDY IN ANOTHER LOCAL AND GLOBAL REGION

Country	Specific activity (Bq/kg)				References
	$^{226}\text{Ra}$	$^{232}\text{Th}$	$^{40}\text{K}$	$^{137}\text{Cs}$	
South Korea	21.9	11.1	661	0.9	Lee et al., 2023
Turkey	60.2	50.1	631	5.5	Turhan, 2023
Turkey	11.65	9.55	369.43	4.57	Isel et al., 2023
Bangladesh	27	64	762	-	Dina et al., 2022
Iran	17.61	35.91	398.65	4.01	Shahroudi and Pouriman, 2023
Egypt	20.35	10.52	158.16	0.13	Mansour et al., 2022
Saudi Arabia	21.16	18.80	202.15	0.16	Mansour et al., 2022
Iraq, Kirkuk	57.8	25.4	479.9	4.2	Taqi and Nomp, 2022
Iraq, Duhok	21.6	35.4	438	1.0	Abdullah and Ahmed, 2012
Iraq, Kurdistan	14.1	6.8	281	7.1	Smail et al., 2021
Iraq, Rabia	12.85	19.66	214.52	-	Wais et al., 2023
Iraq, Hamam	11.17	13.38	158.36	1.52	Present study
AL-Alil					
Worldwide Ave.	33	30	400	-	UNSCEAR, 2000

TABLE IV

The Radiological Hazard Indices of soil sample in this study	Ra <sub>eq</sub> (Bq/kg)	D <sub>r</sub> (nGy/h)	AEDE (μSv/y)		ELCRout×10 <sup>-6</sup>	Hazard indices		I <sub>r</sub>	AGDE (μSv/y)	H*(10) nSv/h
			AEDE <sub>in</sub>	AEDE <sub>out</sub>		H <sub>ex</sub>	H <sub>in</sub>			
H1	31.619	14.613	71.686	17.922	62.725	0.085	0.114	0.230	102.405	19.145
H2	27.223	12.808	62.829	15.707	54.975	0.074	0.096	0.202	90.554	16.704
H3	31.882	14.744	72.326	18.082	63.285	0.086	0.113	0.233	103.536	19.180
H4	50.258	23.236	113.988	28.497	99.740	0.136	0.177	0.367	163.226	30.253
H5	36.899	17.158	84.171	21.043	73.650	0.100	0.125	0.272	121.135	22.229
H6	50.159	23.390	114.742	28.685	100.399	0.135	0.175	0.369	164.941	30.435
H7	42.547	20.055	98.384	24.596	86.086	0.115	0.142	0.318	142.479	26.297
H8	44.128	20.741	101.748	25.437	89.029	0.119	0.155	0.327	146.623	28.305
H9	39.846	18.647	91.473	22.868	80.038	0.108	0.136	0.295	131.911	24.248
H10	42.609	19.947	97.854	24.463	85.622	0.115	0.143	0.316	141.294	26.024
H11	49.080	22.976	112.713	28.178	98.624	0.133	0.171	0.363	162.286	29.902
H12	36.763	17.188	84.317	21.079	73.777	0.099	0.123	0.273	121.712	22.223
H13	52.005	24.307	119.239	29.810	104.334	0.140	0.175	0.386	172.054	31.810
H14	49.636	23.152	113.573	28.393	99.377	0.134	0.173	0.366	163.344	30.266
H15	52.929	24.779	121.558	30.389	106.363	0.143	0.179	0.393	175.420	32.031
Min	27.223	12.808	62.829	15.707	54.975	0.074	0.096	0.202	90.554	16.704
Max	52.929	24.779	121.558	30.389	106.363	0.143	0.179	0.393	175.420	32.031
Ave.	42.506	19.849	97.373	24.343	85.202	0.115	0.147	0.314	140.195	25.937

AGDE: Annual gonadal dose equivalent

(19.849 nGy/h), it could be noted that all values of D<sub>r</sub> were below the world average value (55 nGy/h) (UNSCEAR, 2000).

The indoor equivalent annual effective dose (AEDE<sub>in</sub>) and outdoor equivalent annual effective dose (AEDE<sub>out</sub>) were calculated. The value of (AEDE<sub>in</sub>) ranges between (62.829 – 121.558) μSv/y with a mean value (97.373 μSv/y). The value of (AEDE<sub>out</sub>) ranges between (15.707 – 30.389) μSv/y with a mean value (24.343 μSv/y). The values of (AEDE<sub>in</sub>) and (AEDE<sub>out</sub>) are within the world average which is equal to (1 mSv/y) (UNSCEAR, 2000).

The value of the ELCR ranged between (54.707 × 10<sup>-6</sup>– 106.363 × 10<sup>-6</sup>) with a mean value of (85.202 × 10<sup>-6</sup>). The average value is less than the world average value (290 × 10<sup>-6</sup>) (UNSCEAR, 2000).

For the values of external (H<sub>ex</sub>) and internal (H<sub>in</sub>) radiological indices, they range between (0.074–0.143) a mean value of (0.115) for (H<sub>ex</sub>), and between (0.096 – 0.179) with a mean of (0.147) for (H<sub>in</sub>).

The resulting values of the gamma radiation level index (I<sub>r</sub>) for all soil samples range between (0.202) and (0.393), with an average value of (0.314). All the obtained values of (H<sub>in</sub>), (H<sub>ex</sub>) and (I<sub>r</sub>) are below one (worldwide value), which is suggested by (UNSCEAR, 2000), and the values of these indices for all samples were with the safety standard values.

For the value of AGDE, it ranges between (90.554 and 175.420) μSv/y, with a mean value of (140.195 μSv/y). The values of (AGDE) are less than the global permissible value, which is less than (300 μSv/y) (UNSCEAR, 2000).

The values of the ambient dose equivalent rate H\*(10), it is ranging between (16.704 nSv/h) to (32.031 nSv/h) with a mean value of (25.937 nSv/h).

### V. CONCLUSION

In this study, a 15 soil samples near Al-Hadbaa cement plant have been collected to evaluate the natural and artificial

radioactivity. Gamma-ray spectrometry with (HPGe) detector has been used to determine the activity concentration level for radionuclides (<sup>226</sup>Ra, <sup>232</sup>Th, and <sup>40</sup>K) and (<sup>137</sup>Cs). The radiological hazard indices and the activity concentration of <sup>40</sup>K were the dominating natural radioactivity in soil, which confirmed the abundance of <sup>40</sup>K in the Earth's crust. The radioactivity level of <sup>137</sup>Cs is found to be insignificant. Some variations of the activity concentration measured in soil samples are observed because of the physical, chemical, and geological structure.

The values of the specific activity obtained in the study are lower than the worldwide average values, and <sup>40</sup>K is the main contribution of the radioactivity in this study. The result of all radiological hazard indices such as: Ra<sub>eq</sub>, D<sub>r</sub>, AEDE, ELCR, H<sub>ex</sub>, H<sub>in</sub>, AGDE, and H\*(10) is within the internationally accepted limits, thus it can be concluded that there are no radiological hazards due to the directed and continuous exposure of ionizing radiation from radionuclides to the working workers in this cement plant and organisms that live in this region. This study establishes a significant information base about the radioactivity in the studied region.

### VI. ACKNOWLEDGMENTS

The authors wish to express their gratitude to everyone who helped to complete this work.

### REFERENCES

Abdullah, K.M.S., and Ahmed, M.T., 2012. Environmental and radiological pollution in creek sediment and water from Duhok, Iraq. *The Nucleus A Quarterly Scientific Journal of Pakistan Atomic Energy Commission*, 49(1), pp.49-59.

Ali, K.K., Awadh, S.M., and Al-Auweidy, M.R., 2014. Assessment natural radioactivity of marl as raw material at Kufa Cement Quarry in Najaf Governorate. *Iraqi Journal of Science*, 55(2), pp.454-462.

Cherie, G.Z., and Deressu, T.T., 2023. Assessment of natural radioactivity levels in soil samples from Dejen district, Ethiopia. *Radiation Protection Dosimetry*,

p.ncad214. <https://doi.org/10.1093/rpd/ncad214>

Dina, N.T., Das, S.C., Kabir, M.Z., Rasul, M.G., Deeba, F., Rajib, M., Islam, M.S., Hayder, M. A., and Ali, M.I., 2022. Natural radioactivity and its radiological implications from soils and rocks in Jaintiapur area, North-east Bangladesh. *Journal of Radioanalytical and Nuclear Chemistry*, 331, pp.4457-4468.

El-Taher, A., Najam, L.A., Oraibi, A.H., and Isinkaye, M.O., 2017. Effect of cement factory exhaust on radiological contents of surrounding soil samples in Assuit Province, Egypt. *Journal of Physical Science*, 28, pp. 137-150.

Gruppen, C., and Rodgers, M., 2016. *Radioactivity and Radiation*. Springer International Publishing, Germany.

Hafizoğlu, N., 2023. Radioactivity transfer factors and distribution of the natural and anthropogenic radionuclides in tea, plant and soil samples from the Black Sea Region in Turkey. *The European Physical Journal Plus*, 138, p.353.

Hussein, Z.A., 2019. Assessment of natural radioactivity levels and radiation hazards of soils from Erbil Governorate, Iraq Kurdistan. *ARO-The Scientific Journal of Koya University*, 7(1), pp.34-39.

Isel, P., Sahin, L., Hafizoglu, E., and Mülayim, A., 2023. Natural and artificial radioactive pollution in sediment and soil samples of the bosporus, Istanbul, *Environmental Science and Pollution Research*, 30, pp.70937-70949.

Kafala, S.I., and MacMahon, T.D., 2007. Comparison of neutron activation analysis methods. *Journal of Radioanalytical and Nuclear Chemistry*, 271, pp. 507-516.

Kang, T.W., Park, W.P., Han, Y.V., Bong, K.M., and Kim, K., 2020. Natural and artificial radioactivity in volcanic ash Soil, of Jeju Island, republic of Korea, and assessment of The radiation hazards: Importance of soil properties. *Journal of Radioanalytical and Nuclear Chemistry*, 323, pp. 1113-1124.

Kolo, M.T., Amin, Y.M., Khandaker, M.U., and Abdullah, W.H.B., 2017. Radionuclide concentrations and excess lifetime cancer risk due to gamma radioactivity in tailing enriched soil around maiganga coal mine, Northeast Nigeria. *International Journal of Radiation Research*, 15(1), pp.71-80.

Küçükönder, E., Gümbür, S., Söğütö, Ö., and Doğru, M., 2023. Natural radioactivity in soil samples taken from kahramanmaraş provincial center. *Environmental Geochemistry and Health*, 45, pp.5245-5259.

Lee, J., Kim, H., Kye, Y.U., Lee, D.Y., Jo, W.S., Lee, C.G., Kim, J.K., Baek, J.H., and Kang, Y.R., 2023. Activity Concentrations and radiological hazard assessments of <sup>226</sup>Ra, <sup>232</sup>Th, <sup>40</sup>K, <sup>137</sup>Cs in soil sample obtained from dongham institute of radiological and medical science, Korea. *Nuclear Engineering and Technology*, 55(7), pp.2388-2394.

Mahur, A.K., Kumar, R. Sonkawade, R.G. Sengupta, D., and Prasad, R., 2008. Measurement of natural radioactivity and radon exhalation rate from rock samples of Jaduguda uranium mines and its radiological implications. *Nuclear Instruments and Methods in Physics Research, Section B: Beam Interactions with Materials and Atoms*, 266(8), pp.1591-1597.

Mansour, H., Najam, L.A., and Abd El-Azeem, S.A., 2022. Determination and distribution map for radionuclides in soil samples from different location by gamma spectrometry using software analysis. *Atom Indonesia*, 48(3), pp.179-184.

Marie, Z.M., and Najam, L.A., 2022. Evaluation of natural radioactivity and radiological hazard indicators in soil samples from the environment of Al-Kasik oil refinery in Nineveh Governorate, in Iraq. *Journal of Nuclear sciences and Arab Applications*. 55(4), pp. 57-66.

Najam, L.A., AL-Jomaily, F., and AL-Farha, E., 2011. Natural radioactivity levels of limestone rocks in Northern Iraq using gamma spectroscopy and nuclear track detector. *Journal of Radioanalytical and Nuclear Chemistry*, 289(3), pp.709-715.

Örgün, Y., Altinsoy, N., Şahin, S.Y., Güngör, Y., Gültekin, A.H., Karahan, G., and Karacik, Z., 2007. Natural and anthropogenic radionuclides in rocks and beach sands from Ezine region (Çanakkale), Western Anatolia, Turkey. *Applied Radiation and Isotopes*, 65(6), pp.739-747.

PGT Company., 2002. *Nuclear Products Catalog*. Princeton Gamma-Tech Company, United States, p.101. Available from: [www.Itech-instruments.com](http://www.Itech-instruments.com)

Qureshi, A.A., Jadoon, I.A., Wajid, A.A., Attique, A., Masood, A., Anees, M., Manzoor, S., Waheed, A., and Tubassam, A., 2014. Study of natural radioactivity in Mansehra Granite, Pakistan: Environmental concerns. *Radiation Protection Dosimetry*, 158(4), pp.466-478.

Shahroudi, S.M.M., and Poukimani, R., 2022. Emission pattern of NORMS and <sup>137</sup>Cs in the sediments of the Gaz River and the Gorgan Bay, North Iran. *Iranian Journal of Science*, 47, pp.589-599.

Smail, J.M., Ahmad, S.T., and Mansour, H.H., 2021. Estimation of the natural radioactivity levels in the soil along the little Zab river, Kurdistan Region in Iraq. *Journal of Radioanalytical and Nuclear Chemistry*, 331, pp.119-128.

Taqi, A.H., and Namq, B.F., 2022. Radioactivity distribution in soil samples of the Baba Gurgur dome of Kirkuk oil field in Iraq. *International Journal of Environmental Analytical Chemistry, Online*, pp.1-19.

Taskin, H., Karavus, M.G.L.D.A., Ay, P., Topuzoglu, A.H.M.E.I.T., Hidiroglu, S.E.Y.H.A.N., and Karahan, G., 2009. Radionuclide concentrations in soil and lifetime cancer risk due to gamma radioactivity in Kirklareli, Turkey. *Journal of Environmental Radioactivity*, 100(1), pp.49-53.

Turhan, S., 2022. Radiological assessment of urban Soil Samples in the residents of a central anatolion volcanic province, Turkey. *International Journal of Environmental Health Research*, 20, pp.1-14.

UNSCEAR., 2000. *Sources and Effects of Ionizing Radiation, United Nations Scientific Committee on the Effects of Atomic Radiation UNSCEAR 2000 Report to the General Assembly, with Scientific Annexes*. UNSCEAR, Austria.

Wais, T., and Najam, L., 2021. Radiological hazard assessment of radionuclides in sediment samples of Tigris river in Mosul city, Iraq. *Arab Journal of Nuclear Sciences and Applications*, 55(1), pp.45-52.

Wais, T.Y., Ali, F.N.M., Najam, L.A., Mansour, H., and Mostafa, M.Y.A., 2023. Assessment of natural radioactivity and radiological hazards of soil collected from Rabia town in Nineveh Governorate (North Iraq). *Physica Scripta*, 98(2023), p.65304.

Xinwei, L., and Xiaolan, Z., 2006. Measurement of natural radioactivity in sand samples collected from the Baoji weihe sands park, China. *Environmental Geology*, 50, pp.977-982.

# Manufacturing and Evaluating of Indirect Solar Dryers: A Case Study for the Kurdistan Region of Iraq

Dara K. Khidhir

Department of Manufacturing and Industrial Engineering, Faculty of Engineering, Koya University, Koya, KOY45, Kurdistan Region - F.R. Iraq

**Abstract**—Indirect solar drying uses solar radiation to heat air and dry agricultural products in harvest time to store them for a longer time and reduce waste. The dryer consists of a solar air heater collector, a drying chamber, and an air ventilation system. In this study, an indirect solar dryer system is constructed and ventilated with an electrical fan. Experiments are conducted on the system using eggplant as an agricultural sample on 2 consequent days (29<sup>th</sup> and 30<sup>th</sup> October 2022), to evaluate the system data recorded during the drying process in terms of the temperature for points in the system, solar radiation, and the sample mass. The temperature measurements are ambient, collector, and dried chamber outlet temperatures. The results show that the most effective time for solar drying is between 9:00 and 16:00, and the drying system air temperature is raised to about 40°C when solar radiation reached more than 600 W/m<sup>2</sup> in the noon time. The weighted mass is used to evaluate the drying process, and maximum drying rate and drying efficiency are obtained on the 1<sup>st</sup> day of the drying before noon time.

**Index Terms**—Drying efficiency, Eggplant, Experimentation, Indirect solar dryer, Solar energy.

## I. INTRODUCTION

Solar radiation in the form of solar thermal energy is a suitable energy source and can be used in many applications, drying is one of these applications, particularly for fruits, vegetables, and agricultural grains. Iraq is within areas with high solar radiation intensity and long daylight hours, which makes this approach more feasible (Mahmood and Al-hassany, 2014; Jassim and Hassan, 2018).

Drying is a technique employed to extract moisture from agricultural goods, extending their storage duration. The ancient method of sun drying outdoors has been utilized for preserving edibles and crops. Nevertheless, this approach presents several drawbacks, such as product spoilage caused by elements such as rain, wind, moisture, and dust. There is also the risk of losses from animals and birds, along

with the potential deterioration of harvested crops due to decomposition, insect infestations, fungi, and more. In addition, this process demands substantial manual labor, a significant time investment, and ample space for spreading out the items to facilitate drying (Khan, Kasi and Kasi, 2018; Hii, et al., 2012).

Indirect solar drying is one of the important preservation techniques for fruits and vegetables, to sustain the balance between population growth and food supply, food losses during harvesting and marketing should be minimized. The quality and quantity of agricultural produce suffer due to poor processing methods and a shortage of storage facilities. Many developing countries suffer considerable losses on the agricultural front. It is mentioned that post-harvesting loss of fruits and vegetables in developing countries is about 30–40% of total production (Lingayat, et al., 2020).

Indirect solar drying offers better control over drying and the product obtained is of better quality than sun drying, the foods to be dried are not exposed directly to solar radiation, so they are protected from the harmful effects of UV rays. Drying is carried out indirectly by convection between the heated air and the products to be dried (Krabch, et al., 2022).

Researchers in various geographical areas harnessed accessible solar power for dehydrating items and diverse culinary uses. Their efforts were primarily directed toward drying farm produce during the local harvest season, with some investigations also aimed at enhancing the efficiency of the employed technology.

One application of solar drying is to reduce the weight of waste; in a study, a solar dryer was investigated by Irene Montero, et al. to decrease by-products during olive oil production, and the drying process included olive pomace, olive mill wastewater, and sludge residue. The work aimed to reduce their high moisture content as drying constitutes the main stage for a possible bio-fuel conversion. The work dealt with the analysis of drying for the three main wastes from olive oil using a prototype dryer. Results showed the promising application of the dryer (Montero, et al., 2015).

Experimental research on the solar drying of Ataulfo mango was conducted in a region of Mexico, and the dried sample dried to 8% of its initial moisture in the ambient condition of an average temperature of 25°C and solar radiation 500 W/m<sup>2</sup> (Díaz, et al., 2017).



A Proposal system using solar thermal energy in Iran, as presented Zaredar et al. to dehumidify products in the agricultural and pharmaceutical industries. The researchers suggested that the electronic and control system is embedded in data creation and airflow when necessary. The solar dryer is a device that performs the drying of different products with the use of renewable energies, in other words, no need of supplying the system with electricity performs dehumidifying operations (Zaredar, Effatnejad, and Behnam, 2018).

Different shapes of absorber plates in the collector were investigated to dry maize for Baghdad weather by a mixed-mode forced convection solar dryer. The study was carried out using three solar collector models: a collector with a flat plate, a V-corrugated plate, and tubes. Moreover, the three models were compared with traditional open sun drying. The obtained result showed that the maximum thermal efficiency of the solar collector was 78.5% for 0.057 kg/s when the V-corrugated plate shape was used as the absorber. Furthermore, the moisture content is reduced from the initial moisture content to 13.2% wet basis after about 5 h of drying (Jassim and Hassan, 2018).

A study that includes a hybrid photovoltaic-thermal double-pass counter-flow system connected with the mixed-mode solar dryer system was studied by Jadallah, Alsaadi and Hussien, 2020. The verification of the effectiveness and robustness of the system was explored by drying 300 g of slices of banana. The moisture content dried from 78% to 28.12% after 8 h of the drying process and the obtained range of air temperature is from 43.2 to 60.2°C. It was noticed that the highest thermal efficiency was 52.98% at 1:00 PM when the mass flow rate was 0.031 kg/s (Jadallah, Alsaadi, and Hussien, 2020).

The suggestion of employing phase change material as a means of storing thermal energy was put forward within the thermal framework of an indirect solar dryer. This proposal aimed to extend operational hours through the night. The study delved into the effectiveness of three different models, and the findings indicated an enhancement in the duration of effective drying hours (Ramirez, Palacio, and Carmona, 2020).

Effect of constructed material for constructing experimental model investigated by Fernandes et al., two designs of indirect solar dryers using two different constructed materials (wood and styrofoam) for domestic application and the result showed the possibility of drying fruits and vegetables up to 10% of their initial weight at low cost (Fernandes, Fernandes, and Tavares, 2022).

Using energy and exergy thermodynamic analysis to study the effects of air-drying parameters of the rosemary drying process in a hybrid-solar dryer was performed by Karami, et al. The studied parameters were air temperature and air velocity for optimizing the system operation. The findings showed that the exergy loss rate was affected by temperature and air velocity because the overall heat transfer coefficient was different under these conditions (Fernandes, Fernandes, and Tavares, 2022).

A single dryer compartment indirect solar dryer with a south-oriented roof was used to dry pearl in the Faculty of

Sciences of Rabat city. Thermal performance and economic cost were investigated in the study, and the experimental results showed that the relative humidity inside the dryer can decrease by up to 10%, and the average temperature inside the dryer reached 50°C, allowing the pear to dry just after 24° h and it was concluded that solar dryer is less expensive than conventional two-compartment solar dryers (Krabch, et al., 2022).

A mathematical model based on the experimental model was derived to study design parameters in an indirect solar dryer in case of no load and full load operation capacity. It is concluded the drying efficiency of the solar dryer improved in the case of forced convection with the help of a fan (Kumar, et al., 2022)

This research investigates the potential for utilizing solar energy to achieve a sustainable food drying method. The aim is to address the issue of excessive wastage of agricultural produce, particularly fresh foods and fruits, during the harvest season in the Kurdistan Region of Iraq. The goal is also to extend the shelf life of these food items.

## II. MATERIALS AND METHODS

### A. Experimental Setup

An experimental greenhouse indirect forced convection solar dryer was designed and installed in location Koysinjq-Erbil-Kurdistan Region of Iraq (36.07, N, 44.65 E), Iraq. The solar collector of the dryer is 80 cm in width, 135 cm in length, and 5 cm in height, and the drying chamber dimensions are 50 cm in length, 80 cm in width, and 60 cm in height. The photograph of the dryer is shown in Fig. 1.

The structure of the dryer is made from steel and to minimize heat loss, the system is covered with an ALUCOBOND sandwich. Components and specifications of the solar dryer are shown in Table I.

The drying chamber had three food shelf trays with the dimension of 80 cm × 50 cm and there was 18 cm distance between each tray. The shelves were made from (12 mm × 12 mm) meshed stainless steel to avoid rusting. This meshed hole of the shelf helps pass hot air through the food to be dried. The system is ventilated with a 16 W fan with a volumetric flow rate of 90 m<sup>3</sup>/h.

Experiments to evaluate the drying performance of the indirect solar dryer prototypes were conducted under the Koysinjq local weather conditions. The experiments were conducted from 29<sup>th</sup> to October 30<sup>th</sup>, 2022.

The measured parameters in the experimental work were temperatures of many points in the system as well as solar heat flux and mass of the drying foods.

The measured temperature points include the outside ambient air temperature, collector outlet temperature (cabinet inlet), and air temperature outlet of the cabinet (chamber).

The temperature measuring points are recorded by the temperature data logger V2 and a DS18B20 digital temperature sensor (3 wire) with accuracy: ±0.5°C over a full -50–125°C temperature range, compatible with Arduino Bluetooth module HC05 at 5 min-intervals temperature data logging.



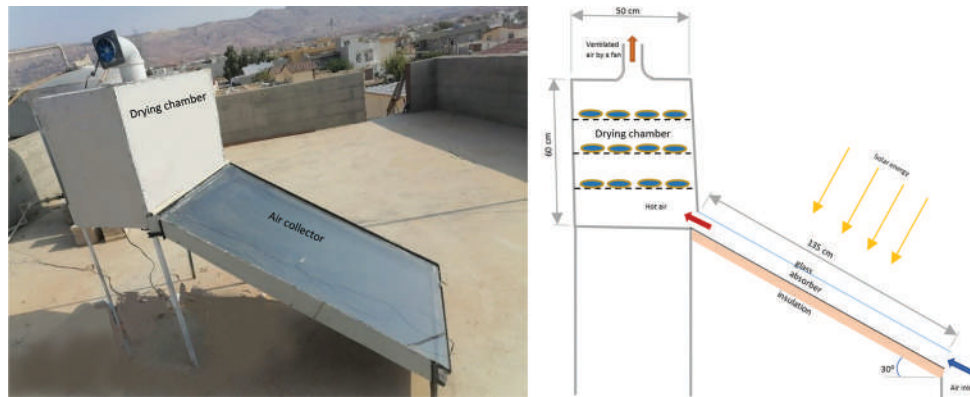


Fig. 1. Photograph and schematic diagram of the experimental model

TABLE I  
SPECIFICATIONS OF THE EXPERIMENTAL MODEL

Item	Description or dimensions
Location of the dryer	Koysenjaq-Erbil-Iraq (36.07, N, 44.65 E)
Standard time of the location	UTC +3
Drying food quantity	3 kg eggplants
Solar collector dimension	W=80 cm, L=135 cm, H=5 cm
Solar collector area	1 m <sup>2</sup>
Solar collector transparent glass thickness	4 mm
Collector's absorber plate material and thickness	Steel, 0.6 mm
Absorber plate painting color	Black
Fan volumetric flow rate	90 m <sup>3</sup> /h
Air exit cross-section diameter	10 cm
Drying chamber	W=80 cm, L=50 cm, H=60 cm
Number of shelf trays	3
Drying shelf trays dimensions	80 cm × 50 cm
Distance between trays	18 cm
Collector's tilt angle	30 due the South

Solar intensity is recorded every 5 min logging by precision; VOLT CRAFT DL-131 LUX Solar data logger instrument with a measuring range (0–2000 W/m<sup>2</sup>) with accuracy: ±10 W/m<sup>2</sup>.

The mass of dried food samples was measured 3 times every day during drying with an accurate electronic weighing scale with accuracy ±0.5 g ranging from 0 to 5000 g.

### B. Drying Performance of the System

To assess the system's effectiveness, eggplants were selected as a representative sample due to their capacity to absorb surplus production during the harvest season in the area, as well as their ability to extend shelf life and enhance the culinary experience.

An eggplant sample was washed with clean water after that slices were cut with a 12 mm thickness to be dried in the solar dryer. The samples were left to water to be dried before they were uniformly distributed between the chamber shelves, and the weight of the samples was scaled.

It is recommended that the drying process take place from 9:00 AM to 4:00 pm in short daytime, in that period solar thermal collector has maximum efficiency for drying grains (Khalil et al., 2012).

The essential measuring parameters taken in this study were ambient air temperature, collector outlet temperature, leaving the drying chamber air temperature, solar heat radiation, and weight of dried food. The measured parameters were used to evaluate the performance of the indirect solar drying system.

During the drying process, the moisture content in the food decreased and a percentage of wet moisture content can be estimated by the following equations (Ssemwanga, Makule, and Kayondo, 2020):

$$Mc = [(m_i - m_d) / m_i] * 100\% \quad (1)$$

Where:

$m_i$  is the mass of the sample before drying  
 $m_d$  is the mass of the sample after drying.

The evaporated water mass is determined by the following equation (Cherotich and Simate, 2016):

$$m_w = [m_i(m_i - m_F) / (100 - m_F)] * 100 \quad (2)$$

Where:

$M_i$  is the initial moisture content and  $M_F$  is the final moisture content.

The drying rate of the food was determined by the equation (Brenndorfer, et al., 1987):

$$m_{dr} = m_w / t_d \quad (3)$$

where  $t_d$  is the considerable drying time.

The drying system efficiency of a solar dryer is the ratio of the energy needed to evaporate moisture from the dried sample to the solar heat energy to the dryer and can be calculated by (Wankhade, Sapkal, and Sapka, 2014):

$$\eta_s = (m_w h_{fg}) / (I_s A_c t_d) \quad (4)$$

Where:

$I_s$  is solar insolation on the collector in W/m<sup>2</sup>.  
 $h_{fg}$  is the latent heat vaporization for water taken from steam tables = 2270 kJ/kg at a mean temperature  $[(T_{coll} + T_o) / 2]$  in J/kg, and  $T_{coll}$  and  $T_o$  are the collector and chamber outlet temperatures at °C (Chouicha, et al., 2013).

### III. RESULTS AND DISCUSSION

Solar radiation and ambient temperature are factors affecting the performance of the drying process. Fig. 2 shows the variation of solar intensity and temperature profiles of ambient, collector exit, and chamber outlet of the dryers with the time of the day during solar drying on October 29, 2022. The findings showed that with increasing solar radiation intensity, the collector and dry chamber temperature rises and the maximum temperature was recorded at noon time when the solar radiation reaches its peak. The maximum solar radiation intensity, collector temperature, and drying

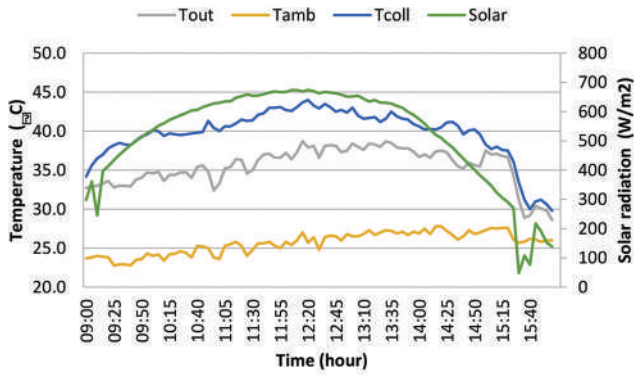


Fig. 2. Ambient, collector, dry chamber air leaving temperatures, and solar radiation on October 29<sup>th</sup>, 2022.

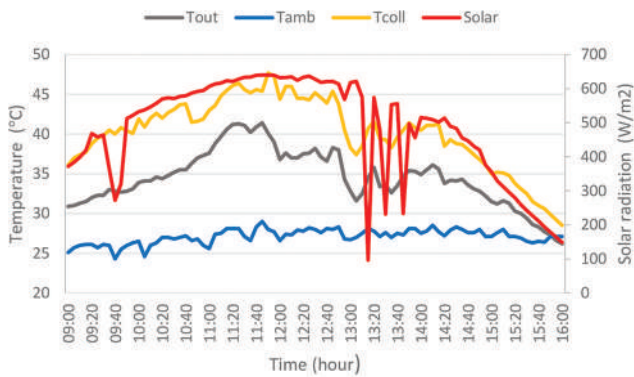


Fig. 3. Ambient, collector, dry chamber air leaving temperatures, and solar radiation on October 30<sup>th</sup>, 2022.

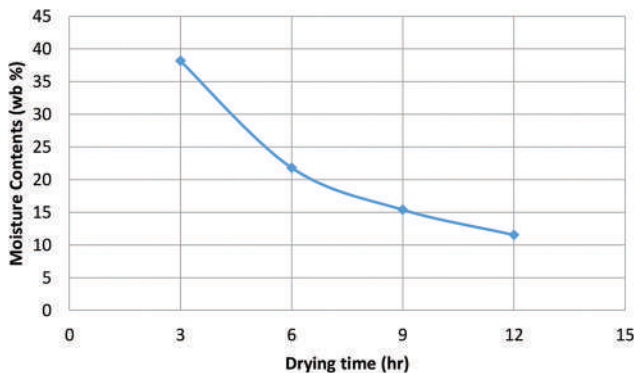


Fig. 4. Relation between the moisture content of the sample and drying time for the system.

chamber temperature were 663 W/m<sup>2</sup>, 43.3°C, and 38.1°C, respectively; on the other hand, the ambient temperature reaches its maximum value 1 h after noon time after that the temperature falls due to diminishing solar radiation.

Fig. 3 shows the variation of temperature profiles and solar insolation on October 30, 2022, it can be noticed that the trend of the curve is similar to the previous day but the collector temperature reached a higher value (more than 45°C), and ambient temperature was higher compared to the previous day (the recorded ambient temperatures were 27.8°C and 28.3°C for the consequent days, respectively).

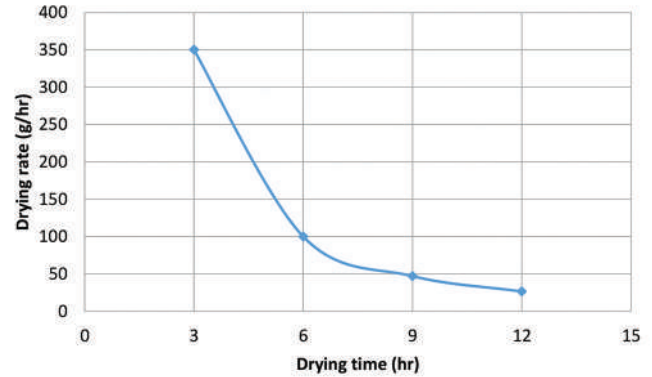


Fig. 5. The variation of drying rate with time for the two consequent drying days.

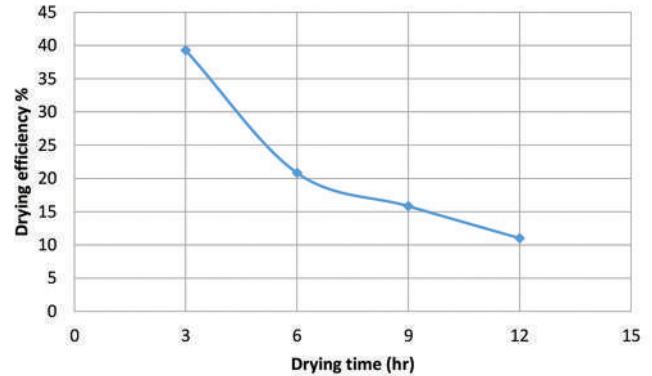


Fig. 6. Drying efficiency during active drying process time

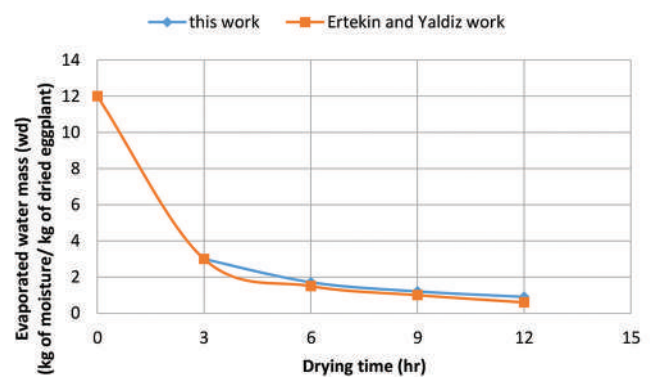


Fig. 7. Comparison between this work to other work at an average drying temperature of 40°C.



Fig. 8. Dried eggplant (a) fresh eggplant before drying (b) 1<sup>st</sup> day after drying (c) 2<sup>nd</sup> day after drying.

For both experimental days, it can be noticed that in the early morning daytime before 9:00 and in the late afternoon daytime after 15:00 h, the temperature difference between ambient and collector decreased resulting non-effecting period for solar drying in that season.

Fig. 4 shows the variation of moisture content with the time of active drying hour of 2 days (October 29<sup>th</sup>, 2022 and October 30<sup>th</sup>, 2022) by the indirect solar drying, the trend of the curve shows moisture content reduction with the time of drying, the most effective moisture reduction is observed in the early time of the drying process, during first 3 h of drying the eggplant lost 60% of its moisture based on wet analysis after 12 h of solar drying only about 10% of the moisture remains in the sample.

The drying duration is the main factor to take into account when assessing a solar dryer system. It is measured in terms of time such as hours or days from the moment the fresh product is placed into the dryer until it reaches the desired moisture level. Drying with higher drying temperatures speed up the drying process, but also it raises the risk of damaging the product in terms of loss of color, flavor, aroma, and vitamins (Leon, Kumar, and Bhattacharya, 2002).

The drying rate is an indication of how fast dehydration takes place in the dryer. Fig. 5 shows the change in the drying rate of the sample with time in the 2 days of drying, it is noticed that there is a sharp fall of the curve trend in early times of drying referring in significant evaporation process in the sample due to rise temperature and forced convection by ventilating the drying chamber with the fan. The rate of the drying process decreases with time, in the late time of drying, the rate tends approach to be constant.

The drying efficiency term is used to measure the overall effectiveness of a drying system, an average drying efficiency for every 3 h is illustrated in Fig. 6, the figure shows that maximum drying efficiency is obtained in the early times of drying, the 1<sup>st</sup> h of drying shows about 40% and decreased with time due to fall in the evaporation rate in the sample, the minimum value of efficiency is obtained in the last hour in the 2<sup>nd</sup> day of the solar drying to reach 11%.

The validation of the authenticity of this study is established through a comparison with prior research concerning the dehydration of eggplants. This current research is contrasted with the findings of (Ertekin and Yaldiz, 2004) and visually presented in Fig. 7. The drying patterns of eggplants, specifically the reduction of moisture content during the drying procedure, exhibit a parallel behavior between the

two datasets. However, a minor distinction between the two curves emerges at an average drying temperature of 40°C.

The utilization of the indirect solar dryer system resulted in achieving high-quality dried eggplants, as determined by their visual attributes, consistency, and fragrance. The images presented in Fig. 8 depict the eggplant samples before drying and after each day of the drying process, illustrating the consistent and desirable coloration observed in the dried samples.

#### IV. CONCLUSION

An indirect type forced convection solar dryer has been designed and fabricated for drying agriculture products; in this study, eggplant was selected to be dried, and the samples were dried for 2 days, it is concluded that:

- The system is suitable for drying foods in the region even in the late summer and fall seasons when the weather is dry and abundant solar radiation is available and it will have a good impact on the economy in the region
- The highest temperature rise in the system is obtained by the collector afternoon time
- During the period of early morning and late afternoon when the solar insolation diminishes, the drying effect of the difference between the collector and ambient temperatures is reduced, de-activate the drying effect in these periods.
- The highest evaporation rate and system efficiency are in the initial time of the drying process on the 1<sup>st</sup> day.

#### REFERENCES

- Brenndorfer, B., Kennedy, L., Bateman, C., Trim, D. S., Mrema, G. C., and Wereko-Brobby, C., 1987. *Solar Dryers-their Role in Post-harvest Processing*. 1st ed. Commonwealth Science Council, London.
- Cherotich, S., and Simate, I. N., 2016. Experimental investigation and mathematical modelling of a natural convection solar tunnel dryer. *International Journal of Scientific and Engineering Research*, 7(5), pp.597-603.
- Chouicha, S., Boubekri, A., Mennouche, D., and Berrbeuh, M. H., 2013. Solar drying of sliced potatoes. an experimental investigation. *Energy Procedia*, 36, pp.1276-1285.
- Díaz, R.I., Gómez, R.A.J., Danguillecourt, O.L., de Paz, P.L., Vázquez, N.F., and Duharte, G.R.I., 2017. Design, construction and evaluation of a solar dryer for Ataulfo mango. *Revista Mexicana de Ciencias Agrícolas*, 8, pp.1719-1732.
- Ertekin, C., and Yaldiz, O., 2004. Drying of eggplant and selection of a suitable thin layer drying model. *Journal of Food Engineering*, 63(3), pp.349-359.
- Fernandes, L., Fernandes, J.R., and Tavares, P.B., 2022. Design of a friendly solar food dryer for domestic over-production. *Solar*, 2(4), pp.495-508.

- Hii, C.L., Jangam, S.V., Ong, S.P., and Mujumdar, A.S., 2012. *Solar Drying: Fundamentals, Applications and Innovations*. TPR Group Publication, Singapore. Available from: <https://www.dergipark.gov.tr/sjmakeu> [Last accessed on 2022 Oct].
- Jadallah, A., Alsaadi, M., and Hussien, S., 2020. The hybrid (PVT) double-pass system with a mixed-mode solar dryer for drying banana. *Engineering and Technology Journal*, 38(8), pp.1214-1225.
- Jassim, N.A., and Hassan, S.S., 2018. *Thermal Performance Evaluation of Solar Air Dryer for Food Drying in Iraq*. Available from: <https://www.researchgate.net/publication/324991813> [Last accessed on 2022 Nov].
- Khan, Y., Kasi, J.K., and Kasi, A.K., 2018. Dehydration of vegetables by using indirect solar dryer. *Techno-Science Scientific Journal of Mehmet Akif Ersoy University*, 1(1), pp.22-28.
- Karami, H., Kaveh, M., Golpour, I., Khalife, E., Rusinek, R., Dobrzański, B. Jr., and Gancarz, M., 2021. Thermodynamic evaluation of the forced convective hybrid-solar dryer during drying process of rosemary (*Rosmarinus officinalis* L.) leaves. *Energies*, 14(18), p.5835.
- Khalil, M. H., Ramzan, M., Rahman, M. U., and Khan, M. A., 2012. Development and evaluation of a solar thermal collector designed for drying grain. *Iranica Journal of Energy and Environment*, 3(4), pp.380-384.
- Krabch, H., Tadili, R., Idrissi, A., and Bargach, M., 2022. Indirect solar dryer with a single compartment for food drying. Application to the drying of the pear. *Solar Energy*, 240, pp.131-139.
- Kumar, A., Singh, K. U., Singh, M. K., Kushwaha, A. K. S., and Kumar, A., 2022. Design and fabrication of solar dryer system for food preservation of vegetables or fruit. *Journal of Food Quality*, 2022, p.6564933.
- Leon, M.A., Kumar, S., and Bhattacharya, S.C., 2002. A comprehensive procedure for performance evaluation of solar food dryers. *Renewable and Sustainable Energy Reviews*, 6(4), pp.367-393.
- Lingayat, A.B., Chandramohan, V.P., Raju, V.R.K., and Meda, V., 2020. A review on indirect type solar dryers for agricultural crops-dryer setup, its performance, energy storage and important highlights. *Applied Energy*, 258, p.114005.
- Mahmood, F.H., and Al-Hassany, G.S., 2014. Study global solar radiation based on sunshine hours in Iraq. *Iraqi Journal of Science*, 55(4), pp.1663-1674.
- Montero, I., Miranda, M.T., Sepúlveda F.J., Arranz, J.I., Rojas, C.V., and Nogales, S., 2015. Solar dryer application for olive oil mill wastes. *Energies*, 8(12), pp.14049-14063.
- Ramirez, C., Palacio, M., and Carmona, M., 2020. Reduced model and comparative analysis of the thermal performance of indirect solar dryer with and without PCM. *Energies*, 13(20), p.5508.
- Ssemwanga, M., Makule, E., and Kayondo, S.I., 2020. Performance analysis of an improved solar dryer integrated with multiple metallic solar concentrators for drying fruits. *Solar Energy*, 204, pp.419-428.
- Wankhade, P. K., Sapkal, R. S., and Sapka, V. S., 2014. Design and performance evaluation of a solar dryer. *Journal of Mechanical and Civil Engineering*, 11, pp. 70-73.
- Zaredar, A., Effatnejad, R., and Behnam, B., 2018. Construction of an indirect solar dryer with a photovoltaic system and optimised speed control. *IET Renewable Power Generation*, 12(15), pp.1807-1812.

# Design and Study of a Nanocavity-based One-dimensional Photonic Crystal for Potential Applications in Refractive Index Sensing

Khalid N. Sediq, Fahmi F. Muhammad, Simko O. Ramadan, and Shalaw Z. Sedeeq

Department of Physics, Faculty of Science and Health, Koya University,  
Danielle Mitterrand Boulevard, Koya KOY45, Kurdistan Region – F.R. Iraq

**Abstract**—Refractive index (RI) can be used to identify a particular substance and determine its purity and concentration. The RI of glucose solution with various concentrations can be determined using a distributed Bragg reflective (DBR) device containing a nanocavity. The optical property of the reflection spectrum produced by DBR is sensitive to the variation of the refractive index. In this study, a DBR with a cavity width of 220 nm, located in the middle of the device, is designed and used to sense the variation in the refractive index of glucose at different concentrations. The proposed design showed a sharp dip pattern within the reflection spectrum. The wavelength of the absorption peak was found to be sensitive to trivial variations in the refractive index of glucose solution. Results showed that the variation in the refractive index of glucose within the order of  $\Delta n = 0.02$  has led to a noticeable shift in the absorption spectrum by  $\Delta \lambda = 2.6$  nm. Furthermore, the sensitivity of the proposed device was found to be 130 nm/RIU which is considered high compared with those reported in the literature. Hence, the proposed structure can be a promising optical device for chemical ultrasensing applications.

**Index Terms**—Distributed Bragg Reflectors, Photonic crystal, Nanocavity, Refractive index, Sensor.

## I. INTRODUCTION

The refractive index (RI) is one of the most important physical properties to determine the composition of solutions (Singh, et al., 2013). Accurate determination of any solution concentration by measuring the RI is usually used in medicine (Elblbesy, 2020), food technology (Harrill, 1994), pollution measurements (Shi, et al., 2014) as well as chemical and physical studies (Reis, et al., 2010). Various studies have demonstrated to measure the refractive index of glucose at different concentrations. Glucose, as an optically active substance, an interferometer measurement system was used

to provide a straightforward means of measuring the optical properties of chiral media (Lin and Su, 2003; Tan and Huang, 2015; Yeh, 2008). Furthermore, the minimum deviation of the prism technique was used to show the dependence RI of glucose solution on the variation of the source wavelength (Belay, 2018).

Distributed Bragg reflector (DBR) mirrors that consist of altered high and low refractive index stacked layers show a high reflectivity phenomenon (Leem and Yu, 2013). The optical property of DBR depends on the stacked layers' thickness and their refractive index. Studies showed that introducing a nanocavity inside the DBR structure produced a sharp dip peak (that is, absorption spectrum) within the reflection spectrum. The peak position is highly sensitive to the refractive index of the introduced cavity and thickness (Shanmugan, et al., 2004; Kumar and Das, 2018). Kumar et al. introduced a refractive index sensor based on the cavity mode formed inside a (200–900) nm thin cavity layer sandwiched between multilayers of  $\text{SiO}_2/\text{Ta}_2\text{O}_5$  and a 40 nm metal film. Their structure showed a relatively high sensitivity for different cavity thicknesses (Kumar and Das, 2018). However, their proposed structure is non-metal layer contained and consists of  $\text{Si}_3\text{N}_4/\text{SiO}_2$  multilayer with nanocavity prepared by plasma-enhanced chemical vapor deposition.

In this study, a DBR structure with nanocavity is used to observe the shift of the absorption spectrum with the variation of the RI of glucose solution. Glucose, known as blood sugar, is an important composition which considered fuel for energy production, especially for the brain, muscles, and several other body organs and tissues. Results showed that the DBR structure containing nanocavity can be used as an ultrasensitive optical device to determine any small variations in the refractive index of solutions.

## II. STRUCTURE DESIGN AND SIMULATION

The proposed nanocavity-based refractive index sensor is shown in Fig. 1a. The structure contains a 220 nm nanocavity sandwiched between the DBR layers which made up of  $\text{Si}_3\text{N}_4$  and  $\text{SiO}_2$ . This structure is also known as one-dimensional photonic crystal (1D PC). The cavity of the DBR structure



is located in the center as it forms the basis of the sensing mechanism. The refractive index of the medium in the cavity region dictates the absorption mode, and hence, any changes in the characteristics of the cavity region alter the absorption wavelength. The DBR is consisting of 14 bilayers of  $\text{Si}_3\text{N}_4/\text{SiO}_2$  having thicknesses of 78 nm and 109 nm, respectively. The thicknesses of the stack layer were chosen to be in the order of quarter wavelength for a band gap centered at  $\lambda_0 = 632.8$  nm based on the following relations:

$$t_H = \frac{\lambda_0}{4n_H} \quad (1)$$

$$t_L = \frac{\lambda_0}{4n_L} \quad (2)$$

Where:  $t_H$ ,  $t_L$ ,  $n_H$  and  $n_L$  are the thickness and refractive index (RI) of both the high  $\text{Si}_3\text{N}_4$  ( $n_H = 2.028$ ) and low  $\text{SiO}_2$  ( $n_L = 1.45$ ) refractive index material, respectively. The photonic band gap is in the visible region (566–718 nm) as shown in Fig. 1b.

However, the DBRs reflectivity calculation is based on the transfer matrix method. Formulation of the boundary conditions at the multilayers' interfaces was derived from both Fresnel and Maxwell's equations for the dielectric medium (Mohammed, 2019).

### III. RESULTS AND DISCUSSION

First of all, the optical resonance of 1D PC containing a noncavity was optimized by manipulating the cavity width and position. To study the effect of cavity position in the DBR structure for 0% glucose concentration solution with  $n = 1.3264$  and cavity width of 220 nm, the cavity position was changed from 10<sup>th</sup> to 20<sup>th</sup> single layer. Calculations indicated that the cavity at the middle of the DBR structure (14 bilayers) shows the highest dip in the reflection spectra (Fig. 2a) and the narrowest width (that is, full width at half maximum [FWHM]) as shown in Fig. 2b.

Second, the cavity thickness was varied from 210 to 240 nm with a step size of  $\pm 5$  nm, to observe the absorption wavelength spectrum for each cavity thickness, as shown in Fig. 3a. For the initial refractive index ( $n = 1.3264$ ), it was observed that the absorption wavelengths have undergone a red shift from 612 to 635 nm within the broad reflection band (Fig. 3b). The intensities of absorption wavelengths and their width were varied due to tuning of the resonance wavelength of the cavity modes with the variation in the cavity thickness. Calculations showed that the cavity of 220 nm supports the highest reflection dip spectrum and the narrowest spectrum width, as shown in Fig 3c.

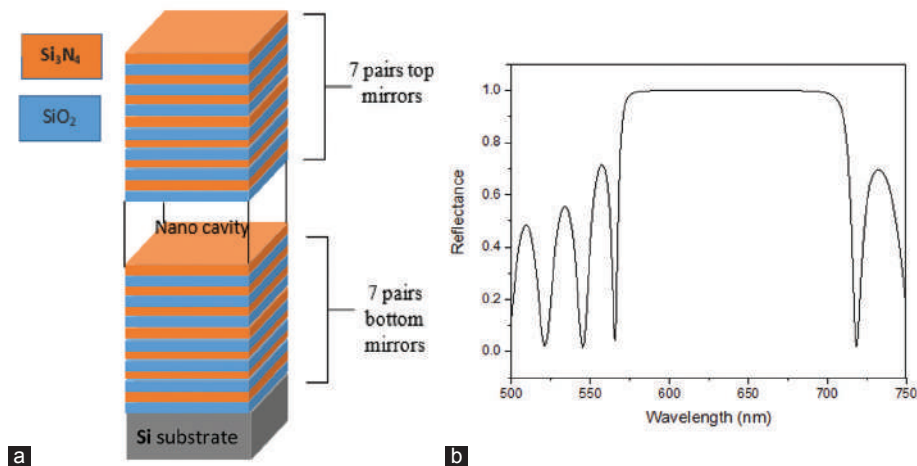


Fig. 1. (a) Fixed nanocavity distributed Bragg reflectors structure (1D PC) between 14 pairs of highly reflecting mirrors on a Si substrate and (b) reflectance spectrum of 14 pair of  $\text{Si}_3\text{N}_4/\text{SiO}_2$  layers.

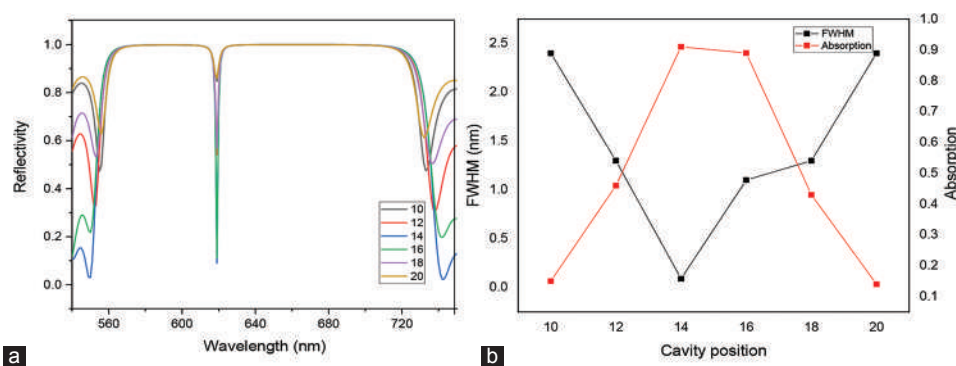


Fig. 2. (a) Absorption spectrum at different position of the nanocavity in the distributed Bragg reflector structure. (b) Absorption and full width at half maximum of produced spectrum versus cavity position.

However, it was found that increment in the solution concentration has led to increase in the refractive index (Tan and Huang, 2015). The DBR mirrors with nanocavity tested as a refractive index sensor device for various concentrations of aqueous glucose solutions in the range of 0–50 mg/mL. The achieved data are illustrated in Table I.

The variation of absorption mode in the reflection spectra as a function of different glucose refractive indices is shown in Fig. 4a. For all guided wavelengths, the absorption spectra were linearly red shifted with the increase in the refractive index, as can be seen in Fig. 4b. By applying a curve fitting technique, the linear correlation between the refractive index of glucose and absorption spectrum dip wavelength was found, which can be expressed as below:

$$\lambda = 130.08n + 445.59 \quad (3)$$

Where  $n$  is the glucose refractive index. Eq. (3) indicates that the average difference of refractive index ( $\Delta n = 0.02$ ) caused a  $\Delta \lambda = 2.6$  nm shift in the absorption peak spectrum. The absorption peak spectrum was found to be comparable to their average FWHM which was around 1.2 nm. Interestingly, the sensitivity for our device which is defined as  $S = \frac{\Delta \lambda}{\Delta n}$  (Shaban, et al., 2017; Zaky, et al., 2022) was found to be  $130 \frac{nm}{RIU}$ . This result showed a high sensitivity for the proposed structure in comparison with the previously reported ones  $20 \frac{nm}{RIU}$  (Yeh, 2008) and  $48 \frac{nm}{RIU}$  (Shaban, et al., 2017). The nm/RIU is typically refers to a change in the refractive index of the region probed by the resonant mode causing a corresponding wavelength shift of the optical resonance of the sensor (White and Fan, 2008).

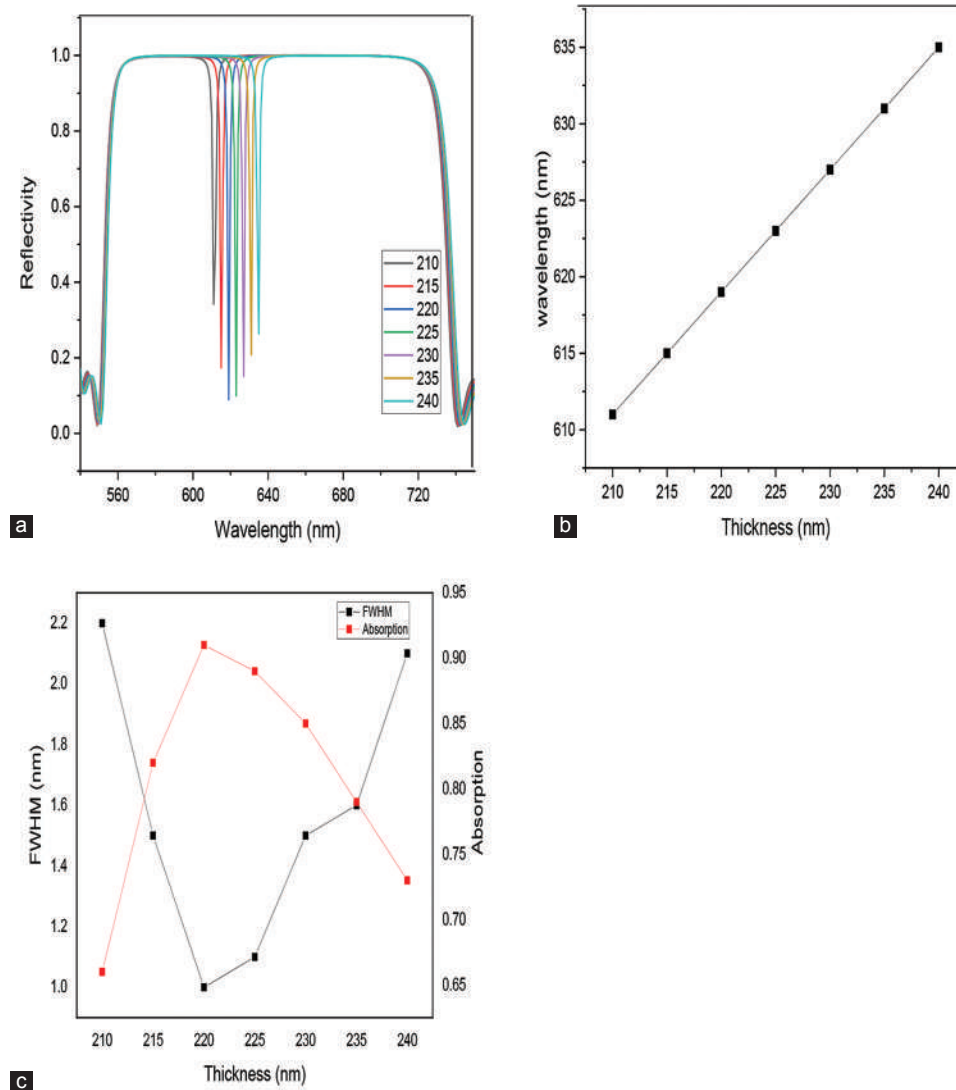


Fig. 3. (a) Absorption spectrum versus different cavity thicknesses. (b) Red shift of absorption spectrum as the cavity thickness increase. (c) Relation between absorption and full width at half maximum spectrum with the cavity thickness.

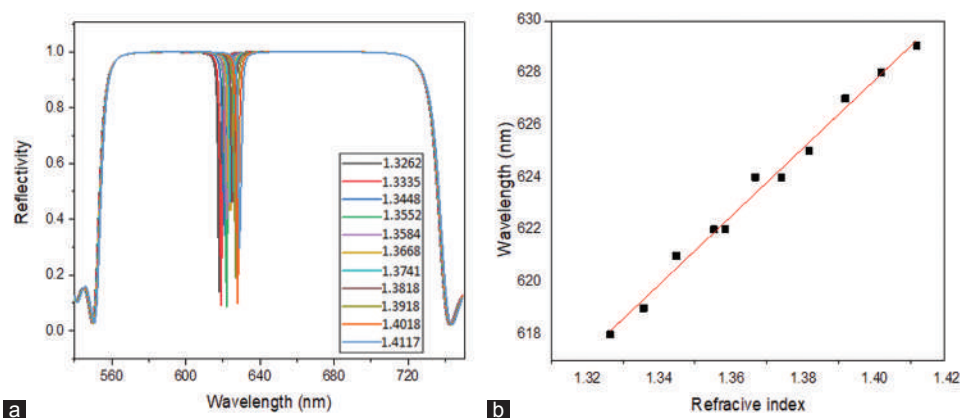


Fig. 4. (a) Absorption spectrum versus variation of glucose refractive index (RI) and (b) Red shift of absorption spectrum as the RI of glucose solution increase.

TABLE I  
SIMULATION RESULTS FOR REFRACTIVE INDEX OF SAMPLES OF GLUCOSE CONCENTRATIONS IN THE RANGE 0–50 MG/ML. THE REFRACTIVE INDEX VALUE EXTRACTED FROM (BELAY, 2018)

Concentration % (mg/mL)	RI	Wavelength $\lambda_{\text{abs}}$ (nm)
0	1.3264	618
5	1.3357	619
10	1.3448	621
15	1.3552	622
20	1.3584	622
25	1.3668	624
30	1.3741	624
35	1.3818	625
40	1.3918	627
45	1.4018	628
50	1.4117	629

#### IV. CONCLUSIONS

The DBR device containing a nanocavity, which is used to detect colugos concentration by means of the variation in the refractive index of the samples, is designed and investigated. This study elucidates that there is a linear relation between the absorption wavelength and the refractive index of glucose solution by which an empirical expression was established. Besides, the cavity widths and positions were changed to optimize the performance of the proposed DBR structure. The results manifest that this design can sense the change of refractive index by  $\Delta n = 0.02$  which in turn produced a 2.6 nm shift in the absorption spectrum. It was concluded that the sensitivity of the device was superior in comparison with those reported in the literature. Thus, these findings can help to improve the fundamental understanding of using DBR stacked layers as a sensitive chemical sensor.

#### REFERENCES

Belay, A., 2018. Concentration, wavelength and temperature dependent refractive index of sugar solutions and methods of determination contents of sugar in soft drink beverages using laser lights. *Journal of Lasers, Optics and Photonics*, 5, p.187.

Elblbesy, M.A., 2020. The refractive index of human blood measured at the visible spectral region by single-fiber reflectance spectroscopy. *AIMS Biophys*, 8, pp.57-65.

Harrill, R., 1994. *Using a Refractometer to Test the Quality of Fruits and Vegetables*. Pine Knoll, California.

Kumar, S., and Das, R., 2018. Refractive index sensing using a light trapping cavity: A theoretical study. *Journal of Applied Physics*, 123, p.233103.

Leem, J.W., and Yu, J.S., 2013. Design and fabrication of amorphous germanium thin film-based single-material distributed Bragg reflectors operating near 2.2  $\mu\text{m}$  for long wavelength applications. *Journal of the Optical Society of America B: Optical Physics*, 30, pp.838-842.

Lin, J.Y., and Su, D.C., 2003. A new method for measuring the chiral parameter and the average refractive index of a chiral liquid. *Optics Communications*, 218, pp.317-323.

Mohammed, Z.H., 2019. The fresnel coefficient of thin film multilayer using transfer matrix method TMM. *IOP Conference Series: Materials Science and Engineering*, 518, p.032026.

Reis, J.C.R., Lampreia, I.M.S., Santos, A.F.S., Moita, M.L.C., and Douh eret, G., 2010. Refractive index of liquid mixtures: Theory and experiment. *ChemPhysChem*, 11, pp.3722-3733.

Shaban, M., Ahmed, A.M., Abdel-Rahman, E., and Hamdy, H., 2017. Tunability and sensing properties of plasmonic/1D photonic crystal. *Scientific Reports*, 7, p.41983.

Shanmugan, V., Shah, M., Teo, S., and Ramam, A., 2004. Dielectric-based Distributed Bragg Reflector (DBR) Mirrors for Tunable MOEMS Applications. In: *Proceedings of SPIE-the International Society for Optical Engineering*, p.5641.

Shi, Q.G., Ying, L.N., Wang, L., Peng, B.J., and Ying, C.F., 2014. A method of the detection of marine pollution based on the measurement of refractive index. *Applied Mechanics and Materials*, 551, pp.347-352.

Singh, V.K., Jaswal, B.B.S., Kumar, V., Prakash, R., and Rai, P., 2013. Application of he-ne laser to study of the variation of refractive index of liquid solutions with the concentration. *Journal of Integrated Science and Technology*, 1, pp.13-18.

Tan, C.Y., and Huang, Y.X., 2015. Dependence of refractive index on concentration and temperature in electrolyte solution, polar solution, nonpolar solution, and protein solution. *Journal of Chemical and Engineering Data*, 60, pp.2827-2833.

White, I.M., and Fan, X., 2008. On the performance quantification of resonant refractive index sensors. *Optics Express*, 16, pp.1020-1028.

Yeh, Y.L., 2008. Real-time measurement of glucose concentration and average refractive index using a laser interferometer. *Optics and Lasers in Engineering*, 64, pp.666-670.

Zaky, Z.A., Alamri, S., Zhaketov, V.D., and Aly, A.H., 2022. Refractive index sensor with magnified resonant signal. *Scientific Reports*, 12, p.13777.



# Enhancing Upper Limb Prosthetic Control in Amputees Using Non-invasive EEG and EMG Signals with Machine Learning Techniques

Huda M. Radha<sup>1</sup>, Alia K. Abdul Hassan<sup>2</sup>, Ali H. Al-Timemy<sup>3</sup>

<sup>1</sup>Department of Computer Science, College of Science, University of Baghdad, Baghdad, Iraq

<sup>2</sup>Department of Computer Science, University of Technology, Baghdad, Iraq.

<sup>3</sup>Department of Biomedical Engineering, Al-Khwarizmi College of Engineering, University of Baghdad, Baghdad, Iraq

**Abstract**—Amputation of the upper limb significantly hinders the ability of patients to perform activities of daily living. To address this challenge, this paper introduces a novel approach that combines non-invasive methods, specifically electroencephalography (EEG) and electromyography (EMG) signals, with advanced machine learning techniques to recognize upper limb movements. The objective is to improve the control and functionality of prosthetic upper limbs through effective pattern recognition. The proposed methodology involves the fusion of EMG and EEG signals, which are processed using time-frequency domain feature extraction techniques. This enables the classification of seven distinct hand and wrist movements. The experiments conducted in this study utilized the binary grey wolf optimization algorithm to select optimal features for the proposed classification model. The results demonstrate promising outcomes, with an average classification accuracy of 93.6% for three amputees and five individuals with intact limbs. The accuracy achieved in classifying the seven types of hand and wrist movements further validates the effectiveness of the proposed approach. By offering a non-invasive and reliable means of recognizing upper limb movements, this research represents a significant step forward in biotechnical engineering for upper limb amputees. The findings hold considerable potential for enhancing the control and usability of prosthetic devices, ultimately contributing to

the overall quality of life for individuals with upper limb amputations.

**Index Terms**—Upper limb amputees, Prosthetic control, EEG and EMG signals, Machine learning, Movement recognition.

## I. INTRODUCTION

Upper limb amputation is a condition that severely limits the capacity of amputees to do daily duties. The myoelectric prosthesis aims to help restore the function of these lost limbs using signals from the remaining muscles. Unfortunately, there are multiple difficulties facing patients with missing upper limbs in terms of the challenge of collecting this signal, and the percentage of upper limb amputation, as much research in this sector is now focused on helping amputees live as normal a life as feasible (Kumar, Singh and Mukaherjee, 2021). The development of fusion bio-signals-based rehabilitation devices has become now very interesting to many biomedical researchers. However, the development of electroencephalography (EEG) and electromyography (EMG)-controlled prostheses remains a challenging issue in developing countries (Khan, Khan and Farooq, 2019). Multiple-source signal fusion is one way to solve the problem of not having enough information to control a prosthesis (Hooda, Das and Kumar, 2020; Radha, Abdul Hassan and Al-Timemy 2023).

In the previous studies, most researchers applied advanced signal processing, robust feature extraction, machine learning, and feature selection algorithms to improve the performance of the biosignal pattern recognition (PR) system (Dey et al., 2018; Udhaya Kumar and Hannah Inbarani, 2017). Signal processing, in general, transforms the signal to obtain useful signal information. The goal of feature extraction is to extract useful information from a signal. The feature selection algorithm attempts to identify the best features from the initial set of features. Finally, machine

ARO-The Scientific Journal of Koya University  
Vol. XI, No. 2 (2023), Article ID: ARO.11269. 10 pages  
DOI: 10.14500/aro.11269

Received: 19 July 2023; Accepted: 05 October 2023  
Regular research paper; Published: 30 October 2023

Corresponding author's e-mail: [huda.rada@sc.uobaghdad.edu.iq](mailto:huda.rada@sc.uobaghdad.edu.iq)  
Copyright © 2023 Huda M. Radha, Alia K. Abdul Hassan, and Ali H. Al-Timemy. This is an open access article distributed under the Creative Commons Attribution License.



learning functions as a classifier, categorizing features to recognize hand movements (Krishnan and Athavale, 2018). Many EEG and EMG features have recently been proposed and used in fusion PR (Al-Quraishi, et al., 2021; Fang, et al., 2020; Radha, Abdul Hassan and Al-Timemy, 2022; Verma and Tiwary, 2014). Increasing in the number of EEG, EMG features not only increase the classifier's complexity but also have a negative impact on the classification process (Cai, et al., 2020). Following this line of thought, feature selection is an important step in removing irrelevant and redundant information, which reduces the number of features and unnecessary complexity (Alelyani, Tang and Liu, 2018). Feature selection methods classify selection approaches based on the participation of the learning algorithm. Filter method (Information Gain) (Singer, Anuar and Ben-Gal, 2020), Gain Ratio (Voelzke, 2015), and Chi-square (Ahakonye, et al., 2023) rely on some data properties without engaging a specific learning process. Wrapper approaches, on the other hand, rely on a specialized learning algorithm (e.g., classifier) to evaluate the specified subset of features (Shahana and Preeja, 2016; Jović, Brkić and Bogunović, 2015). When comparing these families, wrappers are more accurate since they take into account the relationships between the traits themselves. They are, however, more computationally expensive than filters, and their performance is heavily dependent on the learning technique used (Thabtah, et al., 2020). Another important consideration when creating a feature selection algorithm is looking for the (near) optimal subset of features. To choose the best feature subset, wrapper-based feature selection uses a meta-heuristic optimization technique, such as binary grey wolf optimization (BGWO), binary particle swarm optimization, ant colony optimization, and genetic algorithm (Beheshti, 2022). This study proposes an algorithm for classifying the upper limb motions of below-elbow amputees by fusing EMG and EEG data as parallel input. The following is a summary of the main contributions of the current work:

1. Build a dataset for hand and wrist motion detection for two biosignals (EEG, EMG).
2. Binary gray wolf optimization-based feature selection is utilized to select the proper set of features, which improved outcomes for selecting effective features for signal segment classification to categorize seven classes of hand and wrist motion, which are (wrist flexion [WF], flexion of outer part of the wrist [FO], hand close [HC], hand open [HO], pronation [PRO], supination [SUP], and rest [RST]).

## II. METHODOLOGY

### A. Subjects and Data Acquisition

Data were collected from eight subjects, five subjects are intact-limbed, and three are amputees and were recorded in the laboratory of the Department of Biomedical Engineering, Al-Khwarizmi College of Engineering, University of Baghdad. To classify hand movements, a set of seven movements was selected: WF, outward part of the wrist

(WE), HO, HC, PRO, SUP, and RST see Fig. 1. When recording the signal, the following was observed:

- Subjects have given their consent to participate in the study.
- The experimental protocol was done according to the Declaration of Helsinki and its later amendments.

This study was focused on these motions according to their relationship with low-level amputation. Table I displays the demographic data of the amputees. In addition, Fig. 2 provides illustration pictures of amputees in the registration of this dataset. Eight EMG channels were recorded in the data. Moreover, four frontal EEG channels were provided as shown in Fig. 3. Subjects received a thorough explanation of the events, and they received some brief training to get them acclimated to the process. Each participant in the experiment was instructed to do the exercise in turn for a duration of 10 s, after which the motions were recorded three more times. In this setting, two trails were used to train the classifier and the remaining trail was used to test the classifier to calculate the classification error rate. EMG and EEG were recorded simultaneously while performing the movement. EMG signals were collected. They used a high-density EMG system where the signal frequency was 200 Hz for eight channels; Electrodes were placed on the surface of the skin to check for residues arm for each subject. On the other hand, EEG Muse data were collected on 252 Fs, and with 4 channels Raw. At a sampling rate of 1 kHz, raw data are gathered from which

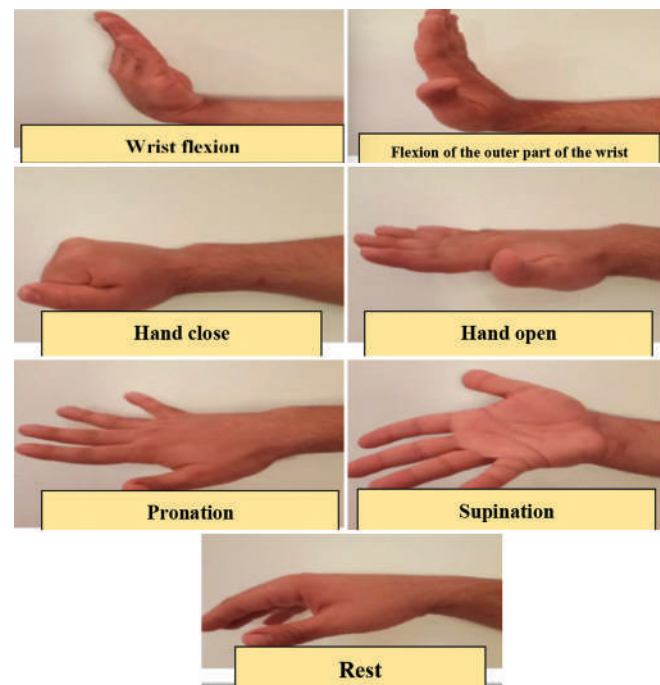


Fig. 1. Hand and wrist motion classes.

TABLE I  
DEMOGRAPHIC DATA FOR AMPUTEE SUBJECTS

Amputee ID	Age (years)	Missing arm	Time since amputation (years)
Amputee 1	67	Left	30
Amputee 2	48	Right	31
Amputee 3	35	Left	7

useful features can be extracted. Fig. 4 depicts a visualization plot comparing both the EEG and EMG signals for an



Fig. 2. Amputee’s participants during the acquisition of the proposed dataset. (a) Amputee subject 1, (b) Amputee subject 2, and (c) Amputee subject 3.



Fig. 3. Electroencephalography Muse four channels and electromyography Armband placement eight channels devices.

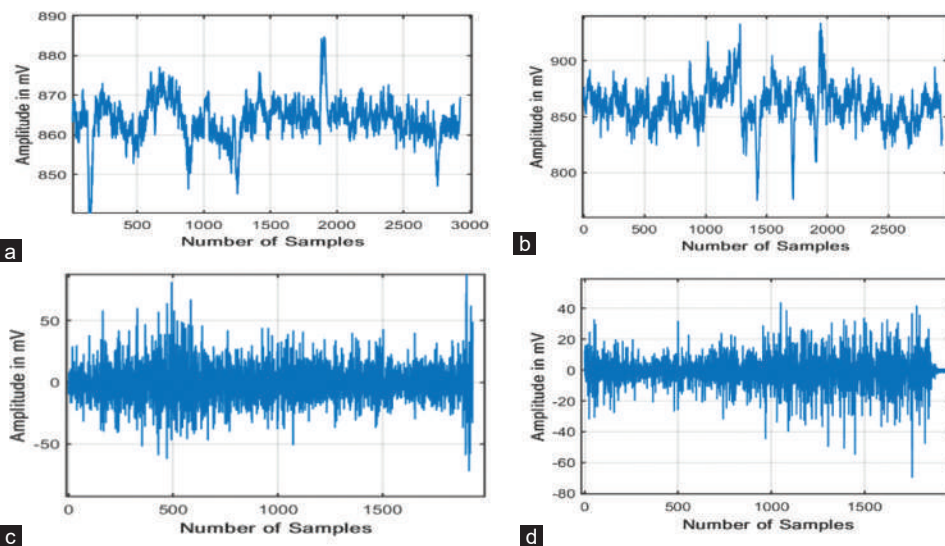


Fig. 4. Waveforms obtained from electroencephalography (EEG) and electromyography (EMG). (a) EEG signal for non-amputee subject, (b) EEG signal for amputee subject, (c) EMG signal for non-amputee subject, and (d) EMG signal for amputee subject.

amputee and intact-limb subject. Because the EMG is based on the acquisition of bioelectrical signals associated with muscular contraction, it appears to acquire more information per motion. The accuracy of the classification was calculated according to the following equation:

$$\text{Classification accuracy(\%)} = \frac{\text{Number of correctly classified motion samples}}{\text{Total number of motion samples}} \quad (1)$$

*B. Data Windowing*

The data were segmented using an overlapped segmentation approach with a window size of 150 ms and an increment of 50 ms, applied on the eight channels for EMG signals and four channels for EEG. Using Bluetooth, the data were transferred from Myo armband and Muse to the computer.

*C. Feature Extraction*

After windowing the EEG and EMG signals, they were included in separate matrices. This was done before extracting the time-frequency domain (TFD) features. One matrix has four columns, one for each channel of EEG, and the other has eight columns, one for each channel of EMG recorded signal, and gets the class for each segment. TFD involves the extraction of fourteen features from EEG signal and six features from EMG signal. Tables II and III provide extracted features equations using in EEG and EMG signals, respectively (Al-Quraishi, et al., 2021, Krishnan and Athavale, 2018).

*D. Dimensionality Reduction*

A significant question in the area of PR is how to extract fewer but more useful features. Dimensionality reduction is a common method employed to resolve this problem. In this

TABLE II  
FEATURES BASED ON THE EEG SIGNAL

Feature Name	Equation
Hjorth Complexity	$Complexity = \frac{Mobility(y'(t))}{Mobility(y(t))}$
Hjorth Mobility	$Mobility = \sqrt{\frac{var(y'(t))}{var(y(t))}}$
Tsallis Entropy	$Ts = \left(\frac{1}{\alpha-1}\right) * (1 - \sum En(x))$ Where $x$ denotes the signal segment, and $\alpha=2$
Shannon Entropy	$Shan En = -\sum_i p_i \log p_i$ Where $p_i$ stands for EEG signal likelihood having a value of $a_i$ , at some certain location, $i$ , within general signal
Band Power Alpha	$BPA = bandpower(x, fs, [f_{low} f_{high}])$ Where $fs=252$ , $flow=8$ , and $fhigh=12$
Band Power Beta	$BPB = bandpower(x, fs, [f_{low} f_{high}])$ Which ranges from 12 to 30 Hz
Band Power Gamma	$BPG = bandpower(x, fs, [f_{low} f_{high}])$ Which ranges from 30 to 64 Hz
Band Power Theta	$BPT = bandpower(x, fs, [f_{low} f_{high}])$ Which ranges from 4 to 8 Hz
Band Power Delta	$bandpower(x, fs, [f_{low} f_{high}])$ which ranges from 1 to 4 Hz
Ratio of Band Power Alpha to Beta	$RBA = \left(\frac{BPB}{BPA}\right)$
Mean energy	ME=mean ( $x^2$ )
Median value	MED=medium ( $x$ )
Maximum value	Max=max ( $x$ )
Minimum value	Min=min ( $x$ )

TABLE III  
FEATURES BASED ON THE EMG SIGNAL

Feature Name	Equation
Wavelength feature Mean absolute value	$MAV = \frac{1}{N} \sum_{i=1}^N  x_i $
Slope sigh changes	$SSC = \sum_{i=2}^{n-1} [f[(x_i - x_{i-1}) \times (x_i - x_{i+1})]]$
Cardinality	$n(A \cup B) = n(A) + n(B) - n(A \cap B)$
Wilson amplitude	$WAMP = \sum_{i=1}^{N-1} f( x_i + 1 - x_i )$
Simple square integral	$SSI = \int_0^1 \int_0^1  x - y ^n dx dy$

study, through the experiments, we used principal components analysis (PCA) as a feature reduction to reduce the features; we found that it is better to reduce the features to 35 features.

PCA provides an orthogonal transformation that converts data with correlated variables into samples with linearly associated features. The main components are new features that have fewer or equivalent variables to the ones that were present at the start. Because PCA is an unsupervised method, data label information is not included. Normally, dispersed data have self-contained primary components (Nanga et al., 2021).

### E. Dimension Reduction Results

The dimension reduction method chosen is determined by the nature of the input data. For example, different strategies apply to continuous, category, count, or distance data. We must also consider our intuition and domain expertise about aggregated measurements. Consider the amount of variance described by each primary component when determining the number of dimensions to keep. We know that the variance of the data is equal to the diagonal sum of matrix D, that is, the sum of the eigenvalues  $Var(X) = \sum |\lambda|$  (García, Luengo and Herrera, 2015).

Recognizing different motions using a single set of features is the most challenging task in biosignal-based motion recognition systems. The feature reduction-based PCA technique has been introduced in this work, with the aim of narrowing down the set of potentially unimportant expert features describing a dataset to a few key features. Fig. 5 displays the classification test error for a different number of features in the proposed dataset.

The testing error obtained for each subject (i.e., intact-limb and amputee) for classification-based PCA feature reduction to EEG signal only (colored red) and EMG signal only (colored yellow) is presented in Fig. 6, by varying the number of features (10, 15, 20, 25, 30, 35), respectively. That the testing error for EEG signal for intact-limb subjects ranges from (36–48%), and for amputee subjects ranges from (32–50%), whereas the testing error for EMG signal for intact-limb subjects ranges from (5–15%), and the testing error for EMG signal for amputee subjects ranges from (20–25%). The results of intact-limb subjects were different from the amputee's subject. This may be due to that the intact-limb have the whole arm that make them apply the motions as required for HO, HC, or other motions. However, the amputees are not having hand that cause them not do the movement as required. This paper presents the BGWO algorithm, which select effective sets of features for each biosignal classification to optimize the results obtained. The following sections explain the fundamental concepts of the BGWO algorithm.

### F. Feature Selection based Binary Grey Wolf Optimization

Through given the nature of each signal acquired in this work and the importance of the characteristics extracted from it to improve the prosthetic limb movement recognition system for upper limb amputees, consideration has been given to suggest the best method of feature selection algorithms to achieve three objective in this proposal. First, enhance the performance of a data-mining module by delivering a faster and more cost-effective learning process as well as a better grasp of the underlying data selection process. The algorithm for BGWO in this work was chosen to since its nature is in line

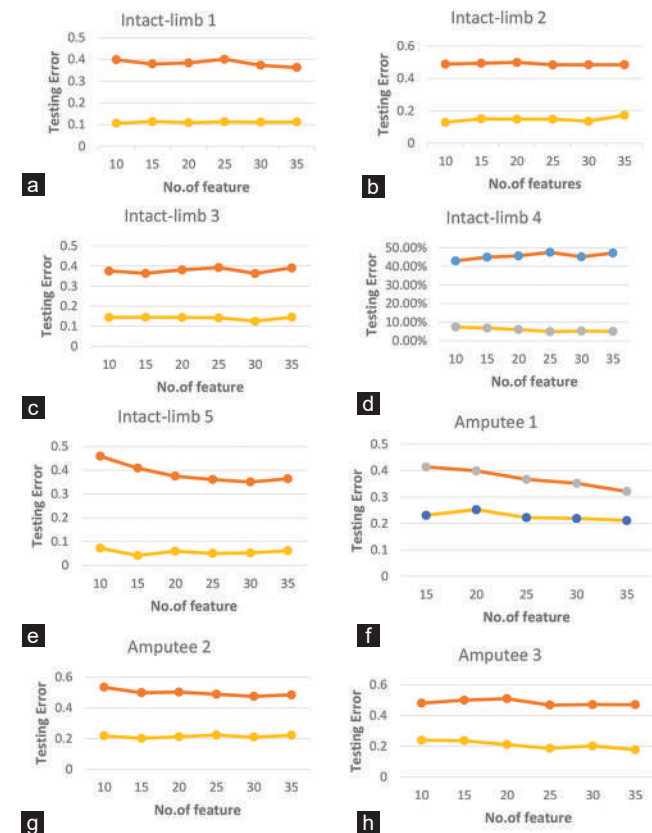


Fig. 5. Testing error for classification using PCA feature reduction for all subjects in proposed dataset, (a) intact-limb 1, (b) intact-limb 2, (c) intact-limb 3, (d) intact-limb 4, (e) intact-limb 5, (f) amputee 1, (g) amputee 2, and (h) amputee 3.

with the set of features extracted from the biological signals used in this work. This algorithm uses the three best levels such as (*alpha*, *beta*, and *delta*), in addition to the secondary (i.e., *omega*, and so on) priority levels. This is consistent with the desire to achieve higher gradient levels to select the best features extracted from the signals recorded in this work. The details of the proposed system are illustrated in Fig. 6. First, wolves' initial populations are randomly initialized (either bit 1 or 0). The fitness of gray wolves is assessed next. The fitness is used to select the three leaders, alpha, beta, and delta, whose positions are denoted by  $X_1$ ,  $X_2$ , and  $X_3$ . After that, update the gray wolf's new location. Following that, the wolves' fitness is evaluated, and alpha, beta, and delta positions are updated (Udhaya Kumar and Hannah Inbarani, 2017).

All the solutions are guided through such three solutions (i.e.,  $[\alpha]$ ,  $[\beta]$ , and  $[\delta]$ ) for discovering the search space to find the optimal solution. The mathematical modeling of the encircling behavior is done using the next equations. The algorithm kept running until the termination criterion was met. The best feature subset ultimately determined to be the alpha solution. Algorithm 1 demonstrates the steps taken during BGWO feature selection.

$$\vec{X}(t+1) = \vec{X}p(t) + \vec{A} \times \vec{D} \quad (2)$$

$$\vec{D} = \left| \vec{C} \times \vec{X}p(t) - \vec{X}(t) \right| \quad (3)$$

ALGORITHM I  
THE PROPOSED BGWO BASED FEATURE SELECTION

**Input:** Extracted EEG , EMG Features matrix (Training file)  
**Output:** Sfeat1(): selected features of EEG matrix  
 SF1(): (index of best selected feature columns from EEG matrix)  
 Sfeat2(): selected features of EMG matrix  
 SF2(): (index of best selected feature columns from EMG matrix)

**Begin**

**Step 1:** Initialized BGWO parameters (Population of grey wolves,  $X=15$ ).  
 (Number of iteration,  $T=100$ ), (Weight of cross-validation value  $cv=0.5$ )

**Step 2:** Initialize the parameter  $a$ ,  $A$  and  $C$

**Step 3:** Compute the fitness of wolves,  $F(X)$ .

**Step 4:** Set  $X_\alpha$  = the position of best wolf.

Set  $X_\beta$  = the position of second best wolf.

Set  $X_\delta$  = the position of third best wolf.

**Step5:** for  $t = 1$  to maximum number of iteration ,  $T$

**Step6:** for  $i = 1$  to number of wolf,  $N$

**Step7:** Compute  $X_1$  ,  $X_2$ , ,&  $X_3$  using Equation (6)

**Step 8:** Generate  $X_i^{new}$  by applying the Equation (7)

**Step 9:** next  $i$

**Step 10:** Compute the fitness of all grey wolves,  $F(X^{new})$

**Step 11:** Update the position of alpha, beta and delta.

**Step 12:** Update the Parameter  $a$ ,  $A$  and  $C$

**Step 13:** next  $t$

**Step 14:** //Select the best features from (EEG, EMG) Testing file according of //Index vector SF1 () and SF2 (), respectively. For testing evaluation,

**Return** Sfeat1 (), SF1 (), Sfeat2 (), SF2 ().

**Step 15: End**

Where  $\vec{D}$  is as defined in equation (3),  $t$  is the number of iterations,  $\vec{X}p(t)$  is the position of the prey,  $\vec{A}$ ,  $\vec{C}$  are coefficient vectors, and  $\vec{X}$  is the gray wolf position.

$$\vec{C} = 2 \times \vec{r}_2 \quad (4)$$

$$\vec{A} = 2 \times \vec{a} \times \vec{r}_1 - \vec{a} \quad (5)$$

The vectors  $\vec{A}$ , and  $\vec{C}$  have been estimated using equations (4) and (5). Components of  $\vec{a}$  are reduced linearly from (2 to 0) over the course of the iterations and  $r1$ ,  $r2$  represent random vectors in  $[0, 1]$ .

Typically, the alpha drives the hunting. In some cases, the beta and delta may be involved in the hunt. For mathematically simulating gray wolf hunting behavior, beta, alpha, and delta (i.e., the highest solutions) are expected to have a better understanding of prey location. Other search agents follow the first three optimal solutions found thus far in the hunting processes to update their position to the search agent's optimal position. The equations below show the wolves' updated positions.

$$\left. \begin{aligned} \vec{D}_\alpha &= \left| \vec{C}_1 \times \vec{X}_\alpha - \vec{X} \right| \\ \vec{D}_\beta &= \left| \vec{C}_2 \times \vec{X}_\beta - \vec{X} \right| \\ \vec{D}_\delta &= \left| \vec{C}_3 \times \vec{X}_\delta - \vec{X}_\alpha \right| \quad \vec{X}_1 = \left| \vec{X}_\alpha - \vec{A}_1 \times \vec{D}_\alpha \right| \\ \vec{X}_2 &= \left| \vec{X}_\beta - \vec{A}_2 \times \vec{D}_\beta \right| \\ \vec{X}_3 &= \left| \vec{X}_\delta - \vec{A}_3 \times \vec{D}_\delta \right| \end{aligned} \right\} \quad (6)$$

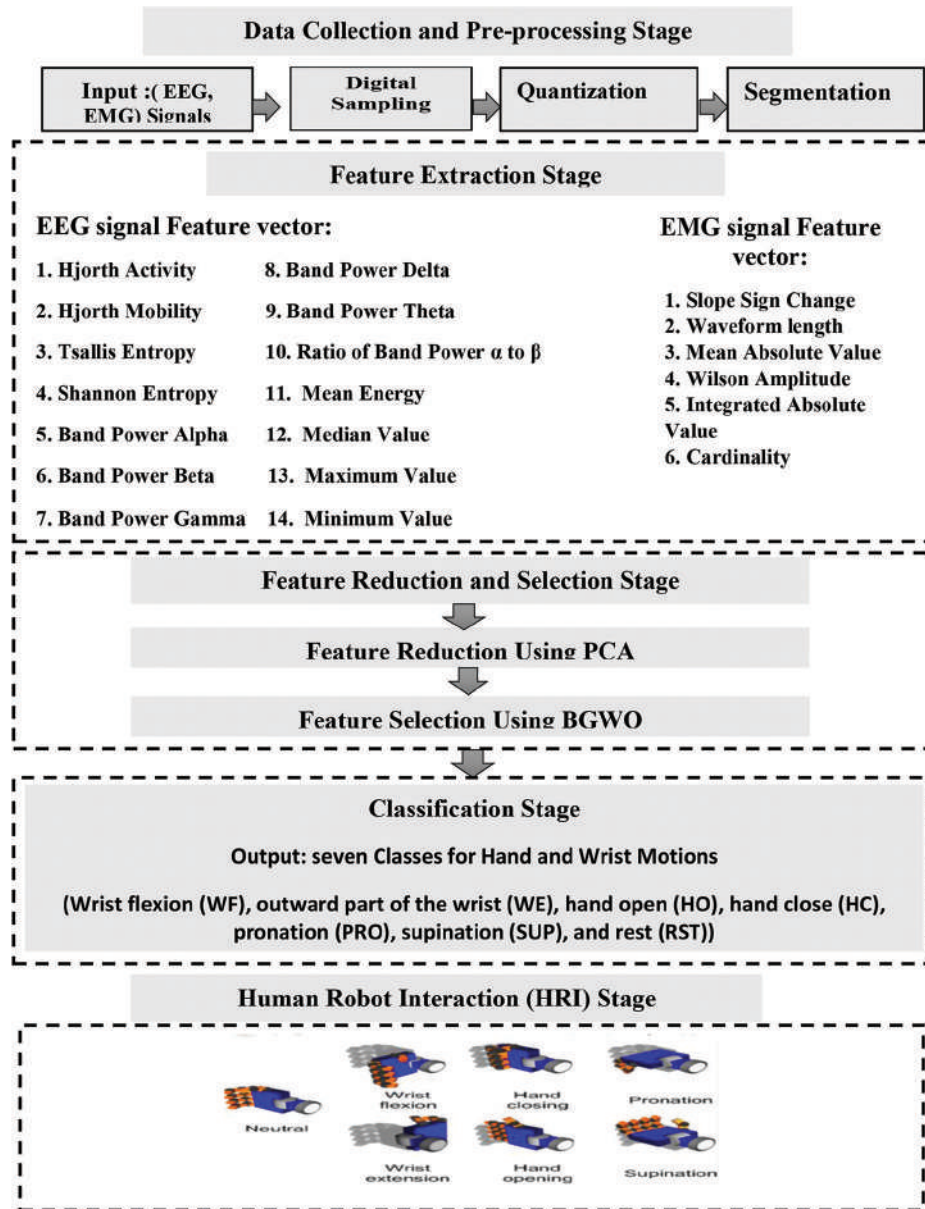


Fig. 6. The proposed system detailed structure.

$$\bar{X}(t+1) = \frac{\bar{X}_1 + \bar{X}_2 + \bar{X}_3}{3} \quad (7)$$

This study proposes a GWO modification. As a binary GWO (BGWO) for modifying binary variables in the search region (i.e., the nature of the Feature Selection problem). The generation function of the solutions and equation of new position (i.e.,  $\bar{X}(t+1)$ ) Equation (7) are adjusted for identifying practical solutions throughout BGWO execution, as follows:

$$Sig(\bar{X}(t+1)) = \frac{1}{1 + e^{-\bar{x}(t+1)}} \quad (8)$$

The  $X$  solution's decision variables are updated by Equation (8), where  $Sig(\bar{X}(t+1))$  denotes the possibility that they will be set to "0" or "1" in the  $X$  solution.

$$\bar{X}(t+1) = \begin{cases} 1 & \text{if } r < Sig(\bar{X}(t+1)) \\ 0 & \text{otherwise} \end{cases} \quad (9)$$

where the sigmoid function is used in Equation (8) to translate the value of  $\bar{X}(t+1)$  in Equation (9) in the range [0, 1],  $r$  denotes random numbers between (0, 1).

Tables IV and V show the final selected feature subset for intact-limbl as an example, using BGWO-based EEG and EMG signals, respectively, whereas Table VI lists the total number of feature subsets that were chosen for the proposed dataset for all subjects.

### G. Classification

Liner discriminant classifier (LDC) was utilized to perform the classification. LDC's primary task is to look

TABLE IV  
FINAL SELECTED FEATURE SUBSET FOR INTACT-LIMB 1 OF CLASSIFICATION FOR IN THE PROPOSED DATASET-BASED ON THE EEG SIGNAL

Feature No.	Feature Name	CH 1	CH 2	CH 3	CH 4
F1	Band Power Alpha			✓	
F2	Band Power Beta			✓	
F3	Band Power Delta				
F4	Band Power Gama	✓	✓		✓
F5	Band Power Theta				
F6	Ratio Band Power Alpha Beta		✓		
F7	Shannon Entropy			✓	
F8	Mean Energy		✓	✓	✓
F9	Median	✓		✓	✓
F10	Maximum		✓	✓	
F11	Minimum	✓	✓	✓	✓
F12	Hjorth Mobility		✓	✓	
F13	Hjorth Complexity			✓	✓
F14	Tsallis Entropy		✓		

No. of selected features=24

TABLE V  
FINAL SELECTED FEATURE SUBSET FOR INTACT-LIMB 1 OF CLASSIFICATION FOR IN THE PROPOSED DATASET BASED ON THE EMG SIGNAL

Feature No.	Feature Name	CH 1	CH 2	CH 3	CH 4	CH 5	CH 6	CH 7	CH 8
F1	Wavelength		✓	✓			✓	✓	
F2	Mean Absolute Value		✓				✓	✓	✓
F3	Slope Sign Change			✓	✓				✓
F4	Cardinality	✓				✓		✓	
F5	Wilson Amplitude	✓		✓	✓				
F6	Integrated Absolute Value	✓		✓		✓		✓	

No. of selected features=21

TABLE VI  
NUMBER OF SELECTED FEATURES FOR ALL SUBJECTS OF CLASSIFICATION FOR PROPOSED HYBRID EEG-EMG DATASET

Signal Type	Intact-limb1	Intact-limb 2	Intact-limb 3	Intact-limb 4	Intact-limb 5	Amputee 1	Amputee 2	Amputee 3	Total number of selected features for all subjects
EEG	24	24	22	29	27	15	26	24	191
EMG	21	24	26	23	23	21	20	26	184

TABLE VII  
COMPARISON WITH PREVIOUS RELATED WORKS

Authors	Type of signal	Methodology	Dataset	Accuracy
Gordleva et al. (2020)	EEG, EMG	CSP features extraction from a combination of EEG+EMG and then classification of the LDA.	Dataset consist of 8 healthy subjects	80% for LDA classifier
Nsugbe et al. (2020)	EMG, EEG	TD time-domain Feature Extraction such as (MAV, WL, ZC, and SSC), PCA dimension reduction with two-classifier K-mean and Gaussian mixture model (GMM).	Case Study for one amputee	88% for GMM classifier 82% for K-mean classifier
Nsugbe and A. H. Al-Timemy (2021)	EMG, Accelerometers (Acc.)	MAV, WL, ZC, and RMS are examples of features extracted from two signals in the time domain. Cepstrum, Auto-regression (AR) coefficients, Sample entropy (SampEN), Maximum fractal length (MFL), Higuchi fractal dimension (HFD), and Detrended fluctuation analysis (DFA) are examples of features extracted from two signals in the frequency domain. With the LDA, SRDA, and SVM three classifiers.	Dataset consists of 10 subjects for four Amputees and six intact-limb	70% for LDA classifier 70% for SRDA classifier 88% for SVM classifier
Colli and Trejos (2022)	EMG, Accelerometers Acc.	Features vector extracted from two signals such as (MAV, MAVS, WL, 4 <sup>th</sup> order auto-regressive coefficients (AR), and ZC) with Adaptive Least-Squares Support Vector Machine	Dataset consists of 22 healthy subjects	92.9% for adaptive SVM classifier
The proposed system	EEG, EMG	Time-Domain with feature for EMG, Frequency-domain with feature for EEG)	Dataset: Proposed Dataset for hand and wrist motion, which consists of 8 subjects (3 amputees and 5 intact limbs).	93.26% For LDA classifier

for any vectors in the vector space that can better separate the different classes of data. The original data points could be projected onto such vectors (s) for evaluating the class separability. Therefore, LDC seeks to better differentiate the classes in the case when they overlap for a given set of data points using a few sorts of transformation method (Alzubi, Nayyar and Kumar, 2018).

In classification stage, the result of extracted EEG and EMG features is separated into training and testing sets. The training data are fed into the feature selection stage which uses BGWO algorithm to select the best features. The output of this algorithm is the set of optimum extracted features known as (Sfeat) see algorithm 1, as well as the index of this optimum column known as (SF), which is utilized to choose the column from the testing set. These steps are also used to obtain EMG training set features. The following phase sends the class labels from the training and testing sets into the LDC classifier, which predicts the class by completing performance measures. The final step is to concatenate the EEG and EMG training and testing sets, as well as their class labels, to feed into the LDC classifier, which will predicate class by performing performance evaluation satisfying fusion concepts.

H. Comparison with the Previous Studies

Table VII shows a comparison of the proposed system’s findings with the state-of-the-art works. The comparison table shows that the proposed system outperformed the current standard in the following:

1. The achieved accuracy is increased by approximately 31.24% and 6.35%, respectively, when only EEG and EMG signals are used.
2. The proposed system has been evaluated utilizing the seven basic hand and wrist motions, including the RST (no movement) class.
3. The proposed system has been tested on a dataset containing people of various ages and conditions. This is a reflection of the suggested system's flexibility and the dependability of the extracted EEG and EMG features, which can distinguish motion regardless of control intensity or presence. This research aimed to combine EEG and EMG to identify upper limb voluntary movement.
4. In general, a method for improving the detection of upper limb voluntary movement intention by combining EEG and EMG patterns was provided, which is important for the interactive control of the upper limb exoskeleton robot.

III. RESULTS AND DISCUSSION

The proposed algorithm was tested and evaluated with the following step. Testing error and classification accuracy based on EEG, EMG, and fusion EEG, and EMG were calculated. Once more, the 1<sup>st</sup> experiment is conducted using the collection of features known as TFD, including 14 features extracted from EEG signal and five features extracted from EMG signal. For intact-limb 1 value-based BGWO (feature selection), the acquired classification accuracy is calculated using the LDC classifier, as shown in Fig. 7.

The classification performance confusion matrix for intact-limb 1 is shown in this figure as example for the single-

signal approaches of (4-ch EEG) which is 60.5%, (8-ch EMG) which is 91.1%, respectively.

Table VIII shows the average testing errors for the single-signal approaches of 8-ch only EMG, 4-ch only EEG, for all subjects.

As shown from Table VIII, the average testing error for all subjects-based EEG signal only is 38.48% and for EMG only is 9.55%. This gives the impression that it is possible to benefit from the EMG signal in terms of taking the characteristics that it is better than the EEG signal; however, due to the difficulty in obtaining the characteristics from the EEG signal, we employed 14 features in this work to benefit from the characteristics of this signal.

IV. EEG – EMG FUSION RESULTS

This section presents the fusion stage results. The accuracy achieved by the fusion method was presented first, followed by a comparison of the results obtained by the fusion method, EEG, and EMG alone.

The fusion of EEG and EMG results is performed at the decision level. LDA classifier is tried to fuse the outputs for seven classes which are (WF, Flexion of the outer part of the wrist, HC, HO, PRO, SUP, and RST), and the achieved results for the proposed dataset are shown in Table IX.

Fig. 8 illustrates the graphical representation of comparison of the achieved results for the proposed dataset using EEG only, EMG only, and Fusion (EEG+EMG). As shown, EMG data often have a higher classification accuracy than EEG data. Therefore, using EMG signals in combination with EEG signals rather than EMG signals alone will always increase accuracy.

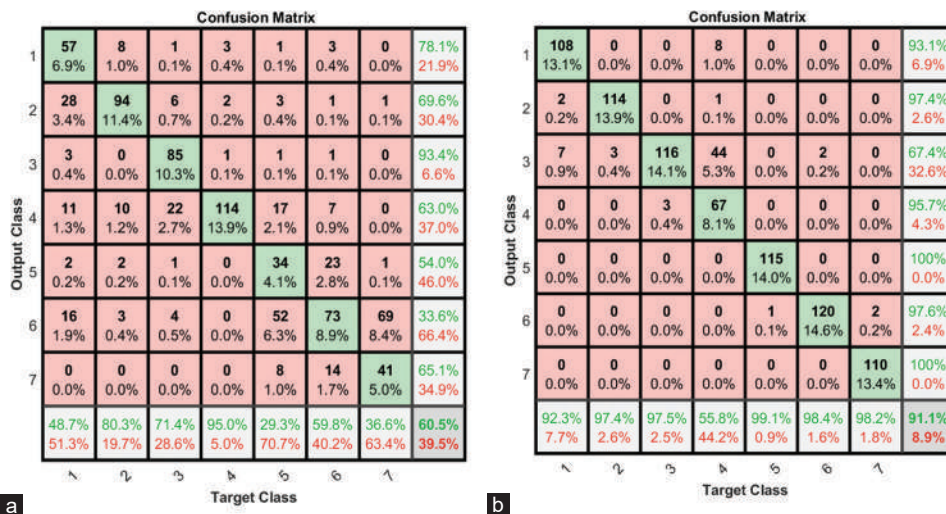


Fig. 7. (a) Confusion matrices for Intact-limb 1 (EEG only). (b) Confusion matrices for Intact-limb 1 (EMG only).

TABLE VIII  
TESTING ERRORS FOR THE SINGLE-SIGNAL APPROACHES FOR ALL SUBJECTS

Signal Type	Intact-limb1	Intact-limb 2	Intact-limb 3	Intact-limb 4	Intact-limb 5	Amputee 1	Amputee 2	Amputee 3	Average Testing Error
EEG only	39.5%	34.8%	34.9%	39.5%	34.2%	43.3%	45.8%	35.9%	38.48%
EMG only	8.9%	2.5%	3.4%	8.0%	8.4%	16.3%	15.7%	13.2%	9.55%

EEG: Electroencephalography, EMG: Electromyography



TABLE IX  
CLASSIFICATION ACCURACY ACHIEVED FOR ALL SUBJECTS WITH THE PROPOSED DATASET

Signal type	Intact-limb1	Intact-limb 2	Intact-limb 3	Intact-limb 4	Intact-limb 5	Amputee 1	Amputee 2	Amputee 3	Average Accuracy for all subjects
Fusion (EEG, EMG)	96.2%	98.3%	98.1%	97.6%	95.6%	86.8%	84.6%	88.9%	93.26%

EEG: Electroencephalography, EMG: Electromyography

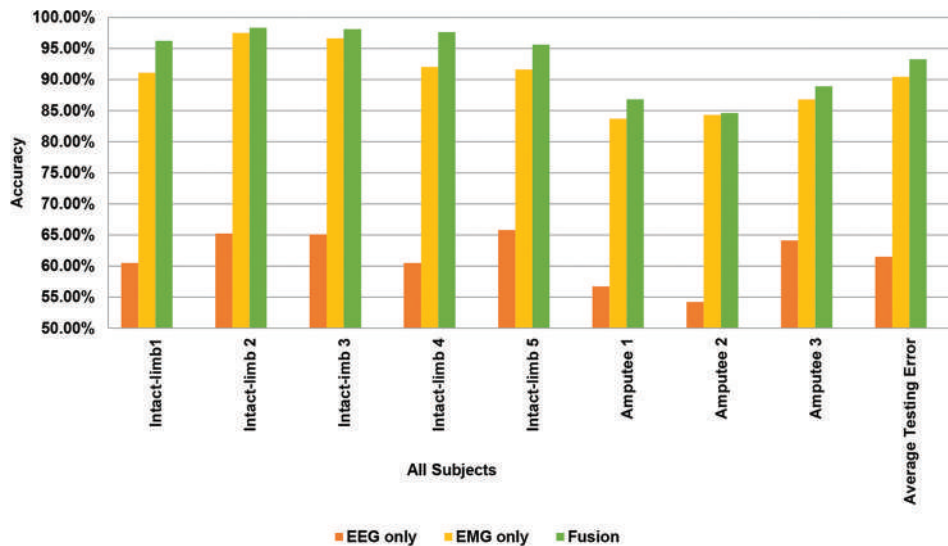


Fig. 8. Comparison of the achieved results for the proposed dataset using electroencephalography (EEG) only, electromyography (EMG) only, and Fusion (EEG+EMG).

As a result, users of the most recent prosthetic devices based on EMG data alone encounter numerous drawbacks.

From the foregoing, we conclude that EEG signals, in conjunction with EMG signals, should be used to determine the direction of development of the prosthesis for movement classification. This work mainly focused on the use of PR algorithms in transfer learning by combining EEG and EMG signals.

As shown to Fig. 8, the fusion of EMG and EEG data can be more accurate, allowing upper-limb amputees to use hand movements as non-invasive and intuitive control cues for prosthetic replacement. The experiment showed that BGWO algorithm for feature selection using an LDC classifier was facilitated by extracting regular patterns of vital signs. With an average classification, accuracy of 97.16% for five intact-limb subjects and of 86.76% for three amputee's subjects. The average classification achieved for all subjects in the proposed dataset is 93.26%.

The proposed PR system was successful in recognizing seven hand-grinding movements based on the obtained results and effective solutions from conducting experiments using the methods approved in this thesis. The findings of the study could be utilized to improve the functionality of electrosurgical prosthetics for persons who have lost lower limbs. To improve control instructions, control speed, and application, future work will focus on building a portable, low-cost, completely synchronous EEG/Electrooculogram/EMG-based multimodal human-machine interface and a synchronous multi-information acquisition system. In the meanwhile, the Multimodal Human-Machine Interface

(mHMI) should be used to help severely injured stroke patients regain hand motor function.

#### IV. CONCLUSION

This study proposed system that was tested and modified to handle a dataset of various hand and wrist movements for low-level upper limb amputees for recording actual dataset. Using different types of biosignals extracted from the human body and pre-processing each one in accordance with the method of acquisition. In the proposed system, TFD features were used for feature extraction, BGWO feature selection was used to improve results for selecting effective features for signal segment classification to categorize seven classes of hand motion, and LDA was used as a classifier with a 75ms window size segment. A novel EEG-EMG fusion method was presented in this study to improve the performance of bioelectrical signal-controlled robotic devices used for assistance and rehabilitation. The PR system was able to identify seven classes for hand and wrist motions with classification accuracy of 86.7% for three amputee subjects and 97.1% for five intact-limb subjects when utilizing EEG and EMG channels.

#### V. ACKNOWLEDGMENT

The authors would like to thank all of the subjects who volunteered for this study, both intact-limbed and amputee. The authors are also grateful to the reviewers for their valuable suggestions.

## REFERENCES

- Ahakonye, L.A.C., Nwakanma, C.I., Lee, J.M., and Kim, D.S., 2023. SCADA intrusion detection scheme exploiting the fusion of modified decision tree and Chi-square feature selection. *Internet of Things*, 21, p.100676.
- Alelyani, S., Tang, J., and Liu, H., 2018. Feature selection for clustering: A review. In: *Data Clustering*. CRC Press, United States, p.29-60. Available from: <https://www.taylorfrancis.com/chapters/edit/10.1201/9781315373515-2/feature-selection-clustering-review-salem-alelyani-jiliang-tang-huan-liu> [Last accessed on 2023 Jul 01].
- Al-Quraishi, M.S., Elamvazuthi, I., Tang, T.B., Al-Qurishi, M., Parasuraman, S., and Borboni, A., 2021. Multimodal fusion approach based on EEG and EMG signals for lower limb movement recognition. *IEEE Sensors Journal*, 21(24), p.27640-27650.
- Alzubi, J., Nayyar, A., and Kumar, A., 2018. Machine learning from theory to algorithms: An overview. *Journal of physics: Conference series*, 1142, p.012012.
- Beheshti, Z., 2022. BMPA-TVSSinV: A binary marine predators algorithm using time-varying sine and V-shaped transfer functions for wrapper-based feature selection. *Knowledge-Based Systems*, 252, p.109446
- Cai, H., Qu, Z., Li, Z., Zhang, Y., Hu, X., and Hu, B., 2020. Feature-level fusion approaches based on multimodal EEG data for depression recognition. *Information Fusion*, 59, pp.127-138.
- Dey, N., Borra, S., Ashour, A., and Shi, F., 2018. *Machine Learning in Bio-Signal Analysis and Diagnostic Imaging*. Academic Press, United States. Available from: [https://books.google.iq/books?id=3OR8DwAAQBAJ&dq=Machine+learning+in+bio-signal+analysis+and+diagnostic+imaging:+academic+press.&lr=&hl=en&source=gbs\\_navlinks\\_s](https://books.google.iq/books?id=3OR8DwAAQBAJ&dq=Machine+learning+in+bio-signal+analysis+and+diagnostic+imaging:+academic+press.&lr=&hl=en&source=gbs_navlinks_s) [Last accessed on 2023 Jul 01].
- Fang, C., He, B., Wang, Y., Cao, J., and Gao, S., 2020. EMG-centered multisensory based technologies for pattern recognition in rehabilitation: State of the art and challenges. *Biosensors (Basel)*, 10(8), p.85.
- García, S., Luengo, J., and Herrera, F., 2015. *Data Preprocessing in Data Mining*. Vol. 72. Springer, Germany.
- Hooda, N., Das, R., and Kumar, N., 2020. Fusion of EEG and EMG signals for classification of unilateral foot movements. *Biomedical Signal Processing and Control*, 60, p.101990.
- Jović, A., Brkić, K., and Bogunović, N., 2015. A review of feature selection methods with applications. In: *Paper Presented at the 2015 38<sup>th</sup> International Convention on Information and Communication Technology, Electronics and Microelectronics (MIPRO)*.
- Khan, S.M., Khan, A.A., and Farooq, O., 2019. Selection of features and classifiers for EMG-EEG-based upper limb assistive devices-a review. *IEEE Reviews in Biomedical Engineering*, 13, pp.248-260.
- Krishnan, S., and Athavale, Y., 2018. Trends in biomedical signal feature extraction. *Biomedical Signal Processing and Control*, 43, pp.41-63.
- Kumar, R., Singh, A.K., and Mukherjee, S., 2021. Review of An EMG-Controlled Prosthetic Arm. In: *Computational Methodologies for Electrical and Electronics Engineers*. IGI Global, United States. pp. 85-92.
- Nanga, S., Bawah, A.T., Acquaye, B.A., Billa, M.I., Baeta, F.D., Odai, N.A., and Nsiah, A.D., 2021. Review of dimension reduction methods. *Journal of Data Analysis and Information Processing*, 9(3), pp.189-231.
- Radha, H.M., Abdul Hassan, A.K., and Al-Timemy, A.H., 2023. Enhanced prosthesis control through improved shoulder girdle motion recognition using time-dependent power spectrum descriptors and long short-term memory. *Mathematical Modelling of Engineering Problems*, 10(3), pp.861-870.
- Radha, H.M., Abdul Hassan, A.K., and H Al-Timemy, A., 2022. Classification of different shoulder girdle motions for prosthesis control using a time-domain feature extraction technique. *Aro-the Scientific Journal of Koya University*, 10(2), pp.73-81.
- Shahana, A., and Preeja, V., 2016, Survey on feature subset selection for high dimensional data. In: Paper Presented at the 2016 International Conference on Circuit, Power and Computing Technologies (ICCPCT).
- Singer, G., Anuar, R., and Ben-Gal, I., 2020. A weighted information-gain measure for ordinal classification trees. *Expert Systems with Applications*, 152, p.113375.
- Thabtah, F., Kamalov, F., Hammoud, S., and Shahamiri, S.R., 2020. Least Loss: A simplified filter method for feature selection. *Information Sciences*, 534, p.1-15.
- Udhaya Kumar, S., and Hannah Inbarani, H., 2017. PSO-based feature selection and neighborhood rough set-based classification for BCI multiclass motor imagery task. *Neural Computing and Applications*, 28, p.3239-3258.
- Verma, G.K., and Tiwary, U.S., 2014. Multimodal fusion framework: A multiresolution approach for emotion classification and recognition from physiological signals. *Neuroimage*, 102, p.162-172.
- Voelzke, J., 2015. Weakening the gain-loss-ratio measure to make it stronger. *Finance Research Letters*, 12, p.58-66.

# Investigating the Role of Metoclopramide and Hyoscine-N-Butyl Bromide in Colon Motility

Sleman Y. Omar<sup>1</sup>, Dyari M. Mamand<sup>2</sup>, Rebaz A. Omer<sup>3</sup>, Rzgar F. Rashid<sup>4</sup> and Musher I. Salih<sup>3</sup>

<sup>1</sup>Department of Biology, College of Science, University of Raparin, Sulaymaniyah, Kurdistan Region – F.R. Iraq

<sup>2</sup>Department of Physics, College of Science, University of Raparin, Sulaymaniyah, Kurdistan Region – F.R. Iraq

<sup>3</sup>Department of Chemistry, Faculty of Science and Health, Koya University, Danielle Mitterrand Boulevard, Koya KOY45, Kurdistan Region – F.R. Iraq

<sup>4</sup>Department of Medical Laboratory Science, College of Science, Knowledge University, Erbil, 44001, Kurdistan Region – F.R. Iraq

**Abstract**—Metoclopramide is a treatment for gastroenteritis accompanied by vomiting. Hyoscine-n-butyl bromide as an anticholinergic agent causes inhibition of the acetylcholine (Ach) by acting on muscarinic receptors. The study aims to ascertain how metoclopramide affects Ach-induced cortical motility and also investigates the effects of metoclopramide alone and in combination with hyoscine-n-butyl bromide drug effects on colon motility. In this study, 1 cm of colon tissue width was cut, 2 cm long strips were made, and both sides of the tissue were secured with surgical silk at both ends of isolated bath tissues of isolated organs with (1 g) tension to the suspended instrument that recorded isometric contractions. Tissue fixation is followed by drug addition: Ach, metoclopramide, and hyoscine-N-butyl bromide. The tissue was treated with metoclopramide and hyoscine-n-butyl bromide and excess Caine for 10 min. The results show changes in colon frequency, peak-to-peak, and amplitude levels for metoclopramide, hyoscine-N-butyl, and metoclopramide and hyoscine. A paired T-test statistically analyzes the results. Metoclopramide by itself, as well as in combination with hyoscine-n-butyl bromide, increases colon motility and induces Ach release. In addition, an analysis of the physicochemical characteristics of hyoscine-n-butyl bromide and metoclopramide molecules is conducted. The study includes theoretical calculations of electronic parameters for both protonated and unprotonated forms of these molecules in both gaseous and aqueous environments. These results show the potential use of metoclopramide as a therapeutic option for gastroenteritis with vomiting, warranting additional study, and clinical evaluation. The research also reveals hyoscine-n-butyl bromide and metoclopramide's molecular features by their physicochemical properties.

**Index Terms**—Acetylcholine, Colon, DFT, Hyoscine-N-butyl bromide, Metoclopramide.

## I. INTRODUCTION

Smooth muscle is a type of muscle tissue whose movements are spontaneous and involuntary. Cells have a single nucleus located in the middle of the cell. Smooth muscle is composed of thin and thick fibers so uniform appear cells (Phillips, 1984). Approximately 10% of the human body's muscle composition consists of smooth muscle, found in organs such as the digestive tract, intestines, and bladder. Although the symptoms of smooth muscle contraction resemble those of skeletal muscle contraction, the structural and internal characteristics of smooth muscle fibers differ significantly. Within the stomach and intestines, muscle fibers play a crucial role in aiding the process of digestion and the absorption of nutrients. In the urinary system, it is also responsible for electrolyte balance and regulating the elimination of waste and harmful substances from the body (Williams and Rubin, 2018, Giuseppe, Paul and Hans-Ulrich, 2015). Smooth muscle is present in all arteries and veins and has an important function in controlling blood pressure and tissue respiration. The human colon performs several majestic and important functions, such as fixation of nutrients, utilization of water and electrolytes, storage of stool contents, and timely excretion (Phillips, 1984). The cortical muscle needs to be activated in a well-coordinated and controlled manner for these processes to occur. Moreover, some medications such as metoclopramide can help and support gastric emptying by stimulating smooth muscle activity (Williams and Rubin, 2018, Giuseppe, Paul and Hans-Ulrich, 2015). The ascending colon expands superiorly until coming to a halt at the right colic flexure (hepatic flexure), which is located close to the liver's inferior right edge (Macfarlane, Gibson and Cummings, 1992). The descending colon rises from the

ARO-The Scientific Journal of Koya University  
Vol. XI, No. 2 (2023), Article ID: ARO.11375. 7 pages  
DOI: 10.14500/aro.11375

Received: 03 September 2023; Accepted: 18 October 2023  
Regular research paper: Published: 10 November 2023

Corresponding author's e-mail: musher.ismael@koyauniversity.org  
Copyright © 2023 Sleman Y. Omar, Dyari M. Mamand, Rebaz A. Omer, Rzgar F. Rashid and Musher I. Salih. This is an open access article distributed under the Creative Commons Attribution License.



left colic flexure to the anterior aperture of the true pelvis, where it creates the sigmoid colon, whereas the transverse colon spreads from the right colic flexure to the left colic flexure. An S-shaped tube that extends into the pelvis and terminates at the rectum is formed by the descending colon (Cody, 2001).

Metoclopramide (Fig. 1) is an important antiemetic drug and is also used as a treatment to stimulate stomach movements. Metoclopramide is indicated for the treatment of individuals with gastroesophageal reflux disease and gastrostomy has been associated with metoclopramide, as described by (Maltepe and Koren, 2013). Metoclopramide is characterized as a dopamine (D2) receptor antagonist with a brief half-life, and it possesses dual properties as both a 5HT3 and 5HT4 receptor antagonist. Its effects encompass antiemetic, antidiarrheal, and gastromotor properties (Smith and Laufer, 2014). Meanwhile, the ability of metoclopramide to affect colon motility remains controversial. Metoclopramide enhanced withdrawal frequency in round sections of the human and animal cortex through smooth muscle contraction *in vitro* (Schulze-Delrieu, 1979).

In clinical practice, stomach pains are treated with hyoscine-n-butyl bromide (buscopan) (Fig. 2), which is an antispasmodic agent of the muscle. It is particularly involved in gastrointestinal inflammation, for example, those with leukemia, especially bowel obstruction and irritable bowel syndrome. They are also used effectively as smooth muscle relaxants and anticholinergic and calcium channel blockers and are very effective in treating conditions associated with stomach pain (Samuels, 2009). Known as hyoscine-n-butyl bromide (scopolamine butyl bromide, Buscopan) that is used to treat smooth muscle relaxation and anticholinergic properties (Hasan, et al., 2013). Example of muscle M2 and M3 receptors has a very good effect on them so hyoscine-n-butyl bromide in smooth muscle causes gastrointestinal tract. Hyoscine-N-butylbromide according to its sustained actions

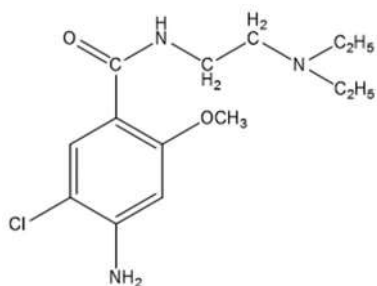


Fig. 1. Chemical formation of metoclopramide is strictly associated with procainamide.

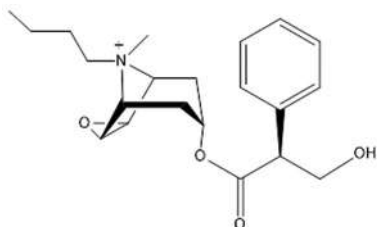


Fig. 2. Chemical formation of hyoscine-N-butyl bromide.

being anti-smooth muscle contraction can inhibit nicotinic receptor in SH-SY5Y cells and human enteric neurons (DeLoid, et al., 2017). In addition, a unique kinematic study of muscle contraction and relaxation was conducted to examine the effects of hyoscine-n-butyl bromide on the digestive system, especially the abdominal colon (Dicken, et al., 2011). To facilitate the long-term preservation of ingested material and promote microbial aging, the complex functioning of the digestive system requires the integration of its kinetics. Therefore, any increase in bowel motility in these areas makes a person more vulnerable (Hasan, et al., 2013).

## II. MATERIALS AND METHODS

### A. Study Design

In the study, for colon tissue recordings, eight animals were utilized from the Firat University Experimental Research Center located in ELAZIĞ, with each animal's tissue strips serving as respective controls. Waited for 10–12 weeks until the mice had reached an average weight ranging between 180 and 200 g. Following the decapitation of the mice, the abdominal area promptly excised and the colon tissues were removed. These colon tissues were subsequently placed in a Petri dish containing Krebs solution. In this study, smooth muscle was focused on the animals that were euthanized without the use of anesthesia to prevent any potential impact on the smooth muscle.

### B. Experimental Setup

The study utilizes a two-chamber organ bath system, enabling the concurrent utilization of two separate smooth muscle strips. This setup comprises several essential components, including the organ bath itself, an amplifier, a recorder, a circulating pump equipped with a thermostat, and a source of oxygen and carbon dioxide. Designed to replicate physiological conditions within a laboratory environment, Krebs's solution incorporates specific elements that support the retention of contractility properties in smooth muscle cells when studied *in vitro*. The Krebs solution is prepared in mmol/L and the pH is adjusted to 7.4 of NaCl: 118, KCl: 4.7 mmol/L, MgSO<sub>4</sub>: 1.2 mmol/L, Glucose: 11.5 mmol/L, CaCl<sub>2</sub>: 2.4 mmol/L, KH<sub>2</sub>PO<sub>4</sub>: 1.18 mmol/L, EDTA: 0.016 mmol/L, and NaHCO<sub>3</sub>: 2.0 mmol/L.

### C. Preparation and Application Protocol of Colon Tissues

After euthanizing male animals, their abdominal areas were carefully opened, and a 1 cm wide incision was made in the colon cecum. A 2 cm long strip of tissue was then meticulously prepared and affixed to both ends of silk sutures, which were embedded at either end of the isolated organ bath. A tension of 1.0 g was applied to the device, which was suspended and used to record isometric contractions. Following this, we allowed 1.5 hours for the colon strips to acclimate. During this time, tissues in the isolated organ baths were subjected to a 15-min treatment with Krebs solution. Once sustained spontaneous contractions became observable, we induced contractions by adding acetylcholine (Ach) at

a dose of 10–4M. Subsequently, we conducted experiments in three distinct protocols after the adjustment period. In the first protocol, we added 35 μM of metoclopramide to the Ach-stimulated colon strips, followed by 15 μM of hyoscine-n-butyl bromide to the same strips after 1 h. Finally, 1 h later, both hyoscine-n-butyl bromide and metoclopramide were simultaneously administered to the Ach-stimulated colon strips. We carefully recorded and analyzed the effects of metoclopramide alone and hyoscine-n-butyl bromide on colonic contractility, with the tissue contraction values before drug administration serving as their respective controls.

*D. Organ Bath Containers*

Divided into two interconnected parts. In addition, the heater contains hot water within the space between these two layers. Inside the inner compartment, you will find Krebs solution along with the smooth muscle strips utilized in the research. The cortex strip is suspended between two hooks, one within the chamber and the other outside, using a silk thread.

*E. Thermocirculator*

It is placed in heat-circulated purified water at 36.7°C. The heated water goes to the area where the Krebs solution is stored and goes to the warehouses in various ways. Because the Krebs solution is stored in two regions, the spaces and reservoirs are intertwined and there are gaps between the layers. The thermostat sensitivity ranges from 36.7 ± 0.1°C. The circulating heated water circulates in this space to keep the environment at body temperature.

*F. Oxygen carbon dioxide source*

A gas mixture required for *in vitro* smooth muscle contraction is ideally made of 95% O<sub>2</sub> and 5% CO<sub>2</sub>. In the isolated organic bath and recording system, the O<sub>2</sub> and CO<sub>2</sub> contents prepared in this mixture were continuously circulated to the chamber.

*G. Statistical Analysis*

Statistical analysis was performed using SPSS software, version 24. For comparison of uptake values (independent test). The significance level used was p = 0.05).

III. RESULTS AND DISCUSSION

*A. Effects of Metoclopramide and Hyoscine-n-butyl Bromide on Frequency of Smooth Muscle Contraction and Relaxation in Colon*

The results provided evidence that all doses of metoclopramide, hyoscine-N-butyl bromide, and a combination of the two were statistically significant (p < 0.05). Specifically, the mean frequency (mean ± SE) of isolated Ach-induced colon strips was 151.5021.38 (n = 8) for 35M metoclopramide, 127.0510.09 (n = 8) for 15 M hyoscine-N-butyl bromide, and 242.3255.00 (n = 8) for 50 M of the mixed concentration. The highest frequency of isolated Ach-induced colon strips was observed in the

combination of metoclopramide and hyoscine-N-butyl bromide, as indicated in Table I.

*B. Effects of metoclopramide and hyoscine-n-butyl bromide on Pile peak (peak-to-peak) on smooth muscle contraction and relaxation in the colon*

Sections of rat colon tissues were tested by treating and administering drugs with 35 μM metoclopramide, 15 μM hyoscine-n-butyl bromide in each drug separately, then by mixing both drugs at 50 μM. The mean and standard deviation error for peak-to-peak of isolated Ach-induced cortical strips from control and treated mice was 62.364.35 (n = 8), 67,225.84 (n = 8), and 73.576.23 (n = 8), respectively. All drugs caused a significant decrease in peak-to-peak static compared with control (35 μM metoclopramide: p < 0.001; 15 μM hyoscine-N-butyl bromide: p < 0.001; 50 μM: p < 0.05). metoclopramide 35 μM showed the most significant reduction compared with other drugs, as shown in Table II.

*C. Effects of Metoclopramide and Hyoscine-n-butyl Bromide on Smooth Muscle Contraction and Relaxation in the Colon*

Results from this analysis are mean ± SE of 48.27 ± 11.42 (n = 8), 46.06 ± 8.75 (n = 8), and 29.28 ± 4.65 (n = 8) for the amplitude of Ach-induced isolated contractile strips, contractile muscle shoulder in rats with 35 μM metoclopramide and 15 μM hyoscine-1. N-butyl bromide we also control 50 μM hyoscine-n-butyl bromide and metoclopramide by combining the two drugs. All of these doses were statistically significant compared with the control, as 35 μM metoclopramide showed the least reduction in muscle contractility (p < 0.05). Relative to the combination of both drugs with 50 μM metoclopramide and hyoscine-n-butyl bromide had the greatest reduction (p < 0.001), as shown in Table III. One dose that captures

TABLE I  
SHOWS MEAN±SE AND P VALUE OF FREQUENCY, BEFORE AND AFTER TREATMENT IN COLON CONTRACTION STRIPS

Dose	Frequency	N	Mean±SE	p
(35μm) Metoclopramide	Before treat.	8	115.352±16.532	0.047
	After treat.		151.507±21.387	
(15 μm) hyoscine-n-butyl bromide	Before treat.	8	98.341±9.220	0.032
	After treat.		127.056±10.093	
(35 μm) metoclopramide+(15 μm) hyosin-n-butyl bromide	Before treat.	8	174.827±38.349	0.03
	After treat.		242.325±55.004	

TABLE II  
THE MEAN±SE AND P VALUE OF PEAK-PEAK, BEFORE AND AFTER TREATMENT IN DUODENUM STRIPS

Dose	Peak-peak	n	Mean±S.E	p
(35 μm) Metoclopramide	Before treat.	8	70.922±3.651	0.0001
	After treat.		62.360±4.359	
(15 μm) hyoscine-n-butyl bromide	Before treat.	8	74.591±6.508	0.001
	After treat.		67.222±5.843	
(35 μm) metoclopramide+(15 μm) hyoscine-N-butyl bromide	Before treat.	8	129.289±48.459	0.004
	After treat.		73.578±6.323	

TABLE III  
MEAN±SE AND P VALUE OF THE AREA, BEFORE AND AFTER TREATMENT  
CONTRACTION 109 COLON STRIPS

Dose	Area	N	Mean±SE	P
(35 µm) Metoclopramide	Before treat.	8	52.246±11.600	0.003
	After treat		48.275±11.432	
(15 µm) hyoscine-n-butyl bromide	Before treat.	8	52.155±8.876	0.001
	After treat.		46.063±8.751	
(35 µm) metoclopramide+ (15 µm) hyoscine -n-butyl bromide	Before treat.	8	35.132±4.647	0.001
	After treat.		29.288±4.659	

the awareness of experts in this sector is metoclopramide. Metoclopramide and its receptor are expressed in multiple organs, mainly the lung, adipose tissue, and female breast (Falcão-Pires and Leite-Moreira, 2005). The results of this study showed that metoclopramide alone and in combination with hyoscine-n-butyl bromide significantly affects slowing of the muscle in vitro in male rats. According to earlier research on the colon, contract happens when intracellular  $Ca^{+2}$  rises as a result of  $Ca^{+2}$  being released from SR and entering the cell through voltage-sensitive  $Ca^{+2}$  channels outside the cell. PLC pathways are used by several hormones that act on receptors, including OT and PGF2 (Catterall, 1988). Two-second messengers are activated by PLC activation. PKC is activated by DAG, which also releases  $Ca^{+2}$  from IP3 SR. Myosin-actin contact causes contraction when the MLCK enzyme is activated by the  $Ca^{+2}$  calmodulin compound, which also causes the phosphorylated of MLC (Sumi, et al., 1991). Actin and myosin levels reduced together with the colon's contraction upon the addition of metoclopramide alone, along with hyoscine-n-butyl bromide in the container (Sumi, et al., 1991). It is well recognized that a variety of regional and global factors influence how the colon constricts when doses are administered. Recent investigations have uncovered the varied ways in which numerous novel hormones and cytokines affect the motility of the colon (Falcão-Pires, et al., 2005). Similar to skeletal muscle, the colon cells are heavily dependent on calcium ions to control their ability to contract. However, because smooth muscle SR does not mature properly, extracellular fluid is mostly responsible for the calcium needed for contraction. Exactly before phasic contractions in the GI,  $Ca^{+2}$  entrance into the cell from the external environment raises intracellular calcium levels (Giannone, et al., 2010). It has been claimed that the availability of exogenous calcium completely determines the amount of stimulation parameters in the colon. It has been demonstrated that if there is no  $Ca^{+2}$  in the environment where duodenal segments are situated, spontaneously contracting ends abruptly and spontaneously activation diminishes. It has been noted that adding  $Ca^{+2}$  to the medium restores activation in response (Hashitani, Brading and Suzuki, 2004). Changes in underdoes levels were statistically significant in male rats. Sequentially, it was observed that the tissue was controlled by the application of 35 µM metoclopramide, 15 µM hyoscine-n-butyl bromide and by combining the drugs with 50 µM metoclopramide and hyoscine-n-butyl bromide. All dose frequencies had

a statistically significant positive effect on slowing muscle contraction. Furthermore, metoclopramide applied alone to compare with hyoscine-n-butyl bromide is preferable, because it increases the effects of metoclopramide on smooth muscle contractility, better than hyoscine-n-butyl bromide. Meanwhile, hyoscine-n-butyl bromide is more effective than the combination of both metoclopramide and hyoscine-n-butyl bromide which significantly reduces smooth muscle contraction at peak-to-peak. However, when hyoscine-n-butyl bromide was added, it showed minimal muscle contractile effects significantly compared to the dosage forms. Furthermore, the effects of metoclopramide and hyoscine-n-butyl bromide on smooth muscle contraction showed the least statistically significant reduction of cortical muscle contraction, compared with each other. Furthermore, the importance of metoclopramide only on muscle contraction in the cortex, the contraction of the region was much less effective than each other.

#### D. Electronic Structure

In drug development, physicochemical qualities are the tangible physical characteristics of molecules related to interactions with various mediums and situations. Physicochemical describes objects that include both physics and chemistry principles, implying that they rely on or are generated by the combined operations of physical and chemical qualities (Mary, et al., 2021). Throughout the study, the B3LYP density functional technique, as implemented in the Gaussian package 09, was used. Basis set 6-311G++(d,p) is used for full optimization of all geometries. With large 6-311++G(d,p) basis sets, the anionic species used in this work were produced (Fig. 3), using the continuous solvation approach, the relaxation energies of the protonated and neutral species were calculated theoretically (Mamand, et al., 2022a, Mamand and Qadr, 2021). The guide-like polarization constant variation was used to implement the polarization constant model (PCM). PCM computations were performed on the gas-phase geometries as single points (without optimization) since this has been demonstrated to produce better results than optimization. Water was given a dielectric constant of = 79.39 (Erdoğan, et al., 2017, Qadr and Mamand, 2021). A characterization of the form and size of the cavity formed by solute molecules in the solvent is required for continuum models.

Numerous novel chemical reactivity descriptors have been proposed to help understand various areas of pharmaceutical sciences such as drug design and prospective ecotoxicological physiognomies of medications. To investigate the properties of these two molecules, some important properties were calculated in this study, which is shown in Tables IV and V.

The features of frontier molecular orbitals are utilized to describe many types of reactions and to calculate the most reactive location in a conjugated system. The HOMO and LUMO energy, as well as their gap, are computed to show a complex's chemical reactivity and biological activity. The HOMO, which is thought to be the outer orbital containing electrons, has a tendency to contribute electrons as e-donors,

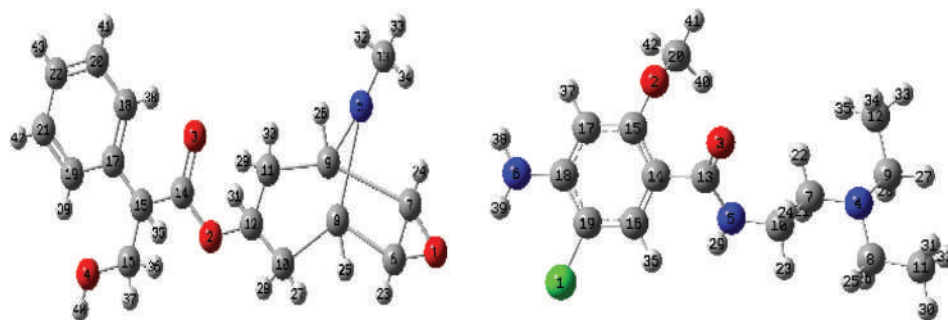


Fig. 3. Optimized molecule structure of hyoscine-n-butyl bromide and metoclopramide is strictly associated with procainamide based on DFT at 6-311G++(d,p) basis set.

TABLE IV  
THEORETICAL CALCULATION OF ELECTRONIC PARAMETERS FOR HYOSCINE-N-BUTYL BROMIDE AT PROTONATED AND NON-PROTONATED SPECIES IN GAS AND AQUEOUS PHASES

A	Non-protonated gas phase	Protonated gas phase	Non-protonated aqueous phase	Protonated aqueous phase
$E_{\text{HOMO}}$ (eV)	-7.20639506	-7.18054423	-5.74922459	-7.91634049
$E_{\text{LUMO}}$ (eV)	-6.570736758	-6.60910483	-5.21996286	-7.42190935
Dipole moment (Debye)	10.6328	17.7123	15.7043	23.1631
Total energy a.u	-1116.8279	-1117.0173	-1116.8121	-1116.8919
Ionization energy (eV)	7.2063	7.1805	5.7492	7.9163
Electron affinity (eV)	6.5707	6.6091	5.2199	7.4219
Band-gap energy (eV)	0.6356	0.5714	0.5292	0.4944
Hardness (eV)	0.31782	0.2857	0.2646	0.2472
Softness (eV)	3.1463	3.4999	3.7788	4.0450
Electronegativity (eV)	6.8885	6.8948	5.4845	7.6691
Chemical potential (eV)	-6.8885	-6.8948	-5.4845	-7.6691
Electrophilicity (eV)	74.6507	83.1909	56.8353	118.955
Nucleophilicity (eV) <sup>-1</sup>	0.0133	0.0120	0.0175	0.0084
Transfer electrons	-0.0794	-0.07142	-0.066	-0.0618
$\Delta E_{\text{Back-donation}}$ (eV)	0.1753	0.1840	2.8632	-1.3533
$\Delta N$	-0.0097	-0.0096	-2.1694	-0.4527
$E_{\text{MEI}}$	68.0799	76.5818	51.6153	111.5339
Nucleophugality	81.8570	90.3715	62.5845	126.8721
Electrphugality	7.2063	7.18054	5.7492	7.9163

TABLE V  
THEORETICAL CALCULATION OF ELECTRONIC PARAMETERS FOR METOCLOPRAMIDE AT PROTONATED AND NON-PROTONATED SPECIES IN GAS AND AQUEOUS PHASES

B	Non-protonated gas phase	Protonated gas phase	Non-protonated aqueous phase	Protonated aqueous phase
$E_{\text{HOMO}}$ (eV)	-7.55089139	-7.42789586	-7.60857955	-5.95902449
$E_{\text{LUMO}}$ (eV)	-6.64529599	-6.89754567	-6.92285227	-4.71328659
Dipole moment (Debye)	8.9873	9.7832	14.6734	18.5133
Total energy a.u	-1320.7281	-1320.440	-1320.4521	-1320.7801
Ionization energy (eV)	7.5508	7.4278	7.6085	5.9590
Electron affinity (eV)	6.6452	6.8975	6.9228	4.7132
Band-gap energy (eV)	0.9055	0.5303	0.6857	1.2457
Hardness (eV)	0.4527	0.2651	0.342	0.6228
Softness (eV)	2.2084	3.771093238	2.9166	1.6054
Electronegativity (eV)	7.0980	7.162720765	7.2657	5.3361
Chemical potential (eV)	-7.098	-7.1627	-7.2657	-5.3361
Electrophilicity (eV) ( $\omega$ )	55.6351	96.7371	76.9848	22.8575
Nucleophilicity (eV) <sup>-1</sup>	0.0179	0.0103	0.0129	0.0437
Transfer electrons	-0.1131	-0.0662	-0.0857	-0.1557
$\Delta E_{\text{Back-donation}}$ (eV)	-0.10831	-0.3068	-0.3874	1.33562
$\Delta N$	-0.00531	-0.0249	-0.05148	-1.1111
$E_{\text{MEI}}$	48.9898	89.8396	70.0620	18.1442
Nucleophugality	63.1860	104.1650	84.5934	28.8166
Electrphugality	7.5508	7.4278	7.6085	5.9590

and so the ionization potential is necessarily connected to the energy of the HOMO. LUMO, on the other hand, may accept electrons, and the LUMO energy is directly related to electron affinity. A high value indicates electron donation and also a high LUMO value causes the molecule to tend to accept electrons. Both molecules have the highest values for HOMO in water, which proves that the ability of these two drugs to donate electrons will be greater. A molecule with a smaller HOMO-LUMO gap is more polarizable and has low kinetic stability and strong chemical reactivity. The softness, therefore, correlates to the HOMO-LUMO gap. The softer the molecule or multicomponent crystal, the narrower the HOMO-LUMO energy gap. Figs. 4 and 5 illustrate the HOMO-LUMO energy gaps of hyoscine-n-butyl bromide has a lower bandgap energy than metoclopramide (Mamand, et al., 2022b, Omar, et al., 2023). The ( $\eta$ ) defines the conflict toward the distortion of the electron cloud of chemical systems in the presence of minor disturbances encountered throughout the chemical process (Chattaraj and Roy, 2007, Parlak, et al., 2022, Omer, Koparir and Ahmed, 2022). Electrophilicity ( $\omega$ ) is

defined as a measure of the sensitivity of chemical species to accept electrons. Low values of ( $\omega$ ) indicate the presence of a good nucleophile; whereas, higher values indicate the presence of good electrophiles. The best electrophilic molecule is in the state, where the first molecule has the highest electrophilicity in non-protonated gas and protonated water. Electrophilicity is a reactivity descriptor that may be used to define the toxicity of these compounds. It also includes a direct link between reaction rates and the ability to determine an electrophile's function or capacity. The inhibitor (A) had higher electrophilicity indices (74.65, 83.19, 56.83, and 118.95 eV) in gas and aqueous phases for protonating and non-protonated states than metoclopramide (55.63, 96.73, 76.98, and 22.85 eV), indicating that they have more biological activity. In addition, the calculations revealed that the hyoscine butyl bromide molecule has a low electronegativity (6.88, 6.89, 484, and 7.66 eV) in gas and aqueous phases for protonating and non-protonated states, which increases the electron releasing power of metoclopramide to the enzyme, and as a result, increases metoclopramide capacity to be oxidized.

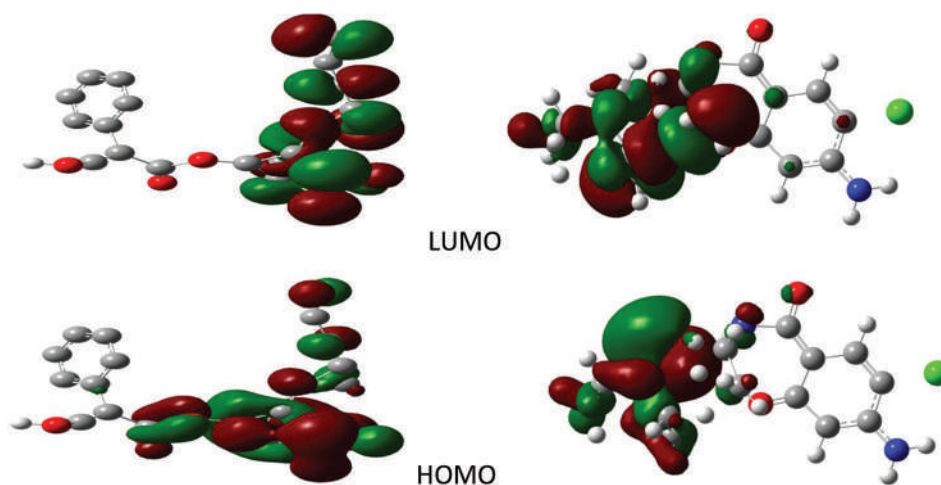


Fig. 4. HOMO and LUMO of hyoscine-n-butyl bromide and metoclopramide compounds in the gas phase.

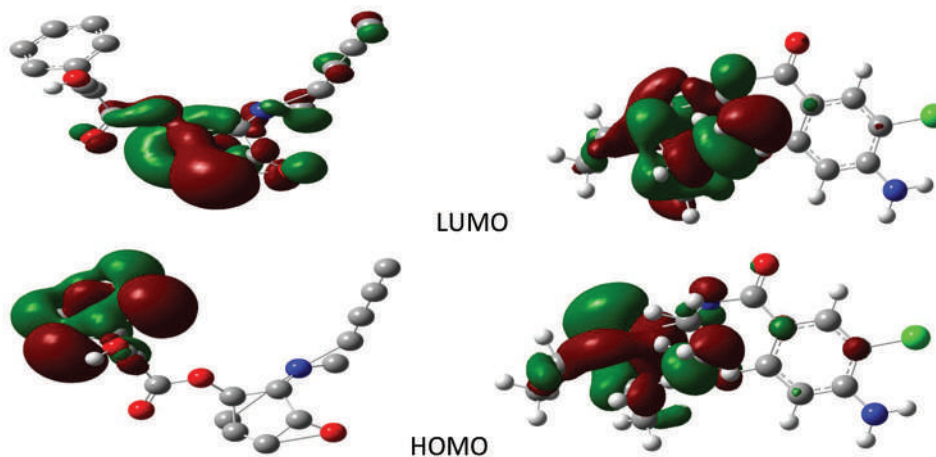


Fig. 5. HOMO and LUMO of hyoscine-n-butyl bromide and metoclopramide compounds in the aqueous phase.



## IV. CONCLUSION

The impact of metoclopramide on the contractile and relaxant responses of colon muscle induced by Ach. To achieve this, we utilized a novel experimental setup, involving 1 cm wide and 2 cm long incisions in the colon tissue attached to organ bath tissues. Ach, metoclopramide, hyoscine-n-butyl bromide, and a combination of metoclopramide and hyoscine-n-butyl bromide were sequentially applied to the colon tissue. This allowed us to observe and analyze changes in frequency, peak-to-peak, and amplitude in the muscle contractions. Using statistical analysis a paired sample T-test, providing valuable insights into the effects of metoclopramide on colon muscle responses to Ach stimulation. The results showed that metoclopramide, hyoscine-n-butyl bromide, and the combination of the two affected colonic contractility by stimulating Ach and increasing intestinal motility. Metoclopramide is thus used in the treatment of gastroenteritis. Physicochemical properties of hyoscine-n-butyl bromide and metoclopramide molecules metoclopramide bromide were found to have a higher electrophilicity index and higher electronegativity than hyoscine-n-butyl bromide, indicating that it has more biological activity and potential to deform more effectively oxidized. Therefore, it can be concluded that metoclopramide bromide is the best molecule for an anticholinergic agent.

## REFERENCES

- Catterall, W.A., 1988. Structure and function of voltage-sensitive ion channels. *Science*, 242, pp.50-61.
- Chattaraj, P.K., and Roy, D.R., 2007. Update 1 of: electrophilicity index. *Chemical Reviews*, 107, pp.PR46-PR74.
- Cody, H.S., 2001. *Sentinel Lymph Node Biopsy*. CRC Press, United States.
- Deloid, G.M., Wang, Y., Kapronezai, K., Lorente, L.R., Zhang, R., Pyrgiotakis, G., Konduru, N.V., Ericsson, M., White, J.C., and De La Torre-Roche, R., 2017. An integrated methodology for assessing the impact of food matrix and gastrointestinal effects on the biokinetics and cellular toxicity of ingested engineered nanomaterials. *Particle and Fibre Toxicology*, 14, p.40.
- Dicken, B.J., Sergi, C., Rescorla, F.J., Breckler, F., and Sigalet, D., 2011. Medical management of motility disorders in patients with intestinal failure: A focus on necrotizing enterocolitis, gastroschisis, and intestinal atresia. *Journal of Pediatric Surgery*, 46, pp.1618-1630.
- Erdoğan, Ş., Safi, Z.S., Kaya, S., Işın, D.Ö., Guo, L., and Kaya, C., 2017. A computational study on corrosion inhibition performances of novel quinoline derivatives against the corrosion of iron. *Journal of Molecular Structure*, 1134, pp.751-761.
- Falcão-Pires, I., and Leite-Moreira, A.F., 2005. Apelin: A novel neurohumoral modulator of the cardiovascular system. Pathophysiologic importance and potential use as a therapeutic target. *Revista Portuguesa de Cardiologia*, 24, pp.1263-1276.
- Falcao-Pires, I., Vasconcelos, M., Magalhaes, J., Bras-Silva, C., and Leite-Moreira, A., 2005. 234 Distinct contractile effects of apelin in intact hearts and isolated papillary muscles. *European Journal of Heart Failure Supplements*, 4, pp.48-49.
- Giannone, F., Malpeli, G., Lisi, V., Grasso, S., Shukla, P., Ramarli, D., Sartoris, S., Monsurro, V., Krampera, M., and Amato, E., 2010. The puzzling uniqueness of the heterotrimeric G15 protein and its potential beyond hematopoiesis. *Journal of Molecular Endocrinology*, 44, pp.259-269.
- Giuseppe, C., Paul, J., and Hans-Ulrich, I., 2015. Use of nitrates in ischemic heart disease. *Expert Opinion on Pharmacotherapy*, 16, pp.1567-1572.
- Hasan, N., Chaiham, M., Khan, S., Khalid, H., Sher, N., Siddiqui, F.A., and Siddiqui, M.Z., 2013. Dual wavelength RP-HPLC method for simultaneous determination of two antispasmodic drugs: An application in pharmaceutical and human serum. *Journal of Analytical Methods in Chemistry*, 2013, p.297285.
- Hashitani, H., Brading, A.F., and Suzuki, H., 2004. Correlation between spontaneous electrical, calcium and mechanical activity in detrusor smooth muscle of the guinea-pig bladder. *British Journal of Pharmacology*, 141, pp.183-193.
- Macfarlane, G., Gibson, G., and Cummings, J., 1992. Comparison of fermentation reactions in different regions of the human colon. *Journal of Applied Bacteriology*, 72, pp.57-64.
- Maltepe, C., and Koren, G., 2013. The management of nausea and vomiting of pregnancy and hyperemesis gravidarum-a 2013 update. *Journal of Population Therapeutics and Clinical Pharmacology*, 20, pp.e184-e194.
- Mamand, D.M., and Qadr, H.M., 2021. Comprehensive spectroscopic and optoelectronic properties of bbl organic semiconductor. *Protection of Metals and Physical Chemistry of Surfaces*, 57, pp.943-953.
- Mamand, D.M., Awla, A.H., Anwer, T.M.K., and Qadr, H.M., 2022a. Quantum chemical study of heterocyclic organic compounds on the corrosion inhibition. *Chimica Techno Acta*, 9, p.20229203.
- Mamand, D.M., Rasul, H.H., Omer, P.K., and Qadr, H.M., 2022b. Theoretical and experimental investigation on ADT organic semiconductor in different solvents. *Condensed Matter and Interphases*, 24, pp.227-242.
- Mary, Y.S., Mary, Y.S., Armaković, S., Armaković, S.J., Yadav, R., Celik, I., Mane, P., and Chakraborty, B., 2021. Stability and reactivity study of biomolecules brucine and colchicine towards electrophile and nucleophile attacks: Insight from DFT and MD simulations. *Journal of Molecular Liquids*, 335, p.116192.
- Omar, R.A., Koparir, P., Sarac, K., Koparir, M., and Safin, D.A., 2023. A novel coumarin-triazole-thiophene hybrid: Synthesis, characterization, ADMET prediction, molecular docking and molecular dynamics studies with a series of SARS-CoV-2 proteins. *Journal of Chemical Sciences (Bangalore)*, 135, p.6.
- Omer, R.A., Koparir, P., and Ahmed, L., 2022. Theoretical determination of corrosion inhibitor activities of 4-allyl-5-(pyridin-4-yl)-4H-1, 2, 4-triazole-3-thiol-thione tautomerism. *Indian Journal of Chemical Technology (IJCT)*, 29, pp.75-81.
- Parlak, A.E., Omar, R.A., Koparir, P., and Salih, M.I., 2022. Experimental, DFT and theoretical corrosion study for 4-(((4-ethyl-5-(thiophen-2-yl)-4H-1, 2, 4-triazole-3-yl) thio) methyl)-7, 8-dimethyl-2H-chromen-2-one. *Arabian Journal of Chemistry*, 15, p.104088.
- Phillips, S., 1984. Functions of the large bowel: an overview. *Scandinavian Journal of Gastroenterology Supplement*, 93, pp.1-12.
- Qadr, H.M., and Mamand, D.M., 2021. Molecular structure and density functional theory investigation corrosion inhibitors of some oxadiazoles. *Journal of Bio-and Tribo-Corrosion*, 7, p.140.
- Samuels, L.A., 2009. Pharmacotherapy update: Hyoscine butylbromide in the treatment of abdominal spasms. *Clinical Medicine Therapeutics*, 1, p.S1134.
- Schulze-Delrieu, K., 1979. Metoclopramide. *Gastroenterology*, 77, pp.768-779.
- Smith, H.S., and Laufer, A., 2014. Opioid induced nausea and vomiting. *European Journal of Pharmacology*, 722, pp.67-78.
- Sumi, M., Kiuchi, K., Ishikawa, T., Ishii, A., Hagiwara, M., Nagatsu, T., and Hidaka, H., 1991. The newly synthesized selective Ca<sup>2+</sup> calmodulin dependent protein kinase II inhibitor KN-93 reduces dopamine contents in PC12h cells. *Biochemical and Biophysical Research Communications*, 181, pp.968-975.
- Williams, D.M., and Rubin, B.K., 2018. Clinical pharmacology of bronchodilator medications. *Respiratory Care*, 63, pp.641-654.

# The Local Anesthetic Activity of *Lavandula angustifolia* and *Eugenia caryophyllata* Essential Oils

Subasini Uthirapathy

Department Pharmacology, Faculty of Pharmacy, Tishk International University,  
Erbil, Kurdistan Region-F.R. Iraq

**Abstract**—Previous studies show that *Lavandula angustifolia* (lavender) and *Eugenia caryophyllata* (clove) essential oils can help relieve dental pain. Clove oil and lavender oil were tested as topical anesthetics in this study on rabbits, and their effects and likely mechanisms of action were analyzed. Clove oil and lavender oil were extracted by hydrodistillation using a Clevenger-setup apparatus. Topically applying lidocaine, clove oil, or lavender oil topically all significantly reduced corneal sensitivity. The sensitivity of the cornea was successfully reduced by treatments consisting of lidocaine at a concentration of 0.5%, 25 µg of clove oil, and 50 µg of lavender oil. When clove oil is applied topically to the cornea, it produces effects similar to those of a local anesthetic due to the involvement of the cholinergic system. To achieve the desired effect of producing local anesthesia in the cornea of the rabbit, lidocaine, clove oil, and lavender oil were applied topically to the animal. A noticeable local anesthetic effect was produced when sub-anesthetic doses of lidocaine were combined with sub-anesthetic doses of lavender or clove oil.

**Index Terms**—Clove oil, Corneal reflex, *Eugenia caryophyllata*, *Lavandula angustifolia*, Lavender oil, Lidocaine, Local anesthesia.

## I. INTRODUCTION

To evaluate anesthetic activity *in vivo* model, one uses the rabbit conjunctival reflex test. The antispasmodic qualities of certain herbal plants, such as “*Lavandula angustifolia* M, *Mentha piperita* M, *Salvia officinalis* M, *Eugenia caryophyllus* M, and *Foeniculum vulgare* M, support their historical use for digestive system diseases” (Koulivand, Khaleghi Ghadiri and Gorji, 2013; Tschiggerl and Bucar, 2010). The chemical phytoconstituents in essential oils are responsible for this biological process. Simpson (2019) reported using it to treat stomach cramps. Numerous *in vitro* investigations on the antispasmodic effects of essential oils derived from the aforementioned medicinal plants. They convert to prevent the contractions brought on by different

spasmogens by acting pharmacologically, which results in an unspecific antagonistic response. Essential oils’ non-polar components may interact well with the plasma membrane’s lipid bilayer. Essential oil blocks the neurotransmission by decreasing Ca<sup>2+</sup> inflow or stopping the increase in Na<sup>+</sup> permeability (Bikmoradi, et al., 2017).

The more than 100 lavender components include “linalool, perillyl alcohol, linalyl acetate, camphor, limonene, tannin, triterpene, coumarin, cineole, and flavonoids” (Wilson, et al., 2021). These chemicals work by dose-dependently binding to glutamate, a key central nervous system excitatory neurotransmitter. Linalool successfully lowers mouse motor activity. The hypnotic and anticonvulsant properties of lavender are attributed to GABA amplification. Menthol is an analgesic and local anesthetic, whereas eugenol stabilizes membranes (Zheljazkov, et al., 2013; Silva, et al., 2015).

These methods of anesthesia involve local anesthetics. Surface anesthetic anesthetizes skin, eyes, ears, and throat. Block or infiltration anesthesia: Nerve endings are sedated by subcutaneous injection of the drug. Nerve block, often called condition block, involves delivering drugs near a nerve. Drugs are injected into the subarachnoid area to provide spinal anesthesia. Epidural anesthesia involves injecting drugs outside the dura (Batiha, et al., 2023).

*Eugenia caryophyllata* is also known as clove. It is a member of the *Myrtaceae* family and is 20 m tall. It is growing in “Madagascar, Tanzania, Sri Lanka, Brazil, and Indonesia” (Arung, et al., 2011). As an oral antibacterial and for treating toothaches, joint pains, and headaches, clove oil and its essential oil have long been utilized in aromatherapy (Chaieb, et al., 2007; Dalai, et al., 2014). The main component of clove essential oil, eugenol, also possesses a variety of biological activities, such as antiallergic (Chioca, et al., 2013), antifungal (Pinto, et al., 2009), and antioxidant (Gülçin, Elmastas and Aboul-Enein, 2012) capabilities. For fish and amphibians, the essential oil of *E. caryophyllata* and its principal constituent, eugenol, has been demonstrated to be a safe, effective, and inexpensive anesthetic (Rosenthal, Baran and Jacobs, 2009). In addition, eugenol’s analgesic activity in several pain models has been thoroughly demonstrated (Lionnet, Beaudry and Vachon, 2010; Daniel, et al., 2009; Park, et al., 2011; Properzi, et al., 2013).

One of the most often studied therapeutic herbs is lavender, also known as *Lavandula*, which belongs to the

ARO-The Scientific Journal of Koya University  
Vol. XI, No. 2 (2023), Article ID: ARO.11426. 6 pages  
DOI: 10.14500/aro.11426

Received: 04 October 2022; Accepted: 28 October 2023

Regular research paper: Published: 10 November 2023

Corresponding author’s e-mail: subasini.uthirapathy@tiu.edu.iq

Copyright © 2023 Subasini Uthirapathy.

This is an open access article distributed under the Creative Commons Attribution License.



*Lamiaceae* family (Prusinowska and Śmigielski, 2014). The purple-blue flower of the shrub has been used for centuries to treat various illnesses. “*L. angustifolia*, *Lavandula latifolia*, *Lavandula stoechas*, and *Lavandula intermedia*” are among the most commonly utilized species of lavender (Tschiggerl and Bucar, 2010). It is grown worldwide for commercial use. It thrives in the Indian states of Himachal Pradesh, Uttar Pradesh, and Kashmir Valley. It is recognized to have calming, anti-inflammatory, anti-nociceptive, antibacterial, and antioxidant properties (Shaw, et al., 2007; Kritsidima, Newton and Asimakopoulou, 2010).

A phytochemical investigation found that lavender essential oils contain “linalool, linalyl acetate, 8-cineole-ocimene, terpinen-4-ol, and camphor.” This structure underpins attribute mechanisms (Jianu, Pop and Gruia, 2013). Herbal therapies such as lavender essential oils can treat antibiotic resistance, invasive procedures, side effects, and medication addiction. Due to these properties and medication tolerance, lavender is an effective therapeutic herb (de Rapper, Viljoen and Vuuren, 2016).

If pain comes from the cornea, it would be very strong and make it hard to do anything. Corneal nociceptor density is approximately 35 times that of dental pulp and 500 times that of skin (Rosenthal, Baran and Jacobs, 2009). Polymodal nociceptors react to high-threshold touch, chemicals, cold, heat, and protons. Dry eye, post-herpetic neuralgia, trigeminal neuralgia, polluted settings, contact lens wear, and recent refractive surgery can all induce eye pain (Hirata and Meng, 2010). Acute and chronic trigeminal neuralgia is difficult to treat due to a lack of knowledge (Miranda, Sierralta and Prieto, 2009).

When adverse effects are considered, herbal therapies outperform opioids and non-steroidal anti-inflammatory medications. Dentistry uses *E. caryophyllata* clove bud oil as a mouth antibacterial, topical anesthetic, and painkiller. In this study, we investigated the potential local anesthetic activity of the essential oils of *L. angustifolia* and *E. caryophyllata*. Linalyl acetate and linalyl linalool are the two main phytoconstituents in this lavender oil. Three major phytoconstituents include eugenol, eugenol acetate, and caryophyllene of clove oil. Two essential oils were investigated to determine their possible local anesthetic activity ratio. The corneal touch thresholds (CTT) and duration of the local anesthetic were also measured after topical instillation of clove oil and lavender oil alone and in combination with lidocaine (Ait Said, et al., 2015). Therefore, the aim of the study was to investigate the local anesthetic effects of clove oil and lavender oil on rabbit corneas.

## II. MATERIALS AND METHODS

### A. Animals

All study methods and animal care practices are approved by the current laboratory animal care recommendations (TIU/FP/2022/07, dated December 15, 2022) and ethical principles for researching conscious animal pain at the Department of Pharmacology Animal House at Tishk International University in Erbil (Pathan, et al., 2020). Randomly selected adult male rabbits weighing 630–660 g were kept in plastic

cages with free access to food and water over a 12-h cycle with temperature control of 22°C (three rabbits per group). All experiments were carried out between 10 am and 4 pm. Each rabbit received topical solution 3 days between trials.

### B. Drugs

Normal saline (0.9% of sodium chloride) was used to dissolve all drugs lidocaine (xylocaine) eye drops, each unit contains approximately 0.5 mL eye drops solution of lidocaine hydrochloride 4% w/v (20 mg), and samples (clove and lavender oil isolated pure essential oil from pharmacognosy laboratory) of oil used in topical studies. Tween 80 (more lipophilic nature) and saline (0.5% v/v) were used as a solvent to create an emulsion of clove oil and lavender oil. Tween 80 is a non-ionic surfactant and emulsifier that emulsifies clove oil and lavender in saline. The pH of each solution was adjusted to 7.4. Before apply.

### C. Extraction of Plant Material and Essential Oil (Figs. 1 and 2)

The buds of *E. caryophyllata* (clove) purchased from local market and *L. angustifolia* (lavender) leaves collected from a TIU campus garden in Erbil, Iraq, and authenticated by Dr. Javed Ahmad, a Pharmacognist, Faculty of Pharmacy, Tishk International University, Erbil, Iraq. The dried clove buds and the fresh lavender leaves were used to extract the essential oil. Hydrodistillation of clove buds and lavender leaves in a Clevenger apparatus for 3 h resulted in a 3 % (v/w) yield of essential oil. The extracted essential oil was dried over anhydrous sodium sulfate until all traces of water were removed and then stored in dark glass bottles at 4°C (Ali, Rozhan and Subasini, 2023).

### D. Methodology

Handle rabbits with caution. Remove the lashes from both eyes. To infuse medications into the eye, use the pouch approach. Make a tiny pouch by pinching the lower eyelid. Using a dropper, add one to two drops of saline/drug. Keep the lower eyelid in contact with the conjunctiva for 1–2 min by pulling it upward. After giving the drug, press the medial canthus for 5 s. Maintain one eye as the control (right or left) and the other as the test. Use saline in the control eye and



Fig. 1. Clove fruits.

medication in the test eye. The criteria include pupil size, light reflex, touch reflex, and corneal reflex (Farazifard, et al., 2005).

### E. Pupil Size Evaluation

Each pupil's diameter should be measured. This can be measured with a pupillometer made of hard paper. Cut a firm piece of paper to the length of a 5-inch ruler. Then, at the lowest to highest of millimeter diameter, cut holes in it. It could be started with 1 mm and work our way up to 10 mm and measured with a simple scale (Fig. 3a). It was tough to force the rabbits' eyes open. As a result, measuring diameter becomes simple with a pupillometer (Fig. 3b). Place the pupillometer in close to the rabbit's eye so it can see the pupil. Match the hole on the pupillometer to the size of the pupil and record the pupil's diameter in millimeters on the corresponding hole (Zagon, et al., 2014).

### F. Examining the Light Reflex

A torch was used to test light reflex. This experiment required the use of a pencil torch. Always bring the light from the side (behind) to the front. The light was not placed from the front side of the rabbits. When light was flashed into the eye, the diameter of the pupil changed. There is no decrease or increase in pupillary diameter, noted down the completed three readings (Kim, et al., 2013).

### G. CTT Evaluation

Fine cotton filaments or wick was used to test it so that no projecting cotton component in the manufacture of the filaments. With the tip of a cotton filament, touch the cornea's periphery. Always bring the cotton filament from the side forward (back). Cotton filament and our hands should not be visible to rabbits. During the testing period, the rabbits were held and restrained by hand with care. Using a set of calibrated cotton filaments, animal withdrawal reactions to corneal touch, such as blinking and head withdrawal (abrupt head movement), were counted as positive. In five tests on the control and test eye, the CTT was characterized as the filament force that triggered at least three withdrawal responses (Zagon, et al., 2014; Kim, et al., 2013).

### H. Dose-dependent study of CTT

The experiment was carried out using modified approach of Pathan, et al. (2020). For the evaluation of corneal



Fig. 2. Lavender leaves in TIU campus garden.

mechanical sensitivity, behavioral corneal responses were used to lower corneal sensitivity in a dose-dependent manner. In brief, a conjunctival response was elicited by stimulating the rabbit eye's external side with a corneal touch. The increased number of stimuli required to cause palpebral closure indicates that the medicines deposited in the rabbit eye sac have local anesthetic activity. Vehicle (Tween 80, 0.5% dissolved in saline), clove oil (50, 100  $\mu\text{L}/\text{eye}$ ), lavender oil (50 and 100  $\mu\text{L}/\text{eye}$ ), lidocaine (0.5% and 2%, 40  $\mu\text{L}/\text{eye}$ ), and combination of clove oil (25  $\mu\text{L}$ ) or lavender oil (25  $\mu\text{L}$ ) with lidocaine (0.5%, 40  $\mu\text{L}/\text{eye}$ ) were topically applied to the cornea in two consecutive 20  $\mu\text{L}$  volumes and rabbits gently restrained by hand to prevent wiping of solution for 1 min in each application. After corneal solution instillation, corneal reflexes were assessed 5–8 min later (Bates, et al., 2010).

### I. Study Depending on the Time of the Duration of Local Anesthetic

In the time-dependent study, the most prominent cotton filament (2  $\mu\text{L}$ ) was used to evaluate the duration of corneal anesthesia induced by clove oil (100  $\mu\text{L}$ ), lavender oil (100  $\mu\text{L}$ ), lidocaine 2%, and combinations of clove oil (25  $\mu\text{L}$ ) or lavender oil (25  $\mu\text{L}$ ) with lidocaine. Five minutes



Fig. 3. Observations for clove oil and lavender oil topical applications. (a) Rabbits gently restrained by hand. (b) Instill one to two drops of a drug in it using a dropper (essential oil). (c) Applications of saline for the control eye. (d) Assessing corneal touch threshold. (e) Evaluation of the length of the corneal anesthesia induced by clove and lavender oils. (f) Application of lidocaine drug. (g) Observed how the diameter of the pupil changed when light was shone into the eye. (h) There is no change in pupillary diameter of any kind.

before, 5 min after, 10 min after, 15 min after, 25 min after, and 40 min after applying each solution topically, corneal touch tests were performed. Caution: Avoid touching the cornea's central portion, since it might cause corneal ulcers or opacities. This can cause blindness, as the central part of the cornea is primarily responsible for vision (Tamaddonfar, et al., 2008).

*J. Statistical Analysis*

All experimental results are given as the Mean ± Standard Deviation. GraphPad - "One-way analysis of variance followed by Dunnett's multiple comparisons test was performed using GraphPad Prism version 10.0.  $p < 0.05$  was considered statistically significant.

III. RESULTS AND DISCUSSION

The iris of the eye is made up of circular and radial muscle fibers. The parasympathetic cholinergic nerve system sends nerve impulses to the circular fibers, which then make the constrictor pupillae contract. The sympathetic adrenergic nerve system sends nerve signals to the radial and dilator pupillae. When sympathetic and parasympathetic nerves are stimulated, mydriasis and miosis happen. However, when these nerves are paralyzed, the opposite effect happens. The above effects can be induced by drugs that affect autonomic nervous systems (Kim, et al., 2013).

It manifests either by interfering with the parasympathetic supply to the eye by activating the sympathetic system excessively. Alpha ( $\alpha_1$ ) selective action causes pupil dilation by stimulating the dilator muscles. They are used to reduce painful ciliary spasms, diagnose Horner's syndrome, examine the retina and deeper structures, and treat chronic simple glaucoma, and corneal ulcers, and retinoscopy in children and elderly patients in particular. Constrict pupil,  $M_3$ -specific action by tightening iris sphincter muscles or by preventing the activity of the enzyme acetylcholinesterase, facilitates the action of acetylcholine at transmitter sites (Uthirapathy, 2023; Zagon, et al., 2014). These mechanisms improve drainage of the aqueous humor and lower intraocular pressure. These medications treat wide-angle glaucoma, xerostomia, and xerostomia during cataract and anterior chamber surgeries. Khalilzadeh, Hazrati, and Vafaei Sayah (2014) reported that the effects of miotics, which are parasympathetic drugs such as pilocarpine, physostigmine, and atropine, and mydriatics, which are sympathetic drugs such as amphetamine, epinephrine, and phenylephrine. When compared to saline

solution, local anesthetics such as cocaine and lignocaine have different effects on corneal reflexes and light perception, according to Hirata and Meng, (2010). Local anesthetics primarily block  $Na^+$  channels, which affects depolarization, and stops the initiation and propagation of action potentials (Dohi, Terasaki and Makino, 2009). Membrane stabilizing effects influence the depolarization process, and subsequently, the failure of the propagation potential. When a cotton wick is touched to the cornea of a rabbit's eye, the corneal reflex takes place. A rabbit's eyelids closing is referred to as a positive corneal reflex, and keeping them open is called to as a negative corneal reflex (Park, et al., 2009).

*A. The Local Anesthetic Activity of Topical Clove Oil, Lavender Oil, and Lidocaine*

Table I shows that the CTT was noticed to be 0.3 g of calibrated force in the cornea that had received a vehicle treatment (Fig. 3c). In the dose-dependent study, clove oil increased at doses of 50  $\mu$ L/eye (Table I,  $p < 0.05$ ) and CTT at 0.5 g of calibrated force. At doses of 50 and 100  $\mu$ L/eye, clove oil significantly produced a local anesthetic effect compared to the vehicle group (Table I,  $p < 0.001$ ) (Fig. 3d). Lavender oil raised the CTT at doses of 50 and 100  $\mu$ L/eye to 1 and 2 g calibrated force, respectively (Fig. 3e). In contrast to the vehicle group, topical lidocaine application at a dose of 2% (40  $\mu$ L/eye) but not 0.5% resulted in a highly effective local anesthetic effect (Table I,  $p < 0.001$ , Fig. 3f). Furthermore, when low doses of lavender or clove oil were mixed with low doses of lidocaine, there was a significant (Table I,  $p < 0.001$ ) local anesthetic effect for all forces tested. However, this effect was insignificant in control group.

Clove oil and lavender oil were used as local anesthetic because the test drug's corneal reflex loss indicates a corneal sensation loss (Fig. 3g and h). In addition, for all forces tested, a significant (Table I,  $p < 0.001$ ) local anesthetic effect was generated, when low doses of lavender or clove oil were combined with low doses of lidocaine (Dohi, Terasaki and Makino, 2009). The same doses of lavender oil and clove also allow an increase in the number of stimuli to induce conjunctival reflex (Zagon, et al., 2014). This was in contrast to the vehicle group. Clove oil and lavender oil were used as a local anesthetic because the test drug's loss of corneal reflex indicates a loss of corneal sensation.

Thin A-delta and C-type fibers on the corneal surface respond to painful chemical, mechanical, and thermal stimuli (Hirata and Meng, 2010). Clove oil's ability to relieve acute

TABLE I  
EFFECT OF DRUGS ON RABBITS EYE

Drugs	Light reflex		Corneal reflex		Pupil size mm (mydriasis)	
	Right (control) eye	Left (test eye)	Right	Left	Right	Left
Clove oil	+++	---	+++	+	11	14.2
Lavender oil	+++	---	+++	+	10.7	13.5
Lidocaine	+++	++	+++	---	No change	No change
Clove oil+lidocaine	+++	+	+++	---	11	15.6
Lavender oil+lidocaine	+++	+	+++	---	12	13.7

corneal pain depends on its cholinergic activity because the muscarinic cholinergic receptor antagonist atropine completely blocks its effect. *In vitro* studies have shown that clove oil and eugenol have potent anti-acetylcholinesterase properties (Dohi, Terasaki and Makino, 2009). Clove oil and eugenol's anti-acetylcholinesterase activity may also be in line with the mechanisms underlying their antinociception, as it has been shown that cholinergic system activation by muscarinic agonist or cholinesterase inhibitors has analgesic effects (Pan, et al., 2011; Uthirapathy and Tahir, 2021).

The findings of the present study demonstrated that lidocaine (as a positive control) and clove oil applied topically decreased the corneal mechanical sensitivity of rabbits. Clove oil and lavender were applied in high doses to produce corneal anesthesia patterns comparable to lidocaine's anesthetic pattern. When a low dose of lidocaine was combined with a low dose of clove oil or lavender oil, it worked well as a local anesthetic. When clove oil or lavender oil with lidocaine is given at the same time, it appears that a concur effect is what causes their local anesthetic effects. In contrast to the combination of lidocaine and a low dose of lavender oil, the lidocaine sub-anesthetic dose and clove oil generated an enduring anesthesia (Kajjari, Joshi and Hugar, 2022); the presence of other substances alongside eugenol in clove essential oil may be cause of this effect.

In the composition of clove oil, Eugenol (54.86%) and  $\beta$ -caryophyllene (20.19%) were exceptionally high in clove oil (Khalilzadeh, Hazrati and Vafaei Sayah, 2014). Eugenol, a phenylpropane derivative, is a popular local anesthetic, analgesic (Properzi, et al., 2013; Park, et al., 2011), and anti-inflammatory (Nardarajah, Dhanraj and Jain, 2018). Eugenol may modulate analgesia and local anesthesia by inhibiting voltage-gated Na<sup>+</sup> channels (Park, et al., 2006). Eugenol may inhibit pain by activating rodent and human trigeminal ganglion neurons' transient receptor potential ankyrin subtype 1 (TRPA1) receptors (Chung, et al., 2014). The effects of local anesthetics like lidocaine, like eugenol, inhibit voltage-gated Na<sup>+</sup> channels and activate TRPV1 (Leffler, et al., 2008). In the rabbit conjunctival reflex test, topical caryophyllene had a strong local anesthetic effect (Ahmed, Altaei and Ahmed, 2020). *L. angustifolia* essential oil has antimuscarinic effects. In the neuromuscular junction of the rabbit, linalool has been shown to shorten the time that the channel is open and inhibit acetylcholine release. These findings suggest that the local anesthetic properties of lavender and clove oils may result from their phytochemicals' capacity to block Na<sup>+</sup> and/or Ca<sup>+</sup> channels.

#### IV. CONCLUSION

The current data suggest that clove oil and lavender oil provided local anesthetic effects through cholinergic mechanisms in acute corneal reflexes. Lidocaine, clove oil, and lavender oil were applied topically to the cornea to diminish corneal sensitivity. However, the maximal anesthetic effect and duration differed according to the essential oils presented, including linalool, linalyl acetate, and eugenol.

Clove or lavender oil was excellent local anesthetics when paired with a sub-anesthetic concentration of lidocaine.

#### V. ACKNOWLEDGMENT

I am grateful to Tishk International University, Erbil, Iraq, for providing research facilities for these small animal models.

#### REFERENCES

- Ahmed, S.A., Altaei, T., and Ahmed, T., 2020. Comparative study of the antioxidant effects of lavender and flax oils in recurrent aphthous ulceration treatment. *Journal of Baghdad College of Dentistry*, 32(1), pp.1-9.
- Ait Said, L., Zahlane, K., Ghalbane, I., El Messoussi, S., Romane, A., Cavaleiro, C., and Salgueiro, L., 2015. Chemical composition and antibacterial activity of *Lavandula coronopifolia* essential oil against antibiotic-resistant bacteria. *Natural Product Research*, 29(6), pp.582-585.
- Ali, O.Y, Rozhan, A., and Subasini, U., 2023. SYBR-Green I fluorescence-based qRT-PCR of clove oil's anticancer, chemical characterization and antidiabetic activities. *Journal of Population Therapeutics and Clinical Pharmacology*, 30(11), pp.125-134.
- Arung, E.T., Matsubara, E., Kusuma, I.W., Sukaton, E., Shimizu, K., and Kondo, R., 2011. Inhibitory components from the buds of clove (*Syzygium aromaticum*) on melanin formation in B16 melanoma cells. *Fitoterapia*, 82, pp.198-202.
- Bates, B., Mitchell, K., Keller, J.M., Chan, C., Swaim, W.D., Yaskovich, R., Mannes, A.J., and Iadarola, M.J., 2010. Prolonged analgesic response of cornea to topical resiniferatoxin, a potent TRPV1 agonist. *Pain*, 149, pp.522-528.
- Batiha, G.E.S., Teibo, J.O., Wasef, L., Shaheen, H.M., Akomolafe, A.P., Teibo, T.K.A., Al-Kuraishy, H.M. Al-Garbeeb, A.I., Alexiou, A., and Papadakis, M. 2023. A review of the bioactive components and pharmacological properties of *Lavandula* species. *Naunyn Schmiedebergs Arch Pharmacol*, 396(5), pp.877-900.
- Bikmoradi, A., Khaleghverdi, M., Seddighi, I., Moradkhani, S., Soltanian, A., and Cheraghi, F., 2017. Effect of inhalation aromatherapy with lavender essence on pain associated with intravenous catheter insertion in preschool children: A quasi-experimental study. *Complementary Therapies in Clinical Practice*, 28, pp.85-91.
- Chaieb, K., Hajlaoui, H., Zmanta, T., Kahla-Nakbi, A.B., Mahmoud, R., Mahdouani, K., and Bakrouf, A., 2007. The chemical composition and biological activity of clove essential oil, *Eugenia caryophyllata* (*Syzygium aromaticum* L. *Myrtaceae*): A short review. *Phytotherapy Research*, 21, pp.501-506.
- Chioca, L.R., Ferro, M.M., Baretta, I.P., Oliveira, S.M., Silva, C.R., Ferreira, J., Losso, E.M., and Andreatini, R., 2013. Anxiolytic-like effect of lavender essential oil inhalation in mice: Participation of serotonergic but not GABAA/benzodiazepine neurotransmission. *Journal of Ethnopharmacology*, 147(2), pp.412-418.
- Chung, G., Im, S.T., Kim, Y.H., Jung, S.J., Rhyu, M.R., and Oh, S.B., 2014. Activation of transient receptor potential ankyrin 1 by eugenol. *Neuroscience*, 261, pp.153-160.
- Dalai, M.K., Bhadra, S., Chaudhary, S.K., Bandyopadhyay, A., and Mukherjee, P.K., 2014. Anti-cholinesterase activity of the standardized extract of *Syzygium aromaticum* L. *Pharmacognosy Magazine*, 10, pp.S276-S282.
- Daniel, A.N., Sartoretto, S.M., Schmidt, G., Caparroz-Assef, S.M., Bersani-Amado, C.A., and Cuman, R.K.N., 2009. Anti-inflammatory and antinociceptive activities A of eugenol essential oil in experimental animal models. *Revista Brasileira de Farmacognosia*, 19, pp.212-217.
- De Rapper, S., Viljoen, A., and Vuuren, S., 2016. The *in vitro* antimicrobial

- effects of *Lavandula angustifolia* essential oil in combination with conventional antimicrobial agents. *Evidence-Based Complementary and Alternative Medicine*, 2016, p.2752739.
- Dohi, S., Terasaki, M., and Makino, M., 2009. Acetylcholinesterase inhibitory activity and chemical composition of commercial essential oils. *Journal of Agricultural and Food Chemistry*, 57, pp.4313-4318.
- Farazifard, R., Safapour, F., Sheibani, V., and Javan, M., 2005. Eye wiping test: A sensitive animal model for acute trigeminal pain studies. *Brain Research Protocols*, 16, pp.44-49.
- Gülçin, I., Elmastas, M., and Aboul-Enein, H.Y., 2012. Antioxidant activity of clove oil - a powerful antioxidant source. *Arabian Journal of Chemistry*, 5, pp.489-499.
- Hirata, H., and Meng, I.D., 2010. Cold-sensitive corneal afferents respond to a variety of ocular stimuli central to tear production: implications for dry eye disease. *Investigative Ophthalmology and Visual Science*, 5, pp.3969-3976.
- Jianu, C., Pop, G., and Gruia, A., 2013. Chemical composition and antimicrobial activity of essential oils of lavender (*Lavandula angustifolia*) and lavandin (*Lavandula x intermedia*) grown in Western Romania. *International Journal of Agriculture and Biology*, 6(4), pp.15-17.
- Kajjari, S., Joshi, R.S., and Hugar, S.M., 2022. The effects of lavender essential oil and its clinical implications in dentistry: A review. *International Journal of Clinical Pediatric Dentistry*, 15(3), pp.385-388.
- Khalilzadeh, E., Hazrati, R., and Vafaei Sayah, G., 2014. Evaluation of chemical composition, anti-inflammatory and anti-nociceptive effects of *Eugenia caryophyllata* buds' essential oil. *Journal of Herbal Drugs*, 5, pp.68-76.
- Kim, J., Kim, N.S., Lee, K.C., Lee, H.B., Kim, M.S., and Kim, H.S., 2013. Effect of topical anesthesia on evaluation of corneal sensitivity and intraocular pressure in rats and dogs. *Veterinary Ophthalmology*, 16, pp.43-46.
- Koulivand, P.H., Khaleghi Ghadiri, M., and Gorji, A., 2013. Lavender and the nervous system. *Evidence-Based Complementary and Alternative Medicine*, 36, pp.235-238.
- Kritsidima, M., Newton, T., and Asimakopoulou, K., 2010. The effects of lavender scent on dental patient anxiety levels: A cluster randomized controlled trial. *Community Dentistry and Oral Epidemiology*, 38(1), pp.83-87.
- Leffler, A., Fischer, M.J., Rehner, D., Kienel, S., Kistner, K., Sauer, S.K., Gavva, N.R., Reeh, P.W., and Nau, C., 2008. The vanilloid receptor TRPV 1 is activated and sensitized by local anesthetics in rodent sensory neurons. *Journal of Clinical Investigation*, 118, pp.763-776.
- Lionnet, L., Beaudry, F., and Vachon, P., 2010. Intrathecal eugenol administration alleviates neuropathic pain in male Sprague-Dawley rats. *Phytotherapy Research*, 24, pp.1645-1653.
- Miranda, H.F., Sierralta, F., and Prieto, J.C., 2009. Synergism between NSAIDs in the orofacial formalin test in mice. *Pharmacology Biochemistry and Behavior*, 92, pp.314-318.
- Nardarajah, D., Dhanraj, M., and Jain, A.R., 2018. Effects of lavender aromatherapy on anxiety levels of patients undergoing mandibular third molar extraction. *Drug Invention Today*, 10(7), pp.1318-1322.
- Pan, Z., Wang, Z., Yang, H., Zhang, F., and Reinach, P.S., 2011. TRPV1 activation is required for hypertonicity stimulated inflammatory cytokine release in human corneal epithelial cells. *Investigative Ophthalmology and Visual Science*, 52, pp.485-493.
- Park, C.K., Kim, K., Jung, S.J., Kim, M.J., Ahn, D.K., Hong, S.D., Kim, J.S., and Oh, S.B., 2009. Molecular mechanism for local anesthetic action of eugenol in the rat trigeminal system. *Pain*, 144, pp.84-94.
- Park, C.K., Li, H.Y., Yeon, K.Y., Jung, S.J., Choi, S.Y., Lee, S.J., Lee, S., Park, K., Kim, J.S., and Oh, S.B., 2006. Eugenol inhibits sodium currents in dental afferent neurons. *Journal of Dental Research*, 85, pp.900-904.
- Park, S.H., Sim, Y.B., Lee, J.K., Kim, S.M., Kang, Y.J., Jung, J.S., and Suh, H.W., 2011. The analgesic effects and mechanisms of orally administered eugenol. *Archives of Pharmacological Research*, 34, pp.501-507.
- Pathan, J.M., Dadpe, M.V., Kale, Y.J., Dahake, P.T., and Kendre, S.B., 2020. Evaluation of lavender oil as a topical analgesic agent before dental anaesthesia through pain rating scales-an *in vivo* study. *IOSR Journal of Dental and Medical Sciences*, 19(7), pp.6-13.
- Pinto, E., Vale-Silva, L., Cavaleiro, C., and Salgueiro, L., 2009. Antifungal activity of the clove essential oil from *Syzygium aromaticum* on *Candida*, *Aspergillus* and dermatophyte species. *Journal of Medical Microbiology*, 58, pp.1454-1462.
- Properzi, A., Angelina, P., Bertuzzi, G., and Venanzoni, R., 2013. Some biological activities of essential oils. *Medicinal and Aromatic Plants*, 2(5), p.000136.
- Prusinowska, R., and Śmigielski, K.B., 2014. Composition, biological properties and therapeutic effects of lavender (*Lavandula angustifolia* L.). A review. *Herbapolonica*, 60, pp.56-66.
- Rosenthal, P., Baran, I., and Jacobs, D.S., 2009. Corneal pain without stain: Is it real? *The Ocular Surface*, 7, 28-40.
- Shaw, D., Annett, J.M., Doherty, B., and Leslie, J.C., 2007. Anxiolytic effects of lavender oil inhalation on open-field behaviour in rats. *Phytomedicine*, 14(9), pp.613-620.
- Silva, G.L., Luft, C., Lunardelli, A., Amaral, R.H., da Silva Melo, D.A., Donadio, M.V.F., Nunes, F.B., de Azambuja, M.S., Santana, J.C., Moraes, C.M.B., Mello, R.O., Cassel, E., de Almeida Pereira, M.A., and de Oliveira, J.R., 2015. Antioxidant, analgesic and anti-inflammatory effects of lavender essential oil. *Anais da Academia Brasileira de Ciências*, 87(2 Suppl), pp.1397-1408.
- Simpson, M.G., 2019. *Plant Systematics*. Academic press, United States.
- Tamaddonfard, E., Khalilzadeh, E., Hamzeh-Gooshchi, N., and Seiednejhad-Yamchi, S., 2008. Central effect of histamine in a rat model of acute trigeminal pain. *Pharmacological Reports*, 60, pp.219-224.
- Tschiggerl, C., and Bucar, F., 2010. Volatile fraction of lavender and bitter fennel infusion extracts. *Natural Product Communications*, 5(9), pp.1431-1436.
- Uthirapathy, S., 2023. "Cytostatic effects of avocado oil using single-cell gel electrophoresis (Comet Assay): An evaluation. *ARO-The Scientific Journal of Koya University*, 11(1), pp.16-21.
- Uthirapathy, S., and Tahir, T.F., 2021. "Withania somnifera: Correlation of phytoconstituents with hypolipidemic and cardioprotective activities. *ARO-The Scientific Journal of Koya University*, 9(2), pp.15-21.
- Wilson, T.M., Poulson, A., Packer, C., Carlson, R.E., and Buch, R.M., 2021. Essential oil profile and yield of corolla, calyx, leaf, and whole flowering top of cultivated *Lavandula angustifolia* Mill. (*Lamiaceae*) from Utah. *Molecules*, 26(8), p.2343.
- Zagon, I.S., Sassani, G.W., Immonen, J.A., and McLaughlin, P.J., 2014. Ocular surface abnormalities related to type 2 diabetes are reversed by the opioid antagonist naltrexone. *Clinical and Experimental Ophthalmology*, 42, pp.159-168.
- Zheljazkov, V.D., Cantrell, C.L., Astatkie, T., and Jeliazkova, E., 2013. Distillation time effect on lavender essential oil yield and composition. *Journal of Oleo Science*, 62(4), pp.195-199.

# Size Reduction and Harmonics Suppression in Microwave Power Dividers: A Comprehensive Review

Sobhan Roshani<sup>1</sup>, Salah I. Yahya<sup>2</sup>, Yazeed Y. Ghadi<sup>3</sup>, Saeed Roshani<sup>1</sup>, Fariborz Parandin<sup>1</sup> and Behnam D. Yaghouti<sup>4</sup>

<sup>1</sup>Department of Electrical Engineering, Kermanshah Branch, Islamic Azad University, Kermanshah, 6718997551, Iran

<sup>2</sup>Department of Communication and Computer Engineering, Cihan University-Erbil, Erbil, Iraq

<sup>3</sup>Department of Software Engineering and Computer Science, Al Ain University, Al Ain, 64141, United Arab Emirates

<sup>4</sup>Department of Information and Communications Technology, Amin University, Tehran, Iran

**Abstract**—In this paper, several types of microstrip power divider are studied and compared in terms of harmonics suppression and size reductions. The importance of this research lies in the fact that power dividers are critical components in various communication systems, and their performance directly affects the overall system efficiency. The conventional structure of the power divider has an acceptable performance at operating frequency in terms of excellent output ports isolation, low insertion loss, and high return loss, but occupies large size and passes unwanted signals at higher frequencies along with desired signal without any suppression. Harmonics are popular distortion and has different distortion impacts in many different facilities. Recently, several techniques are introduced to overcome these drawbacks. Applied open stubs, applied resonators, lumped reactive components such as capacitors and inductors, coupled lines, defected ground structure (DGS), and electronic band gaps are common methods, which are widely used to overcome these drawbacks. Finally, the study results show that the resonator-based power dividers and coupled-line-based power dividers have good performances in terms of size reduction and harmonic suppression but increase insertion loss parameter. Furthermore, the lumped reactive component-based power dividers and applied DGS and electromagnetic bandgap cells suppress unwanted harmonics, but they need extra process to fabrication, which is undesirable. Moreover, the open-stub-based power dividers have moderate performance with simple structure, but size reduction and harmonics suppression are not so superior in this method.

Overall, the results of this study can be used to design power dividers for desirable applications with high performances.

**Index Terms**—Harmonics suppression, Microstrip, Power divider, Size reduction.

## I. INTRODUCTION

Wilkinson power dividers (WPDs) are passive devices that are used to divide an input signal into two or more output signals. They are commonly used in microwave and RF systems, such as in antenna arrays, mixers, and filters. The main advantage of WPD is its ability to provide excellent isolation between the output ports, which helps to minimize the loss of signal power and reduce unwanted reflections. One of the key features of WPDs is their ability to operate over a wide frequency band with good performance. This makes them suitable for use in applications that require high performance and reliability, such as military and aerospace systems., WPDs can be easily integrated into circuit designs due to their compact size and simple construction.

The conventional structure of the Wilkinson divider as depicted in Fig. 1a occupies a large size and pass unwanted signals along with desired signal without any suppression as shown in Fig. 1b. Recently, several techniques are introduced to overcome these drawbacks.

The conventional Wilkinson power dividers (WPDs) have limited performance outside of the center frequency and require a large size. To improve on this, a modified microstrip WPD is presented in Moloudian, et al. (2023) that has better out-of-band performance and high isolation. This is achieved using a lowpass filter (LPF) structure in both branches of the power divider to suppress harmonics. The proposed WPD has a wide stopband from 2.54 GHz to 13.48 GHz and filters the second to seventh harmonics with attenuation levels

ARO-The Scientific Journal of Koya University  
Vol. XI, No. 2 (2023), Article ID: ARO.11385, 15 pages  
DOI: 10.14500/aro.11385

Received: 05 September 2023; Accepted: 28 October 2023

Regular review paper: Published: 10 November 2023

Corresponding authors' email: s\_roshani@iauksh.ac.ir

Copyright © 2023 Sobhan Roshani, Salah I. Yahya, Yazeed Y. Ghadi, Saeed Roshani, Fariborz Parandin, and Behnam D. Yaghouti This is an open access article distributed under the Creative Commons Attribution License.





>20 dB. The size of this WPD is small at  $33.8 \text{ mm} \times 27 \text{ mm}$  ( $0.42 \lambda_g \times 0.33 \lambda_g$ ), where  $\lambda_g$  is the guided wavelength at the operating frequency of 1.8 GHz. This divider is a good candidate for LTE and GSM applications.

In some works, neural networks and artificial intelligence (Jamshidi, et al., 2019; Jamshidi, et al., 2020) are used to model microstrip resonators and power divider, which resulted in accurate model.

In this paper, several types of power dividers in terms of harmonics suppression and size reductions methods are studied.

## II. POWER DIVIDER WITH APPLIED OPEN-ENDED STUBS

Add microstrip stubs in the conventional divider improved divider performances in terms of reducing the size and eliminating harmonics. In Cheng and Ip (2010), by adding three open-ended stubs, the improved divider is designed as depicted in Fig. 2. This divider is fabricated on RT/Duroid substrate with thickness of 0.813 mm and relative permittivity of 3.38.

The frequency response of the proposed divider in Cheng and Ip (2010) is shown in Fig. 3. As results shown,

this divider has acceptable results at 1 GHz frequency and suppresses the second up to fourth harmonics. This power divider has a simple structure and can be easily fabricated, but it only reduces the first three harmonics.

In Hayati and Roshani (2013), a power divider using open-end stubs is presented. The structure of this divider is depicted in Fig. 4. The mentioned power divider is implemented on RT/Duroid 5880 substrate with a relative permittivity of 2.2 and a thickness of 0.381 mm, which in this structure, three open-ended stubs are used at all three ports. The overall dimensions are  $24 \text{ mm} \times 16 \text{ mm}$ , which shows 35% reduction in size compared to the conventional power divider.

The frequency responses of this divider are shown in Fig. 5. This power divider (Hayati and Roshani, 2013) has a good performance at the frequency of 1.65 GHz and suppresses the third and fifth harmonics. The results of the measurements indicate that the power divider allows the 1.65 GHz fundamental signal to pass whereas simultaneously suppressing the 4.95 GHz third-order harmonic and the 8.25 GHz fifth-order harmonic. As shown in Fig. 4, the insertion loss at 1.65 GHz is only 0.1 dB, whereas the third- and fifth-order harmonics are suppressed by 43 dB and 41 dB, respectively.

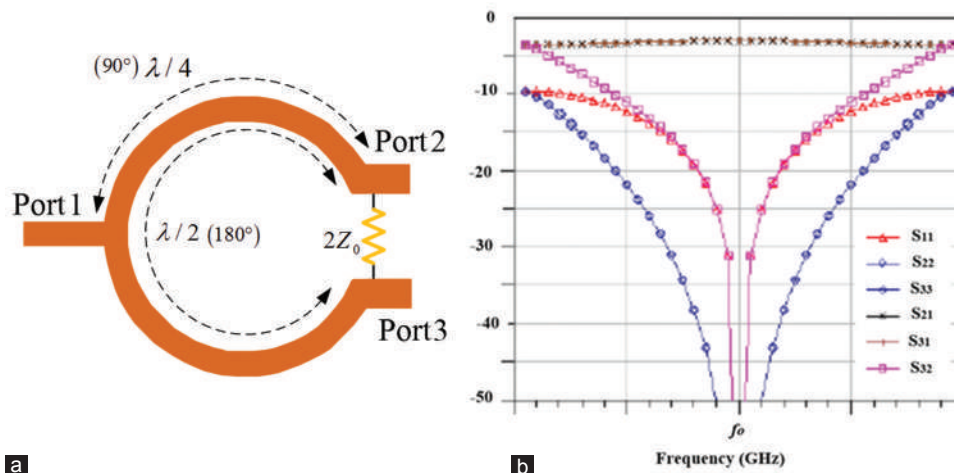


Fig. 1. The structure of the conventional WPD (a) layout; (b) frequency response.

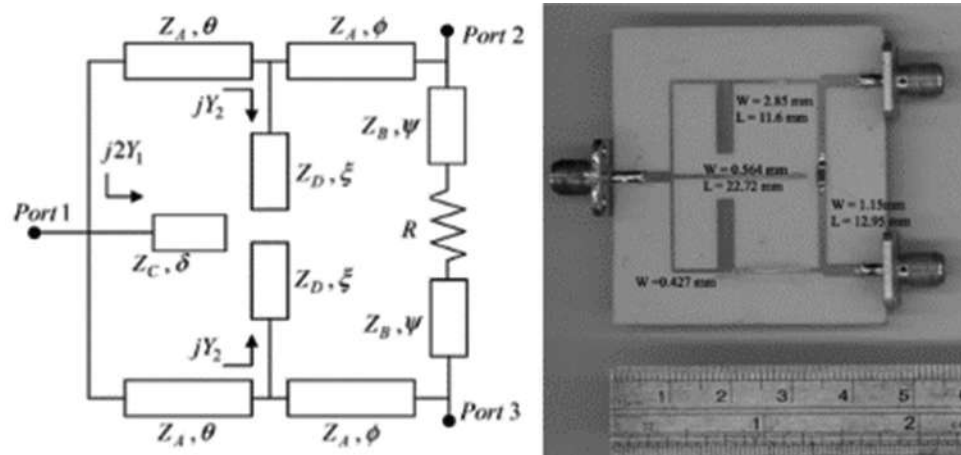


Fig. 2. The structure of the improved Wilkinson power divider with three open stubs (Cheng and Ip, 2010).

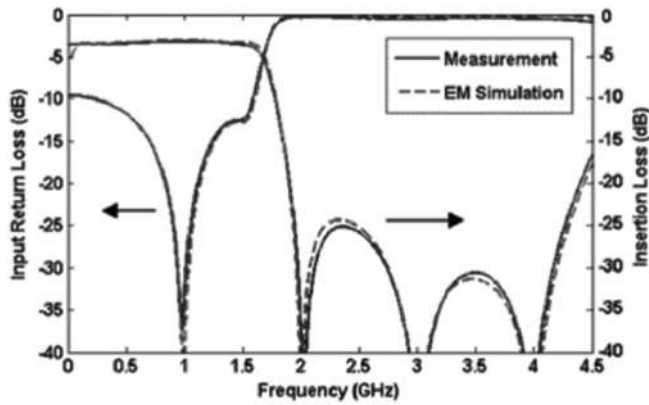


Fig. 3. The frequency response of the improved Wilkinson divider with three open stubs (Cheng and Ip, 2010).

This divider has a simple structure and can be easily fabricated, but it only suppresses two harmonics.

In Hayati, Roshani, and Roshani (2013), a simple divider using three open-ended stubs is presented. The layout of this divider is depicted in Fig. 6. This divider is implemented on RT/Duorid 5880 substrate with 2.2 relative permittivity and a thickness of 0.381 mm. In its structure, three open-ended stubs are applied at all three ports. Occupied size of this divider is 37.5 mm × 30 mm, which does not reduce the size compared to the typical divider.

The frequency responses of the mentioned divider (Hayati, Roshani, and Roshani, 2013) are depicted in Fig. 7. As can be seen, this power splitter has a very good performance at 900 MHz frequency and has the ability to reduce the second to sixth harmonics with a very high attenuation level. Therefore, this structure can be used to remove unwanted harmonics in other radio frequency circuits.

According to the simulations and measurements results, this divider effectively allows the fundamental signal at 0.9 GHz to pass through, whereas suppressing unwanted signals at higher frequencies. The proposed power divider also exhibits good performance in terms of insertion loss and harmonic suppression. The measured insertion loss is better than 0.3 dB at the center frequency of 0.9 GHz, whereas the stopband bandwidth of 1.4–5 GHz has been achieved with a minimum attenuation level of 20 dB. The measured spurious attenuations for the second to sixth harmonic frequencies are 71, 77, 36, 26, and 34 dB, respectively. In addition, this divider provides more than 34 dB of port isolation at the center frequency and good port isolation at harmonic frequencies.

Fig. 8, shows the schematic and implemented photo of the proposed divider (Hayati, Roshani, and Roshani 2013) with the help of microstrip stubs to remove the second and third harmonics. As can be seen, this power divider has a very simple structure, in which, two open-ended stubs and three grounded stubs are used.

Fig. 9 depicted the frequency response of the mentioned divider using two open stubs and three grounded stubs. As can be seen, this divider has a very good performance at 2 GHz frequency and has the ability to eliminate the second and third harmonics with high attenuation level.

According to results, this power divider has an insertion loss of 0.1 dB and an isolation of approximately 30 dB at the operating frequency. The input and output return losses are around 28 dB and 44 dB, respectively. In addition, the third and second harmonics are effectively suppressed with high attenuation levels.

Fig. 10 illustrates the structure of the divider (Lotfi, et al., 2020) using six open-ended and four grounded stubs to eliminate the second up to fourth harmonics. As can be seen, this power divider has a simple structure, which is designed by using six open-end microstrip stubs and four grounded microstrip stubs symmetrically. The mentioned power divider is implemented on RT/Duorid 5880 substrate with 2.2 relative permittivity and a thickness of 0.79 mm.

The frequency responses of this divider are shown in Fig. 11, which shows good performance at 0.9 GHz frequency, with 0.17 dB insertion loss. This WPD can suppress second, third, and fourth harmonics with attenuation levels of 64 dB, 45 dB, and 43 dB, respectively.

In Fig. 12 (Roshani and Roshani, 2020), the structure, fabricated photo, and frequency response of the compact size divider using aperiodic stubs are depicted. This WPD correctly works at 700 MHz and consists of several aperiodic stubs, which each stubs suppresses one desired harmonic. This divider suppresses 2<sup>nd</sup>–15<sup>th</sup> harmonics. These applied stubs reduce circuit size, which this divider has 73% size reductions, compared to the 700 MHz typical divider. This divider is implemented on RO4003 substrate with  $\epsilon_r = 3.36$  and thickness of 20 mil.

Layout, substrate, and advantage of some designed power dividers using open stubs are listed in Table I as follows:

### III. POWER DIVIDER WITH RESONATORS

Resonators are widely used in the communication devices such as filters (Yahya, Rezaei, and Khaleel, 2021), duplexers (Yahya and Rezaei, 2021; Rezaei and Yahya, 2022), and antenna (Roshani, et al., 2023) to improve the functionality of the performance of devices.

Another way to remove harmonics and reduce the size of the power divider is to use resonators in the output branches of the power divider structure. In this method, according to the main frequency of the power divider, specific resonator is designed to remove unwanted frequencies. In Hayati, Roshani, and Roshani (2013), a power divider using a resonator is presented. The layout of this divider is depicted in Fig. 13.

This divider is implemented on RT/Duorid 5880 substrate with  $\epsilon_r = 2.2$  and thickness of 0.381 mm, which works at frequency of 2 GHz and the applied resonator is designed to eliminate the third to fifth harmonics. The frequency response of this divider (Hayati, Roshani, and Roshani, 2013) is shown in Fig. 14. As can be seen, this power divider has a very good performance at 2 GHz frequency and has the ability to reduce the third to fifth harmonics with a good attenuation level.

A microstrip power divider with filtering response is reported in this paper, which uses a front-coupled tapered

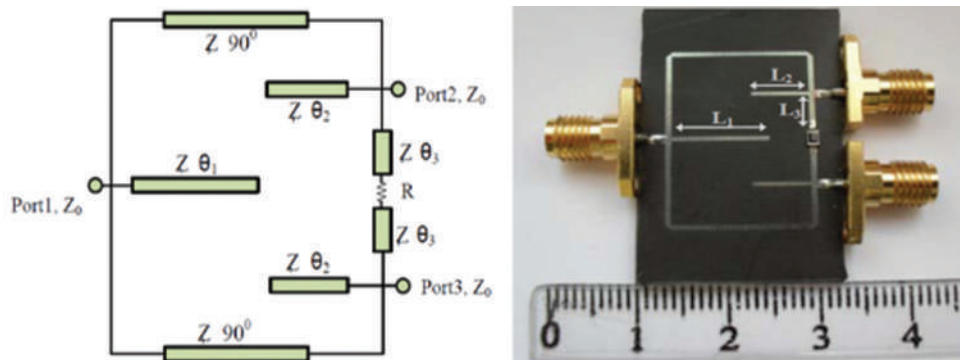


Fig. 4. The structure of the improved Wilkinson power divider with three open stubs (Hayati and Roshani 2013).

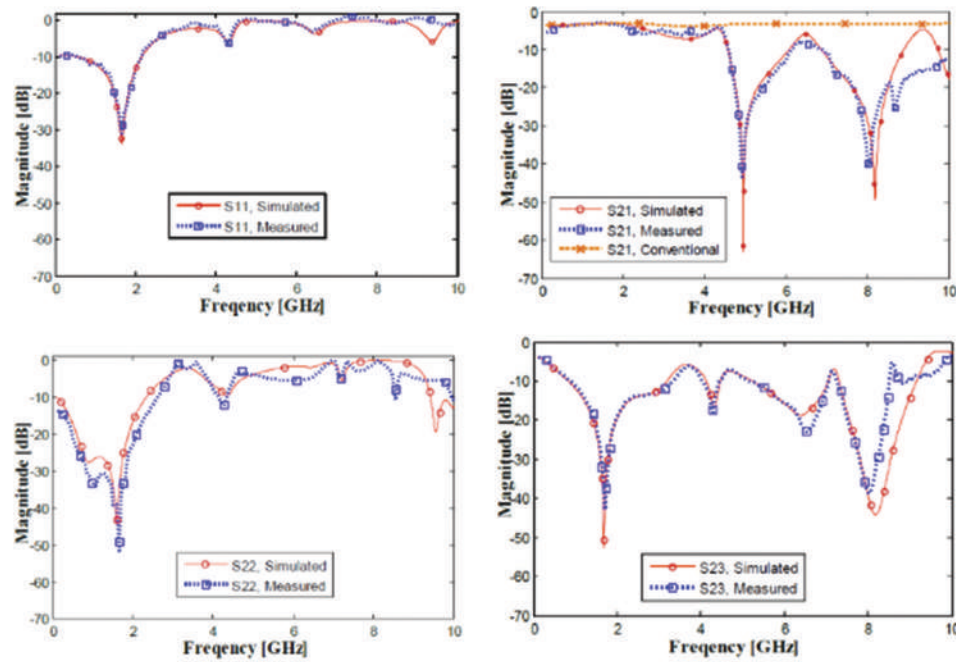


Fig. 5. The frequency response of the improved Wilkinson power divider with three open stubs (Hayati and Roshani 2013).

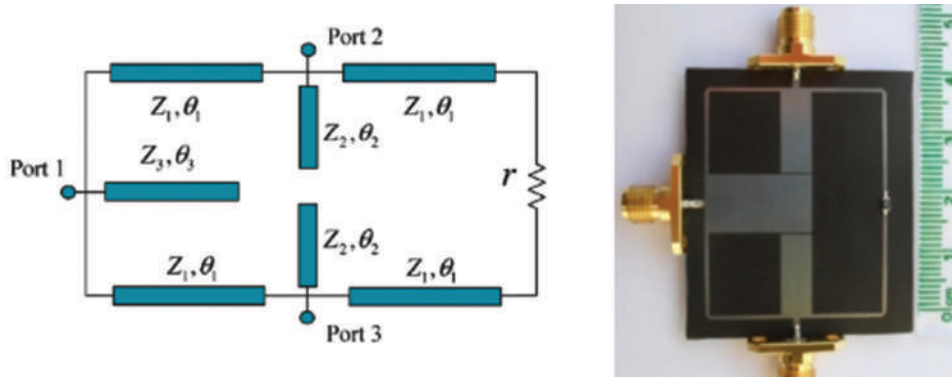


Fig. 6. The structure of the simple Wilkinson power divider with three open stubs (Hayati, Roshani, and Roshani 2013).

compact microstrip resonant cell (FCTCMRC) to achieve high harmonic suppression. This cell is inserted into a quarter-wavelength transmission line of the conventional WPD. This divider not only improves harmonic suppression but also reduces the length of a quarter-wave line by over 29.3% compared to the conventional divider. Measured results

show that the proposed structure achieves wide stop-band bandwidth (6 GHz – 12 GHz) with a minimum attenuation level of 24 dB, whereas maintaining the characteristics of the conventional WPD. The input and output return losses at 2 GHz are 48 and 44 dB, respectively, and the insertion loss is about 0.1 dB. The isolation obtained is better than 45 dB.

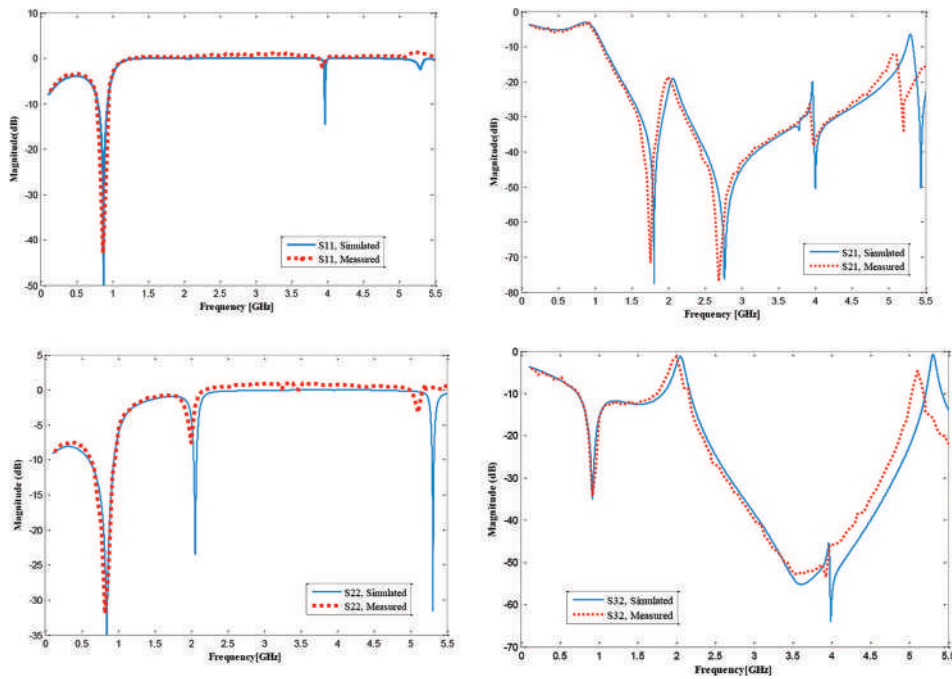


Fig. 7. The frequency response of the simple Wilkinson divider with three open stubs (Hayati, Roshani, and Roshani 2013).

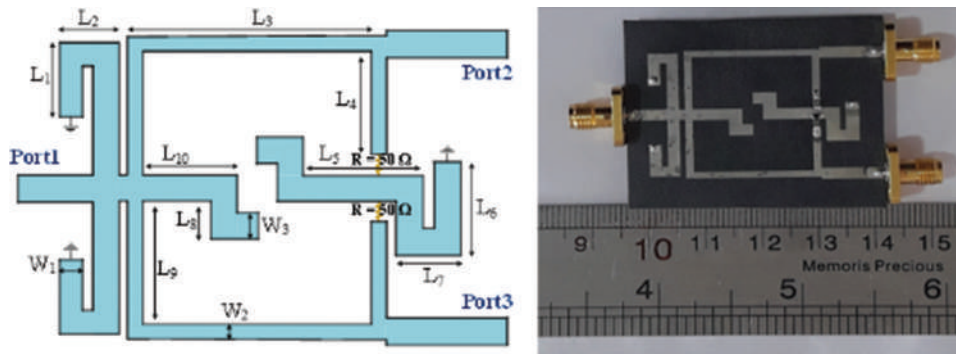


Fig. 8. The structure and fabricated photo of the Wilkinson divider with open and short stubs (Roshani, et al., 2022).

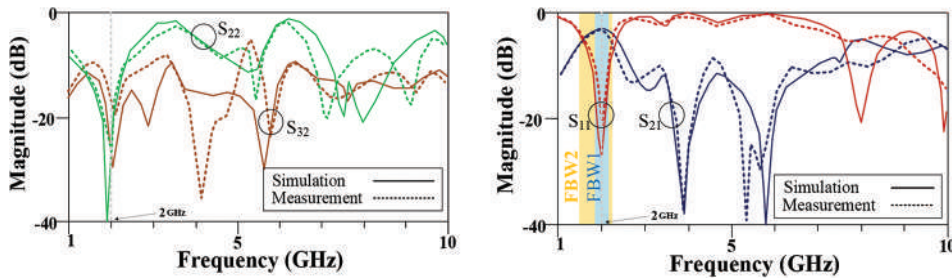


Fig. 9. The frequency response of the Wilkinson divider with open and short stubs (Roshani, et al., 2022).

In Hayati, et al. (2013), a compact low pass filter is designed and located between input and output ports of the Wilkinson divider. The structure of this divider is depicted in Fig. 15. This power divider is more than 71% smaller compared to the conventional power divider. This divider is implemented on RT/Duroid 5880 substrate with  $\epsilon_r = 2.2$  and thickness of 0.508 mm, which works at frequency of 1 GHz and the LPF is designed to eliminate the 4<sup>th</sup>–12<sup>th</sup> harmonics and to suppress second and third harmonics open stubs are

used in the divider structure. In the final structure, to occupy small size, the applied microstrip lines are bent symmetrically. The frequency response of this divider (Hayati, et al., 2013) is shown in Fig. 16. As can be seen, this power divider has a very good performance at 1GHz frequency and has the ability to reduce the 2<sup>nd</sup>–12<sup>th</sup> harmonics with a good attenuation level.

In Roshani (2017), a power divider using resonator and stub is presented. The layout of this divider is depicted in Fig. 17.

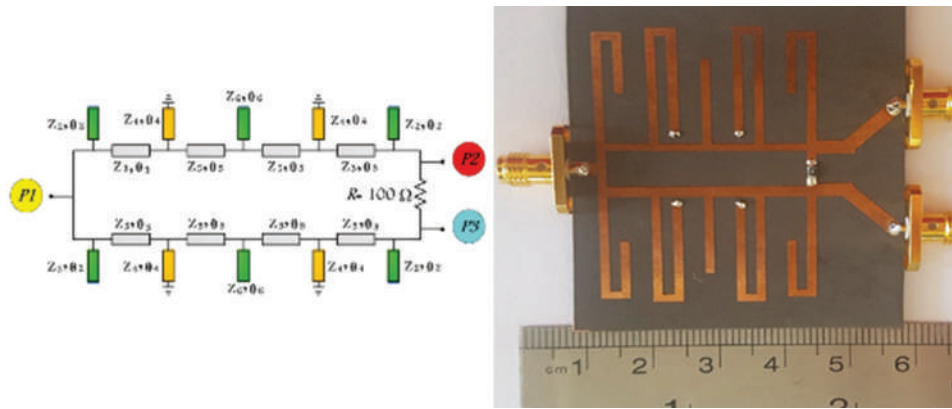


Fig. 10. The structure and fabricated photo of the Wilkinson divider with open and short stubs (Lotfi, et al., 2020).

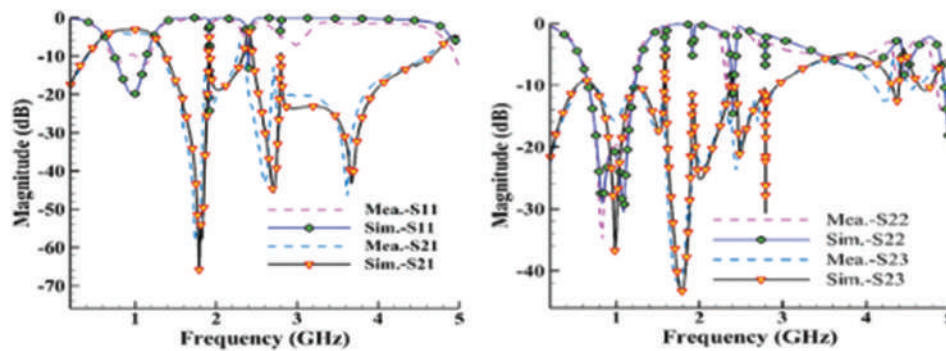


Fig. 11. The frequency responses of the Wilkinson divider with open and short stubs (Lotfi, et al., 2020).

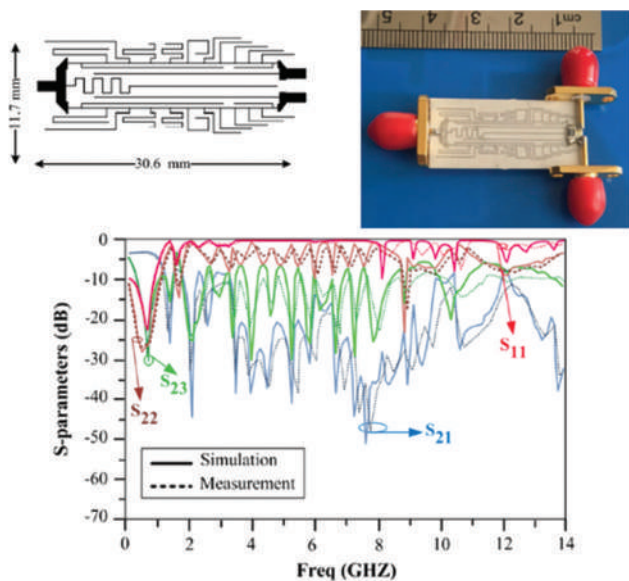


Fig. 12. The structure, fabricated photo, and frequency response of the compact divider using aperiodic stubs (Roshani and Roshani, 2020).

This power divider is more than 65% smaller compared to the typical divider. This divider is implemented on RT/Duorid 5880 substrate with  $\epsilon_r = 2.2$  and thickness of 0.508 mm.

The frequency response of this power divider using resonator and open stub is shown in Fig. 18. This divider works at a frequency of 2 GHz. The design of this divider involves the use of an open stub to suppress the second

harmonic, whereas two MCMRC units are inserted into the quarter-wavelength lines of the conventional divider to suppress the 3<sup>rd</sup>–7<sup>th</sup> harmonics. The proposed power divider is significantly smaller than the conventional one, with a reduction in size of over 65%. The resonator and power divider are fabricated and measured, and the results show impressive harmonic suppression with high attenuation levels.

In Roshani and Siahkamari (2022), a WPD is designed at 2.75 GHz frequency. A compact resonator is designed and placed in this structure, which reduces the size and eliminates harmonics. Fig. 19 illustrates the structure of the Wilkinson divider which is designed and manufactured on RT/Duorid 5880 substrate with thickness of 0.787 mm and 2.2 relative permeability. This divider reduces circuit size more than 37% compared with the typical divider and suppressed 2<sup>nd</sup>–5<sup>th</sup> unwanted harmonics.

In Roshani, et al. (2021), with H-shaped resonators and open stubs, a patch power divider is designed. The structure of the designed patch power is depicted in Fig. 20. This divider is implemented on RT/Duorid 5880 substrate with a relative permeability of 2.2 and a thickness of 0.508 mm.

The frequency response of the designed patch divider is depicted in Fig. 21. This divider is designed to operate at 1.8 GHz and has good performance within the operating bandwidth. It uses two low-pass filters and three open-ended stubs at each port to achieve its performance. The divider has an operating band from 1.62 GHz to 2.1 GHz with a fractional bandwidth of 25.8%. It provides ultra-

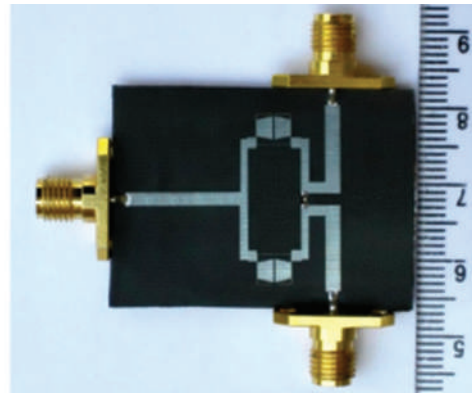
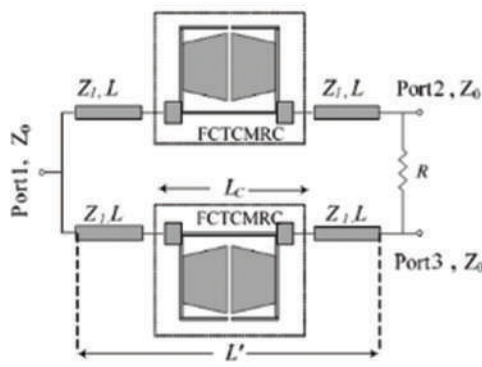


Fig. 13. The structure and implemented photo of the power divider using FCTCMRC (Hayati, Roshani, and Roshani, 2013).

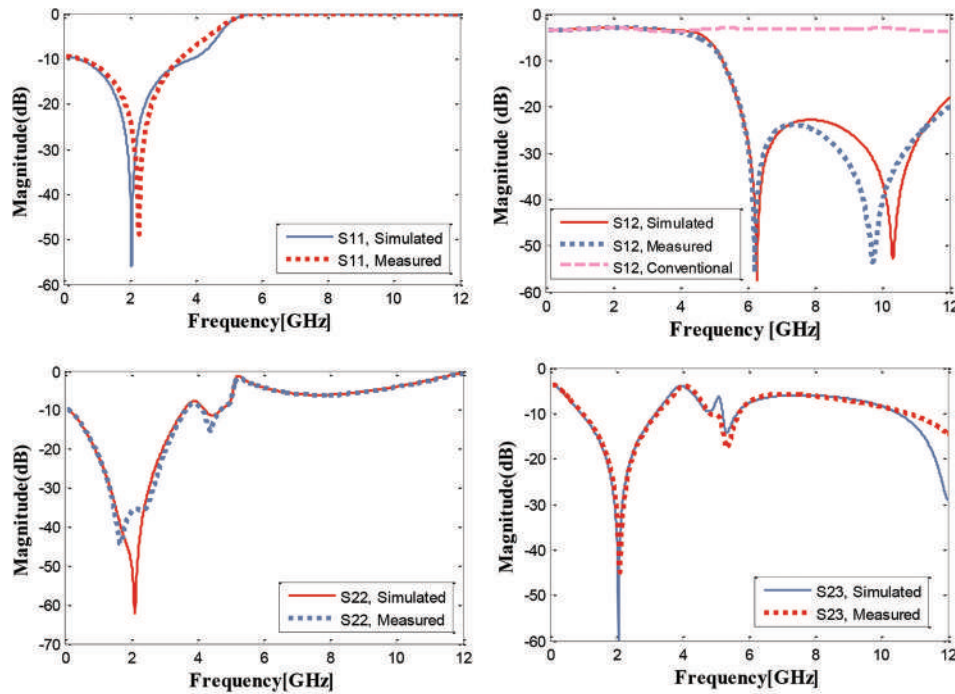


Fig. 14. The frequency responses of the power divider using FCTCMRC (Hayati, Roshani, and Roshani, 2013).

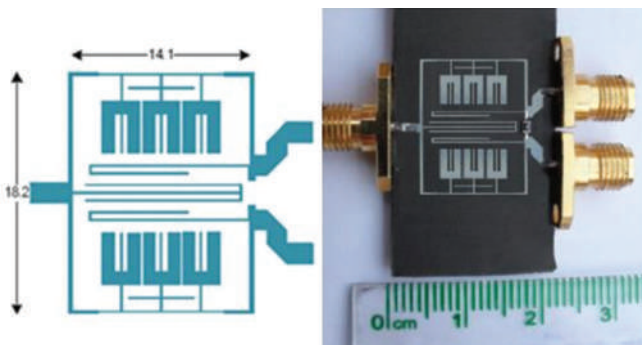


Fig. 15. The structure and fabricated photo of the power divider using LPF (Hayati, et al., 2013).

wide suppression from 3 GHz to 20 GHz, which covers the 2<sup>nd</sup> up to the 11<sup>th</sup> harmonic. The measured results show good agreement with the simulated results, with  $|S_{11}|$ ,  $|S_{12}|$ ,  $|S_{22}|$ , and  $|S_{23}|$  equal to  $-17$  dB,  $-3.5$  dB,  $-20$  dB, and  $-17$  dB, respectively, at the operating frequency.

The Lalbakhsh, et al. (2020) describes a simple and effective design method for a microstrip LPF that outperforms other filters in its class. The proposed filter consists of three polygonal-shaped resonators, two of which improve the stopband and the third enhances selectivity. The filter's performance is evaluated using a Figure of Merit and compared to other filters, demonstrating its superiority. A prototype of the filter was fabricated and tested, with a 3-dB cutoff frequency at 1.27 GHz and a wide stopband with 25 dB suppression from 1.6 to 25 GHz. This device is suitable for satellite communication systems.

In some works like Roshani, et al. (2023) and Roshani and Shahveisi (2022), resonators are applied to reduce mutual coupling effects in microstrip patch antenna arrays. These applied ladder resonators impressively block the surface current between two patch antennas at the operating frequency, which results in mutual effect reduction.

In Jamshidi, et al. (2020), symmetrical modified T-shaped resonators are used to design a WPD. This technique

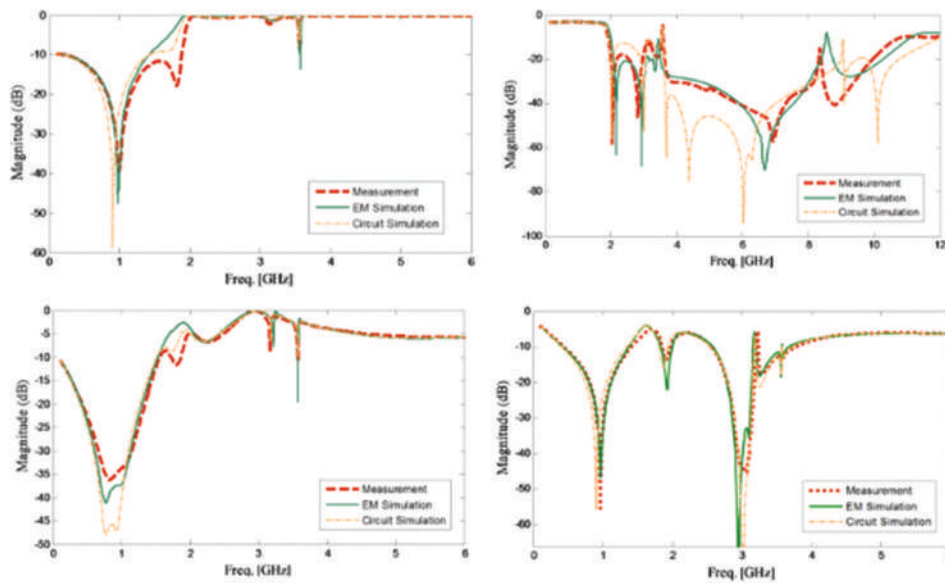


Fig. 16. The frequency responses of the power divider using LPF (Hayati, et al., 2013).

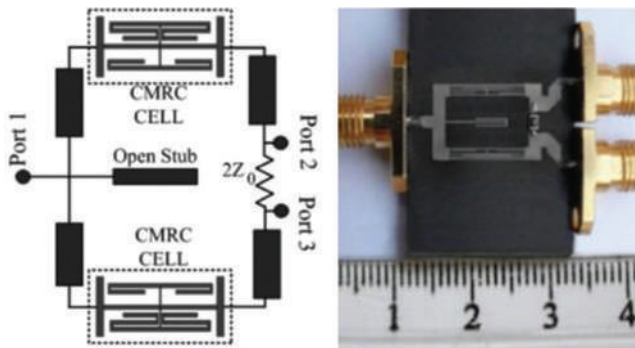


Fig. 17. The structure and implemented photo of the divider using resonator and open stub (Roshani 2017).

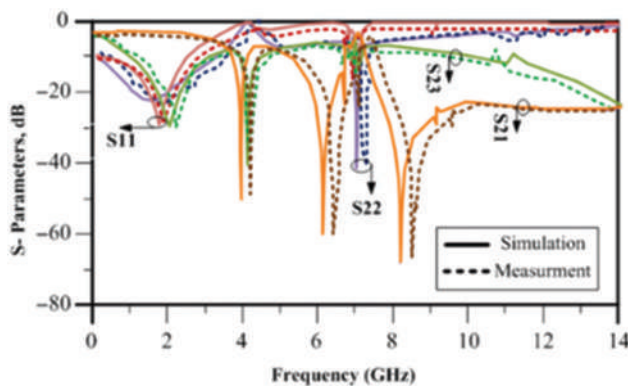


Fig. 18. The frequency responses of the power divider using resonator and open stub (Roshani 2017).

reduces the size of the power divider by 45% and suppresses unwanted bands up to the fifth harmonics. The results show that the insertion loss and the isolation at the center frequency are 0.1 dB and 23 dB, respectively.

In Lalbakhsh, et al., (2020) a narrowband dual-band bandpass filter and in Lalbakhsh, et al. (2020) a simple

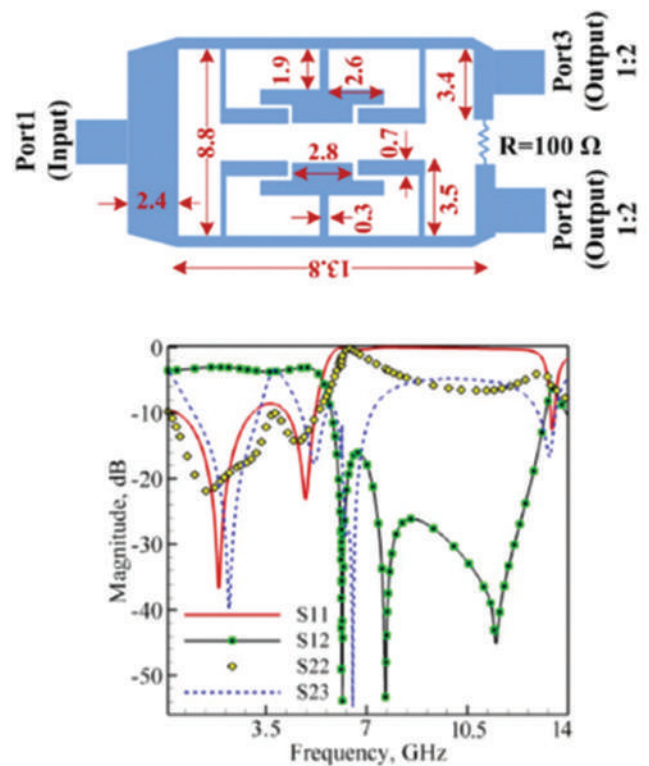


Fig. 19. The structure and frequency responses of the power divider using resonator (Roshani and Siahkamari 2022).

LPF with an ultrawide stopband from 1.6 to 25 GHz, in Pradhan, et al. (2023), substrate integrated waveguide (SIW) bandpass filters using open-loop ring resonators and in Pradhan, et al. (2023) SIW bandpass filters using semi-circular cavities and in Barik, Koziel and Pietrenko-Dabrowska (2023) a compact filter using a half-mode substrate-integrated rectangular cavity are presented, which all of these resonators can be used in dividers structure for harmonics suppression purpose.

Layout, substrate, and advantage of some designed power dividers using resonators are listed in Table II as follows:

IV. POWER DIVIDER WITH LUMPED REACTIVE COMPONENTS

Using lumped reactive elements (L and C) in power divider design is another method to suppress unwanted harmonics and reduce circuit size, which affect the quality of the final product.

In Jamshidi, et al. (2021), as shown in Fig. 22, the structure and layout of the proposed divider using compact elements are depicted. In the above structure, using series inductor and capacitor, very efficient method is presented

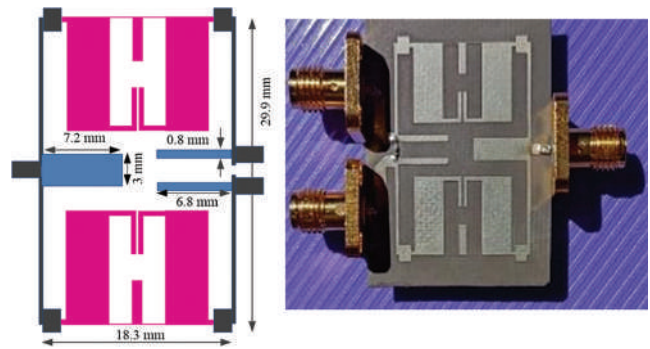


Fig. 20. The structure and fabricated photo of the patch divider using resonator and three open stubs (Roshani, et al., 2021).

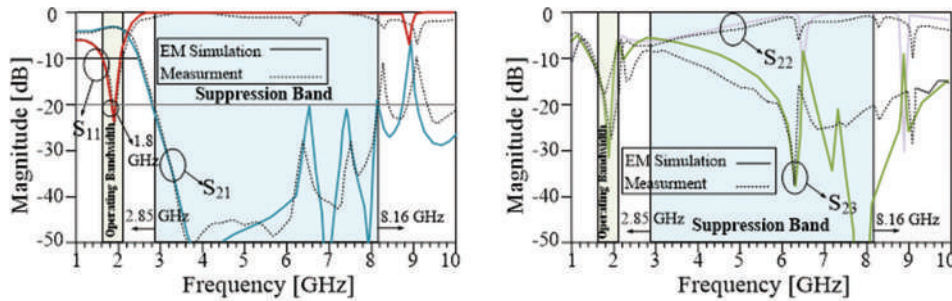


Fig. 21. The frequency responses of the patch divider using resonator and three open stubs (Roshani, et al., 2021).

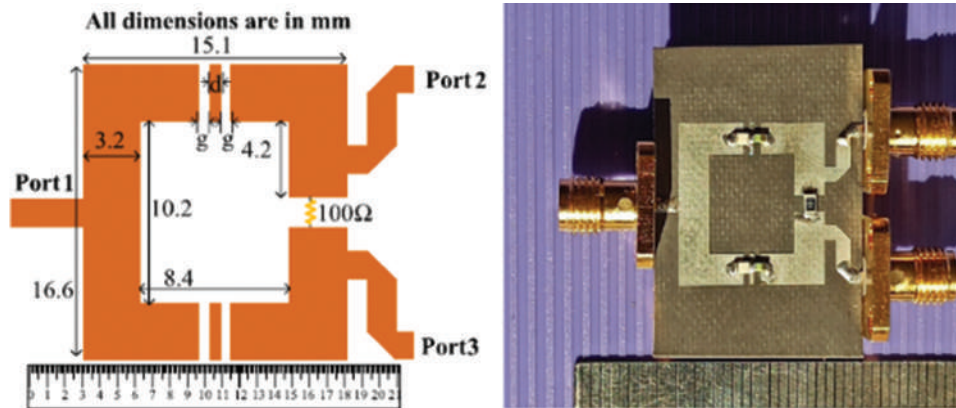


Fig. 22. The structure and fabricated photo of the hybrid power divider using series LC (Jamshidi, et al., 2021).

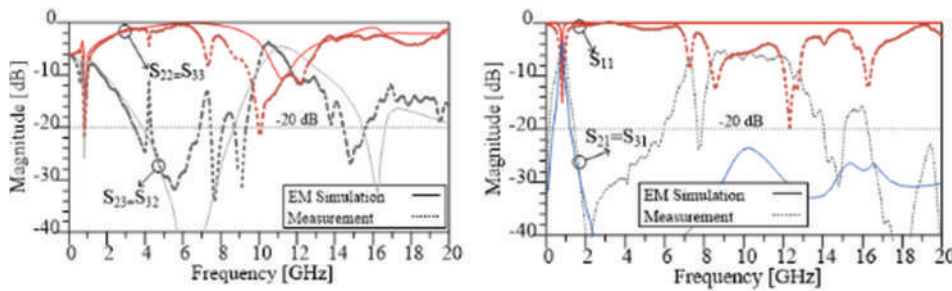


Fig. 23. The frequency responses of the hybrid power divider using series LC (Jamshidi, et al., 2021).

with 100% size reduction and infinite harmonic elimination theoretically. This power divider is fabricated on RT/Duorid 5880 substrate with a relative permeability of 2.2 and a thickness of 0.508 mm.

This power divider is designed at 800 MHz frequency and has a very small size which is 82.5% smaller compared to the conventional divider. This structure is a general design method for working at different frequencies and desired



size reduction percentages in reference Jamshidi, et al. (2021), and several examples are designed with different size reduction percentages. In practice, the above structure was implemented on a frequency of 800 MHz and good results were obtained. The fabricated divider suppresses the 2<sup>nd</sup>–25<sup>th</sup> harmonics with a suitable attenuation level, which frequency response is shown in Fig. 23. The insertion loss of the divider is below 0.1 dB in the operating frequency, and the isolation between output ports is better than 38 dB at the operating frequency.

In Heydari and Roshani (2021), with using resonators, lumped inductors, and capacitors, a compact divider is designed with harmonic suppression. This divider is implemented on RT/Duorid 5880 substrate with a  $\epsilon_r$  of 2.2. In this divider, two series inductors and a parallel capacitor are used as shown in Fig. 24. This divider works at 1500 MHz frequency and has a very small size, which

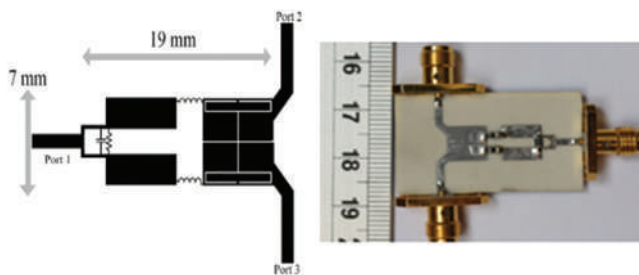


Fig. 24. The structure and fabricated photo of the divider using series inductors and parallel capacitor (Heydari and Roshani 2021).

shows 52% size reduction in compared with the typical divider at 1500 MHz frequency. The frequency response of this divider is depicted in Fig. 25, as seen in this divider, removes the 3<sup>rd</sup> up to 6<sup>th</sup> harmonics well, and has 0.15 dB insertion loss, which shows the proper performance of this designed divider.

A dual-band divider using lumped capacitors, with compact size and suppressed harmonics, is designed in Rostami and Roshani (2018). This divider correctly works at two frequencies of 0.9 and 1.8 GHz. To reduce the size and also eliminate harmonics, lumped capacitors are used in the structure of this divider as seen in Fig. 26. This divider has 80% size reduction compared with the typical dual-band divider at same frequencies.

The frequency response of this divider shows in Fig. 27, as results show, this divider correctly works at two frequencies of 0.9 and 1.8 GHz, with 0.1 dB insertion loss and provides a wide suppression level from 3.1 to 10.6 GHz frequencies.

Layout, substrate, and advantage of some designed power dividers using LC components are listed in Table III as follows:

### V. POWER DIVIDER WITH COUPLED LINES TECHNIQUES

Using coupled lines, in microwave devices particularly in power dividers, can improve the performance of the devices, such as efficient power division, impedance transformation, filtering capabilities, size reduction, and improved performance characteristics. These benefits make coupled-line structures valuable building blocks

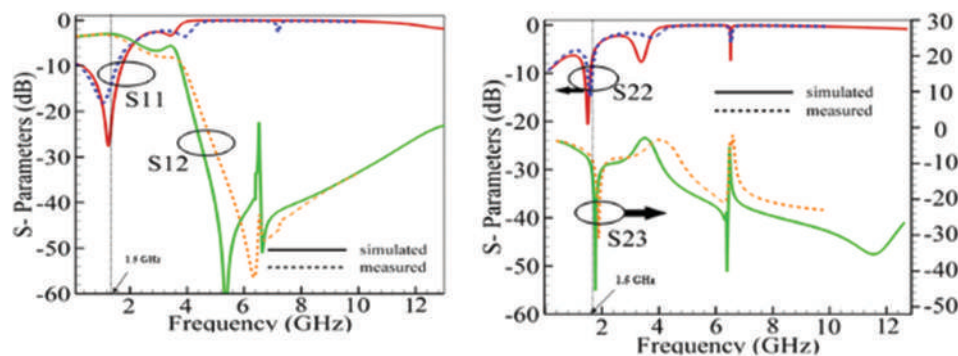


Fig. 25. The frequency responses of the power divider using series inductors and parallel capacitor (Heydari and Roshani 2021).

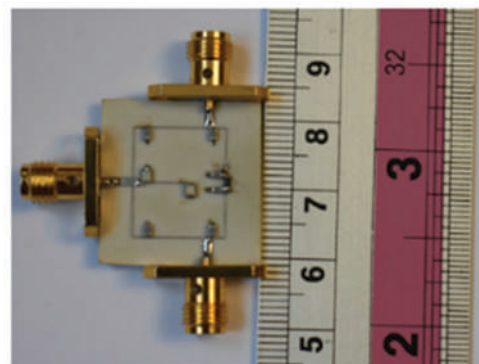
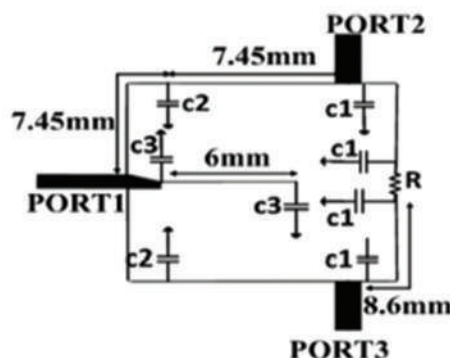


Fig. 26. The structure and fabricated photo of the dual-band divider using lumped capacitors (Rostami and Roshani 2018).

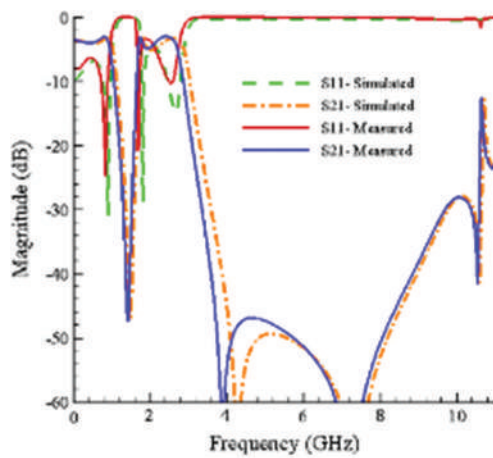


Fig. 27. The frequency responses of the dual-band divider using lumped capacitors (Rostami and Roshani 2018).

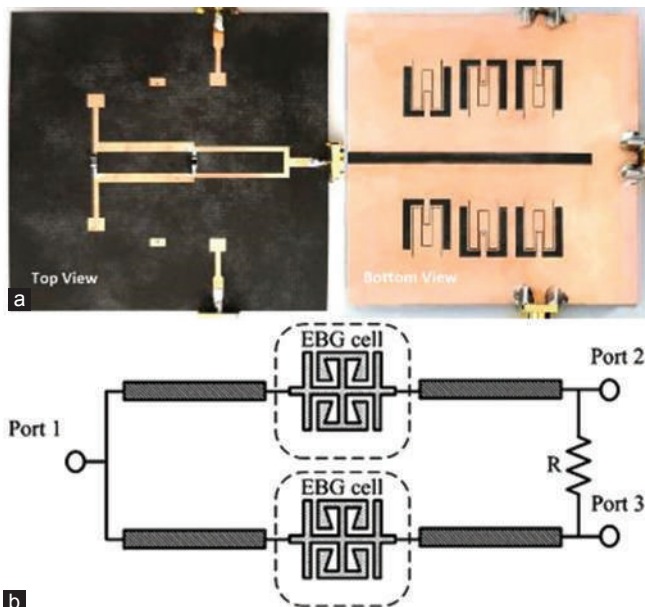


Fig. 28. (a and b) Using defected ground structure (Rao, et al., 2020) and EBG techniques (Lin, et al., 2007) in power divider for performance improvement.

in microwave circuit design and enable the development of advanced and high-performance microwave systems. Coupled-line structures can be used to implement bandpass or band-stop filtering functions. By exploiting the coupling between the lines, specific frequencies can be allowed to propagate whereas suppressing others. Furthermore, coupled-line structures can help in reducing the size of microwave devices.

The presented work in Chen and Ho (2017) introduces the design equations for a coupled-line divider. These equations provide analytical solutions for the design parameters, allowing the divider to be suitable for a desired two-pole Butterworth or Chebyshev response. The derived design equations enable the design of dividers with desired frequency responses, and the concept presented in the paper can be extended to higher-order filtering dividers for

improved selectivity. In Lin and Chu (2010), an approach is introduced to designing a dual-band divider with a selective dividing ratio based on coupled-lines. A dual-band quarter-wave length transformer using coupled-lines is presented as a replacement for the traditional quarter-wave length transformer in a typical divider. The designed divider exhibits a simple and structure with compact size and wide bandwidth performance for a small frequency ratio. A divider using coupled lines and compact size is presented in Singh, Basu and Wang (2009). In this divider, a single-stage coupled line is used in the typical Wilkinson divider structure, resulting in a compact layout. According to the results of this paper, the designed power divider improves bandpass frequency response and offers a compact size.

The performances of some power dividers approaches, which have exploited coupled line techniques, are compared in Table IV.

## VI. POWER DIVIDER WITH ELECTROMAGNETIC BANDGAP (EBG) AND DEFECTED GROUND STRUCTURE (DGS) TECHNIQUES

EBG and DGS techniques are two important concepts which have commonly used in microwave engineering, particularly in the design of power dividers, as shown in Fig. 28. DGS is a technique used to create specific patterns or structures in the ground plane of a microwave circuit to achieve desired electromagnetic characteristics. The DGS is typically implemented by etching slots, patches, or other shapes into the ground plane beneath the transmission lines or other components. Using DGS structures in the power dividers may result in improving isolation between output ports, improve return loss, or provide frequency selectivity, depending on the specific requirements of the design.

On the other hand, EBG techniques involve the use of periodic structures to create bandgaps in the electromagnetic spectrum. In power divider design, EBG techniques can be utilized to achieve performance improvement in terms of isolation, insertion loss, and bandwidth. By using EBG structures into the power divider circuit, unwanted harmonics can be suppressed.

A miniaturized WPD for GSM applications is presented in Gupta, Ghosh, and Toppo (2011). The conventional design is modified by replacing the quarter-wave sections with fractals, resulting in a smaller device. To compensate for the performance degradation caused by miniaturization, a DGS is employed. The proposed design occupies only 56% of the area, compared to the typical divider. In He, et al. (2013), a novel divider that combines SIW and DGS techniques together is presented to provide filtering response. The integration of SIW offers advantages, such as low loss, easy implementation, and seamless integration with planar circuits. By incorporating DGS, the proposed power divider achieves filtering capabilities, reducing the need for an additional filter and resulting in size and cost reduction. Furthermore, the presented work in Mohassieb, et al. (2010), focuses on the design, simulation, and fabrication

TABLE I  
LAYOUT, SUBSTRATE, AND ADVANTAGE OF SOME POWER DIVIDERS USING OPEN STUBS

References	Layout of BLCs	Method	Substrate	$\epsilon_r$	Thickness	Advantages
Cheng and Ip, 2010		Open stubs	RT_Duroid 5880	3.38	0.813 mm	1. Simple structure 2. 2 <sup>nd</sup> -4 <sup>th</sup> harmonics suppression 3. No size reduction
Hayati and Roshani, 2013		Open stubs	RT_Duroid 5880	2.2	0.381 mm	1. Simple structure 2. 3 <sup>rd</sup> -5 <sup>th</sup> harmonics suppression 3. 35% size reduction
Hayati, Roshani and Roshani, 2013		Open stubs	RT/Duroid	2.2	0.381 mm	1. Simple structure 2. 2 <sup>nd</sup> -6 <sup>th</sup> harmonics suppression 3. No size reduction
Roshani, et al., 2022		Open and Short stubs	RT/Duroid	2.2	0.508 mm	1. Simple structure 2. 2 <sup>nd</sup> -3 <sup>rd</sup> harmonics suppression 3. No size reduction
Lotfi, et al., 2020		Open and Short stubs	RT/Duroid	2.2	0.787 mm	1. Simple structure 2. 2 <sup>nd</sup> -4 <sup>th</sup> harmonics suppression 3. No size reduction
Roshani and Roshani 2020		Open stubs	RO4003	3.65	0.508 mm	1. Semi complex 2. 2 <sup>nd</sup> -15 <sup>th</sup> harmonics suppression 3. 73% size reduction

of miniaturized branch-line couplers (BLCs) operating at 2.4 GHz. Two techniques are employed to reduce the size of the conventional BLC: High impedance open stubs (HIOS) and DGS. The HIOS approach reduces the size by over 57.5% without compromising power handling capability. The DGS technique further reduces the size by more than 18% whereas achieving any desired dividing ratio and suppressing higher-order modes.

A design procedure of an unequal Wilkinson divider using a DGS is presented in Lim, et al. (2001). Using the DGS in the unequal Wilkinson topology, a 4:1 power dividing ratio is easily achieved, which would be impractical with conventional microstrip lines due to thin conductor width and low aspect ratio. A 4:1 power divider is designed and measured at 1.5 GHz to validate the proposed approach. The measured performance demonstrates excellent matching, isolation, and accurate dividing ratios at different ports. The DGS implementation allows for a larger conductor width, reduced length, and overall smaller circuit size, making it advantageous for high-impedance lines. The presented work in Rao, et al. (2020) introduces two types of hybrid microstrip/DGS cells, for passive device fabrication with an ultra-wide

stopband. These cells feature dual-resonance characteristics achieved through stepped-impedance DGS and embedded folded slot-line on the ground.

A planar WPD is designed for the suppression of harmonics using microstrip EBG cells in Lin, et al. (2007). The proposed technique utilizes the EBG cells to suppress unwanted harmonics and reduce the circuit size over 30% compared to the typical divider. The planar structure facilitates easy circuit design on printed circuit boards. The measured results demonstrate excellent performance, with third and fourth harmonics suppression. Furthermore, an EBG in-phase hybrid-ring equal power divider is presented in Ooi (2005). A systematic design technique is introduced, utilizing closed-form analytical expressions for the EBG structure. The proposed structure achieves an increase in both input and output impedance bandwidth of approximately 10%, compared to conventional hybrid-ring equal power dividers. The proposed EBG in-phase hybrid-ring equal power divider offers a broader bandwidth, occupies a smaller area, and exhibits good harmonic suppression characteristics. The performances of some power dividers approaches, which have exploited DGS and EBG techniques, are compared in Table V.

TABLE II  
LAYOUT, SUBSTRATE, AND ADVANTAGE OF SOME POWER DIVIDER USING RESONATOR

References	Layout of BLCs	Method	Substrate	$\epsilon_r$	Thickness	Advantages
Hayati, Roshani and Roshani 2013		Resonator	RT_Duroid 5880	2.2	0.381 mm	1. Simple structure 2. 3 <sup>rd</sup> -5 <sup>th</sup> harmonics suppression 3. 29.3% size reduction
Hayati, et al., 2013		Resonator	RT_Duroid 5880	2.2	0.508 mm	1. Simple structure 2. 2 <sup>nd</sup> -12 <sup>th</sup> harmonics suppression 3. 71% size reduction
Roshani, 2017		Resonator	RT_Duroid 5880	2.2	0.508 mm	1. Simple structure 2. 2 <sup>nd</sup> -4 <sup>th</sup> harmonics suppression 3. 65% size reduction
Roshani and Siahkamari, 2022		Resonator	RT/Duroid	2.2	0.787 mm	1. Simple structure 2. 2 <sup>nd</sup> -5 <sup>th</sup> harmonics suppression 3. 37% size reduction
Roshani, et al., 2021		Resonator and Open stubs	RT_Duroid 5880	2.2	0.508 mm	1. Simple structure 2. 2 <sup>nd</sup> -11 <sup>th</sup> harmonics suppression 3. No size reduction

TABLE III  
LAYOUT, SUBSTRATE, AND ADVANTAGE OF SOME POWER DIVIDER USING LC COMPONENTS

References	Layout of BLCs	Method	Substrate	$\epsilon_r$	Thickness	Advantages
Jamshidi, et al., 2021		Lumped L and C	RT_Duroid 5880	2.2	0.508 mm	1. Complex structure 2. 2 <sup>nd</sup> -25 <sup>th</sup> harmonics suppression 3. 82.8% size reduction
Heydari and Roshani 2021		Lumped L and C	RT_Duroid 5880	2.2	0.508 mm	1. Complex structure 2. 2 <sup>nd</sup> -8 <sup>th</sup> harmonics suppression 3. 52% size reduction
Rostami and Roshani, 2018		Lumped L and C	RT_Duroid 5880	2.2	0.508 mm	1. Complex structure 2. 2 <sup>nd</sup> -12 <sup>th</sup> harmonics suppression 3. 80% size reduction

TABLE IV  
LAYOUT, SUBSTRATE, AND ADVANTAGE OF SOME POWER DIVIDER USING COUPLED LINE

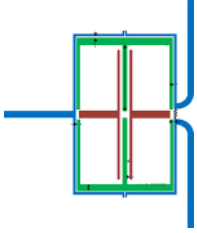
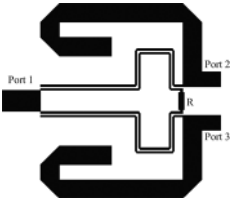
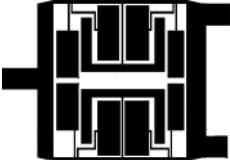
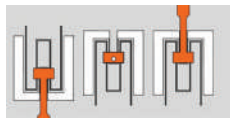
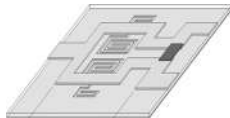
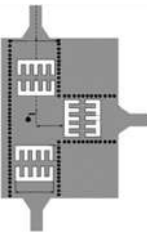
References	Layout of BLCs	Method	Substrate	$\epsilon_r$	Thickness	Advantages and Comments
Roshani, et al., 2022		Coupled lines, open Stubs	RT_Duroid 5880	2.2	30 mil	1. Simple structure 2. 2 <sup>nd</sup> -6 <sup>th</sup> harmonic suppression 3. Dual band operation 4. No size reduction
Soleymani and Roshani, 2020		Coupled lines, Open stubs, bended lines	RT/Duroid	2.2	0.508 mm	1. Simple structure 2. The 2 <sup>nd</sup> Harmonics suppression 3. Wide band operation 4. No size reduction
Lotfi, Roshani and Roshani, 2020		Coupled lines, Open stubs,	RT/Duroid	2.2	31 mil	1. Simple structure 2. The 2 <sup>nd</sup> -14 <sup>th</sup> harmonics suppression 3. Wide band operation 4. Size reduction of 50%

TABLE V  
LAYOUT, SUBSTRATE, AND ADVANTAGE OF SOME POWER DIVIDER USING DGS (RAO, ET AL., 2020) AND EBG TECHNIQUES

References	Layout of BLCs	Method	Substrate	$\epsilon_r$	Thickness	Advantages and Comments
Rao, et al., 2020		DGS Hybrid Microstrip	RT_Duroid 5880	2.2	0.508 mm	1. Dual band operation 2. Harmonics suppression 3. Filtering Response 4. No size reduction
Woo and Lee, 2005		Asymmetric DGS	GML1000	3.2	1.63 mm	1. Simple structure 2. 2 <sup>nd</sup> -3 <sup>rd</sup> harmonic suppression 3. Wide band operation 4. Size reduction of 9%
He, et al., 2013		DGS, SIW	RT_Duroid 5880	2.2	0.254 mm	1. Wide band operation 2. No size reduction

SIW: Substrate integrated waveguide, DGS: Defected ground structures

VII. CONCLUSION

Several methods for size reduction and harmonics suppression in microstrip power divider design, including open-ended stubs, resonators, coupled lines, DGS and EBG cells, and lumped reactive components are reviewed in this work. The topology, substrate, operating performance, advantages, and disadvantages of some of these dividers are investigated. The occupied size and numbers of suppressed harmonics, in these power dividers, are compared with conventional divider and reviewed. Most of reviewed dividers suppress unwanted harmonics and reduced occupied size compared with conventional divider, but some of them only suppress harmonics and increase circuit size.

REFERENCES

Barik, R.K., Koziel, S., and Pietrenko-Dabrowska, A., 2023. Broad stopband, low-loss, and ultra-compact dual-mode bandpass filter based on HMSIRC. *Electronics*, 12(13), p.2831.

Chen, C.J., and Ho, Z.C., 2017. Design equations for a coupled-line type filtering power divider. *IEEE Microwave and Wireless Components Letters*, 27(3), pp.257-259.

Cheng, K.K.M., and Ip, W.C., 2010. A novel power divider design with enhanced spurious suppression and simple structure. *IEEE Transactions on Microwave Theory and Techniques*, 58(12), pp.3903-3908.

Gupta, N., Ghosh, P., and Toppo, M., 2011. A miniaturized Wilkinson power divider using DGS and fractal structure for GSM application. *Progress in Electromagnetics Research Letters*, 7, pp.25-31.

- Hayati, M., and Roshani, S., 2013. A novel Wilkinson power divider using open stubs for the suppression of harmonics. *The Applied Computational Electromagnetics Society Journal (ACES)*, 28(6), pp.501-506.
- Hayati, M., Roshani, S., and Roshani, S., 2013. Miniaturized Wilkinson power divider with nth harmonic suppression using front coupled tapered CMRC. *The Applied Computational Electromagnetics Society Journal (ACES)*, 28(3), pp.221-227.
- Hayati, M., Roshani, S., Roshani, S., and Shama, F., 2013. A novel miniaturized Wilkinson power divider with nth harmonic suppression. *Journal of Electromagnetic Waves and Applications*, 27(6), pp.726-735.
- He, Z., Cai, J., Shao, Z., Li, I., and Huang, Y.M., 2013. A novel power divider integrated with SIW and DGS technology. *Progress in Electromagnetics Research*, 139, pp.289-301.
- Heydari, M., and Roshani, S., 2021. Miniaturized harmonic suppressed Wilkinson power divider using lumped components and resonators. *Wireless Personal Communications*, 117(2), pp.1527-1536.
- Jamshidi, M., Lalbakhsh, A., Lotfi, S., Siahkamari, H., Mohamadzade, B., and Jalilian, J., 2020. A neuro-based approach to designing a Wilkinson power divider. *International Journal of RF and Microwave Computer-Aided Engineering*, 30(3), p.e22091.
- Jamshidi, M.B., Lalbakhsh, A., Mohamadzade, B., Siahkamari, H., and Mousavi, S.M.H., 2019. A novel neural-based approach for design of microstrip filters. *AEU-International Journal of Electronics and Communications*, 110, p.152847.
- Jamshidi, M.B., Roshani, S., Talla, J., Roshani, S., and Peroutka, Z., 2021. Size reduction and performance improvement of a microstrip Wilkinson power divider using a hybrid design technique. *Scientific Reports*, 11(1), p.7773.
- Lalbakhsh, A., Ghaderi, A., Mohyuddin, W., Simorangkir, R.B.V.B., Bayat-Makou, N., Ahmad, M.S., Lee, G.H., and Kim, K.W., 2020. A compact C-band bandpass filter with an adjustable dual-band suitable for satellite communication systems. *Electronics*, 9(7), p.1088.
- Lalbakhsh, A., Jamshidi, M.B., Siahkamari, H., Ghaderi, A., Golestanifar, A., Linhart, R., Talla, J., Roy B.V.B. Simorangkir, R.B.V.B., and Mandal, K., 2020. A compact lowpass filter for satellite communication systems based on transfer function analysis. *AEU-International Journal of Electronics and Communications*, 124, p.153318.
- Lim, J.S., Lee, S.W., Kim, C.S., Park, J.S., Ahn, D., and Nam, S., 2001. A 4:1 unequal Wilkinson power divider. *IEEE Microwave and Wireless Components Letters*, 11(3), pp.124-126.
- Lin, C.M., Su, H.H., Chiu, J.C., and Wang, Y.H., 2007. Wilkinson power divider using microstrip EBG cells for the suppression of harmonics. *IEEE Microwave and Wireless Components Letters*, 17(10), pp.700-702.
- Lin, Z., and Chu, Q.X., 2010. A novel approach to the design of dual-band power divider with variable power dividing ratio based on coupled-lines. *Progress in Electromagnetics Research*, 103, pp.271-284.
- Lotfi, S., Roshani, S., and Roshani, S., 2020. Design of a Miniaturized planar microstrip wilkinson power divider with harmonic cancellation. *Turkish Journal of Electrical Engineering and Computer Sciences*, 28(6), pp.3126-3136.
- Lotfi, S., Roshani, S., Roshani, S., and Gilan, M., 2020. Wilkinson power divider with band-pass filtering response and harmonics suppression using open and short stubs. *Frequenz*, 74(5-6), pp. 169-176.
- Mohassieb, S., Barseem, I.M., Abdallah, E.A.F., and El-Hennawy, H.M., 2010. A compact microstrip power divider using periodic DGS and HIOS. *Progress in Electromagnetics Research*, 531, pp.22-26.
- Moloudian, G., Soltani, S., Bahrami, S., Buckley, J.L., O'Flynn, B., and Lalbakhsh, A., 2023. Design and fabrication of a wilkinson power divider with harmonic suppression for LTE and GSM applications. *Scientific Reports*, 13(1), p.4246.
- Ooi, B.L., 2005. Compact EBG in-phase hybrid-ring equal power divider. *IEEE Transactions on Microwave Theory and Techniques*, 53(7), pp.2329-2334.
- Pradhan, N.C., Koziel, S., Barik, R.K., and Pietrenko-Dabrowska, A., 2023. Bandwidth-controllable third-order band pass filter using substrate-integrated full-and semi-circular cavities. *Sensors*, 23(13), p.6162.
- Pradhan, N.C., Koziel, S., Barik, R.K., Pietrenko-Dabrowska, A., and Karthikeyan, S.S., 2023. Miniaturized dual-band SIW-based bandpass filters using open-loop ring resonators. *Electronics*, 12(18), p.3974.
- Rao, Y., Qian, H.J., Yang, B., Gómez-García, R., and Luo, X., 2020. Dual-band bandpass filter and filtering power divider with ultra-wide upper stopband using hybrid microstrip/DGS Dual-resonance cells. *IEEE Access*, 8, pp.23624-23637.
- Rezaei, A., and Yahya, S.I., 2022. A new design approach for a compact microstrip diplexer with good passband characteristics. *ARO-The Scientific Journal of Koya University*, 10(2), pp.1-6.
- Roshani, S., 2017. A Wilkinson power divider with harmonics suppression and size reduction using meandered compact microstrip resonating cells. *Frequenz*, 71(11-12), pp.517-522.
- Roshani, S., and Roshani, S., 2013. A simple Wilkinson power divider with harmonics suppression. *Electromagnetics*, 33(4), pp.332-340.
- Roshani, S., and Roshani, S., 2020. Design of a compact LPF and a miniaturized wilkinson power divider using aperiodic stubs with harmonic suppression for wireless applications. *Wireless Networks*, 26(2), pp.1493-1501.
- Roshani, S., and Shahveisi, H., 2022. Mutual coupling reduction in microstrip patch antenna arrays using simple microstrip resonator. *Wireless Personal Communications*, 126(2), pp.1665-1677.
- Roshani, S., and Siahkamari, P., 2022. Design of a Compact 1:2 and 1:4 power divider with harmonic suppression using resonator. *Wireless Personal Communications*, 126(3), pp.2635-2645.
- Roshani, S., Koziel, S., Roshani, S., Hashemi Mehr, F.S., and Szczepanski, S., 2022. Design and Implementation of a dual-band filtering wilkinson power divider using coupled T-shaped dual-band resonators. *Energies*, 15(3), p.1189.
- Roshani, S., Koziel, S., Roshani, S., Jamshidi, M.B., Parandin, F., and Szczepanski, S., 2021. Design of a patch power divider with simple structure and ultra-broadband harmonics suppression. *IEEE Access*, 9, pp.165734-165744.
- Roshani, S., Koziel, S., Yahya, S.I., Chaudhary, M.A., Ghadi, Y.Y., Roshani, S., and Golunski, L., 2023. Mutual coupling reduction in antenna arrays using artificial intelligence approach and inverse neural network surrogates. *Sensors*, 23(16), p.7089.
- Roshani, S., Yahya, S.I., Rastad, J., Mezaal, Y.S., Liu, L.W.Y., and Roshani, S., 2022. Design of a filtering power divider with simple symmetric structure using stubs. *Symmetry*, 14(10), p.1973.
- Rostami, P., and Roshani, S., 2018. A miniaturized dual band wilkinson power divider using capacitor loaded transmission lines. *AEU-International Journal of Electronics and Communications*, 90, pp.63-68.
- Singh, P., Basu, S., and Wang, Y.H., 2009. Coupled line power divider with compact size and bandpass response. *Electronics Letters*, 45(17), pp.892-894.
- Soleymani, H., and Roshani, S., 2020. Design and implementation of a bandpass wilkinson power divider with wide bandwidth and harmonic suppression. *Turkish Journal of Electrical Engineering and Computer Sciences*, 28(1), pp.414-422.
- Woo, D.J., and Lee, T.K., 2005. Suppression of harmonics in wilkinson power divider using dual-band rejection by asymmetric DGS. *IEEE Transactions on Microwave Theory and Techniques*, 53(6), pp.2139-2144.
- Yahya, S.I., and Rezaei, A., 2021. Design and fabrication of a novel ultra compact microstrip diplexer using interdigital and spiral cells. *ARO-The Scientific Journal of Koya University*, 9(1), pp.103-108.
- Yahya, S.I., Rezaei, A., and Khaleel, Y.A., 2021. Design and analysis of a wide stopband microstrip dual-band bandpass filter. *ARO-The Scientific Journal of Koya University*, 9(2), pp. 83-90.

# Real-time Traffic Monitoring System based on Deep Learning and YOLOv8

Saif B. Neamah and Abdulmir A. Karim

Department of Computer Sciences, University of Technology,  
Baghdad, Iraq

**Abstract**—Computer vision applications are important nowadays because they provide solutions to critical problems that relate to traffic in a cost-effective manner to reduce accidents and preserve lives. This paper proposes a system for real-time traffic monitoring based on cutting-edge deep learning techniques through the state-of-the-art you-only-look-once v8 algorithm, benefiting from its functionalities to provide vehicle detection, classification, and segmentation. The proposed work provides various important traffic information, including vehicle counting, classification, speed estimation, and size estimation. This information helps enforce traffic laws. The proposed system consists of five stages: The preprocessing stage, which includes camera calibration, ROI calculation, and preparing the source video input; the vehicle detection stage, which uses the convolutional neural network model to localize vehicles in the video frames; the tracking stage, which uses the ByteTrack algorithm to track the detected vehicles; the speed estimation stage, which estimates the speed for the tracked vehicles; and the size estimation stage, which estimates the vehicle size. The results of the proposed system running on the Nvidia GTX 1070 GPU show that the detection and tracking stages have an average accuracy of 96.58% with an average error of 3.42%, the vehicle counting stage has an average accuracy of 97.54% with a 2.46% average error, the speed estimation stage has an average accuracy of 96.75% with a 3.25% average error, and the size estimation stage has an average accuracy of 87.28% with a 12.72% average error.

**Index Terms** – Computer vision, Deep learning, Object detection, Traffic monitoring, YOLOv8.

## I. INTRODUCTION

The emergence of smart cities and intelligent traffic systems nowadays aims at enhancing human lives by enabling efficient use of infrastructure resources, reducing risks such as traffic collisions, and improving drivers' and pedestrians'

safety. The need for these types of systems is increasing across various domains such as transportation, public safety, and infrastructure management. In addition to the growth of cities, the increase in human population, and the number of vehicles, vehicular traffic data represents the most vital data source in smart city management systems. An effective analysis of this data can yield significant benefits for both citizens and governments. Traffic problems have increased as cities become larger. With the increasing number of vehicles, several network protocols have been developed to address this problem. These protocols require a data source that can continuously feed the network with traffic data provided by real-time traffic analysis systems (Dias, et al., 2023) (Farooq and Kanwal, 2023).

Road traffic accidents are one of the leading causes of mortality globally. In Iraq, traffic accidents have increased considerably, especially after 2003, as a result of the growth in the economy and population. The number of vehicles as of 2015 was 5.775 million, according to the 2018 World Health Organization (WHO) road safety report (WHO, 2018).

## II. RELATED WORKS

There are a number of studies that are conducted on vehicle detection and vehicle speed estimation, but very few on vehicle size estimation. Some of these studies are described below:

In 2020, Berna, Swathi, and Devi, presented in their work entitled “*Distance and Speed Estimation of Moving Object Using Video Processing*” a distance and speed estimation in real-time with 90% precision using a fixed camera and a centroid method. Object detection is done by performing frame differencing and thresholding, and the speed is estimated by dividing the manually measured distance by the time difference, and the vehicle length is also estimated (Berna, Swathi, and Devi, 2020).

In 2020, Costa, Rauen and Fronza, presented in their work entitled “*Car Speed Estimation Based on Image Scale Factor*” a vehicle speed estimation with a longitudinal trajectory relative to the camera without reference markers. They used the image scale factor (ISF) in pixels to calculate the distance from the vehicle to the camera in different video



frames, and they proposed to combine the ratio of  $\frac{fw}{W}$  and  $\frac{fh}{H}$  where  $f$  is the camera focal length,  $w$ ,  $h$  are the sensor's width and height, and  $W$ ,  $H$  are the image frame width and height into a single ISF, then estimate the distance and time difference to estimate the vehicle speed. The result of their work shows a maximum deviation of 2.2% for vehicle speed estimation (Costa, Rauen, and Fronza, 2020).

In 2021, Lin, Jeng, and Lioa, presented in their work entitled "A Real-time Vehicle Counting, Speed Estimation, and Classification System Based on Virtual Detection Zone and YOLO" the implementation of a real-time traffic monitoring system to count vehicles and estimate their speed with a classification facility. They based their work on the Gaussian mixture model (GMM) and you only look once v4 (YOLOv4). The GMM and a virtual detection zone are used for vehicle counting and detection. The GMM is used to perform background subtraction and foreground segmentation. The YOLOv4 model is used for vehicle classification, with a classification accuracy of 98.91% and an average absolute percentage error of vehicle speed estimation of 7.6% (Lin, Jeng and Lioa, 2021).

In 2022, Gupta et al. presented in their work entitled "Vehicle Speed Detection System in Highway" the implementation of a vehicle speed detection system using a video-based approach. The Haar cascade approach is used for vehicle detection and a correlation tracker, and speed estimation, they estimated the pixel per meter (PPM) ratio manually and calculated the speed by dividing the distance by the recorded time when the vehicle enters and leaves a region of interest. The detection accuracy was 95%, and for speed measurement, it was 92% (Gupta, et al., 2022).

In 2022, Shihab, Ghani, and Mohammed, presented in their work entitled "Machine Learning Techniques for Vehicle Detection" the implementation of a vehicle detection and classification system using two methods based on Haar cascade and YOLOv3. The detection results they got

were 86.9% for the Haar cascade approach and 91.31% for the YOLOv3 approach, concluding that YOLO-based algorithms have better detection results than Haar cascade-based methods. YOLO-based methods are robust to different lighting conditions (Shihab, Ghani, and Mohammed, 2022).

This paper implements a real-time system based on the most recent CNN-based deep learning models that give more accurate detection results with more critical information regarding traffic, including vehicle counting, vehicle classification, vehicle speed estimation, and vehicle size estimation. The vehicle size can be useful in enforcing speed limit laws on roads, as we know truck speed limits, for example, differ from salon car speed limits. The built-in classification facility in our proposed system can estimate the vehicle speed and vehicle count based on the vehicle class. The vehicle size estimation was not thoroughly researched in previous studies. In this paper, we present a new way to estimate vehicle size in real time. Table I summarizes the related works and their limitations compared with our work.

### III. TRADITIONAL TRAFFIC MONITORING SYSTEMS

A variety of hardware technologies are available for collecting traffic data to facilitate traffic surveillance systems, including sensors, induction loops, and microwave radars. All hardware technologies have their limitations. Induction loops only affect the point of measurements, limiting their spatial coverage, and with significant traffic density, their accuracy can degrade. The majority of surface sensors have high installation and maintenance costs. Handheld radar guns that rely on the principle of the Doppler effect, in addition to their equipment's high cost, require an on-site operator and a line of sight to perform the speed estimation, can only be applied to one vehicle at a time, and suffer from shadowing where more than one wave is reflected from vehicles with different heights (Koyuncu and Koyuncu, 2018).

TABLE I  
SUMMARY OF RELATED WORKS LIMITATIONS

Work	Year	Related works (limitations and comparison)
Distance and speed estimation of moving object using video processing	2020	Vehicle detection is based on the frame-differencing method. It is not clear if the system can track multiple vehicles; no vehicle size information is provided, and there is no vehicle counting facility. Our system tracks multiple vehicles and estimates the vehicle size with a counting facility.
Car speed estimation based on ISF	2020	It is not clear if the system works on multiple vehicles, and the system is not robust to motion blur; no vehicle size information is provided, and there is no counting facility. Our system works on multiple vehicles, is robust to motion blur, and the size information is estimated with a counting facility.
A real-time vehicle counting, speed estimation, and classification system based on a virtual detection zone	2021	There is no estimation of the vehicle's size. The system used an outdated YOLOv4 as a pre-trained object detector and classifier. Our system estimates the vehicle size, and the detection accuracy is higher based on the YOLOv8 model.
Vehicle speed detection system on highway	2022	The system used Haar cascades for vehicle detection and a correlation tracker. The detection and tracking are not powerful enough to deal with heavy traffic. There is no estimation of vehicle size information and no vehicle counting facility. Our system uses a deep-learning-based method that is more robust in vehicle detection and suitable for real-time applications. It also provides a counting facility with size estimation.
Machine learning techniques for vehicle detection	2022	The system is limited to multi-object detection and classification; there is no tracking applied and no counting facility; neither vehicle speed nor size information is provided. Used an outdated YOLOv3 model. Our system also provides multiple vehicle tracking and speed estimation in real time, based on the recent YOLOv8 model.

ISF: Image scale factor



#### IV. DEEP LEARNING-BASED TRAFFIC MONITORING SYSTEMS

Deep learning and convolutional neural network (CNN)-based object detection techniques can automatically extract features from input images and are more resilient to changes in illumination, shadows, and partial occlusions. The two primary methodologies of detection are the one-stage approach and the two-stage approach, which dominate the field of object detection. One-stage detectors, such as you only look once (YOLO) and single-shot detectors (SSD), approach object identification as a regression problem in which the bounding box coordinates and the object classes are predicted directly. However, two-stage detectors, like the region-based CNN (R-CNN), have two phases. Using a search approach, such as a selective method or a region proposal network, the first step is to produce a large number of region suggestions. The second step is to submit these region proposals for classification and bounding box regression. Two-stage detectors often have greater detection rates than one-stage detectors, but since there are more processes, they also take longer processing time (Liu, et al., 2021; Yasir and Ali, 2021).

#### V. CNNs

The CNN, also called ConvNet, is a very popular deep learning architecture that can learn directly from the input data without the need for manual human feature extraction. It includes *multiple* convolution and pooling layers. CNNs are specifically intended to deal with a variety of 2-dimensional shapes and are widely employed in the applications of computer vision, image segmentation, and object detection. The rapid development of GPU technology made CNNs so popular. In fact, one of the bottlenecks of deep neural networks is that training takes a long time because of the

many hidden units in the network. But as GPUs became faster, this bottleneck was overcome (Sarker, 2021; Raheem and AbdulHussain, 2020).

In CNNs, the states of each layer are arranged according to a spatial grid structure; these spatial relationships are inherited from one layer to the next because each feature value is based on a small local spatial region in the previous layer. Each layer in the convolutional network is a 3-dimensional grid structure that has a *height*, *width*, and *depth*. The depth of a single layer refers to the number of *channels* in each layer; in the case of colored RGB images, the depth is three. Fig. 1 demonstrates the traditional CNN model (Alzubaidi, et al., 2021; Awotunde, et al., 2023).

#### VI. OBJECT DETECTION WITH CNN

The problem of object detection can be efficiently solved with deep learning models. Object detection based on CNNs consists of two tasks: recognizing and localizing objects in the image. Recognition is a classification task that involves providing category information and the probability of the target. The other is a positioning task that involves finding the specific location of the target by utilizing bounding boxes with labels. There are various algorithms for object detection using CNNs, which are mainly divided into two main categories (Alzubaidi, et al., 2021) (AlNujaidi, AlHabib and AlOdhieb, 2023).

1. *Two-stage algorithms*: Like the R-CNN series, which generates at the first stage set ROIs that represent a set of category-independent bounding boxes in the image; at the second stage, it makes corrections based on the bounding box region to improve the final detection results. The two-stage algorithms give more accurate results, but they are more computationally expensive as they require the classification

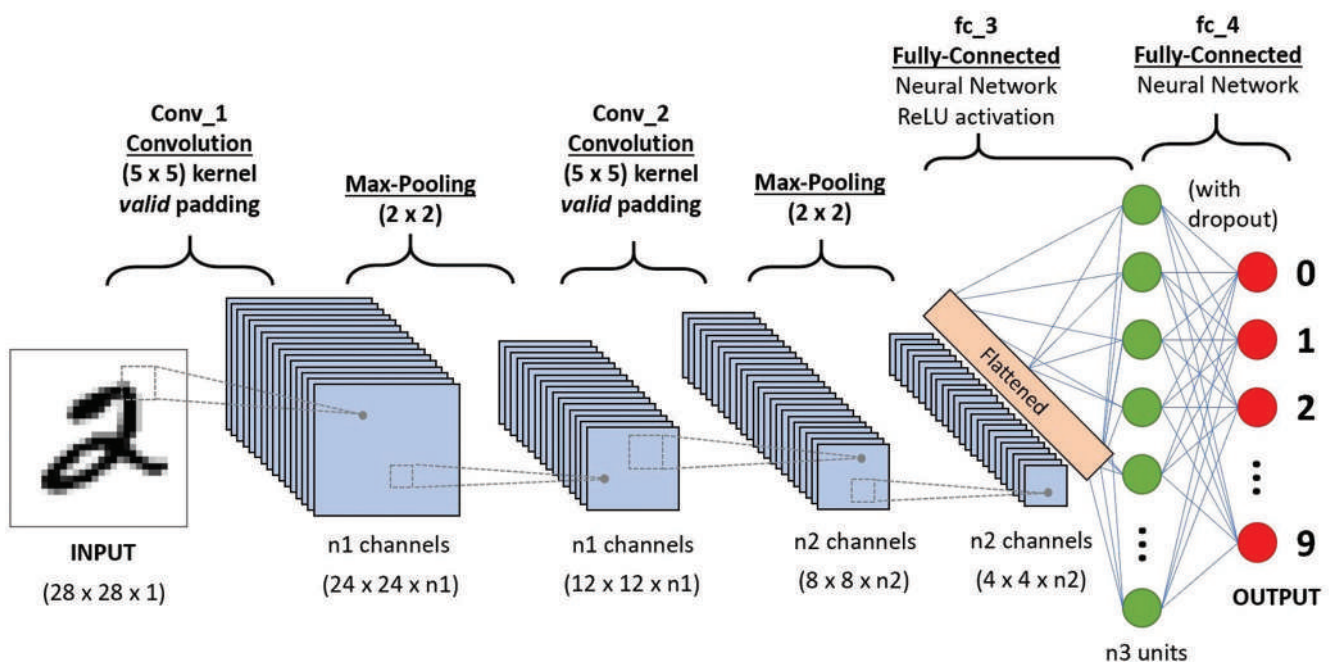


Fig. 1. Traditional CNN model. n is the number of image color channels.

network to be applied to a large number of ROIs, so this approach is slower than the one-stage algorithms (AlNujaidi, AlHabib and AlOdhieb, 2023) (Alzubaidi, et al., 2021).

2. *One-stage algorithms*: They merge the classification and regression into a single pass, like the YOLO series and SSD, divide the image into a fixed grid, and apply a classification network to each segment. The one-stage algorithms are fast but give less accurate detection results than the R-CNN algorithms (AlNujaidi, AlHabib and AlOdhieb, 2023) (Hakim and Fadhil, 2021).

## VII. YOLO ONE-STAGE DNN MODEL

YOLO is a real-time object detection algorithm that uses a single CNN to predict the bounding boxes and class labels of objects in an image. *YOLOv1* was introduced in 2015, which frames the object detection problem as a regression problem instead of a classification problem that classifies each pixel in the image. To eliminate duplicate detections, YOLO divides the input image into a grid and predicts the bounding boxes for the same class along with its confidence values; the output is then followed by a non-maximum suppression (NMS). There are 24 CNN layers in *YOLOv1* architecture, then two fully connected layers. All layers use leaky ReLU except for the last one, which uses a linear activation function. YOLO used (1\*1) convolutional layers to reduce the number of feature maps and the network parameters. The loss function used is composed of multiple sum-squared errors. *YOLOv2* was introduced in 2016 with various improvements, including detecting over 9000 object categories, adding batch normalization, using anchor boxes, using the Darknet-19 architecture composed of 19 convolutional layers and five max-pooling layers. *YOLOv3* was introduced in 2018 and evolved from Darknet-19 to Darknet-53 with residual connections. *YOLOv4* was introduced in 2020 with weighted residual connections, cross-stage partial connections (CSP), cross-mini-batch normalization, self-adversarial training, and mish-activation function as the backbone. *YOLOv5* was introduced in 2021 and implemented under the PyTorch framework. It has a focus layer to reduce the number of parameters and a CSP, which extends shallow information in the focus layer to maximize functionality. *YOLOv6* was introduced in 2022 with a plain single-path backbone for small models and efficient multi-branch blocks for

large models; this was done by proposing two scaled, re-parametrizable backbones and necks to accommodate models of different sizes. *YOLOv7*, which was introduced in 2022, proposed a planned re-parameterized model by merging multiple computational modules into one at the inference stage and made some architectural reforms. *YOLOv8* was introduced in 2023 and outperformed all previous models, as illustrated in Fig. 2 (Hussain, 2023) (Jocher, Chaurasia and Qiu, 2023).

## VIII. YOLOv8 ARCHITECTURE

*YOLOv8* proposed a new backbone network with a new anchor-free detection head, which means it predicts directly the center of an object instead of the offset from a known anchor box. It also proposes a new loss function. The basic architecture of *YOLOv8* consists of two major parts: the backbone for extracting feature maps and the head for detection, as illustrated in Fig. 3 (King, 2023).

The backbone contains a series of convolutional layers for different image resolutions and sizes, and then the features detected are passed through the advanced head for detection based on a loss function. New convolutional layers are used. The stem's first (6\*6) convolution is replaced by a (3\*3); the main building block was changed, and C2f replaced the *YOLOv5* C3. The bottleneck is the same as in *YOLOv5*, but the first convolution's kernel was changed from (1\*1) to (3\*3) in the neck, and features are concatenated directly without forcing the same channel dimensions. This reduces the parameter count and the overall size of the tensors (Jocher, Chaurasia and Qiu, 2023).

## IX. BYTETRACK MULTI-OBJECT TRACKING ALGORITHM

A state-of-the-art algorithm based on a combination of feature pyramids, anchor-free detection, and multiple-scale training makes it compatible with *YOLOv8*. The algorithm tracks by associating every bounding box instead of only the high-scoring ones. Data association is the core of multi-object tracking, which first computes the similarity between tracklets and detection boxes. A tracklet is a sequence of detections that are likely to belong to the same object. The similarity metrics may include location, motion, and

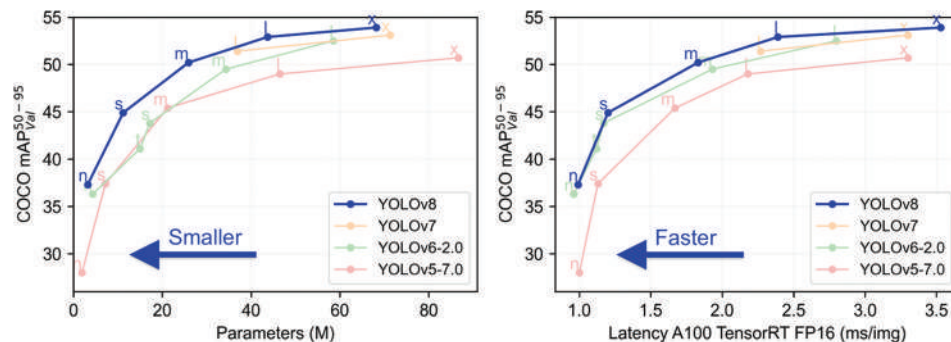


Fig. 2. YOLOv8 evaluation against recent YOLO models.

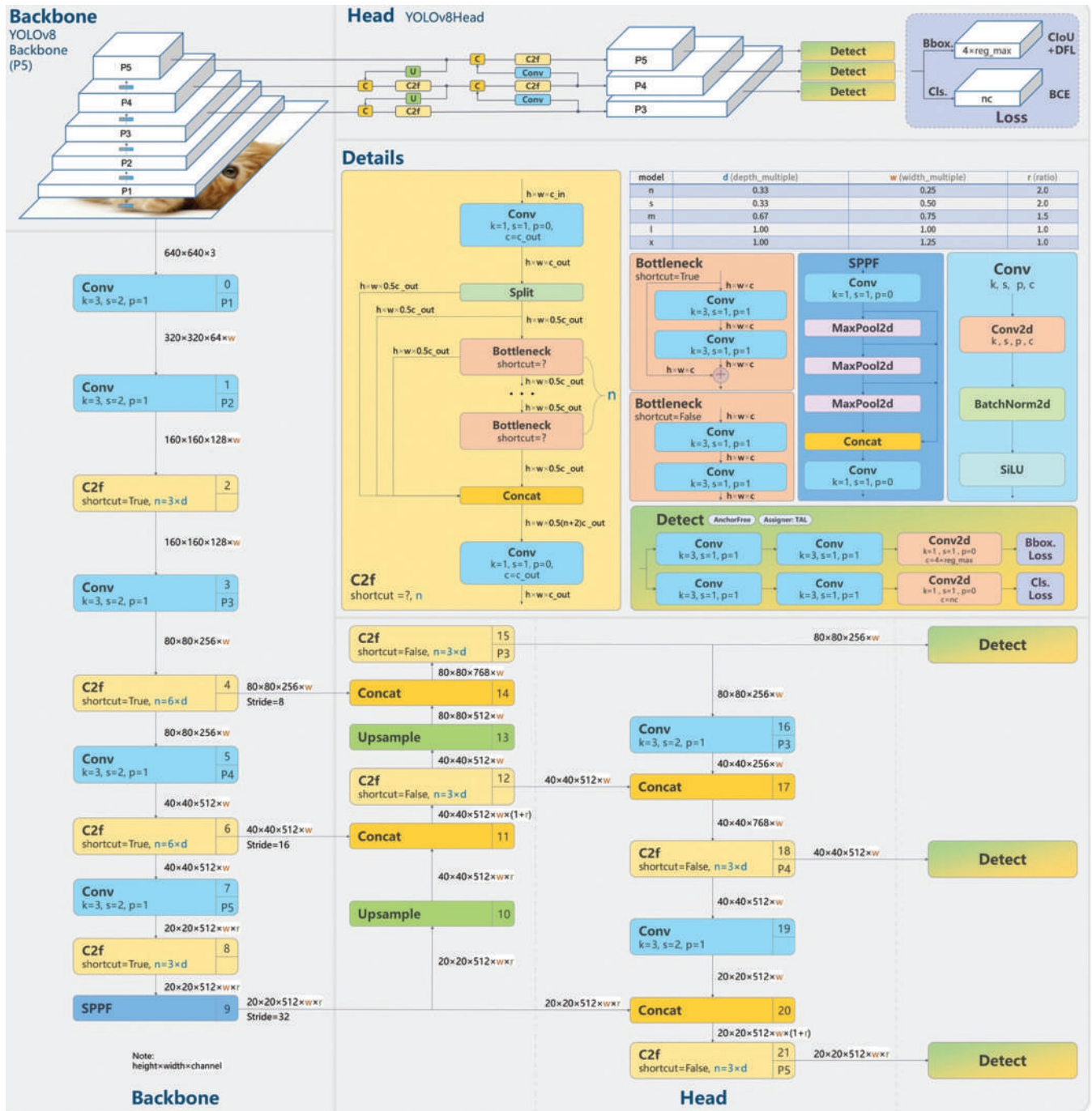


Fig. 3. YOLOv8 architecture.

appearance features. The ByteTrack algorithm tracks objects with high or low values of confidence by presenting a BYTE method for each detection box. First, the high-scoring boxes are tracked based on motion similarity or appearance similarity, and a Kalman filter is adopted to predict the location of the objects in the next frame. The similarity can be computed by the IoU or Re-ID feature distance between the predicted box and the detection box. After similarity computation, the matching strategy assigns identities to the objects using the Hungarian algorithm. Algorithm 1 provides the pseudocode for the BYTE algorithm (Zhang, et al., 2022).

### X. THE PROPOSED SYSTEM ARCHITECTURE

The general architecture of the proposed system consists of several stages that start with the preprocessing stage, which includes the camera calibration and calculation of the PPM ratio, calculating the ROIs, determining the video source, preparing to read the live video feed, dividing the live video into a series of frames, and resizing the video frames into the standard resolution (640\*640). Then comes the detection stage for specified classes of vehicles that implement the YOLOv8 pretrained classification and segmentation model, and then a tracking algorithm is applied to the detected vehicles to track their movements. The tracking stage is

**Algorithm 1:** BYTE Algorithm**Input:**  $V$ : video file;  $D$ : object detector;  $\theta$ : detection score threshold**Output:**  $T$ : tracks**Begin:****Step 1:** Initialize  $T=0$ **Step 2:** for frame  $f_k$  in  $V$  do $D_k \leftarrow Det(f_k)$  $D_{high} \leftarrow 0$  $D_{low} \leftarrow 0$ **Step 3:** for  $d$  in  $D_k$  doIf  $d$ . score  $> \theta$  then $D_{high} \leftarrow D_{high} \cup \{d\}$ 

else

 $D_{low} \leftarrow D_{low} \cup \{d\}$ **Step 4:** for  $t$  in  $T$  $t.KalmanFilter(t)$ **Step 5:** Associate  $T$  and  $D_{high}$  using similarity1**Step 6:**  $D_{remain} \leftarrow$  remaining boxes from  $D_{high}$ **Step 7:**  $T_{remain} \leftarrow$  remaining tracks from  $T$ **Step 8:** Associate  $T_{remain}$  in  $D_{low}$  using similarity2**Step 9:**  $T_{re-remain} \leftarrow$  remaining tracks from  $T$ **Step 10:**  $T \leftarrow T \setminus T_{re-remain}$  // delete unmatched tracks**Step 11:** for  $d$  in  $D_{remain}$  do $T \leftarrow T \cup \{d\}$ 

end for

return

**End**

essential for the speed estimation stage; it assigns track IDs to the detected vehicles. Finally, size estimation is performed to calculate the size of segments provided by the segmentation model according to the calibration parameters. The following block diagram in Fig. 4 illustrates a general block diagram of the proposed system.

The system also includes a vehicle counting process, which counts the vehicles passing through the ROIs in real-time based on the center of the detected vehicle passing within the coordinates of the ROI lines. The counter is displayed on the video output, and the total number of vehicles passed during the observation period is recorded in the log file in CSV format. The tracking trial drawing process, which is an optional process that draws a tracking trail behind the tracked vehicles to give the viewer a sense of tracking, the output of the proposed system is presented as a video stream that is displayed to the viewer as long as the system is running. The stream can also be saved to the hard disk as a video file in MP4 format. The proposed system will also produce a log file that will contain all the important information calculated by the system, including the timestamp for the system's first run, each car's estimated speed and estimated size associated with the car tracking ID and class ID, the timestamp for each calculation, and the total car count number.

## XI. THE PROPOSED SYSTEM'S STAGES

The proposed system consists of five stages; each stage leads to the next one, and every stage contains specific details that will be explained in the following sub-sections.

## A. The Preprocessing Stage

The first stage contains three main steps, which are the camera calibration step, the ROI calculation step, and the input preparation step. The camera calibration step is essential for the speed and size estimation stages. The calibration is done using a reference object with known dimensions (one known car dimension, e.g.,) at the speed and size estimation ROIs. It is necessary to calculate the PPM ratio, which is used to estimate the real distance in the ROI and the real size of the detected vehicles. The second step is the ROI calculation. In the proposed system, two ROIs are specified, namely, ROI1 and ROI2, and three lines, namely, Line 1, Line 2, and Line 3, as illustrated in Fig. 5. The picture was taken by a phone camera at Mohammed Al Qassim Highway Street in Baghdad, Iraq.

The reason behind dividing the ROI into two regions is that we want to get the most accurate results possible, so the speed is calculated in ROI1, then calculated again in ROI2, and the average speed will be taken as the final result for the vehicle's estimated speed. The final step at this stage is

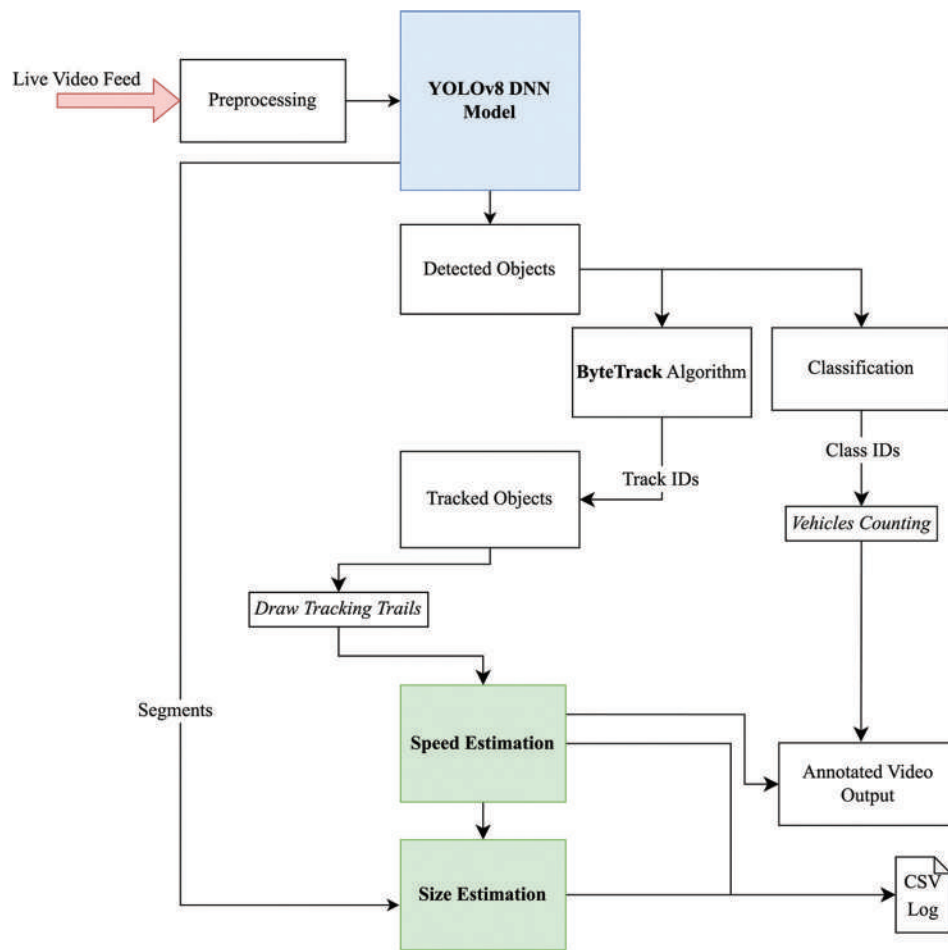


Fig. 4. The proposed system's block diagram.



Fig. 5. The proposed system's ROIs.

the input preparation step, where the source video input is determined and resized to (640\*640) resolution, and then the video frames are extracted.

### B. The Vehicle Detection Stage

The detection stage deploys the pretrained YOLOv8 DNN models. The detection algorithm consists of multiple layers of convolution (Conv), coarse-to-fine (C2f), concatenation (Concat), upsampling (Upsample), spatial pixel per feature (SPPF), and finally the segmentation process. The Conv layer involves the standard convolution operation of a

sliding window with predefined kernels, a stride of 1, no padding, and the SiLU activation function, followed by batch normalization to improve the overall learning process. The C2f process involves a convolution operation with a kernel of size (1\*1), no padding, and a stride of 1, then the output is entered into a split operation that is fed to the bottleneck; the bottleneck itself consists of two convolutional layers with residual connections. Then the concatenation operation is performed, and finally another convolution is performed.

The SPPF is spatial pyramid pooling (fast), similar to the SPP used in YOLOv5, which involves two convolution layers and three max-pooling layers, used to capture multi-scale information and improve the detection performance of the network, enabling the network to detect objects at different sizes more accurately. The upsample process involves increasing the size of the matrices by using a transposed convolution process with a stride of 2 and a padding of 1. It increases the spatial resolution of the feature maps, which helps improve object localization. The Concat process involves the concatenation of a list of tensors into a tensor of one dimension. This will enable feature fusion, model flexibility, and the handling of multiple inputs. Fig. 6 demonstrates the multiple layers of the DNN segmentation model.

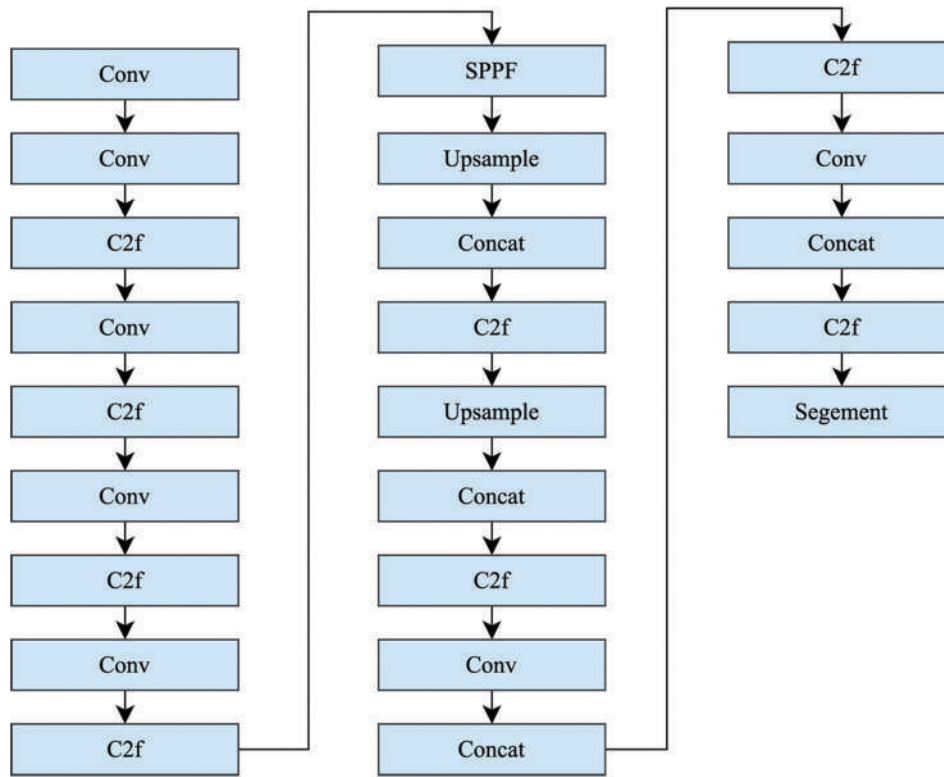


Fig. 6. YOLOv8 segmentation model layers.

### C. The Vehicle Tracking Stage

The tracking stage depends on the results of the detection stage as the tracker tracks the detected bounding boxes of the vehicles. The ByteTrack algorithm is applied to track the moving vehicles in the scene based on their detected bounding boxes, and then the algorithm will assign a track identification number (*track ID*) for each tracked vehicle. The tracking stage is essential to the proposed system as it will be used in the vehicle counting process and the speed estimation stage for calculating the speed of the tracked vehicle in the scene. The vehicle counting process starts after the detection stage and during the tracking stage. The counting process is performed in the predefined ROIs. Line 1 of ROI1 will be used to define the vehicle's entering point, and Line 2 will define the vehicle's leaving point. At the entry line, the center of each detected vehicle is calculated using the following equation:

$$(cx, cy) = \left( \frac{x + (x + w)}{2}, \frac{y + (h + y)}{2} \right) \quad (1)$$

Where:  $(x, y)$  is the detected object's bounding box top left corner coordinates.  $(w, h)$  is the detected object's bounding box width and height.  $(cx, cy)$  is the center coordinate of the detected object.

Several important pieces of information are stored in a queue, including the car ID, the time of entering in seconds (TIME1), and the vehicle's calculated center (CENTER1). This information will be used later in the speed estimation stage. When the vehicle approaches Line 1 by a predefined

offset, it will be considered that the vehicle has entered ROI1, and a vehicle counter will increase. The offset is manually fine-tuned and is essential to the system's performance because, in real-time systems that employ heavy processing of DNN models, the system will encounter some cases of missed detections during the vehicle's movement that can be solved with this offset to expand the detection zone. Fig. 7 demonstrates the three lines in the ROI with offset values.

### D. The Speed Estimation Stage

The object counting process provides this stage with three queues (CARS\_Q1, CARS\_Q2, and CARS\_Q3), each corresponding to a line in the ROI. The queues contain the car ID, the timestamp, and the car center coordinates. The speed will be calculated two times in the proposed system: The first speed calculation will be between Line 1 and Line 2, and the second is between Line 2 and Line 3. Finally, the two calculations are averaged to produce the final estimated speed that will be displayed on the screen and stored in the log file along with the car ID number and the timestamp. Equations 2 and 4 use the Euclidean distance to calculate the distance between two centers, and Equations 3 and 5 divide the results by a calibration parameter (PPM) ratio.

$$distance1 = \sqrt{(CENTER2.x - CENTER1.x)^2 + (CENTER2.y - CENTER1.y)^2} \quad (2)$$

$$real\ distance1 = \frac{distance1}{PPM} \quad (3)$$

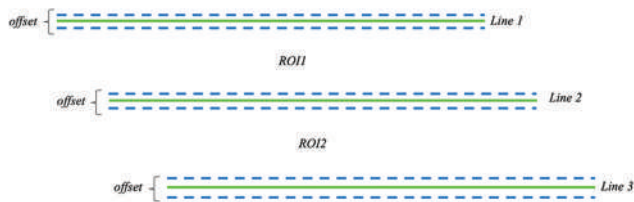


Fig. 7. The detection lines offsets.

$$distance2 = \sqrt{(CENTER3.x - CENTER2.x)^2 + (CENTER3.y - CENTER2.y)^2} \quad (4)$$

$$real\ distance2 = \frac{distance2}{PPM} \quad (5)$$

The time difference is also calculated for the two regions as the difference between the time recorded at Line 2 and the time recorded at Line 1, as in Equation 6, and the difference between the time recorded at Line 3 and Line 2, as in Equation 7.

$$\Delta Time1 = Time2 - Time1 \quad (6)$$

$$\Delta Time2 = Time3 - Time2 \quad (7)$$

Finally, the speed is calculated for the two regions as in Equations 8 and 9, and then the average speed is calculated between the two speeds as in Equation 10.

$$Speed1 = \frac{real\ distance1}{\Delta Time1} \quad (8)$$

$$Speed2 = \frac{real\ distance2}{\Delta Time2} \quad (9)$$

$$Average\ Speed = \frac{Speed1 + Speed2}{2} \quad (10)$$

The average speed is calculated in meters per second units; to display the speed in kilometers per hour (kmh) or miles per hour (mph), unit conversion equations 11 and 12 are applied.

$$Speed_{kmh} = Average\ speed * 3.6 \quad (11)$$

$$Speed_{mph} = Speed_{kmh} * 1.6093470879 \quad (12)$$

The details of the speed estimation at ROI1 and ROI2 are demonstrated in Algorithm 2.

### E. The Size Estimation Stage

The size estimation stage depends on the output of the pretrained segmentation model of YOLOv8 in the detection stage, which generates segments (masks) for each vehicle. The following steps are performed to estimate the area and size: Step 1: The generated mask, which is a series of points that surround the detected vehicle, is used to draw a polygon filling the detected vehicle using the *fillPoly* OpenCV method. Step 2: The area of the polygon is calculated using the *contourArea* OpenCV method, as in Equation 13.

$$pixel_{area} = contourArea(mask) \quad (13)$$

Step 3: The calculated area is divided by PPM to get an estimation of the real area of the detected vehicle, as Equation 14 shows.

$$real_{area} = \frac{pixel_{area}}{PPM} \quad (14)$$

As the vehicle gets closer to the camera, its image will increase in area, so we need to have a fixed region for measuring the area of the vehicle in that region. In the proposed system, the area of the vehicle is measured if the center of the vehicle's bounding box reaches line 2. The estimated area is stored in the log file alongside the car ID. Step 4: The size of the vehicle is a three-dimensional measurement, and since the proposed system utilizes a single camera, one dimension of the detected vehicle will be lost since images are stored in computers as two-dimensional data structures. The least variable vehicle dimension is the vehicle width, and since our proposed system performs vehicle classification into four vehicle classes (car, bus, truck, and motorcycle), we assumed that the width of these vehicle types is approximately equal for each class; vehicles usually vary greatly in length and height. Through an Internet search, we found that the average salon car width is approximately 1.5 m. The average bus width is approximately 2 m. The average truck width is approximately 2.5 m, and the average motorcycle width is approximately 0.5 m. Estimating the size of the vehicle requires calculating the vehicle's length and height. Using the top-side view camera position and acquiring the vehicle mask through the segmentation stage, we can find the two dimensions by taking the point with the lowest y value and the point with the highest y value to represent the two points of the vehicle length. Applying the Euclidian distance, we will obtain the vehicle's length. Similarly, from these points, we can find the height, then apply the size equation 15 to get the approximated size in pixels, and then apply equation 16 to estimate the real size in meters by dividing the size in pixels over the PPM ratio.

$$pixel_{size} = vehicle_{length} * vehicle_{width} * vehicle_{height} \quad (15)$$

$$real_{size} = \frac{pixel_{size}}{PPM} \quad (16)$$

Fig. 8 demonstrates the approximated vehicle's length and height from the segmentation polygon points. Algorithm 3 demonstrates the steps to estimate the size of detected vehicles.

## XII. RESULTS AND DISCUSSION

The results of the proposed system are presented on the system's output screen with all the annotations applied to it by the multiple stages of the proposed system. Fig. 9 shows the proposed system's screen of results.

The detection stage will draw a bounding box around the detected vehicles; the bounding box of each vehicle will be annotated with the vehicle's tracking ID assigned by the ByteTrack tracking algorithm, the class name extracted from

**Algorithm 2:** The Speed Estimation Algorithm**Input:** CAR\_ID, CAR\_Q1, CAR\_Q2, CAR\_Q3: list of queues, PPM**Output:** SPEED\_Q1, SPEED\_Q2: queues with estimated speed values**Start:**

```

Step 1: SPEED_Q1 = [ ], SPEED_Q2 = [ ]
        offset = 20
        speed = speed1 = speed2 = 0
Step 2: check5 = cy <= (L2.start.y1 + offset)           // object at Line 2
        check6 = cy >= (L2.start.y1 - offset)
        check7 = cx <= L2.end.x2
Step 3: if check5 and check6 and check7
        For each object in CARS_Q1:
Step 4: dx = CENTER2.x - CENTER1.x
        dy = CENTER2.y - CENTER1.y
Step 5: distance1 = math.sqrt(math.pow(dx, 2) + math.pow(dy, 2))
Step 6: real_distance1 = distance1 / PPM
Step 7: delta_time1 = TIME2 - TIME1
Step 8: speed1 = (real_distance1 / delta_time1) * 3.6    // km/h
Step 9: SPEED_Q1.append([CAR_ID, speed1])
        End For
Step 10: check8 = cy <= (L3.start.y1 + offset)         // object at Line 3
        check9 = cy >= (L3.start.y1 - offset)
        check10 = cx <= L3.end.x2
Step 11: if check8 and check9 and check10
Step 12: For each object in CARS_Q2:
Step 13: dx = CENTER3.x - CENTER2.x
        dy = CENTER3.y - CENTER2.y
Step 14: distance2 = math.sqrt(math.pow(dx, 2) + math.pow(dy, 2))
Step 15: real_distance2 = distance2 / PPM
Step 16: delta_time2 = TIME3 - TIME2
Step 17: speed2 = (real_distance2 / delta_time2) * 3.6 // km/h
Step 18: SPEED_Q2.append([CAR_ID, speed2])
        End For
Step 19: if CAR_ID in SPEED_Q1 and CAR_ID in SPEED_Q2
        speed = int( (SPEED_Q1[CAR_ID] + SPEED_Q2[CAR_ID]) / 2 )
        speed_mph = int(speed * 1.6093470879)
        now = datetime.now()
Step 20: display (CAR_ID, speed, now) // show car id, speed, time on screen
        log (CAR_ID, speed, now). // store car id, speed, time on log file
        log (CAR_ID, speed_mph, now). // store car id, speed, time on log file
End

```



Fig. 8. Vehicle's height and length.

also provided in the proposed system, and it will produce a segment mask for each detected vehicle; the segment masks are filled with red to reflect the vehicle's blob. The speed estimation will also be shown at the top center of the screen. The text consists of the estimated speed, the vehicle ID, and a timestamp. This text will dynamically change as every vehicle passes through the ROI.

The classification process will assign different colors to each vehicle class as demonstrated in Fig. 10.

The proposed system was evaluated on test videos taken at different locations and lengths with different camera positions to evaluate the detection, tracking, classification, and counting processes, while the system was running on an

the COCO dataset after performing classification by the CNN model, and the confidence score. Instance segmentation is



**Algorithm 3:** The Area and Size Estimation Algorithm

**Input:** CAR\_ID, CLASS\_IDS, MASKS, PPM  
**Output:** SIZE\_Q: queue with estimated size values

```

Start:
    SIZE_Q = [ ]; offset = 20
Step 1: For each mask in MASKS:
    x1 = mask [0][0] // get the first point
    y1 = mask [0][1]
Step 2: check_mask1 = y1 <= (L2.start.y1 + offset) // object at Line 2
    check_mask2 = y1 >= (L2.start.y1 - offset)
    check_mask3 = x1 <= L2.end.x2
Step 3: if check_mask1 and check_mask2 and check_mask3:
Step 4: pixels_area = contourArea(mask)// calculate mask area
Step 5: real_area = pixels_area / PPM
Step 6: if CAR_ID not in SIZE_Q:
    SIZE_Q.append([CAR_ID, real_area])
    now = datetime.now( )
    log (CAR_ID, real_area, now) // store car id, area, time on log file
Step 7: p1 = min(mask[1]) // vehicle length points
    p2 = max(mask[1])
    v_length = math.sqrt((p2[0] - p1[0])**2+(p2[1] - p1[1])**2)
Step 8: p1 = min(mask[0]) // vehicle height points
    p2 = max(mask[6])
    v_height = math.sqrt((p2[0] - p1[0])**2+(p2[1] - p1[1])**2)
Step 9: v_width = 1.5 // default for salon cars
    If CLASS_ID == 3:
    v_width = 0.5 // motorcycle class
    else if CLASS_ID == 5:
    v_width = 2 // bus class
    else if CLASS_ID == 7:
    v_width = 2.5 // truck class
    End if
Step 10: real_size = (v_length * v_height * v_width) / PPM
    now = datetime.now( )
    log (CAR_ID, real_size, now) // store car id, size, time on log file
End For
End
    
```

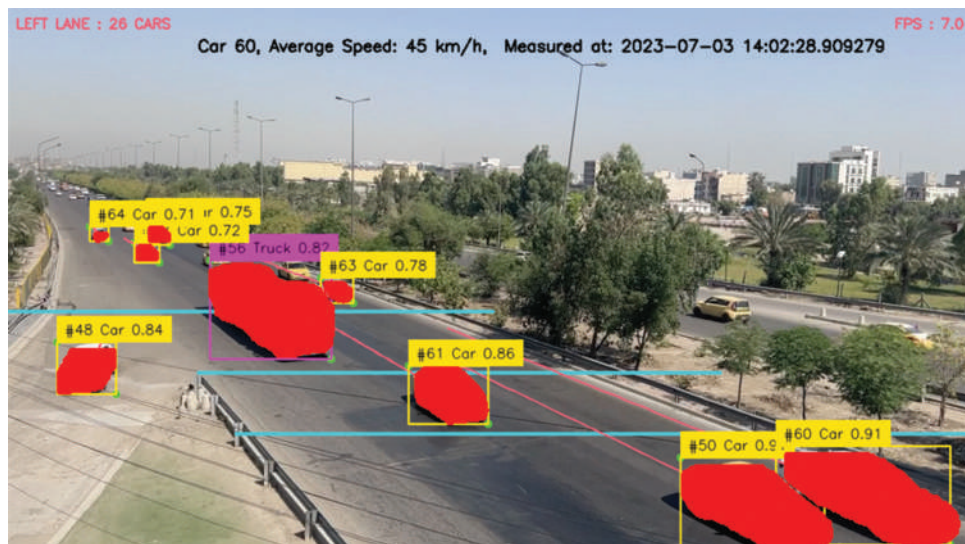


Fig. 9. System's output screen.



Fig. 10. System's vehicle classification.

TABLE II  
VEHICLE DETECTION WITH TRACKING EVALUATION

Test video	Model size	Ground-truth vehicles	System's detections	FPS	Accuracy (%)	Error (%)
Video1	Nano	70	67	48.8	95.7	4.3
Video1	Small	70	68	42	97.1	2.9
Video1	Medium	70	69	28.7	98.5	1.5
Video1	Large	70	69	21.5	98.5	1.5
Video1	Extra-Large	70	69	15.9	98.5	1.5
Video2	Nano	45	41	50.2	91.1	8.9
Video2	Small	45	43	43.8	95.5	4.5
Video2	Medium	45	43	29.6	95.5	4.5
Video2	Large	45	43	21.7	95.5	4.5
Video2	Extra-Large	45	44	16	97.7	2.3
Video3	Nano	28	25	50	89.2	10.8
Video3	Small	28	26	43.3	92.8	7.2
Video3	Medium	28	27	29.3	96.4	3.6
Video3	Large	28	28	21.7	100	0
Video3	Extra-Large	28	28	16	100	0
Video4	Nano	50	48	48	96	4
Video4	Small	50	49	41.5	98	2
Video4	Medium	50	49	28.5	98	2
Video4	Large	50	50	21	100	0
Video4	Extra-Large	50	50	15.6	100	0
Video5	Nano	37	34	46	91.8	8.2
Video5	Small	37	35	40	94.5	5.5
Video5	Medium	37	36	28	97.2	2.8
Video5	Large	37	36	21	97.2	2.8
Video5	Extra-Large	37	37	15.7	100	0
<b>Averages</b>					<b>96.58</b>	<b>3.42</b>

Nvidia GTX 1017 GPU with different YOLOv8 model sizes as listed in the following Tables II-IV.

For speed estimation evaluation, the VS13 dataset (Djukanović, et al., 2022) with known ground truth vehicle speed values is used to evaluate the system, and the results are demonstrated in Table V.

The size estimation stage is also evaluated by known ground truth values of known vehicle sizes; the result obtained is shown in Table VI.

The results of the proposed system showed excellent estimations for the multiple system stages. For the detection and tracking stage, the results we tested on multiple video samples and different CNN model sizes showed an average accuracy of 96.58% and an average error of 3.42%. For the vehicle counting process, the results show an average accuracy of 97.54% with a 2.46% average error. For the vehicle classification stage, the results from a single test video show an accuracy of 94.7% for the salon car class, 94.7% for the bus class, 96.2% for the truck class, and

TABLE III  
VEHICLE COUNTING EVALUATION

Test video	Model size	Ground-truth count	System's count	FPS	Accuracy (%)	Error (%)
Video1	Nano	60	61	49.4	98.3	1.7
Video1	Small	60	60	42.6	100	0
Video1	Medium	60	60	28.9	100	0
Video1	Large	60	61	21.5	98.3	1.7
Video1	Extra-Large	60	62	16	96.6	3.4
Video2	Nano	45	45	50.8	100	0
Video2	Small	45	44	43.6	97.7	2.3
Video2	Medium	45	43	29.3	95.5	4.5
Video2	Large	45	45	21.6	100	0
Video2	Extra-Large	45	45	16	100	0
Video4	Nano	40	40	47.6	100	0
Video4	Small	40	43	41	93	7
Video4	Medium	40	44	28.1	90	10
Video4	Large	40	43	21.1	93	7
Video4	Extra-Large	40	43	15.7	93	7
Video5	Nano	21	22	44.6	95.4	4.6
Video5	Small	21	21	39.8	100	0
Video5	Medium	21	21	27.5	100	0
Video5	Large	21	21	20.7	100	0
Video5	Extra-Large	21	21	15.5	100	0
<b>Averages</b>					<b>97.54</b>	<b>2.46</b>

TABLE IV  
VEHICLE CLASSIFICATION EVALUATION

Class	Precision (%)	Recall (%)	Accuracy (%)	F1-score (%)
Car	95	97.9	94.7	96.3
Bus	100	36.3	94.7	53.2
Truck	81.4	100	96.2	89.7
Motorcycle	100	66.6	99.7	79.9

99.7% for the motorcycle class. The precision values for the car, bus, truck, and motorcycle were 95%, 100%, 81.4%, and 100%, respectively. The recall values obtained were 97.9%, 36.3%, 100%, and 66.6%. The f1-score values were 96.3%, 53.2%, 89.7%, and 79.9% for the four vehicle classes. For the speed estimation stage, the results obtained had an average accuracy of 96.75% and a 3.25% average error. Finally, for the size estimation stage, the results obtained compared with ground-truth values of vehicle size gave 87.28% average accuracy with a 12.72% average error. The low accuracy in the bus class is because there are no buses in the test videos, only minibuses, and the model is trained on large regular buses; minibuses are classified as salon cars.

TABLE V  
VEHICLE SPEED ESTIMATION EVALUATION

Test video	Ground-truth speed value (km/h)	System's speed estimation (km/h)	FPS	Accuracy (%)	Error (%)
Eval30	30	28	29	93.3	6.7
Eval42	42	41.4	29	98.5	1.5
Eval56	56	53.8	29	96	4
Eval64	64	62.4	29	97.5	2.5
Eval71	71	68.4	29	96.3	3.7
Eval88	88	90	29	97.7	2.3
Eval94	94	90.6	29	96.3	3.7
Eval101	101	99.4	29	98.4	1.6
<b>Averages</b>				<b>96.75</b>	<b>3.25</b>

TABLE VI  
VEHICLE SIZE ESTIMATION EVALUATION

Vehicle ID	Ground-truth size value (m <sup>3</sup> )	System's size estimation (m <sup>3</sup> )	FPS	Accuracy (%)	Error (%)
1	11.53	15	30	76.8	33.2
5	13.7	14	30	97.8	2.2
11	16.52	16	30	96.8	3.2
15	14.37	13	30	90.4	9.6
24	9.18	9	30	98	2
37	14.18	13	30	91.6	8.4
39	14.18	14	30	98.7	1.3
65	16.68	7	30	41.9	58.1
97	10.14	11	30	92.2	7.8
118	19.03	24	30	79.2	20.8
<b>Averages</b>				<b>87.28</b>	<b>12.72</b>

### XIII. CONCLUSIONS AND FUTURE WORKS

The proposed system provided traffic monitoring information in real-time using a combination of cutting-edge deep learning technology and state-of-the-art algorithms. The system gave excellent results in all of its stages compared with previous works, with high accuracy and low error rates.

The system was implemented with various adjustable parameters such as frame skipping, enabling and disabling segmentation, and device-agnostic code that made the system run on different hardware configurations and GPUs, which made the system flexible and configurable for any video input type, resolution, or weather condition. The classification stage in the proposed system is useful in enforcing different speed limits based on the vehicle class. The counting process can also count vehicles in general or count them based on their classes for more specific information.

The proposed system estimates the vehicle's size with a novel approach based on segmentation masks generated from the YOLOv8 segmentation model, fixing one dimension (the vehicle's width) and calculating the other two (the vehicle's length and height) from the polygon points of the segmentation mask. The vehicle size information is useful for traffic control, as speed limits differ for different vehicle sizes. For example, trucks have speed limits that are different from those of salon cars. Size information can also help detect large vehicles that are not allowed to drive on certain roads at certain times of the day. The vehicle height is also important for driving in tunnels and under bridges.

As suggestions for future work to further develop the system, an automatic ROI detection algorithm can be implemented, and for size estimation, a stereo camera can be deployed to get more accurate estimations. In addition, the system can be integrated with an OCR algorithm for reading the vehicle's license plate for vehicles with speed limit violations.

### REFERENCES

AlNujaidi, K., AlHabib, G., and AlOdhieb, A., 2023. Spot-the-camel: Computer vision for safer roads. *International Journal of Artificial Intelligence and Applications (IJAAI)*, 14(2), pp.1-10.

Alzubaidi, L., Zhang, J., Humaidi, A.J., Al-Dujaili, A., Duan, Y., Al-Shamma, O., Santamaria, J., Fadhel, M.A., Al-Amidie, M., and Farhan, L., 2021. Review of deep learning: Concepts, CNN architectures, challenges, applications, future directions. *Journal of Big Data*, 8(1), p.53.

Awotunde, J.B., Jimoh, R.G., Imoize, A.L., Abdulrazaq, A.T., Li, C.T., and Lee, C.C., 2023. An enhanced deep learning-based deepfake video detection and classification system. *Electronics*, 12(1), p.87.

Berna, S.J., Swathi S., Devi, C.Y., and Varalakshmi, D., 2020. Distance and speed estimation of moving object using video processing. *International Journal for Research in Applied Science and Engineering Technology (IJRASET)*, 8(5), pp.2605-2612.

Costa, L.R., Rauen, M.S., and Fronza, A.B., 2020. Car speed estimation based on image scale factor. *Forensic Science International*, 310, p.110229.

Dias, T., Fonseca, T., Vitorino, J., Martins, A., Malpique, S., and Praça, I., 2023. *From Data to Action: Exploring AI and IoT-Driven Solutions for Smarter Cities*. Springer, Cham.

Djukanović, S., Bulatović, N., and Čavor, I., 2022. *A Dataset for Audio-video Based Vehicle Speed Estimation*. Cornell University, New York, pp.1-4.

Farooq, M.S., and Kanwal, S., 2023. Traffic Road Congestion System using by the Internet of Vehicles (IoV), *Networking and Internet Architecture*, Cornell University, New York, arXiv:2306.00395, pp.1-9.

Gupta, U., Kumar, U., Kumar, S., Shariq, M., and Kumar, R., 2022. Vehicle speed detection system in highway. *International Research Journal of Modernization in Engineering Technology and Science*, 4(5), pp.406-411.

Hakim, H., and Fadhil, A., 2021. Survey: Convolution neural networks in object detection. *Journal of Physics: Conference Series*, 1804, pp.1-18.

Hussain, M., 2023. YOLO-v1 to YOLO-v8, the rise of YOLO and its complementary nature toward digital manufacturing and industrial defect detection. *Machines*, 11, p.677.

Jocher, G., Chaurasia, A., and Qiu, J., 2023. *YOLO by Ultralytics (Version 8.0.0)*. Available from: <https://github.com/ultralytics/ultralytics> [Last accessed on 2023 Aug 07].

Jocher, G., Chaurasia, A., and Qiu, J., 2023. *YOLOv8 Docs by Ultralytics (Version 8.0.0)*. Available from: <https://docs.ultralytics.com> [Last accessed on 2023 Aug 07].

King, R., 2023. *Github Repo MMYOLO*. Available from: <https://github.com/open-mmlab/mmyolo/tree/main/configs/yolov8> [Last accessed on 2023 Aug 07].

Koyuncu, H., and Koyuncu, B., 2018. Vehicle speed detection by using camera and image processing software. *The International Journal of Engineering and Science (IJES)*, 7(9), pp.64-72.

Lin, C.J., Jeng, S.Y., and Lioa, H.W., 2021. A real-time vehicle counting, speed estimation, and classification system based on virtual detection zone and YOLO. *Mathematical Problems of Applied System Innovations for IoT Applications*, 2021, p.1577614.

Liu, C., Huynh, D., Sun, C., Reynolds, M., and Atkinson, S., 2021. A vision-based pipeline for vehicle counting, speed estimation, and classification. *IEEE Transactions on Intelligent Transportation Systems*, 22(12), pp.7547-7560.

Raheem, F.A., and AbdulHussain, A.A., 2020. Deep learning convolution neural networks analysis and comparative study for static alphabet ASL hand gesture recognition. *Journal of Xidian University*, 14(4), pp.1871-1881.

Sarker, I.H., 2021. Deep learning: A comprehensive overview on techniques, taxonomy, applications and research Directions. *SN Computer Science*, 2, p.420.

Shihab, M.R., Ghani, R.F., and Mohammed, A.J., 2022. Machine learning techniques for vehicle detection. *Iraqi Journal of Computers, Communications, Control and Systems Engineering (IJCCCE)*, 22(4), pp.1-12.

WHO, 2018. *Global Status Report on Road Safety 2018*. World Health

Organization, Geneva.

Yasir, M.A., and Ali, Y.H., 2021. Review on real time background extraction: Models, applications, environments, challenges and evaluation approaches. *International Journal of Online and Biomedical Engineering*, 17(2), pp.37-68.

Zhang, Y., Sun, P., Jiang, Y., Yu, D., Weng, F., Yuan, Z., Luo, P., Liu, W., and Wang, X., 2022. ByteTrack: Multi-Object Tracking by Associating Every Detection Box, *Computer Vision and Pattern Recognition*, Cornell University, New York, arXiv:2110.06864, pp.1-14.

# Atherogenic Index of Plasma in the Three Trimesters of Pregnancy

Bana K. Hamadameen and Sara S. Hamad

Department of Chemistry, Faculty of Science and Health, Koya University  
Koya KOY45, Kurdistan Region – F.R. Iraq

**Abstract**—This study investigates the change that occurs for atherogenic index of plasma (AIP) which is a very good marker for the evaluation of the risk of atherogenicity and cardiometabolic health. This study indicates the logarithm of the triglyceride and high-density lipoprotein cholesterol ( $\log [TG/HDL-c]$ ). The parameters of triglycerides (TG) and high-density lipoprotein cholesterol (HDL-c) are estimated and compared with the control cases. The AIP is calculated for each case during pregnancy in first, second, and third trimesters separately and each is compared with control cases. The study population comprised (80) women aged between (20–40) years distributed to (20) healthy non-pregnant women, (20) in the first trimester, (20) in the second trimester, and (20) in the third trimester in Koya health centers. The results of this study showed a significant increase in the TG level in both the second and third trimesters of pregnancy compared to the control cases. Whereas, in the first trimester of pregnancy, it can be assumed that there is a non-significant decrease of TG level rather than control cases. As well as the serum levels of HDL for all three trimesters of pregnancy displayed non-significant changes when compared to non-pregnant cases. These data illustrate that the AIP levels during both the second and third trimesters of pregnancy are significantly higher, as compared to control cases, whereas the AIP levels in the first trimester are non-significantly elevated, as compared with control cases.

**Index Terms**—Atherogenicity, Lipoproteins, Plasma, Pregnancy, Trimester.

## 1. INTRODUCTION

Pregnancy is a significant life experience that influences identities, relationships, and the pregnant mother's capacity to adjust to the growing fetus through substantial physiological and physical transformations. The alterations commence after conception and affect each of the body's organ systems (Chikhaoui, et al., 2023, Adam, et al., 2022). Pregnancy-related physiological changes, for example, alterations in lipid metabolism, promote growth,

and prenatal development. During a normal pregnancy, there is an increase in the levels of total cholesterol (TC), triglycerides (TG), and low-density lipoprotein cholesterol (LDL-c), and a reduction in high-density lipoprotein cholesterol (HDL-c) (Bartha, et al., 2023). During the pregnancy, the lipoprotein lipid physiology has significant effects on the pregnant woman and her unborn child as well as the developing fetus. High triglyceride levels meet the mother's energy requirements while sparing glucose for the fetus. For a fetus to develop normally, cholesterol and essential fatty acids are not necessary. During pregnancy, many physiological changes take place and affect the healthy and gestating women's lipid profile, that to prepare for the fetal development energy required for the late of pregnancy, for increased lipid synthesis and fat storage initially that is anabolic phase, and as lipid physiology enters to the net catabolic phase and the fat been breakdowns in the third trimester. Overall, during pregnancy, the mother's lipid physiology changed to reflect her increasing insulin resistance and facilitate the provision of adequate nutrients to the fetus (Wild and Feingold, 2023). The physiological adjustments that occur during pregnancy benefit the growing fetus and get the mother ready for birth and delivery. While some of these changes affect biochemical values, which are frequently stable, others could mimic disease symptoms. Distinguishing between typical physiological changes and the pathophysiology of diseases is crucial (Muhammad, Aghatise and Bello, 2023).

## II. CHARACTERIZATION OF PREGNANCY BY TRIMESTERS

Figured from the 1<sup>st</sup> day of the last menstrual cycle or 256–270 days after ovulation, the normal human pregnancy lasts an average of 280 days, or 40 weeks (Muralidhara, 2023). This is divided into three sections named trimesters, each of which is approximately 3 months long, corresponding to about nine calendar months. These three trimesters are distinguished by particular fetal changes. Infants delivered before the end of 37 weeks are regarded as preterm. A pregnancy is deemed to be full-term at 40 weeks. Premature babies may struggle with breathing and digestive problems, as well as growth and development problems (Hadi, Mahmoodb and Hadi, 2021, Butt and Lim, 2019).

ARO-The Scientific Journal of Koya University  
Vol. XI, No. 2 (2023), Article ID: ARO.11337. 6 pages  
DOI: 10.14500/aro.11337

Received: 08 August 2023; Accepted: 10 November 2023  
Regular research paper: Published: 21 November 2023

Corresponding author's e-mail: sara.sardar@koyauniversity.org  
Copyright © 2023 Bana K. Hamadameen and Sara S. Hamad. This is an open access article distributed under the Creative Commons Attribution License.



### A. First Trimester of Pregnancy

Pregnancy's first trimester is generally considered to be the past weeks 1–13. The first trimester was analyzed and correlated with the normal menstrual cycle and the day of the previous menstrual period. Medical professionals have historically relied on the day of the last menstrual cycle, ovulation, fertilization, implantation, and chemical detection to establish the occurrence of pregnancy, as shown in Fig. 1 (Vinh, 2021). Beginning in the 12<sup>th</sup> week of pregnancy, TC, TG, LDL-c, HDL-c, and phospholipids all started to rise in pregnant women's serum lipid levels (Zhu, et al., 2021). During the first trimester, lipid levels, including TG, typically decrease, while HDL cholesterol levels may increase. This phenomenon is apparent to be a protective mechanism, ensuring sufficient lipid supply for fetal development. As a result, the AIP may decrease during this period (Wild and Feingold, 2023).

### B. Second Trimester of Pregnancy

The pregnancy in the second trimester is known as weeks 13–26. During this time, most women report feeling more energized and start to gain weight as the morning sickness symptoms gradually become better. After 14 weeks: Gender can be determined and at about 16–20 weeks: Pregnant women usually feel the movements of the fetus. Women who have had previous pregnancies usually feel movement about 2 weeks earlier than women who are pregnant for the first time. The pineal gland appears and the female reproductive tract appears (Shah, et al., 2023).

In the second trimester, lipid levels start to rise gradually due to increased energy demands for both the mother and the growing fetus. TG may increase, while HDL cholesterol levels could remain stable or show slight changes. The AIP may increase slightly during this period but is still likely to be lower than pre-pregnancy values (Wild and Feingold, 2023, Musa, 2023).

### C. Third Trimester of Pregnancy

The third trimester of pregnancy is well-known as weeks 26–40. Fetal lungs mature between 30 and 34 weeks with each

passing week spent in the womb. However, the kicks and fetal movements are stronger than ever. Approximately 38 weeks of development the average weight of a fetus is 3250 g for females and 3300 g for male. The face is distinctly appearance and nearly all muscles appear in adult form. Due to the fetus's downward turn as it prepares to birth, the woman's abdomen will change shape and drop (Shah, et al., 2023).

During the third trimester, there is a further increase in lipid levels, particularly TG. This rise is partly attributed to increased insulin resistance in late pregnancy. HDL cholesterol may also increase, but it might not keep pace with the rise in TG. As a result, the AIP may increase during this trimester, indicating a relatively higher risk of atherogenicity (Wild and Feingold, 2023).

## III. LIPID PROFILES

The serum lipid profile is determined, prediction of cardiovascular risk and present nearly in common tests (Mora, et al., 2019). Most importantly, cardiac risk assessments can help in determining whether a person may have experienced a coronary event because of blood vessel obstruction or arteriosclerosis (Ireshanavar, et al., 2019). It is ordinarily done in fasting blood specimens. Fasting is 12–14 h complete overnight diet with exceptional water and medicine. It may be true there are two main reasons: Postprandial TG remained boosted for several hours (Galal, et al., 2020, Zhang, et al., 2023) and the majority of serum lipid reference values has been determined using fasting blood samples. A shift to a catabolic state promotes the use of maternal tissue lipids as the source of energy, preventing the fetus from consuming glucose and amino acids. Moreover, fetus utilization of maternal lipids, including cholesterol, is accessible for the development of cell membranes as well as for use for the precursor to bile acids, and steroid hormones (Sobik, et al., 2023). Dobiasová showed that the atherogenic index of the plasma (AIP), calculated as the logarithm ratio of TG to HDL cholesterol, is connected with lipoprotein particle size (Paleari, et al., 2023) and may function as a plasma atherogenicity measure (Chen, et al., 2023, Chen, et al., 2020).

To assess the risk to the cardiovascular system, National Cholesterol Education Programme (NCEP) and Europe Guidelines also propose lipid profiling fasting blood tests. These recommendations do permit TC and HDL, though. There is little variation in cholesterol levels between fed samples and non-fed samples of these lipids. In addition, panel III's non-HDL cholesterol (TC minus HDL cholesterol) can be used in the non-fasting state as a secondary target treatment for adults (Nordestgaard and Varbo, 2021, Marou, 2021). The lipid profile serum includes the measurements of the following tests: TC, TG, HDL-c, and low-density lipoprotein (LDL-c) (Bailey and Mohiuddin, 2022). Lipids such as cholesterol and TG can be carried through the bloodstream via lipoproteins (Liu, et al., 2022).

LDL-c is frequently used to calculate how much LDL-c drives certain medical outcomes advancement of

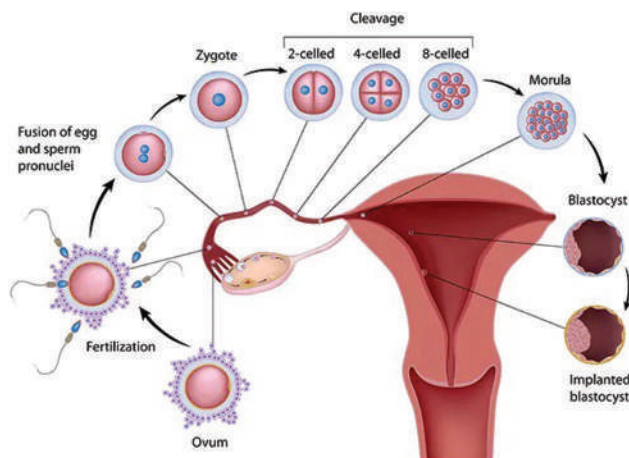


Fig. 1. Fertilization steps and development of blastocyst and implantation (Shah, et al., 2023).

atherosclerosis. The assessment of the risk of cardiovascular disease (CVD) sometimes involves comparing the ratio of TC to HDL-c (Castañer, et al., 2020, Rajab, 2012).

#### A. TC

The TC level of the patient is determined by measuring all of the lipoproteins (Brown, 2007). High cholesterol can cause atherosclerosis due to the excessive buildup of cholesterol and other deposits on the walls of the arteries. There are no symptoms associated with elevated cholesterol, but these deposits (plaques) might decrease blood flow through your arteries. Moreover, the only way to know if you have it is the blood test. Levels below 5 mmol/L = 200 mg/dl were confirmed by both the European Society of Cardiologists and the American NCEP (Bartels and O'Donoghue, 2011).

#### B. TG

TG, a specific type of fat, are carried by the blood. Your body either makes TG on its own or gets them from food. For optimal health, the body requires some TG (Wang, et al., 2013). Elevated blood TG levels do not cause any symptoms. However, if left unmanaged, they can increase the risk of significant problems including stroke and coronary heart disease (Jadhav and Annapure, 2023). Triglyceride levels can be assessed when not fasting or while doing so, and levels between 2 and 10 mmol/L are linked to a higher risk of CVD (Yildiz, et al., 2023), levels  $\geq 150$  mg/dl were linked to relating non-coronary atherosclerosis (Hao, et al., 2022) and concentrations exceeding 10 mmol/L may induce CVD and an increased risk of acute pancreatitis (Yildiz, et al., 2023).

#### C. HDL-c

One of the main classes of plasma lipoproteins, HDL-c, is referred to as the "good cholesterol" because the main role of HDL-c is to carry and absorb the amount the Cholesterol in the blood and carry it back to the liver, and HDL removed the excess cholesterol from tissues (it cleans blood) (Jomard and Osto, 2020, Bailey and Mohiuddin, 2022). A high level of (HDL-c), in the presence of hypertriglyceridemia, increases hepatic lipase (HL) activity, and increased HDL-c catabolism (degradation of HDL-c). For every 1 mg of HDL-c lost, the risk of coronary artery disease (CAD) increases by 2% (Rajab, 2012). Normal values are more than 50 mg/dl for women and 40 mg/dl for men (Karizi, et al., 2023).

#### D. LDL-c

Low-density lipoprotein contains less protein and more cholesterol and indicated the "bad" cholesterol, also well-known as LDL-c, which moves cholesterol metabolites from the liver throughout the body. The accumulation of LDL cholesterol can cause narrowing and hardening of arteries which leads to the development of atherosclerotic lesions. Accurate LDL-c assessment is crucial for medications that target lipid reduction to slow or stop the development of atherosclerosis and prevent plaque. Normal values:  $<70$  mg/dl (Pownall, et al., 2021).

### IV. ATHEROGENIC INDEX OF PLASMA

TG and HDL-c make up the AIP, a new marker for evaluating atherogenicity risk and cardiometabolic health. Among patients with type 2 diabetes mellitus and high cardiovascular (CV) disease risk, there is a correlation between AIP and a higher frequency of major adverse cardiovascular events (MACEs). In just a few studies has the connection between AIP and CV risk in general populations been examined (Kim, et al., 2022). To investigate the association with the AIP, researchers examine the logarithm of the molar ratio of TG/HDL-c. A measure of plasma atherogenesis, (AIP) is established with lipoprotein particle size (Chen, et al., 2020). Several factors have been used to predict the risk of CVD. In the early 1990s, the ratio of LDL/HDL and TC/HDL were the best-correlated predictor of future CVD. The latest indicator of atherogenicity is the AIP, which is directly associated with the risk of developing atherosclerosis (Castañer, et al., 2020, Rajab, 2012).

### V. MATERIALS AND METHODS

#### A. Chemicals and Procedures

The biochemical parameters of TG and HDL-C were measured by enzymatic colorimetric assay by the (Fuji dry-chem slide TG-Piii) and (Fuji dry-chem slide HDL-C-piii) respectively, with a company of Fuji film and Japanese origin. As well as, the common instrument and model of (Fujifilm dri-chem NX500) with Japan origin and also the (800-1 centrifuge) with China origin used for this study (Nakamura, et al., 2011).

#### B. Study Population

Participants in the study were (80) healthy pregnant women and (20) healthy non-pregnant women, the ages between (20–40 years).

#### C. Sampling

This study, which was conducted at koya health centers in November 2022, found that (60) pregnant women were between the ages of 20 and 40, were not clearly experiencing any pregnancy-related complications, and were grouped into three groups:

1. (20) in the first trimester of pregnancy (up to 13 weeks).
2. (20) in the second trimester of pregnancy (13–28 weeks).
3. (20) in the third trimester of pregnancy (28–40 weeks).

Twenty healthy, non-pregnant women served as controls in addition. A venous sample of 3 ml was taken from each group being tested. The blood samples were placed in gel tube, and the serum was extracted by centrifuge at 1500 rpm about 10 min. The serum was then separated into small parts and kept frozen until further analysis. As well as the AIP was determined as  $\log$  (TG/HDL-c) using the Czech online atherogenic risk calculator.

#### D. Statistical Analysis

The GraphPad prism with version 9 (Graphpad Software, Inc.) was used to conduct the statistical analysis. As well as,

the student t-test was used to analyze the differences between the groups. The data results represented as mean and standard error of mean (mean ± standard error of the mean [SEM]), p value (p < 0.05), was regarded as statistically significant, while if (p > 0.05) represented as no significant (N.S) and the results represented as median.

VI. RESULTS AND DISCUSSION

A. Serum TG Level Results

The results of this study reveal that the value of TG in sera of healthy pregnant women in three trimesters and non-pregnant women (control cases) from the Table I, Figs. 2 and 3. The (mean ± SEM) of TG is (148.7 ± 4.82) for control case, however, the (Mean ± SEM) of the second and third trimesters are (236.7 ± 27.84 and 259.9 ± 24.78) respectively. On the other hand, the median for the first trimester is (142.0).

As well as, from Table I it can be seen that the TG level in first trimester has recorded the lowest level but the decrease is non-significant difference if compared to control cases,

TABLE I  
SERUM LEVEL OF TG FOR BOTH PREGNANT WOMEN (IN EACH TRIMESTER) AND NON-PREGNANT WOMEN

Groups	N	Serum level of TG (mg/dl)	p
Control	20	148.7±4.82	-
First trimester	20	142.0	0.7603 (N.S)
Second trimester	20	236.7±27.84	0.0042 (S)
Third trimester	20	259.9±24.78	0.0001 (S)

\*The values expressed as (mean±SEM) for significant value and (median) for non-significant value

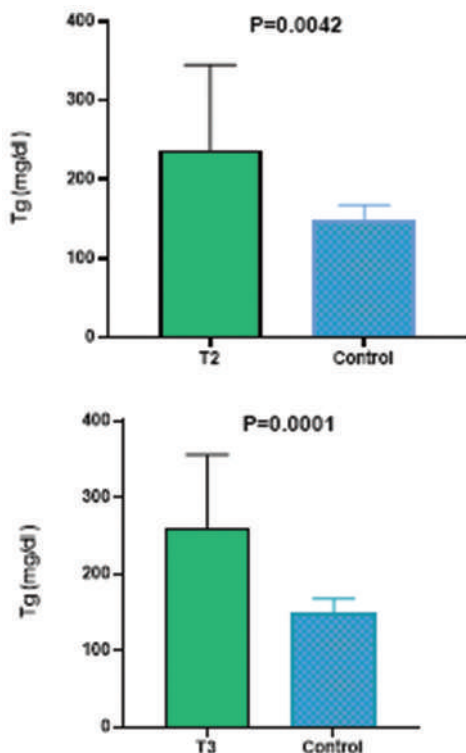


Fig. 2. Serum levels of triglycerides in both second trimester (T2) and third trimester (T3) of pregnancy with non-pregnant women.

inversely we can notice that there is a significant increase in TG level for both second and third trimester of pregnant cases if compared with control cases, and this may be according to the biochemical, hormonal, and physiological changes that occur during these two trimesters of pregnancy and growth of the fetus inside the womb.

B. Serum HDL Level Results

The data from Table II and Fig. 4, that show the serum level of HDL during the three trimesters of pregnancy and healthy non-pregnant women cases. The median HDL level of each trimester and control cases was investigated to be (44.00) for non-pregnant women and (45.00, 53.00, and 51.00) for first, second, and third trimesters, respectively. From the results, it can be assumed that there are no significant differences in serum HDL levels in all three trimesters of pregnancy compared with non-pregnant women.

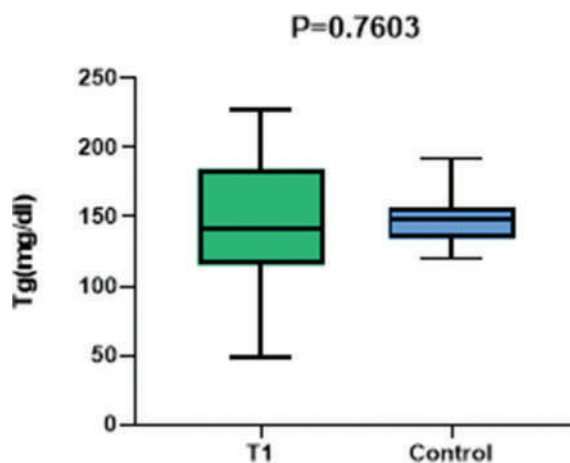


Fig. 3. Serum levels of triglycerides in both first trimester (T1) of pregnancy with non-pregnant women.

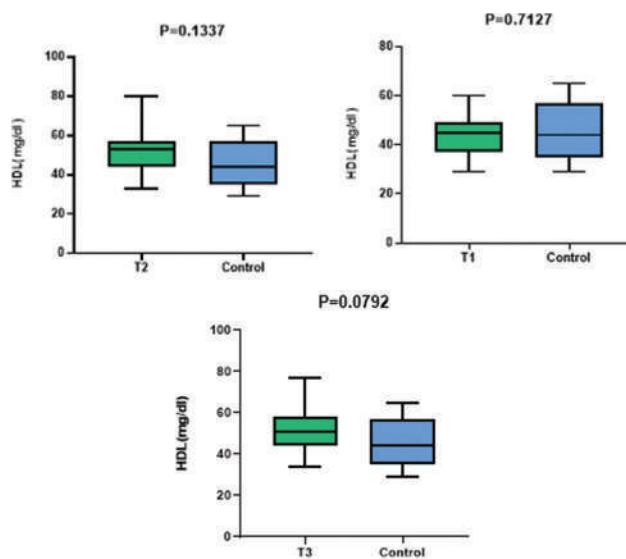


Fig. 4. Serum levels of high density lipoprotein in three trimesters of pregnancy with non-pregnant women.



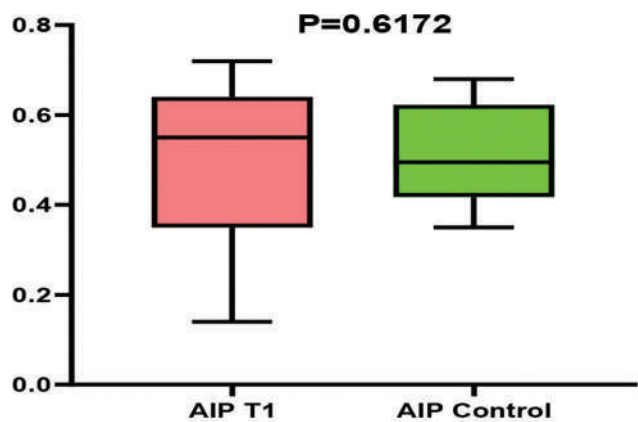


Fig. 5. Calculated atherogenic index of plasma for first trimester (T1) and non-pregnant women.

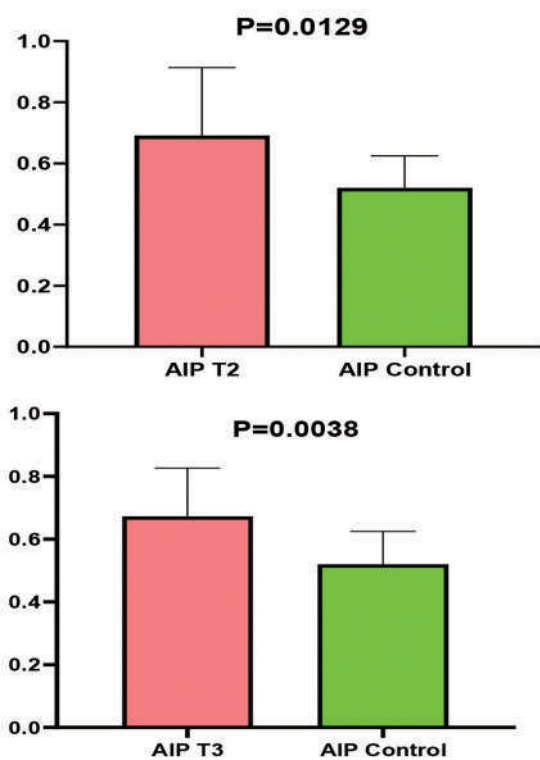


Fig. 6. Calculated atherogenic index of plasma for second trimester (T2) and third trimester (T3) with non-pregnant women.

C. Calculated AIP Level Results

The data from Table III, Figs. 5 and 6, illustrate the values of calculated AIP for all three trimesters of pregnancy and non-pregnant women. The (mean ± SEM) of AIP for non-pregnant women, second and third trimesters are (0.5200 ± 0.02710, 0.6915 ± 0.06168, and 0.6722 ± 0.03984) respectively, while the median of AIP for the first trimester is (0.5500).

From the evaluated results for the first trimester of pregnancy we can conclude that there is a non-significant increase of AIP level compared with control cases, while it can be assumed that there are significant elevates of AIP level in both the second and third trimesters compared with AIP level of non-pregnant women, and this may also relate

TABLE II  
SERUM LEVEL OF HDL FOR BOTH PREGNANT WOMEN (IN EACH TRIMESTER) AND NON-PREGNANT WOMEN

Groups	N	Serum level of HDL (mg/dl)	p
Control	20	44.00	-
First trimester	20	45.00	0.7127 (N.S)
Second trimester	20	53.00	0.1337 (N.S)
Third trimester	20	51.00	0.0792 (N.S)

\*The values expressed as (median) for non-significant value

TABLE III  
CALCULATED AIP OF BOTH PREGNANT WOMEN (IN EACH TRIMESTER) AND NON-PREGNANT WOMEN

Groups	N	AIP (Log (TG/HDL))	p
Control	20	0.5200±0.0271	-
First trimester	20	0.5500	0.7603 (N.S)
Second trimester	20	0.6915±0.0616	0.0129 (S)
Third trimester	20	0.6722±0.0398	0.0038 (S)

\*The values expressed as (mean±SEM) for significant value and (median) for non-significant value

to the big physiological and biochemical changes in the both second and third trimesters of pregnancy.

VII. CONCLUSION

From the results of this study, we conclude that the TG level is significantly higher in both the second and third trimesters of pregnancy compared with the control cases. While for the first trimester of pregnancy, it can be assumed that there is a non-significant decrease of TG level if compared with the control cases. Non-significant changes were found in the estimation of serum HDL levels for all three trimesters of pregnancy if compared with non-pregnant cases. It can be concluded a significant increase in AIP level during both the second and third trimesters of pregnancy if compared to control cases, while a non-significant increase can be seen in AIP level of the first trimester compared with the control cases.

VIII. RECOMMENDATIONS AND FUTURE WORK

1. To evaluate some other lipids profile parameters such as TC, LDL-c, and VLDL-c.
2. Study and measured some other Lipid ratios such as: Cardiac risk ratio 1 (TC/HDL-c), and Cardiac risk ratio 2 (LDL-c/HDL-c).
3. Studying if there is association between these factors and the future cardiac complications for the mom and after the baby is born.

ACKNOWLEDGMENT

The authors would like to acknowledge the Department of Chemistry, Faculty of Science and Health, Koya University.

REFERENCES

Adam, S., Pheiffer, C., Dias, S., Hlongwane, T., Vannevel, V., Soma-Pillay, P., and Abdullah, F. 2022. Coronavirus and pregnancy: The challenges of the 21<sup>st</sup> century: A review. *Frontiers in Microbiology*, 13, p.923546.

- Bailey, A., and Mohiuddin, S.S. 2022. *Biochemistry, High Density Lipoprotein*. StatPearls Publishing, Treasure Island, FL.
- Bartels, Ä., and O'Donoghue, K. 2011. Cholesterol in pregnancy: A review of knowns and unknowns. *Obstetric Medicine*, 4, pp.147-151.
- Bartha, I., Joumady, I., Cuerva, M., and Bartha, J.L. 2023. The effect of maternal obesity and lipid profile on first-trimester serum progesterone levels. *American Journal of Obstetrics and Gynecology MFM*, 5, p.100959.
- Brown, W.V. 2007. High-density lipoprotein and transport of cholesterol and triglyceride in blood. *Journal of Clinical Lipidology*, 1, pp.7-19.
- Butt, K., and Lim, K.I. 2019. Guideline no. 388-determination of gestational age by ultrasound. *Journal of Obstetrics and Gynaecology Canada*, 41, pp.1497-1507.
- Castañer, O., Pintó, X., Subirana, I., Amor, A.J., Ros, E., Hernáez, Á., Martínez-González, M.Á., Corella, D., Salas-Salvadó, J., and Estruch, R. 2020. Remnant cholesterol, not LDL cholesterol, is associated with incident cardiovascular disease. *Journal of the American College of Cardiology*, 76, pp.2712-2724.
- Chen, M., Fang, C.Y., Guo, J.C., Pang, L.M., Zhou, Y., Hong, Y., Yang, L.F., Zhang, J., Zhang, T., and Zhou, B.F. 2023. Predictive value of atherogenic index of plasma and atherogenic index of plasma combined with low-density lipoprotein cholesterol for the risk of acute myocardial infarction. *Frontiers in Cardiovascular Medicine*, 10, p.1117362.
- Chen, Z., Hu, H., Chen, M., Luo, X., Yao, W., Liang, Q., Yang, F., and Wang, X. 2020. Association of Triglyceride to high-density lipoprotein cholesterol ratio and incident of diabetes mellitus: A secondary retrospective analysis based on a Chinese cohort study. *Lipids in Health and Disease*, 19, p.33.
- Chikhaoui, M., Smail, F., Aiche, S., and Benamor, N. 2023. Comparing hematological and biochemical profiles of pregnant and non-pregnant barb mares raised in Tiaret, Algeria. *Iranian Journal of Veterinary Medicine*, 17, pp.309-320.
- Galal, H., Samir, A., and Shehata, M. 2020. Assessment of apolipoprotein B/ apolipoprotein AI ratio in non-ST segment elevation acute coronary syndrome patients. *The Egyptian Heart Journal*, 72, pp.1-8.
- Hadi, N.A., Mahmoodb, R.T., and Hadi, H.A. 2021. Estimation of calcium, iron, zinc and some antioxidants in the serum of pregnant women in samarra. *Annals of the Romanian Society for Cell Biology*, 25, pp.10536-10542.
- Hao, Q.Y., Gao, J.W., Yuan, Z.M., Gao, M., Wang, J.F., Schiele, F., Zhang, S.L., and Liu, P.M. 2022. Remnant cholesterol and the risk of coronary artery calcium progression: Insights from the CARDIA and MESA study. *Circulation: Cardiovascular Imaging*, 15, p.e014116.
- Ireshanavar, D.S., Shetty, S., Rao, A., Patil, V.S., Patil, V.P., and Shilpasree, A.S. 2019. Establishment of reference intervals for fasting and nonfasting serum lipid profile from healthy population in Mangaluru, Karnataka, India. *Indian Journal of Medical Biochemistry*, 23, pp.327-330.
- Jadhav, H.B., and Annapure, U.S. 2023. Triglycerides of medium-chain fatty acids: A concise review. *Journal of Food Science and Technology*, 60, pp.2143-2152.
- Jomard, A., and Osto, E. 2020. High density lipoproteins: Metabolism, function, and therapeutic potential. *Frontiers in Cardiovascular Medicine*, 7, p.39.
- Karizi, S.R., Armanmehr, F., Azadi, H.G., Zahroodi, H.S., Ghalibaf, A.M., Bazzaz, B.S.F., Abbaspour, M., Boskabadi, J., Eslami, S., and Taherzadeh, Z. 2023. A randomized, double-blind placebo-controlled add-on trial to assess the efficacy, safety, and anti-atherogenic effect of *Spirulina platensis* in patients with inadequately controlled type 2 diabetes mellitus. *Phytotherapy Research*, 37, pp.1435-1448.
- Kim, S.H., Cho, Y.K., Kim, Y.J., Jung, C.H., Lee, W.J., Park, J.Y., Huh, J.H., Kang, J.G., Lee, S.J., and Ihm, S.H. 2022. Association of the atherogenic index of plasma with cardiovascular risk beyond the traditional risk factors: A nationwide population-based cohort study. *Cardiovascular Diabetology*, 21, p.81.
- Liu, C., Yin, J., Lu, B., and Lin, W. 2022. Exploring of blood viscosity in injured liver tissues of hyperlipidemic mice. *Dyes and Pigments*, 202, p.110272.
- Marou, A. 2021. Non-high-density-lipoprotein cholesterol in Morocco hemodialysis patients. *Scholars International Journal of Biochemistry*, 4, pp.52-56.
- Mora, S., Chang, C.L., Moorthy, M.V., and Sever, P.S. 2019. Association of nonfasting vs fasting lipid levels with risk of major coronary events in the Anglo-Scandinavian cardiac outcomes trial-lipid lowering arm. *JAMA Internal Medicine*, 179, pp.898-905.
- Muhammad, H., Aghatise, E.K., and Bello, F.S. 2023. Evaluation of some hemostatic Changes in pregnant women attending FMC keffi, Nasarawa state, Nigeria. *Asian Hematology Research Journal*, 6, pp.243-248.
- Muralidhara, M. 2023. Exploring the neuro-ameliorative propensity of *Withania somnifera*-Indian ginseng. In: *Ayurvedic Herbal Preparations in Neurological Disorders*. Elsevier, Amsterdam.
- Musa, M.I.S. 2023. Effect of pregnancy stages on changes in lipid profiles. *Journal for Research in Applied Sciences and Biotechnology*, 2, pp.26-30.
- Nakamura, K., Kageyama, S., Tanaka, H., Kawasaki, K., and Terashima, K. 2011. Development of Fuji Dri-chem v-LIP-P slide that has the high specificity to pancreatic lipase. *Fujifilm Research and Development*, 56, pp.5-10.
- Nordestgaard, B.G., and Varbo, A. 2021. Triglyceride-rich lipoprotein cholesterol (remnant cholesterol) as a therapeutic target for cardiovascular disease risk. In: *Therapeutic Lipidology*. Humana, Cham, pp.139-158.
- Paleari, R., Vidali, M., Ceriotti, F., Pintaudi, B., De Angelis, M.L., Vitacolonna, E., Cataldo, I., Torlone, E., Succurro, E., and Angotti, E. 2023. Reference intervals for glycated albumin during physiological pregnancy of Europid women: Evidences from a prospective observational study. *Clinica Chimica Acta*, 541, p.117246.
- Pownall, H.J., Rosales, C., Gillard, B.K., and Gotto, A.M. Jr. 2021. High-density lipoproteins, reverse cholesterol transport and atherogenesis. *Nature Reviews Cardiology*, 18, pp.712-723.
- Rajab, T. 2012. Comparative study for atherogenic index of plasma (AIP) in patient with type 1 diabetes mellitus, type 2 diabetes mellitus, beta thalassemia and hypothyroidism. *International Journal of Chemical Research*, 2, pp.1-9.
- Shah, A., Patel, J., Isath, A., Virk, H.U.H., Jneid, H., Zelop, C.M., Mehta-Lee, S., Economy, K.E., Gulati, M., and Krittanawong, C. 2023. Cardiovascular complications in pregnancy. *Current Treatment Options in Cardiovascular Medicine*, 25, pp.1-24.
- Sobik, S., Sims, C.R., Crimmins, M., Bimali, M., Williams, D.K., and Andres, A. 2023. Associations between maternal physical activity, maternal lipid levels, and infant anthropometric outcomes at two weeks of age. *Maternal and Child Health Journal*, 27, pp.168-177.
- Vinh, P.Q. 2021. Changes in hematology parameters in the first trimester pregnant women. *Scientific Journal Current Research*, 45, pp.44-47.
- Wang, T.Y., Liu, M., Portincasa, P., and Wang, D.Q.H. 2013. New insights into the molecular mechanism of intestinal fatty acid absorption. *European Journal of Clinical Investigation*, 43, pp.1203-1223.
- Wild, R., and Feingold, K.R. 2023. Effect of pregnancy on lipid metabolism and lipoprotein levels. In: *Endotext*. MDText.com, Inc., South Dartmouth.
- Yildiz, M., Miedema, M.D., Murthy, A., Henry, T.D., Bergstedt, S., Okeson, B.K., Schmidt, C.W., Volpenhein, L., Garcia, S., and Sharkey, S.W. 2023. Association of triglyceride levels with adverse cardiovascular events in patients with ST-segment elevation myocardial infarction. *Heliyon*, 14, p.e17308.
- Zhang, P., Zhang, Z., Li, D., Han, R., Li, H., Ma, J., Xu, P., Qi, Z., Liu, L., and Zhang, A. 2023. Association of remnant cholesterol with intracranial atherosclerosis in community-based population: The ARIC study. *Journal of Stroke and Cerebrovascular Diseases*, 32, p.107293.
- Zhu, Y., Zhu, H., Dang, Q., Yang, Q., Huang, D., Zhang, Y., Cai, X., and Yu, H. 2021. Changes in serum TG levels during pregnancy and their association with postpartum hypertriglyceridemia: A population-based prospective cohort study. *Lipids in Health and Disease*, 20, p.119.

# Peperites: Insight into the Submarine Eruptions within Walash Volcanosedimentary Group, Mawat Area, Iraqi Kurdistan Region

Jabbar M. A. Qaradaghi and Tola A. Mirza

Department of Geology, College of Science, Sulaimani University,  
Sulaimani, Kurdistan Region–F.R, Iraq

**Abstract**—Peperites are volcanosedimentary materials generated by the mingling of magma and unconsolidated wet sediments. They have unique insights into submarine volcanisms and the tectonic environments where they form. For the 1<sup>st</sup> time, the authors identified two types of peperites (blocky and fluidal) hosted by micritic limestone rocks in the Walash Volcanosedimentary Group of the Mawat area, Kurdistan Region-Iraq. They are designated as peperitic facies one and two (PF1 and PF2) and consist of black basaltic rocks mixed with chocolate-brown micritic limestone rocks. Their abundance demonstrates the contemporaneity of deep marine sediment deposition and submarine volcanism during Walash's nascent arc. Despite hydrothermal alteration, the basaltic rocks retained their magmatic textures. Basaltic rocks comprise mainly albite, anorthite, diopside, hematite, and alkali-feldspar. Calcite dominates micritic limestone rocks, while quartz is minor. Based on geochemical data, igneous sections are basaltic rocks with tholeiitic series that are strongly enriched in Light Rare Earth Elements with low concentration ratios of (La/Yb) and (Sr/Y), indicating geochemical affinity to normal island arc basalt with a primitive arc signature. Furthermore, their formation is thought to be caused by partial melting of subducted slabs deep within 30 km and the associated derived fluids above the subducted slab. Thirteen species of planktonic foraminifera (*Morozovella*) are identified through paleontological research and biostratigraphy. Using these various tools lead the authors to illustrate the tectonic setting of the formation of peperitic rocks in arc fronts of the subducted Walash arc during the Middle to Late Paleocene (60 Ma).

**Index Terms**—Mawat, Paleocene, Peperite, Primitive Arc, Volcanic Arc, Walash.

## I. INTRODUCTION

The term “peperite,” comes after “peperino,” first used by (Scrope, 1827) to describe clastic rocks from the Limagne d' Auvergne region of central France (now considered the

type locality for “peperite”). It comprises mixtures of wet sediment or lacustrine limestone and basalt (Skilling, et al., 2002). Peperite is a combined rock formed essentially *in situ* by the disintegration of magma which intrudes and mingles with unconsolidated or poorly consolidated, typically wet sediment (Busby-Spera and White, 1987; White, McPhie and Skilling, 2000; Skilling, et al., 2002; Brown and Bell, 2007; El Desoky and Shahin, 2020). However, most peperites described as basaltic extrusion involve relatively fine-grained sediment (White and Busby-Spera, 1987; Hanson, 1991; Boulter, 1993; Hanson and Wilson, 1993; Rawlings, 1993; Brooks, 1995; Goto and McPhie, 1996; Hanson and Hargrove, 1999; Skilling, et al., 2002; Waichel, et al., 2007; Branney, et al., 2008; Palinkaš, et al., 2008; Chen, et al., 2013; Famelli, et al., 2021; Bann, Jones and Graham, 2022). While few exceptions involve basaltic extrusions into coarse-grained host sediment (Wilson, 1991; Squire and McPhie, 2002). Peperite may extend its range from minor occurrences adjacent to igneous extrusions up to deposits with quantities of several km<sup>3</sup> (Brown and Bell, 2007). Texturally, peperites have different juvenile clast morphologies, including blocky and fluidal types, and numerous magma-sediment relationships (Busby-Spera and White, 1987). Peperite may occur in any tectonic environment, where magmatism and sedimentation are contemporaneous, frequently in arc-related and other volcanosedimentary sequences (Hanson and Hargrove, 1999; Mueller, Garde and Stendal, 2000; Skilling, et al., 2002; Dadd and Van Wagoner, 2002; Templeton and Hanson, 2003; Nemeth, Breitreutz and Wilke, 2004; Chen, et al., 2016; Fontboté, 2019; Mawson, White and Palin, 2020). Consequently, petrologists have defined peperites in different ways, some authors may mistakenly define this rock as sedimentary rock, while others more properly define peperites as a combined volcano-sedimentary succession (White, McPhie and Skilling, 2000; Skilling, et al., 2002; Brown and Bell, 2007; Chen, et al., 2016; Krobicki, 2018; Krobicki, et al., 2019; Memtimin, et al., 2020).

The Walash Group was first named by Bolton (1958) and later subjected to numerous studies (e.g., Aziz, 1986; Jassim and Goff, 2006; Al-Banna and Al-Mutwali, 2008; Koyi, 2009; Ali, 2012; Al-Qayim, Ghafor and Jaff, 2012; Ali and Aswad, 2013; Ali, et al., 2013; Aswad, et al., 2013; Al-



Qayim, Ghafor and Jaff, 2014; Ali, et al., 2017; Koshnaw, et al., 2017; Karim and Hamza, 2021). Aziz (1986) studied the geochemistry and petrogenesis of the volcanic rocks within the Walsh Volcanosedimentary Group (WVSg) for the first time, and he concluded that the volcanic rocks of the Walsh composed of basalts and andesites, which display tholeiitic to calc-alkaline affinity, formed as a result of the subduction of the oceanic crust beneath the Iranian microcontinent. Previously, the  $^{40}\text{Ar}$ - $^{39}\text{Ar}$  geochronological data suggested an age of 43–32 Ma for the volcanic rocks of Walsh in the Mawat ophiolite complex (Aswad, et al., 2013). Despite the aforementioned studies for WVSg, it is reasonable to do more meticulous petrological studies as it is the most complex volcanosedimentary unit in the Iraqi Zagros Suture Zone (IZSZ).

The occurrence of basaltic pillow lava, peperitic rocks, and host micritic carbonate rocks together within the lower part of WVSg is designated as the peperitic facies (PF) in this study. The primary goals of our research are to use peperite and basaltic rock compositions obtained from the WVSg in the Mawat area to reconstruct the tectonic setting of the basaltic rocks within the aforementioned volcanosedimentary group. In addition to covering the occurrence and genesis of peperites in the Mawat area within WVSg.

## II. TECTONIC SETTING OF THE REGION

The Zagros orogeny is an active orogeny that includes the Zagros mountains, which formed as the Arabian and Eurasian plates collided (Agard, et al., 2011; Austermann and Iaffaldano, 2013; Elias, Sissakian and Al-Ansari, 2018). Tectonically, the Zagros orogen is divided into four subparallel divisions, which are the Urumieh-Dokhtar Magmatic Arc; the Sanandaj-Sirjan Zone; the Zagros Fold-Thrust Belt and the Mesopotamian Foreland Basin (Alavi, 2004; Mohammad, et al., 2014; English, et al., 2015). Iraq also is a part of the Zagros orogeny. It is divided into different tectonic zones, which are Zagros Suture Zone (ZSZ), Unstable shelf, and Stable shelf. The studied area is located within the Penjween Walsh sub-zone, which is a part of the IZSZ (Jassim and Goff, 2006) (Fig. 1). Jassim and Goff, (2006) defined the Penjween-Walash subzone as a unit of the main (Central) Neo-Tethys, which consists of volcanosedimentary sequences formed during Cretaceous Ocean spreading in the Neo-Tethys and Paleogene arc volcanics and syn-tectonic basic intrusions formed during the ocean's final closure. Thus, the oceanic sediments were deposited on both Arabian and Iranian microplates during the middle Paleocene. Later, Zagros orogeny was followed by the late Eocene 38 Ma continent-continent collision of the Arabian plate with

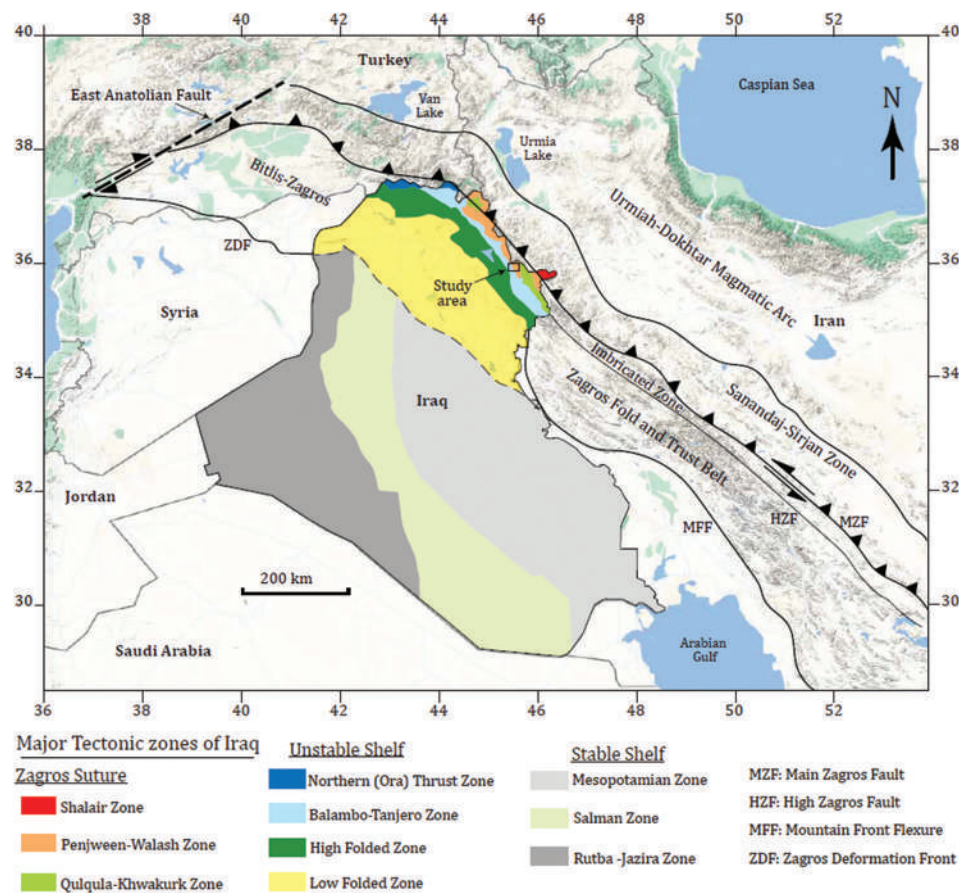


Fig. 1. Tectonic map of the studied area illustrating the tectonic division of Kurdistan and Iraq after (Jassim and Goff, 2006) and surroundings after (Alavi, 2004; English, et al., 2015).

Eurasia (Mohammad, et al., 2014). Furthermore, in the study area, the WVSg exposed in the Thrust Zone and the Mawat nappe stack consists of two allochthonous sheets, namely, the upper and lower allochthonous thrust sheets (Aswad et al., 2011; Aziz et al., 2011a). The lower allochthonous thrust sheet consists of Walash volcanosedimentary rocks, which undergo lateral transitions to the Naopurdan sedimentary group, thereby forming the Walash-Naopurdan allochthonous thrust sheet.

Peperite literature along the Zagros orogeny (Turkey-Iraq-Iran) is rare. Recently, Nouri et al., (2017) have recorded peperites within western Iran along the ZSZ. As well as Erkül, Helvaci and Sözbilir, (2006) recorded peperites within Miocene units in Western Turkey. The formation of peperites, which occurred by the interaction of lava with wet sediment, is a vitally significant environmental indicator. Nonetheless, few examples of this phenomenon have been comparatively documented, which happened during Archean successions (Beresford, et al., 2002; Wilson and Grant, 2006; Moulton, et al., 2011; Barnes and Van Kranendonk, 2014; Barnes and Arndt, 2019); Proterozoic succession (McPhie, 1993; Rawlings, 1993; Biske, Romashkin and Rychanchik, 2004; Sinha, et al., 2011; Constenius, et al., 2017); Palaeozoic succession (Brooks, 1995; Doyle, 2000; Cas, et al., 2001; Chen, et al., 2013; Zhu, et al., 2014; Chen, et al., 2016; Memtimin, et al., 2020; Bann, Jones and Graham, 2022); Mesozoic succession (Wilson, 1991; Wilson, 1993; Hanson and Hargrove, 1999; Templeton and Hanson, 2003; Hanson and Nemeth, Breitreutz and Wilke, et al., 2004; Palinkaš, et al., 2008; Asvesta and Dimitriadis, 2013; Krobicki, et al., 2019); Cenozoic succession (Erkül, Helvaci and Sözbilir, 2006; Martin and Németh, 2007; Busby, et al., 2008; Haller and Németh, 2009; Nouri, et al., 2017); and to the most recent Pleistocene succession around 43,000-12,400 years ago (Mercurio, 2011). However, it has also been pointed out by (Skilling, et al., 2002) that in ancient deposits, it may be difficult to differentiate fragments obtained from this process from those of tectonic origin. Despite this fact, the presence of peperite in oceanic island arcs may infer the primitive arc settings.

Although according to Jassim and Goff (2006) along Iraqi part of Zagros orogeny, the WVsg comprises from the base: Basal Red Beds, Lower Volcanics consisting of mafic, minor felsic lavas and frequently pillow lavas laterally adjacent to the sedimentary sequence (i.e., volcano-flysch unit), Middle Red Beds ( $\pm$ limestones), Upper Volcanics and finally the Upper Red Beds, peperites were not recorded in any sequences within whole succession of WVsg.

### III. GEOLOGY OF THE STUDIED AREA AND FIELD INVESTIGATIONS

Peperites in the studied area are exposed at two locations along Mawat-Shasho road, which lies between longitudes  $45^{\circ} 25' 21.10''$  E (PF1) –  $45^{\circ} 27' 11.21''$  E (PF2) and latitudes  $35^{\circ} 54' 16.80''$  N –  $35^{\circ} 55' 29.65''$  N, respectively, and 1–4 Km away from East of Mawat town and 37 km north of

Sulaimani city (Figs. 2b, 3-5). Stratigraphically, both sites are within the base of WVsg. The WVsg within the Mawat area covers almost 70 km<sup>2</sup>. It is adjacent to the Mawat Ophiolite complex (Fig. 2). Along the Mawat-Shasho road, basaltic intrusions and its intermingling with deep-sea sediments have been observed at different locations in the basal part of the WVsg.

Based on the field investigations, the peperite-bearing successions in both PF1 and PF2 show variation in thickness at different sites and are widespread in the study area along the Mawat-Shasho section (Figs. 3-5). PF are discontinuously exposed on both the eastern and western sides of the Mawat-Shasho section. The distance between these two outcrops is about 6–7 km. PF1 and PF2 exhibit lateral lithological changes involving basaltic lava flows interlayered with deep marine succession involving micritic carbonate rocks occasionally associated with shale (a thrust product of basaltic pillow lava) beds. Two lithofacies types are recognized within peperites in the studied area (PF1 and PF2), both are illustrated in discussion section scenarios. Lithofacies Type 1 (PF1) is made up of coherent basaltic pillow lava that is sandwiched between peperites and micritic limestone rocks (Figs. 3, 4 and 6). While lithofacies 2 (PF2) comprises, coherent massive basalt intercalated with host micritic limestone rocks, closely packed vesicular pillow basalt, and peperites (Figs. 5 and 7). The host rocks for both lithofacies types (PF1 and PF2) are deep marine micritic carbonate rocks rich in planktonic Forams (Figs. 4 and 8).

PF1 in the field is characterized by blocky peperites and vesicular pillowed basaltic intrusions with well-layered, thick, and chocolate-colored micritic limestones. The jigsaw texture in the peperitic rocks is well exposed, especially in PF1 (Fig. 3). Even though PF2 is distinguished by fluidal peperites and vesicular to amygdaloidal pillowed basaltic intrusions with well-layered thick chocolate-colored micritic limestones (Fig. 5). In both PF1 and PF2 basaltic intrusions appear as grayish black having normal to the mega-pillow morphologies based on (Walker, 1992) classification and their rounded vesicles diameter range 1–5 mm are often filled with the secondary minerals such as calcite, chlorite, and quartz. The sedimentary rocks have attitudes of  $240^{\circ}/54^{\circ}/NW$ , occur as layers to massive chocolate micritic limestones, and cover more than 30–50 m within PF (Fig. 4). Manganese mineralization is well exposed on the micritic limestones in the form of surficial pods (3–5 cm), small tubes, and dendritic structures within PF1, which may indicate the deposition of micritic limestone within a deep marine environment (Fig. 4).

### IV. SAMPLING AND ANALYTICAL TECHNIQUES

The intensive fieldwork encompasses the meticulous collection of samples for peperites, basaltic rocks, and host micritic carbonate rocks, in addition to the comprehensive examination of the petrological and stratigraphical features of the PF. Almost 35 samples have been taken from PF. All 35 samples were cut for thin sections preparation (15 thin sections of basaltic rocks, 10 thin sections of peperitic rocks,

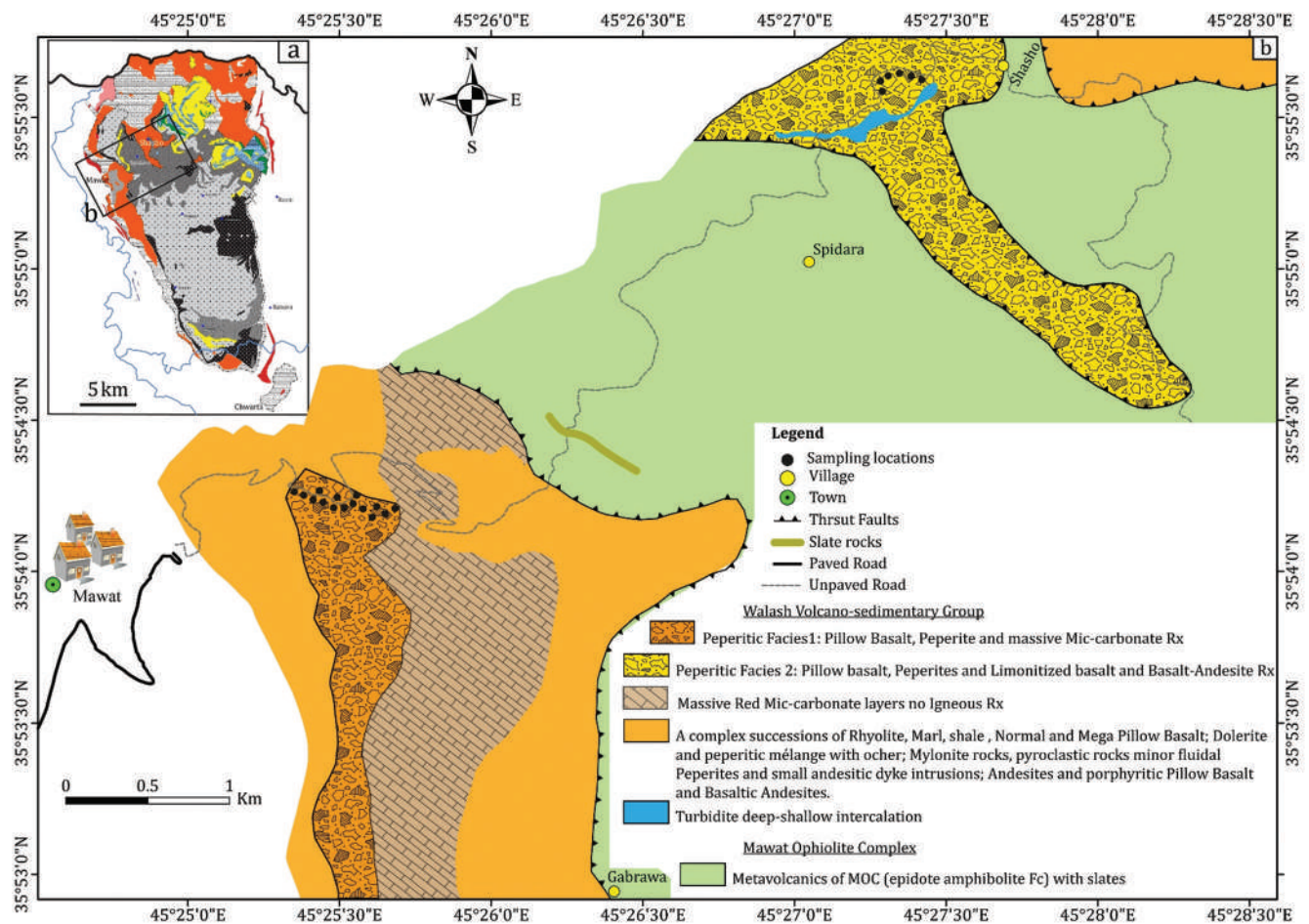


Fig. 2. (a) Location and geological map of the Mawat-Chwarta area of the study area after (Al-Mehaidi, 1974). (b) Detail geological map of the WVsg Mawat-Shasho section.

and 10 thin sections of host micritic carbonate rocks) and for studying their internal structures, textures, mineralogy (modal analysis), and paleontology polarized light microscope were used.

Twenty-six fresh samples have been selected for the mineralogical study. Among them, 20 samples were taken from peperitic rocks (basaltic rocks) and five samples from host micritic carbonate rocks, and one sample from thrust shale which is located between host micritic carbonate rocks and peperitic-basaltic rocks. All samples were grounded into powders for X-ray diffraction analysis at the University of Soran using a Panalytical X'Pert MRD machine. The samples were scanned using a Ni filter and K-Alpha1 radiation (1.54060 Å) at generator settings of 40 mA and 45 kV and recorded diffraction peaks are between  $2\theta=5^\circ$  and  $2\theta=70^\circ$ . Mineral patterns were identified using Match 3 software.

Within (PF1) 10 fresh samples from basaltic rocks and three samples from host micritic carbonate rocks and also 10 fresh samples from basaltic rocks and two samples from host micritic carbonate rocks within (PF2) have been selected for the whole rock geochemistry (major, trace and REE elements) analysis within ALS Laboratories in Seville, Spain.

At the geology department Research Laboratories at the University of Sulaimani, the slabbed whole-rock samples

were prepared with a water-cooled diamond-blade saw to remove any weathered or calcified parts of the rock samples. All rock samples were powdered in hardened steel with a chromium-free tool steel vibrating cup mill by using PULVERISSETTE 9 machine. Further sample preparations, such as pulverizing to get particle size  $<75 \mu\text{m}$  and lithium borate fusion before acid dissolution, have been done at ALS Labs. Whole-rock powders were analyzed by inductively coupled plasma-atomic emission spectroscopy (ICP) and Mass spectrometer (ICP-MS) methods for major, trace, and rare earth element (REE) abundances in the ALS laboratories using geochemical procedures (ME-ICP06; ME-MS81; ME-4ACD81). For major and trace element analyses, structural water was removed from sample powders by heating in a furnace at  $1000^\circ\text{C}$  for 30 min. Loss on ignition (LOI) was determined from 1 g of the powdered samples by heating in a furnace at  $1000^\circ\text{C}$ , and then the total weight change of the sample powder is calculated. Detection limits are  $<0.01\%$  for major elements and 0.01–1 ppm for trace and REE elements, except for As and Cr, which have relative errors of 5 ppm. Mg numbers are calculated using the formula  $\text{Mg\#} = (100 * \text{MgO} / [\text{MgO} + \text{Fe}_2\text{O}_3])$  [molar]. Eu anomalies ( $\text{Eu}/\text{Eu}^*$ ) have been calculated as  $\text{Eu}/\text{Eu}^* = (\text{Eu})_{\text{cn}} / [(\text{Sm})_{\text{cn}} \times (\text{Gd})_{\text{cn}}]^{0.5}$  after McLennan (1989). The Chemical Index of Alterations

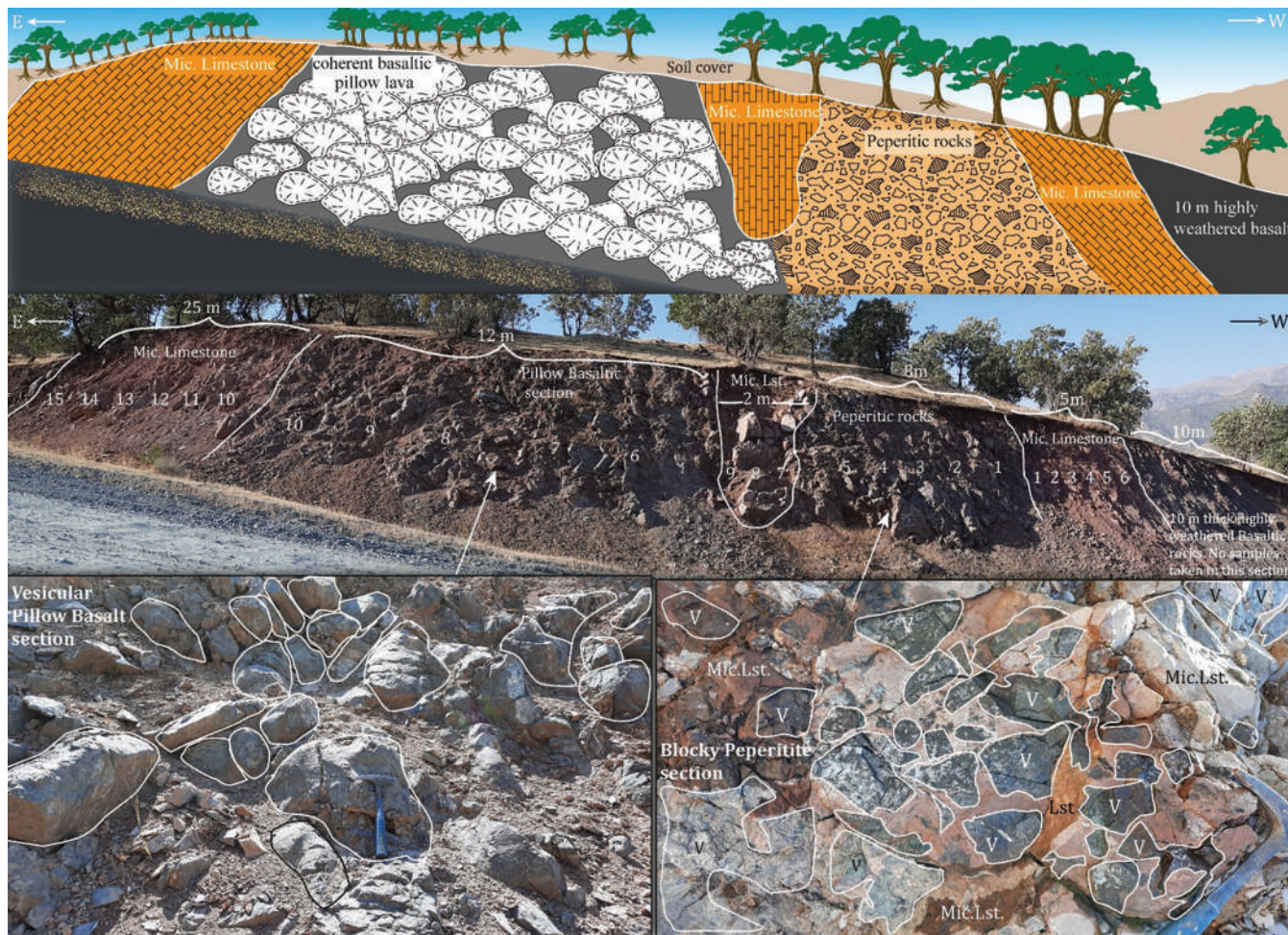


Fig. 3. Panoramic view and illustration of the PF1 outcrop within the Mawat area, comprising intercalation of the basaltic pillow with micritic limestone thick layers, blocky peperites, and coherent basaltic pillow lava. Numbers refer to the sampling locations.

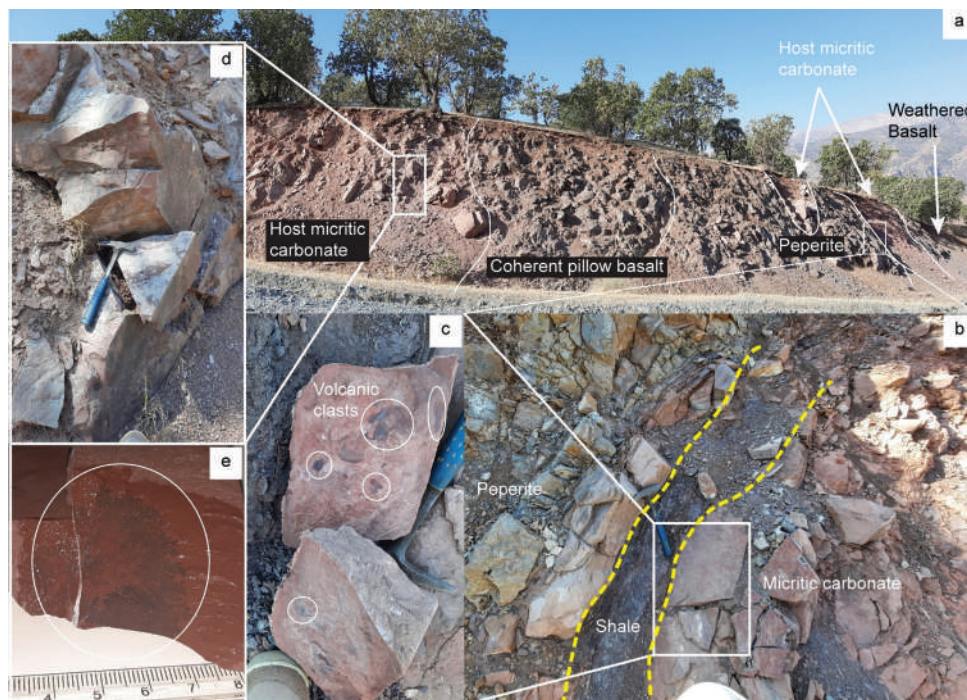


Fig. 4. (a) Panoramic view (~70 m horizontal) of the PF1 outcrop. (b) Shale (thrust) contact between peperite and host micritic carbonate rocks. (c) Centimetric pods of volcanic clasts (white circles) within micritic carbonate rocks. (d) Reddish brown host micritic carbonate rocks. (e) Dendritic structures of manganese mineralization within host micritic carbonate rocks.

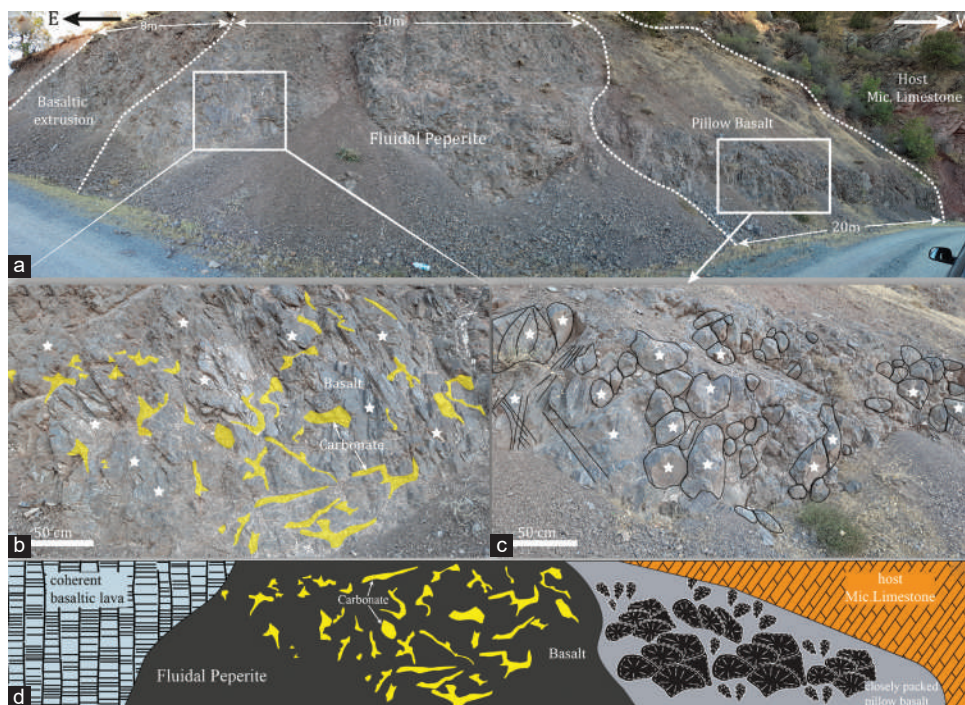


Fig. 5. (a) Panoramic view of the PF2 outcrop near Shasho village. (b) Fluidal peperites. (c) Vesicular pillow basalt outcrop, white stars represent sampling locations. (d) Representative illustration for fluidal peperite outcrop of panoramic view (a). White stars represent sampling locations.

(CIA%) is also calculated using the formula  $CIA\% = 100 * m. Al_2O_3 / (m. Al_2O_3 + m. CaO + m. Na_2O + m. K_2O)$  after Nesbitt and Young (1982).

## V. RESULTS

### A. Petrography

Petrographically, both PF1 and PF2 are composed primarily of plagioclase (45–50%) and clinopyroxene (20–25%) phenocrysts, set in an aphanitic groundmass of the same minerals and associated with hematite (10%) and orthoclase (8%), nepheline and sphene as accessory phases. Although PF1 and PF2 mineralogically are the same, they are showing different textures. PF1 samples tend to be more aphanitic in textures and are characterized by the presence of tachylite, in which skeletal grains of plagioclase (only the outer rim) set in the glassy groundmass (Fig. 9a). PF2 samples indicate more evolved magma and are characterized by porphyritic textures (Fig. 9c-f) in which boxy cellular plagioclase serves an initial mixing stage of magma. It indicates the typical volcanic texture of these rocks (Hibbard, 1995) and references therein (Fig. 9c and d). Amygdaloidal textures are clearly seen in both PF, vesicles are of circular and amoeboid forms and filled with secondary minerals, such as hematite, calcite, and dolomite. This might indicate hydrothermal alterations or submarine weathering in these volcanic rocks (Thompson, 1991) (Fig. 9a, b and e). Pyroxenes in PF1 samples are extremely altered while in PF2 samples, they are less altered (Fig. 9a and e). Despite the submarine hydrothermal alteration, the basaltic rocks in both PF1 and PF2 maintained their original igneous textures such as interstitial, glomerophytic, and intersertal textures.

### B. Mineralogy

Detailed mineralogical studies for the PF1, PF2, and host micritic limestone are shown in Table I. XRD analysis shows that the basaltic pillow lavas from PF1 and PF2 comprise major phases, such as albite, andesine, and diopside. While the minor phases comprise hematite, ilmenite, and titanite (Table I). As well as host micritic limestone rocks comprising calcite as major phases and quartz as minor. A 20cm shale in PF1 (thrust product) is between peperites and host micritic limestone rocks. It comprises montmorillonite, quartz, calcite, and anorthite as major phases and pyroxene as minor phases.

### C. Geochemistry

Within the studied area, 20 volcanic and five micritic limestones (host) rock representative samples from PF1 and PF2 were analyzed for geochemical classification and interpretation of the peperitic rock types. The major, trace, and REE concentrations of these volcanic and micritic limestone rocks in the PF are given in Tables II and III. Micritic limestone host rocks are characterized by a narrow range in  $SiO_2$  (10.75–11.65 wt.%) and high contents of CaO (45.3–46.7 wt.%) with LOI (36.0–36.8 wt.%). While the concentrations of  $Al_2O_3$ ,  $Fe_2O_3$ , MgO,  $Na_2O$ , and  $K_2O$  are around 6 wt.%. The geochemical signature of these micritic limestone rocks indicates that the host carbonate rocks in both PF1 and PF2 are deposited in a deep-marine environment.

Meanwhile, the volcanic rock samples in both PF1 and PF2 occupy a narrow range of  $SiO_2$  (43.63–47.57wt.%),  $Al_2O_3$  (16.05–17.85 wt.%), and  $Fe_2O_3$  (10.15–11.35 wt.%) with relatively high  $Na_2O$  and CaO and low  $K_2O$ . Furthermore, the amounts of  $Cr_2O_3$ , MnO,  $P_2O_5$ , SrO, and BaO are <0.5 wt.%. Almost all samples are influenced by



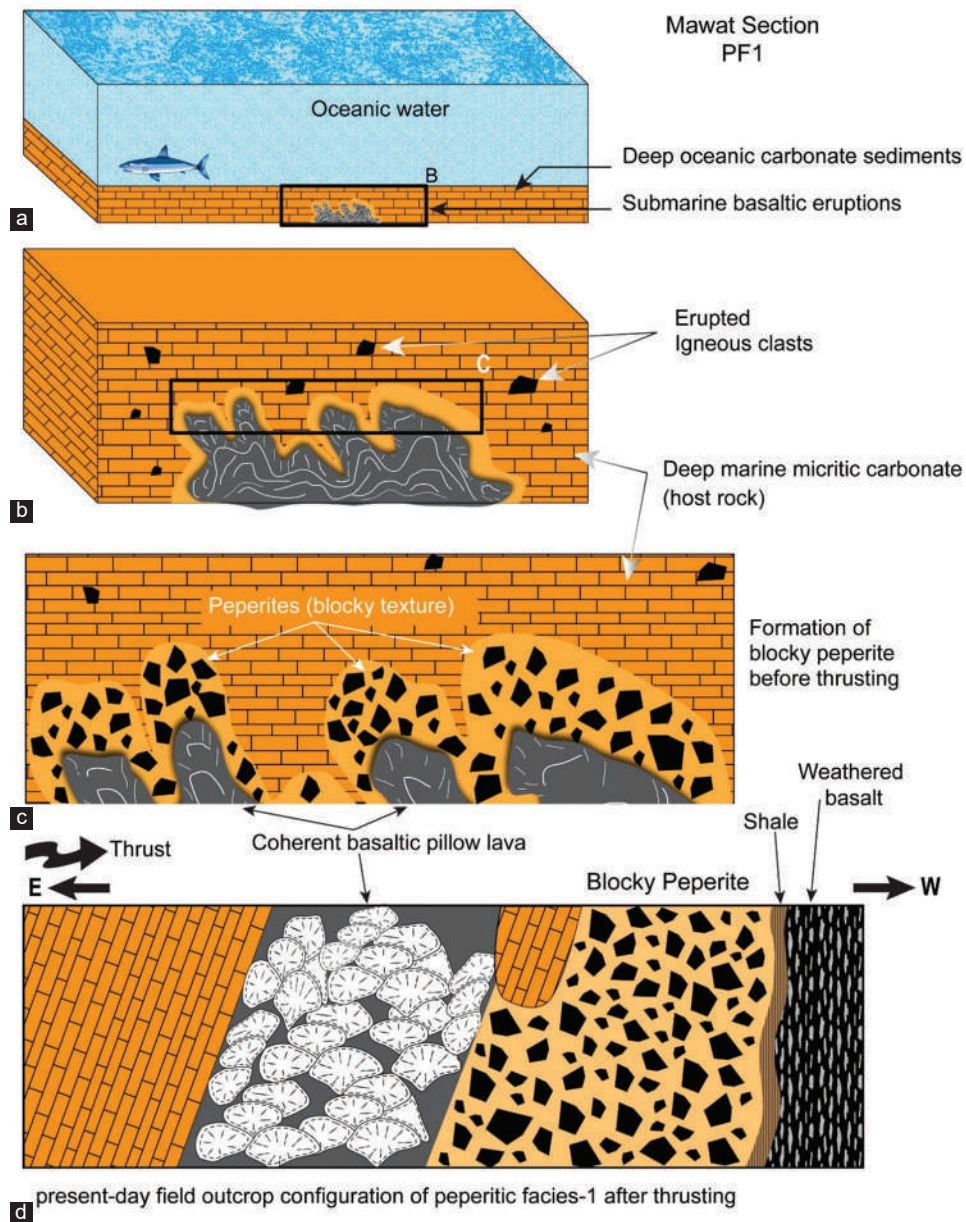


Fig. 6. (a-d) Scenario 1 for the formation of blocky peperite within PF1 (Mawat section).

hydrothermal alteration (Fig. 9a-f). The alteration effects on the volcanic rocks are consistent with the high value of LOI (7.0–9.46%) and the high ratio of alkalis ( $\text{Na}_2\text{O}+\text{K}_2\text{O}$ ).

The use of Harker diagrams reveals a discernible negative or positive correlation between the majority of major oxides and the increasing  $\text{SiO}_2$  content. The observed correlations indicate the significant influence of fractional crystallization processes in the development of volcanic rocks within PF 1 and 2. The observed patterns in the concentrations of  $\text{Al}_2\text{O}_3$ ,  $\text{CaO}$ ,  $\text{Na}_2\text{O}$ ,  $\text{TiO}_2$ , and  $\text{Fe}_2\text{O}_3$  relative to  $\text{SiO}_2$  indicate a potential process of fractionation involving diopside, plagioclase, sphene, and other iron-titanium oxides, as illustrated in (Fig. 10).

The low concentration of  $\text{MgO}$  observed in both sections PF1 and PF2 may be attributed to the absence of olivine and amphibole (specifically, Mg-hornblende). Besides, low  $\text{TiO}_2$

concentrations of around 1% may reflect the eruption of basaltic submarine eruptions near frontal arc settings (Shuto, et al., 2015). Conversely, the greater concentrations of  $\text{Fe}_2\text{O}_3$ , as indicated by the elevated modal percentage of hematite, are evident in both PF1 and PF2.

The concentrations of trace elements, specifically Nb, Ta, and Ti, exhibit a distinct depletion characteristic in volcanic rocks found in PF1 and PF2. This depletion feature is believed to be an inherent characteristic of the source region of the island arc (Ryerson and Watson, 1987). Furthermore, the concentrations of compatible trace elements, such as chromium (Cr) and nickel (Ni), in the volcanic samples from PF1 and PF2 exhibit a range of (205–380 ppm) and (82–171 ppm), respectively (Tables II and III). As reported by (Humphris and Thompson, 1978), the observed values generally align with the Cr and Ni concentrations found in

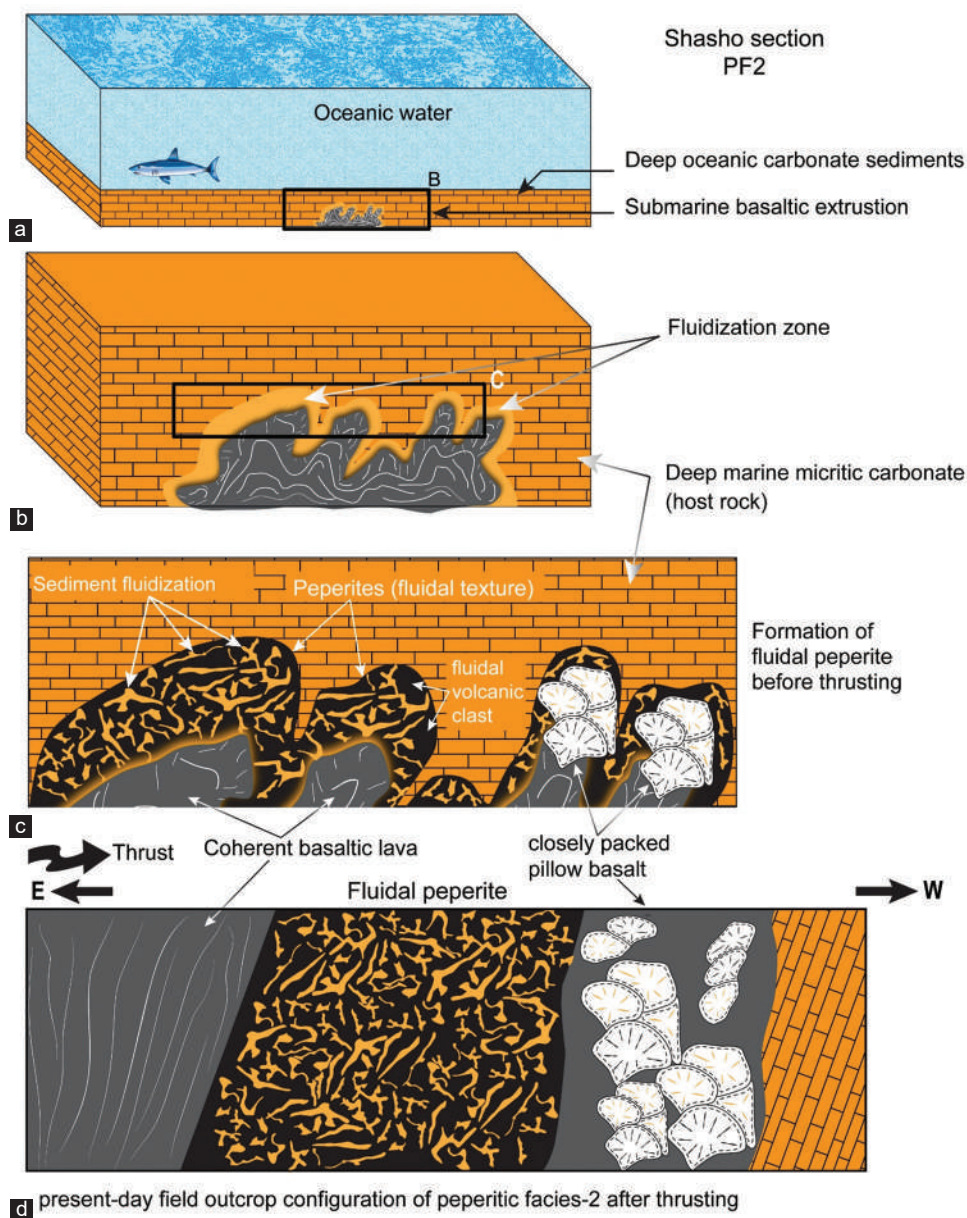


Fig. 7. (a-d) Scenario 2 for the formation of fluidal peperite within PF2 (Shasho section).

fresh basalt, which typically, fall within the range of 280–550 ppm and 75–140 ppm, respectively.

Zirconium (Zr) concentration serves as a reliable indicator of geochemical diversity, functioning as an independent index. It demonstrates a strong correlation with various other elements, thereby enabling the assessment of their mobility (Pearce, et al., 1992; Liu, et al., 2012; Wang, et al., 2016). Therefore, the utilization of Zr as a fractionation index allows for the identification of mafic fractionation processes involving pyroxene and/or olivine, as evidenced by the observed decrease in Cr and Ni (Fig. 11). The presence of a positive correlation between Zr and Y, as well as Zr and Nb, in conjunction with the presence of Ce, may suggest the absence of amphibole and monazite minerals. In general, there is a notable correlation between Zr and REEs (La, Ce, Nd, and Sm), which serves to confirm the immobile nature of

these elements during hydrothermal or secondary alteration processes within PF1 and PF2 rock samples (Fig. 11).

All samples, that were plotted on the diagram (Zr/TiO<sub>2</sub>–Nb/Y) after (Pearce, 1996), are in the basaltic field and show sub-alkaline characteristics (Fig. 12a). The magmatic nature classification diagrams, after (Miyashiro, 1974) and (Ross and Bédard, 2009), show all samples in the field of tholeiitic nature (Fig. 12b and c). All basaltic rock samples within both PF are characterized by the following elemental ratios: low Nb/Y (0.10–0.15), La/Yb (1.4–2.3), and Nb/La (0.61–0.77); adequately high Zr/Nb (23–30), Hf/Ta (12–22) and Th/Ta (2–5); relatively low contents of major elements, such as TiO<sub>2</sub> and P<sub>2</sub>O<sub>5</sub> in contrast to the high ratios of FeO<sub>t</sub>/MgO (Tables II and III). Furthermore, on well-known tectonic diagrams, such as Th/Yb versus Ta/Yb after (Pearce, 1982), Ce–Sr–Sm normalized ternary after (Ikeda, 1990), and

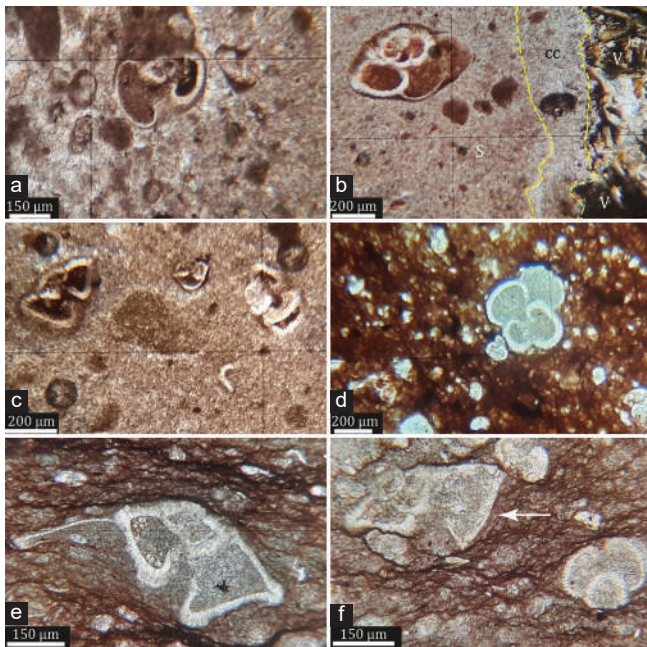


Fig. 8. (a) *Acarinina nitida*, (b) *Morozovella praeangulata*, (c) *Morozovella subbotinae* (left up), *Morozovella apantesma* (right up), (d) *Morozovella aequa*, (e) *Morozovella velascoensis*, (f) *Morozovella subbotina* (with arrow), *Acarinina soldadoensis* (bottom right). Figures (a-c) are for PF rocks and (d-f) are for host micritic carbonate rocks (S). Volcanic rocks (V), calcite vein represented by cc.

Zr-Ti-Sr ternary after (Pearce and Cann, 1973), these basaltic rocks are plotted in the fields of volcanic arc basalt and island arc tholeiitic basalt, respectively (Fig. 13a-c). Based on the primitive mantle-normalized multielement spider diagram (Fig. 14a), the basaltic rocks in both PF1 and PF2 show selective enrichment in Large-Ion Lithophile Elements (LILEs) (e.g., Rb, Ba, and K) and depletion in the High Field Strength Elements (HFSEs) (e.g., Ta, Nb, Nd, and Ti). It compared with the field of island arc basalts (IAB) after (Perfit, et al., 1980). While on the REE chondrite-normalized diagram (Fig. 14b), these basaltic rocks are characterized by slight enrichment and with flat REE patterns. It compared with the average composition of IAB after (Elliott, 2003) and Izu-Bonin-Mariana arc basalts (IBM Arc) field after (Elliott, et al., 1997).

#### D. Paleontological Investigation

The authors concentrated on whole PF1 sections for paleontological investigations because the PF1 consists of well crops out of micritic carbonate sequences that sandwiched peperitic rocks in the area (Figs. 3 and 4). The distinguishable facies throughout peperites within WVSg indicated deep marine environments that lack benthonic foraminifera in contrast with the high percentage of planktonic foraminifera, especially *Morozovella* and *Acarinina* which they reflect the deep marine environment

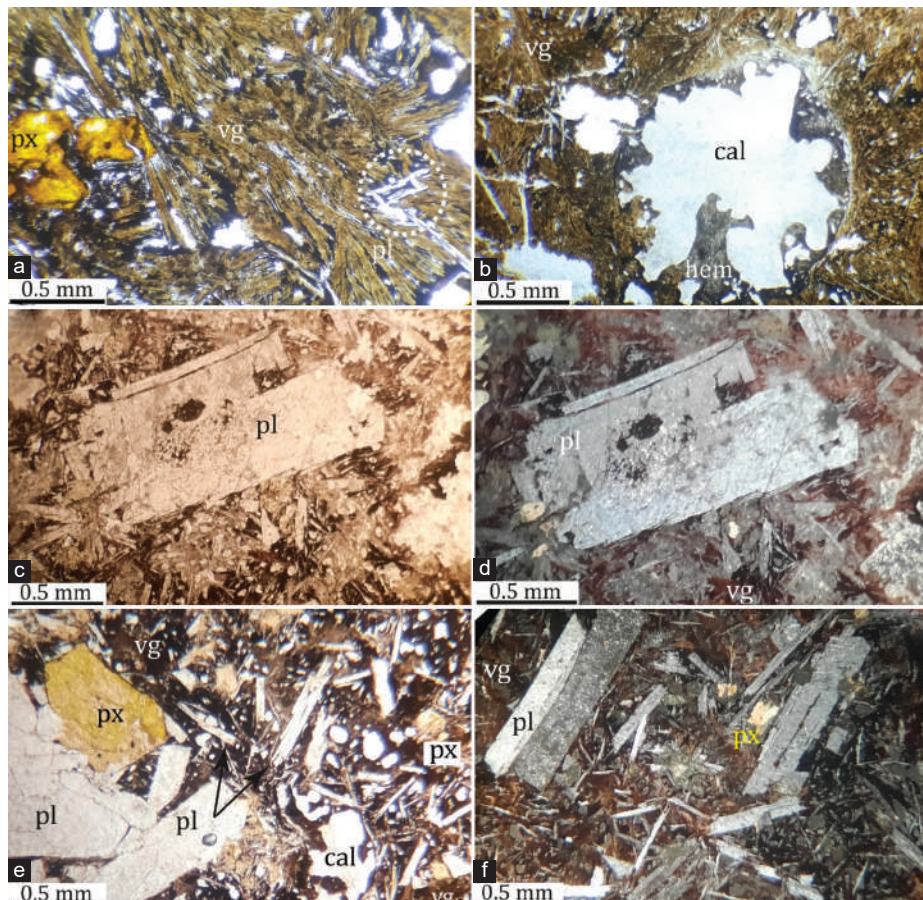


Fig. 9. (a) Tachylite, skeletal plagioclase (pl) with extremely altered pyroxene (px) and volcanic glass (vg) groundmass in PF1 (sample JB1). (b) Amygdule filled with hematite (hem) and calcite (cal) (sample JB6). (c and d) Boxy cellular plagioclase in PF2 (sample JB16). (e and f) Porphyritic basalt in PF2 (sample JB20). Mineral abbreviations after (Whitney and Evans, 2010). Photomicrographs of a, b, c, and e are PPL view; d and f are XPL view.

TABLE I  
XRD MINERALOGY (MAJOR & MINOR PHASES) WITHIN PF1 AND PF2 AND HOST MICRITIC CARBONATE ROCKS (MC). (BST.) STANDS FOR BASALT

Sample	Location	Field description	Major minerals	Minor minerals	Sections
JB1	Mawat	Basaltic-Peperitic rocks contacted with host micritic carbonate rocks	Diopside and Albite	Sodalite and Hematite	
JB2	Mawat	Basaltic-Peperitic rocks 50 cm away from host micritic carbonate rocks	Albite, Andesine and Diopside	Calcite and Hematite	
JB3	Mawat	Fresh pillowed basalt 10m away from Peperitic rocks	Albite, Augite and Anorthite	Hematite	
JB4	Mawat	Fresh pillowed basalt 12m away from Peperitic rocks	Albite, Andesine and Hematite	Calcite and Ilmenite	
JB5	Mawat	Fresh pillowed basalt contacted with host micritic carbonate rock	Albite, Calcite and Ilmenite	Hematite	
JB6	Mawat	Fresh pillowed basalt 12.5m away from Peperitic rocks	Albite, Augite and Ilmenite	Calcite and Hematite	
JB7	Mawat	Fresh pillowed basalt 13m away from Peperitic rocks	Albite, Andesine, Augite and Ilmenite	Calcite and Hematite	
JB8	Mawat	Fresh pillowed basalt 14m away from Peperitic rocks	Albite, Andesine and Ilmenite	Calcite and Hematite	
JB9	Mawat	Fresh pillowed basalt 15m away from Peperitic rocks	Albite, Andesine, Augite and Ilmenite	Calcite and Hematite	
JB10	Mawat	Fresh pillowed basalt 16m away from Peperitic rocks	Albite, Diopside, Anorthite and Ilmenite	Hematite	
JB11	Mawat	Host Micritic carbonate rock, Right side of peperitic rocks	Calcite	Colusite and Quartz	
JB12	Mawat	Host Micritic carbonate rock, Left side of peperitic rocks	Calcite	Quartz	
JB13	Mawat	Host Micritic carbonate rock, Left side of peperitic rocks	Calcite	Quartz	
Shale	Mawat	20 cm Thick Shale rock contacted with samples IMP and IMPF	Montmorillonite, Quartz, Calcite and Anorthite	Pyroxene	
JB14	Shasho	Vesicular- amygdaloidal basalt- Peperite	Albite and Diopside	Ilmenite and Hematite	
JB15	Shasho	Vesicular- amygdaloidal basalt- Peperite	Albite and Diopside	Ilmenite and Hematite	
JB16	Shasho	Vesicular- amygdaloidal basalt- Peperite	Albite and Diopside	Ilmenite and Hematite	
JB17	Shasho	Vesicular- amygdaloidal basalt- Peperite	Albite and Diopside	Ilmenite and Hematite	
JB18	Shasho	Vesicular- amygdaloidal basalt- Peperite	Albite and Diopside	Ilmenite and Hematite	
JB19	Shasho	Vesicular- amygdaloidal basalt- Peperite	Albite and Diopside	Titanite and Ilmenite	
JB20	Shasho	Vesicular- amygdaloidal basalt- Peperite	Albite and Diopside	Titanite and Ilmenite	
JB21	Shasho	Vesicular- amygdaloidal basalt- Peperite	Albite and Diopside	Titanite and Ilmenite	
JB22	Shasho	Vesicular- amygdaloidal basalt- Peperite	Albite and Diopside	Titanite and Ilmenite	
JB23	Shasho	Vesicular- amygdaloidal basalt- Peperite	Albite and Diopside	Titanite and Ilmenite	
JB24	Shasho	Micritic carbonate rock, within peperitic rocks	Calcite	Quartz and Colusite	
JB25	Shasho	Micritic carbonate rock, within peperitic rocks	Calcite	Quartz	

TABLE II  
WHOLE-ROCK MAJOR, TRACE, AND REE CONCENTRATIONS (ICP-MS) OF PF1 ROCK SAMPLES IN THE MAWAT AREA

PEPERITIC FACIES	PF1																				
	Sample number	JB1	JB2	JB3	JB4	JB5	JB6	JB7	JB8	JB9	JB10	D.L.	Average STDEV.	JB11	JB12	JB13	D.L.	Average STDEV.			
Rock type	Basalt	Basalt	Basalt	Basalt	Basalt	Basalt	Basalt	Basalt	Basalt	Basalt	Basalt		Mean	Precision	Mic. Lst.	Mic. Lst.	Mic. Lst.		Mean	Precision	
Oxides (Wt.%)																					
SiO <sub>2</sub>	47.57	46.11	43.87	45.74	43.99	43.63	46.45	46.00	46.50	46.20	<0.01	45.61	1.32	11.50	11.60	11.65	<0.01	11.58	0.08		
Al <sub>2</sub> O <sub>3</sub>	16.80	16.40	17.85	17.15	16.05	17.25	17.10	17.00	17.20	17.15	<0.01	17.00	0.49	3.06	3.08	3.07	<0.01	3.07	0.01		
Fe <sub>2</sub> O <sub>3</sub>	10.40	10.60	11.35	10.95	10.15	10.20	10.95	10.90	10.92	10.85	<0.01	10.73	0.38	1.62	1.68	1.64	<0.01	1.65	0.03		
CaO	11.00	12.90	11.10	13.35	13.75	14.70	11.80	11.60	11.70	11.50	<0.01	12.34	1.26	46.40	46.50	46.70	<0.01	46.53	0.15		
MgO	3.45	4.46	3.33	2.65	3.04	1.82	3.61	3.50	3.45	3.40	<0.01	3.27	0.68	1.00	1.08	1.06	<0.01	1.05	0.04		
Na <sub>2</sub> O	4.75	4.06	3.62	3.67	3.97	3.65	4.09	4.00	4.05	4.00	<0.01	3.99	0.33	0.34	0.36	0.35	<0.01	0.35	0.01		
K <sub>2</sub> O	0.94	0.48	1.38	1.44	0.85	1.35	1.05	1.00	0.95	0.98	<0.01	1.04	0.29	0.62	0.61	0.62	<0.01	0.62	0.01		
Cr <sub>2</sub> O <sub>3</sub>	0.05	0.04	0.04	0.04	0.04	0.04	0.04	0.04	0.05	0.04	<0.01	0.04	0.01	0.01	0.01	0.01	<0.01	0.01	0.00		
TiO <sub>2</sub>	1.04	1.08	1.13	1.24	1.08	1.04	1.20	1.10	1.20	1.15	<0.01	1.13	0.07	0.15	0.17	0.16	<0.01	0.16	0.01		
MnO	0.17	0.15	0.16	0.16	0.16	0.15	0.18	0.17	0.15	0.16	<0.01	0.16	0.01	0.10	0.10	0.10	<0.01	0.10	0.00		
P <sub>2</sub> O <sub>5</sub>	0.15	0.10	0.25	0.66	0.33	0.59	0.21	0.40	0.55	0.50	<0.01	0.37	0.20	0.20	0.20	0.21	<0.01	0.20	0.01		
SrO	0.07	0.07	0.05	0.06	0.05	0.06	0.07	0.06	0.07	0.07	<0.01	0.06	0.01	0.02	0.02	0.02	<0.01	0.02	0.00		
BaO	0.02	0.02	0.03	0.02	0.02	0.03	0.02	0.03	0.03	0.03	<0.01	0.03	0.01	0.01	0.01	0.01	<0.01	0.01	0.00		
LOI	7.31	7.44	8.74	7.15	8.45	9.46	7.04	7.10	7.00	7.05	<0.01	7.67	0.88	36.70	36.50	36.00	<0.01	36.40	0.36		
TOTAL	103.72	103.92	102.90	104.27	101.92	103.97	103.82	102.89	103.82	103.08		103.43		101.73	101.92	101.60		101.75			
Mg#	58.82	63.58	55.94	52.63	59.70	48.08	58.82	57.14	58.82	52.63		56.62		-	-	-					
CIA%	35.56	34.04	40.00	34.69	33.33	34.00	36.96	37.78	36.96	37.78		36.11		-	-	-					
Trace (ppm)																					
Ag	0.5	0.5	0.5	0.5	0.5	0.5	0.5	0.5	0.5	0.5	0.01-1	0.50	0.00	0.4	0.4	0.5	0.01-1	0.43	0.06		
As	5	5	12	27	20	25	19	13	15	22	5	16.30	7.67	9	9	9	5	9.00	0.00		
Cd	0.5	0.5	0.5	0.5	0.5	0.5	0.5	0.5	0.5	0.5	0.01-1	0.50	0.00	0.6	0.6	0.6	0.01-1	0.60	0.00		

(Contd...)

TABLE II  
(CONTINUED)

PEPERITIC FACIES											PF1									
Sample number	JB1	JB2	JB3	JB4	JB5	JB6	JB7	JB8	JB9	JB10	D.L.	Average	STDEV.	JB11	JB12	JB13	D.L.	Average	STDEV.	
Rock type	Basalt	Basalt	Basalt	Basalt	Basalt	Basalt	Basalt	Basalt	Basalt	Basalt		Mean	Precision	Mic. Lst.	Mic. Lst.	Mic. Lst.		Mean	Precision	
Co	48	51	54	53	49	45	44	43	46	49	0.01-1	48.20	3.74	7	7	7.2	0.01-1	7.07	0.12	
Cu	87	53	133	39	28	27	38	35	44	51	0.01-1	53.50	32.80	31	31	30	0.01-1	30.67	0.58	
Li	40	40	40	20	20	10	30	40	38	35	0.01-1	31.30	10.91	10	10	10	0.01-1	10.00	0.00	
Mo	1	1	1	1	1	1	1	1	1	1	0.01-1	1.00	0.00	2	1	2	0.01-1	1.67	0.58	
Ni	150	160	171	106	121	142	119	120	125	130	0.01-1	134.40	20.64	71	72	71	0.01-1	71.33	0.58	
Pb	2	3	2	3	2	4	2	3	2	3	0.01-1	2.60	0.70	4	4	4	0.01-1	4.00	0.00	
Sc	35	36	36	40	35	32	37	35	36	35	0.01-1	35.70	2.00	4	4	4	0.01-1	4.00	0.00	
Tl	10	10	10	10	10	10	10	10	10	10	0.01-1	10.00	0.00	10	9	10	0.01-1	9.67	0.58	
Zn	85	79	115	115	106	104	101	100	105	102	0.01-1	101.20	11.47	30	30	30	0.01-1	30.00	0.00	
Ba	203	125	215	149.5	120	204	246	225	240	235	0.01-1	196.25	47.43	126	126.5	127	0.01-1	126.50	0.50	
Ce	9.5	9.6	11	13.6	12.2	11.5	14.3	11.2	13.5	12.4	0.01-1	11.88	1.63	10.9	10.8	10.9	0.01-1	10.87	0.06	
Cr	380	300	270	240	250	230	230	260	280	265	5	270.50	44.38	51	50	50.5	5	50.50	0.50	
Cs	0.72	0.44	1.01	0.94	0.38	1.04	0.86	0.7	0.9	0.85	0.01-1	0.78	0.23	1.15	1.14	1.15	0.01-1	1.15	0.01	
Dy	4.09	4.28	4.37	5.32	4.38	3.89	4.74	4.2	4.7	4.5	0.01-1	4.45	0.40	2.38	2.39	2.36	0.01-1	2.38	0.02	
Er	2.58	2.87	2.96	3.38	2.99	2.68	3.02	2.7	3	2.95	0.01-1	2.91	0.23	1.43	1.45	1.44	0.01-1	1.44	0.01	
Eu	1	0.96	1.09	1.26	1.1	1.04	1.1	1	1.1	1.05	0.01-1	1.07	0.08	0.57	0.59	0.57	0.01-1	0.58	0.01	
Ga	15.6	17.2	17.2	17.3	16.1	17.6	17.6	16	17.5	17	0.01-1	16.91	0.73	4.5	4.4	4.6	0.01-1	4.50	0.10	
Gd	3.51	3.56	4.03	4.46	3.84	3.78	4.24	3.86	4.2	4	0.01-1	3.95	0.30	2.62	2.62	2.61	0.01-1	2.62	0.01	
Hf	1.9	1.9	2	2.2	1.9	2.1	2.4	2	2.3	2.1	0.01-1	2.08	0.18	0.7	0.7	0.7	0.01-1	0.70	0.00	
Ho	0.86	0.95	0.97	1.14	0.95	0.92	0.97	0.88	0.98	0.9	0.01-1	0.95	0.08	0.48	0.48	0.49	0.01-1	0.48	0.01	
La	3.6	3.8	4.1	5.9	4.8	4.8	6	4.2	5.4	4.9	0.01-1	4.75	0.84	14.6	14.7	14.5	0.01-1	14.60	0.10	
Lu	0.38	0.4	0.45	0.53	0.44	0.43	0.46	0.41	0.47	0.45	0.01-1	0.44	0.04	0.18	0.19	0.18	0.01-1	0.18	0.01	
Nb	2.4	2.6	2.6	3.6	3.1	3.1	3.6	3.2	3.5	2.3	0.01-1	3.00	0.49	2.6	2.7	2.6	0.01-1	2.63	0.06	
Nd	7.9	8.3	8.5	10.6	9.6	9.2	11.2	8.8	10.5	9.8	0.01-1	9.44	1.09	11.4	11.3	11.4	0.01-1	11.37	0.06	
Pr	1.54	1.57	1.66	2.18	1.84	1.78	2.11	1.7	2.1	1.9	0.01-1	1.84	0.23	2.64	2.66	2.65	0.01-1	2.65	0.01	
Rb	15.4	7.3	22.2	17.8	11.6	16.8	15	15.5	18	16	0.01-1	15.56	3.96	15	15	15	0.01-1	15.00	0.00	
Sm	2.59	2.55	2.64	3.37	2.74	2.77	3.05	2.6	3	2.8	0.01-1	2.81	0.26	2.08	2.07	2.08	0.01-1	2.08	0.01	
Sn	1	1	1	1	1	1	1	1	1	1	0.01-1	1.00	0.00	1	1	1	0.01-1	1.00	0.00	
Sr	705	667	538	556	467	577	651	670	700	680	0.01-1	621.10	80.94	252	250	253	0.01-1	251.67	1.53	
Ta	0.1	0.1	0.1	0.1	0.1	0.1	0.2	0.1	0.2	0.1	0.01-1	0.12	0.04	0.2	0.2	0.2	0.01-1	0.20	0.00	
Tb	0.62	0.66	0.7	0.78	0.62	0.66	0.72	0.67	0.71	0.69	0.01-1	0.68	0.05	0.37	0.37	0.38	0.01-1	0.37	0.01	
Th	0.34	0.4	0.38	0.48	0.41	0.41	0.52	0.44	0.5	0.47	0.01-1	0.44	0.06	1.4	1.3	1.4	0.01-1	1.37	0.06	
Tm	0.39	0.42	0.43	0.5	0.41	0.37	0.46	0.42	0.48	0.46	0.01-1	0.43	0.04	0.17	0.17	0.16	0.01-1	0.17	0.01	
U	0.28	0.21	0.36	0.32	0.24	0.38	0.26	0.3	0.36	0.33	0.01-1	0.30	0.06	0.24	0.24	0.23	0.01-1	0.24	0.01	
V	220	208	219	218	206	218	219	218	222	220	0.01-1	216.80	5.33	17	16	17	0.01-1	16.67	0.58	
W	1	1	1	1	1	1	1	1	1	1	0.01-1	1.00	0.00	1	1	1	0.01-1	1.00	0.00	
Y	26	25.4	25.3	30.1	26	25.9	27.8	26.5	28	27	0.01-1	26.80	1.48	16.6	16.6	16.7	0.01-1	16.63	0.06	
Yb	2.42	2.68	2.85	3.18	2.9	2.64	2.59	2.67	2.8	2.7	0.01-1	2.74	0.21	1.22	1.21	1.23	0.01-1	1.22	0.01	
Zr	72	74	75	93	84	79	100	85	95	90	0.01-1	84.70	9.66	27	28	26	0.01-1	27.00	1.00	
Eu/Eu*	1.02	0.98	1.03	1	1.04	0.99	0.94	0.97	0.95	0.97				-	-	-				
(La/Sm)N	0.76	0.82	0.85	0.96	0.96	0.95	1.08	0.89	0.99	0.96				-	-	-				
(La/Yb)N	0.9	0.86	0.87	1.12	1	1.1	1.4	0.95	1.17	1.1				-	-	-				
(Tb/Yb)N	1.09	1.05	1.05	1.04	0.91	1.06	1.18	1.07	1.08	1.09				-	-	-				

Mic Lst.: Micritic Limestone, D.L.: Detection Limit, STDEV.:Standard Deviations

with tropical to subtropical climate condition (BouDagher-Fadel, 2015).

Ten samples were dated using planktonic foraminifera, five samples were from peperitic rocks taken from the contact of basaltic-carbonate clasts (blocky peperites). The other five samples were taken from host micritic carbonate rocks. Both of these section samples gave us the same planktonic foram species (Figs. 8 and 15). The systematic investigation of planktonic foraminifera enabled us to identify 13 species and subspecies in the studied sections (Fig. 8) including *Morozovella praeangulata*; *Morozovella apantesma*; *Morozovella angulata*; *Morozovella subbotinae*; *Morozovella*

*accuta*; *Morozovella occlusal*; *Morozovella cf. apantesma*; *Morozovella velascoensis*; *Morozovella aequa*; *Acarinina nitida*; *Acarinina soldadoensis*; *Subbotina cancellate*; and *Globanomalina chapmani*. To recognize these species, a lot of sources were used including (Cushman, 1925; White, 1928; Parr, 1938; Morozova, 1939; Toulmin, 1941; Cushman, 1942; Martin, 1943; Bronnimann, 1952; Loeblich Jr. and Tappan, 1957; Blow, 1979; Olsson, et al., 1999; Berggren, et al., 2006). The stratigraphic distribution of these planktonic foraminiferal assemblages permits the recognition of 15 biozones, two dominant biozones (P3 and P4) after (Wade, et al., 2011) have established in WVSg (Middle Paleocene). The



TABLE III  
(CONTINUED)

Peperitic Facies											PF2							
Sample number	JB14	JB15	JB16	JB17	JB18	JB19	JB20	JB21	JB22	JB23	D.L.	Average	STDEV.	JB24	JB25	D.L.	Average	STDEV.
Rock type	Basalt	Basalt	Basalt	Basalt	Basalt	Basalt	Basalt	Basalt	Basalt	Basalt		Mean	Precision	Mic. Lst.	Mic. Lst.		Mean	Precision
W	1	1	1	1	1	1	1	1	1	1	0.01-1	1.00	0.00	1	1	0.01-1	1.00	0.00
Y	24.5	25	25.5	25.8	26.2	26.9	27.2	26.5	27.6	28.3	0.01-1	26.35	1.19	12.8	13	0.01-1	12.90	0.14
Yb	2.67	2.65	2.68	2.66	2.9	2.73	2.75	2.69	2.82	2.78	0.01-1	2.73	0.08	0.86	0.9	0.01-1	0.88	0.03
Zr	86	84	86	85	87	83	88	82	87	89	0.01-1	85.70	2.21	20	21	0.01-1	20.50	0.71
Eu/Eu*	1.05	1.04	1.05	1.11	1.09	1.1	1.13	1.06	1.16	1.15				-	-			
(La/Sm)N	0.87	0.86	0.89	0.86	0.85	0.94	1.06	0.98	0.9	0.79				-	-			
(La/Yb)N	1.09	1.07	1.11	0.93	0.94	1.11	1.15	1.15	0.99	0.87				-	-			
(Tb/Yb)N	1.08	1.06	1.1	1.12	0.95	1.12	0.99	1.15	1.13	1.18				-	-			

Mic Lst.: Micritic Limestone, D.L.: Detection Limit, STDEV.:Standard Deviations

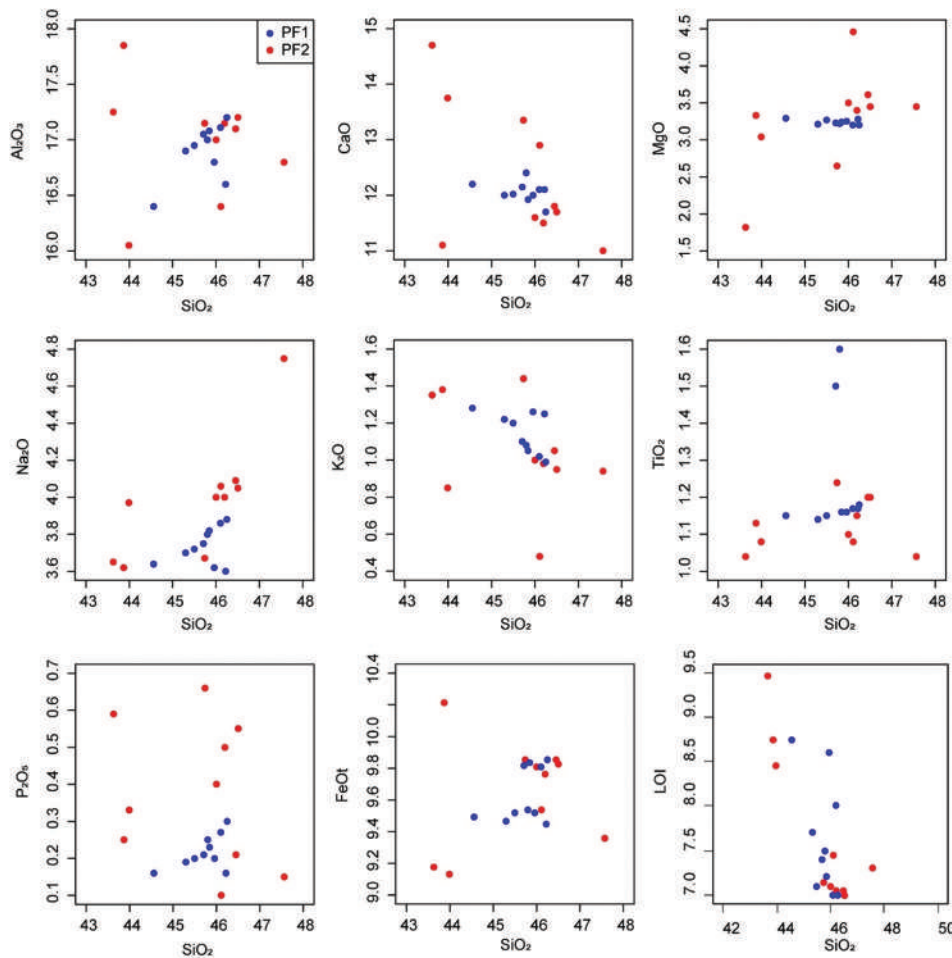


Fig. 10. Harker diagram SiO<sub>2</sub> based versus major elements (Wt.%) for the basaltic rock samples from PF1 and PF2 within WVSg.

peperitic rocks in WVSg were dated to 60 million years ago, corresponding to the Selandian stage of the Middle Paleocene, based on the presence of a *Morozovella* assemblage zone.

## VI. DISCUSSION

### A. PF in WVSg

As a first attempt, in this paper, two kinds of PF have been recognized in the WVSg. However, to define any PF in

any tectonic setting, two principal rules of (White, Mcphie and Skilling, 2000; Skilling, et al., 2002) must be fulfilled: (1) The presence of unconsolidated wet sediment or poorly consolidated sediment; (2) The confirmation of hot magma and its in-situ disintegration and intermingling with the host sediment. Regarding WVSg, the PF1 and PF2 possess the two principal rules as they are clearly seen in the fields. Thus, volcanic rocks and peperites are ubiquitous components within the WVSg of all studied sections in the Mawat area.

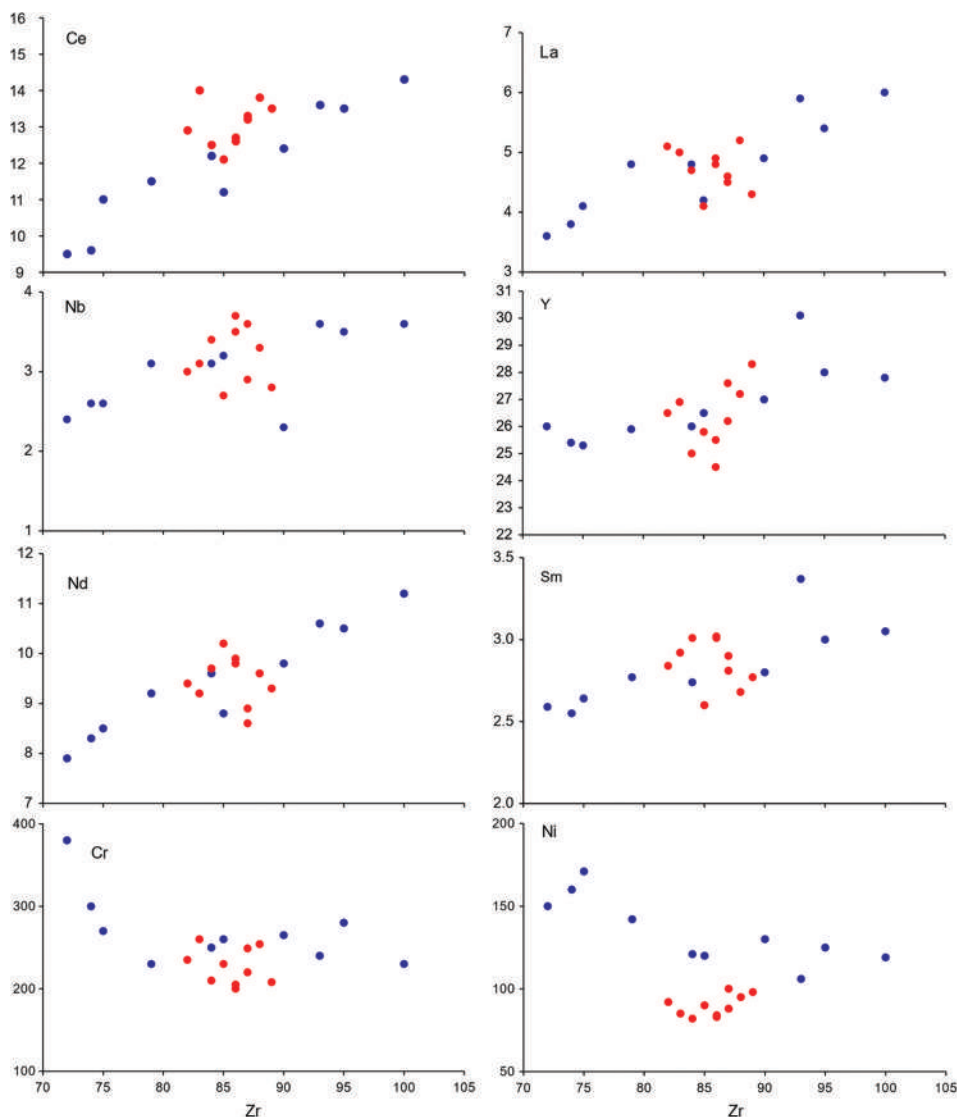


Fig. 11. Binary plots of Zr (ppm) vs selected trace and REE elements (ppm) for the volcanic rocks within PF1 and PF2. Symbols are the same as in Fig. 10.

TABLE IV

WALASH PEPERITE MAJOR-TRACE ELEMENTAL RATIOS COMPARISON TO THE WPB-MORB AND ARCB-NMORB AFTER (CONDIE, 1989).

Major-Trace elemental ratios	WPB-MORB	ARCB-NMORB	Walash Peperite
Nb/La	>1	≤1	0.47-0.77
Hf/Ta	<5	≥5	12-22
Ti/Y	≥350	<350	240-281
Ti/V	>30	≤30	27-31
TiO <sub>2</sub> %	>1.25	≤1.25	1.04-1.2
Ta(ppm)	>0.7	≤0.7	0.1-0.2
Nb(ppm)	>12	≤12	2.4-3.7

WPB: Within Plate Basalt; MORB: Mid Oceanic Ridge Basalt; NMORB: Normal Mid Oceanic Ridge Basalt; ARCB: Arc Basalt.

The peperite-bearing successions in WVSg have varying thicknesses at several places across the research area, which includes the PF1 and PF2 study areas (Figs. 3-5). Their deposits are exposed in a discontinuous fashion across the entirety of the Walash volcanic arc basin (Fig. 2b), including both its eastern and western sides of

TABLE V

WALASH PEPERITE MAJOR-TRACE ELEMENTAL RATIOS COMPARISON TO THE NMORB AND ARCB AFTER (CONDIE, 1989).

Trace elemental ratios	NMORB	ARCB	Walash Peperite
Th/Yb	≤0.1	>0.1	0.13-0.2
Th/Nb	≤0.07	>0.07	0.11-0.2
Nb/La	>0.8	≤0.8	0.47-0.77
Hf/Th	≥8	<8	4.33-5.88

NMORB: Normal Mid Oceanic Ridge Basalt; ARCB: Arc Basalt.

the WVSg. Peperite-bearing successions are often made up of basaltic lava flows that have intruded carbonates and volcanoclastics, as their primary constituents. A deep carbonate sequence has been found in both the eastern and western sides of the PF (Figs. 3-5). This succession displays a lateral lithological change as it moves right and left flanks. In general, both PF 1 and 2 are composed of basaltic lava flows that are interlayered with deep marine-rich planktonic rocks that consist of micritic carbonate horizons.



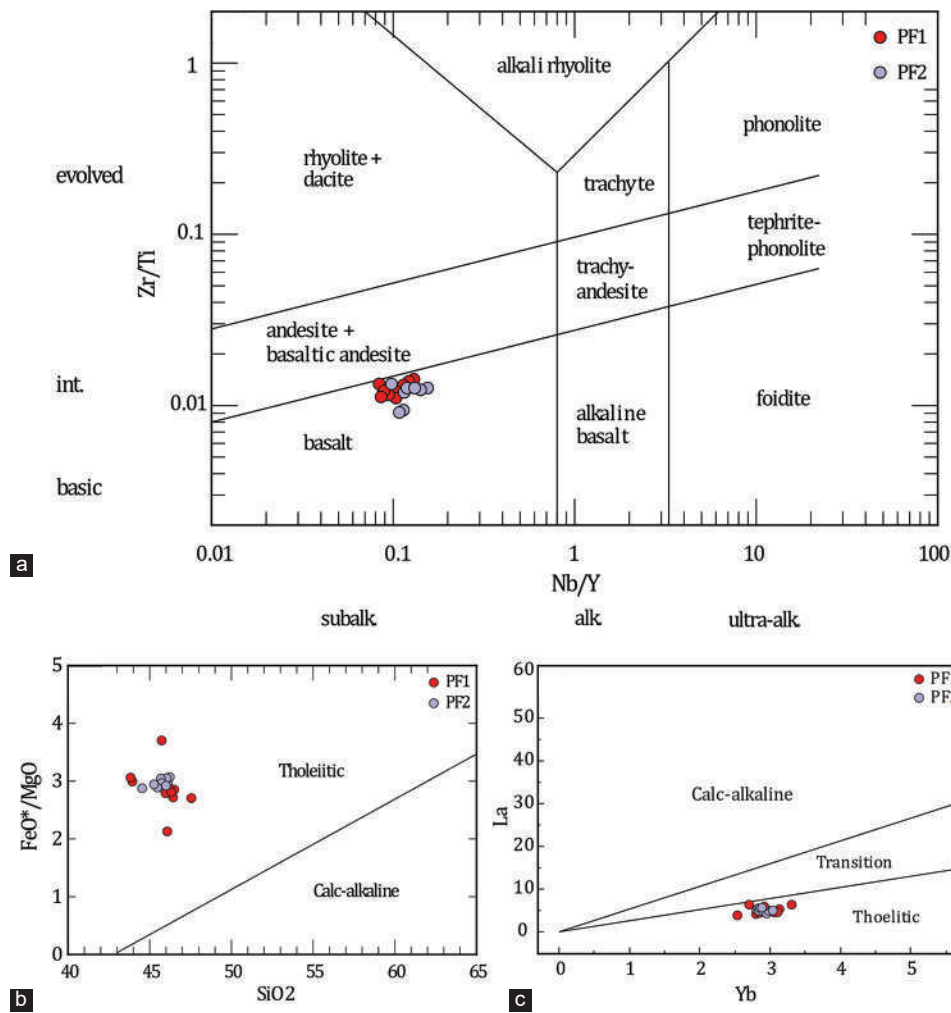


Fig. 12. Rock classification and characteristics of volcanic rocks within PF1 and PF2 (a)  $Zr/TiO_2$  versus  $Nb/Y$  of (Pearce, 1996) after (Winchester and Floyd, 1977). (b)  $SiO_2$  versus  $(FeO^*/MgO)$  diagram of (Miyashiro, 1974) and (c)  $La$  versus  $Yb$  after (Ross and Bédard, 2009), showing the tholeiitic nature of the PF1 and PF2 volcanic rocks.

Two types of peperite occur in the Mawat-Shasho area, these include (a) PF1 characterized by blocky peperite related to the rapid submarine eruption of basaltic rocks into wet, unconsolidated deep-marine sediments (host micritic limestone) (Figs. 3, 6, and 9). (b) PF2 is characterized by fluidal peperite associated with the more evolved palagonitized basaltic lava flows into wet, unconsolidated deep-marine sediment (Figs. 5, 7 and 9e, f). Base lithology extension of the Walash arc and PF in the Mawat area was compared with the similar peperites and their extended range from minor occurrences adjacent to igneous extrusions up to deposits with quantities of several  $km^3$  within Mull lava field of NW Scotland by (Brown and Bell, 2007). In this way, the Walash arc base distance may extend to several kilometers based on petrological field evidence.

Accurate and effective volcanic age estimates necessitate a meticulous differentiation between primary and secondary volcanic deposits and volcanosedimentary rocks. Primary volcanoclastic deposits and volcano-sedimentary rocks are non-reworked deposits formed directly from volcanic eruptions (i.e., pyroclastic, autoclastic, hyaloclastic, and peperitic)

(White and Houghton, 2006; Sohn and Sohn, 2019). They are distinguished from other volcanoclastic deposits that are not directly related to eruptions but are reworked, modified, and redeposited by surface or gravitational processes (e.g., tides, waves, currents, or non-eruptive gravitational density flows in the oceanic realm) and are classified as epiclastic or secondary (White and Houghton, 2006).

Contemporaneous and non-reworked beds of peperitic rocks have been found throughout the whole section of Mawat-Shasho. According to (Nayudu, 1971), it is conclusive that fossils can be discovered in primary volcanoclastic piles, even in solid basalts. When there is a good record of foraminiferal assemblages with chronostratigraphic value, such as planktonic forams, biochronostratigraphic methods can be used to date volcanic events. Dating peperitic rocks with the presence of short-geologic-range planktonic Foram species, including specifically *Morozovella praeangulata* and *Morozovella angulata* (ranging only 1–2 Ma), is vital and helpful to understand the contemporaneous idea behind the eruption of submarine volcanism into wet, unconsolidated sediments throughout the Walash volcanic area. In this

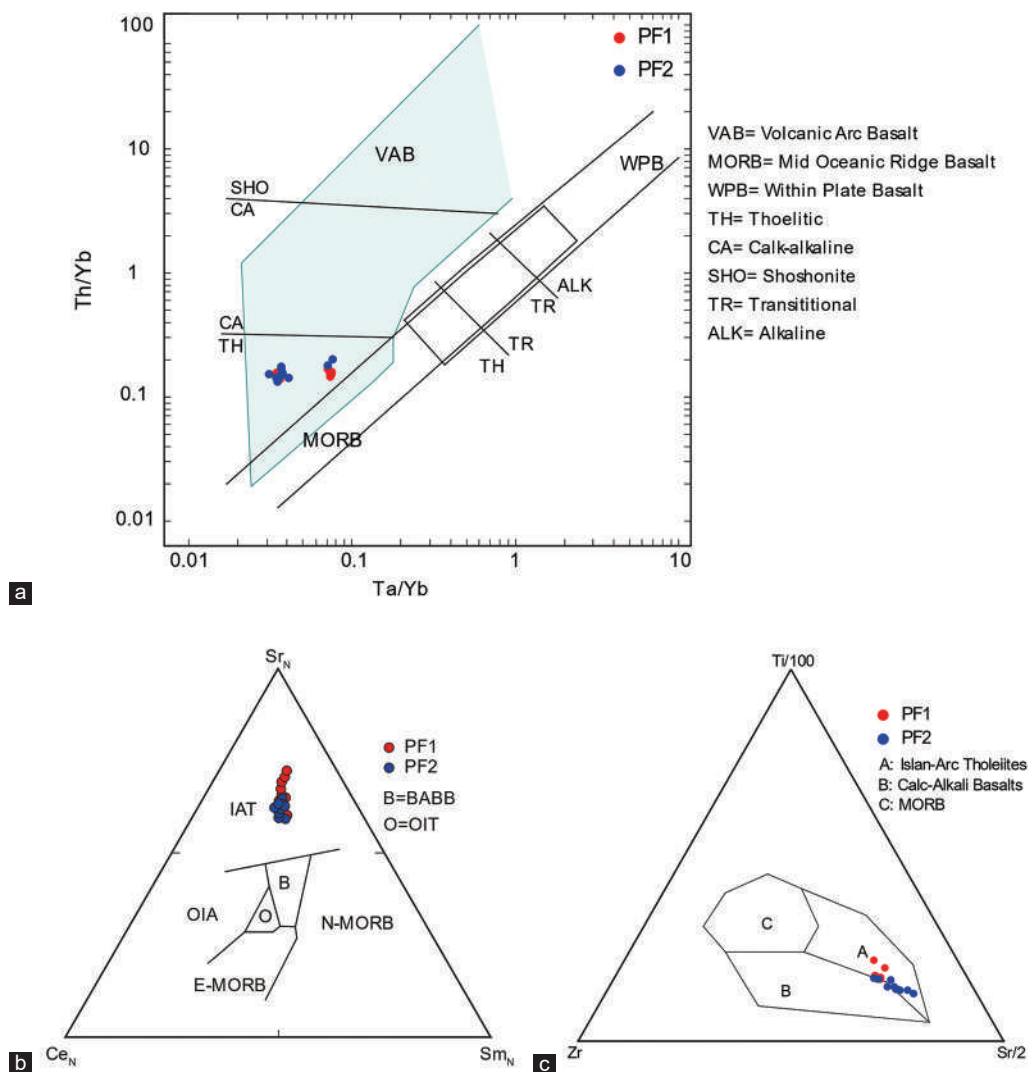


Fig. 13. Tectonic diagrams for PF1 and PF2 Basaltic rocks. (a) Th/Yb versus Ta/Yb after (Pearce, 1982). (b) Ce<sub>N</sub>-Sr<sub>N</sub>-Sm<sub>N</sub> ternary after (Ikeda, 1990) and (c) Zr-Ti-Sr ternary after (Pearce and Cann, 1973).

particular instance, we used planktonic fauna to date volcanic rocks (contemporaneous with the age of deep-marine micritic carbonate rocks) within PF due to the absence of normative zircon and numerous problems within hydrothermally altered volcanic rocks, including grain size and freshness of phenocrysts; whole rock low K content and low K/Ca content; common replacement of crystalline plagioclase and other K-rich phenocrysts. The aforementioned obstacles represent particular difficulties for dating these volcanic rocks using U-Pb and Ar/Ar dating geochronological methods, respectively.

The results indicate that the presence of basaltic rocks, peperites, host micritic carbonate rocks, and shales with some volcanoclastic rocks as well as mélangé of mentioned rocks are robust to the presence of a complex primitive volcanic arc in the studied area. Furthermore, because volcanic arcs are large and geologically comprise heterogeneous structures (Stern, 2010), different perspectives of geoscience have been used in this research, such as field investigations, geochemistry, sedimentology, and paleontology. All mentioned tools together will explain the contemporaneity of

the basaltic rocks with deep marine sediments in both PF1 and PF2 and based on a precise paleontological study the peperitic rocks dated to the Middle Paleocene, that is, 60 Ma. This age represents the beginning of submarine eruptions in the initial volcanic arc stage within WVSg. These peperites and initial arc volcanic rocks were formed by the subduction of the Arabic Plate beneath the Iranian Plate (Fig. 16).

#### B. Geochemical Signatures and Tectonic Implications

The peperite concept has changed greatly since its original application, and how and where the peperite form is still a lively topic of debate. The authors precisely prepared volcanic rock samples for geochemical analysis by removing all altered and weathered parts, thus the chemical index of alteration (CIA) value is consistent with fresh basaltic rocks after Nesbitt and Young (1982) and ranging between (33.33–40.0)%. Besides, a minor amount of nepheline in these basaltic rocks may refer to the assimilation of the basic magma with carbonate rocks (Iacono Marziano, et al., 2008), and this will allow the magma to be rich in Na and nepheline

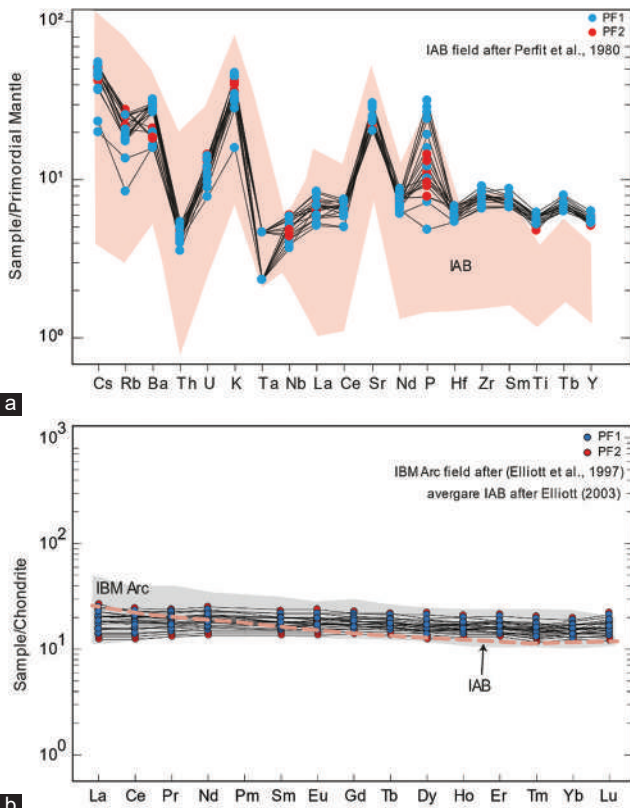


Fig. 14. (a) Multi-element spider diagram normalized to the primordial mantle (normalizing values are from [Wood, et al., 1979] and IAB field after [Perfit, et al., 1980]). (b) Chondrite-normalized REE patterns (normalizing values are from [Sun and McDonough, 1989]) for the basaltic rocks within PF1 and PF2 (average composition of IAB is from [Elliott, 2003], IBM Arc: Izu – Bonin – Mariana arc basalts field after [Elliott, et al., 1997]).

as a minor phase may found in the peperitic rocks despite their tholeiitic nature.

Considering altered arc volcanic rocks, the diagram (Zr/TiO<sub>2</sub>-Nb/Y) can be used to replace the total alkali-Silica diagram (Winchester and Floyd, 1977; Pearce, 1996; Hastie, et al., 2007). It is not reasonable to use (Winchester and Floyd, 1977) classification, because it is not robust in classifying altered volcanic rocks (Hastie, et al., 2007). Thus, to determine the classification of mafic volcanic rocks from PF1 and PF2, the data were plotted on a Zr/TiO<sub>2</sub> versus Nb/Y diagram, as shown in Figure 12a. All samples fell within the basaltic field and exhibited sub-alkaline characteristics. Furthermore, their tholeiitic nature is obvious from petrochemical discrimination diagrams of SiO<sub>2</sub> versus (FeO<sub>T</sub>/MgO) after Miyashiro (1974) and La versus Yb after Ross and Bédard (2009) (Fig. 12b and c). Basaltic rocks within both PF are characterized by the following elemental ratios: low Nb/Y (0.10-0.15), La/Yb (1.4–2.3), and Nb/La (0.61–0.77); adequately high Zr/Nb (23–30), Hf/Ta (12–22) and Th/Ta (2–5); relatively low contents of major elements like TiO<sub>2</sub> and P<sub>2</sub>O<sub>5</sub> (Tables II and III) in contrast to the high ratios of FeO<sub>T</sub>/MgO, which are diagnostic features of subalkaline (tholeiitic) rocks in primitive arc basalts (Miyashiro, 1974; Winchester and Floyd, 1977; Condie, 1989; Ross and Bédard, 2009).

Using Condie (1989) basaltic trace elemental ratios, a comparison is made between the Walsh peperite and the various types of basalt, such as Within Plate Basalt-Normal Mid Oceanic Ridge Basalt (WPB-NMORB) and Arc Basalt-Normal Mid Oceanic Ridge Basalt (ARCB-NMORB). The trace elemental ratios of Walsh peperite are in agreement with those of ARCB and NMORB (Table IV). It should be noted that the ARCB and NMORB are difficult to

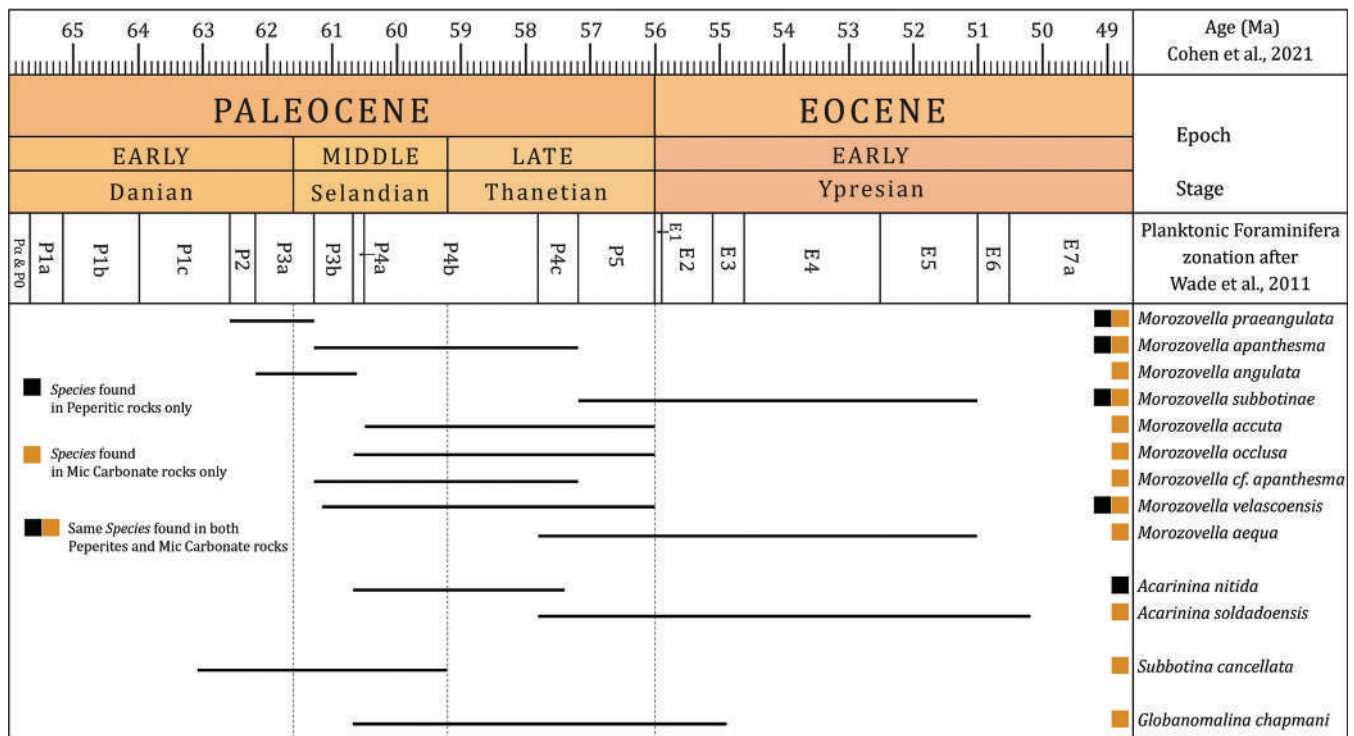


Fig. 15. Biozonation study for Paleocene peperitic rocks (PF1) within WVSg. Ages after (Cohen, et al., 2021)

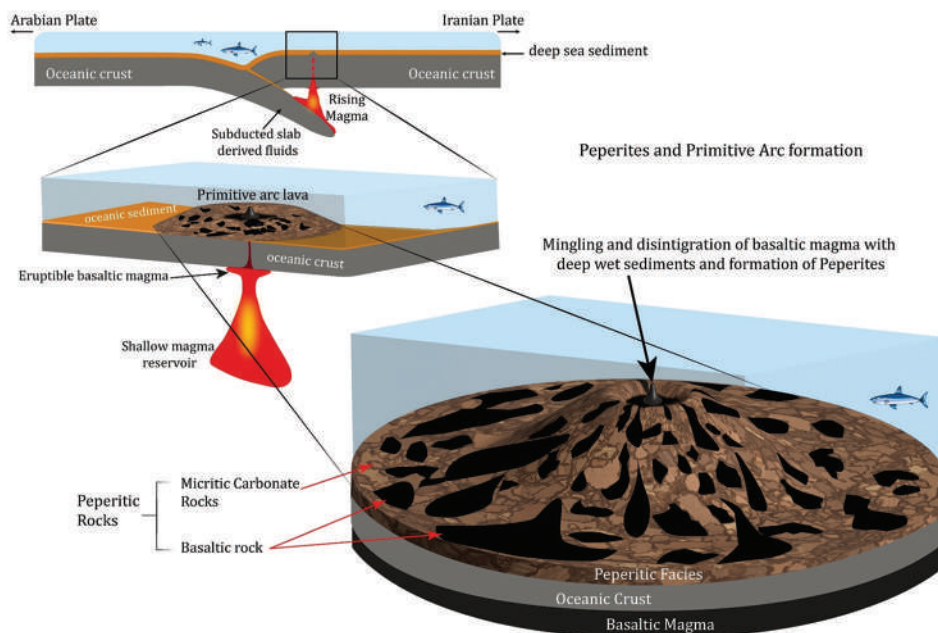


Fig. 16. Generalized tectonic model (not to scale) to illustrate the formation of peperitic facies within the Walsh volcano-sedimentary group in the Mawat area in response to the subduction of the Arabian Plate beneath the Iranian Plate in Paleocene (60 Ma).

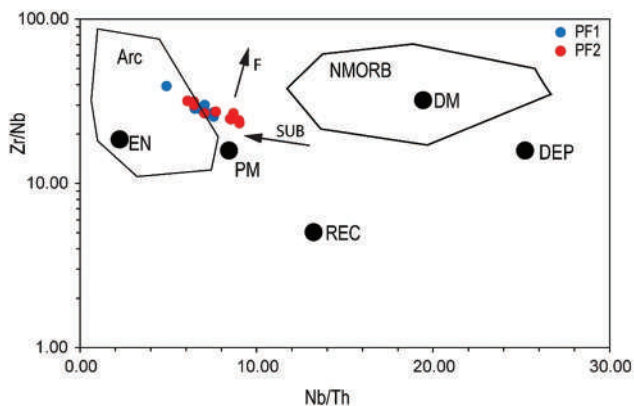


Fig. 17. Nb/Th vs. Zr/Nb elemental ratios for PF1 and PF2 volcanic rock sample, showing samples plotted within the Arc field and their consistent trends with the partial melting subduction-derived fluid trends after Condie (2005). Arrows indicate the effects of batch melting (F) and Subduction-derived fluids. EN: Enriched component; PM: Primitive mantle; DM: Shallow depleted mantle; DEP: Deep depleted mantle; REC: Recycled component; Arc: Arc-related basalts; NMORB: Normal ocean ridge basalt.

differentiate in general; however, using several different ratios of trace elements, such as Th/Yb, Th/Nb, Nb/La, and Hf/Th (Tables IV and V), it is possible to overcome this issue (Condie, 1989).

Using trace elemental ratios, such as Nb/Th and Zr/Nb, the arc basaltic source for Walsh peperites can be distinguished from the NMORB basaltic source (Fig. 17). According to (Condie, 2005), arc basalts may have similar Zr/Nb ratios, but they are quite different in Nb/Th ratios. Thus, arc basaltic sources for Walsh peperite on an Nb/Th–Zr/Nb plot seem robust. Furthermore, the headed arrows are quite consistent

with the Walsh volcanic data, which indicate subduction-related derived fluid effects (Condie, 2005).

Based on the primitive mantle-normalized multielement spider diagram (Fig. 14a), the basaltic rocks in both PF1 and PF2 show selective enrichment in LILEs (e.g., Rb, Ba, and K) and depletion in HFSEs (e.g., Ta, Nb, Nd, and Ti) indicate an arc volcanic feature (Saunders and Tarney, 1979) and compared with the field of IAB after (Perfit, et al., 1980). While on the REE chondrite-normalized diagram (Fig. 14b), these basaltic rocks are characterized by slight enrichment and with flat REE patterns which is consistent with the same normalized ratio of (La/Yb)  $\approx 1$  for IAB (Perfit, et al., 1980; Philpotts and Ague, 2022). As well as, the absence of the negative Europium (Eu) anomaly suggests that the plagioclase role is insignificant during magma evolution in the area (Slovenec, Lugovic and Vlahovic, 2010; Philpotts and Ague, 2022). Furthermore, in Figure 14a and b, these basaltic rocks were compared and consistent with the average composition of IAB after (Elliott, 2003) and Izu-Bonin-Mariana arc basalts (IBM Arc) field after (Elliott, et al., 1997).

However, PF1 and PF2 basaltic rocks have a geochemical affinity to normal island arcs. In the Sr/Y versus Y diagram (Fig. 18a), basaltic rocks were plotted in the normal island arc magma field suggesting a high concentration of Y with low concentration ratios of Sr/Y. This low ratio of Sr/Y suggests partial melting or fractionation at lower pressure ( $\ll 1$  GPa.), in addition, the absence of garnet  $\pm$  amphibole will cause Y to behave incompatibly, and simultaneously stable plagioclase absorbs Sr as a result, a melt with low Sr/Y will form (Lieu and Stern, 2019). Based on these incompatible trace ratios and tectonic models of Lieu and Stern (2019), we infer that basaltic rocks in the PF1 and PF2 were generated by the partial melting of subducted slabs deep within 30 km and accompanying derived fluids above the subducted slab.

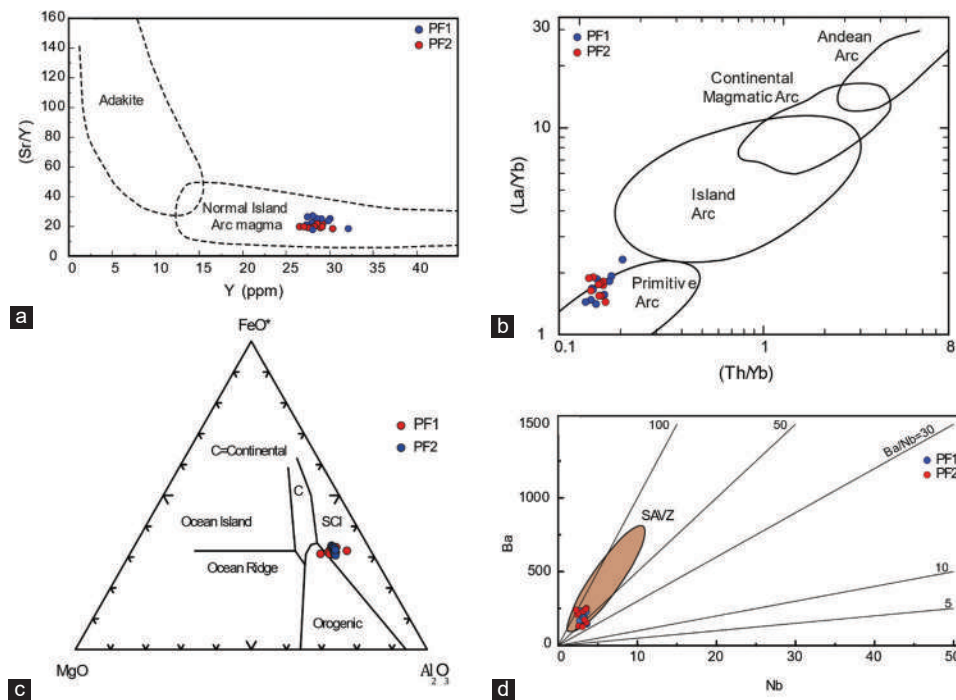


Fig. 18. (a) Sr/Y versus Y diagram showing Island arc magmatic field for the basaltic rocks in PF1 and PF2 after Rogers and Hawkesworth (1989), adakite field is after Defant and Drummond (1990). (b) La/Yb versus Th/Yb tectonic discrimination diagram showing primitive arc setting for basaltic rock samples from the PF1 and PF2 after Condie (1989). (c) FeO-MgO-  $Al_2O_3$  showing Spreading center Island arc (SCI) tectonic setting for PF1 and PF2 basaltic rocks after Pearce, *et al.*, 1977. (d) Ba versus Nb diagram for arc front volcanic rocks, (SAVZ) field represents south Andes volcanic rocks after Aragón, *et al.* (2013).

Furthermore, positive Sr, Ba, and K and negative Nb and Ta anomalies indicate magma generated at the subduction zone (Pearce, 1983). Peperites uniquely suggest a tectonic signature for the submarine eruptions into host sediments. However, their identification indicates contemporaneous magmatism and sedimentation. It helps to reconstruct facies architecture, paleoenvironmental conditions, and tectonic settings. In this circumstance and using available data, the PF1 and PF2 volcanic rocks yielded a primitive arc setting. As well as, their formation in the spreading center of the Island basalts suggest their eruption might happen at the initial arc stage of the volcanic arcs in the arc fronts (Fig. 18b and d), respectively. In addition, the Ba vs. Nb diagram was utilized to confirm the depiction of arc fronts in these PF, and their arc front signatures were compared to those of the South Andes arc front volcanic rocks after (Aragón, *et al.*, 2013) (Fig. 18d). Thus, all geochemical indicators suggest that the PF1 and PF2 should be considered as a part of the subduction zone arc front tectonic settings. Consequently, the authors proposed a tectonic model and two scenarios to illustrate the formation of peperitic rocks in the arc fronts and indicate the submarine eruptions into wet host sediments (Figs. 6, 7, 16). The details of the proposed scenarios for the formation of peperites within WVSg are illustrated in Figures 6 and 7. The first scenario deals with the explosive eruptions of submarine basaltic pillow lava into wet, unconsolidated sediments within the base of the Walsh arc (Fig. 6). While the second scenario is represented by the submarine extrusions of massive coherent basalt and closely packed basaltic pillow lava into

wet, unconsolidated deep marine carbonate sediments within the base of the Walsh arc (Fig. 7).

## VII. CONCLUSIONS

Peperitic rocks in WVSg are classified into blocky and globular (fluidal) peperitic rocks based on field investigations and textural evidences. In contrast to previous interpretations of the Walsh stratigraphy base unit as volcanoclastics, detail mapping and petrological study during this work have revealed a coherent stratigraphy of volcano-sedimentary made up of intrusions of basaltic pillow lavas into micritic carbonate sequence. The newly mapped unit nominated as PF, outcropped in two locations consequently as PF1 and PF2, are texturally classified as blocky and fluidal peperitic rocks, respectively. Volcanic intrusions in the PF classified as basaltic rocks showing tholeiitic magma series based on geochemical signature and positive Sr, Ba, and K and negative Nb and Ta anomalies indicate magma generated at the subduction zone. Dating of the host micritic carbonates and sedimentary clasts in contact with the basaltic rocks within the PF, using planktonic foraminifera, shows that the submarine eruptions occurred during the middle of Paleocene time around 60 Ma and might continue to the 43 Ma which is compatible with the age determined using Ar-Ar geochronology. Geochemical data suggest these basaltic rocks formed as a result of partial melting of subducting slab under the influence of slab-derived fluids at an approximate depth of 30 km and their eruption into wet sediment also

suggests a spreading center of arc front at the early stage of the Walsh volcanic arcs.

In summary, for the first time, we have reported the simultaneous occurrence of basaltic pillow lava and deep-marine micritic carbonate rocks using comprehensive and precise field investigations, petrological, geochemical, and biostratigraphical studies. The identified peperites present within the WVSg indicate simultaneous volcanism and sedimentation and that the Neo-Tethys was still open throughout the Paleocene (~60 Ma).

#### ACKNOWLEDGMENTS

The authors are grateful to Dr. Yadollah Ezampanah from Bu-Ali Sina University (Hamadan, Iran) and Professor Dr. Khalid M. I. Sharbazheri from Sulaimani University (Sulaimani, Kurdistan Region-Iraq) for their help in recognizing and identifying the planktonic species.

#### REFERENCES

- Agard, P., Omrani, J., Jolivet, L., Whitechurch, H., Vrielynck, B., Spakman, W., Monié, P., Meyer, B., and Wortel, R., 2011. Zagros orogeny: A subduction-dominated process. *Geological Magazine*, 148, pp.692-725.
- Alavi, M., 2004. Regional stratigraphy of the Zagros fold-thrust belt of Iran and its proforeland evolution. *American Journal of Science*, 304, pp.1-20.
- Al-Banna, N.Y., and Al-Mutwali, M.M., 2008. Microfacies and age determination of the sedimentary sequences within Walsh volcano-sedimentary group, Mawat complex, Northeast Iraq. *Tikrit Journal of Pure Science*, 13, pp.46-52.
- Al-Mehaidi, H., 1974. *Report on Geological Investigation of Mawat-Chowarta Area*, NE Iraq.
- Ali, S.A., and Aswad, K.J., 2013. SHRIMP U-Pb dating of zircon inheritance in Walsh arcvolcanic rocks (paleogene age), Zagros suture zone, NE Iraq: New insights into crustal contributions to trachytic andesite generation. *Iraqi National Journal of Earth Sciences*, 13, pp.45-58.
- Ali, S.A., 2012. *Geochemistry and Geochronology of Tethyan-arc Related Igneous rocks, NE Iraq*, Doctor of Philosophy Thesis, School of Earth and Environmental Sciences. University of Wollongong. Available from: <https://ro.uow.edu.au/theses/3478>
- Ali, S.A., Buckman, S., Aswad, K.J., Jones, B.G., Ismail, S.A., and Nutman, A.P., 2013. The tectonic evolution of a Neo-Tethyan (eocene-oligocene) island-arc (Walsh and Naopurdan groups) in the Kurdistan region of the Northeast Iraqi Zagros suture zone. *Island Arc*, 22, pp.104-125.
- Ali, S.A., Sleabi, R.S., Talabani, M.J.A., and Jones, B.G., 2017. Provenance of the Walsh-Naopurdan back-arc-arc clastic sequences in the Iraqi Zagros Suture Zone. *Journal of African Earth Sciences*, 125, pp.73-87.
- Al-Mehaidi, H., 1974. *Report on Geological Investigation of Mawat-Chowarta area, NE Iraq*.
- Al-Qayim, B., Ghafor, I., and Jaff, R., 2012. Contribution to the stratigraphy of the Walsh Group, Sulaimani area, Kurdistan, Iraq. *Arabian Journal of Geosciences*, 7, pp.181-192.
- Al-Qayim, B., Ghafor, I., and Jaff, R., 2014. Contribution to the stratigraphy of the Walsh Group, Sulaimani area, Kurdistan, Iraq. *Arabian Journal of Geosciences*, 7, pp.181-192.
- Aragón, E., Pinotti, L., Fernando, D., Castro, A., Rabbia, O., Coniglio, J., Demartis, M., Hernando, I., Cavarozzi, C.E., and Aguilera, Y.E., 2013. The Farallon-Aluk ridge collision with South America: Implications for the geochemical changes of slab window magmas from fore-to back-arc. *Geoscience Frontiers*, 4, pp.377-388.
- Asvesta, A., and Dimitriadis, S., 2013. Magma-sediment interaction during the emplacement of syn-sedimentary silicic and mafic intrusions and lavas into and onto Triassic strata (Circum-Rhodope Belt, Northern Greece). *Geologica Carpathica*, 64, pp.181-194.
- Aswad, K.J., Aziz, N.R., and Koyi, H.A., 2011. Cr-spinel compositions in serpentinites and their implications for the petroectonic history of the Zagros Suture Zone, Kurdistan Region, Iraq. *Geological Magazine*, 148(5-6), pp.802-818.
- Aswad, K.J.A., Al-Samman, A.H.M., Aziz, N.R.H., and Koyi, A.M.A., 2013. The geochronology and petrogenesis of Walsh volcanic rocks, Mawat nappes: Constraints on the evolution of the Northwestern Zagros suture zone, Kurdistan Region, Iraq. *Arabian Journal of Geosciences*, 7, pp.1403-1432.
- Austermann, J., and Iaffaldano, G., 2013. The role of the Zagros orogeny in slowing down Arabia-Eurasia convergence since ~5 Ma. *Tectonics*, 32, pp.351-363.
- Aziz, N.R.H., 1986. *Petrochemistry, Petrogenesis and Tectonic Setting of Spilitic Rocks of Walsh Volcanic Sedimentary Group in Qala Diza Area, NE Iraq*. MSc Thesis, Mosul University, Iraq, p.164. (in Arabic).
- Aziz, N.R., Aswad, K.J., and Koyi, H.A., 2011. Contrasting settings of serpentinite bodies in the northwestern Zagros Suture Zone, Kurdistan Region, Iraq. *Geological Magazine*, 148(5-6), pp.819-837.
- Bann, G.R., Jones, B.G., and Graham, I.T., 2022. A mid-Permian mafic intrusion into wet marine sediments of the lower Shoalhaven Group and its significance in the volcanic history of the Southern Sydney Basin. *Australian Journal of Earth Sciences*, 69, pp.1-17.
- Barnes, S.J., and Arndt, N.T., 2019. Distribution and geochemistry of komatiites and basalts through the archaic. In: *Earth's Oldest Rocks*. Elsevier, Amsterdam.
- Barnes, S.J., and Van Kranendonk, M.J., 2014. Archaean andesites in the East Yilgarn craton, Australia: Products of plume-crust interaction? *Lithosphere*, 6, pp.80-92.
- Beresford, S., Cas, R., Lahaye, Y., and Jane, M., 2002. Facies architecture of an Archaean komatiite-hosted Ni-sulphide ore deposit, Victor, Kambalda, Western Australia: Implications for komatiite lava emplacement. *Journal of Volcanology and Geothermal Research*, 118, pp.57-75.
- Berggren, W.A., Pearson, P.N., Huber, B., and Wade, B.S., 2006. *Taxonomy, Biostratigraphy and Phylogeny of Eocene Acarina*. Cushman Foundation for Foraminiferal Research, New York.
- Biske, N., Romashkin, A., and Rychanchik, D., 2004. Proterozoic peperite-structures of Lebestchina. In: *Geology and Mineral Deposits, Proceedings of the Institute of Geology*. Vol. 7. Karelian Research Centre of RAS, Petrozavodsk, pp.193-199.
- Blow, W.H., 1979. *The Cainozoic Globigerinida*. Atlas. Brill Archive, Leiden.
- Bolton, C., 1958. The Geology of the Ranya Area. Manuscript Report No. 271. GEOSURV, Baghdad.
- Boudagher-Fadel, M.K., 2015. *Biostratigraphic and Geological Significance of Planktonic Foraminifera*. Newnes, Oxford.
- Boulter, C., 1993. High-level peperitic sills at Rio Tinto, Spain: Implications for stratigraphy and mineralization. *Transactions of the Institution of Mining and Metallurgy. Section B. Applied Earth Science*, 102, pp.30-38.
- Branney, M.J., Bonnicksen, B., Andrews, G.D.M., Ellis, B., Barry, T.L., and Mccurry, M., 2008. 'Snake River (SR)-type' volcanism at the yellowstone hotspot track: Distinctive products from unusual, high-temperature silicic super-eruptions. *Bulletin of Volcanology*, 70, pp.293-314.
- Bronnimann, P., 1952. Trinidad paleocene and lower eocene globigerinidae. *Bulletins of American Paleontology*, 34, p.134.
- Brooks, E.R., 1995. Paleozoic fluidization, folding, and peperite formation, Northern Sierra Nevada, California. *Canadian Journal of Earth Sciences*, 32, pp.314-324.

- Brown, D.J., and Bell, B.R., 2007. How do you grade peperites? *Journal of Volcanology and Geothermal Research*, 159, pp.409-420.
- Busby-Spera, C.J., and White, J.D., 1987. Variation in peperite textures associated with differing host-sediment properties. *Bulletin of Volcanology*, 49, pp.765-776.
- Busby, C.J., Hagan, J.C., Putirka, K., Pluhar, C.J., Gans, P.B., Wagner, D.L., Rood, D., Deoreo, S.B., and Skilling, I., 2008. *The Ancestral Cascades Arc: Cenozoic Evolution of the Central Sierra Nevada (California) and the Birth of the New Plate Boundary*. The Geological Society of America, Boulder.
- Cas, R.A.F., Edgar, C., Allen, R.L., Bull, S., Clifford, B.A., Giordano, G., and Wright, J.V., 2001. Influence of magmatism and tectonics on sedimentation in an extensional lake basin: The upper devonian bunga beds, boyd volcanic complex, South-Eastern Australia. *Volcaniclastic Sedimentation in Lacustrine Settings*. Wiley-Blackwell, Hoboken, pp.81-108.
- Chen, S., Guo, Z.J., Pe-Piper, G., and Zhu, B.B., 2013. Late paleozoic peperites in West Junggar, China, and how they constrain regional tectonic and palaeoenvironmental settings. *Gondwana Research*, 23, pp.666-681.
- Chen, S., Guo, Z., Qi, J., Zhang, Y., Pe-Piper, G., and Piper, D.J.W., 2016. Early permian volcano-sedimentary successions, Beishan, NW China: Peperites demonstrate an evolving rift basin. *Journal of Volcanology and Geothermal Research*, 309, pp.31-44.
- Cohen, K.M., Finney, S.C., Gibbard, P.L., and Fan, J., 2021. The ICS international chronostratigraphic chart. *Episodes*, 36, pp.199-204.
- Condie, K.C., 1989. Geochemical changes in basalts and andesites across the Archean-Proterozoic boundary: Identification and significance. *Lithos*, 23, pp.1-18.
- Condie, K.C., 2005. High field strength element ratios in Archean basalts: A window to evolving sources of mantle plumes? *Lithos*, 79, pp.491-504.
- Constenius, K.N., Mcgimsey, R.G., Valencia, V., Ibanex-Mejia, M., and Domanik, K.J., 2017. *Peperite in the Purcell Lava and a Revised Age of the Upper Proterozoic Belt-Purcell Supergroup*. Geological Society of America Abstracts with Programs, Boulder, pp.1-7.
- Cushman, J.A., 1925. Some new foraminifera from the Velasco Shale of Mexico. *Contributions from the Cushman Laboratory for Foraminiferal Research*, 1, pp.18-23.
- Cushman, J.A., 1942. Eocene, midway, foraminifera from Soldado Rock, Trinidad. *Contributions from the Cushman Laboratory for Foraminiferal Research*, 18, pp.1-20.
- Dadd, K.A., and Van Wagoner, N.A., 2002. Magma composition and viscosity as controls on peperite texture: An example from Passamaquoddy Bay, Southeastern Canada. *Journal of Volcanology and Geothermal Research*, 114, pp.63-80.
- Defant, M.J., and Drummond, M.S., 1990. Derivation of some modern arc magmas by melting of young subducted lithosphere. *Nature*, 347, pp.662-665.
- Doyle, M.G., 2000. Clast shape and textural associations in peperite as a guide to hydromagmatic interactions: Upper permian basaltic and basaltic andesite examples from Kiama, Australia. *Australian Journal of Earth Sciences*, 47, pp.167-177.
- El Desoky, H.M., and Shahin, T.M., 2020. Characteristics of lava-sediments interactions during emplacement of mid-tertiary volcanism, Northeastern Desert, Egypt: Field geology and geochemistry approach. *Arabian Journal of Geosciences*, 13, p.328.
- Elias, Z., Sissakian, V.K., and Al-Ansari, N., 2018. New tectonic activity within Zagros-Taurus belt: A case study from North Iraq using region shuttle radar topography mission (SRTM). *Journal of Earth Sciences and Geotechnical Engineering*, 8, pp.51-63.
- Elliott, T., 2003. Tracers of the slab. In: *Geophysical Monograph-American Geophysical Union*. Vol. 138. American Geophysical Union, Washington, D.C., pp.23-46.
- Elliott, T., Plank, T., Zindler, A., White, W., and Bourdon, B., 1997. Element transport from slab to volcanic front at the Mariana arc. *Journal of Geophysical Research: Solid Earth*, 102, pp.14991-15019.
- English, J.M., Lunn, G.A., Ferreira, L., and Yacu, G., 2015. Geologic evolution of the Iraqi Zagros, and its influence on the distribution of hydrocarbons in the Kurdistan Region. *AAPG Bulletin*, 99, pp.231-272.
- Erkül, F., Helvacı, C., and Sözbilir, H., 2006. Olivine basalt and trachyandesite peperites formed at the subsurface/surface interface of a semi-arid lake: An example from the early miocene bigadiç basin, Western Turkey. *Journal of Volcanology and Geothermal Research*, 149, pp.240-262.
- Famelli, N., Millett, J.M., Hole, M.J., Lima, E.F., de O.Carmo, I., Jerram, D.A., Jolley, D.W., Pugsley, J.H., and Howell, J.A., 2021. Characterizing the nature and importance of lava-sediment interactions with the aid of field outcrop analogues. *Journal of South American Earth Sciences*, 108, p.103108.
- Fontboté, L., 2019. Volcanogenic Zn-Pb±Cu massive sulfide deposits in the upper cretaceous plutono-volcanic arc in central Peru. In: *Proceedings of Proexplo 2019*. Extended Abstracts, Peru.
- Goto, Y., and McPhie, J., 1996. A Miocene basanite peperitic dyke at Stanley, Northwestern Tasmania, Australia. *Journal of Volcanology and Geothermal Research*, 74, pp.111-120.
- Haller, M., and Németh, K., 2009. Cenozoic diatremes in Chubut, Northern Patagonia, Argentina. In: *3ICM International Maar Conference, Malargüe, Argentina, Extended Abstract*.
- Hanson, R.E., and Hargrove, U.S., 1999. Processes of magma/wet sediment interaction in a large-scale Jurassic andesitic peperite complex, northern Sierra Nevada, California. *Bulletin of Volcanology*, 60, pp.610-626.
- Hanson, R.E., and Wilson, T.J., 1993. Large-scale rhyolite peperites (Jurassic, Southern Chile). *Journal of Volcanology and Geothermal Research*, 54, pp.247-264.
- Hanson, R.E., 1991. Quenching and hydroclastic disruption of andesitic to rhyolitic intrusions in a submarine Island-arc sequence, Northern Sierra Nevada, California. *Geological Society of America Bulletin*, 103, pp.804-816.
- Hastie, A.R., Kerr, A.C., Pearce, J.A., and Mitchell, S.F., 2007. Classification of altered volcanic Island arc rocks using immobile trace elements: Development of the Th-Co discrimination diagram. *Journal of Petrology*, 48, pp.2341-2357.
- Hibbard, M.J., 1995. *Petrography to Petrogenesis*. Macmillan College, London.
- Humphris, S.E., and Thompson, G., 1978. Trace element mobility during hydrothermal alteration of oceanic basalts. *Geochimica et Cosmochimica Acta*, 42, pp.127-136.
- Iacono Marziano, G., Gaillard, F., and Pichavant, M., 2008. Limestone assimilation by basaltic magmas: An experimental re-assessment and application to Italian volcanoes. *Contributions to Mineralogy and Petrology*, 155, pp.719-738.
- Ikeda, Y., 1990. CeN/SrN/SmN: A trace element discriminant for basaltic rocks from different tectonomagmatic environments. *Neues Jahrbuch für Mineralogie Monatshefte*, 4, pp.145-158.
- Jassim, S.Z., and Goff, J.C., 2006. *Geology of Iraq*. DOLIN, Sro, Distributed by Geological Society of London, Burlington House.
- Karim, K.H., and Hamza, B.J., 2021. Relation between Walsh Group and Kolosh Formation: A key to the stratigraphy of the Penjween area. In: *The 1st International Conference for Natural Resources Research Center, Geo Iraq I*, University of Tikrit, Tikrit City.
- Koshnaw, R.I., Horton, B.K., Stockli, D.F., Barber, D.E., Tamar-Agha, M.Y., and Kendall, J.J., 2017. Neogene shortening and exhumation of the Zagros fold-thrust belt and foreland basin in the Kurdistan region of northern Iraq. *Tectonophysics*, 694, pp.332-355.
- Koyi, A.M.A., 2009. Sr-Nd isotopic significance of Walsh volcanic rocks, Mawat area, NE Iraq. *Zanco Journal of Pure and Applied Sciences*, 21, pp.39-45.
- Krobicki M., 2018. The earliest Cretaceous (Berriasian) peperites in volcano-sedimentary units of the Ukrainian Carpathians. In: Šujan, M., Csibri, T., Kiss,

- P., and Rybár, S. (Eds.): *Environmental, Structural and Stratigraphical Evolution of the Western Carpathians, Abstract Book, 11<sup>th</sup> ESSEWECA Conference, 29th–30th November 2018*, Bratislava, Slovakia, pp.52–53.
- Krobicki, M., Feldman-Olszewska, A., Hnylko, O., and Iwańczuk, J., 2019. Peperites and other volcano-sedimentary deposits (lowermost Cretaceous, Berriasian) of the Ukrainian Carpathians. *Geologica Carpathica*, 70, p.146.
- Lieu, W.K., and Stern, R.J., 2019. The robustness of Sr/Y and La/Yb as proxies for crust thickness in modern arcs. *Geosphere*, 15, pp.621-641.
- Liu, S., Zhang, J., Li, Q., Zhang, L., Wang, W., and Yang, P., 2012. Geochemistry and U-Pb zircon ages of metamorphic volcanic rocks of the paleoproterozoic lüliang complex and constraints on the evolution of the trans-North China orogen, North China craton. *Precambrian Research*, 222, pp.173-190.
- Loeblich, A.R., and Tappan, H.N., 1957. Planktonic foraminifera of paleocene and early eocene age from the. *Bulletin United States National Museum*, 215, pp.173-198.
- Martin, L.T., 1943. *Eocene Foraminifera from the Type Lodo Formation, Fresno County, California*, Stanford University Press, Redwood City.
- Martin, U., and Németh, K., 2007. Blocky versus fluidal peperite textures developed in volcanic conduits, vents and crater lakes of phreatomagmatic volcanoes in mio/pliocene volcanic fields of Western Hungary. *Journal of Volcanology and Geothermal Research*, 159, pp.164-178.
- Mawson, J.F., White, J., and Palin, J.M., 2020. Contemporaneously emplaced submarine volcanoclastic deposits and pillow lavas from multiple sources in the Island arc brook street Terrane, Southland, New Zealand. *New Zealand Journal of Geology and Geophysics*, 63, pp.562-577.
- McLennan, S.M., 1989. Rare earth elements in sedimentary rocks: Influence of provenance and sedimentary process. *Reviews in Mineralogy*, 21, pp.169-200.
- Mcphe, J., 1993. The tennant creek porphyry revisited: A synsedimentary sill with peperite margins, early proterozoic, Northern Territory. *Australian Journal of Earth Sciences*, 40, pp.545-558.
- Memtimin, M., Zhang, Y., Furnes, H., Pe-Piper, G., Piper, D.J.W., and Guo, Z., 2020. Facies architecture of a subaqueous volcano-sedimentary succession on Bogda Mountains, NW China-evidence of extension in late carboniferous. *Geological Journal*, 55, pp.3097-3111.
- Mercurio, E.C., 2011. *Processes, Products and Depositional Environments of Ice-Confined Basaltic Fissure Eruptions: A Case Study of the Sveifuhals Volcanic Complex, SW Iceland*. University of Pittsburgh, Pittsburgh.
- Miyashiro, A., 1974. Volcanic rock series in island arcs and active continental margins. *American Journal of Science*, 274, pp.321-355.
- Mohammad, Y.O., Cornell, D.H., Qaradaghi, J.H., and Mohammad, F.O., 2014. Geochemistry and Ar-Ar muscovite ages of the Daraban Leucogranite, Mawat Ophiolite, Northeastern Iraq: Implications for Arabia-Eurasia continental collision. *Journal of Asian Earth Sciences*, 86, pp.151-165.
- Morozova, V.G., 1939. K stratigrafii verkhnego mela i paleogena Embenskoj oblasti po faune foraminifer [On the stratigraphy of the upper cretaceous and paleogene of Emba region according to the foraminiferal fauna]. *Biulleten Moskovskogo Obshchestva Ispytatelei Prirody, Otdel Geologicheskii*, 17, pp.59-86.
- Moulton, B.J.A., Fowler, A.D., Ayer, J.A., Berger, B.R., and Mercier-Langevin, P., 2011. Archean subaqueous high-silica rhyolite coulées: Examples from the Kidd-Munro assemblage in the abitibi subprovince. *Precambrian Research*, 189, pp.389-403.
- Mueller, W.U., Garde, A.A., and Stendal, H., 2000. Shallow-water, eruption-fed, mafic pyroclastic deposits along a paleoproterozoic coastline: Kangerluluk volcano-sedimentary sequence, southeast Greenland. *Precambrian Research*, 101, pp.163-192.
- Nayudu, Y.R., 1971. Geologic implications of microfossils in submarine volcanics. *Bulletin Volcanologique*, 35, pp.402-423.
- Nemeth, K., Bretkreutz, C., and Wilke, H.G., 2004. *Volcano-sedimentary Successions within an Intra-arc Related Jurassic Large Igneous Province (LIP): La Negra Formation, Northern Chile (a Preliminary Scientific Report on the Br 997/22-1 DFG Pilot Project)*.
- Nesbitt, H.W., and Young, G.M., 1982. Early proterozoic climates and plate motions inferred from major element chemistry of lutites. *Nature*, 299, pp. 715-717.
- Nouri, F., Asahara, Y., Azizi, H., Yamamoto, K., and Tsuboi, M., 2017. Geochemistry and petrogenesis of the eocene back arc mafic rocks in the Zagros suture zone, Northern Noorabad, Western Iran. *Geochemistry*, 77, pp.517-533.
- Olsson, R.K., Berggren, W.A., Hemleben, C., and Huber, B.T., 1999. *Atlas of Paleocene Planktonic Foraminifera*. Smithsonian Institution Press, Washington, D.C.
- Palinkaš, L.A., Bermanec, V., Šoštarić, S.B., Kolar-Jurkovšek, T., Palinkaš, S.S., Molnar, F., and Kniewald, G., 2008. Volcanic facies analysis of a subaqueous basalt lava-flow complex at Hruškovec, NW Croatia-Evidence of advanced rifting in the Tethyan domain. *Journal of Volcanology and Geothermal Research*, 178, pp.644-656.
- Parr, W.J., 1938. Upper eocene foraminifera from deep borings in King's park, Perth, Western Australia. *Journal of the Royal Society of Western Australia*, 24, pp.69-101.
- Pearce, J.A., 1982. In: Thorpe, R.S., editor. *En: Andesites: Orogenic Andesites and Related Rocks*. John Wiley and Sons, Hoboken.
- Pearce, J.A., and Cann, J.R., 1973. Tectonic setting of basic volcanic rocks determined using trace element analyses. *Earth and Planetary Science Letters*, 19, pp.290-300.
- Pearce, J.A., 1983. *Role of the Sub-Continental Lithosphere in Magma Genesis at Active Continental Margins*. Shiva Cheshire, UK, Cheshire.
- Pearce, J.A., 1996. A user's guide to basalt discrimination diagrams. In: *Trace element Geochemistry of Volcanic Rocks: Applications for Massive Sulphide Exploration*. Vol. 12. Geological Association of Canada, Short Course Notes, Canada, p.113.
- Pearce, J.A., van der Laan, S.R., Arculus, R.J., Murton, B.J., Ishii, T., Peate, D.W., and Parkinson, I.J., 1992. Boninite and harzburgite from Leg 125 (Bonin-Mariana forearc): A case study of magma genesis during the initial stages of subduction. In: *Proceedings of the Ocean Drilling Program, Scientific Results*. Ocean Drilling Program, College Station, TX, pp.623-659.
- Pearce, T.H., Gorman, B.E., and Birkett, T.C., 1977. The relationship between major element chemistry and tectonic environment of basic and intermediate volcanic rocks. *Earth and Planetary Science Letters*, 36, pp.121-132.
- Perfit, M.R., Gust, D.A., Bence, A.E., Arculus, R.J., and Taylor, S.R., 1980. Chemical characteristics of island-arc basalts: Implications for mantle sources. *Chemical Geology*, 30, pp.227-256.
- Philpotts, A.R., and Ague, J.J., 2022. *Principles of Igneous and Metamorphic Petrology*. Cambridge University Press, Cambridge.
- Rawlings, D.J., 1993. Mafic peperite from the gold creek Volcanics in the middle proterozoic McArthur Basin, Northern Territory. *Australian Journal of Earth Sciences*, 40, pp.109-113.
- Rogers, G., and Hawkesworth, C.J., 1989. A geochemical traverse across the North Chilean Andes: Evidence for crust generation from the mantle wedge. *Earth and Planetary Science Letters*, 91, pp.271-285.
- Ross, P.S., and Bédard, J.H., 2009. Magmatic affinity of modern and ancient subalkaline volcanic rocks determined from trace-element discriminant diagrams. *Canadian Journal of Earth Sciences*, 46, pp.823-839.
- Ryerson, F.J., and Watson, E.B., 1987. Rutile saturation in magmas: Implications for Ti-Nb-Ta depletion in island-arc basalts. *Earth and Planetary Science Letters*, 86, pp.225-239.
- Saunders, A.D., and Tarney, J., 1979. The geochemistry of basalts from a back-



- arc spreading centre in the East Scotia Sea. *Geochimica et Cosmochimica Acta*, 43, pp.555-572.
- Scrope, G.P., 1827. *Memoir on the Geology of Central France: Including the Volcanic Formations of Auvergne, the Velay, and the Vivarsais*. Longman, Rees, Orme, Brown, and Green, London.
- Shuto, K., Nohara-Imanaka, R., Sato, M., Takahashi, T., Takazawa, E., Kawabata, H., Takanashi, K., Ban, M., Watanabe, N., and Fujibayashi, N., 2015. Across-arc variations in geochemistry of oligocene to quaternary basalts from the NE Japan arc: Constraints on source composition, mantle melting and slab input composition. *Journal of Petrology*, 56, pp.2257-2297.
- Sinha, K.K., Pandey, P., Bhairam, C.L., and Parihar, P.S., 2011. Peperite occurrence and its implications on origin and temporal development of the proterozoic Dhala Basin, Mohar area, Shivpuri district, Madhya Pradesh. *Journal of the Geological Society of India*, 77, pp.183-189.
- Skilling, I.P., White, J.D.L., and Mcphie, J., 2002. Peperite: A review of magma-sediment mingling. *Journal of Volcanology and Geothermal Research*, 114, pp.1-17.
- Slovenec, D., Lugovic, B., and Vlahovic, I., 2010. Geochemistry, petrology and tectonomagmatic significance of basaltic rocks from the ophiolite mélange at the NW external-internal dinarides junction (Croatia). *Geologica Carpathica*, 61, pp.273-292.
- Sohn, C., and Sohn, Y.K., 2019. Distinguishing between primary and secondary volcanoclastic deposits. *Scientific Reports*, 9, p.12425.
- Squire, R.J., and Mcphie, J., 2002. Characteristics and origin of peperite involving coarse-grained host sediment. *Journal of Volcanology and Geothermal Research*, 114, pp.45-61.
- Stern, R.J., 2010. *The Anatomy and Ontogeny of Modern Intra-Oceanic Arc Systems*. Vol. 338. Geological Society, London, Special Publications, London, pp.7-34.
- Sun, S.S., and McDonough, W.F., 1989. *Chemical and Isotopic Systematics of Oceanic Basalts: Implications for Mantle Composition and Processes*. Vol. 42. Geological Society, London, Special Publications, London, pp.313-345.
- Templeton, J.H., and Hanson, R.E., 2003. Jurassic submarine arc-apron deposits and associated Magma/Wet-sediment interaction, northern Sierra Nevada, California. *Journal of Volcanology and Geothermal Research*, 128, pp.299-326.
- Thompson, G., 1991. Metamorphic and hydrothermal processes: Basalt-seawater interactions. In: *Oceanic Basalts*. Springer, Berlin.
- Toulmin, L.D., 1941. Eocene smaller foraminifera from the Salt Mountain Limestone of Alabama. *Journal of Paleontology*, 15, pp.567-611.
- Wade, B.S., Pearson, P.N., Berggren, W.A., and Pälike, H., 2011. Review and revision of cenozoic tropical planktonic foraminiferal biostratigraphy and calibration to the geomagnetic polarity and astronomical time scale. *Earth-Science Reviews*, 104, pp.111-142.
- Waichel, B.L., de Lima, E.F., Sommer, C.A., and Lubachesky, R., 2007. Peperite formed by lava flows over sediments: An example from the central paraná continental flood basalts, Brazil. *Journal of Volcanology and Geothermal Research*, 159, pp.343-354.
- Walker, G.P.L., 1992. Morphometric study of pillow-size spectrum among pillow lavas. *Bulletin of Volcanology*, 54, pp.459-474.
- Wang, T., Wang, Z., Yan, Z., Ma, Z., He, S., Fu, C., and Wang, D., 2016. Geochronological and geochemical evidence of amphibolite from the Hualong Group, Northwest China: Implication for the early Paleozoic accretionary tectonics of the Central Qilian belt. *Lithos*, 248, pp.12-21.
- White, J., and Houghton, B., 2006. Primary volcanoclastic rocks. *Geology*, 34, pp.677-680.
- White, J.D.L., and Busby-Spera, C.J., 1987. Deep marine arc apron deposits and syndepositional magmatism in the Alisitos Group at Punta Cono, Baja California, Mexico. *Sedimentology*, 34, pp.911-927.
- White, J.D.L., Mcphie, J., and Skilling, I., 2000. Peperite: A useful genetic term. *Bulletin of Volcanology*, 62, pp.65-66.
- White, M.P., 1928. Some index foraminifera of the Tampico Embayment area of Mexico. Part I. *Journal of Paleontology*, 2, pp.177-215.
- Whitney, D.L., and Evans, B.W., 2010. Abbreviations for names of rock-forming minerals. *American Mineralogist*, 95, pp.185-187.
- Wilson, A.H., and Grant, C.E., 2006. *Physical Volcanology and Compositions of the Basaltic Lavas in the Archean Nzuse Group, White Mfolozi Inlier, South Africa*. Geological Society of America, Boulder.
- Wilson, T.J., and Hanson, R.E., 1991. Submarine rhyolitic volcanism in a Jurassic proto-marginal basin; southern Andes, Chile and Argentina. In: *Andean Magmatism and its Tectonic Setting*. Vol. 265. Geological Society of America, Boulder, p.13.
- Winchester, J.A., and Floyd, P.A., 1977. Geochemical discrimination of different magma series and their differentiation products using immobile elements. *Chemical Geology*, 20, pp.325-343.
- Wood, D.A., Joron, J.L., Treuil, M., Norry, M., and Tarney, J., 1979. Elemental and Sr isotope variations in basic lavas from Iceland and the surrounding ocean floor. *Contribution to Mineralogy and Petrology*, 70, pp.319-339.
- Zhu, B., Guo, Z., Zhang, Z., and Cheng, F., 2014. Peperites in the permian tarim large igneous province in Northwest China and their constraints on the local eruption environments. *Science China Earth Sciences*, 57, pp.2914-2921.

# Effect of Waste Glass on Properties of Treated Problematic Soils: A Comprehensive Review

Jaylan H. Sherwany<sup>1</sup>, Jamal I. Kakrasul<sup>1</sup> and Jie Han<sup>2</sup>

<sup>1</sup>Department of Civil and Environmental Engineering, Faculty of Engineering, Soran University, Soran, 44008, Kurdistan Region, Iraq

<sup>2</sup>Department of Civil, Environmental and Architectural Engineering, The University of Kansas, Lawrence, Kansas, USA

**Abstract**—Soils are the most commonly used construction material in engineering projects. Fine-grained soils especially clayey soil may expand and lose strength when wet and shrink when dry, resulting in a significant volume change. Construction on weak soils has created challenges for various civil engineering projects worldwide, including roadways, embankments, and foundations. As a result, improving weak soil is vital, particularly for highway construction. The properties of this type of soil can be improved by waste-recycled materials such as waste glass (WG). The WG must be crushed and ground to a fine powder first and then can be mixed in various proportions with the soil. The primary objective of this study is to review the effect of WG on geotechnical properties of fine-grained soils treated by WG. To demonstrate the effects, the treated fine-grained soils at varying percentages of WG are compared with untreated soils. Physical properties (e.g., Atterberg limits, swelling, and maximum dry density), mechanical properties (e.g., California bearing ratio, and unconfined compressive strength) are evaluated. The test results from the literature show that adding a certain percentage of WG leads to a substantial effect on the properties of fine-grained soils; hence, using WG could reduce the required thickness of subbases in the construction of driveways and roads.

**Index Terms**—Stabilization, Problematic Soil, Waste Glass, Physical Properties, Mechanical Properties.

## I. INTRODUCTION

Clayey soils are extensively spread on many parts of the earth (Behnood, 2018; Ramos, et al., 2015). Some of the clayey soils are expansive soils whose volumes are directly proportional to moisture content, they expand when the water content increases and shrink when the water content decreases (Sharma and Bhardwaj, 2018). These soils also lose strength when they get wet. The swelling and low-strength properties of the clayey soils make them problematic and difficult to

be handled in civil engineering projects (Ikeagwuani and Nwonu, 2019; Thyagaraj and Zodinsanga, 2014), such as pavement foundations, slopes, embankments, and retaining walls (Fatta, et al., 2003). Therefore, it is often necessary to improve their properties before or during construction by stabilization of these soils (Sharma and Hymavathi, 2016). Soil stabilization (mechanical and chemical stabilization) may be achieved through mixing clayey soils with another geomaterial or chemicals to improve their geotechnical engineering properties according to the project's requirements (Gangwar and Tiwari, 2021; Olufowobi, et al., 2014; Patel, 2019). Mechanical stabilization by mixing soil with another soil of different gradation (e.g., sands and crushed stones) changes the soil gradation and properties. However, chemical stabilization, such as lime, cement, and fly ash, involves the alteration of soil properties (Patel, 2019). Increased uses of sand, crushed stones, and chemicals increase their prices and reduce natural resources, which are not sustainable. To provide sustainable construction, waste materials have been increasingly used as alternative materials in recent years to save natural resources and protect the environment. It is even more beneficial when wastes are used to strengthen soils and reduce their potential to swell (Parihar, Garlapati and Ganguly, 2019). Mixing waste materials with clayey soils to improve their soil properties is one of such applications, which makes the clayey soils more suitable for construction and more beneficial to the environment (Sharma and Hymavathi, 2016) because the waste materials from industrial processes negatively influence the environment (Balkaya, 2019; Ibrahim, Mawlood and Alshkane, 2019).

Waste glass (WG) is one of the most widely used in the world. WG is non-biodegradable; it does not decompose in landfills, causing it to its permanent accumulation in ever-increasing amounts and posing serious risks to the environment and ecosystems (Balan, Anupam and Sharma, 2021). According to the data from Environmental Protection Agency (EPA) in 2005, WG accounted for 12.5 million tons of municipal solid waste in the USA, with only 18.8% being recycled (Parihar, Garlapati and Ganguly, 2019; Rivera, et al., 2018). In 2006, the percentage of recycled WG in the USA increased to 22%. According to the EPA report in 2018, 12.3 million tons of WG was generated in the USA

ARO-The Scientific Journal of Koya University  
Vol. XI, No. 2 (2023), Article ID: ARO.11284. 11 pages  
Doi: 10.14500/aro.11284

Received: 22 July 2023; Accepted: 28 October 2023  
Review paper: Published: 08 December 2023

Corresponding author's email: [jamal.kakrasul@soran.edu.iq](mailto:jamal.kakrasul@soran.edu.iq)  
Copyright © 2023 Jaylan H. Sherwany, Jamal I. Kakrasul and Jie Han. This is an open access article distributed under the Creative Commons Attribution License.



which consists of 4.2% of municipal solid waste, of which only 3.1 million tons were recycled. However, according to the National Waste Report in 2020, Australia generated 1.16 million tons of WG from 2018 to 2019 with only 57% to 59% was recycled (Nacini, et al., 2019; Parera, et al., 2022). It was reported that 180 million tons of glass is produced every year and this quantity continues rising at the rate of 2 % to 4 % yearly (Bilgen, 2020a). Glass is produced in different forms: container or packaging glass (e.g., jars and bottles); flat glass (e.g., windows and windscreens); bulb glass (e.g., light globes); and cathode ray tube glass (e.g., TV screens and monitors) (Shayan and Xu, 2004; Siddique, 2007). Among all the glass materials, flat glass and container glass cover nearly 90% of the worldwide manufactured glass. Only approximately 20% of 90% of waste flat and container glass materials has been recycled, in other words, approximately 70% of the manufactured waste flat and container glass is disposed of as waste materials in landfills (Bilgen, 2020a; Rivera, et al., 2018). This situation is even worse in the Iraqi Kurdistan region because there is no factory for recycling waste. As a result, massive waste materials are thrown away yearly (Aziz, et al., 2011). In addition, this practice has undesirable environmental effects (Olofinnade, et al., 2018; Rashad, 2014).

Actually, some waste materials like WG have favorable properties, such as durability, high resistance, and strength, which can provide economic and environmental benefits when they are used for the construction of highways and structure foundations (Igwe and Adepehin, 2017; Zhang, Korkiala-Tanttu and Borén, 2019). For example, WG can be used to stabilize clayey soils and reduce negative impacts on the environment and waste degradation (Ibrahim, Mawlood and Alshkane, 2019). WG has been used in various forms for soil stabilization purposes including WG powder. The study (Bilgen, 2020b) showed that using WG powder for soil stabilization is the most economical way among other ways of recycling all WG.

#### *A. Objective and Significance of the Research*

Table I lists the published articles on the effects of WG on the characteristics of various treated problematic soils reviewed in this study. Table II shows that very few reviews on the use of WG in soil stabilization are available in the literature. Mohajerani, et al. (2017) reviewed the uses of crushed WG, glass powder, and foamed WG to improve the properties of base and subbase materials. They also found that crushed WG could be used as an aggregate alternative in asphalt mixtures. In addition, Mohajerani, et al. (2017) determined the optimum ratio of glass to aggregate used in the mixture to have appropriate performance and durability of the mixture. Rai, Singh and Tiwari (2020) conducted a comparative investigation of the engineering properties of a soil mixed with varying percentages of WG powder.

Perera, et al. (2021) reviewed the application of glass in base, subbase, and subgrade and assessed the effects of glass powder, glass fibers, foamed glass, WG aggregates, fine to coarse recycled glass, and glass geopolymers with

various particle sizes on the properties of these soils, such as maximum dry density (MDD), optimum moisture content (OMC), unconfined compressive strength (UCS), California bearing ratio (CBR), resilient modulus, swelling-shrinkage, direct shear strength, and triaxial shear strength.

However, a comprehensive review of the effect of WG powder with particle sizes smaller than 4.75 mm on problematic subgrade soils has not been conducted yet based on the recent publications from 2013 to 2021. Therefore, the objective of this study is to fill the above gap. Table III shows the differences between the present study and the published literature by Perera, et al. (2021), in terms of the reviewed papers and the particle size of WG. Table III shows that only a few papers (in bold fonts) were used by these two review papers. This study reviewed the effect of WG powder on the physical and mechanical properties of subgrade soil including: Atterberg limits (liquid limit [LL], plastic limit [PL], and plasticity index [PI]), linear shrinkage (LS)/swelling, MDD, OMC, UCS, and CBR. In addition, pavement thickness design based on the CBR value of subgrade treated with WG has not been well considered yet.

## II. TYPES, PREPARATION, AND UTILIZATION OF WG FOR SOIL STABILIZATION

Glass is produced from melting limestone, dolomite, sand, sodium sulfate, and soda at 1500–1600°C. Various techniques, such as cast rolling, rolling, blowing, flotation, and pressing, are used to obtain the most desired forms of glass. Some glass forms need cutting, tempering, and coloring (Chesner, et al., 2012). Several forms of WG have been produced, researched, and applied in the practice, such as glass powder (Bilgen, 2020b; Mohajerani, et al., 2017; Rai, Singh and Tiwari, 2020), waste soda lime (Canakci, Aram and Celik, 2016), fine to coarse recycled glass (Disfani, et al., 2011), recycled crushed glass, foamed glass, glass fibers, and glass geopolymers (Alqaisi, Le and Khabbaz, 2019). Most of these WG materials are produced from damaged windows of demolished buildings (Sharma and Bhardwaj, 2018) and drinking containers (Olufowobi, et al., 2014). Soda-lime glass is the most obtainable type of WG. The main uses of waste soda lime glass are in bottles and jars, tableware, and flat glass (Siddique, 2008). The chemical compositions of waste soda lime glass are as follows; SiO<sub>2</sub> (70–75%), Al<sub>2</sub>O<sub>3</sub> (1.3–2%), CaO (9.1–10.5%), and Na<sub>2</sub>O (13–14.4%) (Canakci, Aram and Celik, 2016; Siddique, 2008). WG is crushed in a crusher machine and then thoroughly powdered in a planetary mill passing a No. 200 sieve. Particles passing the No. 200 sieve (i.e., smaller than 75 μm) have been used as a source material for soil stabilization and geo-polymerization. Finally, the glass powder should be uniformly mixed for required tests (de Jesús Arrieta Baldovino, et al., 2020). Table I provides the information about soil type, WG type, content, waste size, and properties investigated in the past studies.

TABLE I  
UTILIZATION OF WASTE GLASS IN POOR SOILS

References	Soil type	Waste or binder type	Content of waste or binder (%)	Optimum content of waste glass (%)	Waste size (mm)	Properties of waste
Blayi, et al., 2020	Low-plasticity clay	Glass powder	2.5, 5, 10, 15, and 25	15	<0.250	$G_s=2.55$
Bilgen, 2020a	Clayey soil	Glass powder	10, 20 and 25		<0.425	$G_s=2.57$
de Jesús Arrieta Baldovino, et al., 2020	Silty soil	Glass powder	5, 15, and 30		<0.075	$G_s=2.40$ , $C_u=5.43$ , $C_c=1.09$ and $D_{50}=0.015$ mm
Bilgen, 2020b	Clayey soil	Glass powder Lime	10, 20 and 25 5		<0.425	
Arrieta Baldovino, et al., 2020	Silty soil	Glass powder Cement	5, 15, and 30 3, 6, 9		<0.075	$G_s=2.40$
Ibrahim, Mawlood and Alshkane, 2019	Clayey soil	Glass powder	6, 12, 18, 27, and 36	18	<0.075	$G_s=2.52$
Siyab Khan, Tufail and Mateeullah, 2018	Loose subsoil (CL-ML)	Glass powder	4, 8, and 12		<0.075	$G_s=2.56$
Adetayo, et al., 2021	Fine sand and silty or clayey gravel sand	Glass powder Cow Bone Ash	1, 2, 3, 4, and 5 1, 2, 3, 4, and 5		<0.075	
Canakci, Aram and Celik, 2016	Clayey soil	Waste soda lime glass	3, 6, 9, and 12		<0.075	
Sharma and Bhardwaj, 2018	High-plasticity clay	Glass waste Construction and demolition waste	3, 5, 7, and 9 12, 16, 20, and 24		<4.75 <4.75	
Parihar, Garlapati and Ganguly, 2019	Clayey soil	Waste soda lime glass	3, 6, 9, and 12		<0.425	
Bilondi, Toufigh and Toufigh, 2018a	Low-plasticity clay	Glass powder	3, 6, 9, 12, 15, 20, and 25	15	<0.075	
Fauzi, Djauhari and Fauzi, 2016	Clayey soil	Crushed glass and waste plastic	4, 8, and 12		<0.075	
Olufowobi, et al., 2014	Clayey soil (high and medium plasticity)	Glass powder Cement	1, 2, 5, 10, and 15 15		<0.075	$G_s=2.5-2.9$
Baldovino, et al., 2021	Sedimentary silty soil (with sand)	Glass Powder Lime	5, 15, and 30 5		<0.075	$G_s=2.4$
Güllü, Canakci and Al Zangana, 2017	Low-plasticity clay	Waste soda lime glass	3, 6, and 9		<0.150	
Kumar, et al., 2020	Clay, loam, and red soil	Crushed glass Reclaimed asphalt pavement	5 30, 50, 55, 60, 65		<4.75 <12.5, >4.75	$G_s=2.51$ $G_s=2.63$
Mujtaba, et al., 2020	Clayey soil	Glass powder	2, 4, 6, 8, 10, 12, 14		<4.75	$G_s=2.70$
Fauzi, Rahman and Jauhari, 2013	Clayey soil	Crushed glass Waste plastic bottle	4, 8, 12 4, 8, 12			$G_s=0.96$ $G_s=2.53$

$G_s$ : Specific gravity,  $C_u$ : Coefficient of uniformity,  $C_c$ : Coefficient of curvature,  $D_{50}$ : Mean particle size

### III. EVALUATED SOIL PROPERTIES

This study presented the physical properties (e.g., LL, PL, PI, LS, swelling, and MDD) and the mechanical properties (e.g., CBR, and UCS) of WG powder treated soils in the literature, as summarized in Table IV. In the reviewed studies, the soil was dried and sieved. Subsequently, the soils were mixed with WG. Grain-size analysis, Atterberg limits, MDD, OMC, and swelling tests were conducted following the ASTM standard. In addition, CBR and UCS also were carried out according to ASTM standards; the studies used modified mold for UCS tests.

### IV. RESULTS AND DISCUSSIONS

This study evaluated the physical and mechanical properties of different soils treated by the WG in the literature. The effects of WG on the soil property changes are discussed below.

#### A. Effects on Soil Physical Properties

##### Atterberg limits and LS

Atterberg limits (e.g., LL, PL, and PI), LS, and swelling are basic indices to describe soil behavior with moisture (Parihar, Garlapati and Ganguly, 2019). These limits can be used to evaluate soil plasticity characteristics and deformation behavior of treated and untreated soils (Blayi, et al., 2020). These indices of soils (e.g., clayey soils) can be changed by adding WG and will be discussed below.

##### LL

LL is a basic property for fine-grained soils, which is defined as a boundary moisture content of the soil to distinguish its liquid and plastic states. Adding WG to fine-grained soils is expected to influence the LLs of the soil. Fig. 1 shows the effect of WG on the LL ratios of fine-grained soils. The LL ratio is defined as the ratio of the LL of the soil after treatment to that before treatment. Fig. 1 shows a general trend that an increase in the WG content

TABLE II  
COMPARISON BETWEEN REVIEW ARTICLES AND THE CURRENT REVIEW STUDY ON THE USE OF WG FOR SOIL STABILIZATION

References	Published year of reviewed articular	Papers reviewed	Pavement layer	Replacement/addition	Specific gravity	Chemical composition (%)	Physical properties	Mechanical properties
Mohajerani, et al., 2017	2012–2019	8	Base and subbase	Crushed WG	2.4–2.8	SiO <sub>2</sub> =(32-75), Al <sub>2</sub> O <sub>3</sub> =(0.5–24.5), Na <sub>2</sub> O=(0.5–17), CaO=(2-10), MgO=(0.1–10.5)	Particle Size Distribution, MDD, OWC	Los Angeles abrasion test, CBR, modified compaction test, direct shear, and UCS
Rai, Singh and Tiwari, 2020	2016–2019	5	subgrade	Glass Powder Waste	2.62		PL, LL, PI, MDD, OMC	Proctor test, UCS, CBR
Perera, et al., 2021	1996–2021	29	Base and Subbase	Glass powder, Glass fibres, Foamed glass,	1.3–14.79	SiO <sub>2</sub> = 72.58, Al <sub>2</sub> O <sub>3</sub> = 1.48, Na <sub>2</sub> O = 12.54, CaO = 10.49	Specific gravity, bulk density, index of flakiness, particle size distribution, water absorption, permeability, pH value	Compaction , Direct Shear, Triaxial shear, Resilient Modulus, Swelling-Shrinkage, UCS and CBR
	1999–2021	29	Subgrade	Glass aggregates ( WG), (fine, medium, coarse) recycled glass, and Glass geopolymers				
Current study	2014–2021	19	Subgrade	WG (WG powder, crushed glass)	0.96–2.7	SiO <sub>2</sub> =(63-81), Al <sub>2</sub> O <sub>3</sub> =(0.4–2.61), Na <sub>2</sub> O=(4-17), CaO=(0.26–13.3), MgO = (0.2–3.89)	LL, PL, PI, LS, MDD, OMC	UCS, and CBR

WG: Waste glass, UCS: Unconfined compressive strength, CBR: California bearing ratio, LL: Liquid limit, PL: Plastic limit, PI: Plasticity index, LS: Linear shrinkage, MDD: Maximum dry density, OMC: Optimum moisture content

TABLE III  
VARIATIONS BETWEEN THE CURRENT REVIEW AND THE PUBLISHED REVIEW (PERERA, ET AL., 2021) OF USING WASTE GLASS ON SUBGRADE SOIL (2013–2021)

Year	Current study		Study (Perera, et al., 2021)	
	Paper reviewed	Waste glass particle size (mm)	Paper reviewed	Waste glass particle size (mm)
2013	Fauzi, Rahman and Jauhari (2013)	-	Fauzi, Rahman and Jauhari (2013)	-
2014	Olufowobi, et al. (2014)	<0.075		
2016	Canakci, Aram and Celik (2016)	<0.075	Canakci, Aram and Celik (2016)	<0.075
	Fauzi, Djauhari and Fauzi (2016)	<0.075	Ateş (2016)	l=4, w=2, t=0.4
2017	Güllü, Canakci and Al Zangana (2017)	<0.150	Patel and Singh (2017a)	d=0.15
			Patel and Singh (2017b)	l=10,20,30
2018	Sharma and Bhardwaj (2018)	<4.75	Bilondi, Toufigh and Toufigh (2018a)	<0.075
	Siyab Khan, Tufail and Mateullah (2018)	<0.075	Bilondi, Toufigh and Toufigh (2018b)	<0.075
	Bilondi, Toufigh and Toufigh (2018a)	<0.075		
2019	Parihar, Garlapati and Ganguly (2019)	<0.425	Arulrajah, et al. (2019)	1.5
	Ibrahim, Mawlood and Alshkane (2019)	<0.075	Onyelowe, et al. (2019)	10
			Patel and Singh (2019)	0.15
2020	Bilgen (2020a)	<0.425	Pacheco-Torres and Varela (2020)	≤10
	Bilgen (2020b)	<0.425	Blayi, et al. (2020)	<0.250
	de Jesús Arrieta Baldovino, et al. (2020)	<0.075	Mujtaba, et al. (2020)	<4.75
	Blayi, et al. (2020)	<0.250	Sujatha, et al. (2020)	l=12, d=0.019
	Arrieta Baldovino, et al. (2020)	<0.075	Más-López, et al. (2020)	≤40
	Kumar, et al. (2020)	<4.75	Patel and Singh (2020)	l=20, d=0.15
	Mujtaba, et al. (2020)	<4.75		
2021	Adetayo, et al. (2021)	<0.075	Yaghoubi, et al. (2021)	≤4.75
	Baldovino, et al. (2021)	<0.075	Rabab'ah, et al. (2021)	l=30

l: Length of glass fiber, w: Width, t: Thickness, d: Diameter.

reduced the LL of the soil. Blayi, et al. (2020) used five WG contents (2.5%, 5%, 10%, 15%, and 25%) and found that when the WG content increased by 25%, the LL of the soil decreased from 44.10% to 22.19%, that is, by approximately 50% reduction ( $[(22.19-44.10)/49.19]*100$ ). Bilgen (2020a) investigated the influence of WG on three different types of soil (Alapli clay soil, Eregli clay soil, and Bentonite clay soil). This research showed that an increase in the WG content from 10% to 25% reduced LL by 14.3%, 12%, and 8.8%, respectively, for these three types of soil. Ibrahim, Mawlood, and Alshkane (2019) also showed that when the

WG content increased by 0%, 6%, 12%, 18%, 27%, and 36 %, the LLs of the soil decreased by 50.93%, 48.97%, 46.90%, 41.92%, 39.96%, and 38.84%. This change is equivalent to a 23.7% reduction in the LL ratio of the soil when 36% WG was added, as shown in Fig. 1. This reduction in LL is due to lower water absorption properties of WG particles compared to that of the clay particles.

Fig. 1 shows a decreasing trend with the WG content (red line) since WG works as an inner material and its particles' ability to absorb water is less than soil particles. In addition, all studies in Fig. 1 used clayey soils with specific gravity

TABLE IV  
PHYSICAL AND MECHANICAL PROPERTIES OF SOILS TREATED BY WASTE GLASS POWDER IN THE LITERATURE

Refererences	Physical properties					Mechanical properties			
	LL (%)	PL (%)	PI (%)	LS (%)	Swelling (%)	Compaction test		UCS (kPa)	CBR (%)
						OMC (%)	MDD (g/cm <sup>3</sup> )		
Blayi, et al., 2020	✓	✓	✓	✓	✓	✓	✓	✓	✓
Bilgen, 2020a	✓	✓	✓			✓	✓	✓	✓
de Jesús Arrieta Baldovino, et al., 2020	✓	✓	✓			✓	✓		
Bilgen, 2020b	✓	✓	✓			✓	✓	✓	✓
Arrieta Baldovino, et al., 2020	✓	✓	✓			✓	✓	✓	
Ibrahim, Mawlood and Alshkane, 2019	✓	✓	✓	✓	✓	✓	✓	✓	
Siyab Khan, Tufail and Matecullah, 2018	✓	✓	✓			✓	✓		✓
Adetayo, et al., 2021	✓	✓	✓			✓	✓		✓
Nacini, et al., 2019						✓	✓		✓
Canakci, Aram and Celik, 2016	✓	✓	✓		✓	✓	✓	✓	✓
Sharma and Bhardwaj, 2018	✓	✓	✓			✓	✓	✓	
Parihar, Garlapati and Ganguly, 2019	✓	✓	✓			✓	✓		✓
Bilondi, Toufigh and Toufigh, 2018a	✓	✓	✓			✓	✓	✓	
Fauzi, Djauhari and Fauzi, 2016	✓	✓	✓			✓	✓		✓
Olufowobi, et al., 2014	✓	✓	✓			✓	✓		✓
Baldovino, et al., 2021	✓	✓	✓			✓	✓	✓	
Güllü, Canakci and Al Zangana, 2017	✓	✓	✓			✓	✓	✓	
Kumar, et al., 2020						✓	✓		✓
Mujtaba, et al., 2020	✓	✓	✓		✓	✓	✓	✓	✓
Fauzi, Rahman and Jauhari, 2013	✓	✓	✓			✓			

UCS: Unconfined compressive strength, CBR: California bearing ratio, LL: Liquid limit, PL: Plastic limit, PI: Plasticity index, LS: Linear shrinkage, MDD: Maximum dry density, OMC: Optimum moisture content

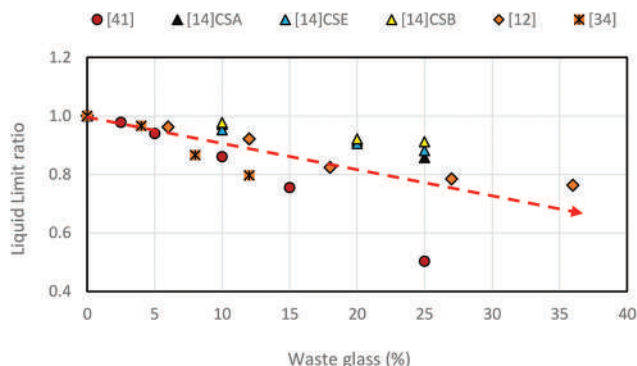


Fig. 1. Liquid limit ratios of soils treated with waste glass.

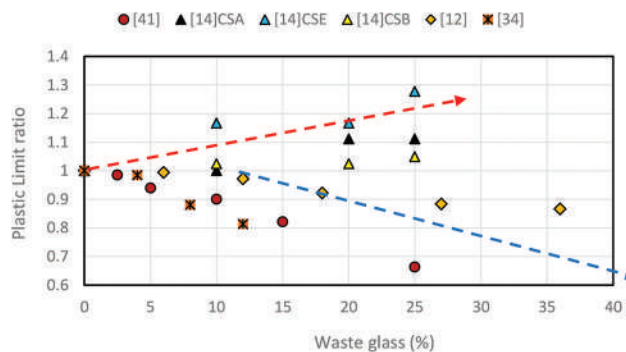


Fig. 2. Plastic limit ratios of treated soils from the literature.

between 2.51 and 2.74, particle sizes of WG between 0.075 and 0.425 mm, and the silica content of WG between 70.2% and 72%. It is noticed that the decrease in LL in the study (Blayi, et al., 2020) is more significant and affected by the addition of WG as compared to that in other studies. The reason behind this difference is due to the quality and accuracy of the test procedure by studies.

PL

Fig. 2 shows the collected data from the previous research on the effect of WG on the PL (PL) ratios of fine-grained soils. The PL ratio is defined as the ratio of the PL of the soil treated by WG to that without any WG. Fig. 2 shows two different trends: (1) The use of WG reduced PL and (2) the use of WG increased PL. The study (Blayi, et al., 2020) indicated that the PL of low-plasticity clay was 24.81% and WG at different contents reduced

PL. When the WG content was increased by 25%, the PL was reduced by 16.44% due to a large amount of silica in WG, which is equivalent to nearly 34% loss in the PL for this soil [i.e., (16.44 - 24.81)/24.81\*100%]. Bilgen (2020a) evaluated three soils treated at WG contents of 0%, 10%, 20%, and 25% and found that the use of WG at 25% increased PL by 11%, 28%, and 5%, respectively, for Alapli, Eregli, and Bentonite clayey soils. Ibrahim, Mawlood, and Alshkane (2019) reported that the use of WG at different contents of 0%, 6%, 12%, 18%, 27%, and 36% reduced PL by a maximum of 13.4% (i.e., from 22.5% to 19.5%). However, PL changed slightly when the WG content was more than 18%, in other words, adding 27% and 36% WG led to a less significant change in PL for the clayey soil.

Fig. 2 shows both increase (red line) and decrease (blue line) trends. The increased trend due to the addition of WG

is related to its independence of the percentage of additives but dependence on the clay type (Ahmed, Swindale and EL-Swaify, 1969). However, the reason for the decreasing trend of PL is that WG acts as a non-plastic material due to a large amount of silica in the content of WG.

PI

Fig. 3 shows the collected data from the literature about the effect of WG on the PI ratios for fine-grained soils. The PI ratio is defined as the ratio of the PI of the soil treated by WG to that without any WG. Fig. 3 clearly shows that all the PI ratios except for one are below 1.0, indicating PI decreases with the addition of WG and the increase of the WG content. Blayi, et al. (2020) indicated that the PI decreased from 19.5% to 6.3% (i.e., 68% reduction)  $[(6.3\% - 19.5\%) / 19.5\%] * 100$  as the WG content increased from 2.5% to 25%. Bilgen (2020a) reported that the increase of the WG content from 0% to 25% reduced their PIs by 41.2%, 41.7%, and 12.1%, respectively, for Alapli, Eregli, and Bentonite clayey soils. Ibrahim, Mawlood, and Alshkane (2019) found that the increase of the WG content from 0% to 36% reduced the soil PI from 28.5% to 19.5% (i.e., nearly 32% reduction). A similar result was obtained by Canakci, Aram and Celik (2016), in which they showed that WG at the contents of 3%, 6%, 9%, and 12% with a clayey soil reduced their plastic indices by 13.13%, 12.29%, 11.38%, and 10.04% (i.e., a maximum 44% deduction). The reduction of the plasticity indices of soils treated by WG is attributed to the fact that WG is a cohesionless material due to a large amount of silica (a non-plastic material) (Ibrahim, Mawlood and Alshkane, 2019).

This decreasing trend in PI in all studies due to the addition of WG is related to the cohesionless behavior of WG.

LS

Fig. 4 shows the collected data from two past studies about the effect of WG on the LS ratios of soils. The LS ratio is defined as the ratio of the LS of the soil treated by WG to that without any WG. Fig. 4 clearly shows that adding WG to soils reduced their LS ratios. For example, in the study (Blayi, et al., 2020), the LS of the natural soil was 9.1% and decreased by 8.7%, 8.0%, 7.0%, 5.5%, and 2.8%, respectively, when the WG content was increased by 2.5%, 5%, 10%, 15%, and 25%. These results indicate that

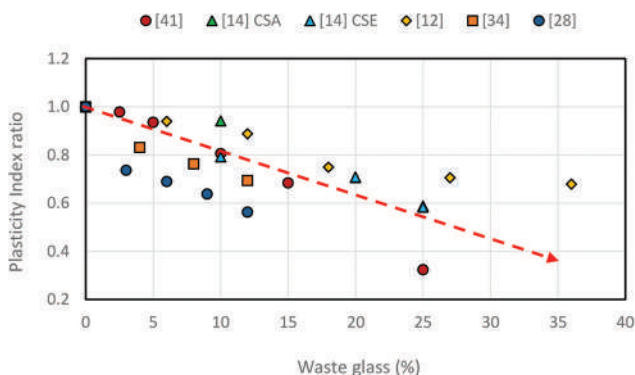


Fig. 3. Plasticity indices of soils treated by waste glass from the literature.

the maximum percentage reduction in the LS was 69% (i.e.,  $[2.8 - 9.1] / 9.1 * 100\%$ ) when 25% of WG was added (Blayi, et al., 2020). Ibrahim, Mawlood, and Alshkane (2019) also found that, as the WG content increased from 0% to 36%, the LS decreased from 13.4% to 9.0% (i.e., a 33% reduction in the LS).

Fig. 4 shows that the results in Ibrahim, Mawlood and Alshkane (2019) were less affected by WG as compared with those in Blayi, et al. (2020) because the soil in the study (Ibrahim, Mawlood and Alshkane, 2019) was a high plasticity clay while that in the study (Blayi, et al., 2020) was a low plasticity clay. Hence, the LS of the low-plasticity clay decreased more.

MDD and OMC

MDD and OMC of soil with or without any treatment by additives can be determined by compaction tests. Compacted specimens can also be used to determine their UCSs and CBRs. Compaction tests can provide valuable information about the quality of compacted soil and help evaluate the suitability of the soil for construction and service.

Fig. 5 shows the collected data for the MDD ratios of soils treated by WG from the literature whereas Fig. 6 shows their OMC ratios. The MDD or OMC ratio is defined as the ratio of the MDD or OMC of soil treated by WG to that without any WG. Figs. 5 and 6 show that MDD increased but OMC

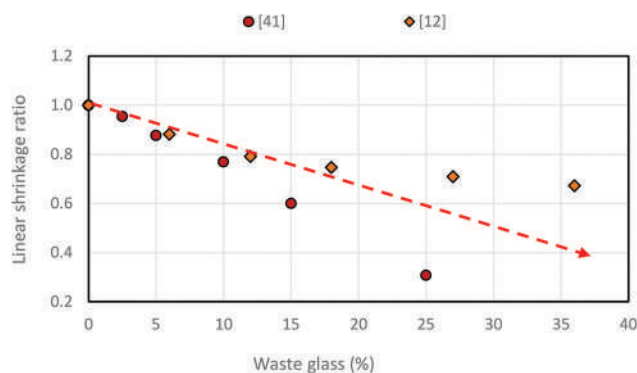


Fig. 4. Linear shrinkage ratios of soils treated by waste glass from the literature.

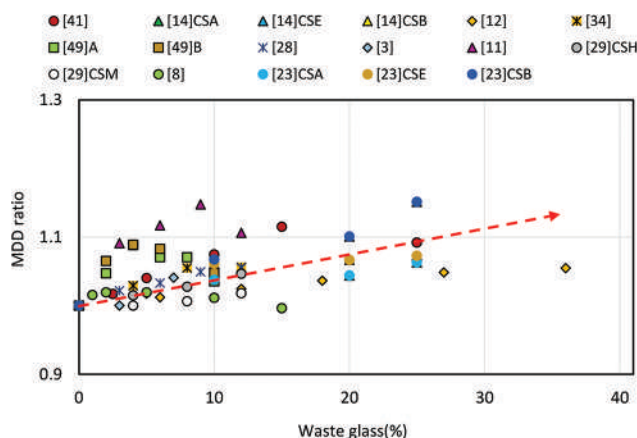


Fig. 5. Maximum dry density ratios of compacted soils treated by waste glass from the literature.

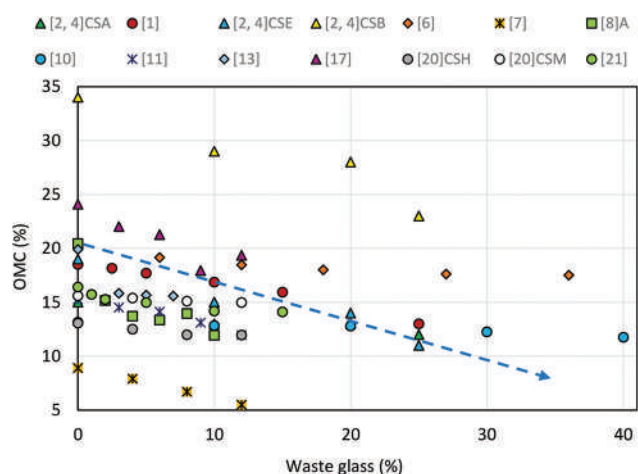


Fig. 6. Optimum moisture content ratios of compacted soil treated by waste glass from the literature.

decreased as the WG content increased. Ibrahim, Mawlood, and Alshkane (2019) investigated the effect of WG using different WG contents (6%, 12%, 18%, 27%, and 36%) in soils on their MDDs and OMCs and found that adding WG resulted in a maximum increase of MDD by 5.5% and a maximum reduction of OMC by nearly 15%. Bilgen (2020a) found that as the WG content increased from 0% to 25%, the MDD increased by approximately 5%, 7%, and 16%, but the OMC decreased by nearly 20%, 42%, and 32%, respectively, for Alapli, Eregli, and Bentonite clayey soils. Bilgen (2020b) use the same soils that used by the study (Bilgen, 2020a) with addition of 5% of cement. The results show that an increase of WG by 25% increased the MDD by 6%, 7%, and 15% and reduced the OMC by 11%, 32%, and 18%, respectively, for Alapli, Eregli, and Bentonite clayey soils. Canakci, Aram, and Celik (2016) found that the increase of the WG content from 0% to 12% reduced the MDD of the soil by more than 5% but reduced the OMC by nearly 22%. Parihar, Garlapati, and Ganguly (2019) investigated the effect of WG with different contents of 0%, 3%, 6%, 9%, and 12% (same as those in the study [Canakci, Aram and Celik, 2016]) and found that adding 9% WG to the soil increased its MDD by 14.7% but reduced its OMC by 25.6%. Blayi, et al. (2020) used different WG contents of 0%, 2.5%, 5%, 10%, 15%, and 25% in soils and found that the increase in the WG content from 0% to 25% led to a decrease in the OMC from 18.5% to 13% and an increase in the MDD from 1.74 g/cm<sup>3</sup> to 1.94 g/cm<sup>3</sup>, which are equivalent to nearly 30% reduction in the OMC and more than 9% increase in the MDD when the WG content increased from 0% to 25%. Adetayo, et al. (2021) conducted field tests with two test pits (Pits A and B) at different depths (1.5 m and 1.25 m, respectively) to evaluate the effect of WG and Cow Bone Ash and found that the MDD of the treated soil in Pit A was increased by 8.8% (from 1.7 to 1.85 g/cm<sup>3</sup>) by adding 4% WG and Cow Bone Ash. However, a further increase in the WG and Cow Bone Ash content (e.g., 8%) in the soil reduced the MDD from 1.85 to 1.76 g/cm<sup>3</sup> (the same result obtained by [Kumar, et al., 2020]). The increase in MDD in some studies after

an increase in the percentage of WG in clay soils may be attributed to an increase in the voids within the soil structure, which reduces the MDD of the WG-soil mixture (Salpadoru Tholkamudalige, et al., 2022). In Pit B, the MDD increased from 1.69 to 2.87 g/cm<sup>3</sup> when the WG and Cow Bone Ash increased from 0% to 8%, but decreased to 1.77 g/cm<sup>3</sup> when the WG and Cow Bone Ash content increased to 10% (i.e., nearly 5% increase in the MDD). In addition, the OMC decreased by 1.7% (from 17.01% to 16.73%) when the WG and Cow Bone Ash content increased from 0% to 10% (same as those in the study [Fauzi, Rahman and Jauhari, 2013]). The above discussion shows that adding WG into a soil increased its MDD and reduced its OMC. The increase in the MDD is attributed to the fact that WG has a higher density than clayey soils whereas the reduction in the OMC is attributed to the fact that WG has a lower absorption than clayey soils (Nuruzzaman and Hossain, 2014). In addition, the fineness of WG plays an important role (de Jesús Arrieta Baldovino, et al., 2020).

The increase of MDD with the WG content in Fig. 5 can be explained as WG is a cohesionless material that makes particles more easily rearranged into a dense state. The decrease of OMC with the WG content in Fig. 6 can be explained as WG having a lower water absorption ability.

#### Swelling

The percentage of expansion at a stable pressure of 1 kPa is known as free swelling (Ibrahim, Mawlood and Alshkane, 2019). Fig. 7 shows the collected data for the swelling ratios of soils treated by WG from the literature. The swelling ratio is defined as the ratio of the swelling of soil treated by WG to that without any WG. Mujtaba, et al. (2020) reported the influence of WG on the swelling of expansive soil. The study shows that increasing WG by 14% reduced the percentage of swelling from 4% to 0.5%. Blayi, et al. (2020) investigated the effect of WG on the swelling of expansive clayey soil and found that increasing WG by 25% reduced free swelling from 5.28% to 0.88% (i.e., 83.3% reduction in swelling). Canakci, Aram and Celik (2016) also observed that, the swelling of the soil with 0% WG was 5.51% and reduced by 4.5, 3.1, 2.02, and 1.65% as the WG content was increased by 3, 6, 9, and 12%. Ibrahim, Mawlood, and Alshkane (2019) examined WG's impact on the swelling of high-plasticity clayey soil and found that increasing WG from 0% to 36% reduced the swelling by 50.7%. In general, as the WG content increases in expansive soils, their swelling decreases due to the cohesionless behavior of WG. Furthermore, the reason for decrease in swelling is the breakdown of the bond between clay particles (clay-clay) and clay with water (clay – double diffused layer of water) breakage and replaced with clay-silica bonds along with enhancing particle packing (Parihar, Garlapati and Ganguly, 2019).

#### B. Effect on Soil Mechanical Properties

##### UCS

Fig. 8 shows the collected data for the UCS ratios of soils treated by WG from the literature. The UCS ratio is defined as the ratio of the UCS of soil treated by WG to



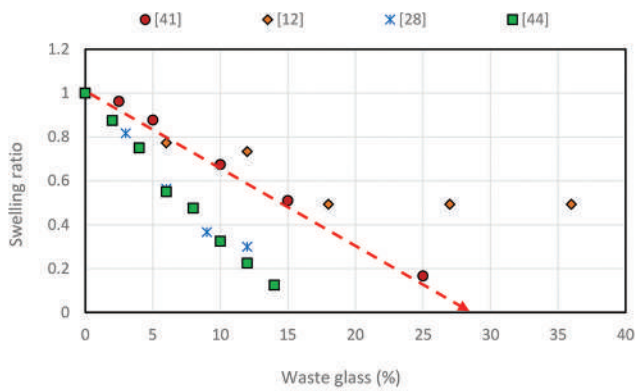


Fig. 7. Swelling ratios of compacted soil treated by waste glass from the literature.

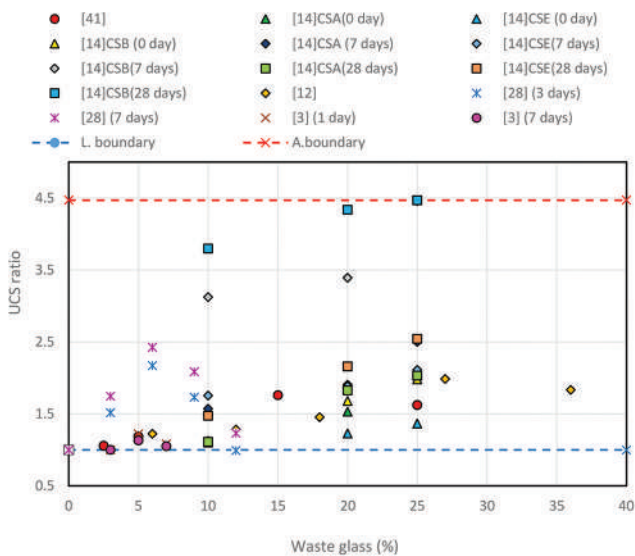


Fig. 8. Unconfined compressive strength ratios of soils treated by waste glass from the literature.

that of native soil (without any WG). Fig. 8 shows that UCS generally increased as the WG content increased. Sharma and Bhardwaj (2018) conducted UCS tests on a high-plasticity clay treated by WG at three different contents (3%, 5%, and 7%) at curing ages of 1, 7, and 28 days and found that as the WG content increased, the UCS increased. For example, adding 3% WG to the soil increased UCS from 303 kPa at 1 day, 678 kPa at 7 days, and 1155 kPa at 28 days of curing. Adding 5% WG to the soil increased the UCS to 371, 678, and 1239 kPa at 1, 7, and 28 days of curing, respectively. However, when 7% WG was used, the increase of UCS became less, 329, 713, and 1193 kPa at 1, 7, and 28 days of curing, respectively. The above changes in UCS at three curing ages can also be expressed as a percentage increase, for example, more than 13%, and 22% increase in USC at the WG content of 3%, and 5%. Blayi, et al. (2020) examined the effect of various percentages of WG (i.e., 0% to 25% of WG by dry weight of native soil) on UCS. They reported that as the WG content increased from 0% to 15%, its UCS increased from 205 to 360 kPa. However, with a further increase in

the WG content (e.g., 25%), its UCS decreased to 332 kPa. The decrease in the UCS by adding an extra amount of WG might be due to the reduction of its cohesion due to the high amount of silica in WG (Ibrahim, Mawlood and Alshkane, 2019).

Bilgen (2020a) also investigated the effect of WG on USCs for three types of soil: Alapli, Eregli, and Bentonite clayey soils at different curing ages and found the UCS increased by 106%, 150%, and 103%, 36%, 111%, and 154%, and 97%, 345%, and 346% at 1, 7, and 28 days of curing, respectively. Ibrahim, Mawlood, and Alshkane (2019) evaluated the properties of soils mixed with WG at five different contents (6%, 12%, 18%, 27%, and 36%). They found that as the WG content increased by 18%, the UCS increased by more than 45%. When the WG content increased from 18% to 27%, the UCS increased from 410 to 565 kPa. However, the WG content increased from 27% to 36%, the UCS decreased to 517 kPa. Canakci, Aram and Celik (2016) found that as the WG content increased by 6%, the UCS increased by nearly 117%, from 238 to 518 kPa; however, at the WG contents of 9% and 12%, the UCSs were 412 and 236 kPa, respectively, at 3 days of curing.

Fig. 8 shows that an increase of the WG content generally increased the UCS ratio and different soils had different responses to the WG content. The soil with high plasticity (e.g., the Bentonite clay in the study (Bilgen, 2020a)) had the highest UCS ratio.

*CBR*

CBR is an essential geotechnical engineering parameter for evaluating subgrade and base course strengths and stiffness for pavement design including the determination of pavement thicknesses (Adetayo, et al., 2021; Siyab Khan, Tufail and Matecullah, 2018). The typical range for CBR value of a subgrade layer is in the range of 2% to 12% [59]. Fig. 9 shows the collected data for the CBR ratios of soils treated by WG from the studied literature. The CBR ratio is defined as the ratio of the CBR of soil treated by WG to that without any WG. Fig. 9 shows that CBR generally increased as the WG content increased. Canakci, Aram and Celik (2016) investigated the effect of WG on the CBR value of the soil treated by WG at different contents (e.g., 3%, 6%, 9%, and 12%) and found that adding 12% WG to a clayey soil increased its CBR value by nearly 143%. Siyab Khan, Tufail and Matecullah (2018) also showed that an increase of the WG content from 0% to 12% increased the CBR by 59% (i.e., more than 32% increase). Consequently, Blayi, et al. (2020) concluded that an increase in the WG content from 0% to 15% increased the CBR by 12.2%; however, with a further increase in the WG content to 25%, the CBR decreased to 10.8%. Blayi, et al. (2020) also concluded that the optimum WG content was 15%. Bilgen (2020a) showed that an increase in the WG content from 0% to 25% increased the CBR value by a lot and curing periods also affected the CBR of the treated soil. The results showed that, for immediately tested samples when 25% WG was added, the CBR increased by approximately 167%, 191%,

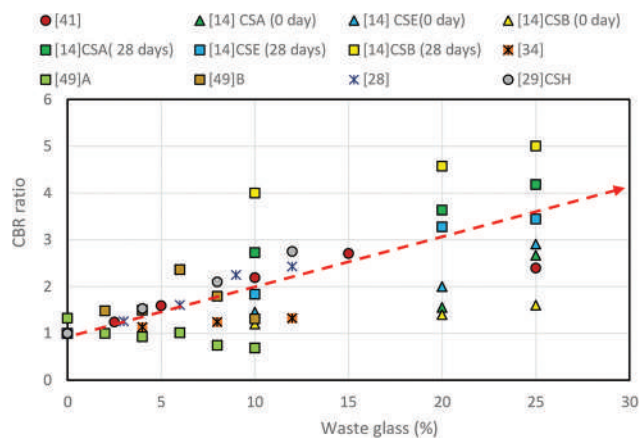


Fig. 9. California bearing ratio ratios of soils treated by waste glass from the literature.

and 60%, respectively, for Alapli, Eregli, and Bentonite clayey soils. Consequently, after 28 days of curing, the CBR of soils treated with 25% WG increased by more than 318%, 244%, and 400% respectively, for Alapli, Eregli, and Bentonite clayey soils. Adetayo, et al. (2021) reported that an increase of the WG content by 10% increased the CBR value by 38% and 31%, respectively, for soil in pit A and soil in pit B.

#### V. EFFECT ON PAVEMENT THICKNESS DESIGN

A design manual for roads and bridges (HD 26/06, 2006) provides the details needed to determine the thicknesses of capping and subbase layers of pavements based on subgrade CBR. This design manual suggests that, for a subgrade with a CBR equal to or greater than 15%, only a 150 mm thick sub-base is needed; however, for a subgrade with a CBR value lower than 15%, a capping layer of variable thickness is needed. Therefore, determination of the thicknesses of capping and subbase layers depends on the CBR of the subgrade. Blayi, et al. (2020) showed that adding 15% WG into a subgrade soil increased its CBR from 4.5% to 12.2%, thus reducing the subbase thickness from 240 to 150 mm; however, increasing the WG content to 25% increased the subgrade CBR to 10.8%, thus requiring a subbase thickness of 160 mm. Bilgen (2020a) reported that, adding 25% WG to Alapli, Eregli, and Bentonite clayey soils increased their CBRs from 9% to 24%, 11% to 32%, and 5% to 8%, respectively. As a result, their required subbase thicknesses decreased from 180 to 150 mm, 160 to 150 mm, and 200 to 190 mm, respectively, as shown in Fig. 10. Canakci, Aram and Celik (2016) also reported that, increasing the WG content from 0% to 12% increased the subgrade CBR from 2.47% to 6%, which required a 150 mm subbase and a 235 mm capping layer. All these studies showed that an increase in the WG content increased the subgrade CBR, thus reducing the thicknesses of pavement layers.

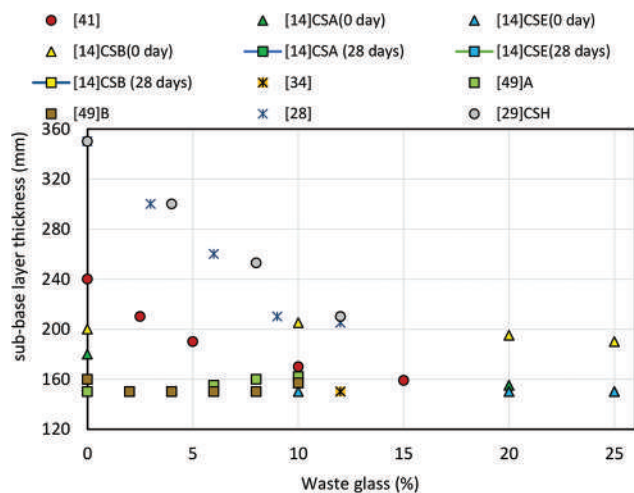


Fig. 10. Subbase thicknesses for subgrade soils treated by waste glass from the literature.

#### VI. CONCLUSIONS

This paper reviewed the utilization and research results of WG for soil stabilization in the literature. The review focused on the effects of WG and its content on the physical and mechanical properties of treated soils and pavement thicknesses on treated subgrade soils. The following conclusions can be made from this study:

- The content of WG utilized for soil stabilization ranged from 2% to 25%.
- WG is composed of a high content of non-plastic silica, which generally reduces the Atterberg limits of soils after being mixed with WG.
- WG has low absorption property and when it is mixed with fine-grained soil, it reduces its OMC.
- WG powder is a cohesionless material. When an appropriate amount of WG is mixed with soil, it makes particles more easily rearranged to a dense state thus increasing its MDD and soil strengths, such as UCS and CBR. However, when an excessive amount of WG is used, it may reduce soil strength.
- Since the use of WG generally increases a subgrade CBR, it reduces the thicknesses of subbase and surface layers in pavements.

#### VII. LIMITATION

In recent years, the use of WG to enhance the geotechnical properties of problematic soils has been the subject of numerous studies. This assessment was limited to the impact of WG on subgrade soil in terms of its physical and mechanical properties. To gain a better understanding of the effect of WG on the durability, drainage, and deformation behavior of problematic soils, additional tests, such as freezing-thawing, one-dimensional consolidation, and direct shear tests, could be conducted. Furthermore, various types of glass and particle sizes (<4.75 mm) were investigated.

Therefore, there is a lack of utilization of specific categories of WG. The composition, particle size, and type of WG could potentially influence the properties of different soil types.

#### REFERENCES

- Adetayo, O.A., Umego, O.M., Faluyi, F., Odetoeye, A.O., Bucknor, A.O., Busari, A.A., and Sanni, A., 2021. Evaluation of pulverized cow bone ash and waste glass powder on the geotechnical properties of tropical laterite. *Silicon*, 14(5), pp.2097-2106.
- Ahmed, S., Swindale, L.D., and EL-Swaify, S.A., 1969. Effects of adsorbed cations on physical properties of tropical red earths and tropical black earths. I. Plastic limits, percentage of stable aggregates, and hydraulic conductivity. *Journal of Soil Science*, 20(2), pp.255-268.
- Alqaisi, R., Le, T.M., and Khabbaz, H., 2019. Applications of recycled sustainable materials and by-products in soil stabilization. In: *International Congress and Exhibition "Sustainable Civil Infrastructures"*. Springer, Cham, pp.91-117.
- Arrieta Baldovino, J.J., dos Santos Izzo, R.L., da Silva, É.R., and Lundgren Rose, J., 2020. Sustainable use of recycled-glass powder in soil stabilization. *Journal of Materials in Civil Engineering*, 32(5), p.04020080-1.
- Arulrajah, A., Kua, T.A., Suksiripattanapong, C., and Horpibulsuk, S., 2019. Stiffness and strength properties of spent coffee grounds-recycled glass geopolymers. *Road Materials and Pavement Design*, 20(3), pp.623-638.
- Ateş, A., 2016. Mechanical properties of sandy soils reinforced with cement and randomly distributed glass fibers (GRC). *Composites Part B: Engineering*, 96, pp.295-304.
- Aziz, S.Q., Aziz, H.A., Bashir, M.J.K., and Yusoff, M.S., 2011. Appraisal of domestic solid waste generation, components, and the feasibility of recycling in Erbil, Iraq. *Waste Management and Research*, 29(8), pp.880-887.
- Balan, L.A., Anupam, B.R., and Sharma, S., 2021. Thermal and mechanical performance of cool concrete pavements containing waste glass. *Construction and Building Materials*, 290, p.123238.
- Baldovino, J.J.A., Izzo, R.L.S., Rose, J.L., and Domingos, M.D.I., 2021. Strength, durability, and microstructure of geopolymers based on recycled-glass powder waste and dolomitic lime for soil stabilization. *Construction and Building Materials*, 271, p.121874.
- Balkaya, M., 2019. Beneficial use of dredged materials in geotechnical engineering. In: *Recycling and Reuse Approaches for Better Sustainability*. Springer, Cham, Switzerland, pp.21-38.
- Behnood, A., 2018. Soil and clay stabilization with calcium-and non-calcium-based additives: A state-of-the-art review of challenges, approaches and techniques. *Transportation Geotechnics*, 17, pp.14-32.
- Bilgen, G., 2020a. Utilization of powdered glass as an additive in clayey soils. *Geotechnical and Geological Engineering*, 38(3), pp.3163-3173.
- Bilgen, G., 2020b. Utilization of powdered glass in lime-stabilized clayey soil with sea water. *Environmental Earth Sciences*, 79(19), p.437.
- Bilondi, M.P., Toufigh, M.M., and Toufigh, V., 2018a. Experimental investigation of using a recycled glass powder-based geopolymer to improve the mechanical behavior of clay soils. *Construction and Building Materials*, 170, pp.302-313.
- Bilondi, M.P., Toufigh, M.M., and Toufigh, V., 2018b. Using calcium carbide residue as an alkaline activator for glass powder-clay geopolymer. *Construction and Building Materials*, 183, pp.417-428.
- Blayi, R.A., Sherwani, A.F.H., Ibrahim, H.H., Faraj, R.H., and Daraei, A., 2020. Strength improvement of expansive soil by utilizing waste glass powder. *Case Studies in Construction Materials*, 13, p.e00427.
- Canakci, H., Aram, A.L., and Celik, F., 2016. Stabilization of clay with waste soda lime glass powder. *Procedia Engineering*, 161, pp.600-605.
- Chesner, W.H., Collins, R.J., MacKay, M.H., and Emery, J., 2012. *User Guidelines for Waste and by-Product Materials in Pavement Construction*. Recycled Materials Resource Center, New Hampshire.
- De Jesús Arrieta Baldovino, J., dos Santos Izzo, R., Rose, J.L., and Avanci, M.A., 2020. Geopolymers based on recycled glass powder for soil stabilization. *Geotechnical and Geological Engineering*, 38(4), pp.4013-4031.
- Disfani, M.M., Arulrajah, A., Bo, M.W., and Hankour, R., 2011. Recycled crushed glass in road work applications. *Waste Management*, 31(11), pp.2341-2351.
- Fatta, D., Papadopoulos, A., Avramikos, E., Sgourou, E., Moustakas, K., Kourmoussis, F., Mentzis, A., and Loizidou, M., 2003. Generation and management of construction and demolition waste in Greece-an existing challenge. *Resources, Conservation and Recycling*, 40(1), pp.81-91.
- Fauzi, A., Djauhari, Z., and Fauzi, U.J., 2016. Soil engineering properties improvement by utilization of cut waste plastic and crushed waste glass as additive. *International Journal of Engineering and Technology*, 8(1), pp.15-18.
- Fauzi, A., Rahman, W.M.N.W.A., and Jauhari, Z., 2013. Utilization waste material as stabilizer on kuantan clayey soil stabilization. *Procedia Engineering*, 53, pp.42-47.
- Gangwar, P., and Tiwari, S., 2021. Stabilization of soil with waste plastic bottles. *Materials Today: Proceedings*, 47, pp.3802-3806.
- Güllü, H., Canakci, H., and Al Zangana, I.F., 2017. Use of cement based grout with glass powder for deep mixing. *Construction and Building Materials*, 137, pp.12-20.
- HD 26/06., 2006. *Pavement Design and Maintenance-Foundation. Design Manual for Roads and Bridges (DMRB)*. Vol. 7., The Stationery Office Ltd, London.
- Ibrahim, H.H., Mawlood, Y.I., and Alshkane, Y.M., 2019. Using waste glass powder for stabilizing high-plasticity clay in Erbil city-Iraq. *International Journal of Geotechnical Engineering*, 15(4), pp.496-503.
- Igwe, O., and Adepehin, E.J., 2017. Alternative approach to clay stabilization using granite and dolerite dusts. *Geotechnical and Geological Engineering*, 35(4), pp.1657-1664.
- Ikeagwuani, C.C., and Nwonu, D.C., 2019. Emerging trends in expansive soil stabilisation: A review. *Journal of Rock Mechanics and Geotechnical Engineering*, 11(2), pp.423-440.
- Kumar, C.R., Gadekari, R.S., Vani, G., and Mini, K.M., 2020. Stabilization of black cotton soil and loam soil using reclaimed asphalt pavement and waste crushed glass. *Materials Today: Proceedings*, 24, pp.379-387.
- Más-López, M.I., García del Toro, E.M., Luizaga Patiño, A., and García, L.J.M., 2020. Eco-friendly pavements manufactured with glass waste: Physical and mechanical characterization and its applicability in soil stabilization. *Materials*, 13(17), p.3727.
- Mohajerani, A., Vajna, J., Cheung, T.H.H., Kurmus, H., Arulrajah, A., and Horpibulsuk, S., 2017. Practical recycling applications of crushed waste glass in construction materials: A review. *Construction and Building Materials*, 156, pp.443-467.
- Mujtaba, H., Khalid, U., Farooq, K., Elahi, M., Rehman, Z., and Shahzad, H.M., 2020. Sustainable utilization of powdered glass to improve the mechanical behavior of fat clay. *KSCE Journal of Civil Engineering*, 24(12), pp.3628-3639.
- Naeini, M., Mohammadinia, A., Arulrajah, A., Horpibulsuk, S., and Leong, M., 2019. Stiffness and strength characteristics of demolition waste, glass and plastics in railway capping layers. *Soils and Foundations*, 59(6), pp.2238-2253.
- Nuruzzaman, M., and Hossain, M.A., 2014. Effect of soda lime glass dust on the properties of clayey soil. *Global Journal of Research In Engineering: Civil and Structural Engineering*, 14, pp.17-22.
- Olofinnade, O.M., Ede, A.N., Ndambuki, J.M., Ngene, B.U., Akinwumi, I.I., and Ofuyatan, O., 2018. Strength and microstructure of eco-concrete produced using waste glass as partial and complete replacement for sand. *Cogent Engineering*, 5(1), p.1483860.

- Olufowobi, J., Ogundoju, A., Michael, B., and Aderinlewo, O., 2014. Clay soil stabilisation using powdered glass. *Journal of Engineering Science and Technology*, 9(5), pp.541-558.
- Onyelowe, K., Igboayaka, C., Orji, F., Ugwuanyi, H., and Van, D.B., 2019. Triaxial and density behaviour of quarry dust based geopolymer cement treated expansive soil with crushed waste glasses for pavement foundation purposes. *International Journal of Pavement Research and Technology*, 12(1), pp.78-87.
- Pacheco-Torres, R., and Varela, F., 2020. Mechanical performance of cement-stabilised soil containing recycled glass as road base layer. *Road Materials and Pavement Design*, 21(8), pp.2247-2263.
- Parihar, N.S., Garlapati, V.K., and Ganguly, R., 2019. Stabilization of black cotton soil using waste glass. In: *Handbook of Environmental Materials Management*. Springer, Cham, pp.3099-3114.
- Patel, A., 2019. Soil stabilization. In: *Geotechnical Investigations and Improvement of Ground Conditions*. Elsevier, Amsterdam, pp. 19-27.
- Patel, S.K., and Singh, B., 2017a. Experimental investigation on the behaviour of glass fibre-reinforced cohesive soil for application as pavement subgrade material. *International Journal of Geosynthetics and Ground Engineering*, 3(2), p.13.
- Patel, S.K., and Singh, B., 2017b. Strength and deformation behavior of fiber-reinforced cohesive soil under varying moisture and compaction states. *Geotechnical and Geological Engineering*, 35(4), pp.1767-1781.
- Patel, S.K., and Singh, B., 2019. Shear strength response of glass fibre-reinforced sand with varying compacted relative density. *International Journal of Geotechnical Engineering*, 13(4), pp.339-351.
- Patel, S.K., and Singh, B., 2020. A comparative study on shear strength and deformation behaviour of clayey and sandy soils reinforced with glass fibre. *Geotechnical and Geological Engineering*, 38(5), pp.4831-4845.
- Perera, S.T.A.M., Saberian, M., Zhu, J., Roychand, R., and Li, J., 2022. Effect of crushed glass on the mechanical and microstructural behavior of highly expansive clay subgrade. *Case Studies in Construction Materials*, 17, p.e01244.
- Perera, S.T.A.M., Zhu, J., Saberian, M., Liu, M., Cameron, D., Maqsood, T., and Li, J., 2021. Application of glass in subsurface pavement layers: A comprehensive review. *Sustainability (Switzerland)*, 13(21), p.11825
- Rabab'ah, S., Al Hattamleh, O., Aldeeky, H., and Alfoul, B.A., 2021. Effect of glass fiber on the properties of expansive soil and its utilization as subgrade reinforcement in pavement applications. *Case Studies in Construction Materials*, 14, p.e00485.
- Rai, A.K., Singh, G., and Tiwari, A.K., 2020. Comparative study of soil stabilization with glass powder, plastic and e-waste: A review. *Materials Today: Proceedings*, 32, pp.771-776.
- Ramos, M.R., Melo, V.F., Uhlmann, A., Dedecek, R.A., and Curcio, G.R., 2015. Clay mineralogy and genesis of fragipan in soils from Southeast Brazil. *Catena*, 135, pp.22-28.
- Rashad, A.M., 2014. Recycled waste glass as fine aggregate replacement in cementitious materials based on Portland cement. *Construction and Building Materials*, 72, pp.340-357.
- Rivera, J.F., Cuarán-Cuarán, Z.I., Vanegas-Bonilla, N., and Mejía de Gutiérrez, R., 2018. Novel use of waste glass powder: Production of geopolymeric tiles. *Advanced Powder Technology*, 29(12), pp.3448-3454.
- Sharma, R.K., and Bhardwaj, A., 2018. Effect of Construction Demolition and Glass Waste on Stabilization of Clayey Soil. In: *International Conference on Sustainable Waste Management through Design*, pp.87-94.
- Sharma, R.K., and Hymavathi, J., 2016. Effect of fly ash, construction demolition waste and lime on geotechnical characteristics of a clayey soil: A comparative study. *Environmental Earth Sciences*, 75(5), p.377.
- Shayan, A., and Xu, A., 2004. Value-added utilisation of waste glass in concrete. *Cement and Concrete Research*, 34(1), pp.81-89.
- Siddique, R., 2007. *Waste Materials and by-Products in Concrete*. Springer Science and Business Media, Berlin.
- Siddique, R., 2008. *Waste Glass*. Springer, Berlin, Heidelberg.
- Siyab Khan, M., Tufail, M., and Mateullah, 2018. Effects of waste glass powder on the geotechnical properties of loose subsoils. *Civil Engineering Journal*, 4(9), p.2044.
- Sujatha, E.R., Atchaya, P., Darshan, S., and Subhashini, S., 2020. Mechanical properties of glass fibre reinforced soil and its application as subgrade reinforcement. *Road Materials and Pavement Design*, 22(10), pp.2384-2395.
- Thyagaraj, T., and Zodinsanga, S., 2014. Swell-shrink behaviour of lime precipitation treated soil. *Proceedings of the Institution of Civil Engineers-Ground Improvement*, 167(4), pp.260-273.
- Yaghoubi, E., Yaghoubi, M., Guerrieri, M., and Sudarsanan, N., 2021. Improving expansive clay subgrades using recycled glass: Resilient modulus characteristics and pavement performance. *Construction and Building Materials*, 302, p.124384.
- Zhang, Y., Korkiala-Tanttu, L.K., and Borén, M., 2019. Assessment for sustainable use of quarry fines as pavement construction materials: Part II-stabilization and characterization of quarry fine materials. *Materials*, 12(15), p.2450.

# Magnetic and Electrical Properties of Electrodeposited Nickel Films

Musaab S. Sultan

Department of Networks and Information Security, Technical College of Informatics, University of Akre for Applied Sciences, 42004, Kurdistan Region, Iraq

**Abstract**—Magnetic and electrical properties of nickel (Ni) thin films produced by the electrodeposition technique under a range of growth times (30, 40, and 60 s) are investigated thoroughly using Magneto-Optical Kerr Effect (MOKE) magnetometry and Magneto-Resistance setup, respectively. To deeply understand these properties, the elemental composition, surface morphology, and bulk crystalline structure are analyzed using energy dispersive X-ray spectroscopy (EDS) with high-resolution scanning electron microscopy (HRSEM), grazing incidence X-ray reflectivity (GIXR), and X-ray diffraction measurements, respectively. EDS analysis confirms that these samples are free from impurities and contamination. An increase in coercive fields (~67 Oe) with wide distribution (58–85 Oe) across the film area and a slight variation in the shape of the loops are noticed by decreasing the film growth time (30 s). This is attributed to the deviations in the film surface morphology (defects), as confirmed by HRSEM and GIXR measurements. The angular dependence of the coercivity is nearly constant for each sample and most angles, indicating the similarity in the reversal behavior in such films. The sample resistance is found to be ~20.3  $\Omega$  and ~2.8  $\Omega$  for films with growth times of 40 s and 60 s, respectively. The coercivity of the AMR profiles and MOKE loops is consistent with each other, indicating that the magnetization at the surface performs similarly to that of their bulks. This article gives an indication that Ni films produced by this technique under such conditions are soft at longer deposition times and largely isotropic, which is more preferable in some magnetic applications.

**Index Terms**—Ferromagnetic Nickel films, Electrodeposition, Elemental composition, Magnetic and Electrical properties.

## I. INTRODUCTION

Ferromagnetic thin films and nanostructures of cobalt, nickel (Ni), iron, and their alloys have been the topic of increasing interest for the past 40 years. This is due to their importance in scientific research and their significant demand in many industrial applications, such as giant magneto resistance (Elhoussine, et al., 2005; Karahan, Bakkalo and Bedir, 2007;

Thompson, 2008), magneto optical devices (Lee, et al., 2007; Sun, et al., 2005), and ultra-high density magnetic storage media in hard disk drives (Kunz, et al., 2010), as well as magnetic sensors (MS) (Kunz, et al., 2010; Sun, et al., 2005), and volatile magneto resistive random access memory (VMR-RAM) (Allwood, et al., 2005; Atkinson, Eastwood and Bogart, 2008; Kunz, et al., 2010; Lodder, 2004).

A variety of fabrication systems have been extensively used to produce these magnetic structures. These techniques include sputtering (Donald, 2003; Murakami and Birukawa, 2008; Uehara and Ikeda, 2003), thermal evaporation (Allwood, et al., 2005; Atkinson, Eastwood and Bogart, 2008; Donald, 2003), laser ablation (Donald, 2003), molecular beam epitaxy (Donald, 2003), electroless plating (Nazila and Georges, 2007), and electrodeposition (Peter, 2008; Possin, 1970; Sultan, 2013). Each method, however, has its own benefits and drawbacks. Among these systems, electrodeposition has been proven to be a simple, fast, and low-cost method. It also has benefits regarding reduced limitations on the shape and dimensions of the samples (Sun, et al., 2005).

The crystalline structure of such films has been extensively considered during the past few decades using different analytical techniques, which include transmission electron microscopy with selected area electron diffraction, and X-ray diffraction (XRD) analysis. These studies were carried out by changing the conditions or parameters under which they were produced. For instance, pH (Daimon and Kitakami, 1993; Fert and Piraux, 1999; Kafil, Fernando and Saibal, 2009; Lihu, et al., 2009; Nasirpouri, 2007; Possin, 1970; Rahman, et al., 2004; Ren, et al., 2009), temperature (Kafil, Fernando and Saibal, 2009; Nasirpouri, 2007), concentration of the electrolyte solution, growth voltage (Lihu, et al., 2009), deposition voltage mode (alternating current [AC] or direct current), annealing the samples at high temperatures (Guo, et al., 2003; Koohbor, et al., 2012; Qin, et al., 2002), and using a permanent magnet during the deposition process (Aravamudhan, et al., 2009; Coey and Hinds, 2001; Das, et al., 2008; Jin, et al., 2003; Sun and Chen, 2009; Tian, et al., 2005; 2008) are thoroughly discussed.

The magnetic properties of such ferromagnetic thin films were also investigated using a range of characterization systems, which include superconducting quantum interference device, vibrating sample magnetometry, torque



magnetometry, and alternating gradient magnetometry, as well as magnetic force microscopy. On the other hand, the Magneto-Optical Kerr Effect (MOKE) setup has also been used to demonstrate the magnetization behavior of a range of magnetic thin films (Azzawi, et al., 2016; Ganguly, et al., 2015; Michelini, et al., 2002), nanodots (Heyderman, et al., 2004), nanowires (Allwood, et al., 2003; Bryan, Atkinson and Allwood, 2006; Maruyama, et al., 1997), and more complex geometric shapes of nanostructures (Chen, et al., 2010; Das, et al., 2016; Eider, et al., 2016; Ester, et al., 2015; Lupu, Lostun and Chiriac, 2010; Philip, et al., 2016; Sharma, et al., 2009; Sultan, et al., 2012; Sultan, 2017a, 2017b; 2018; Vega, et al., 2012). However, in this setup, the reflected light is proportional to the amount of magnetization within the surface of the film, which depends on the polarization rotation of a polarized laser light following its reflection from a ferromagnetic sample to the skin depth (Allwood, et al., 2003). This is due to the absorption of the laser light in the medium, which is called the optical skin depth (Allwood, et al., 2003; Lupu, Lostun and Chiriac, 2010).

Magneto-Resistance (MR) setup is a powerful system adopted by many investigators to gain insight into the magnetic and electrical transport properties of ferromagnetic thin films (Alcer and Atkinson, 2017; Tokaç, et al., 2015), individual rectangular nanowires (Fernández-Pacheco, et al., 2008; Oliveira, et al., 2010; Oliveira, Rezende, and Azevedo, 2008 Tokaç, et al., 2015), rod nanowires embedded in their membranes (Fert and Piraux, 1999; Ferré, et al., 1997; Pignard, et al., 2000), and isolated rod wires (Rheem, 2007a; 2007b; 2007c; 2007d; Sultan, 2017) using the Anisotropic Magneto Resistance (AMR) effect. This is due to the sensitivity of AMR to the relative direction of the magnetic spins within the bulk of such materials with respect to the applied electrical current. Where the electrical resistance is at its highest value when the magnetic spins are parallel to the applied electrical current and at its lowest value when they are orthogonal to each other. This behavior is related to the anisotropic property of the electrons in the spin-orbit coupling, as investigated in further detail elsewhere (Cullity and Graham, 2009; Jiles, 1998).

Nevertheless, an understanding of the magnetic and electrical transport properties of electrodeposited

ferromagnetic thin films and nanostructures using surface and bulk characterization techniques such as MOKE and MR setup is crucial from a scientific and technological point of view. Therefore, in this article, ferromagnetic Ni thin films were prepared under different growth times using electrodeposition technique, and then their magneto- and electrotransport behavior was analyzed at room temperature using longitudinal MOKE magnetometry and MR setup, respectively. To deeply understand these properties, the chemical composition, surface structural variations (defects or imperfections), and bulk crystalline structure of such Ni films were thoroughly analyzed across the whole sample area.

## II. EXPERIMENTAL DETAILS

Ferromagnetic Ni thin films with three different thicknesses were deposited onto Au/Cr/SiO<sub>2</sub>/Si chips using the electrodeposition technique. The substrates (Si/SiO<sub>2</sub>) were first thoroughly cleaned using acetone and isopropanol alcohol (IPA) and then dried with argon gas. The area of these substrates was approximately 2.4 × 22 mm<sup>2</sup>. A gold (Au) film of 99.99% purity was placed onto these substrates with a thickness of ~10 nm on the SiO<sub>2</sub> side using thermal evaporation technique. To increase the adhesion of the gold film to the substrate, chromium (Cr) was deposited before the gold deposition of a thickness of ~3 nm. A schematic diagram of the gold-coated substrate (Au/Cr/SiO<sub>2</sub>/Si) is shown in Fig. 1a.

These substrates were then used as cathodes (working electrodes) in the electrochemical cell, which is shown schematically in Fig. 1b with the gold-coated side facing toward the platinum counter electrode (anode) and electrically connected to the external circuit by a copper wire using silver paste. The reference electrode had a standard voltage of around 0.23 V and it was Ag/AgCl in saturated KCl solution.

To create Ni films, the chemical solution was ~0.57 M of NiSO<sub>4</sub>, ~0.32 M of H<sub>3</sub>BO<sub>3</sub>, and the hydrogen ion concentration in the electrolyte solution was fixed at about 3.5–4. The voltage applied between the reference and counter electrodes was around -0.84 V. This voltage was selected

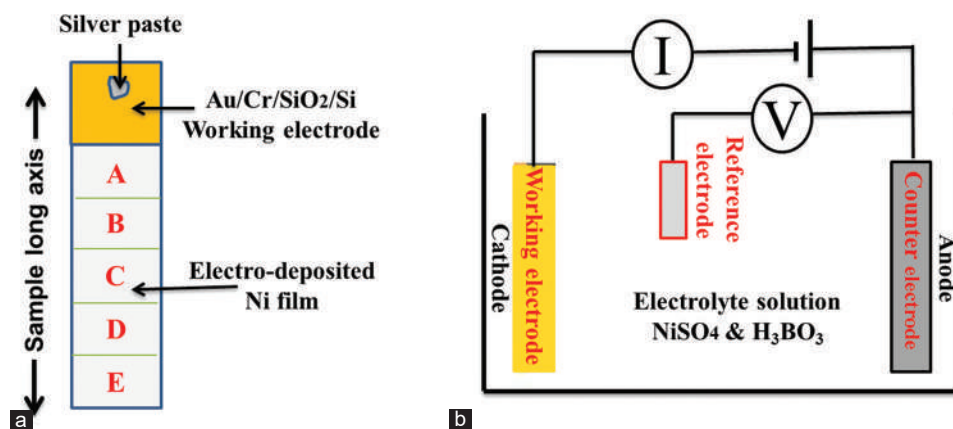


Fig. 1. (a) Gold-coated substrate (Au/Cr/SiO<sub>2</sub>/Si) and (b) electrochemical cell with the gold-coated side (working electrode) facing toward the platinum counter electrode and electrically connected to the external circuit by a copper wire using silver paste.

according to a linear sweep voltammetry result. To prepare different thicknesses of Ni film, various deposition times of 30 s, 40 s, and 60 s were utilized. These growth times were chosen arbitrarily because most magnetic devices use ultra-thin ferromagnetic films. Once the electrodeposition was finished, the chips were washed thoroughly in distilled water, followed by IPA, and blown with argon gas. Further, information on the deposition procedure using this technique can be found in (Das, et al., 2008; Possin, 1970; Sultan, et al., 2012; Sultan, 2017a; 2017b; 2018).

Now, to analyze the elemental composition of these samples, energy-dispersive X-ray spectroscopy (EDS) analysis on the Hitachi-SU 70 was used. Whereas, to study the film roughness (surface morphology) and film thickness, high-resolution scanning electron microscopy (HRSEM) and grazing incidence X-ray reflectivity (GIXR) measurements were established, respectively. Finally, to measure the bulk crystalline structure of such thin films, the XRD system equipped in the Jordan Valley Bede diffractometer D1 was utilized. For more theoretical (Bowen and Tanner, 2006; Brundle, Evans and Wilson, 1992; Cullity and Stock, 2001; Cullity and Graham, 2009) and experimental (Bede REFS, 2007; Bowen and Mendis, 2012; Jordan Valley, 2007; 2008; Parratt, 1954; Wormington, et al., 1999) details on these analytical investigative techniques, please refer to the references (Bede REFS, 2007; Bowen and Tanner, 2006; 2012; Brundle, Evans and Wilson, 1992; Cullity and Stock, 2001; Cullity and Graham, 2009; Jordan Valley, 2007; 2008; Parratt, 1954; Wormington, et al., 1999).

The magnetic analyses were performed at room temperature using a highly sensitive longitudinal MOKE setup. In this technique, the laser light was focused onto the chip with a spot radius of around 2.5–3  $\mu\text{m}$ . The change in the angle of reflected light (Kerr signal) is proportional to the longitudinal component of the magnetic state within the film surface plane.

All the chips were placed on a movable stage holder, which was located between the two poles of an AC electromagnet coil with a magnetic strength of  $\pm 450$  Oe, at an angle of  $\sim 45^\circ$  with respect to the optical axis. To distinguish the real measurements from the background noise, all the MOKE measurements were done for repeated loops averaged over 3.5 min to satisfactorily reduce the noise and increase the reflected Kerr signal. The obtained hysteresis loops were the reflected Kerr light against the externally applied magnetic

field. More theoretical (Brundle, Evans and Wilson, 1992; Cullity and Graham, 2009; Jiles, 1998) and experimental (Eastwood, 2009; Lupu, Lostun and Chiriac, 2010; Sultan, et al., 2012; Sultan, 2017a; 2017b; 2018) details on the MOKE setup and its measurements can be found elsewhere.

The electrical and magnetic transport behavior of such films was also investigated using a room-temperature Magneto-Resistance setup, which is schematically shown in Fig. 2. This system was controlled by a digital computer using the LabVIEW program. The chips were placed on a rotation step between the pole pieces of an electromagnet with a maximum magnetic field of around  $\pm 1$  kOe and covered with an electrically and thermally shielded cover.

Fig. 3 shows a schematic diagram and a photograph of the sample holder of the four-point probe used in this research. It consisted of four equally spaced pieces of phosphor bronze plates (plated with gold) with a finite diameter. These tips were supported by springs on the other end to reduce film damage during the measurements. Further, details on the MR setup and its measurements can be found in (Armstrong, 2010; Brundle, Evans and Wilson, 1992; Cullity and Graham, 2009; Jiles, 1998; Sultan, 2017).

To perform the electrical measurements, the current was applied to the outer probes using a high-impedance current supply, whereas a voltmeter was connected to measure the voltage across the inner probes. The inner probe spacing was  $\sim 0.7$  cm, whereas the outer probe spacing was  $\sim 1.2$  cm, as schematically shown in Fig. 3. These measurements were performed using an electrical direct current of around 1 mA at room temperature. However, using higher electrical currents might increase the joule heating and destroy the sample.

The applied magnetic field was scanned between +1 kOe and  $-1$  kOe. The chip carrier could be rotated at an angle between  $0^\circ$  and  $90^\circ$  with respect to the external magnetic field, allowing the investigations to be carried out at different angles. Once the current was applied to the sample, 50 measurements would be made and averaged to determine the electrical resistance. For each chip, the measurements were repeated four times to gain insight into the signal and noise background.

### III. RESULTS AND DISCUSSION

The following subsections investigate the magneto- and electro-transport properties of electrodeposited Ni films

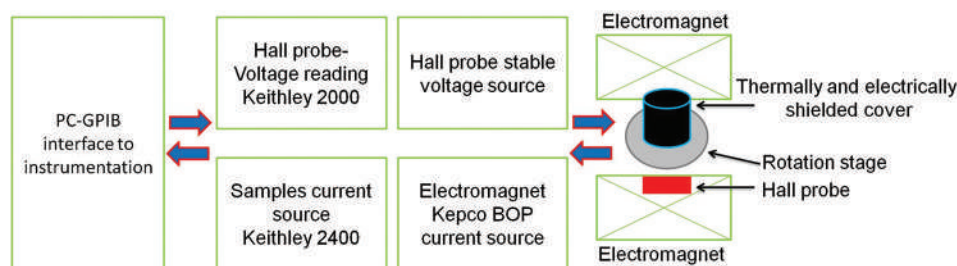


Fig. 2. A block diagram of the magneto resistance setup used in this article to discuss the electro- and magneto-transport properties of electrodeposited Ni thin films. Modified from (Armstrong, 2010).

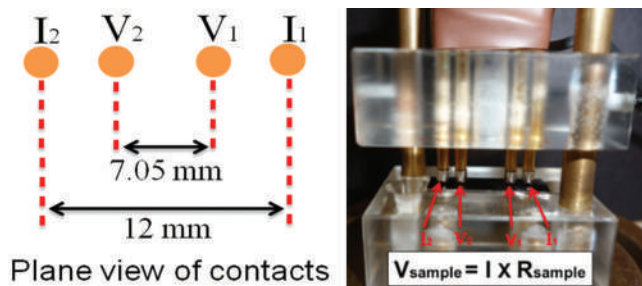


Fig. 3. A schematic diagram of the plane view of contacts for a four-point probe and a photograph of its sample holder. It consists of four equally gold-plated tips with a finite diameter.

prepared under different growth times using MOKE and MR setups, respectively, which are the main purpose of this study (Kacel, et al., 2018; Parlaka, et al., 2015; Rizwan, et al., 2021). To precisely analyze these properties, the chemical composition, surface morphology, thickness, and bulk crystalline structure of such thin films were firstly investigated using EDS with HRSEM, GIXR, and XRD measurements, respectively.

#### A. Elemental Composition, Surface, and Bulk Structure Analyses

To ascertain the elemental composition of such Ni films, all the samples were measured at different arbitrary locations (A, B, C, D, and E shown in Fig. 1a) using EDS analysis. These analyses were performed with support from (Bowen and Mendis, 2012). An example of the EDS measurement of Ni film prepared under a 40 s deposition time is shown in Fig. 4. The identification of the peaks is related to Ni, Au, O, and Si. The Au and Si contents reflect the elemental composition of the substrate.

A small amount of oxygen was noticed in most of the samples and might have been formed by oxidation during or after the electrodeposition. Significantly, these analyses confirm that these samples are free from impurities and contamination, which has been observed elsewhere (Das, et al., 2008).

Now, to investigate the surface morphology of such Ni samples, detailed of HRSEM imaging was undertaken. Micrographs example at three different locations on the surface of Ni film that was produced under 40 s deposition time is shown in Fig. 5. These measurements demonstrated that there were defects or imperfections of different sizes distributed randomly on these specimens. These defects were found to be more remarkable at lower film growth times. This is because decreasing the film growth time will decrease the film thickness which in turn increases the defects and non-uniformity. These imperfections are more likely to occur as a result of gas bubbles occurring during the electrodeposition process or might be due to the inhomogeneous density of the electrolyte solution throughout the electrochemical cell during the fabrication process. Thus, the Ni films prepared by this technique under such conditions are more likely to be non-uniform and have an irregular surface morphology. This result will be discussed in more detail in other research using other compositions of ferromagnetic thin films.

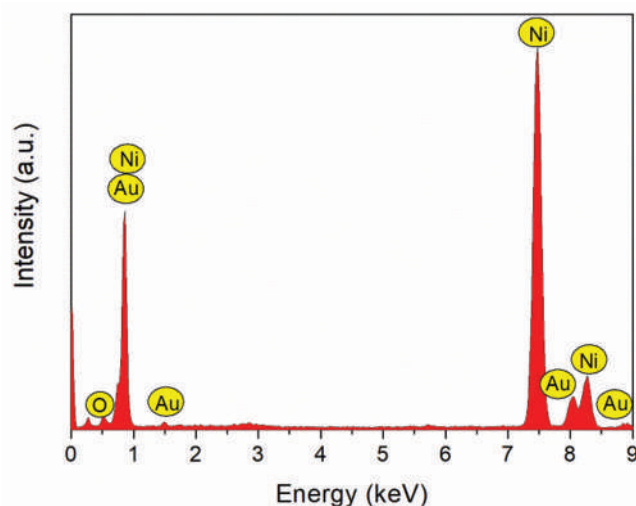


Fig. 4. An example of energy-dispersive X-ray spectroscopy measurement of nickel film prepared under a 60 s deposition time (Bowen and Mendis, 2012).

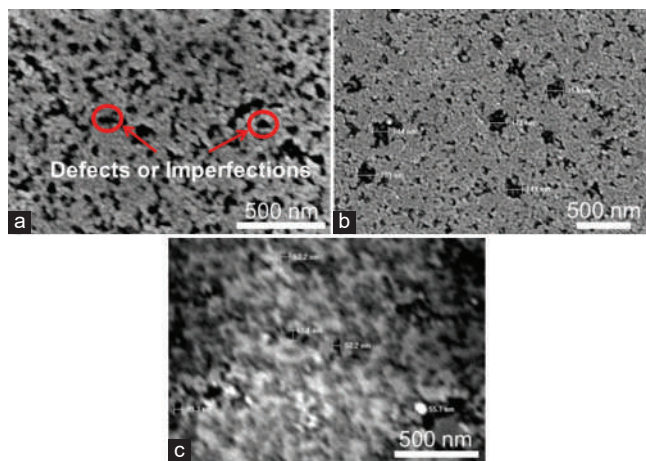


Fig. 5. Examples of high-resolution scanning electron microscopy micrographs showing the surface of nickel film prepared under 40 s deposition time at (a-c) three different locations.

In spite of the surface non-uniformity of these films, which was beyond the limit of the GIXR technique, the structural surface variations were confirmed, as demonstrated in Fig. 6, which shows the true specular and simulated scans of electrodeposited Ni films with deposition times of (a) 40 s and (b) 60 s. The true specular scan was fitted using Bede REFS simulations program (Bede REFS, 2007) which is based on the Parratt recursive formulism (Cullity and Stock, 2001). Using this simulation package, the thickness was found to be ~22, ~31, and ~228 nm for Ni films produced at 30 s, 40 s, and 60 s, respectively. The details of this simulation package and GIXR system can be found elsewhere (Bowen and Tanner, 2006; Bowen and Mendis, 2012; Brundle, Evans and Wilson, 1992; Cullity and Stock, 2001; Jordan Valley, 2007; 2008; Parratt, 1954; Wormington, et al., 1999).

Fig. 7 shows an example of XRD pattern of Ni film fabricated under a 60 s deposition time. As expected (Jin, et al., 2003; Rheem, et al., 2007), the crystalline structure of



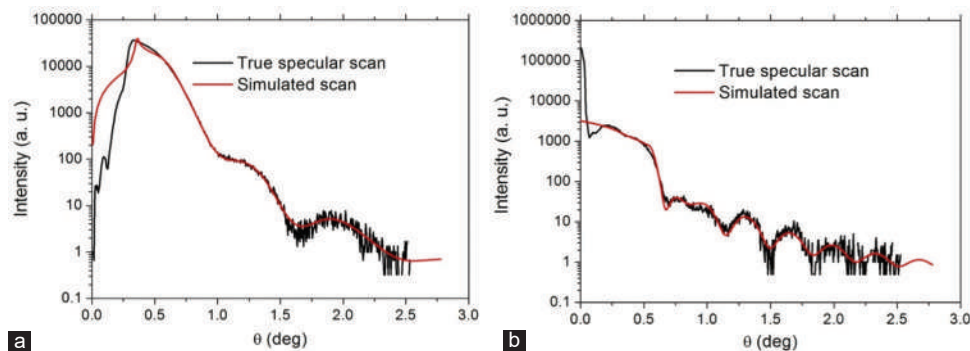


Fig. 6. True specular and simulated scans of electrodeposited nickel films with deposition times of (a) 40 s and (b) 60 s.

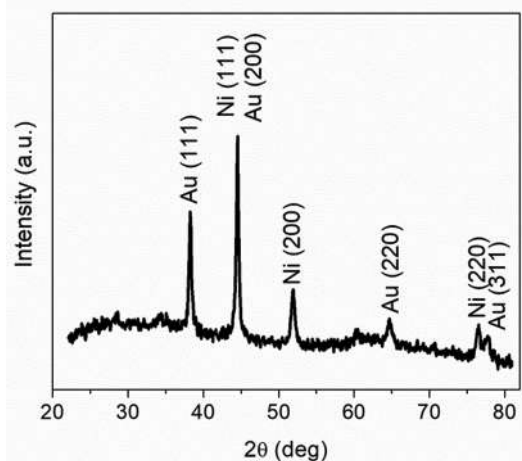


Fig. 7. Example of an X-ray diffraction pattern of the nickel film prepared at 60 s deposition time.

such films is FCC structure, where the peaks correspond to the FCC phase of Ni and the FCC of the Au-coated substrate, as compared with the standard reference patterns (Inorganic Crystal Structure Data base [ICSD]) (Mark, 2023).

From Fig. 7, it is also clear that there are no peaks related to the Si, SiO<sub>2</sub>, and Cr elements due to the dominance of the amorphous SiO<sub>2</sub> layer on the behavior, which is in full agreement with the literature (Jian, et al., 2005). Furthermore, the peaks are quite sharp, indicating that the crystallites within such films are relatively large (Bowen and Tanner, 2006; Brundle, Evans and Wilson, 1992; Cullity and Stock, 2001). The intensity of the peaks is related to the presence of a preferred crystallite orientation or the sample thickness. The calculated intensity ratio of the Ni peaks shows that these samples have no preferred orientation in any direction. This result means that there is no effect of crystallites on the magnetization behavior, as will be seen in the following discussion.

### B. Moke Measurements – Magnetic Properties

To discuss the distribution of magnetization across the whole sample area and to deeply understand the angular dependence of the magnetic state of such films, MOKE measurements were carried out at different arbitrary places (A, B, C, D, and E shown in Fig. 1a) on these films when the magnetic field was applied at two orthogonal angles with respect to the chip long axis (defined in Fig. 1a).

In general, square hysteresis loops were obtained from most of these studies, with very small local variations. Typical examples of MOKE loops obtained from such measurements are shown in Fig. 8. The similarity in the hysteresis shape among the majority of cases indicated an isotropic magnetic nature in the surface plane of such films. The reversal behavior was sharper for samples with higher growth times and more rounded for samples with lower deposition times.

To understand in more detail the magnetic state in these films, distribution histograms of the coercive field were obtained by repeating the measurements at many different positions on these films, as shown in Fig. 9a. The average coercivity as a function of film growth time is also shown in Fig. 9b. A reduction in coercivity was observed with increased growth time. As an example, the coercivity peaked around ~67 Oe, ~65 Oe, and ~35 Oe for samples with growth times of 30 s, 40 s, and 60 s, respectively. It has also been noticed from Fig. 9 that there is a broad distribution of coercivity throughout the film area of the same sample, which decreases considerably for samples with longer growth times. As an example, the distribution of coercivity was found to range between approximately 24–35 Oe and 58–85 Oe for the samples with the longest (60 s) and shortest (30 s) deposition times, respectively.

The coercivity distributions obtained here may reasonably be attributed to the changes in the film surface morphology discussed earlier in the previous section by HRSEM and GIXR measurements. This result is in full agreement with the result reported in the literature (Oliveira, Rezende, and Azevedo, 2008), which showed that the presence of surface structural variations (defects or imperfections) can act as pinning centers during the reversal, distort the spin configuration structure, and give different values of coercive field (Oliveira, Rezende, and Azevedo, 2008).

Hence, the surface structural variations in the samples under investigation may contribute to the change observed in the coercive field and the shape of the MOKE hysteresis loops. Fig. 9b clearly shows that decreasing the growth time decreases the film thickness, which, in turn, increases the film surface structure variations and non-uniformity and ultimately increases the pinning sites and coercive fields.

To understand the magnetic reversal in such ferromagnetic thin films, the average coercivity as a function of sample

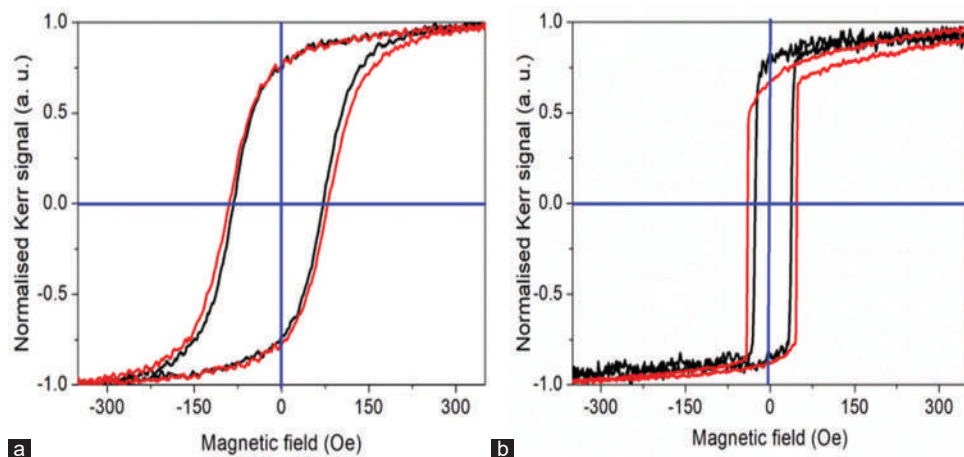


Fig. 8. Normalized Magneto-Optical Kerr Effect hysteresis loops of electrodeposited nickel films prepared under (a) 30 s and (b) 60 s growth times and measured along two perpendicular in-plane axes.

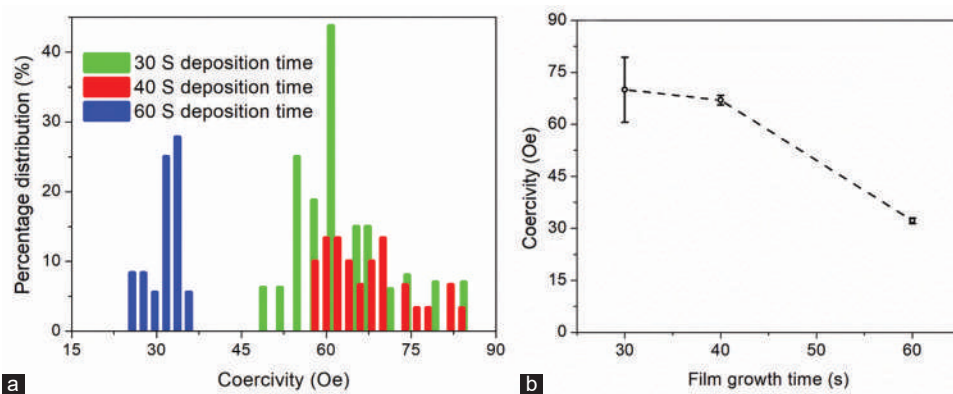


Fig. 9. (a) Distribution histogram of the coercive field acquired from repeating Magneto-Optical Kerr Effect examinations on the electrodeposited nickel films at different arbitrary positions; and (b) average coercive field as a function of deposition time.

long axis angles with respect to the externally applied magnetic field is plotted in Fig. 10. Clearly, for each chip, the coercive field was nearly constant (dash line) for most angles discussed here, indicating the similarity in the magnetization reversal in these samples. The similarity in the reversal behavior, however, might be due to the lack of preferred orientation of the crystallites within such Ni thin films, as confirmed by the XRD measurements stated previously. However, the data for the shortest deposition time (30 s) demonstrate an increase in coercive field with a broader distribution of different angles. This may also reflect the differences in surface morphology discussed earlier. Nonetheless, the results acquired here give an indication that these films are soft at longer growth times and are generally isotropic.

Now, to gain a fuller understanding of the magnetic properties of such films, the coercivity acquired here was compared with other results reported in the literature discussing isolated Ni and NiFe nanowires prepared under the same conditions and measured also by MOKE magnetometry (Sultan, et al., 2012; Sultan, 2017a; 2017b; 2018), a large difference was noticed. This large difference is quite acceptable since the crystallites within such ferromagnetic thin films have no preferred orientations and

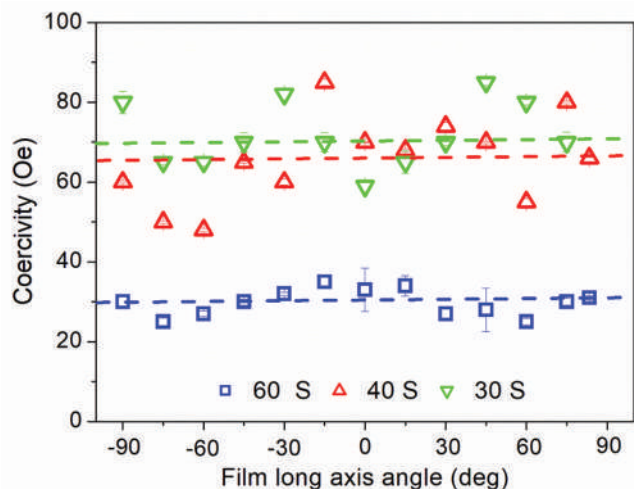


Fig. 10. Derived coercivity from the loops obtained from Magneto-Optical Kerr Effect measurements at various positions on the electrodeposited Ni films (with different deposition times as indicated in the figure title) as a function of the sample long axis angle with respect to the applied magnetic field. The dashed lines provide a guide for the eye.

have no shape anisotropy dominating the behavior as in the nanowires.

*C. MR Measurements – Electrical and Magnetic Properties*

The electro- and magneto-transport measurements of these films were implemented by applying an external magnetic field in two orthogonal directions with respect to the current flow (sample long axis) using a four-point probe arrangement (Fig. 3) after connecting these samples to the external electrical circuit. The measured electrical resistance,  $R_o$ , (overall sample resistance) at zero field for these films with deposition times of 40 s and 60s, was  $\sim 26.4 \Omega$  and  $\sim 3.4 \Omega$ , respectively, and the behavior was ohmic. The electrical resistance of such films is expected to be relatively lower than that of individual nanowires (see, for example, References [Cullity and Graham, 2009; Rheem, et al., 2007]). This is due to the large sizes of the samples investigated here with respect to their counterpart’s ferromagnetic nanowires and the increased volume-to-surface ratio. This resistance, however, is due to the sample bulk resistance,  $R_s$ , connected wire resistance,  $R_w$ , and contact resistance,  $R_c$ .

The value of the sample resistance,  $R_s$ , depends on various parameters, such as the dimension of the chip, the scattering rates of the electrons with phonons, defects, and grain boundaries within the films (Rheem, et al., 2007). On the other hand, the connection wire resistance,  $R_w$ , appears as a result of the electrical connection of these films with the external electrical circuitry. This electrical resistance is extremely small and can be neglected. Finally, the contact resistance,  $R_c$ , arises from the connections of the four probes with the samples. This resistance, however, arises as a result of the presence of hydroxide or oxide layers or any other residual impurities on these chips, as discussed elsewhere. Thus, the overall electrical resistance,  $R_o$ , in such films can be written as:

$$R_o = R_s + R_w + R_c \quad (1)$$

The sample resistance,  $R_s$ , was estimated approximately depending on the film size and their bulk resistivity ( $\rho = \sim 6.99 \times 10^{-8} \Omega \cdot \text{cm}$  at room temperature) using the following relation (Cullity and Graham, 2009; Helmenstine, 2020; Jiles, 1998; Sultan, 2017):

$$R_s = \rho L/A \quad (2)$$

where,  $L$  and  $A$  are the length and cross-sectional area of the Ni film, respectively. Accordingly, the calculated sample resistance was found to be  $\sim 20.3 \Omega$  and  $\sim 2.8 \Omega$  for films

with growth times of 40 s and 60 s, respectively. Comparing this theoretical result with the experimental result discussed earlier from MR measurements, an agreement is clearly seen, which is quite reasonable since the rest of the electrical resistances belonged to the contact resistance,  $R_c$ , and wire resistance,  $R_w$ .

Fig. 11 shows typical results obtained from these MR measurements of Ni films with deposition times of (a) 40 s and (b) 60 s by applying the external magnetic field in longitudinal (parallel) and transverse (normal) orientations to the sample long axis. These experiments were performed 4 times by sweeping the external magnetic field in both directions, as shown in Fig. 11. From these MR measurements, it is interesting to note the excellent quality of the signal-to-noise ratio. For both samples and both longitudinal and transverse profiles, two regions were recognized (Fig. 11). At high magnetic field strengths  $\geq \pm 150$  Oe, the resistance shows saturation, indicating that the spins within these films are directed normal (with minimum electrical resistance) and parallel (with maximum electrical resistance) to the applied external magnetic field. At magnetic fields  $\leq \pm 150$  Oe, the resistance falls rapidly, followed by positive jumps in the parallel directions, and jumps up, followed by a drop in the orthogonal directions. The variations in electrical resistance are symmetric about the zero magnetic fields when changing the magnetic field direction.

Comparing the electrical resistance of longitudinal and transverse measurements with each other at maximum field strengths (saturation), a reduction in the saturated resistance was seen as the implementation changed from parallel to perpendicular directions. This can be understood in terms of the magnetic spin orientations within these films. When the spins lie parallel (normal) to the film’s long axis, the magnetization will be collinear (orthogonal) to the current flow, giving maximum (minimum) electrical resistance. This is the maximum and minimum electrical resistance relative to the current and magnetic moments in the AMR effect (Cullity and Graham, 2009; Armstrong, 2010; Jian, et al., 2005).

The difference in resistance,  $\delta R$ , is defined as the changes between the resistance when the external applied magnetic field is longitudinal,  $R_L$ , and transverse,  $R_T$ , to the current flow (demonstrated in Fig. 11b), and it is given by (Brundle, Evans and Wilson, 1992; Sultan, 2013):

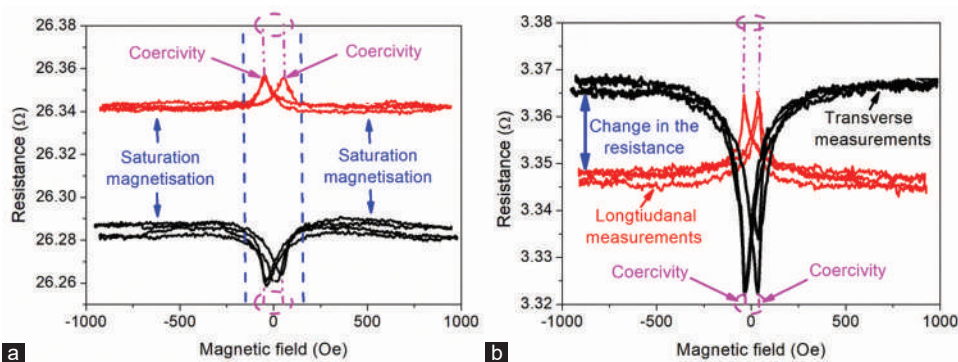


Fig. 11. Magneto-resistance profiles obtained from electrodeposited nickel samples with (a) 40 s and (b) 60 s deposition times by applying the external magnetic field either longitudinally (parallel) or transversely (perpendicular) to the current flow.

$$\delta R = R_{\parallel} - R_{\perp} \quad (3)$$

The difference in resistance,  $\delta R$ , for the sample with a 40 s deposition time was found to be 0.06  $\Omega$ , which is larger than the difference in resistance (0.02  $\Omega$ ) of the films with a 60 s deposition time.

Since the electrical resistance in the absence of the external magnetic field depends on the structure of the domain, which depends on the magnetic history of the sample, it is more suitable to use the following equation to show the average electrical resistance (Armstrong, 2010):

$$R_{ave} = \frac{1}{3}(R_{\parallel} + 2R_{\perp}) \quad (4)$$

The  $\delta R$  of a ferromagnetic sample on applying an external magnetic field is usually expressed as  $\delta R/R_{ave}$ , and is known as the AMR ratio, which is given by combining equations 3 and 4 (Yoo, et al., 2006):

$$\frac{\delta R}{R_{ave}} = \frac{R_{\parallel} - R_{\perp}}{\frac{1}{3}(R_{\parallel} + 2R_{\perp})} \quad (5)$$

Thus, the AMR ratio was calculated here using equation 5, and it was found to be  $\sim 0.7$  and  $\sim 1.8$  for samples with 40 s and 60 s growth times, respectively. The difference between these values can be attributed to the difference in film thickness. Comparing the AMR ratio obtained here with the AMR ratio reported in the literature for individual nanowires with the same composition and prepared under similar conditions, an agreement was noticed (Yoo, et al., 2006).

As discussed earlier, the average coercive field acquired from MOKE hysteresis loops of Ni films of 40 s and 60 s deposition times (Fig. 9) was  $\sim 67$  Oe and  $\sim 35$  Oe, respectively. Comparing these findings with the coercivities extracted from the magnetic fields at which the peaks (troughs) happened in the MR profiles (Fig. 11), an excellent agreement was found, indicating that the magnetic state at the surface of such films behaves similarly to that of their bulks. This result is quite reasonable since the thickness of these films is extremely thin. Finally, studying the saturation magnetization and annealing the samples under different temperatures (Kamrul and Johurul, 2015) are very important and needs further research.

#### IV. CONCLUSIONS

To sum up, the magnetic and electrical properties of electrodeposited Ni thin films prepared at different growth times were studied in detail. The chemical composition of these films was analyzed using EDS measurements, which confirm that these films are free from impurities and contamination. HRSEM measurements indicated the existence of defects or imperfections distributed randomly on these samples. These imperfections were attributed to the inhomogeneous density of the electrolyte solution throughout the electrochemical cell or to the occurrence of gas bubbles during the fabrication process. Thus, the Ni films prepared using this technique under such conditions is more likely to be non-uniform and have an irregular surface morphology. XRD analysis showed that

the crystalline structure of such films is FCC with quite large crystallites of no preferred orientation in any direction.

MOKE measurements were executed at many arbitrary locations on these films by applying the magnetic field at different angles with respect to the sample's long axis. Square loops were noticed with a high squareness ratio. The similarity in the hysteresis shape between the two orthogonal in-plane axes in most measurements indicates an isotropic magnetic nature in such films. This result was attributed to the lack of preferred orientation of the crystallites within such samples, as confirmed by XRD measurements. The coercivity falls by increasing the film growth time ( $\sim 67$  Oe to  $\sim 35$  Oe for samples with growth times of 30–60 s, respectively). This was attributed to a reduction in surface non-uniformity on increasing the film thickness, which, in turn, minimizes the pinning sites and coercive fields. The experimental and theoretical resistances were in agreement with each other and were found to be around 20.3  $\Omega$  and 2.8  $\Omega$  for films with growth times of 40 s and 60 s, respectively. The difference in resistance,  $\delta R$ , for the sample with a 40 s deposition time was found to be  $\sim 0.06$   $\Omega$ , which is larger than the difference in resistance  $\sim 0.02$   $\Omega$  of the films with a 60 s deposition time. This result was in full agreement with the literature. The coercivities acquired from MR measurements were consistent with the coercivities obtained from MOKE measurements, indicating that the magnetization at the surface of such films behaves similarly to that of their bulks.

#### ACKNOWLEDGMENTS

The author wishes to express his deep sense of appreciation and many thanks to Prof. Dr. Del Atkinson at the Physics Department, Durham University, England, for his valuable assistance throughout this work. Acknowledgments are also due to Dr. Jennifer King, Dr. Bipul Das, and Prof. Dr. Kalyan Mandal for providing these Ni samples.

#### REFERENCES

- Aler, D., and Atkinson, D., 2017. The role of mesoscopic structuring on the intermixing of spin-polarised conduction channels in thin-film ferromagnets for spintronics. *Nanotechnology*, 28(37), p.375703.
- Allwood, D.A., Xiong, G., Cooke, M.D., and Cowburn, R.P., 2003. Magneto-optical Kerr effect analysis of magnetic nanostructures. *Journal of Physics D: Applied Physics*, 36, p.2175.
- Allwood, D.A., Xiong, G., Faulkner, C.C., Atkinson, D., Petit, D., and Cowburn, R.P., 2005. Magnetic domain-wall logic. *Science*, 309, p.1688.
- Aravamudhan, S., Singleton, J., Goddard, P.A., and Bhansali, S., 2009. Magnetic properties of Ni-Fe nanowire arrays: Effect of template material and deposition conditions. *Journal of Physics D: Applied Physics*, 42, p.115008.
- Armstrong, H., 2010. *Magnetoresistance Measurement System Instruction Manual V3.0*. Durham University, Physics Department, Durham, England [Last accessed on 2023 Nov 28].
- Atkinson, D., Eastwood, D.S., and Bogart, L.K., 2008. Controlling domain wall pinning in planar nanowires by selecting domain wall type and its application in a memory concept. *Applied Physics Letters*, 92(2), p.022510.
- Azzawi, S., Ganguly, A., Tokaç, M., Rowan-Robinson, R.M., Sinha, J., Hindmarch, A.T., Barman, A., and Atkinson, D., 2016. Evolution of damping

- in ferromagnetic/nonmagnetic thin film bilayers as a function of nonmagnetic layer thickness. *Physical Review B*, 93(5), p.054402.
- Bede REFS., 2007. (*Version 4.5*): *User Manual, Bede PLC, Durham*. Available from: <https://jordanvalleyplc> [Last accessed on 2023 Nov 28].
- Bowen, K.D., and Tanner, B.K., 2006. *X-Ray Metrology in Semiconductor Manufacturing*. Taylor and Francis Group, LLC, United Kingdom.
- Bowen, L., and Mendis, B., 2012. *Electron Microscopy Facility. Physics Department, Durham University, U.K.*, in Private Communication.
- Brundle, R.C., Evans, C.A. Jr., and Wilson, S., 1992. *Encyclopaedia of Materials Characterization*. Butterworth-Heinemann, a division of Reed publishing Inc., Oxford.
- Bryan, M.T., Atkinson, D., and Allwood, D.A., 2006. Multimode switching induced by a transverse field in planar magnetic nanowires *Applied Physics Letters*, 88(3), p.032505.
- Chen, T.C., Kuo, C.Y., Mishra, A.K., Das, B., and Wu, J.C., 2015. Magnetic domain wall motion in notch patterned permalloy nanowire devices. *Physica B: Condensed Matter*, 476, p.161.
- Coe, J.M.D., and Hinds, G., 2001. Magnetic electrodeposition. *Journal of Alloys and Compounds*, 326(1-2), pp.238-245.
- Cullity, B.D., and Graham, C.D., 2009. *Introduction to Magnetic Materials*. 2<sup>nd</sup> ed., John Wiley and Sons Inc., Hoboken, New Jersey.
- Cullity, B.D., and Stock, S.R., 2001. *Elements of X-Ray Diffraction*. 3<sup>rd</sup> ed., Prentice-Hall Inc., Hoboken.
- Daimon, H., and Kitakami, O., 1993. Magnetic and crystallographic study of Co electrodeposited alumite films. *Journal of Applied Physics*, 73(10), p.5391.
- Das, B., Chen, T.C., Shiu, D.S., Lance, H., and Wu, J.C., 2016. Differential domain wall propagation in Y-shaped permalloy nanowire devices. *World Science*, 6(1), p.1650006.
- Das, B., Mandal, K., Sen, P., and Bandopadhyay, S.K., 2008. Effect of aspect ratio on the magnetic properties of nickel nanowires. *Journal of Applied Physics*, 103, p.013908.
- Donald, M.M., 2003. *The Foundations of Vacuum Coating Technology*. Noyes Publications William Andrew Publishing Norwich, New York.
- Eastwood, D., 2009. *Technical Note DSE4, Durham Longitudinal Focused MOKE: Operation Guide*. Physics Department, Durham University, UK.
- Eider, B., Cristina, B., Miriam, J., Manuel, V., and Agustina, A., 2016. Domain wall pinning in FeCoCu bamboo-like nanowires. *Scientific Reports*, 6, p.29702.
- Elhoussine, F., Vila, L., Piraux, L., and Faini, G., 2005. Multiprobe perpendicular giant magnetoresistance measurements on isolated multilayered nanowires. *Journal of Magnetism and Magnetic Materials*, 290-291, pp.116-119.
- Ester, M.P., Cristina, B., del Real, R.P., and Manuel, V., 2015. Vortex domain wall propagation in periodically modulated diameter FeCoCu nanowire as determined by the magneto-optical Kerr effect. *Nanotechnology*, 26, p.461001.
- Fernández-Pacheco, A., De Teresa, J.M., Córdoba, R., and Ibarra, M.R., 2008. Magnetotransport properties of high-quality cobalt nanowires grown by focused-electron-beam-induced deposition. *Journal of Physics D: Applied Physics*, 42, p.055005.
- Fernández-Pacheco, A., De Teresa, J.M., Szkudlarek, A., Córdoba, R., Ibarra, M.R., Petit, D., O'Brien, L., Zeng, H.T., Lewis, E.R., Read, D.E., and Cowburn, R.P., 2009. Magnetization reversal in individual cobalt micro- and nanowires grown by focused-electron-beam-induced-deposition. *Nanotechnology*, 20(47), p.475704.
- Ferré, R., Ounadjela, K., George, J.M., Piraux, L., and Dubois, S., 1997. Magnetization processes in nickel and cobalt electrodeposited nanowires. *Physical Review B*, 56(21), pp.14066-14075.
- Fert, A., and Piraux, L., 1999. Magnetic nanowires. *Journal of Magnetism and Magnetic Materials*, 200, pp.338-358.
- Ganguly, A., Azzawi, S., Saha, S., King, J.A., Rowan-Robinson, R.M., Hindmarch, A.T., Sinha, J., Atkinson, D., and Barman, A., 2015. Tunable magnetization dynamics in interfacially modified Ni<sub>81</sub>Fe<sub>19</sub>/Pt bilayer thin film microstructures. *Scientific Reports*, 5, p.17596.
- Guo, Y., Qin, D.H., Ding, J.B., and Li, H.L., 2003. Annealing and morphology effects on the Fe<sub>0.39</sub>Co<sub>0.61</sub> nanowire arrays. *Applied Surface Science*, 218(1-4), pp.107-113.
- Helmenstine, A.M., 2020. *Table of Electrical Resistivity and Conductivity*. ThoughtCo, New York. Available from: <https://thoughtco.com/table-of-electrical-resistivity-conductivity-608499> [Last accessed on 2023 Nov 28].
- Heyderman, L.J., Solak, H.H., David, C., Atkinson, D., Cowburn, R.P., and Nolting, F., 2004. Arrays of nanoscale magnetic dots: Fabrication by x-ray interference lithography and characterization. *Applied Physics Letters*, 85(21), p.4989.
- Jian, Q., Josep, N., Maria, M., Anna, R., Juan, S.M., and Mamoun, M., 2005. Differences in the magnetic properties of Co, Fe, and Ni 250-300 nm wide nanowires electrodeposited in amorphous anodized alumina templates. *Chemistry of Materials*, 17, pp.1829-1834.
- Jiles, D., 1998. *Introduction to Magnetism and Magnetic Materials*. 2<sup>nd</sup> ed., Chapman and Hall/CRC, New York.
- Jin, C.G., Liu, W.F., Jia, C., Xiang, X.Q., Cai, W.L., Yao, L.Z., and Li, X.G., 2003. High-filling, large-area Ni nanowire arrays and the magnetic properties. *Journal of Crystal Growth*, 258, pp.337-341.
- Jordan Valley applications Staff., 2007. In: Lafford, T., Ryan, P., Wormington, M., Matney, K., Jacques, D., Bytheway, R., Bo, Q., Hofmann, F., and Trussell, R. (eds). *Bede X-Ray Applications Manual*. Jordan Valley Semiconductors Ltd., Texas.
- Jordan Valley applications staff., 2008. Lafford, T., Ryan, P., Wormington, M., Matney, K., Jacques, D., Bytheway, R., Bo, Q., Hofmann, F., and Trussell, R. (eds). *D1 Installation, Operation and Maintains Manual*. Jordan Valley Semiconductors Ltd., Texas.
- Kacel, T., Guittoum, A., Hemmous, M., Dirican, E., Öksüzoglu, R.M., Azizi, A., Laggoun, A., and Zergoug, M., 2018. Effect of thickness on the structural, microstructural, electrical and magnetic properties of Ni films elaborated by pulsed electrodeposition on Si substrate. *Surface Review and Letters*, 25(2), p.1850058.
- Kafil, M.R., Fernando, M.F.R., and Saibal, R., 2009. Magnetic properties of nickel nanowires: Effect of deposition temperature. *Journal of Applied Physics*, 105, p.083922.
- Kamrul, H.M., and Johurul, I.M., 2015. Effect of Substrate and Annealing on Electrical, Magnetic and Morphological Properties of Ni Thin Films. In: *International Conference on Materials, Electronics and Information Engineering, ICMEIE*.
- Karahan, I.H., Bakkalo, O.F., and Bedir, M., 2007. Giant magnetoresistance of electrodeposited Cu-Co-Ni alloy film. *Pramana-Journal of Physics*, 68, pp.83-90.
- Koohbor, M., Soltanian, S., Najafi, M., and Servati, P., 2012. Fabrication of CoZn alloy nanowire arrays: Significant improvement in magnetic properties by annealing process. *Materials Chemistry and Physics*, 131(3), pp.728-734.
- Kunz, A., Reiff, S.C., Priem, J.D., and Rentsch, E.W., 2010. Controlling Individual Domain Walls in Ferromagnetic Nanowires for Memory and Sensor Applications. In: *International Conference on Electromagnetics in Advanced Applications*, p.248.
- Lee, S.W., Jeong, M.C., Myoung, J.M., Chae, G.S., and Chung, I.J., 2007. Magnetic alignment of ZnO nanowires for optoelectronic device applications. *Applied Physics Letters*, 90(13), p.133115.
- Lihu, L., Haitao, L., Shenghua, F., Jianjun, G., Yaopeng, L., and Huiyuan, S., 2009. Fabrication and magnetic properties of Ni-Zn nanowire arrays. *Journal of Magnetism and Magnetic Materials*, 321, pp.3511-3514.
- Lodder, J.C., 2004. Methods for preparing patterned media for high-density recording. *Journal of Magnetism and Magnetic Materials*, 272-276.

- pp.1692-1697.
- Lupu, N., Lostun, M., and Chiriac, H., 2010. Surface magnetization processes in soft magnetic nanowires. *Journal of Applied Physics*, 107(9), p.09E315.
- Mark, W., 1993-2023. *Web Elements*. Available from: <https://www.webelements.com> [Last accessed on 2023 Nov 28].
- Maruyama, K., Namikawa, K., Konno, M., and Maruyama, H., 1997. Magnetization process of iron surface observed by transverse Kerr magnetometry. *Journal of Applied Physics*, 81(8), pp.5675-5677.
- Michelini, F., Ressler, L., Degauque, J., Baule's, P., Fert, A.R., Peyrade, J.P., and Bobo, J.F., 2002. Permalloy thin films on MgO (001): Epitaxial growth and physical properties. *Journal of Applied Physics*, 92, pp. 7337-7340.
- Murakami, M., and Birukawa, M., 2008. Sputtering gases and pressure effects on the microstructure, magnetic properties and recording performance of TbFeCo films. *Journal of Magnetism and Magnetic Materials*, 320(5), pp.608-611.
- Nasirpour, F., 2007. Template electrodeposition of magnetic nanowire arrays. *Transworld Research Network*, 661, p.37.
- Nazila, D., and Georges, J.K., 2007. Electroless fabrication of cobalt alloys nanowires within alumina template. *Journal of Nanomaterials*, 2007, p.46919.
- Oliveira, A.B., de Silva, G.L., Rezende, S.M., and Azevedo, A., 2010. Magnetization reversal in single ferromagnetic rectangular nanowires. *Journal of Physics: Conference Series*, 200(7), p.072023.
- Oliveira, A.B., Rezende, S.M., and Azevedo, A., 2008. Magnetization reversal in permalloy ferromagnetic nanowires investigated with magnetoresistance measurements. *Physical Review B*, 78(2), p.024423.
- Parlaka, U., Aköz, M.E., Tokdemir Öztürk, S., and Erkovanc, M., 2015. Thickness dependent magnetic properties of polycrystalline nickel thin films. *Acta Physica Polonica Series A*, 127(4), pp.995-997.
- Parratt, G.L., 1954. Surface studies of solids by total reflection of X-rays. *Physical Review*, 95, p.359.
- Peter, T.T., 2008. *Utilising Electrochemical Deposition for Micro Manufacturing*. Cardiff University, Whittles Publishing Ltd., Cardiff, UK.
- Philip, S., Javier, G.F., Stefan, M., Michael, Z., Tim, B., Victor, V.M., de la Prida, V.M., Detlef, G., and Kornelius, N., 2016. Statistical magnetometry on isolated NiCo nanowires and nanowire arrays: A comparative study. *Journal of Physics D: Applied Physics*, 49(14), p.145005.
- Pignard, S., Goglio, G., Radulescu, A., Piroux, L., Dubois, S., Declémy, A., and Duval, J.L., 2000. Study of the magnetization reversal in individual nickel nanowires. *Journal of Applied Physics*, 87(2), pp.824-829.
- Possin, E.G., 1970. A method for forming very small diameter wires. *Review of Scientific Instruments*, 41, pp.772-774.
- Qin, D.H., Wang, C.W., Sun, Q.Y., and Li, H.L., 2002. The effects of annealing on the structure and magnetic properties of CoNi patterned nanowire arrays. *Applied Physics A*, 74, pp.761-765.
- Rahman, I.Z., Razeed, K.M., Kamruzzaman, M., and Serantoni, M., 2004. Characterisation of electrodeposited nickel nanowires using NCA template. *Journal of Materials Processing Technology*, 153-154, pp.811-815.
- Ren, Y., Liu, Q.F., Li, S.L., Wang, J.B., and Han, X.H., 2009. The effect of structure on magnetic properties of Co nanowire arrays. *Journal of Magnetism and Magnetic Materials*, 321(3), pp.226-230.
- Rheem, Y., Yoo, B.Y., Beyermann, W.P., and Myung, N.V., 2007a. Magnetotransport studies of a single nickel nanowire. *Nanotechnology*, 18, p.015202.
- Rheem, Y., Yoo, B.Y., Beyermann, W.P., and Myung, N.V., 2007c. Magneto-transport studies of single ferromagnetic nanowire. *Physica Status Solidi (A)*, 204(12), pp.4004-4008.
- Rheem, Y., Yoo, B.Y., Beyermann, W.P., and Myung, N.V., 2007d. Electro-and magneto-transport properties of a single CoNi nanowire. *Nanotechnology*, 18(12), p.125204.
- Rheem, Y., Yoo, B.Y., Koo, B.K., Beyermann, W.P., and Myung, N.V., 2007b. Synthesis and magnetotransport studies of single nickel-rich NiFe nanowire. *Journal of Physics D: Applied Physics*, 40(23), p.7267.
- Rizwan, M.N., Bell, C., Kalyar, M.A., Makhdoom, A.R., Anwar-ul-Haq, M., and Gilory M., 2021. Structural, magnetic and electrical properties of nickel thin films deposited on Si (100) substrates by pulsed laser deposition. *Journal of Ovonic Research*, 17(3), pp.225-230.
- Sharma, S., Barman, A., Sharma, M., Shelford, L.R., Kruglyak, V.V., and Hicken, R.J., 2009. Structural and magnetic properties of electrodeposited cobalt nanowire arrays. *Solid State Communications*, 149(39), pp.1650-1653.
- Sultan, M.S., 2013. *Experimental and Micromagnetic Study of Magnetisation Behaviour in Isolated Ferromagnetic Nanowires*. PhD thesis submitted to Durham University.
- Sultan, M.S., 2017a. Angular dependence of switching behaviour in template released isolated NiFe nanowires. *Physics Letters A*, 381(46), pp.3896-3903.
- Sultan, M.S., 2017b. Surface morphology and magnetic properties of isolated cylindrical nickel nanowires. *American Journal of Nanosciences*, 3(3), pp.30-38.
- Sultan, M.S., 2017c. Electro- and magneto-transport behavior of template-released isolated ferromagnetic nanowires. *IEEE Transactions on Magnetics*, 53(12), pp.1-10.
- Sultan, M.S., 2018. Magnetic State of Template Released Isolated Nickel Nanowires. In: *International Conference on Pure and Applied Science*, Koya University, Kurdistan.
- Sultan, M.S., Das, B., Sen, P., Mandal, K., and Atkinson, D., 2012. Template released ferromagnetic nanowires: Morphology and magnetic properties. *Journal of Spintronics and Magnetic Nanomaterials*, 1(1), pp.113-121.
- Sun, L., and Chen, Q., 2009. Magnetic field effects on the formation and properties of nickel nanostructures. *European Journal of Inorganic Chemistry*, 2009, pp.435-440.
- Sun, L., Hao, Y., Chien, C.L., and Searson, P.C., 2005. Tuning the properties of magnetic nanowires. *IBM Journal of Research and Development*, 49(1), pp.79-102.
- Thompson, S.M., 2008. The discovery, development and future of GMR: The nobel prize 2007. *Journal of Physics D: Applied Physics*, 41, p.093001.
- Tian, F., Chen, J., Zhu, J., and Wei, D., 2008. Magnetism of thin polycrystalline nickel nanowires. *Journal of Applied Physics*, 103, p.013901.
- Tian, F., Zhu, J., Wei, D., and Shen, Y.T., 2005. Magnetic field assisting DC electrodeposition: General methods for high-performance Ni nanowire array fabrication. *The Journal of Physical Chemistry B*, 109, p.14852.
- Tokaç, M., Wang, M., Jaiswal, S., Rushforth, A.W., Gallagher, B.L., Atkinson, D., and Hindmarch, A.T., 2015. Interfacial contribution to thickness dependent in-plane anisotropic magnetoresistance. *AIP Advances*, 5(12), p.127108.
- Uehara, Y., and Ikeda, S., 2003. Dependence of magnetic properties on sputtering pressure for Fe-Al-O alloy films made by carousel-type sputtering. *Japanese Journal of Applied Physics*, 42(7A), pp.4297-4301.
- Vega, V., Bohnert, T., Martens, S., Waleczek, M., Montero-Moreno, J.M., Görlitz, D., Prida, V.M., and Nielsch, K., 2012. Tuning the magnetic anisotropy of Co-Ni nanowires: Comparison between single nanowires and nanowire arrays in hard-anodic aluminum oxide membranes. *Nanotechnology*, 23(46), p.465709.
- Wormington, M., Panaccione, C., Matney, K.M., and Bowen, D.K., 1999. Characterization of structures from X-ray scattering data using genetic algorithms. *Philosophical Transactions of the Royal Society of London-Series A*, 357, pp.2827-2848.
- Yoo, B., Rheem, Y., Beyermann, W.P., and Myung, N.V., 2006. Magnetically assembled 30 nm diameter nickel nanowire with ferromagnetic electrodes. *Nanotechnology*, 17(10), pp.2512-2517.

# An Ultra-wideband Low-power Low-noise Amplifier Linearized by Adjusted Derivative Superposition and Feedback Techniques

Mohsen Alirezapoori<sup>1</sup>, Mohsen Hayati<sup>1</sup>, Mohammad A. Imani<sup>1</sup>, Farzin Shama<sup>2</sup>, and Pouria Almasi<sup>3</sup>

<sup>1</sup>Department of Electrical Engineering, Faculty of Engineering, Razi University, Kermanshah, Iran

<sup>2</sup>Department of Electrical Engineering, Kermanshah Branch, Islamic Azad University, Kermanshah, Iran

<sup>3</sup>Department of Electrical Engineering, School of Electrical and Computer Engineering, College of Engineering, University of Tehran, Iran

**Abstract**—Ultra-wideband (UWB) applications require low-power and low-noise amplifiers (LNAs) that can operate over a wide frequency range. However, conventional LNAs often suffer from poor linearity and high-power consumption. This research work proposes a novel LNA design that uses the adjusted derivative superposition (DS) technique and feedback to improve the linearity and reduce the power consumption of UWB LNAs. The DS technique enhances the third-order intermodulation (IM3) cancellation by adjusting the bias currents of the transistors, whereas the feedback improves the stability and input matching of the LNA. The LNA is implemented using a degenerated common source topology in a 180 nm standard CMOS technology. The simulation results show that the LNA achieves a power gain of 10–12.2 dB, an input third-order intercept point (IIP3) of about 12 dBm, and a noise figure of less than 2.5 dB over the UWB frequency band of 3.1–10.6 GHz. The input reflection coefficient is less than -10 dB, and the power consumption is 11.6 mW with a 1.5 V power supply. The designed LNA offers a novel and innovative solution for UWB applications that significantly improve the performance and efficiency of UWB LNAs whereas reducing the cost and complexity of implementation.

**Index Terms**—Derivative superposition technique, Low-noise amplifier, Low power, Linearization.

## I. INTRODUCTION

One of the frequently used blocks in wireless receiver systems is low-noise amplifiers (LNAs) (Nakhlestani, Hakimi, and Movahhedi, 2012; Hu, et al., 2014; Kim, 2009). There are many technologies to implement the

LNAs, such as optical amplifiers (Chaqmaqchee, 2016; Yaba and Chaqmaqchi, 2022) or CMOS technology (Mohebi, et al., 2020). The most important characteristics of the LNAs include low noise, high linearity, and high-power gain. Ultra-wideband (UWB) applications are needed in electronic consumers, such as vehicular radars with high-accuracy operations (Rafati, Qasemi and Amiri, 2019; Kumaravel, et al., 2016; Zhang and Sánchez-Sinencio, 2010; Kazemi and Hayati, 2021; Wang, 2021; Roobert and Rani, 2020). Ultra-wideband systems are approved for use in 3.1–10.6 GHz bandwidth. An ultra-wideband LNA must benefit from appropriate wideband input matching as well as the low and flat noise figure. Power consumption is another major parameter for portable devices to extend the battery lifetime. To decrease the power consumption of the circuit, a simple way is to use a lower supply voltage. Lowering the voltage leads to achieving lower power-consuming circuits (Zhang and Sánchez-Sinencio, 2010; Rastegar and Jee-Youl, 2015; Eskandari, Ebrahimi and Sobhi, 2018; Sahoolizadeh, Jannesari and Dousti, 2018; Huang, et al., 2018). Resistive feedback topology in LNAs delivers suitable input matching, and high-power gain, as well as ultra-wideband operation (Singh, Arya and Komar, 2018; Saberkari, et al., 2016; Kim, et al., 2005). In Gm-boosting technique, the input signal is applied to the gate and source of MOSFET, simultaneously, which has been presented by (Kim and Kim, 2006). It increases the  $V_{GS}$  swing whereas it decreases the power consumption and provides a suitable noise figure. However, it is still challenging to achieve a lower than 2 dB noise figure (Hu, et al., 2014). The derivative superposition (DS) method (Aparin and Larson, 2005) is a specific expression of the feed-forward technique, where the main or auxiliary amplifiers are realized with transistors that are operating in distinct regions. In addition, the gate-induced noise of the weak-inversion transistor declines the noise figure. The DS technique complicates input matching (Ganesan, Sánchez-Sinencio, and Silva-Martinez, 2006; Guo and Li, 2013).

ARO-The Scientific Journal of Koya University  
Vol. VIII, No. 2 (2023), Article ID: ARO.11267. 9 pages  
Doi: 10.14500/aro.11267

Received: 20 July 2023; Accepted: 02 December 2023  
Regular research paper: Published: 23 December 2023

Corresponding author's e-mail: f.shama@aut.ac.ir

Copyright © 2023 Mohsen Alirezapoori, Mohsen Hayati, Mohammad A. Imani, Farzin Shama, and Pouria Almasi. Rahmah.

This is an open access article distributed under the Creative Commons Attribution License.



Post-distortion is another technique presented by (Kim, 2009). This method is noteworthy for improving the IP3 and easing input matching (Kim, et al., 2006; Sturm, Popuri and Xiang, 2016). However, the auxiliary amplifier in (Zhang, Fan and Sánchez-Sinencio, 2009) solves problems in canceling the non-linear distortion. Another post-distortion method is introduced for ultra-wideband low-noise amplifiers. Controlling the bias absorbs the second and third-order distortion current over a wide frequency band. This technique improves  $IIP2$  and  $IIP3$ ; however, it is still challenging to achieve a lower than 2 dB noise figure.

In (Chung, et al., 2015), authors have used the single ended input and differential input modes. According to the Capacitive Cross Coupled Dual-Gm-Enhancement architecture, the circuit might be reconfigured as distinct versions of single-ended or differential inputs (Chung, et al., 2015). In single-ended input mode, the noise figure is not sufficient and does not provide wide bandwidth, whereas, in differential input mode, the frequency varies from 1.4 dB to 11.4 dB, which is a good bandwidth. However, achieving flat gain and sufficient linearity is still challenging.

This manuscript is formed as follows: The next part describes the proposed ultra-wideband (UWB) LNA circuit design. In this part, the input matching has been discussed first. Then, gain calculations have been explained. Noise and linearity issues have been described within this part. The simulated results have been provided in the next part. Eventually, an overall conclusion has been presented.

## II. PROPOSED UWB LNA

The step-by-step design procedure for the presented LNA can be followed as:

- Step 1: The transistor size and the bias voltage for the main and the auxiliary transistors have been selected, based on the desired noise figure, gain, linearity, and power consumption of the LNA.
- Step 2: The input and the output matching networks for the LNA have been designed, using the source inductance ( $L_s$ ), the gate inductance ( $L_g$ ), the output inductance ( $L_o$ ), and the output capacitance ( $L_c$ ). The matching networks are used to match the input and the output impedance of the LNA to the source and the load impedance, which are usually  $50\ \text{ohms}$ . The matching networks also affect the noise figure, the gain, and the stability of the LNA. The matching networks are designed using the Smith chart and the lumped element model. The goal is to minimize the noise figure and maximize the gain and the stability of the LNA over the entire frequency band.
- Step 3: The feedback network for the LNA has been designed, using the feedback resistance ( $R_f$ ) and the output resistance ( $R_o$ ). The feedback network is used to provide negative feedback to the LNA, which improves the stability and the linearity of the LNA. The feedback network also affects the gain and the noise figure of the LNA. The feedback network can be designed using the feedback theory and the small-signal model of the device. The goal is to achieve a

trade-off between the stability, the linearity, and the gain of the LNA.

- Step 4: The performance of the LNA has been simulated and verified, using the pre-layout and post-layout simulation tool, respectively. The simulation and verification are used to check if the LNA meets the design specifications and the quality standards.

Between different linearization methods, derivative superposition (DS) and feedback techniques have been adjusted and applied to improve the linearity. This technique is called “derivative superposition” since it adds the third-order derivative of  $g_3$  of the drain current to cancel the distortion. Both transistors biased in weak and strong inversion regions are used, respectively. The auxiliary transistor produces a positive third-order derivative of  $g_3$  to cancel the negative  $g_3$  of the main MOSFET. Thus, the linearity is increased within a full dc performance limit. However, second-order interaction at high frequencies often limits the effect. The DS technique reduces major issues whereas it entangles input matching (Aparin and Larson, 2005). For designing the low-noise amplifier, a common-source amplifier is used for the input stage. The proposed UWB LNA has been illustrated in Fig. 1.

In common source, the gate-drain capacitor can be considered as a Miller feedback capacitor so that it causes the loading effect on input matching. In fact, in low frequencies, the gate-drain capacitor acts like negative feedback, and whereas most of the loads are inductive, an inductor in the source of the transistor is applied to reduce the input inductive loading effect. This method is called source degeneration. As mentioned before, positive a third-order derivative of  $g_3$  from the auxiliary transistor cancels the negative term created by the main transistor. The values of different parameters of the proposed LNA have been illustrated in Table I.

### A. Input Matching

In the design of low-noise amplifiers, common gate or common source is used for the input stage. In ultra-wideband applications, usually, the best choice is common gate which provides a wide bandwidth (Kumar and Kumar Deolia, 2019). As shown in Fig. 2, there is Miller’s effect in the common source, whereas in the common gate, Miller’s effect does not exist. Miller’s effect in the gate-drain capacitor makes the total capacitance connected to the gate increased so that the inverse relation between  $f_t$  and the capacitors connected to the gate causes a decrement in  $f_t$  of the transistor.

In source degeneration, an inductor in the gate of the transistor has been put to adjust input matching to reduce  $L_s$ . Thus, the input impedance seen in source resistance is:

$$Z_{in} = s(L_S + L_g) + \frac{1}{sC_{gs}} + \frac{L_S g_{ma}}{C_{gs}} \quad (1)$$

The inductor placed in the source of the transistor provides a real part in the input so that if this real part will be equated with source impedance, a proper input matching will be achieved. By neglecting the channel length modulation, total input impedance consists of two transfer zeros and a pole at the origin that is explained below:



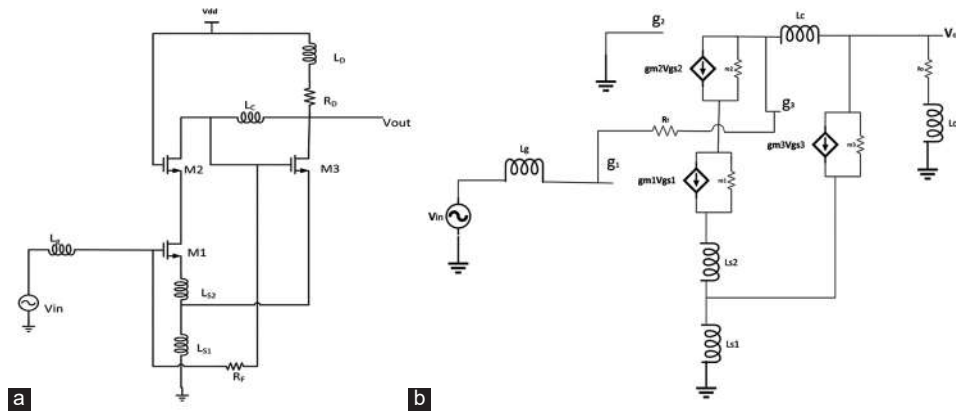


Fig. 1. A complete scheme and small signal equivalent circuit of proposed ultra-wideband (a) complete scheme (b) small signal equivalent circuit.

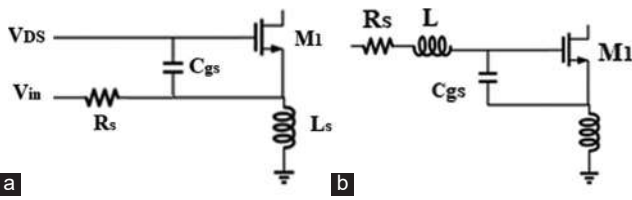


Fig. 2. The input stage (a) without the Miller effect (b) with the Miller effect.

$$Z_{in} = \frac{S^2 + S \frac{g_m L_s}{(L_s + L_g) C_{gs1}} + \frac{1}{(L_s + L_g) C_{gs1}}}{\frac{S}{(L_s + L_g)}} \quad (2)$$

As known, the real part is strongly dependent on variations of transistor length/width and inductor. This point causes sensitivity increment on the variation of the parameters that reduce input matching bandwidth. Finally, a new technique has been suggested to solve this problem. As shown in Fig. 3, any inductor value increment increases the real part. As seen in the figure, the most optimized inductor value has been chosen between 0.2 and 0.5 nH. Furthermore, frequency increment causes a reduction in the real part so that the gate-source capacitance can be controlled by  $L_g$  variations, but the imaginary part is increased by  $L_s$  and frequency increment; this makes the circuit inductive. However, the effect of the noisy gate-source capacitor increases by frequency increment so that the circuit treats like a capacitor at frequencies up to 10 GHz.  $\Omega$

At the frequency of 9 GHz, the real and imaginary parts are in the best condition, but whereas the good input matching should be  $<-10$  dB, this situation achieves 0.2 to 0.5 nH. The input matching is calculated as follows:

$$S_{11} = \frac{Z_{in} - Z_s}{Z_{in} + Z_s} = \frac{1 + s^2 C_{gs} (L_g + L_s) + s g_m L_s - s R_s C_{gs}}{1 + s^2 C_{gs} (L_g + L_s) + s g_m L_s + s R_s C_{gs}}$$

$$= \frac{1 + s^2 C_{gs} (L_g + L_s)}{1 + s(g_m L_s + R_s C_{gs}) + s^2 C_{gs} (L_g + L_s)} \quad (3)$$

Whereas the input matching has an inverse relation with the bandwidth, it does not provide enough bandwidth, so the quality factor to achieve input matching should be reduced in an ultra-

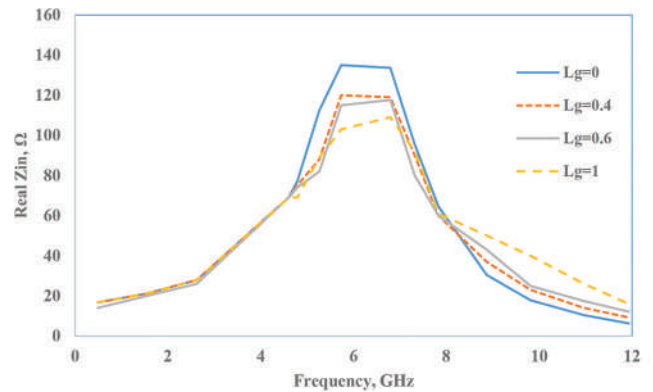


Fig. 3. The plot of real part variation for different  $L_g$ .

TABLE I  
VALUES OF DIFFERENT PARAMETERS OF THE PROPOSED LNA

Parameter	Value	Parameter	Value
$\left(\frac{w}{L}\right)_{M_1}$	$\frac{320 \mu\text{m}}{180 \text{nm}}$	$L_{s1}$	0.05 nH
$\left(\frac{w}{L}\right)_{M_2}$	$\frac{320 \mu\text{m}}{180 \text{nm}}$	$L_{s2}$	0.29 nH
$\left(\frac{w}{L}\right)_{M_3}$	$\frac{230 \text{nm}}{180 \text{nm}}$	$L_g$	0.48 nH
$V_{dd}$	1.5 V	$L_o$	5.04 nH
$R_o$	9.42 $\Omega$	$L_c$	1.19 nH
$r_{o1}$	25.62 $\Omega$	$r_{o2}$	34.47 $\Omega$
$R_f$	3.39 K $\Omega$	$g_{m1}$	0.018 A/v
$g_{m2}$	0.018 A/v	$R_s$	50 $\Omega$

wideband frequency. An  $R_f$  resistor can be used to improve input matching as seen in Fig. 4, although it reduces the gain.

$$S_{11} = \frac{Z_{in} - Z_s}{Z_{in} + Z_s} = \frac{1 + s^2 C_{gs} (L_g + L_s)}{1 + s \left( \frac{R_f g_m L_s}{g_m L_s + R_f C_{gs}} + R_s \right) + s^2 C_{gs} (L_g + L_s)}$$

$$= 20 \log \left( \left| \frac{3 f^2}{62500 f \times i - 3 f^2 + 1250} \right| \right) \quad (4)$$

Hence, the input matching is expressed as follows:

$$Q_{in} = \frac{1}{\omega CR} = \frac{1}{\omega C_{gs}(R_s + g_m L_s / C_{gs})}$$

$$= \frac{1}{\omega(R_s C_{gs} + g_m L_s)} = \frac{1}{2\omega R_s C_{gs}} \quad (5)$$

$$\omega_0^2 = \frac{1}{(L_s + L_g)C_{gs}} \cdot Q = \frac{1}{2R_s \omega_0 C_{gs}} \quad (6)$$

**B. Gain Analysis**

Whereas  $R_f$  is used in the feedback form to achieve full input matching, it reduces the gain. Furthermore, adding transistor  $M_2$  causes a limited increment in the gain, but as known,  $M_2$  noisy gate-drain capacitor reduces bandwidth by adding a dominant pole. Inductor  $L_o$  is used to improve the gain. The effect of  $L_o$  on the gain is shown in Fig. 5.

Calculating total gain with channel length modulation neglecting the  $M_1$  gate capacitor is:

$$G_{eff}(S) = \frac{I_{out}}{V_s} = \frac{g_m}{(R_s + Z_{in})sC_{gs}}$$

$$= \frac{g_m}{1 + s \left( \frac{R_f g_m L_s}{g_m L_s + R_f C_{gs}} + R_s \right) sC_{gs} + s^2 C_{gs}(L_g + L_s)} \quad (7)$$

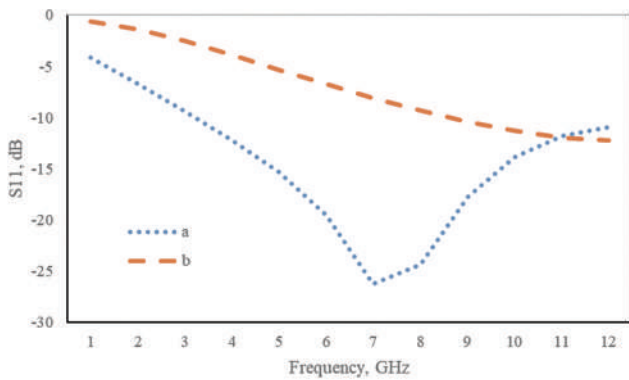


Fig. 4. The plot of  $S_{11}$  (a) with  $R_f$  (b) without  $R_f$ .

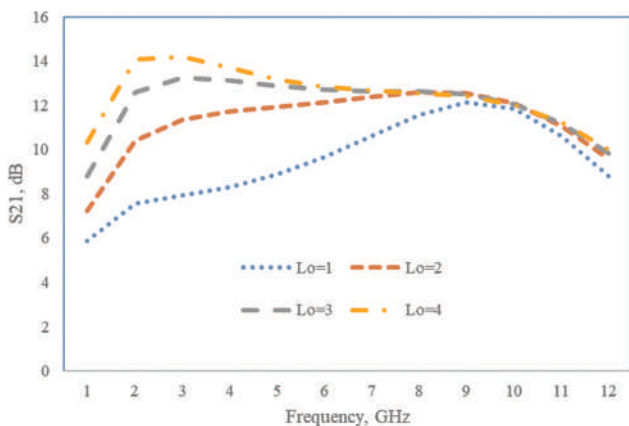


Fig. 5. The plot of  $S_{21}$  variation for different  $L_o$  (nH).

$$G = G_{eff} = \sqrt{\frac{g_m^2}{[1 - \omega^2 C_{gs}(L_g + L_s)]^2 + \omega^2 \left( \frac{R_f g_m L_s}{g_m L_s + R_f C_{gs}} + R_s \right)^2}} \quad (8)$$

$$S_{21} = 2G_{eff}R_L = \frac{2g_m R_D 20}{+s \left( \frac{R_f g_m L_s}{g_m L_s + R_f C_{gs}} + R_s \right)} \Big|_{\omega=\omega_0}$$

$$= 20 \log \left( \frac{1 - 2.76333 \times 10^{-29} f^2}{1 + (f(2.63 \times 10^{-14} i) - 2.76333 \times 10^{-29} f)} \right) \quad (9)$$

This pole that is created in high frequency must be shifted to the right (reducing capacitive effect), so the best choice for getting this pole away is using  $L_c$ . The effect of the variation of  $L_c$  on bandwidth is shown in Fig. 6.

The voltage gain of the LNA is easily obtained as follows:

$$G_m = \frac{I_{out}}{V_s} = \frac{r_{o2} - \frac{g_{m1}R_1(1+g_{m2}r_{o2})}{\frac{1}{r_{o1}} + \frac{1}{r_{o2}} + g_{m2}}}{r_{o2}(R_1 + R_2)} \quad (10)$$

If  $g_{m1}r_{o1} \gg 1$  then  $r_{o2} \ll r_{o1}(1 + g_{m2}r_{o2})$

$$G_m \cong \frac{g_m R_1}{(R_1 + R_s)} \quad (11)$$

$$R_{out} = [R_D \parallel (R_1 + R_s) \parallel (r_{o2} + (1 + g_{m2}r_{o2})r_{o1})] \quad (12)$$

$$A_V = G_m R_{out} \text{ (Aparin and Larson, 2005)} \quad (13)$$

**C. Noise Analysis**

In the proposed LNA, there are four different noise sources consisting of  $M_1$ ,  $M_2$ ,  $R_1$ , and  $R_D$ .  $M_3$  noise and gate noise current have been neglected whereas the transistor is biased in the triadic region (Fig. 7).

Noise of  $M_1$ :

$$\frac{V_1}{R_s} + \frac{V_1}{R_1} = 0 \rightarrow V_1 = 0 \quad (14)$$

$$I_{nM1} + \frac{V_2}{r_{o1}} + \frac{V_2}{r_{o2}} + g_{m2}V_2 = 0 \quad (15)$$

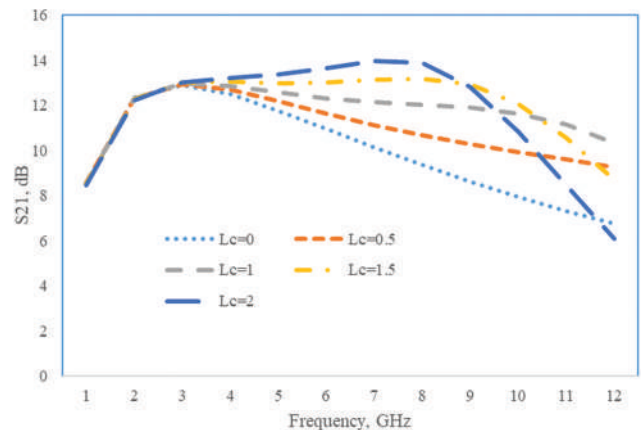


Fig. 6. The plot of  $S_{21}$  variation for different values of  $L_c$  (nH).

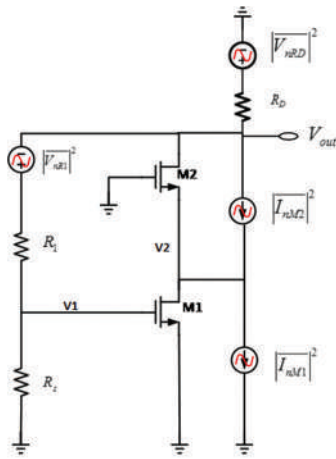


Fig. 7. Equivalent noisy circuit of the proposed low-noise amplifiers.

$$V_2 = \frac{-I_{nM1}}{\frac{1}{r_{o1}} + \frac{1}{r_{o2}} + g_{m2}} \quad (16)$$

$$I_{out} = g_{m2}V_2 + \frac{V_2}{r_{o2}} \quad (17)$$

$$I_{out} = -\frac{1+g_{m2}r_{o2}}{r_{o1}} \frac{I_{nM1}}{\frac{1}{r_{o1}} + \frac{1}{r_{o2}} + g_{m2}} \quad (18)$$

Considering  $g_{m2}r_{o2} \gg 1$  and  $r_{o2} \ll r_{o1}(1+g_{m2}r_{o2})$

$$I_{out} \cong \frac{r_{o2}}{r_{o1}} I_{nM1} \quad (19)$$

According to the above calculations, the noise of  $M_1$  is shown in equation (20):

$$F_{M1} = \left[ \frac{r_{o2}}{r_{o1}} \left( 1 + \frac{R_s}{R_1} \right) \right]^2 \frac{\gamma}{g_{m1}R_s} \quad (20)$$

The channel length modulation  $M_1$  must be reduced to reduce the input transistor noise effect in the output.

Noise of  $M_2$ :

$$g_{m2}V_2 + \frac{V_2}{r_{o1}} + \frac{V_2}{r_{o2}} + I_{nM2} = 0 \quad (21)$$

$$I_{out} = g_{m2}V_2 + I_{nM2} + \frac{V_2}{r_{o2}} \quad (22)$$

$$I_{out} = -\frac{V_2}{r_{o1}} \quad (23)$$

$$V_2 = \frac{-I_{nM2}}{\frac{1}{r_{o1}} + \frac{1}{r_{o2}} + g_{m2}} \quad (24)$$

$$I_{out} = \frac{I_{nM2}}{1 + \frac{r_{o1}}{r_{o2}} + g_{m2}r_{o1}} \quad (25)$$

$$-r_{o1}I_{out} = \frac{-I_{nM2}}{g_{m2} + \frac{1}{r_{o1}} + \frac{1}{r_{o2}}} \quad (26)$$

Considering  $g_{m2}r_{o2} \gg 1$ , noise of  $M_2$  is shown in equation (27):

$$F_{M2} = \frac{\gamma}{(g_{m1}g_{m2}r_{o1})^2} \left( 1 + \frac{R_s}{R_1} \right)^2 \quad (27)$$

Noise of  $R_1$

$$V_1 = \frac{R_s}{R_1 + R_2} V_{nR1} \quad (28)$$

$$g_{m1}V_1 + \frac{V_2}{r_{o1}} + \frac{V_2}{r_{o2}} + g_{m1}V_2 = 0 \quad (29)$$

$$I_{out} = -\frac{V_{nR1}}{R_1 + R_2} + g_{m2}V_2 + g_{m1}V_2 + \frac{V_2}{r_{o2}} \quad (30)$$

$$r_{o2}I_{out} = -\frac{r_{o2}}{R_1 + R_2} V_{nR1} + (g_{m2}r_{o2} + 1)V_2 \quad (31)$$

$$V_2 \left( \frac{1}{r_{o1}} + \frac{1}{r_{o2}} + g_{m2} \right) = -\frac{g_{m1}R_s}{R_1 + R_2} V_{nR1} \quad (32)$$

$$r_{o2}I_{out} = -\frac{r_{o2}}{R_1 + R_2} V_{nR1} - (1 + g_{m2}r_{o2})$$

$$\left( \frac{g_{m1}R_s}{\frac{1}{r_{o1}} + \frac{1}{r_{o2}} + g_{m2}} \frac{1}{R_s + R_1} \right) V_{nR1} \quad (33)$$

$$r_{o2}I_{out} = -\frac{V_{nR1}}{R_1 + R_2} V_{nR1} - \left( r_{o2} + \frac{g_{m1}R_s(1+g_{m2}r_{o2})}{\frac{1}{r_{o1}} + \frac{1}{r_{o2}} + g_{m2}} \right) V_{nR1} \quad (34)$$

$$I_{out} = \left( \frac{1-g_{m1}R_s}{R_1 + R_s} \right) V_{nR1} \quad (35)$$

If  $g_{m1}R_s \gg 1$  then:

$$F_{R1} = \frac{R_s}{R_1} \quad (36)$$

The noise of  $R_1$  motivates  $M_2$ . To reduce the effects of the output noise of  $R_1$ ,  $M_1$ , and  $M_2$ , channel length modulation must be reduced and increased, respectively. This is the same way to reduce the noise of  $M_1$  and  $M_2$  at the output. Hence, the noise of  $R_1$  reduces by  $M_1$  and  $M_2$  noise decrement spontaneously. Furthermore, the value of  $R_1$  must be bigger than the source resistance to decrease noise effects in output.

Noise of  $R_d$ :

The noise of  $R_d$  directly appears in the output, so the noise figure is:

$$F_{RD} = \frac{\left( 1 + \frac{R_s}{R_1} \right)^2}{g_{m1}^2 R_D R_s} \quad (37)$$

$$NF = \frac{f^{3.5}}{3.4 \times 10^3} + 1 \quad (38)$$

#### D. Linearity

Among different linearization techniques, the derivative superposition (DS) and feedback are chosen to improve linearity.

Whereas source degeneration has two different effects, the increment of linearity by  $(1+g\omega L_s)^{3/2}$  and decrement of it, originated from second-order interactions, a technique is explained to reduce second-order interactions in the rest. Furthermore, a feedback has been used to improve the linearity. For  $IIP3$  (Jafari and Yavari, 2015):

$$A_{IIP3, \text{amplifier}} = \sqrt{\frac{4}{3} \left| \frac{g_1}{g_3} \right|} \quad (\text{Jafari and Yavari, 2015}) \quad (39)$$

$$A_{IIP3, \text{close loop}} = \sqrt{\frac{4}{3} \left| \frac{b_1}{b_3} \right|} = \sqrt{\frac{4}{3} \frac{g_1}{g_3} \frac{(1+T_0)^3}{(1-\frac{2g_2^2}{g_1g_3} \frac{T_0}{1+T_0})}} \quad (40)$$

Negative feedback improves  $IIP3$  by  $(1+T_0)^{3/2}$ , where  $T_0=g_f\beta$  is the linear feedback factor.

If  $g_2 \neq 0$  then  $IIP3$  decreases, LNA non-linearity originates from two primary sources:

The other used technique to improve linearity is utilizing the auxiliary transistor in the triode region that is connected with the main transistor. As known, the non-linear relation of a transistor is defined as:

$$i_{ds} = g_1 v_{gs} + g_2 v_{gs}^2 + g_3 v_{gs}^3 \quad (41)$$

$$g_1 = \frac{\partial I_{DS}}{\partial V_{GS}} \quad g_2 = \frac{\partial^2 I_{DS}}{\partial V_{GS}^2} \quad g_3 = \frac{\partial^3 I_{DS}}{\partial V_{GS}^3} \quad (42)$$

Where  $g_1$ ,  $g_2$ , and  $g_3$  are the linear gain, the second-order, and the third-order non-linearity factors, respectively.

The  $g_1$  and  $g_2$  are both positive but  $g_3$  is negative, then the reduction of  $g_3$  is the goal of linearity improvement. To achieve this goal, an auxiliary transistor has been used in the triode region whereas creating positive  $g_3$ . By paralleling transistors, the third-order non-linear factor is reduced.

If  $g_{mb} \gg C_{gsb}$ , the non-linear effects of  $M_2$  can be neglected. The presented LNA linearity equivalent circuit is shown in Fig. 8.

The inductor in the source causes second-order interactions. To solve this problem, the source inductor was divided into two sections. This technique is called Modified Derivative Superposition. When there is no inductor in the source, the vector block diagram is Fig. 9:

However, by placing an inductor in the source, the block diagram is Fig. 10:

By breaking the inductor placed in the source of the transistor, a third-order non-linear factor angle can be easily chosen to neutralize the second-order interaction factor using  $L_{s2}$ .

The Volterra series has been applied to analyze linearity. First, some variables must be defined:

$$I_{m1} = g_{m1} V_{gs1} + g_{m2} V_{gs1}^2 + g_{m3} V_{gs1}^3 \quad (43)$$

Whereas transistor  $M_3$  is in the triode region, the first and second-order currents are neglected.

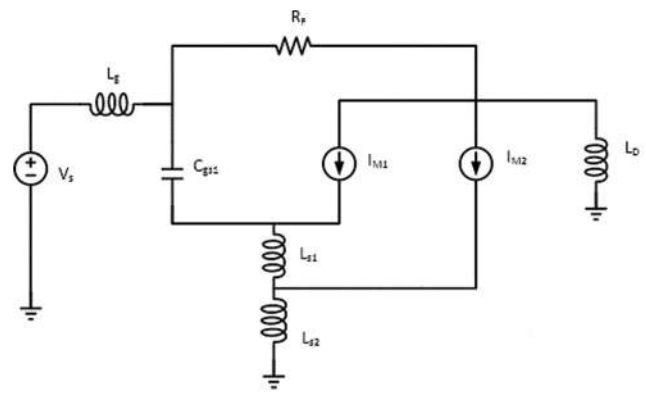


Fig. 8. The linearity equivalent circuit of the proposed low-noise amplifiers.

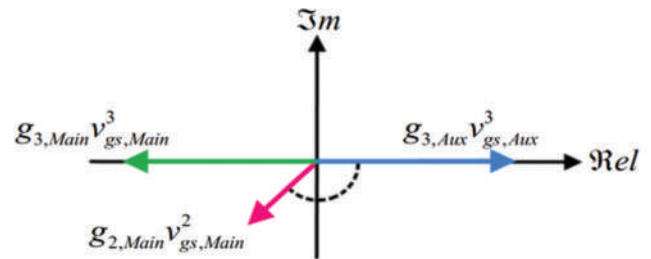


Fig. 9. The vector block diagram without the inductor in the source.

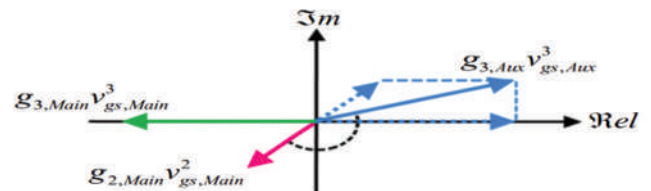


Fig. 10. The vector block diagram with the inductor in the source.

$$I_{out} = A_1 V_s + A_2 V_s^2 + A_3 V_s^3 \quad (44)$$

where:

$$A_1 = \frac{1 + [sR_f C_{gs1} - (R_f + sL_g)(g_{m1} + sR_f C_{gs1})] B_1}{R_f + s(L_g + L_D)} \quad (45)$$

$$A_2 = \frac{sR_f C_{gs1} B_2 - sL_D A_2}{R_f + sL_g} - (g_{ma1} B_2 + g_{ma2} B_1 B_1) - sR_f C_{gs1} B_2 \quad (46)$$

$$A_3 = \left( \frac{sR_f C_{gs1}}{R_f + sL_g} - g_{ma1} \right) B_3 - (2g_{ma2} B_1 B_2 + g_{ma3} B_1 B_1 B_1) - g_{mc3} C_1 C_1 C_1 \quad (47)$$

### III. SIMULATION AND POST-LAYOUT RESULTS

The presented UWB-LNA has been designed with a 180 nm standard CMOS technology model. The LNA has

been worked under a power supply of 1.5 V. The ADS and Cadence software were used for designing, simulations, pre-layout, and post-layout of the proposed LNA.

The design of the LNA aimed to achieve low-noise figure (NF) and high third-order intercept point (IIP3), which are important parameters for the performance and linearity of the amplifier. The simulated gain ( $S_{21}$ ) of the LNA across the frequency range of 3.1 to 10.6 GHz is depicted in Fig. 11 which varies from 10 dB to 12.2 dB at this frequency range. The primary goals in the design of the LNA were to improve NF and IIP3. The figure shows that the LNA provides a consistent and flat gain of about 10–12.2 dB over the entire bandwidth, which is desirable for wideband applications. The NF of the LNA, which measures the amount of noise added by the amplifier to the input signal, is presented in Fig. 12. The figure demonstrates that the LNA exhibits a very low NF of 1.5–2.5 dB within the operating frequency band, which indicates a high signal-to-noise ratio (SNR) at the output. The IIP3 of the LNA, which measures the ability of the amplifier to handle large input signals without distortion, is displayed in Fig. 13. The figure reveals that the LNA achieves a high IIP3 of about 10 dBm at the center frequency of 6.85 GHz, which implies a good linearity and dynamic range for the amplifier. The input reflection coefficient ( $S_{11}$ ) of the LNA, which measures the degree of impedance matching between

the amplifier and the source, is illustrated in Fig. 14. The figure indicates that the LNA has a low  $S_{11}$  of less than -10 dB over the entire frequency band, which means that most of the input power is delivered to the amplifier and the reflection is minimized. The stability factors (K and Delta) of the LNA, which measures the tendency of the amplifier to oscillate, are shown in Fig. 15. The figure confirms that the

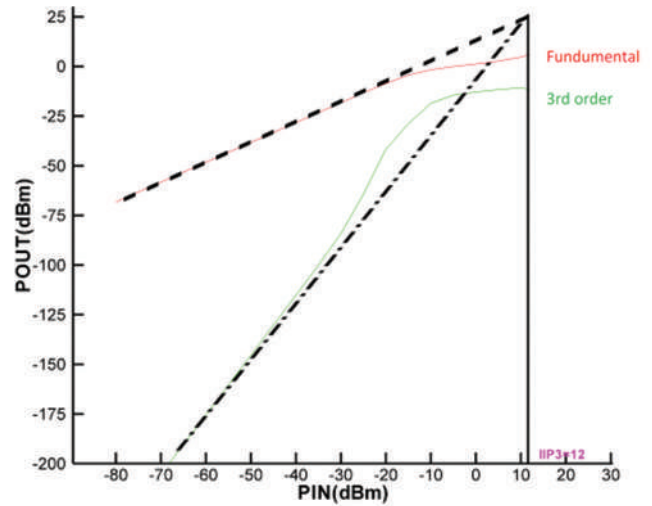


Fig. 13. The IIP3 of the proposed CMOS low-noise amplifiers.

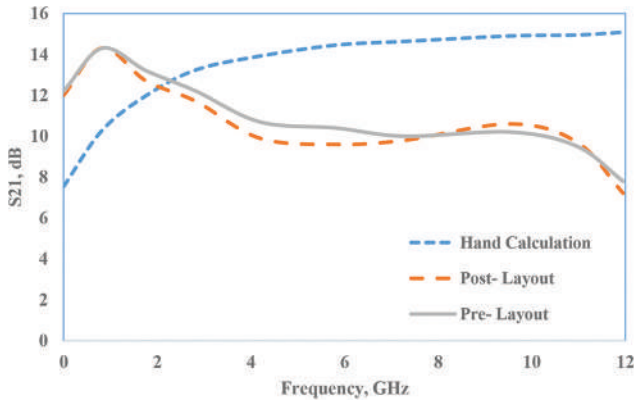


Fig. 11. The  $S_{21}$  parameter.

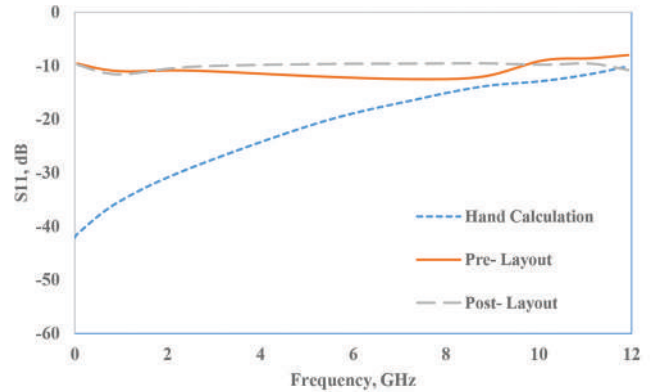


Fig. 14. The  $S_{11}$  parameter.

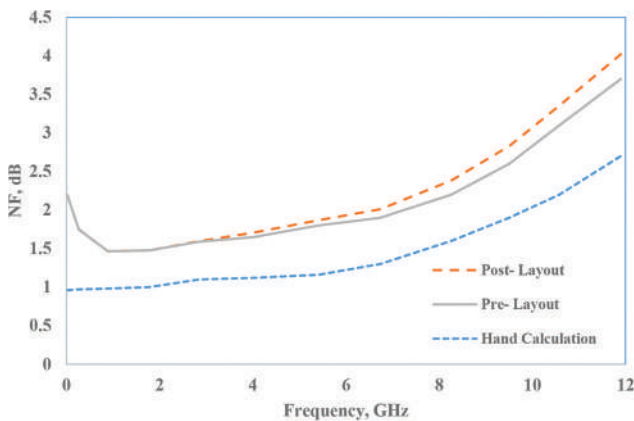


Fig. 12. The noise figure

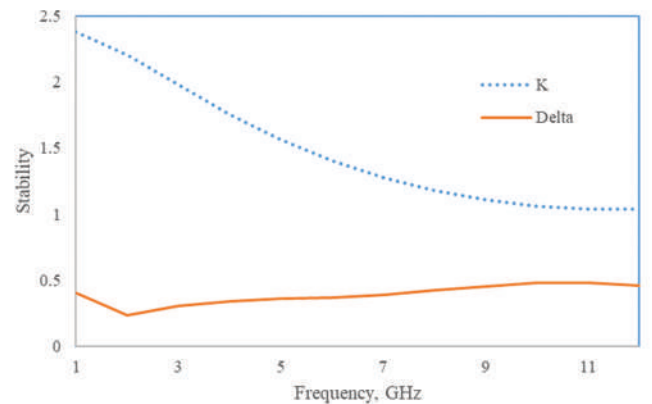


Fig. 15. The stability factor.

TABLE II  
PERFORMANCE COMPARISON OF THE PROPOSED LNA WITH SIMILAR WORKS

Ref.	$T_{ec}$ (nm)	Results type	$BW$ (GHz)	$S_{11}$ (dB)	$S_{21}$ (dB)	$NF_{min}$ (dB)	$P_{dc}$ (mw)	$IIP3$ (dBm)
Rafati, Qasemi and Amiri, 2019	130	Post-layout	3.1–10.6	<−10	12	1.8	11.2	13.8
Kumaravel, et al., 2016	180	Post-layout	2.44	−15	14.6	2.9	3.8	4.19
Rastegar and Jee-Youl, 2015	130	Pre-layout	3.1–10.6	NA	10.24	0.9	17.92	6.8
Eskandari, Ebrahimi and Sobhi, 2018	180	Post-layout	0.6–3.15	−13	20.2	3.1	6	−2.1
Sahoolizadeh, Jannesari and Dousti, 2018	130	Post-layout	3.1–4.8	<−10	15.8	1.7	11.28	8.32
Huang, et al., 2018	180	Post-layout	3–3.5	<−10	14.6	2.9	14.8	1.2–4.7
Kazemi and Hayati, 2021	180	Post-layout	3.1–10.6	−11	15.6–16.5	2.2–3	6.8	−4
Hayati, et al., 2020	180	Post-layout	3–10.6	<−10	12.79	2	11.56	−8
Kazemi and Hayati, 2021	180	Post-layout	1–8	−11	14.7–15.4	2.3–4.4	5.4	2.7
This work	180	Post-layout	3.1–10.6	<−10	10–12.2	1.5–2.5	11.6	12

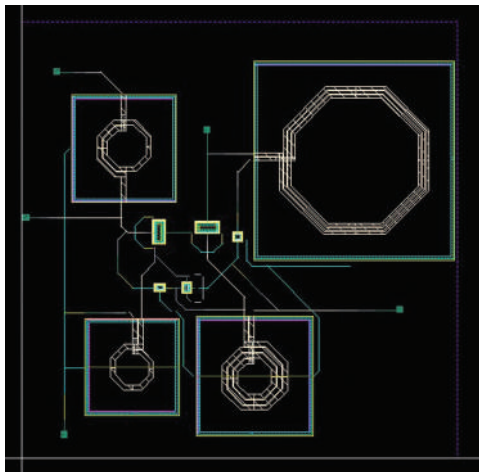


Fig. 16. The layout of the low-noise amplifiers.

LNA has a K value of greater than one for all frequencies, which ensures that the amplifier is unconditionally stable and does not generate any unwanted oscillations.

The characteristics of the proposed ultra-wideband LNA have been compared with similar published articles, as can be seen in Table II. Moreover, as shown in the physical layout in Fig. 16, the presented LNA occupies a 0.58 mm × 0.7 mm chip area.

A figure of merit (FOM) factor has been defined by (Zhang and Sánchez-Sinencio, 2010) to cover all important characteristics of an ultra-wideband LNA as below:

$$FOM = \frac{IIP3[mW] \times Gain[abs] \times BW[GHz]}{P_{dc}[mW] \times (F-1)} \quad (\text{Zhang and Sánchez-Sinencio, 2010}) \quad (48)$$

Where IIP3 is the maximum value for third-order input intercept point, gain has been considered as the maximum power gain in magnitude; BW covers the -3-dB bandwidth;  $P_{dc}$  has been set as the power dissipation; and (F-1) has been considered as the minimum excess noise figure in magnitude. FOM of this work is equal to 83.3.

#### IV. CONCLUSION

In this paper, both the adjusted derivative superposition technique and the feedback technique have been used to improve linearity since using the feedback technique alone

was not enough. An auxiliary transistor that is biased in the deep triode region was connected with the main transistor, generates positive  $g_3$ , and improves linearity. An inductor in the source is divided into two parts to change phase direction. In this LNA, very low-noise and low-power consumptions have been achieved. Furthermore, the gain, linearity, and input matching are adjusted in a suitable range.

#### REFERENCES

- Aparin, V., and Larson, L.E., 2005. Modified derivative superposition method for linearizing FET low-noise amplifiers. *IEEE Transactions on Microwave Theory and Techniques*, 53(2), pp.571-581.
- Chaqmaqchee, F.A.I., 2016. Optical design of dilute nitride quantum wells vertical cavity semiconductor optical amplifiers for communication systems. *Aro-The Scientific Journal of Koya University*, 4(1), pp.8-12.
- Chung, T., Lee, H., Jeong, D., Yoon, J., and Kim, B., 2015. A wideband CMOS noise-canceling low-noise amplifier with high linearity. *IEEE Microwave and Wireless Components Letters*, 25, pp.547-549.
- Eskandari, R., Ebrahimi, A., and Sobhi, J., 2018. A wideband noise cancelling balun LNA employing current reuse technique. *Microelectronics Journal*, 76, pp.1-7.
- Ganesan, S., Sánchez-Sinencio, E., and Silva-Martinez, J., 2006. A highly linear low noise amplifier. *IEEE Transactions on Microwave Theory and Techniques*, 54(12), pp.4079-4085.
- Guo, B., and Li, X., 2013. A 1.6-9.7 GHz CMOS LNA linearized by post distortion technique. *IEEE Microwave and Wireless Components Letters*, 23(11), pp.608-610.
- Hu, B., Yu, X.P., Lim, W.M., and Yeo, K.S., 2014. Analysis and design of ultra-wideband low-noise amplifier with input/output bandwidth optimization and single-ended/differential-input reconfigurability. *IEEE Transactions on Industrial Electronics*, 61(10), pp.5672-5680.
- Huang, D., Yang, X., Chen, H., Khan, M.I., and Lin, F., 2018. A 0.3-3.5 GHz active-feedback low-noise amplifier with linearization design for wideband receivers. *AEU-International Journal of Electronics and Communications*, 111, pp.192-198.
- Jafari, B.M., and Yavari, M., 2015. A UWB CMOS low-noise amplifier with noise reduction and linearity improvement techniques. *Microelectronics Journal*, 46(2), pp.198-206.
- Kazemi, A.H., and Hayati, M., 2021. Analysis and design of ultra-wideband low noise amplifier using complementary structure with series inductive peaking technique and shunt feedback. *International Journal of Circuit Theory and Applications*, 49(10), pp.3209-3229.
- Kazemi, A.H., and Hayati, M., 2021. Design and analysis of a flat gain and linear low noise amplifier using modified current reused structure with feedforward

- structure. *Integration*, 81, pp.123-136.
- Kim, C.W., Kang, M.S., Anh, P.T., Kim, H.T., and Lee, S.G., 2005. An ultra-wideband CMOS low noise amplifier for 3-5-GHz UWB system. *IEEE Journal of Solid-State Circuits*, 40(2), pp.544-547.
- Kim, N., Aparin, V., Barnett, K., and Persico, C., 2006. A cellular-band CDMA 0.25-/spl mu/m CMOS LNA linearized using active post-distortion. *IEEE Journal of Solid-State Circuits*, 41(7), pp.1530-1534.
- Kim, T., Im, D., and Kwon, K., 2020. 360- $\mu$ W 4.1-dB NF CMOS MedRadio receiver RF front-end with current-reuse Q-booster resistive feedback LNA for biomedical IoT applications. *International Journal of Circuit Theory and Applications*, 48(4), pp.502-511.
- Kim, T.S., and Kim, B.S., 2006. Post-linearization of cascode CMOS low noise amplifier using folded PMOS IMD sinker. *IEEE Microwave and Wireless Components Letters*, 16(4), pp.182-184.
- Kim, T.W., 2009. A common-gate amplifier with transconductance nonlinearity cancellation and its high-frequency analysis using the Volterra series. *IEEE Transactions on Microwave Theory and Techniques*, 57, pp.1461-1469.
- Kumar, M., and Kumar Deolia, V., 2019. Performance analysis of low power LNA using particle swarm optimization for wide band application. *AEU-International Journal of Electronics and Communication*, 111, p.152897.
- Kumaravel, S., Kukde, A., Venkataramani, B., and Raja, R., 2016. A high linearity and high gain folded cascode LNA for narrowband receiver applications. *Microelectronics Journal*, 58, pp.101-108.
- Mohebi, Z., Parandin, F., Shama, F., and Hazeri, A., 2020. Highly linear wide band low noise amplifiers: A literature review (2010-2018). *Microelectronics Journal*, 95, p.104673
- Nakhlestani, A., Hakimi, A., and Movahhedi, M., 2012. A novel configuration for UWB LNA suitable for low-power and low-voltage applications. *Microelectronics Journal*, 43(7), pp.444-451.
- Rafati, M., Qasemi, S.R., and Amiri, P., 2019. A 0.65 V, linearized cascade UWB LNA by application of modified derivative superposition technique in 130 nm CMOS technology. *Analog Integrated Circuits and Signal Processing*, 99, pp.693-706.
- Rastegar, H., and Ryu, J.Y., 2015. A broadband low noise amplifier with built-in linearizer in 0.13- $\mu$ m CMOS process. *Microelectronics Journal*, 46(8), pp.698-705.
- Roobert, A.A., and Rani, D.G.N., 2020. Design and analysis of 0.9 and 2.3-GHz concurrent dual-band CMOS LNA for mobile communication. *International Journal of Circuit Theory and Applications*, 48(1), pp.1-14.
- Saberkari, A., Kazemi, S., Shirmohammadi, V., and Yagoub, M.C.E., 2016. Gm-booster flat gain UWB low noise amplifier with active inductor-based input matching network. *Integration*, 52, pp.323-333.
- Sahoolizadeh, H., Jannesari, A., and Dousti, M., 2018. Noise suppression in a common-gate UWB LNA with an inductor resonating at the source node. *AEU-International Journal of Electronics and Communications*, 96, pp.144-153.
- Singh, V., Arya, S.K., and Kumar, M., 2018. Gm-booster current-reuse inductive-peaking common source LNA for 3.1-10.6 GHz UWB wireless applications in 32 nm CMOS. *Analog Integrated Circuits and Signal Processing*, 97, pp.351-363.
- Sturm, J., Popuri, S., and Xiang, X., 2016. A 65 nm CMOS resistive feedback noise canceling LNA with tunable bandpass from 4.6 to 5.8 GHz. *Analog Integrated Circuits and Signal Processing*, 87, pp.191-199.
- Wang, T.P., 2021. Design and analysis of simultaneous wideband input/output matching technique for ultra-wideband amplifier. *IEEE Access*, 9, pp.46800-46809.
- Yaba, H.I., and Chaqmaqchee, F.A., 2022. Design, modeling, and characterization of hot electron light emission and lasing in semiconductor heterostructure-VCSSOA with optical gain up to 36 dB. *Aro-The Scientific Journal of Koya University*, 10(1), pp.111-115.
- Zhang, H., and Sánchez-Sinencio, E., 2010. Linearization techniques for CMOS low noise amplifiers: A tutorial. *IEEE Transactions on Circuits and Systems I: Regular Papers*, 58(1), pp.22-36.
- Zhang, H., Fan, X., and Sánchez-Sinencio, E., 2009. A low-power, linearized, ultra-wideband LNA design technique. *IEEE Journal of Solid-State Circuits*, 44(2), pp.320-330.

## General Information

**ARO's Mission:** ARO seeks to publish those papers that are most influential in their fields or across fields and that will significantly advance scientific understanding. Selected papers should present novel and broadly important data, syntheses, or concepts. They should merit the recognition by the scientific community and general public provided by publication in ARO, beyond that provided by specialty journals.

We welcome submissions from all fields of natural science and technology, and from any source. We are committed to the prompt evaluation and publication of submitted papers. ARO is published biannually; selected papers are published online ahead of print.

### Submission

Manuscripts should be submitted by the correspondent authors of the manuscript via the on-line submission page. Regardless of the source of the word-processing tool, only electronic Word (.doc, .docx, .rtf) files can be submitted online. There is no page limit. Only online submissions are accepted to facilitate rapid publication and minimize administrative costs. Submissions by any other one but the authors will not be accepted. The submitting author takes responsibility for the paper during submission and peer review. If for some technical reason submission through the email is not possible, the author can contact [aro.journal@koyauniversity.org](mailto:aro.journal@koyauniversity.org) for support. Before submitting please check ARO's guide to authors thoroughly to avoid any delay in the review and publication process.

Authors are explicitly responsible for the language of their texts. Paper should be submitted in a well written in understandable English. Authors should not expect the editor or editorial board to rewrite their paper. Prior to submission, authors should have their paper proofread by a possible academic native speaker of English.

- Submit the Article with contact Information
- File name should be your article title
- Don't submit your article in multiple journal, we are taking only minimum time for review process. please don't waste our time
- Once the paper is accepted, it can't be withdrawn
- Please follow publication ethics and regulation
- Avoid plagiarism and copied material
- Strictly Follow ARO's template

### Terms of Submission

Papers must be submitted on the understanding that they have not been published elsewhere and are not currently under consideration by another journal or any other publisher. ARO accepts original articles with novel impacts only. Post conference papers are not accepted "as is", however, regular papers on the same topic but with a different title can be submitted. The new paper should contain significant improvements in terms of extended content, analysis, comparisons with popular methods, results, figures, comments, etc. Please do not forget that the publication of the same or similar material in ARO constitutes the grounds for filing of an (auto) plagiarism case.

The submitting author is responsible for ensuring that the article's publication has been approved by all the other co-authors. It is also the authors' responsibility to ensure that the articles emanating from a particular institution are submitted with the approval of the necessary institution. Only an acknowledgement from the editorial office officially establishes the date of receipt. Further correspondence and proofs will be sent to the author(s) before publication unless otherwise indicated. It is a condition of submission of a paper that the authors permit editing of the paper for readability. All enquiries concerning the publication of accepted papers should be addressed to [aro.journal@koyauniversity.org](mailto:aro.journal@koyauniversity.org).



## Peer Review

All manuscripts are subject to peer review and are expected to meet standards of academic excellence. Submissions will be considered by an editor and “if not rejected right away” by peer-reviewers, whose identities will remain anonymous to the authors.

## Guide to Author

We welcome submissions from all fields of science and from any source. We are committed to the prompt evaluation and publication of submitted papers. Selected papers are published online ahead of print. Authors are encouraged to read the instructions below before submitting their manuscripts. This section arranged into an overview speedy guidelines below and more detailed at the bottom section of this page

### Manuscript Preparation

Submitting your manuscript will be in two stages namely before final acceptance and after.

#### *Stage One:*

For the initial submission, the manuscript should be prepared electronically in Microsoft Word (.doc, .docx, .rtf) and PDF formats. Submit it through the online submission system after completing the registration. The Word file should be in a single-column format, double-spaced, with Times New Roman font, and 12-point font size. The authors' names and affiliations should be removed from the manuscript for the double-blind review process. Referencing and citation should follow the Harvard/ARO system. You can download the stage-one manuscript template by clicking [here](#).

#### *Stage Two:*

Once the manuscript is accepted, the production team of ARO Journal will prepare the camera-ready paper.

### Units of Measurement

Units of measurement should be presented simply and concisely using System International (SI) units.

### Title and Authorship Information

The following information should be included;

- Paper title.
- Full author names.
- Affiliation.
- Email addresses.

### Abstract

The manuscript should contain an abstract. The abstract should be self-contained and citation-free and should not exceed 250 words.

## **Introduction**

This section should be succinct, with no subheadings.

## **Materials and Methods**

This part should contain sufficient detail so that all procedures can be repeated. It can be divided into subsections if several methods are described.

## **Results and Discussion**

This section may each be divided by subheadings or may be combined.

## **Conclusions**

This should clearly explain the main conclusions of the work highlighting its importance and relevance.

## **Acknowledgements**

All acknowledgements (if any) should be included at the very end of the paper before the references and may include supporting grants, presentations, and so forth.

## **References**

References must be included in the manuscript and authors are responsible for the accuracy of references. Manuscripts without them will be returned. ARO is following Harvard System of Referencing. (Learn how to import and use Harvard Styling in your Microsoft Office by following this link:

<http://bibword.codeplex.com/releases/view/15852>)

## **Preparation of Figures**

Upon submission of an article, authors are supposed to include all figures and tables in the PDF file of the manuscript. Figures and tables should be embedded in the manuscript. Figures should be supplied in either vector art formats (Illustrator, EPS, WMF, FreeHand, CorelDraw, PowerPoint, Excel, etc.) or bitmap formats (Photoshop, TIFF, GIF, JPEG, etc.). Bitmap images should be of 300 dpi resolution at least unless the resolution is intentionally set to a lower level for scientific reasons. If a bitmap image has labels, the image and labels should be embedded in separate layers.

## **Preparation of Tables**

Tables should be cited consecutively in the text. Every table must have a descriptive title and if numerical measurements are given, the units should be included in the column heading. Vertical rules should not be used.

## **Copyright**

Open Access authors retain the copyrights of their papers, and all open access articles are distributed under the terms of the Creative Commons Attribution License, which permits unrestricted use, distribution and reproduction in any medium, provided that the original work is properly cited.

The use of general descriptive names, trade names, trademarks, and so forth in this publication, even if not specifically identified, does not imply that these names are not protected by the relevant laws and regulations.

While the advice and information in this journal are believed to be true and accurate on the date of its going to press, neither the authors, the editors, nor the publisher can accept any legal responsibility for any errors or omissions that may be made. The publisher makes no warranty, express or implied, with respect to the material contained herein.

## ARO Reviewer/Associate Editor Application Form

ARO is a scientific journal of Koya University (p-ISSN: 2410-9355, e-ISSN: 2307-549X) which aims to offer a novel contribution to the study of Science. The purpose of ARO is twofold: first, it will aim to become an ongoing forum for debate and discussion across the sciences and Engineering. We hope to advance our problem solving capacity and deepen our knowledge regarding a comprehensive range of collective actions. Second, ARO accepts the challenges brought about by multidisciplinary scientific areas and aspires to expand the community of academics who are able to learn from and help to produce advances in a variety of different disciplines.

The Journal is seeking reviewers who can provide constructive analysis of papers thus enhancing overall reputation of the Journal. If any expert is interested in participating of the review process, we highly encourage you to sign up as a reviewer for our Journal and help us improve our presence in domain of your expertise. Appropriate selection of reviewers who have expertise and interest in the domain relevant to each manuscript are essential elements that ensure a timely, productive peer review process. We require proficiency in English.

### How to apply

To apply for becoming a reviewer of ARO, please submit the application form by following the link:

<https://aro.koyauniversity.org/user/register>

To apply for becoming a member of the Editorial Board of ARO, please submit the application form by completing the [application form](#).

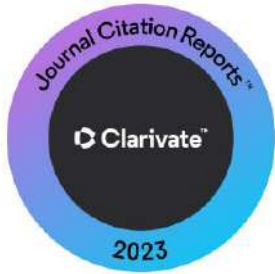
Both Associate Editor and Reviewers should specify their areas of research and expertise. Applicants must have a doctorate (or an equivalent degree), and if Master degree they need to have significant publishing experience. Please note that;

- You will need to write your full official name.
- Please provide an email which reflects your official name, such as nameOne.NameTwo@... , or your institute's official email.
- All data need to be written in English.

**Note:** For more information, kindly visit the following websites:

1. [aro.koyauniversity.org](http://aro.koyauniversity.org).
2. <http://libweb.anglia.ac.uk/referencing/harvard.htm>.
3. <http://bibword.codeplex.com/releases/view/15852>.







Koya University is a young University established in 2003 and it is located in the city of Koya (Koinsinjq), short distance to the East of regional capital city of Erbil (Arbil, Hewlêr) in Kurdistan Region of Iraq. It is on the foothills of beautiful High Mountain. Its campus has been carefully laid out to embrace the beautiful mountainous nature. The Koya University has a Faculty system which enhances the interactions between similar academic fields. Today, Koya University has four Faculties: Engineering, Science and Health, Humanities and Social Sciences and Education in addition to the School of Medicine, which all consist of twenty-five scientific departments in different fields, such as Petroleum Engineering, Geotechnical Engineering, Software Engineering, Physics, Chemistry, Clinical Psychology, Social Science, Medical Microbiology and Sport Education.

ARO-The Scientific Journal of Koya University is a biannual journal of original scientific research, global news, and commentary in the areas of Science and Technology. ARO is a Peer-reviewed Open Access journal with CC BY-NC-SA 4.0 license. It provides immediate, worldwide and barrier-free access to the full text of research articles without requiring a subscription to the journal, and has no article processing charge (APC). ARO Journal seeks to publish those papers that are most influential in their fields or across fields and that will significantly advance scientific understanding. ARO Journal is a member of ROAD and Crossref agencies and has got ESCI, DOAJ seal, SHERPA/RoMEO deposit policy, and LOCKSS archiving policy.

**ARO**

---

The Scientific Journal of Koya University

---

Koya University (KOU)  
University Park  
Danielle Mitterrand Boulevard  
Koya KOY45, Kurdistan Region - Iraq